East European Journal of Physics. 3. 269-279 (2026)
DOI:10.26565/2312-4334-2026-3-21 ISSN 2312-4334

THERMODYNAMIC AND EXERGY ANALYSIS OF AN AP1000-BASED STEAM TURBINE UNIT WITH OPTIMIZED CYCLE CONFIGURATION

Andrii V. Rusanov[1], Andrii O. Kostikov[1], Viktoriia O. Tarasova[1]*, Roman A. Rusanov[1], Marina O. Chugay[1], Maksym V. Lytvynenko[2]
[1]*A. Pidhornyi Institute of Power Machines and Systems of the NAS of Ukraine, Komunalnykiv 2/10 str., Kharkiv, 61046, Ukraine*
[2]*Institute of Fluid-Flow Machinery Polish Academy of Sciences, Fiszera 14 st. Gdańsk 80-231, Poland*
**Corresponding Author e-mail: vat523710@gmail.com*
Received May 22, 2026; revised July 30, 2026; accepted August 21, 2026

Given the strategic importance of Ukraine's nuclear energy sector modernization, the paper presents the results of the investigation into the development and analysis of the cycle configuration of a steam turbine unit (STU) intended for operation with the AP1000 nuclear reactor. The K-1000-60/1500-2 turbine unit was selected as the reference configuration. Based on this design, a new cycle configuration was proposed that includes a combined single-flow high- and intermediate-pressure turbine (HIPT), two low-pressure turbines (LPTs), a steam separator, and a two-stage steam reheating system. A thermodynamic and exergy analysis of the proposed STU configurations was performed to evaluate the influence of steam extraction pressures, regenerative feedwater heating parameters, and turbine stage distribution on the cycle performance. Numerical simulations and flow-path calculations of the turbine sections were performed using modern gas-dynamic design methods. The results show that the optimal selection of steam extraction parameters and intermediate reheating conditions significantly improves the cycle efficiency. The maximum internal efficiency of the STU cycle reached 38.96 %. Exergy analysis demonstrated that the largest exergy destruction occurs in the low-pressure turbine section, while both investigated configurations exhibit high exergy efficiency. A comparative analysis of the turbine stage configurations and the axial dimensions of the turbine flow parts was also conducted. The developed approaches can be applied in the design and optimization of next-generation steam turbine units for nuclear power plants.
Keywords: *Nuclear energy; AP1000; Steam turbine unit; Thermodynamic analysis; Exergy analysis; Regenerative feedwater heating; Nuclear power plant*

1. INTRODUCTION

Nuclear energy is a fundamental component of Ukraine's energy security and one of the most important factors in long-term decarbonization, particularly amid wartime destruction and the loss of a significant share of heat and power generation capacity. Since 2022, the demand for reliable baseload electricity sources in Ukraine has increased substantially, making Generation III+ nuclear units a priority direction for development.

The AP1000 nuclear reactor, developed by Westinghouse Electric Company, is one of the most advanced pressurized water reactors (PWRs), with a thermal output of 3415 MW and an electrical output of 1117–1200 MW [1–3]. It is characterized by passive safety systems and high operational performance. Therefore, the AP1000 appears to be promising for deployment at Ukrainian nuclear power plants (NPPs), including the Khmelnitsky NPP [4].

However, integrating the AP1000 requires developing an optimized cycle configuration for the steam turbine unit (STU) that fully matches the parameters of the saturated steam produced in the steam generator. Existing cycle configurations designed for VVER-1000 units do not fully utilize the thermodynamic potential of the AP1000, necessitating the modeling and implementation of new engineering solutions [5–7].

Therefore, the development and analysis of an STU cycle configuration for the AP1000, aimed at improving the efficiency through the optimal distribution of extraction pressures, is a relevant and practically significant research task.

2. LITERATURE REVIEW ON THE AP1000

The current scientific literature on Generation III+ reactors focuses on the AP1000 model, which is one of the most widely used in the global nuclear energy industry. Several key sources can be identified to cover the design, characteristics, and operation of AP1000 reactors. Papers [2–3] show the basic technical characteristics of the reactor, including a thermal power of 3415 MW, an electrical power of over 1100 MW, core parameters, and a detailed description of the passive safety systems. This material is fundamental, as it contains the official nominal parameters, a diagram of the steam generators, a description of the primary cooling system, as well as safety systems.

The report [8] provides an independent expert assessment of the project. It focuses on the reliability of the safety systems, the behavior of the core under emergency conditions, and the design's compliance with international requirements. The document provides a detailed overview of the reactor plant, steam generators, and the emergency heat exchange system, making it one of the most valuable sources for analyzing the AP1000 engineering design.

Cite as: A.V. Rusanov, A.O. Kostikov, V.O. Tarasova, R.A. Rusanov, M.O. Chugay, M.V. Lytvynenko, East Eur. J. Phys. 3, 269 (2026), https://doi.org/10.26565/2312-4334-2026-3-21

The research paper [9] reveals key features of the commercial operation of the AP1000 reactor at the Sanmen NPP in China. Such key issues as the reliability of passive safety systems, scalability, and verification and validation experiments needed to improve the safety of the AP1000, are discussed in the paper.

A thermal and hydraulic analysis of the AP1000 reactor vessel under nominal operating conditions using a 3D CFD model is presented in paper [10]. The AP1000 Advanced Nuclear Reactor (NR) stands out among other PWRs in terms of generation technology due to its innovative features of reliability, modularity and, most importantly, passive safety systems.

In the study [11], an assessment of the possibilities of deploying AP1000 reactors at existing and new sites was carried out. The document contains technical and economic aspects, including a comparison of implementation options, impact on energy infrastructure, and cost parameters. This source is important in the context of strategic planning for the introduction of AP1000 into state power systems.

Also, the leading areas of research are neutron-physical analysis, core safety indicators and the operation of reactivity control systems, described in papers [12 – 15]. So, the paper [12] shows the influence of fuel temperature, moderator density, boron concentration and control rod condition for AP1000 reactor on the safety parameters.

Thus, the analyzed literature demonstrates that AP1000 is mainly studied in three areas:

– design and passive safety systems [1 – 3, 5, 9, 10];

– neutron and thermal hydraulic analysis of the reactor [12 – 15];

– economic and strategic aspects of implementation [11].

These sources form a complete picture of the capabilities of the AP1000, its design features, safety and implementation prospects.

In contrast to the significant number of papers on design review and neutron-physical analysis, the literature that considers the cycle configuration of a steam turbine plant of a nuclear power plant with the AP1000 nuclear reactor is much less common.

In [16], a system that is designed for reliable and efficient storage and recovery of thermal energy from the steam system of a nuclear power plant (NPP) to ensure flexible electricity production using an economical and scalable design is presented. In [17], the role of energy storage technologies in their integration into NPPs is assessed.

In papers [18 – 20], combined cycles are proposed to increase the efficiency of NPP power units, in particular with gas turbines and hydrogen combustors.

All these measures [16 – 20] significantly increase the output power and efficiency of NPPs. But they are also associated with special safety conditions and require additional research before their implementation into existing NPPs.

Therefore, the problem of increasing the efficiency of a steam turbine unit through thermodynamic analysis and exergy optimization of the cycle, as well as improving the steam turbine flow path using 3D design and modeling [21 – 22] remains relevant.

3. AIM AND OBJECTIVES OF THE STUDY

The aim of the paper is to develop and analyze the cycle configuration of a steam turbine unit intended for operation with the AP1000 nuclear reactor, as well as to determine optimal steam extraction parameters and turbine stage configurations that ensure high thermodynamic and exergy efficiency of the cycle.

To achieve this goal, the following objectives were formulated:

1 To analyze existing condensing steam turbine units of nuclear power plants and select a baseline turbine configuration suitable for adaptation to operation with the AP1000 reactor, taking into account the parameters of saturated steam.

2 To develop a new cycle configuration of the steam turbine unit with a combined high- and intermediate-pressure turbine, regenerative feedwater heating system, steam separator, and intermediate steam reheating.

3 To perform thermodynamic modeling of the AP1000-based steam turbine unit and determine optimal steam extraction pressures that provide maximum cycle efficiency.

4 To develop and compare several options of the turbine flow part configuration with different numbers of turbine stages and steam extraction arrangements.

5 To carry out an exergy analysis of the proposed cycle configuration, including determination of exergy destruction and exergy efficiency of the main elements of the steam turbine unit using the fuel–product approach.

6 To analyze the geometric characteristics of the turbine flow parts and evaluate the influence of turbine stage distribution on the axial dimensions of the steam turbine unit.

4. DEVELOPMENT OF THE CYCLE CONFIGURATION OF AN AP1000-BASED STEAM TURBINE UNIT

4.1. OVERVIEW OF CONDENSING-TYPE STEAM TURBINES OF NUCLEAR POWER PLANT UNITS

Several models of low-speed condensing-type steam turbines K-1000-60/1500, developed by the Joint-Stock Company "Ukrainian Power Machines", are implemented on nuclear power plant units with VVER-1000 reactors. The

K-1000-60/1500 turbine has several modifications. The K-1000-60/1500-1 has a capacity of 1030 MW. The turbine unit is 57.4 m long (50.7 m without the generator), contains one high-pressure turbine (HPT), one intermediate-pressure turbine (IPT) and three low-pressure turbines (LPT). It is equipped with side single-flow condensers. A turbine of the STU K-1000-60/1500-2 has a reduced length of up to 52.2 m. The total mass is reduced by 350 tons. For the cycle configuration developing, the K-1000-60/1500-2 steam turbine unit was taken as a basis [6, 7]. This turbine unit is designed for a nuclear power plant with an electric power of 1200 MW at 3000 rpm. K-1000-60/1500-2 steam turbine unit is intended to operate in a monoblock with an AP1000 PWR with a thermal power of 3400 MW on saturated steam.

4.2. DEVELOPMENT OF A CYCLE CONFIGURATION OF A STU WITH AP1000 REACTOR

A new STU cycle configuration with a combined HIPT is proposed. Unlike the K-1000-60/1500-2 STU, the new configuration includes a single-flow HIPT, two LPTs, and two condensers instead of the three LPTs and three condensers used in the K-1000-60/1500-2 (Fig. 1).

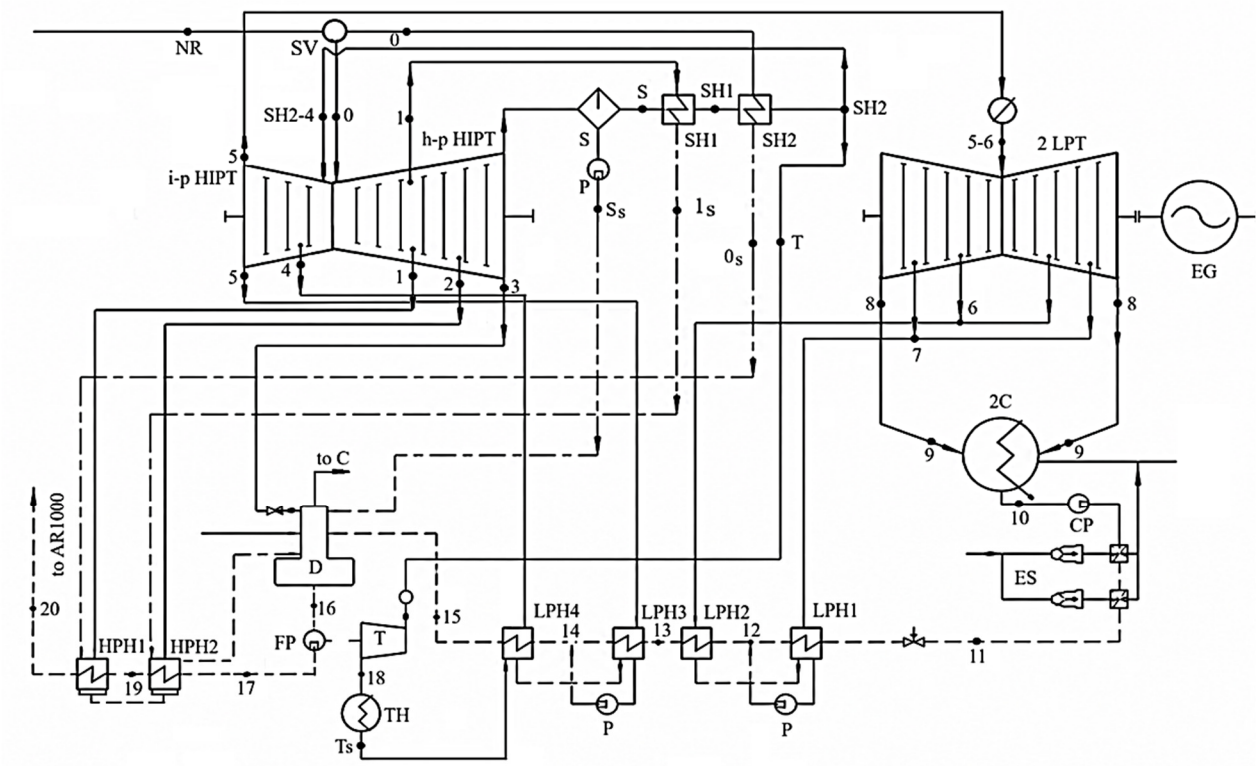

Figure 1. Cycle configuration of a steam turbine unit with AP1000
P– pump; SV – steam stop valve; ES – ejector system; T – turbine; TH – heater; EG – electric generator

The scheme includes a single separation and two-stage reheating of steam. In this case, fresh steam is supplied to the high-pressure part of the HIPT (h-p HIPT). After reaching the permissible humidity, the steam is directed to the external separator (S), where it is dried. After drying and superheating in the superheaters (SHs), the steam enters the intermediate-pressure turbine part (i-p HIPT), and then is directed towards two LPTs. Next, the exhaust steam is directed to the two condensers (C), and then the condensate – to the regeneration system. In the second SH, the steam is reheated by a fresh steam. The main condensate is pumped from the C to the deaerator (D) by condensate pumps (CP). The feed water from the deaerator through the high-pressure heater (HPH) to the steam generator is supplied by a feed pump (FP) with an electric drive.

Pressure losses during steam throttling in the turbine control elements are assumed to be 5%. Pressure losses of 5% are also taken into account in the steam lines leading to the HPHs and low-pressure heaters (LPH).

The initial data for calculating the cycle configuration of a steam turbine unit with the AP1000 reactor:

Steam mass flow rate per turbine – 1878 kg/s;

Absolute fresh steam pressure – 5.877 MPa;

Fresh steam temperature – 274.3 °C;

Absolute condenser pressure – 5 kPa;

Feed water temperature – 226.8 °C.

The distribution pressure at the outlet of the high-pressure part of HIPT is $P_3 = 1.1331$ MPa, and the saturation temperature at this pressure is $T_3 = 185.4$°C. Then the temperatures of the superheated steam after superheater SH1 and SH2 are determined as follows:

$$\Delta T_{\mathrm{SH2}} = T_0 - T_{\mathrm{SH2}}. \tag{1}$$

The saturation temperature of the heating steam and the pressure of the first extraction are:

$$T_{\mathrm{s,SH1}} = T_1 = T_{\mathrm{SH1}} + \Delta T_{\mathrm{SH1}};\ P_1 = f\left(T_{\mathrm{s,SH1}}\right). \tag{2}$$

The pressure of the first extraction is also the pressure of the heating steam in superheater SH1.

To determine the enthalpy at the end of the theoretical and actual expansion processes, it is necessary to determine the entropy at the inlet to the HIPT or LPT section as:

$$s_j = f\left(P_j, h_j\right), \tag{3}$$

where j is the extraction number.

The enthalpy at the end of the theoretical process can be found from:

$$h_{jt} = f\left(P_j, s_{j-1}\right). \tag{4}$$

The enthalpy at the end of the actual steam expansion process in the cylinder can be determined from:

$$h_j = h_{j-1} - \eta_{0i}\left(h_{j-1} - h_{jt}\right). \tag{5}$$

Further, the parameters of the steam expansion process in the HIPT and LPT are calculated using Eqs. (3), (4), and (5).

The enthalpies of the main condensate after the condenser, the LPH, HPH, and the feedwater are determined as functions:

$$T_{sj} = f\left(P_j\right); h_{sj} = f\left(T_{sj}\right); t_{fw} = t_{sj} - \theta; h_{fw} = f\left(P_{fw}, t_{fw}\right). \tag{6}$$

where t_{sj}– saturation temperature at the extraction pressure; h_{sj} – enthalpy of saturated water; t_{fw}– feedwater temperature after the regenerative heater; θ – feedwater terminal temperature difference relative to the saturation temperature of the heating steam; h_{fw}– feedwater enthalpy.

Further calculations of the cycle configuration were carried out to determine the steam extraction parameters in the regenerative system that ensure the maximum efficiency of the K-1000-60/1500-2 steam turbine unit. It should be noted that, during the variation of steam extraction parameters, the division of turbine sections into stages was not taken into account.

The steam extraction pressures were varied within the following ranges: $P_1 = 2.4$–3.5 MPa; $P_2 = 1.3$–1.9 MPa; $P_4 = 0.45$–0.8 MPa.

The minimum pressure value $P_1 = 2.4$ MPa was selected based on the condition that $T_{\mathrm{s,SH1}}$ should not be lower than $206\,^{\circ}\mathrm{C}$ in order to ensure a uniform distribution of heating between SH1 and SH2.

The temperatures T_{SH2} and T_{SH1}were determined using Eqs. (1) and (2) at:

$$\Delta T_{\mathrm{SH2}} = 10^{\circ}\mathrm{C}; \Delta T_{\mathrm{SH1}} = 15^{\circ}\mathrm{C}.$$

The extraction pressures of the LPT were specified as follows:

$$P_6 = 0.075 \text{ MPa}; P_7 = 0.015 \text{ MPa}.$$

We obtained the dependence of STU efficiency on steam extraction pressure in the HIPT (Fig. 2).

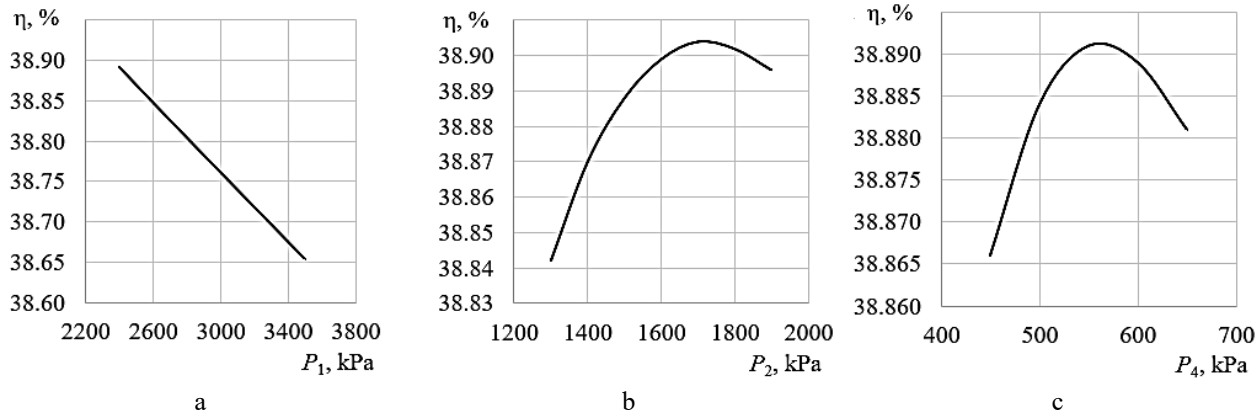

a b c

Figure 2. Dependence of the STU efficiency on steam extraction pressures in the HIPT: a –P_1 at $P_2 = 1.7$ MPa and $P_4 = 0.55$ MPa; b – P_2 at $P_1 = 2.4$ MPa and $P_4 = 0.55$ MPa; c – P_4 at $P_1 = 2.4$ MPa and $P_2 = 1.7$ MPa

Figure 2 shows that the highest efficiency values are observed at:

$$P_1 = 2.4 \text{ MPa}; P_2 = 1.7 \text{ MPa}; P_4 = 0.55 \text{ MPa}.$$

For these parameters corresponding to the maximum efficiency, an analysis of the LPT extraction parameters was carried out within the ranges presented on Fig. 3.

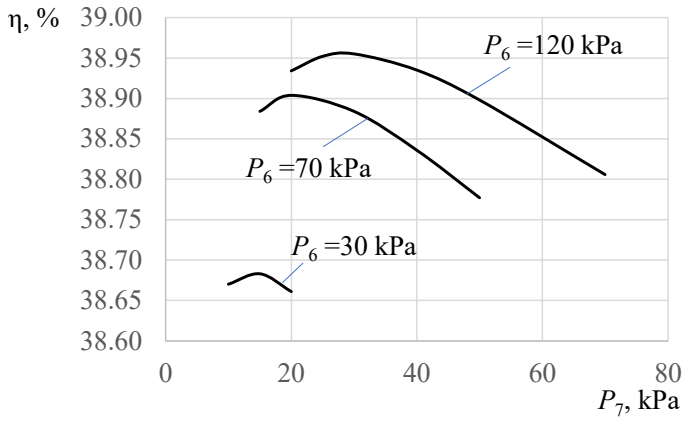

Figure 3. Dependence of the STU efficiency on P_6 and P_7

The results demonstrate that the maximum efficiency values are achieved at: $P_6 = 120$ kPa, $P_7 = 30$ kPa; $P_6 = 70$ kPa, $P_7 = 20$ kPa; $P_6 = 30$ kPa, $P_7 = 15$ kPa.

4.3 DETERMINATION OF OPTIMAL STEAM EXTRACTION PARAMETERS FOR THE AP1000-BASED STEAM TURBINE UNIT CONSIDERING THE NUMBER OF TURBINE STAGES

Several AP1000-based STU options with different numbers of turbine stages were considered. The calculations used modern numerical methods for gas-dynamic analysis and flow-part design of steam turbines [21–22].

Two options are given as an example.

In the first option, the number of stages in the high-pressure turbine part (HIPT, before the separator) was set to 6. In the first option, the number of stages in the high-pressure turbine part (HIPT, before the separator) was selected as 6 stages. The intermediate-pressure turbine part (HIPT, after the separator) had 3 stages. The number of cylinders/steam flow parts was 1. The LPT had 5 stages, and the number of cylinders/steam flow parts was 2.

In the second option, the high-pressure turbine had 4 stages. The intermediate-pressure turbine had 2 stages. The LPT had 6 stages.

Tables 1 and 2 present the steam pressures after each stage for both options.

The energy characteristics of the first option are as follows: the heat transferred to the steam in the steam generator is $Q_h = 3416$ MW; the gross electric power output is $N_e = 1330$ MW; and the internal efficiency of the STU cycle is $\eta = 38.93$ %.

Table 1. Steam pressure between turbine stages and steam mass flow rate, Option 1

Steam extraction number	Axial clearance between stages No. – No	Pressure in the axial clearance, MPa	Steam mass flow rate in the extraction, kg/s
High-pressure turbine part of the HIPT – 6 stages			
	1-2	4.214	
	2-3	3.182	
1	3-4	2.405	131
2	4-5	1.819	84
	5-6	1.377	
3	Steam exhaust	1.133	74
Intermediate-pressure turbine part of the HIPT – 3 stages			
	1-2	0.760	
4	2-3	0.548	35
5	Steam exhaust	0.372	59
2 LPT– 5 stages			
6	1-2	0.166	89
	2-3	0.075	
7	3-4	0.034	65
	4-5	0.015	

Table 2. Steam pressure between turbine stages and steam mass flow rate, Option 2

Steam extraction number	Axial clearance between stages No. – No	Pressure in the axial clearance, MPa	Steam mass flow rate in the extraction, kg/s
High-pressure turbine part of the HIPT – 4 stages			
	1-2	3.578	
1	2-3	2.296	172
2	3-4	1.477	37
3	Steam exhaust	1.133	68
Intermediate-pressure turbine part of the HIPT – 2 stages			
4	1-2	0.586	41
5	Steam exhaust	0.372	83
2 LPT– 6 stages			
	1-2	0.207	
6	2-3	0.113	70
	3-4	0.060	
7	4-5	0.031	63
	5-6	0.015	

The energy characteristics of the second option are as follows: $Q_h = 3416$ MW; $N_e = 1331$ MW; and the internal efficiency of the STU cycle is $\eta = 38.96$ %.

As can be seen, both options demonstrate high efficiency. To finalize the cycle configuration, an exergy analysis of the proposed STU configuration options is necessary.

5. EXERGY ANALYSIS OF THE STU CYCLE CONFIGURATION FOR OPERATION WITH THE AP1000 NUCLEAR REACTOR

The analysis of power generation systems is of significant scientific interest and is essential for the efficient use of energy resources. The most common method for analyzing energy conversion systems is energy analysis, which is based on the first law of thermodynamics. However, this approach does not provide a complete assessment of system efficiency and losses. Therefore, a combined approach that accounts for both the first and second laws of thermodynamics is becoming increasingly widespread.

Exergy analysis, based on the second law of thermodynamics, allows a clear distinction between losses to the environment and internal process irreversibility. This method provides an effective assessment of equipment and processes within energy conversion chains. Process exergy is a measure of its efficiency or inefficiency and enables a better understanding of the mechanisms of energy losses.

The modern approach to process analysis is based on the exergy method, which provides a clear understanding of the process and allows the quantitative assessment of exergy destruction. The main objective of traditional thermodynamic analysis is the conservation of energy.

The mass, energy, and exergy balances for any control volume operating under steady-state conditions with a steady flow, in which changes in kinetic and potential energy are negligible, can be expressed as follows [23]:

$$\sum G_i = \sum G_o, \tag{7}$$

$$\sum_k Q_k + \sum_i (G_i h_i)_k = \sum_e (G_e h_e)_k + N_k, \tag{8}$$

$$\sum_k E_{Q,k} + \sum_i G_i e_i = \sum_j G_j e_j + N_k + E_{D,k,} \tag{9}$$

where i and j are indices corresponding to the inlet and outlet states, and k denotes a specific cycle component; $\dot{Q}$ and $\dot{N}$ are the thermal and mechanical energy flow rates; $\dot{G}$ is the mass flow rate of the working fluid; h is the enthalpy; $\dot{E}_D$ is the exergy loss during the process, or exergy destruction; $\dot{E}_Q$ is the exergy transferred through heat transfer at temperature T, defined as:

$$E_{Q,k} = \sum \left(1 - \frac{T_{amb}}{T}\right) Q_k, \tag{10}$$

where T_{amb} is the ambient temperature. The temperature was assumed to be 25 °C.

The specific flow exergy is determined by the following expression:

$$e_{i,k} = h_{i,k} - h_0 - T_{amb}(s_{i,k} - s_0), \tag{11}$$

where $s_{i,k}$ – the specific entropy; the subscript "0" denotes the ambient environment.

The exergy flow rate is obtained:

$$E_{i,k} = G_{i,k} e_{i,k}. \tag{12}$$

Using the fuel–product (F–P) concept definitions [23, 24], the fuel and product terms can be expressed through exergy flows.

The exergy balance for an individual component (k) is written as:

$$E_{F,k} = E_{P,k} + E_{D,k}. \tag{13}$$

where E_P is the exergy flow of the useful product, and E_F is the fuel exergy required to obtain it.

Thus, the exergy efficiency can be determined:

$$\eta_{ex,k} = \frac{E_{P,k}}{E_{F,k}} = 1 - \frac{E_{D,k}}{E_{F,k}}. \tag{14}$$

The exergy efficiency of the cycle is calculated using the following equation:

$$\eta_{ex} = 1 - \frac{\sum E_{D,k}}{Q_h}. \tag{15}$$

The exergy flow into fuel and product is decomposed using the *F-P* method [23, 24], where fuel is considered as the decrease in exergy, while product is the increase in exergy within the component. The exergy E_i is determined using Eq. (12), where G is the total steam flow rate leaving the reactor heat exchanger.

For example, the exergy of the high-pressure part (h-p) of the HIPT is defined as the difference in exergy at the input and output, taking into account the change in steam mass:

$$E_{F,\text{h-p HIPT}} = (1 - y_1) \cdot (E_0 - E_1) + (1 - y_1 - y_2 - \alpha_1) \cdot (E_1 - E_2) + (1 - y_1 - y_2 - \alpha_1 - \alpha_2) \cdot (E_2 - E_3),$$

where: α_i– fraction of steam extracted to the LPHs and HPHs; γ_i– fraction of steam extracted to the steam SHs.

The exergy product is the power of the high-pressure part of the HIPT. The difficulty lies in separating the fuel and product flows within the deaerator. Fuel exergy is defined as the sum of all incoming flows, and product is defined as the outgoing flow. Table 3 shows the decomposition of exergy flows into fuel and product flows.

Table 3. Decomposition of exergy flows into fuel and product of the STU (Fig. 1).

Element Name	$E_{F,k}$	$E_{P,k}$
NR	Q_h	$E_{\text{NR}} - E_{20}$
SV	E_{NR}	E_0
h-p HIPT	$(1–y_1)\cdot(E_0– E_1)+(1–y_1– y_2–\alpha_1)\cdot(E_1– E_2)+$ $+(1–y_1– y_2–\alpha_1–\alpha_2)\cdot(E_2 – E_3)$	$N_{\text{h-p HIPT}}= G\,((1–y_1)\cdot(h_0– h_1)+ (1–y_1– y_2–\alpha_1)\cdot(h_1– h_2)+(1–y_1– y_2–\alpha_1–\alpha_2)\cdot(h_2 – h_3))$
S	$(1–y_1– y_2–\alpha_1–\alpha_2–\alpha_3)\cdot E_3 – \alpha_S E_{\text{Ss}}$	$(1–y_1– y_2–\alpha_1–\alpha_2–\alpha_3–\alpha_s)\cdot E_{\text{S}}$
SH1	$y_2\,(E_1–E_{1s})$	$(1–y_1– y_2–\alpha_1–\alpha_2–\alpha_3–\alpha_S)\cdot(E_{\text{SH1}}– E_S)$
SH2	$y_1\,(E_0–E_{0s})$	$(1–y_1– y_2–\alpha_1–\alpha_2–\alpha_3–\alpha_S)\cdot(E_{\text{SH2}}– E_{\text{SH1}})$
i-p HIPT	$(1–y_1 – y_2 –\alpha_1–\alpha_2–\alpha_3–\alpha_s– \alpha_T)\cdot(E_{\text{SH2}}–E_4)+(1–y_1– y_2–\alpha_1–\alpha_2–\alpha_3–\alpha_c – \alpha_T–\alpha_4)\cdot(E_4– E_5)$	$N_{\text{i-p HIPT}} = G\,((1–y_1 – y_2 –\alpha_1–\alpha_2–\alpha_3–\alpha_s– \alpha_{18})\cdot(h_{\text{SH2-4}} – h_4)+ (1–y_1 – y_2 –\alpha_1–\alpha_2–\alpha_3–\alpha_c – \alpha_T– \alpha_4)\cdot(h_4 – h_5))$
LPT	$(1–y_1– y_2–\alpha_1–\alpha_2–\alpha_3–\alpha_c– \alpha_{18}– \alpha_4– \alpha_5)\cdot(E_5 – E_6)+ (1–y_1– y_2–\alpha_1–\alpha_2–\alpha_3–\alpha_c– \alpha_T–\alpha_4– \alpha_5–\alpha_6)\cdot(E_6 – E_7)+ (1–y_1– y_2–\alpha_1–\alpha_2–\alpha_3–\alpha_c– \alpha_T– \alpha_4– \alpha_5–\alpha_6– \alpha_7)\cdot(E_7 – E_8)$	$N_{\text{LPT}} = G\,(1–y_1– y_2–\alpha_1–\alpha_2–\alpha_3–\alpha_c– \alpha_{18}– \alpha_4– \alpha_5)\cdot(h_{5\text{-}6} – h_6)+ (1–y_1– y_2–\alpha_1–\alpha_2–\alpha_3–\alpha_c– \alpha_{18}– \alpha_4– \alpha_5–\alpha_6)\cdot(h_6 – h_7)+ (1–y_1– y_2–\alpha_1–\alpha_2–\alpha_3–\alpha_c– \alpha_T– \alpha_4– \alpha_5–\alpha_6– \alpha_7)\cdot(h_7 – h_8)$
C	$(1–y_1– y_2–\alpha_1–\alpha_2–\alpha_3–\alpha_c– \alpha_T– \alpha_4– \alpha_5 –\alpha_6– \alpha_7 –\alpha_T)\cdot(E_8– E_{10})$	$E_{Q0}\,(10)$
CP	$N_{\text{CP}}= \dot{G}\,(1–y_1– y_2–\alpha_1–\alpha_2–\alpha_3–\alpha_c–\alpha_4– \alpha_5 –\alpha_6– \alpha_7–\alpha_T)\cdot(h_{11} – h_{10})$	$(1–y_1– y_2–\alpha_1–\alpha_2–\alpha_3–\alpha_c–\alpha_4– \alpha_5 –\alpha_6– \alpha_7–\alpha_T)\cdot(E_{11} – E_{10})$
LPH1	$\alpha_7\cdot(E_7– E_{7s})+ \alpha_6\cdot E_{6s}$	$(1–y_1– y_2–\alpha_1–\alpha_2–\alpha_3–\alpha_c–\alpha_4– \alpha_5–\alpha_T)\cdot E_{12} – (1–y_1– y_2–\alpha_1–\alpha_2–\alpha_3–\alpha_c–\alpha_4– \alpha_5 – \alpha_6– \alpha_7–\alpha_T)\cdot E_{11}$
LPH2	$\alpha_6\cdot(E_6– E_{6s})$	$(1–y_1– y_2–\alpha_1–\alpha_2–\alpha_3–\alpha_c–\alpha_4– \alpha_5–\alpha_T)\cdot(E_{13} – E_{12})$
LPH3	$\alpha_5\cdot(E_5– E_{5s})+ \alpha_4\cdot E_{4s}$	$(1–y_1– y_2–\alpha_1–\alpha_2–\alpha_3–\alpha_s–\alpha_T)\cdot E_{14} – (1–y_1– y_2–\alpha_1–\alpha_2–\alpha_3–\alpha_c–\alpha_4– \alpha_5–\alpha_T)\cdot E_{13}$
LPH4	$\alpha_4\cdot(E_4– E_{4s})+ \alpha_T\cdot E_{Ts}$	$(1–y_1– y_2–\alpha_1–\alpha_2–\alpha_3–\alpha_s)\cdot E_{15} – (1–y_1– y_2–\alpha_1–\alpha_2–\alpha_3–\alpha_s–\alpha_T)\cdot E_{14}$
D	$\alpha_3\cdot E_3 + \alpha_s\cdot E_S +(1–y_1–y_2–\alpha_1–\alpha_2–\alpha_3–\alpha_s)\cdot E_{15} + (\alpha_1+ y_1+ \alpha_2+ y_2)\cdot E_{2s}$	E_{16}
T and TH	$\alpha_T\cdot(E_T– E_{Ts})$	$N_T= G\,\alpha_T\cdot(h_T– h_{21})$
FP	N_{FP}	$E_{17} – E_{16}$
HPH1	$\alpha_2\cdot(E_2 – E_{2s})+ y_2\,E_{1s} + (\alpha_1 + y_1)\,E_{1s}$	$E_{19}–E_{17}$
HPH2	$\alpha_1\cdot(E_1 – E_{1s})+ y_1\,E_{0s}$	$E_{20} – E_{19}$
EG	$N_e = (N_{\text{h-p HIPT}} + N_{\text{i-p HIPT}} + N_{\text{LPT}}) – (N_{\text{CP}} + N_{\text{FP}})$	$N_{\text{EG}}= N_e \cdot \eta_{\text{EG}}$, where η_{EG}– efficiency of an electric generator

Figure 4 shows the destruction of exergy in the elements of the STU. The exergy destruction in the nuclear reactor (NR) is not shown on Fig. 4, since it accounts for approximately 90% of the total exergy destruction in the STU. Figure 5 shows the exergy efficiency of each element.

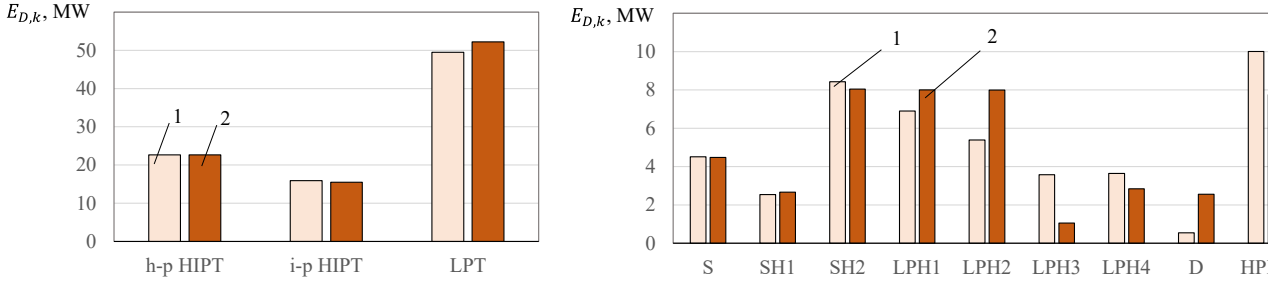

Figure 4. Destruction of exergy in the elements of the STU

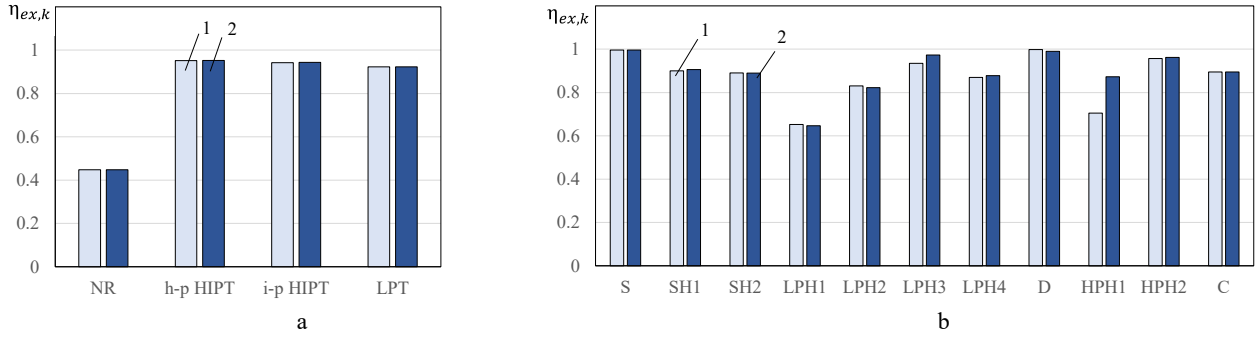

Figure 5. Exergy efficiencies of the STU elements

Figure 4a shows that exergy destruction is highest in the low-pressure turbine section. In the second option, exergy destruction in the LPT is 3 MW higher (Fig. 4a). However, the exergy efficiency of the low-pressure turbine is the same for both variants and equals 0.92. (Fig. 5a).

Figure 4b shows that the highest exergy destruction among the regenerative heaters occurs in HPH1. For the second option, it is lower by 2.3 MW. At the same time, Fig. 5b shows that HPH1 efficiency in the second option is higher by 0.17.

Figure 4 also shows that when exergy destruction decreases in some components of the second option, it increases in others. As a result, the total exergy destruction of the second option is lower by only 0.5 MW. This indicates that both options demonstrate high exergy efficiency.

For further analysis, it is necessary to evaluate the mass-dimensional characteristics. Table 4 presents some geometric characteristics of the turbine flow paths.

Table 4. Axial dimension of the turbine flow paths

Turbine parts	Number of stages	Axial dimension, m
Option 1		
High-pressure turbine part of the HIPT	6	2.195
Intermediate-pressure turbine part of the HIPT	3	1.841
LPT	5	3.237
Option 2		
High-pressure turbine part of the HIPT	4	1.744
Intermediate-pressure turbine part of the HIPT	2	1.092
LPT	6	3.598

Table 4 shows that the largest axial dimension is observed in the LPT of the second option, while the total number of stages is lower by 2 stages.

The final decision can be made based on a techno-economic analysis.

6. DISCUSSION

The obtained results demonstrate that the proposed AP1000-based steam turbine unit provides high thermodynamic and exergy performance while maintaining a relatively compact turbine configuration. The internal cycle efficiency of both investigated options exceeds 38.9 %, which corresponds to the performance level of modern saturated-steam nuclear power units with Generation III+ reactors. The small difference in efficiency between the investigated options indicates that the redistribution of turbine stages mainly affects the distribution of thermodynamic losses within the cycle rather than the overall cycle efficiency.

The performed exergy analysis showed that the largest exergy destruction occurs in the low-pressure turbine section. This is primarily associated with steam moisture formation during the final stages of expansion and with significant irreversible losses caused by large volumetric steam flow rates at low pressures. Similar tendencies are reported in studies devoted to exergy analysis of steam turbine units for nuclear power plants and saturated-steam cycles.

At the same time, the redistribution of stages between the high-, intermediate-, and low-pressure turbine sections changes the local exergy destruction in individual components. In the second option, the exergy destruction in the low-pressure turbine section increases, whereas the exergy destruction in some regenerative heaters decreases. As a result, the total exergy destruction differs only slightly between the investigated configurations. This indicates that both options are thermodynamically balanced and characterized by high exergy efficiency.

The obtained results also show that increasing the number of stages in the low-pressure turbine section leads to an increase in the axial dimensions of the turbine flow path. However, the second configuration simultaneously reduces the total number of turbine stages and simplifies the overall structure of the steam turbine unit. Such an approach may reduce the metal consumption, simplify maintenance, and decrease the dimensions of the turbine hall.

Compared with conventional steam turbine units designed for VVER-1000 reactors, the proposed configuration is better adapted to the thermodynamic parameters of the AP1000 saturated steam cycle. The use of a combined single-flow high- and intermediate-pressure turbine, together with a two-stage reheating system, enables improved distribution of thermal and exergy losses within the cycle.

The obtained results confirm that exergy analysis is an effective tool for evaluating the thermodynamic perfection of nuclear steam turbine cycles and for identifying the components with the highest irreversible losses. The developed approaches may be used to further optimize AP1000-based steam turbine units, including detailed 3D flow-path optimization, moisture reduction in the low-pressure stages, and further improvement of the regenerative feedwater heating system.

7. CONCLUSIONS

1. A review of steam turbine units for nuclear power plants was carried out, and the K-1000-60/1500-2 turbine was selected as the baseline configuration for operation with the AP1000 nuclear reactor. Based on this turbine, a new cycle configuration of the steam turbine unit was developed. The proposed configuration includes a combined single-flow high- and intermediate-pressure turbine, two low-pressure turbines, a steam separator, and a two-stage steam reheating system.

2. Thermodynamic modeling of the AP1000-based steam turbine unit was performed. Optimal steam extraction pressures ensuring the maximum cycle efficiency were determined. The obtained results showed that the highest efficiency values correspond to the extraction pressures $P_1 = 2.4$ MPa, $P_2 = 1.7$ MPa, and $P_4 = 0.55$ MPa for the HIPT extraction system. For the LPT extraction system, the optimal parameters correspond to $P_6 = 120$ kPa and $P_7 = 30$ kPa.

3. Several options of the cycle configuration that consider different numbers of turbine stages were developed and analyzed. Two main configurations were investigated. The first option includes a 6-stage high-pressure part, a 3-stage intermediate-pressure part, and a 5-stage low-pressure turbine. The second option includes a 4-stage high-pressure part, a 2-stage intermediate-pressure part, and a 6-stage low-pressure turbine. Both options demonstrated high thermodynamic performance, with internal cycle efficiencies of 38.93% and 38.96%, respectively. The obtained efficiency values are comparable to those of modern saturated-steam nuclear power units reported in the literature, where the cycle efficiency typically ranges from 37–39% [25, 26].

4. A full exergy analysis of the steam turbine unit was carried out. The exergy destruction in the main elements of the cycle configuration was determined using the fuel–product approach. The results showed that the largest exergy destruction occurs in the low-pressure turbine section. At the same time, the redistribution of exergy destruction between the components of the two investigated options results in only a small difference in the total exergy destruction. Both configurations demonstrated high exergy efficiency characteristics.

5. The analysis of the geometric characteristics of the turbine flow paths showed that the second option has larger axial dimensions in the low-pressure turbine section despite the lower total number of stages.

6. The obtained results can be used for further development and optimization of AP1000-based steam turbine units. The final selection of the cycle configuration should be based on a comprehensive thermodynamic, exergy, and economic analysis.

Acknowledgements

This work was carried out within the framework of the research project "Development of a highly efficient and competitive steam turbine plant for promising power units of Ukrainian NPPs with AP1000 nuclear reactors. Section 1. Power generating steam turbine

plant. Stage I "Analysis of existing thermal schemes of steam turbine plants and their loading modes for promising power units of Ukrainian NPPs with AP1000 nuclear reactors" with state registration number 0125U001698.

ORCID

Andrii V. Rusanov, https://orcid.org/0000-0002-9957-8974, **Andrii O. Kostikov,** https://orcid.org/0000-0001-6076-1942,
Viktoriia O. Tarasova, https://orcid.org/0000-0003-3252-7619, **Roman A. Rusanov**, https://orcid.org/0000-0003-2930-2574,
Marina O. Chugay, https://orcid.org/0000-0002-0696-4527, **Maksym V. Lytvynenko,** https://orcid.org/0000-0003-2805-234X

REFERENCES

[1] Westinghouse Electric Company. AP1000® Plant Overview. Available at: https://westinghousenuclear.com/energy-systems/ap1000-pwr/overview

[2] W.E. Cummins, M.M. Corletti, and T.L. Schulz, "Westinghouse AP1000 Advanced Passive Plant," in: *Proceedings of ICAPP'03*, (Cordoba, Spain, 2003). Paper 3235. Available at: http://large.stanford.edu/courses/2022/ph241/beskind1/docs/cummins-may03.pdf

[3] AP1000 Design Control Document Rev. 16 – Tier 2 Chapter 1 – Introduction and General Description of the Plant – Section 1.9 Compliance with Regulatory Criteria. Available at: https://www.nrc.gov/reactors/new-reactors/design-cert/ap1000/dcd.html

[4] On Siting, Design and Construction of Energy Blocks N3 and N4 of the Khmelnitsky Nuclear Power Plant: Law of Ukraine No. 5217-VI of September 6, 2012. Database "Legislation of Ukraine". Verkhovna Rada of Ukraine. Available at: https://zakon.rada.gov.ua/laws/show/en/5217-17?utm_source=chatgpt.com#Text

[5] T.V. Petik, and H.P. Lisiuk, "Automatic system of regulation of water level in the steam generator of the 1000 MW nuclear power plant," Scientific notes of Taurida National V.I. Vernadsky University, series «Technical Sciences», **30**(69), Part 2, No. 3, 7–13 (2019). (in Ukrainian). https://doi.org/10.32838/2663-5941/2019.3-2/02

[6] O.M. Uss, S.T. Patsiuk, O.V. Panchenko, O.V. Shavlaklov, and D.Kh. Kharlampidi, "New Generation 'Block-Modular' Condenser for K-1000-60/1500-2 Turbine Units in Zaporozhskaya NPP," J. of Mech. Eng. **21**(1), 4-10 (2018). https://doi.org/10.15407/pmach2018.01.004

[7] O.V. Shavlakov, M.O. Feofentov, O.V. Panchenko, O.G. Kasatkin, O.M. Uss, S.T. Patsyuk, O.V. Vavilov, *et al*., *Development and implementation of condensers for steam turbines of nuclear power plants*, (FOP Panov A.M., Kharkiv, 2018). (in Ukrainian)

[8] New nuclear reactors: Generic Design Assessment. Report by the Office for Nuclear Regulation on the Generic Design Assessment of new nuclear reactor designs. 2011. Available at: https://www.onr.org.uk/media/sbkc5dng/ap1000-onr-gda-sr-11-002-rev-0.pdf

[9] S.A. Olatubosun, A. Ayodeji, and M.A. Amidu, "Safety assessment of AP1000: Common transients and their analysis," Nuclear Engineering and Design, **375**, 111100 (2021). https://doi.org/10.1016/j.nucengdes.2021.111100

[10] L.T. Borges, D.G. Rodríguez, C.J.C.M.R. da Cunha, J. de Lima Bezerra, and C.A.B. de Oliveira Lira, CFD Analysis of the AP1000 Reactor Pressure Vessel under Normal Operating Conditions. 2024. Available at: https://sencir.nuclear.ufmg.br/wp-content/uploads/2024/11/956358.pdf

[11] Idaho National Laboratory. Opportunities for AP1000 Deployment at Existing and Planned Nuclear Sites. 2024. Available at: https://inldigitallibrary.inl.gov/sites/STI/STI/Sort_128167.pdf.

[12] X. Niu, J. Liu, Z. Dong, J. Wei, and W. Zhou, "Research on Neutronics Safety Parameters of the AP1000 Nuclear Reactor under Different Conditions," Energies, **16**, 7549 (2023). https://doi.org/10.3390/en16227549

[13] Z. Winfried, B. Nadine, A. Alexander, and V. Kiril, "Sensitivities of delayed neutron fractions in the framework of SCALE 6.2," Annals of Nuclear Energy, **153**, 108068 (2021). https://doi.org/10.1016/j.anucene.2020.108068

[14] M. Rahgoshay, and O. Noori-Kalkhoran, "Calculation of control rod worth and temperature reactivity coefficient of fuel and coolant with burn-up changes for VVRS-2 MWth nuclear reactor," Nuclear Engineering and Design, **256**, 322–331 (2013). https://doi.org/10.1016/j.nucengdes.2012.08.033

[15] H. Mazrou, D. Lababsa, and O. Mokhtari, "Assessment of the safety impact caused by the variations of the critical position of control rods and by the presence of an in-core flux trap on the power peaking factors in an MTR-type research reactor," Nuclear Engineering and Design, **414**, 112553 (2023). https://doi.org/10.1016/j.nucengdes.2023.112553

[16] A. Kluba, and R. Field, "Optimization and Exergy Analysis of Nuclear Heat Storage and Recovery," Energies, **12**(21), 4205 (2019). https://doi.org/10.3390/en12214205

[17] J.Y. Heo, J.H. Park, Y.J. Chae, S.H. Oh, S.Y. Lee, J.Y. Lee, N. Gnanapragasam, *et al*., "Evaluation of various large-scale energy storage technologies for flexible operation of existing pressurized water reactors," Nuclear Engineering and Technology, **53**(8), 2427–2444 (2021). https://doi.org/10.1016/j.net.2021.02.023.

[18] W.M. Conlon, and Ch.W. Forsberg, "Storage-Coupled Nuclear Combined Cycle," ASME Open Journal of Engineering, **1**, 015001-1 (2022). https://doi.org/10.1115/1.4055277

[19] A.V. Rusanov, A.O. Kostikov, V.O. Tarasova, R.A. Rusanov, and S.P. Tretiak, "The concept of creating a maneuverable powerplant based on a small modular reactor." Naukovyi Visnyk Natsionalnoho Hirnychoho Universytetu, (5), 37–44 (2024). https://doi.org/10.33271/nvngu/2024-5/037

[20] M.A. Darwish, F.M. Al Awadhi, and A.O. Bin Amer, "Combining the nuclear power plant steam cycle with gas turbines," Energy, **35**, 4562–4571 (2010). https://doi.org/10.1016/j.energy.2010.04.031

[21] R. Rusanov, A. Rusanov, and M. Chugay, "Analysis of the Influence of Operational and Geometrical Characteristics on the Efficiency of Axial Turbine Stage Profile Cascades," Science and Innovation, **21**(2), 73–87 (2025). https://doi.org/10.15407/scine21.02.073

[22] A. Rusanov, R. Rusanov, P. Klonowicz, P. Lampart, G. Żywica, and A. Borsukiewicz, "Development and experimental validation of real fluid models for CFD calculation of ORC and steam turbine flows," Materials, **14**(22), 6879 (2021). https://doi.org/10.3390/ma14226879

[23] G. Tsatsaronis, "The future of exergy-based methods," Energy, **302**, 131881 (2024). https://doi.org/10.1016/j.energy.2024.131881

[24] D. Kharlampidi, V. Tarasova, M. Kuznetsov, and E. Voytenko, "Thermodynamic analysis of air-compression refrigerating machine based on the exergy cost theory," Eastern-European Journal of Enterprise Technologies, **5**(8(89)), 30–38 (2017). https://doi.org/10.15587/1729-4061.2017.112113

[25] A. Ohji, and M. Haraguchi, "2 - Steam turbine cycles and cycle design optimization: The Rankine cycle, thermal power cycles, and IGCC power plants," Advances in Steam Turbines for Modern Power Plants, 11–40 (2017). https://doi.org/10.1016/B978-0-08-100314-5.00002-6

[26] V. Solovey, M. Zipunnikov, and R. Rusanov, "Increasing the manoeuvrability of power units of the thermal power plants due to applying the hydrogen-oxygen systems," J. Phys. Energy, **5**, 014012 (2023). https://doi.org/10.1088/2515-7655/aca9ff

ТЕРМОДИНАМІЧНИЙ ТА ЕКСЕРГЕТИЧНИЙ АНАЛІЗ ПАРОТУРБІННОЇ УСТАНОВКИ НА БАЗІ AP1000 З ОПТИМІЗОВАНОЮ КОНФІГУРАЦІЄЮ ЦИКЛУ

Андрій В. Русанов[1], Андрій О. Костіков[1], Вікторія О. Тарасова[1], Роман А. Русанов[1], Марина О. Чугай[1], Максим В. Литвиненко[2]

[1]Інститут енергетичних машин і систем ім. А.М. Підгорного Національної академії наук України, вул. Комунальників, 2/10, м. Харків, 61046, Україна

[2]Інститут гідродинамічних машин Польської академії наук, вул. Фішера, 14, м. Гданськ, 80-231, Польща

З огляду на стратегічну важливість модернізації ядерної енергетики України у статті наведено результати дослідження з розроблення та аналізу термодинамічного циклу та структури теплової схеми паротурбінної установки (ПТУ), призначеної для роботи з ядерним реактором AP1000. За базову було обрано теплову схему турбоустановки К-1000-60/1500-2. На її основі запропоновано нову конфігурацію ПТУ, що включає комбінований однотечійний циліндр високого та середнього тиску (ЦВСТ), два циліндри низького тиску (ЦНТ), сепаратор пари та двоступеневу систему проміжного перегріву пари. Для оцінювання впливу тисків відборів пари, параметрів регенеративного підігріву живильної води та розподілу ступенів турбіни на показники циклу було проведено термодинамічний та ексергетичний аналіз запропонованих конфігурацій ПТУ. Чисельне моделювання та розрахунки проточної частини секцій турбіни виконано із застосуванням сучасних методів газодинамічного проєктування. Результати показали, що оптимальний вибір параметрів відборів пари та умов проміжного перегріву суттєво підвищує ефективність циклу. Максимальний внутрішній ККД циклу ПТУ досяг 38,96 %. Ексергетичний аналіз продемонстрував, що найбільші втрати ексергії спостерігаються в циліндрі низького тиску, водночас обидві досліджувані конфігурації характеризуються високою ексергетичною ефективністю. Також проведено порівняльний аналіз компонування ступенів та осьових розмірів проточних частин турбіни. Розроблені підходи можуть бути застосовані під час проєктування та оптимізації паротурбінних установок нового покоління для атомних електростанцій.

Ключові слова: *ядерна енергетика; AP1000; паротурбінна установка; термодинамічний аналіз; ексергетичний аналіз; регенеративний підігрів живильної води; атомна електростанція*

East European Journal of Physics. 3. 280-285 (2026)
DOI:10.26565/2312-4334-2026-3-22 ISSN 2312-4334

A HIGH-SENSITIVITY, ZERO-BIAS SILICON PHOTODIODE FOR DETECTION OF ECO-FRIENDLY $AgInS_2$ та $CuInS_2$ QUANTUM DOT EMISSION

Mykola S. Kukurudziak[1,2*], Vasylyna V. Kopach[1], Serhii A. Voitovych[3], Yuriy B. Khalavka[1], Mykola S. Solodkyi[1]
[1]*Yuriy Fedkovych Chernivtsi National University, Kotsyubyns'kogo str. 2, 58012, Chernivtsi, Ukraine*
[2]*Rhythm Optoelectronics Shareholding Company, Holovna str. 244, 58032, Chernivtsi, Ukraine*
[3]*Ivano-Frankivsk National Medical University, Halytska str. 2, 76018, Ivano-Frankivsk, Ukraine*
**Corresponding Author e-mail: mykola.kukurudzyak@gmail.com*
Received May 24, 2026; revised July 23, 2026; accepted August 20, 2026

Silicon *p-n* photodiodes optimized for detecting a broad spectrum of photoluminescent radiation from $AgInS_2$ and $CuInS_2$ quantum dots have been developed and fabricated. By adjusting fabrication parameters and carefully selecting the substrate material, the sensor's spectral sensitivity peak (0.34 A/W) aligns with the nanocrystal emission range (550–700 nm). To maximize resolution, we operated the detector in zero-bias mode. This minimized dark current to approximately 6 pA, reduced thermal noise, and enabled high detection sensitivity. It has been experimentally established that, with a load resistance of 10 kΩ, the cutoff frequency of the photodiode is 1 MHz and is entirely limited by the RC time constant of the circuit. This frequency response is sufficient not only for steady-state radiometry of colloids and films with a radiation power of 0.29–0.35 mW, but also for precise study of the microsecond kinetics of quantum dot luminescence decay without risking photodegradation.
Keywords: *Quantum dots; $AgInS_2$; $CuInS_2$; Detector; Sensitivity; Photodiode*

A current trend in electronic sensor development is the use of various nanomaterials to miniaturize devices and enhance sensor sensitivity. The wide range of electronic, optical, and mechanical properties across different classes of nanomaterials opens up opportunities to develop sensors with unprecedented sensitivity, fast response, and reliability [1]. By principle of operation, most sensors developed today are electrical (resistive, capacitive, diode, electrochemical, or transistor type), while optical sensors (luminescent) are much less developed [2]. Existing optical and luminescent sensors use quantum dots (QDs), but are often based on toxic materials (Cd, Pb, etc.) [3,4], which limits their application in environmentally sensitive environments (e.g., water, bioenvironment). Therefore, interest is growing in "environmentally friendly" quantum dots—AgInS2 and CuInS2—that combine good optical/electronic properties with lower ecotoxicological risk [5-7]. The band gap of $AgInS_2$ varies between 1.8 and 2.2 eV, depending on the stoichiometric ratio of silver and indium during the synthesis of quantum dots. One of the key features of $AgInS_2$ is a broad emission band with a Stokes shift, mainly in the red-yellow region (550–750 nm). The band gap of $CuInS_2$ is approximately 1.45–1.55 eV. The main advantages of this material are high photosensitivity, good stability, and susceptibility to point-defect formation, particularly copper vacancies (V_{Cu}). Unlike linear defects, which usually degrade the spectroscopic and electrical properties of semiconductor structures [8], these intrinsic point defects positively affect photoluminescence (PL), significantly expanding the spectral range in which the material can operate. Using $AgInS_2$ and $CuInS_2$ nanoparticles, easy-to-use photoluminescence-based sensors with high selectivity, detection range, and sensitivity can be created [9].

The practical application of $AgInS_2$ and $CuInS_2$ nanoparticles in luminescent sensors is limited by detector sensitivity and the intensity of light emitted by these quantum dots. The intensity of the radiation in turn depends on several factors: intensity of the excitation diode; stability of the quantum dots; quantum yield of the nanoparticles; efficiency of absorption of the excitation light; spectral sensitivity of the detector. Thus, for optimal sensor performance based on these quantum dots, all these factors must be considered and balanced.

Our previously published experimental results [10] showed that the PL peak of AgInS2 nanocrystals (colloid) exhibits an emission from 700 nm (1.8 eV) to 575 nm (2.2 eV) with a change in the molar ratio of In/Ag precursors from 3 to 20. The PL spectrum of the layer-by-layer assembled $AgInS_2$ thin films (Fig. 1) are slightly shifted towards higher energy compared to the spectra of the original $AgInS_2$ solution and are in the range from 650 nm (1.9 eV) to 550 nm (2.3 eV). Despite the different shifts of the PL peak positions, the full width at half maximum (FWHM) of the PL spectra of the films are approximately the same for the corresponding colloids: 0.32-0.41 eV.

Increasing the irradiation intensity cannot be infinite, as it can cause photodegradation of quantum dots under real operating conditions. Therefore, the system design should be based on the detector's characteristics, which will determine whether to select nanoparticles with higher intensity. Such $AgInS_2$ and $CuInS_2$ quantum dot colloids can emit power around 0.29-0.35 mW that then require detection.

Cite as: M.S. Kukurudziak, V.V. Kopach, S.A. Voitovych, Y.B. Khalavka, M.S. Solodkyi, East Eur. J. Phys. 3, 280 (2026), https://doi.org/10.26565/2312-4334-2026-3-22

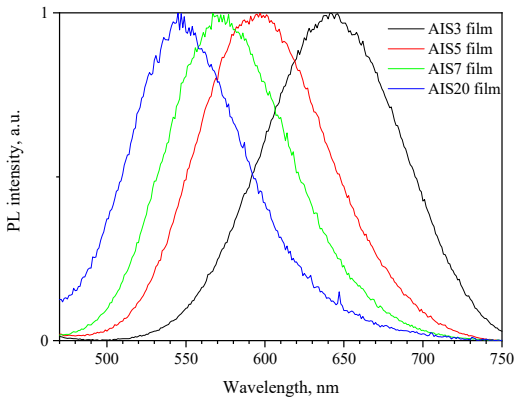

Figure 1. Photoluminescnece spectra of $AgInS_2$ QDs films; λ exc = 441.6 nm

Accordingly, developing quantum dot luminescence detectors is essential for the effective operation of the proposed systems. Undoubtedly, the use of photomultipliers [11] or avalanche photodiodes (PD) [12] could be effective; however, such detectors are expensive and complex to manufacture. One of the main advantages of the proposed system, in addition to its environmental friendliness, is the affordability and relative simplicity of manufacturing its components. Silicon *p-i-n* [13] and *p-n* [14] PDs can serve as an effective replacement for these photodetectors, as they possess sufficient sensitivity in the visible wavelength range that needs to be detected (λ = 550 nm, λ = 570 nm, λ = 590 nm, λ = 600 nm, λ = 650 nm). It is worth noting that *p-i-n* PDs are less suitable for the described purpose, since they typically operate at high reverse bias and have high sheet resistance and a long lifetime of minority carriers in the base, which, as is known, significantly shifts the peak of the photodiode's spectral sensitivity curve toward longer wavelengths up to λ = 1.02 μm [13, 15]. Furthermore, in *p-i-n* photodiodes, there is a need for high-concentration doping of the front region, which in turn absorbs a significant portion of the visible-range radiation; additionally, to mitigate surface generation, *p-i-n* photodiodes should be fabricated with guard ring systems, which subsequently requires the measurement and control of additional parameters [16]. These factors complicate the use of *p-i-n* photodiodes; therefore, it is proposed to use silicon *p-n* photodiodes for detecting visible luminescent radiation from $AgInS_2$ and $CuInS_2$ quantum dots. Accordingly, the aim of this work is to develop a silicon single-element *p-n* PD with enhanced detection sensitivity, which is planned to be achieved through the zero-bias mode, and to evaluate its performance during quantum dot irradiation simulations.

EXPERIMENTAL

The photodetectors were fabricated using *n*-type single-crystal dislocation-free FZ-Si with a [100] orientation and a resistivity of ρ ≈ 100–150 Ω·cm. The fabricated detectors are shown in Fig. 2. The area of the responsive element (RE) was A_{RE}=0.64 mm². The fabrication was carried out using planar diffusion technology.

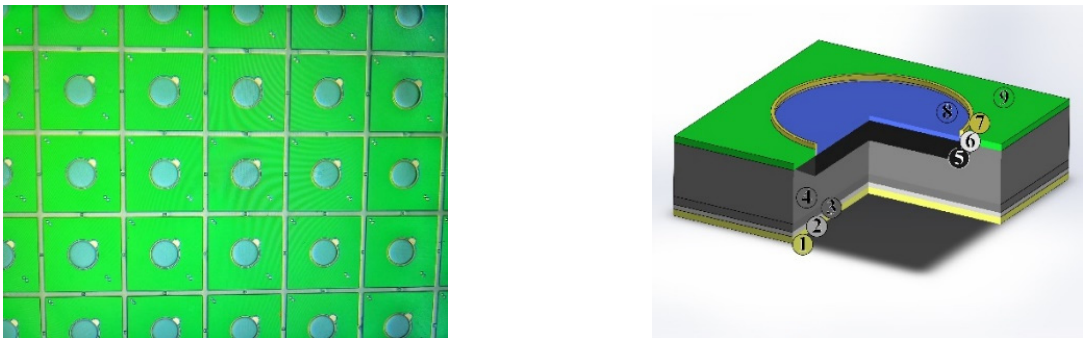

a b

Figure. 2. Image of photosensitive PD-crystals on a substrate (a) and three-dimensional view of the PD-crystal with a quarter cross-section illustrating (b): 1 — back-side Au-metallization, 2 — back-side Cr-sublayer, 3 — phosphorus-doped n^+-region, 4 — *n*-Si substrate, 5 — boron-doped p^+-RE, 6 — front-side Cr-sublayer, 7 — front-side Au-metallization, 8 — antireflection oxide layer of the RE; 9 — protective SiO_2

The photodiode fabrication process consisted of the following steps: oxidation of Si substrates in a hydrochloric acid vapor atmosphere at *T*=1403–1453 K; boron diffusion to form p^+-type photosensitive regions at 1273–1323 K, boron drive-in in an oxidizing atmosphere to form an anti-reflective coating and redistribute the dopant at temperatures of *T*=1403–1453 K, phosphorus diffusion toward the substrate at *T*=1203–1253 K to passivate generation-recombination centers within the photodiode crystal volume and form an ohmic n^+-layer; Cr-Au metallization and contact formation.

Given that visible radiation is absorbed in the near-surface layers of silicon [17], to ensure minimal recombination of photogenerated charge carriers in the n^+-layer, its thickness was approximately x_{p+-n}=1.5–2 μm. The anti-reflective coating was designed to satisfy the minimum reflection condition (1)[18], according to which for a wavelength of λ = 550 nm the oxide thickness is d_{SiO2}=96 nm, and for a wavelength of λ=650 nm it is d_{SiO2}=114 nm; accordingly, the SiO_2 thickness was selected to be approximately d_{SiO2}=100–110 nm.

$$\frac{\lambda}{4} = nd_{SiO_2} \quad (1)$$

where *n* is the refractive index of SiO_2.

Additionally, the method of forming a passivation coating in an atmosphere of hydrochloric acid vapor was selected for the manufacturing process, as this method minimizes the influence of uncontrolled impurities and contamination, particularly Na^+ and K^+ ions, and surface recombination [19, 20], which is particularly relevant for the design of devices without guard rings.

The dark current (I_d) and *I–V*-characteristics of PDs were measured using a hardware-software complex implemented on the basis of the Arduino platform, an Agilent 34410A digital multimeter and a Siglent SPD3303X programmable power source, which were controlled by a personal computer using software created by the authors in the LabView environment.

Monitoring of current monochromatic responsitivity ($S_{I\lambda}$) was carried out by method of comparing responsitivity of the investigated PD with a reference photodiode. Measurements were performed when illuminating the PD with a radiation flux of a power of not over P=2,5·10^{-5} W; load resistance across the responsive element R_l= 10 kΩ, at the reverse bias voltages of V = 0-15 V and modulation frequency f=1 kGz. The spectral characteristic of PD responsivity ($S(\lambda)$) at different bias was obtained out using the KSVU-23 automated spectral complex.

RESULTS OF THE RESEARCH AND THEIR DISCUSSION

From the dark *I-V* characteristics of the PD, it was established that its dark current increases with increasing reverse-bias voltage. The diffusion [21] and surface generation [16] components of the dark current can be considered constant and unchanging with increasing bias, while the volume generation component (I^G_d) increases due to the expansion of the space charge region (SCR) with increasing voltage (2) [21], so in this case, it can be assumed that the current of the fabricated photodiode is determined by the volume generation current. At 0 V, the dark current reaches 6 pF with a depletion-layer width of W_i = 3–4 μm (3) [22]. The dark current does not reach saturation within the voltage range studied because, at these voltages, its SCR does not saturate (Fig. 3).

$$I_d^G = e\frac{n_i}{2\tau}W_i A_{RE} \tag{2}$$

where n_i is own concentration of charge carriers in the substrate; e is the charge of the electron; τ is life time of minor charge carrier.

$$W_i = \left(\frac{2\varepsilon\varepsilon_0(\phi_c - U_{bias})}{eN_A}\right)^{\frac{1}{2}} \tag{3}$$

where ε, ε_0 are dielectric constants for silicon and vacuum, respectively; φ_c is contact potential difference.

It should also be noted that the base material used and the photodiode's operating mode allowed us to achieve the peak of the PD`s spectral response at λ_m≈650-670 nm (Fig. 4). This indicates that this wavelength is characterized by the most efficient collection of minority charge carriers in the silicon bulk, since according to the Beer–Lambert–Bouguer law [23], the intensity of light decreases by a factor of 2.72 at a depth of about 3–4 μm (absorption coefficient $\alpha \approx 2.5\cdot10^3$-$3\cdot10^3$ cm^{-1} [16]), and for light of this wavelength to be absorbed almost completely (by 95–99%), a silicon thickness of about 10–15 μm is required. Accordingly, it can be assumed that the effective diffusion length of holes in the PD base reaches about L_P=5–10 μm, which ensures the effective collection of photogenerated carriers in a silicon layer equal to W_i+L_p [24], since the quantum efficiency (QE) of the photodiode is determined by the probability of radiation absorption in this thickness (4).

$$QE(\lambda) \approx 1 - e^{-\alpha(\lambda)\cdot(W_i + L_n)} \tag{4}$$

We also obtained the dependencies of the photodiode's current monochromatic sensitivities at the wavelengths under study (Fig. 5).

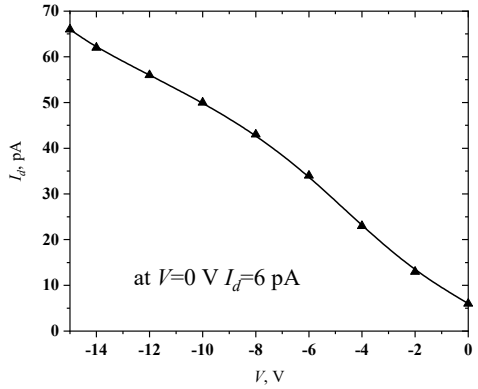

Figure 3. Dark *I-V* characteristic of the *p-n* PD

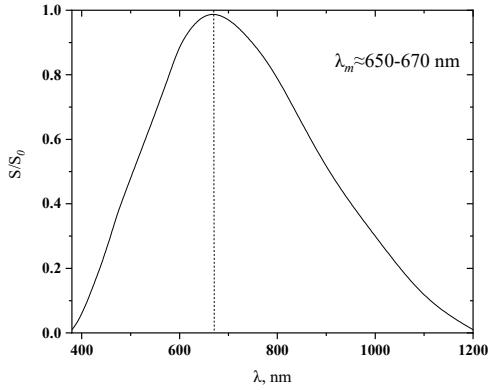

Figure 4. Relative spectral characteristic of the PD at V=0 V

Using these values, we determined the spectral characteristic of the quantum efficiency of the fabricated PD (Fig. 6) from the relationship between quantum efficiency and spectral sensitivity (5) [25]. It should be noted that in *p-n* PDs, as in the case under study, the photosensitivity is practically independent of voltage, since the effective collection region for photogenerated carriers increases minimally with an increase in reverse bias voltage due to the minimal resistivity, and the actual sensitivity of such PD is determined primarily by the diffusion length of the photogenerated charge carriers in the doped front zone and the base region.

Note, that the p^+-layer exhibits a gradual decrease in concentration as the depth of the p^+-n-junction increases; accordingly, the contribution of photogenerated charge carriers to the total sensitivity is significant. However, it should be noted that a significant amount of radiation is absorbed in the doped front p^+-region, so the PD`s *QE* in the visible range is less than 1 (Fig. 6).

$$S_\lambda = \frac{QE \cdot \lambda}{1.24} \tag{5}$$

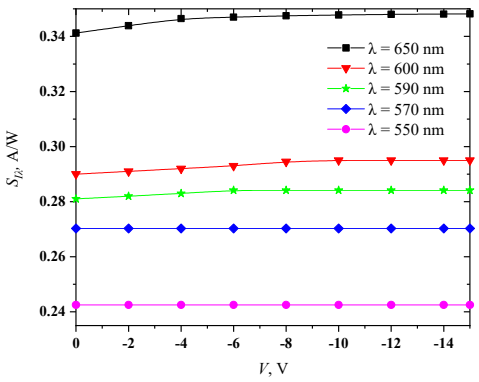

Figure 5. Dependence of the $S_{I\lambda}(V)$ of PDs

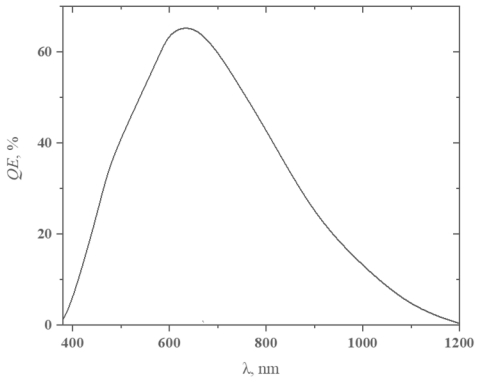

Figure 6. Spectral characteristic of the PD`s QE at V=0 V.

To evaluate the detection properties of the photodiodes, their specific detectivity (D^*) (6)[26] was determined. The fabricated photodiodes showed the highest detectivity at λ = 650 nm, since sensitivity is highest at this wavelength (Fig. 7). Furthermore, the detectivity decreases with increasing bias voltage due to the rise in dark current; however, at V = 0 V, the photodiodes exhibited a $D^* \approx 1.4$–2 cm·Hz$^{1/2}$ W^{-1}, which is a quite high value and can compete with analogues on the market.

$$D^* = \sqrt{\frac{A_{RE}}{2eI_d}} S_{I\lambda} \tag{6}$$

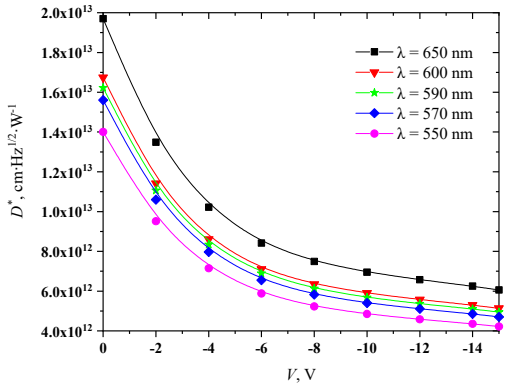

Figure 7. Dependence of the $D^*(V)$ of PDs

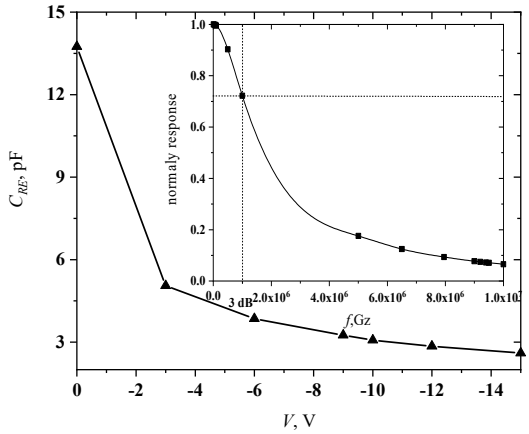

Figure 8. The *C-V* characteristic of a *p-n* photodiode and its amplitude-frequency response at 0 V (inset)

To evaluate the performance of the *p-n* photodiode, its *C-V* characteristics were investigated (Fig. 8). Based on the measured barrier capacitance, which is C_{RE} ≈14 pF at zero bias, the amplitude-frequency response of the sensor was calculated, taking into account a load resistance of 10 kΩ and a series base resistance of 150–200 Ω·cm. It was found that the cutoff frequency of the PD is 1MHz (τ_{RC}=150 ns) (Fig. 8 inset). Since the high value of the load resistance significantly exceeds the internal resistance of the base, the overall response of the structure in photogeneration mode without an external bias is entirely determined by the RC component of the circuit, while the contribution of the photon carrier transit time through the depleted region remains negligible.

The photodiodes produced can be used to measure a steady-state integral photocurrent. In addition to analyzing the steady-state spectral-energy characteristics, a crucial step in the comprehensive testing of the developed photodetector is the investigation of the photoluminescence decay kinetics of $AgInS_2$ and $CuInS_2$ quantum dots. Due to the dominant mechanism of donor-acceptor recombination, the lifetime of charge carriers in such triple nanostructures is abnormally long and typically lies in the microsecond range 100 ns — 1μs. Recording such relaxation processes in dynamic mode imposes stringent requirements on the response speed of the measurement circuit. Since the established cutoff frequency of the photodiode 1 MHz corresponds to a time constant of 150 ns, the developed system is capable of accurately recording long-duration kinetic decay curves, which opens up the prospect of its use in time-resolved photoluminescence spectroscopy.

Given that the PL spectra of the studied $AgInS_2$ nanocrystals cover a spectral range from 550 nm to 700 nm, depending on the In/Ag molar ratio (Fig. 1), an assessment of the photodetector's integral sensitivity for detecting this type of radiation was performed. By convolving the emission spectra of the QDs with the experimental curve of the PD`s relative spectral sensitivity at S_m = 0.34 A/W at a maximum of λ=650–670 nm, it was established that the device's integral sensitivity is 0.32 A/W for long-wavelength samples and gradually decreases to 0.26 A/W for short-wavelength samples. Since the output optical power of quantum dot luminescence is in the range of P=0.29–0. 35 mW, this level of integral sensitivity ensures the generation of a reliable photocurrent of ~75–110 μA, allowing for reliable signal detection without the risk of QDs photodegradation due to excessive excitation.

CONCLUSIONS

High-efficiency silicon *p-n* photodiodes have been developed with a spectral range optimized for detecting the luminescence of $AgInS_2$ and $CuInS_2$ quantum dots (550-700 nm). The detector's operation in zero-bias mode ensures a low dark current (~ 6 pA) and high system detectivity (1.4–2 cm·Hz$^{1/2}$ W^{-1}). With a response rate of 150 ns, the developed module is a reliable tool both for stationary radiometry of QDs emissions with power in the range of 0.29–0.35 mW, as well as for analyzing their microsecond decay kinetics.

Acknowledgments

This work was partially supported by the Ministry of Education and Science of Ukraine (grant number 0126U002507); YK is supported by MESU grant 0126U002293.

ORCID ID

Mykola S. Kukurudziak, https://orcid.org/0000-0002-0059-1387; **Vasylyna V. Kopach,** https://orcid.org/0009-0004-7927-983X
Serhii A. Voitovych, https://orcid.org/0000-0001-9141-808X; **Yuriy B. Khalavka,** https://orcid.org/0000-0002-6832-447X
Mykola S. Solodkyi, https://orcid.org/0000-0001-7432-9202

REFERENCES

[1] X. Sui, J.R. Downing, M.C. Hersam, and J. Chen, Materials Today, **48**, 135-154 (2021). https://doi.org/10.1016/j.mattod.2021.02.001
[2] Ya.O. Linevych, and V.M. Koval, Microsystems, Electronics and Acoustics, **27**(2), 264376–1 (2022). https://doi.org/10.20535/2523-4455.mea.264376
[3] E. Benavente, M. Alegría, P. Cortés, J. Aliaga, R. Villarroel, D. Guzmán, L. and Ballesteros, G., Journal of Environmental Chemical Engineering, **11** (3), 110025 (2023). https://doi.org/10.1016/j.jece.2023.110025
[4] Freeman, R., and Willner, I., Chem. Soc. Rev. **41**, 4067-4085 (2012). https://doi.org/10.1039/C2CS15357B
[5] X. Gao, X. Liu, Z. Lin, S. Liua, and X. Su. Analyst, **137**, 5620-5624 (2012). https://doi.org/10.1039/C2AN35888C
[6] A.S. Fuhr, H.J. Yun, N.S. Makarov, H. Li, H. McDaniel, and V.I. Klimov, ACS Photonics, **4**(10), 2425-2435 (2017). https://doi.org/10.1021/acsphotonics.7b00560
[7] Liu J., Zhao X., Xu H., Wang Z., and Dai Z. Anal Chem. **91**(14), 8987-8993 (2019). https://doi.org/10.1021/acs.analchem.9b01183
[8] I. Fodchuk, A. Kuzmin, O. Maslyanchuk, I. Hutsuliak, M. Solodkyi, Y. Roman, M. Solovan, and O. Gudymenko, Physics and Chemistry of Solid State, **23**(1), 114-149 (2022). https://doi.org/10.15330/pcss.23.1.144-149
[9] T. Xue, Y. Shi, J. Guo, M. Guo, and Y. Yan, Vacuum, **193**, 110514 (2021). https://doi.org/10.1016/j.vacuum.2021.110514
[10] V. Kopach, Y. Khalavka, Y. Yosypenko, N. Doskaliuk, O. Kopach, M. Dmytruk, I. Dmytruk, *et al*., Luminescence, **39**(10), e70001 (2024). https://doi.org/10.1002/bio.70001
[11] S.J. van der Sar, S.E. Brunner, and D.R. Schaart, Medical Physics, **48**(10), 6324-6338 (2021). https://doi.org/10.1002/mp.14886
[12] J. Jegal, H.W. Park, and H.J. Kim, IEEE Transactions on Nuclear Science, **68**(6), 1304-1308 (2021). https://doi.org/10.1109/TNS.2021.3070040
[13] M.S. Kukurudziak, E.V. Maistruk, R. Yatskiv, I.P. Koziarskyi, and D. P. Koziarskyi, Journal of Physics D: Applied Physics, **58**(16), 165106 (2025). https://doi.org/10.1088/1361-6463/adbd4d
[14] V.G. Verbitskiy, V.S. Antonyuk, A.O. Voronko, L.M. Korolevych, D.V. Verbitskiy, and D.O. Novikov, Journal of Nano- and Electronic Physics, **13**(4), 1-6 (2021). https://doi.org/10.21272/jnep.13(4).04029
[15] A. Voronko, D. Novikov, and O. Shymanovskyi, Radioelectronics and Communications Systems, **66**(2), 74-84 (2023). https://doi.org/10.3103/S073527272302005X
[16] M.S. Kukurudziak, Journal of Instrumentation, **19**(09), P09006 (2024). https://doi.org/10.1088/1748-0221/19/09/P09006
[17] S.M. Sze, and K.K. Ng, *Physics of semiconductor devices*, (Wiley, 2006).
[18] S.B. Khan, S. Irfan, Z. Zhuanghao, and S.L. Lee, Materials, **12**(9), 1483 (2019). https://doi.org/10.3390/ma12091483

[19] H. B. Zhang, W. Q. Li, and D. W. Wu, J. Electron Microsc. **58**(1), 15–19 (2009). https://doi.org/10.1093/jmicro/dfn024
[20] N. Akchurin, G. Altopp, B. Burkle, W.D. Frey, U. Heintz, N. Hinton, M. Hoeferkamp, *et al*., Journal of Instrumentation, **18**, P08001 (2023). https://doi.org/10.1088/1748-0221/18/08/P08001
[21] K.V. Ravi, *Imperfections and impurities in semiconductor silicon*, (Wiley, New York, 1981).
[22] A.V. Fedorenko, Technology and design in electronic equipment, **17**(3–4), 17 (2020). https://doi.org/10.15222/TKEA2020.3
[23] A.V. Igo, Opt. Spectrosc. **128**, 1125 (2020). https://doi.org/10.1134/S0030400X20080135
[24] M.S. Kukurudziak, and E.V. Maistruk, East Eur. J. Phys. **1**, 386 (2024). https://doi.org/10.26565/2312-4334-2024-1-39
[25] F. Alghannam, N.S. Alharthi, & M. Alayed, Frontiers in Physics, **13**, 1563838 (2025). https://doi.org/10.3389/fphy.2025.1563838
[26] S.N. Moger, and M. Mahesha, Sensors and Actuators A: Physical, **315**, 112294 (2020). https://doi.org/10.1016/j.sna.2020.112294

ВИСОКОЧУТЛИВИЙ КРЕМНІЄВИЙ ФОТОДІОД ІЗ НУЛЬОВИМ ЗМІЩЕННЯМ ДЛЯ ВИЯВЛЕННЯ ВИПРОМІНЮВАННЯ ЕКОЛОГІЧНО БЕЗПЕЧНИХ КВАНТОВИХ ТОЧОК $AgInS_2$ ТА $CuInS_2$ †

Микола С. Кукурудзяк[1,2], Василина В. Копач[1], Сергій А. Войтович[3], Юрій Б. Халавка[1], Микола С. Солодкий[1]
[1]Чернівецький національний університет імені Юрія Федьковича, 58002, м. Чернівці, вул. Коцюбинського, 2, Україна
[2]АТ «Центральне конструкторське бюро Ритм», 58032, м. Чернівці, вул. Головна, 244, Україна
[3]Івано-Франківський національний медичний університет, 76018, м. Івано-Франківськ, вул. Галицька, 2, Україна

Розроблено та виготовлено кремнієві *p-n* фотодіоди, оптимізовані для детектування широкого спектра фотолюмінесцентного випромінювання квантових точок $AgInS_2$ та $CuInS_2$. Завдяки коригуванню технологічних режимів виготовлення структури та прецизійному вибору базового матеріалу, максимум спектральної чутливості сенсора (0.34 А/Вт) повністю узгоджено з діапазоном емісії нанокристалів (550-700 нм). Для забезпечення максимальної роздільної здатності визначено роботу детектора в режимі нульового зміщення. Це дозволило мінімізувати темновий струм до значення близько 6 пА, зменшити теплові шуми й досягти високої детективності вимірювальної системи. Експериментально встановлено, що за опору навантаження 10 кОм гранична частота фотодіода становить 1МГц і повністю лімітується *RC*-постійною кола. Такий частотний відгук є цілком достатнім не лише для стаціонарної радіометрії колоїдів і плівок із потужністю випромінювання 0.29-0.35 мВт, а й для точного дослідження мікросекундної кінетики затухання люмінесценції квантових точок без ризику їхньої фотодеградації.

Ключові слова: *квантові точки; $AgInS_2$; $CuInS_2$; детектор; чутливість; фотодіод*

EAST EUROPEAN JOURNAL OF PHYSICS. 3. 286-291 (2026)
DOI:10.26565/2312-4334-2026-3-23 ISSN 2312-4334

TCAD-BASED CAPACITANCE ANALYSIS FOR IDENTIFYING LONGITUDINALLY LOCALIZED OXIDE-TRAPPED CHARGE IN SOI FinFETS

Mirzabaxhrom Foziljonov[1], Biloliddin M. Ergashev[2]*, Nuritdin Y. Yunusaliyev[1], Masudjon Norbutayev[3], Kumush Orinboyeva[2]
[1]*Andijan State University named after Z.M. Babur, Andijan, Uzbekistan*
[2]*Andijan State Pedagogical Institute, Dostlik Street 4, Andijan 170100, Uzbekistan*
[3]*Fergana State Technical University, Fergana Street 86, Fergana 150107, Uzbekistan*
**Corresponding Author e-mail: biloliddiner@gmail.com*
Received March 31, 2026; revised June 17, 2026; accepted June 23, 2026

This study examines the effect of the spatial position of locally trapped oxide charge on the gate-to-source and gate-to-drain capacitances of an SOI FinFET using three-dimensional TCAD Sentaurus simulations. The results reveal that the location of the trapped charge strongly influences the gate-to-source capacitance via charge-carrier redistribution near the channel surface, whereas a distinct response is observed when the trapped charge is near the oxide edge. Moreover, the gate-drain-to-gate-source capacitance ratio varies systematically with the trapped-charge position along the channel, suggesting that this parameter can serve as a reliable electrical indicator for detecting oxide-trapped charge and estimating its spatial distribution in FinFET devices.
Keywords: *SOI FinFET; Oxide trapped charge; Gate-source capacitance; Gate-drain capacitance; Charge distribution; TCAD simulation*

INTRODUCTION

Metal–oxide–semiconductor field-effect transistors (MOSFETs), particularly Fin field-effect transistors (FinFETs), are highly susceptible to various electrical stresses and radiation-induced effects during operation, which may degrade their electrical characteristics. Among the most significant degradation mechanisms are hot-carrier injection [1-3], bias temperature instability [4], off-state stress, and radiation-induced charge buildup [5]. These effects arise primarily from charge injection into, or generation within, the oxide layer and at the semiconductor–oxide interface. Since such degradation directly influences the performance and reliability of analog and digital integrated circuits, its impact must be carefully considered in modern device design. Oxide-trapped charge can alter key MOSFET parameters, including the threshold voltage, subthreshold swing, and transconductance, thereby deteriorating the overall device performance. For this reason, the development of reliable methods for identifying the localization and spatial distribution of trapped charge along the channel is of considerable importance. One of the simplest and fastest diagnostic approaches for detecting charge trapped in the oxide or at the interface is based on capacitance–voltage measurements of lateral source(dr.)-channel p–n junctions [6-9]. Previous studies have shown that a nonuniform charge distribution in the oxide layer or at the semiconductor–oxide interface is reflected in the electrical behavior of source–channel and drain–channel p–n junctions. Therefore, the longitudinal distribution of trapped charge along the channel should also affect other capacitances associated with these lateral junctions [10–12]. In the present work, this approach, originally proposed for planar MOSFETs, is adapted for application to SOI FinFET structures. The underlying concept is based on the sensitivity of lateral source–channel and drain–channel p–n junction capacitances to oxide- and interface-trapped charge [13–14]. Accordingly, the most suitable electrical configuration for such an analysis is one in which the capacitance of the lateral source–channel (drain–channel) p–n junction, $C_{p\text{-}n}$ makes a substantial contribution to the measured total capacitance. In SOI FinFETs, one of the relevant configurations satisfying this condition is the gate–source (or gate–drain) connection, as illustrated in Fig. 1.

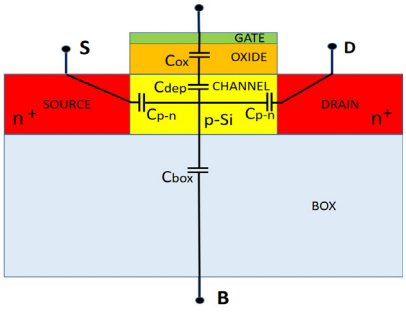

Figure 1. Cross-section of the simulated SOI FinFET with capacitances between contacts

Cite as: M. Foziljonov, B.M. Ergashev, N.Y. Yunusaliyev, M. Norbutayev, K. Orinboyeva, East Eur. J. Phys. 3, 286 (2026), https://doi.org/10.26565/2312-4334-2026-3-23

The gate–source and gate–drain configurations in the considered SOI FinFET can be represented by a series combination of three capacitance components: the gate-oxide capacitance C_{ox}, the depletion-layer capacitance at the oxide–semiconductor interface C_{dep}, and the source–channel p–n junction capacitance C_{p-n}. Among these contributions, C_{dep} becomes significant only when the device operates in the depletion regime. In the present analysis, however, only the barrier capacitance of the source–channel p–n junction is considered. To satisfy this condition, a positive voltage is applied to the n-type source with respect to the gate, thereby establishing carrier accumulation near the oxide-semiconductor interface. Under such bias conditions, the contribution of the depletion-layer capacitance can be neglected, and the total gate–source capacitance is determined predominantly by the series coupling between C_{ox} and C_{p-n}. Accordingly, the resulting capacitance can be written as

$$C_{gs} = \frac{C_{p-n} \cdot C_{ox}}{C_{p-n} + C_{ox}} \tag{1}$$

where C_{ox} denotes the gate-oxide capacitance per unit area and is essentially independent of the applied voltage.

Since the estimated depletion width of the source–channel (or drain–channel) p–n junction is about 0.1 μm, whereas the gate-oxide thickness is only t_{ox}=2.5 nm, the junction capacitance C_{p-n} remains much smaller than C_{ox}. As a consequence, the equivalent capacitance C_{gs} is governed mainly by C_{p-n}, making it highly sensitive to electrostatic perturbations associated with oxide-trapped charge. This feature is particularly important for charge-diagnostics applications, because any local trapped charge in the oxide modifies the potential distribution in the channel region and, in turn, alters the depletion characteristics of the lateral p–n junction. Therefore, variations in C_{gs} can be directly related to the spatial localization of trapped charge along the channel. On this basis, the present work focuses on simulating the dependence of C_{gs} on the position of a local oxide-trapped charge in the SOI FinFET structure.

MATERIALS AND METHODS

Three-dimensional numerical simulations were performed using the Advanced TCAD Sentaurus platform to investigate the effect of localized oxide-trapped charge on the capacitance characteristics of an SOI FinFET structure. The capacitance–voltage (C-V) response of the gate–source and gate–drain configurations was analyzed using a small-signal AC simulation at 1 MHz. This method was selected because it provides a reliable means of evaluating capacitance variations caused by local electrostatic perturbations in nanoscale transistor structures.

The geometry of the simulated SOI FinFET is illustrated in Fig. 2. The gate length, L_{gate}, was fixed at 25 nm, while the gate oxide thickness was taken as 2.5 nm. The silicon channel thickness, T_{Si}, and buried oxide thickness, T_{box}, were set to 30 nm and 100 nm, respectively. The channel width was chosen as 12 nm. The active channel region was assumed to be p-type silicon with a doping concentration of 1×10^{15} cm^{-3}. These geometrical and doping parameters were selected to represent a realistic SOI FinFET structure suitable for analyzing the sensitivity of gate-related capacitances to trapped-charge effects.

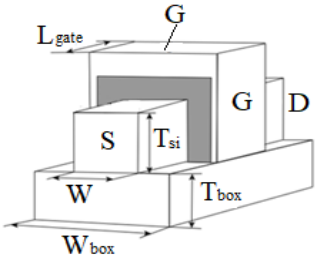

Figure 2. 3D structure of the simulated SOI FinFET

The gate–source capacitance, C_{gs}, was simulated for different positions of a localized trapped charge in the oxide layer, with the position defined by the distance between the center of the charged region and the source–channel boundary. It should be noted that L does not represent the depth of the trapped charge across the oxide thickness. In all simulations, the localized charged region remains embedded inside the gate oxide, while only its longitudinal position along the channel direction is varied. Thus, L is measured from the source–channel boundary to the center of the charged region along the source-to-drain direction. The case L=2.5 nm corresponds to the position where the 5 nm-long charged region touches the source-side edge of the gate oxide, and it does not imply that the charge is located inside the semiconductor. The local oxide-trapped charge was modeled as a uniformly charged region embedded in the oxide. The charge density in this region was set to 10^{12} cm^{-2} (equivalent to 4×10^{18} cm^{-3}), which is a physically reasonable value for trapped charge that may occur in MOSFET structures under electrical or radiation-induced stress conditions. The characteristic size of the local charged region along the channel direction was fixed at d = 5 nm.

Since the depletion width of the lateral source–channel (drain–channel) p–n junction exceeds the channel length, a local trapped charge situated at a distance L from the source–channel junction can appreciably modify the carrier distribution inside the channel [15,16]. This electrostatic perturbation is expected to affect the junction capacitance and, consequently, the overall C–V behavior of the gate–source connection. Owing to the structural symmetry of the FinFET with respect to the channel center, the gate–source and gate–drain capacitances are expected to exhibit equivalent behavior

under symmetric conditions. For this reason, the present analysis is focused primarily on the gate–source capacitance, while the behavior of the gate–drain capacitance can be inferred from the device symmetry.

RESULTS AND DISCUSSION

The simulated C–V characteristics of the gate–source capacitance, C_{gs}, are presented in Fig. 3. In Fig. 3, each curve corresponds to a different longitudinal position L of the localized oxide-trapped charge. Here, L denotes the distance from the source–channel boundary to the center of the localized charged region along the channel direction. The reference curve corresponds to the case without trapped charge, while the other curves represent different values of L, as indicated in the legend. As can be observed, the capacitance behavior is strongly influenced by the position of the local oxide-trapped charge along the channel. At relatively high applied voltages, C_{gs} exhibits a pronounced and nearly monotonic dependence on the trapped-charge location, indicating that the electrostatic effect of the localized charge becomes increasingly important under these bias conditions. This trend is more clearly illustrated in Fig. 4, where the capacitance is plotted as a function of the distance L. An exceptional behavior is observed for the case L = 2.5 nm (point B in Fig. 4). This deviation from the general monotonic trend can be attributed to the fact that, at this position, the local charged region comes into direct contact with the edge of the oxide layer. Such a configuration modifies the local electrostatic environment differently from the other trapped-charge positions and leads to a distinct capacitance response. Therefore, although the overall trend confirms a systematic dependence of C_{gs} on the trapped-charge position, the oxide-edge case should be considered separately due to its specific geometrical and electrostatic conditions.

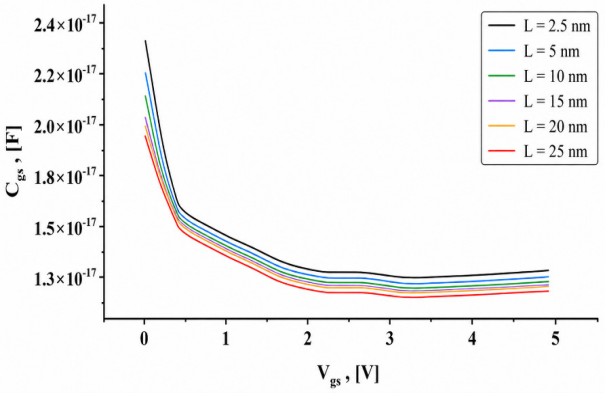

Figure 3. C–V characteristics of the gate–source capacitance, C_{gs}, for different longitudinal positions L of the localized oxide-trapped charge in the gate oxide. The reference curve corresponds to the case without a trapped charge. The legend indicates the corresponding L value for each curve

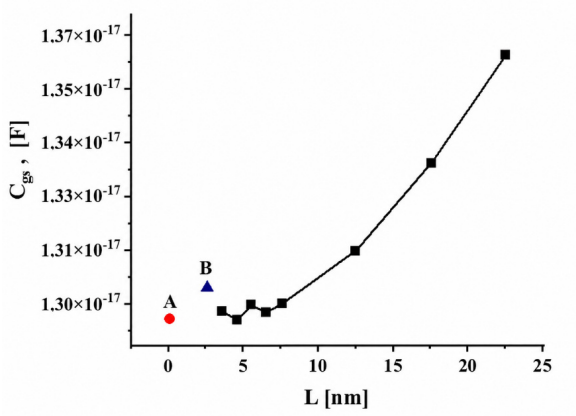

Figure 4. Figure 4. Dependence of C_{gs} on the longitudinal position L of the localized oxide-trapped charge at V_{gs}=4.5 V. Point A corresponds to the reference case without trapped charge, whereas point B corresponds to L=2.5 nm, where the localized charged region touches the source-side edge of the gate oxide

The increase in C_{gs} is attributed to the influence of locally trapped charge in the oxide on the channel carrier concentration. To avoid ambiguity in charge localization, Fig. 5 includes a schematic inset showing the gate oxide, the silicon channel, the source–channel boundary, and the longitudinal positions of the localized trapped charge under investigation. The grey region represents the localized charged domain embedded inside the gate oxide. During the simulation, this charged region is shifted only along the channel direction, whereas its position across the oxide thickness is kept fixed. As shown in Fig. 5, the presence of trapped charge in the oxide layer increases the electron concentration near the channel surface, thereby increasing the gate–source capacitance. From a physical perspective, this behavior reflects the sensitivity of capacitance to charge redistribution in the near-surface region of the channel. By definition, the capacitance can be expressed as follows:

$$C_{gs} = dQ_V/dV. \quad (2)$$

Here, dQ_V represents the change in charge stored in the Cgs capacitance in response to a change in applied voltage, dV.

When a local charge is trapped in the gate oxide, the electron concentration in the channel is modified, which gives rise to an additional charge variation, denoted as dQ_{LC}, in the gate–source capacitance. Consequently, Eq. (2) can be reformulated as follows:

$$C_{gs} = (dQ_V + dQ_{LC})/ dV. \quad (3)$$

This expression explains the increase observed in the gate–source capacitance, C_{gs}, as a consequence of the additional charge redistribution induced by the localized oxide-trapped charge. In the simulated SOI FinFET structure, the maximum variation of C_{gs} caused by the localized trapped charge is approximately 5%. Although this magnitude of variation may appear moderate and does not necessarily indicate severe degradation of the transistor's static current–voltage characteristics, it remains physically meaningful and important for capacitance-based defect diagnostics. The

significance of this variation lies in its systematic dependence on the longitudinal position of the trapped charge. In other words, the change in C_{gs} is not random but follows a clear trend as the localized charge is shifted along the channel. Such a position-dependent capacitance response indicates that the gate–source capacitance is sensitive to local electrostatic perturbations caused by oxide-trapped charge. Therefore, even a several-percent change in capacitance can serve as an electrical signature for detecting localized trapped charge and estimating its approximate position along the channel.

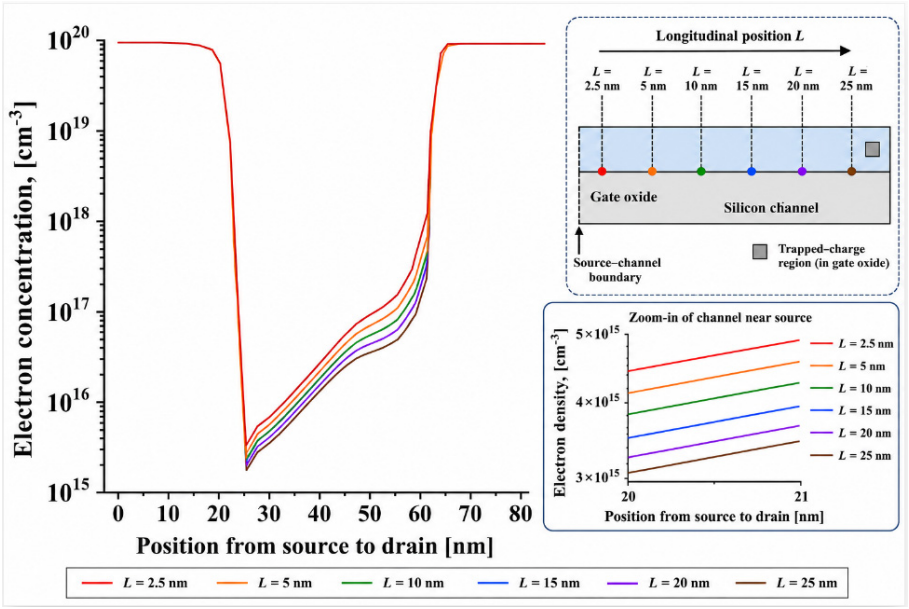

Figure 5. Electron density distribution along the channel at a depth of 2 nm from the channel surface for different longitudinal positions L of the localized oxide-trapped charge. The inset schematically shows the investigated charge positions inside the gate oxide; the charged region remains embedded in the oxide and is shifted only along the source-to-drain direction.

From a device-operation perspective, gate-related capacitances in nanoscale FinFETs contribute to parasitic capacitance, small-signal response, signal delay, and switching behavior. Therefore, a 5% variation in C_{gs} may become relevant in highly scaled devices and in circuits where capacitance matching, transient response, or high-frequency performance is important. However, in the context of the present work, the observed variation should primarily be interpreted not as evidence of catastrophic transistor degradation, but as a measurable and reproducible diagnostic indicator of localized oxide-trapped charge. Thus, the results demonstrate that capacitance variations of this magnitude can be useful for reliability monitoring and defect localization analysis in SOI FinFET structures.

At position L= 2.5 nm of the oxide trapped charge the configuration of the capacitance C_{gs} is changed because the local charge will be in contact with the end of the oxide layer (Fig. 6). In this case the electron density in the channel surface will be redistributed which result in sufficiently increasing the capacitance C_{gs} more than in unbiased case and relatively capacitances corresponding to other positions (Fig. 3). At high applied voltages the redistribution of the carrier densities leads to increasing the C_{gs} with increasing L (Fig. 7).

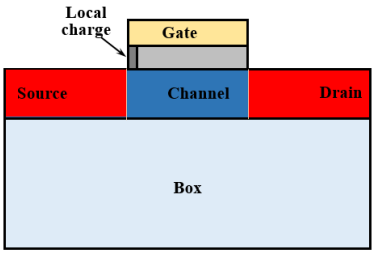

Figure 6. Cross-section of the FinFET with a local charge trapped in the oxide, which is located at the end of the oxide layer. L=2.5 nm.

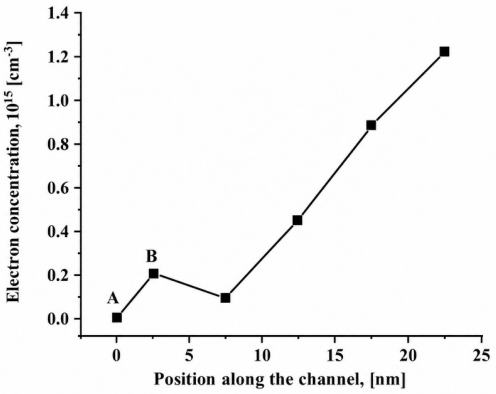

Figure 7. The change in electron density in the channel at a depth of 2 nm from the surface traps local charge in the oxide layer at different positions. A is point is the case without trapped charge, and B is the position with L=2.5 nm

Owing to the structural symmetry of the FinFET, the dependence of the gate–drain capacitance, C_{gd}, on the trapped-charge position L is expected to exhibit a trend opposite to that of the gate–source capacitance, C_{gs}. In other words, as L

increases, C_{gd} decreases, as illustrated in Fig. 8. The positional dependences of both C_{gs} and C_{gd} can therefore be utilized to estimate the location of the oxide-trapped charge along the channel. In this context, the ratio C_{gs}/C_{gd} provides a particularly convenient diagnostic parameter, as shown in Fig. 9. It can be seen that when the trapped charge is located on the source side of the channel center, the ratio C_{gs}/C_{gd} is less than unity, whereas it becomes greater than unity when the trapped charge is positioned on the drain side. If the trapped charge is located at the channel center, the ratio C_{gs}/C_{gd} approaches unity.

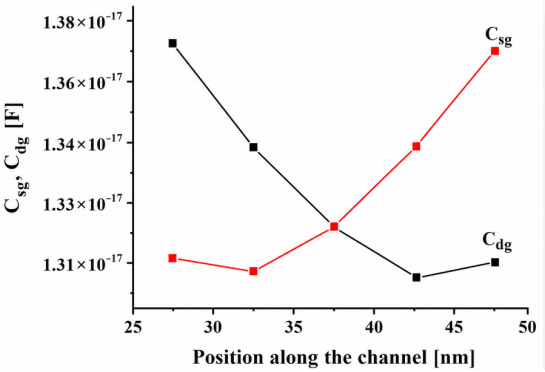

Figure 8. C_{gs} and C_{gd} dependence on the position of the local oxide trapped charge along the channel

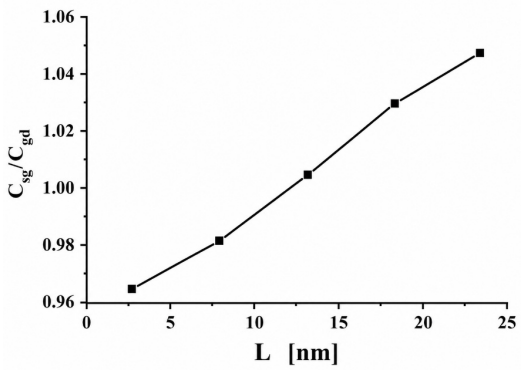

Figure 9. The ratio C_{gs}/C_{gd} dependence on the position of the local oxide trapped charge along the channel

CONCLUSIONS

In this work, the influence of a local oxide-trapped charge on the gate-source and gate-drain capacitances of an SOI FinFET was systematically analyzed using 3D TCAD simulations with the small-signal AC method. The results show that the gate-source capacitance increases monotonically as the trapped charge shifts from the source-side region toward the channel center, except when the charge is positioned at the oxide edge. This behavior is governed by the redistribution of electron concentration near the channel surface induced by the trapped charge. Owing to the device's structural symmetry, the gate-drain capacitance shows the opposite trend, while the Cgs/Cgd ratio varies regularly with the trapped-charge position along the channel. These findings confirm that even a moderate, approximately several-percent variation in gate-related capacitance can serve as a useful diagnostic indicator for identifying localized oxide-trapped charge and estimating its longitudinal position in SOI FinFET structures.

ORCID

M. Foziljonov, https://orcid.org/0009-0005-0073-1713; **N. Yunusaliyev**, https://orcid.org/0009-0002-5714-8658;
M. Norbutayev, https://orcid.org/0000-0003-0471-2593; **B.M. Ergashev**, https://orcid.org/0009-0007-9392-6548;
K. Orinboyeva, https://orcid.org/0009-0000-7677-3964

REFERENCES

[1] J. Martín-Martínez, S. Gerardin, E. Amat, R. Rodríguez, M. Nafría, X. Aymerich, et al., "Channel-Hot-Carrier Degradation and Bias Temperature Instabilities in CMOS Inverters" IEEE Transactions on Electron Devices, **56**, 2155–2159 (2009). https://doi.org/10.1109/TED.2009.2026206

[2] Z. Yu, Z. Zhang, Z. Sun, R. Wang and R. Huang, "On the Trap Locations in Bulk FinFETs After Hot Carrier Degradation (HCD)" IEEE Transactions on Electron Devices, **67**, 3005–3009 (2020). https://doi.org/10.1109/TED.2020.2994171

[3] S. Zaynabidinov, A. Boboev, A. Xakimov, et al. "Thermal evolution of impurity-induced energy levels in platinum-doped silicon", in: *Proc. SPIE 14126, Third International Conference on Optics, Materials Science, and Computing in Condensed-Matter Physics (OMCCP-2025)*, 141260E, 69-74 (2026); https://doi.org/10.1117/12.3110009

[4] B. Kaczer, T. Grasser, P. J. Roussel, J. Franco, R. Degraeve, L. A. Ragnarsson, E. Simoen, *et al*., "Origin of NBTI Variability in Deeply Scaled pFETs" in: *IEEE International Reliability Physics Symposium Proceedings*, (2010), pp. 26–32. https://doi.org/10.1109/IRPS.2010.5488856

[5] A. Y. Boboev, B. M. Ergashev, N. Y. Yunusaliyev, and J. S. Madaminjonov, "Electrophysical Nature of Defects in Silicon Caused by Implanted Platinum Atoms," East European Journal of Physics. (2), 431–435 (2025). https://doi.org/10.26565/2312-4334-2025-2-53

[6] I. Chatterjee, E. X. Zhang, B. L. Bhuva, M. A. Alles, R. D. Schrimpf, D. M. Fleetwood, *et al*., "Bias Dependence of Total-Dose Effects in Bulk FinFETs" IEEE Transactions on Nuclear Science, **60**, 4476–4482 (2013) https://doi.org/10.1109/TNS.2013.2287872

[7] N.-H. Lee, H. Kim, and B. Kang, "Impact of Off-State Stress and Negative Bias Temperature Instability on Degradation of Nanoscale pMOSFET" IEEE Electron Device Letters, **33**(2), 137–139 (2012). https://doi.org/10.1109/led.2011.2174026

[8] A. E. Atamuratov, A. Yusupov, and K. Adinaev, "Experimental Assessment of the Nonuniform Radiation-Induced Space-Charge Distribution in the Surface Region of Silicon," Inorganic Materials, **37**(8), 767–768 (2001). https://doi.org/10.1023/a:1017918911606

[9] A. Y. Boboev, B. M. Ergashev, N. Y. Yunusaliyev, G. G. Tojiboyev, and F. A. Abdulkhaev, "SRIM Simulation of Cobalt Ions Interaction with ZnO-Based Thin Films" Journal of Ovonic Research. **21**(4), 481–493 (2025). https://doi.org/10.15251/JOR.2025.214.481

[10] E. A. Atamuratov, A. Yusupov, A. Z. Atamuratova, J. C. Chedjou, and K. Kyandoghere, "Lateral Capacitance–Voltage Method of NanoMOSFET for Detecting the Hot Carrier Injection," Applied Sciences, **10**(21), 7935 (2020). https://doi.org/10.3390/app10217935

[11] B. M. Ergashev, et al., "The effect of thermal treatment on the absorption spectra of background impurity (oxygen and carbon) atoms in p-Si< B, Pt> structures," in: *Third International Conference on Optics, Materials Science, and Computing in Condensed-Matter Physics (OMCCP-2025)*, vol. 14126, (SPIE, 2026). pp. 13-17.

[12] A. E. Atamuratov, D. U. Matrasulov, and P. K. Khabibullaev, "Detection of a Charge Built in the Oxide Layer of a Metal–Oxide–Semiconductor Field-Effect Transistor by Lateral C-V Measurement," Doklady Physics, **52**(6), 322–325 (2007). https://doi.org/10.1134/s1028335807060080

[13] A. Y. Boboev, B. M. Ergashev, N. Y. Yunusaliyev, and M. M. Xotamov, "Study of the Formation of Low-Dimensional Defect States in Single-Crystal Silicon with the Participation of Oxygen," East European Journal of Physics. (2), 299–306 (2025). https://doi.org/10.26565/2312-4334-2025-2-36

[14] I. Starkov, and A. S. Starkov, "Investigation of the Threshold Voltage Turn-Around Effect in Long-Channel n-MOSFETs Due to Hot-Carrier Stress," Microelectronics Reliability, **54**, 33–36 (2014). https://doi.org/10.1016/j.microrel.2013.08.015

[15] A. E. Abdikarimov, "The Influence of a Single Charged Interface Trap on the Subthreshold Drain Current in FinFETs with Different Fin Shapes," Technical Physics Letters, **46**(5), 494–496 (2020). https://doi.org/10.1134/s106378502005017x

[16] A. E. Atamuratov, M. M. Khalilloev, A. Yusupov, J. C. Chedjou, and K. Kyandoghere, "Contribution to the Physical Modelling of Single Charged Defects Causing the Random Telegraph Noise in Junctionless FinFET," Applied Sciences, **10**(15), 5327 (2020). https://doi.org/10.3390/app10155327; O.V. Kharissova, B.I. Kharisov, and U.O. Mendez, *Nanosilicon*, (CRC Press, 2014). pp. 57-136. https://doi.org/10.1201/b17170-5

АНАЛІЗ ЄМНОСТІ НА ОСНОВІ TCAD ДЛЯ ІДЕНТИФІКАЦІЇ ПОЗДОВЖНЬОГО ЛОКАЛІЗОВАНОГО ЗАРЯДУ, ЗАХОПЛЕНОГО ОКСИДОМ, У SOI FinFETS

Мірзабаххром Фозильонов[1], Білоліддін М. Ергашев[2], Нурітдін Ю. Юнусалієв[1], Масуджон Норбутаєв[3], Кумуш Орінбоєва[2]

[1]Андижанський державний університет імені З.М. Бабура, Андижан, Узбекистан

[2]Андижанський державний педагогічний інститут, вулиця Достлік, 4, Андижан 170100, Узбекистан

[3]Ферганський державний технічний університет, вулиця Фергана, 86, Фергана 150107, Узбекистан

У цьому дослідженні розглядається вплив просторового положення локально захопленого заряду оксиду на ємності затвор–виток та затвор–сток SOI FinFET за допомогою тривимірного моделювання в TCAD Sentaurus. Результати показують, що розташування захопленого заряду сильно впливає на ємність затвор-витік через перерозподіл носіїв заряду поблизу поверхні каналу, тоді як спостерігається чітка реакція, коли захоплений заряд розташований поблизу краю оксиду. Більше того, співвідношення ємностей затвор-стік до затвор-витік систематично змінюється залежно від положення захопленого заряду вздовж каналу, що свідчить про те, що цей параметр може служити надійним електричним індикатором для виявлення захопленого заряду в оксиді та оцінки його просторового розподілу в FinFET-пристроях.

Ключові слова: *SOI FinFET; захоплений заряд в оксиді; ємність затвор-витік; ємність затвор-стік; розподіл заряду; TCAD-моделювання*

East European Journal of Physics. 3. 292-297 (2026)
DOI:10.26565/2312-4334-2026-3-24 ISSN 2312-4334

BIDIRECTIONAL BAND GAP MODULATION IN ZnO-BASED THIN FILMS VIA CATION AND ANION-INDUCED LATTICE ENGINEERING

Javohir Sh. Khudoykulov[1]*, Shavkat U. Yuldashev[1,2], Azamat O. Arslanov[1], Jamoliddin X. Murodov[2], Andrey A. Nebesniy[1], Noiba U. Botirova[2], Ra'no Sh. Sharipova[2]
[1]*Department of Physics, National University of Uzbekistan, University Street 4, Tashkent 100174, Uzbekistan*
[2]*Center for Nanotechnologies Development, National University of Uzbekistan, University Street 4, Tashkent 100174, Uzbekistan*
**Corresponding Author email: xjavokhir1799@gmail.com*
Received April 13, 2026; revised June 22, 2026; accepted June 25, 2026

$Zn_{1-x}Mg_xO$ and $ZnO_{1-\gamma}S_\gamma$ thin films were synthesized by ultrasonic spray pyrolysis (USP) and investigated to achieve bidirectional band gap engineering in ZnO-based materials. X-ray diffraction confirmed a single-phase wurtzite structure with strong c-axis orientation for all samples. Mg incorporation induced a shift of the (002) peak toward higher angles, indicating lattice contraction, whereas S substitution caused a shift toward lower angles, corresponding to lattice expansion. UV–Vis analysis revealed a systematic blue shift of the band gap with Mg doping (from ~3.26 eV to ~3.33 eV) and a red shift with S incorporation (down to ~3.01 eV). These changes are attributed to lattice deformation and its influence on the electronic structure. Additionally, increased dopant concentration led to reduced crystallite size and increased microstrain and disorder. The results establish a clear correlation between lattice deformation and optical band gap modulation, demonstrating an effective approach for tuning ZnO-based thin films for optoelectronic applications.
Keywords: *ZnMgO; ZnOS; Band gap; Lattice deformation; Tauc plot; USP*

INTRODUCTION

ZnO is an II–VI semiconductor with a wide direct band gap of ~3.3 eV at room temperature and a large exciton binding energy (~60 meV), which makes it a promising material for optoelectronic applications such as ultraviolet (UV) lasers, light-emitting diodes, and photodetectors [1]. One of the most effective approaches to tailor its electronic and optical properties is alloying with suitable elements. In particular, Mg incorporation into ZnO leads to band gap widening due to the substitution of Zn^{2+} ions with smaller Mg^{2+} ions, resulting in lattice contraction and modification of the electronic band structure. This tunability is essential for the design of heterojunctions, quantum wells, and transparent optoelectronic devices [2].

In addition to cation substitution, anion substitution provides an alternative pathway for band-gap engineering. The incorporation of sulfur into ZnO ($ZnO_{1-\gamma}S_\gamma$) leads to lattice expansion due to the larger ionic radius of S^{2-} ions, typically resulting in band gap narrowing. Although ZnMgO and $ZnO_{1-\gamma}S_\gamma$ thin films have been widely studied using various deposition techniques, such as sol–gel processing, spray pyrolysis, pulsed laser deposition, and magnetron sputtering, a unified and quantitative understanding of the relationship among lattice deformation, microstructural disorder, and optical band gap modulation remains incomplete [3,4]. In particular, direct experimental comparison of cation- and anion-induced lattice effects within a single framework is still limited.

In this work, we systematically investigate the structural and optical properties of $Zn_{1-x}Mg_xO$ and $ZnO_{1-\gamma}S_\gamma$ thin films deposited on Si(100) substrates by ultrasonic spray pyrolysis (USP). X-ray diffraction (XRD) is employed to analyze crystal structure, lattice parameters, strain, and crystallite size, while UV–Vis spectroscopy is used to determine the optical band gap and Urbach energy [5]. By correlating lattice deformation with optical properties, this study aims to establish a comprehensive framework for bidirectional band gap engineering in ZnO-based thin films.

By combining qualitative figure analysis with the data, this study establishes a clear structure–property relationship, demonstrating how lattice contraction and expansion directly govern band gap widening and narrowing in ZnO-based alloys.

MATERIALS AND METHODS

ZnO-based thin films-undoped, Mg-doped (x = 0.05, 0.10), and S-doped (y = 0.05, 0.10) were deposited on Si(100) substrates by ultrasonic spray pyrolysis (USP). Aqueous precursor solutions were prepared from zinc acetate dihydrate, $Zn(C_2H_3O_2)_2{\cdot}2H_2O$ (0.5 mol/L). For Mg incorporation, magnesium acetate tetrahydrate, $(C_2H_3O_2)_2Mg{\cdot}4H_2O$, was added to achieve the desired Mg/(Zn+Mg) ratios; for S incorporation, thiourea, $SC(NH_2)_2$, was used as the sulfur source. Prior to deposition, Si(100) substrates were sequentially cleaned for 10 minutes each in hydrofluoric acid (10 % in DI) to remove the native SiO_2 layer, acetone and then ethanol to eliminate organic contaminants, followed by a final rinse in deionized (DI) water to remove residual species. All steps were performed under ultrasonic agitation to enhance cleaning efficiency [6-8]. Oxygen (O_2) at a flow of 500 sccm served as the carrier gas. The precursor aerosol was generated using a 1.7 MHz ultrasonic nebulizer and delivered to substrates maintained at 450 °C. After growth, all films were annealed at

Cite as: J.Sh. Khudoykulov, Sh.U. Yuldashev, A.O. Arslanov, J.X. Murodov, A.A. Nebesniy, N.U. Botirova, R.Sh. Sharipova, East Eur. J. Phys. 3, 292 (2026), https://doi.org/10.26565/2312-4334-2026-3-24

600°C for 15 minutes. The resulting thickness was approximately 200 nm. The experimental setup used in this work is illustrated in Figure 1. [10,11]

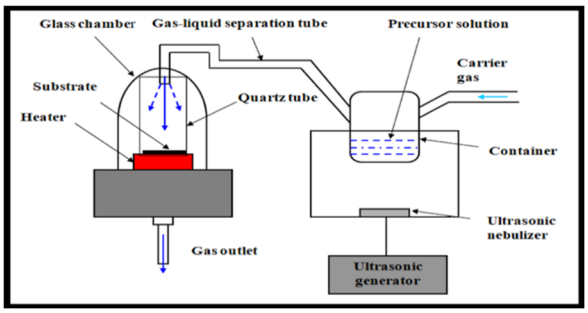

Figure 1. Scheme of Ultrasonic Spray Pyrolysis (USP)

Structural and optical characterization. X-ray diffraction (XRD) was carried out on a Rigaku MiniFlex diffractometer using Cu Kα radiation (λ = 1.5406 Å) over a 2θ range of 30°-60°. The average crystallite size was estimated from the full width at half maximum (FWHM) of the (002) reflection using the Scherrer relation. Optical absorption was measured with a UV-Vis spectrometer in the 300–500 nm wavelength range.[9] Surface morphology and grain structure were examined by field-emission scanning electron microscopy operated at 30 kV in secondary-electron mode using an Everhart–Thornley detector. Plan-view micrographs were spatially calibrated from the instrument pixel size (0.899 nm/px and 1.124 nm/px for the ZnMgO and ZnOS micrographs, respectively). Grain-size distributions were extracted by marker-controlled watershed segmentation, and the maximum Feret diameter was recorded for each grain (N ≥ 284 grains per sample); the distributions were described by a log-normal function.

RESULTS AND DISCUSSION

Figure 2 (a) shows the x-ray diffraction patterns of undoped ZnO and Mg doped $Zn_{1-x}Mg_xO$ thin films deposited on Si(100). All samples indicate a dominant diffraction peak corresponding to the (002) plane of hexagonal wurtzite ZnO, showing a strong preferential orientation along the c-axis. The absence of additional diffraction peaks related to MgO or other secondary phases confirms that Mg incorporation does not lead to phase segregation within the detection limit of XRD. With increasing Mg content, the (002) peak shifts slightly to higher 2θ values, indicating lattice contraction due to Mg substitution.[12]

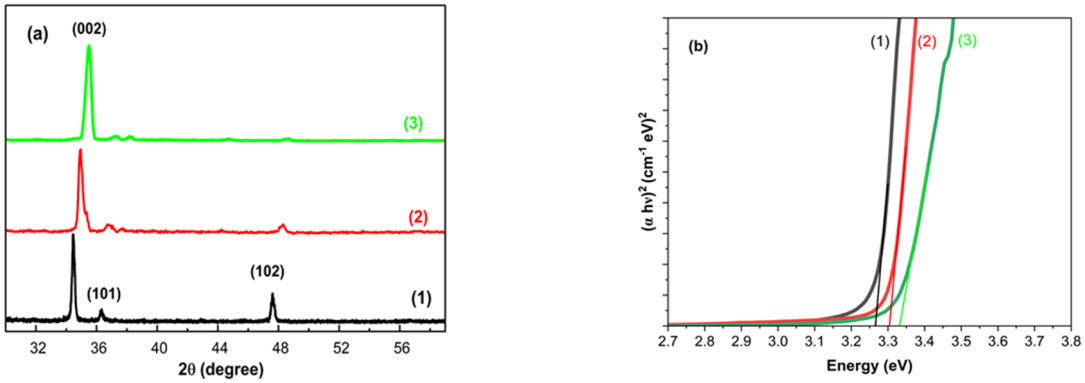

Figure 2. (a) XRD patterns and (b) Tauc plots of $Zn_{1-x}Mg_xO$ films grown on Si by USP; curves (1), (2), and (3) correspond to 0%, 5%, and 10% Mg, respectively

Figure 2 (b) shows the Tauc plots of $(\alpha h\nu)^2$ as a function of photon energy (hν) for undoped ZnO and Mg-doped $Zn_{1-x}Mg_xO$ thin films. The linear regions of the plots confirm that all films exhibit a direct allowed optical transition characteristic of the wurtzite ZnO crystal structure. As shown in Fig. 2(b), the absorption edge shifts progressively toward higher photon energies as the Mg concentration increases, indicating a systematic blue shift of the band gap. The extracted band gap values increase from 3.26 eV for undoped ZnO to 3.30 eV and 3.33 eV for 5% and 10% Mg-doped films, respectively, as summarized in Table 1. The observed band gap widening can be attributed to Mg-induced modification of the electronic band structure, which increases the energy separation between the conduction and valence bands [13].

Table 1. Some essential lattice parameters of ZnMgO thin film

Con. (%)	[002] (°)	FWHM (°)	c (Å)	E_g (eV)	D_{avg} (Å)	ε 10^{-3}	E_u (eV)
0	34.469	0.21541	5.199	3.26	340.55	3.03	0.180
5	34.949	0.34198	5.130	3.30	215.20	4.7	0.210
10	35.465	0.40687	5.058	3.33	150.821	5.5	0.235

The quantitative structural parameters extracted from Fig. 2(a) are summarized in Table 1 and provide strong support for the observed diffraction trends. As the Mg concentration increases from 0% to 10%, the (002) peak position shifts from 34.469° to 35.465°, confirming a continuous lattice contraction. Correspondingly, the calculated c-lattice parameter decreases significantly from 5.199 Å to 5.058 Å, which is consistent with Vegard's law behavior and reflects the smaller ionic radius of Mg^{2+} compared to Zn^{2+}. In addition to peak shifting, Fig. 2(a) shows noticeable peak broadening with increasing Mg content. This effect is quantified in Table 1 by the increase in full width at half maximum (FWHM) from 0.215° for pure ZnO to 0.407° for the 10% Mg-doped film.

The average crystallite size calculated from the (002) peak using the Debye–Scherrer equation:

$$D = 0.9\,\lambda / (\beta \cos\theta). \quad (1)$$

D_{avr} decreases dramatically from 340.55 Å to 150.82 Å as Mg concentration increases. This grain refinement is a direct consequence of Mg-induced strain and inhibited grain growth during film deposition. Despite this reduction in crystallite size, the films retain a strong c-axis orientation, indicating that Mg incorporation affects microstructural features without destroying overall crystallographic alignment.

The strain (ε) and dislocation density (δ) were calculated as:

$$\varepsilon = \beta / (4 \tan\theta),\ \delta = 1 / D^2. \quad (2)$$

The evolution of microstrain (ε) further supports this interpretation. As shown in Table 1, ε increases from 3.03×10^{-3} to 5.5×10^{-3} with Mg content, reflecting enhanced lattice distortion arising from ionic size mismatch and local compositional fluctuations. The simultaneous increase in Urbach energy (E_u) from 0.178 eV to 0.235 eV suggests an increase in localized states and structural disorder, which correlates well with the observed peak broadening and strain evolution. These calculations confirm that ZnMgO films possess nanocrystalline grains with low dislocation density, suitable for optoelectronic integration.

Figure 3 presents the structural and optical evolution of $ZnO_{1-x}S_x$ thin films as a function of sulfur concentration. Figure 3(a) shows the XRD patterns, while Fig. 3(b) displays the corresponding Tauc plots used to extract the optical band gap. As seen in Fig. 3(a), increasing sulfur concentration results in a progressive shift of the (002) diffraction peak toward lower diffraction angles. This behavior indicates an increase in the interplanar spacing along the c-axis, suggesting lattice expansion induced by sulfur incorporation. The absence of secondary phases in the diffraction patterns confirms that sulfur is incorporated into the ZnO lattice without forming separate sulfide phases. The qualitative trends observed in Fig. 3(a) are quantitatively supported by the data summarized in Table 2. The c-axis lattice parameter increases systematically from 5.1999 Å for undoped ZnO to 5.2928 Å for 10% S, confirming a clear expansion of the wurtzite lattice. This lattice dilation originates from the substitution of O^{2-} ions by larger S^{2-} ions, which introduces tensile strain along the growth direction.

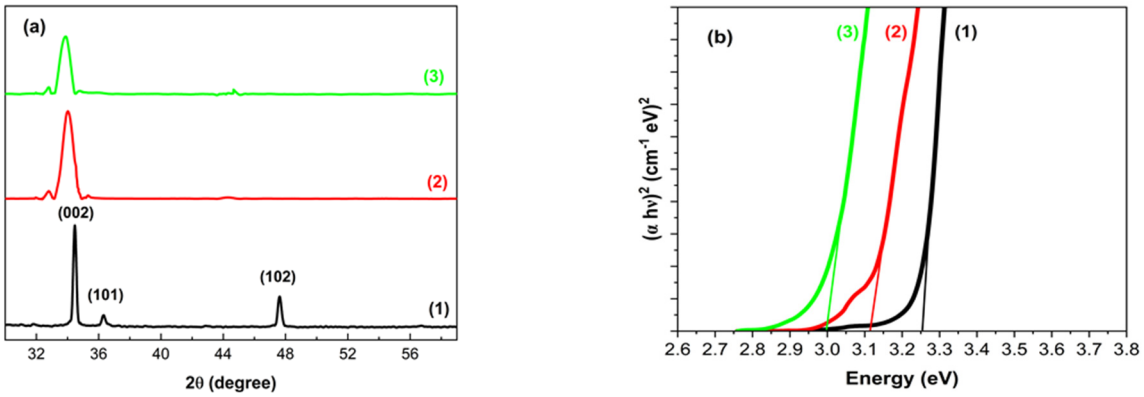

Figure 3. (a) XRD patterns and (b) Tauc plots of $ZnO_{1-x}S_x$ films grown on Si by USP; curves (1), (2), and (3) correspond to 0%, 5%, and 10%, respectively

Accordingly, Fig. 3(b) shows a continuous red shift in the optical absorption edge as the sulfur concentration increases. The extracted band gap values decrease from 3.26 eV (0%) to 3.01 eV (10%), as listed in Table 2.

Table 2. Some essential lattice parameters of ZnOS thin film

Con. (%)	[002] (°)	FWHM	c (Å)	E_g (eV)	D_{avg} (Å)	ε 10^{-3}	E_u (eV)
0	34.4696	0.21541	5.1999	3.26	340.55	3.03	0.180
5	34.0322	0.68788	5.2644	3.11	120.77	9.81	0.264
10	33.8442	0.77724	5.2928	3.01	106.87	11.1	0.292

This band gap narrowing is directly correlated with lattice expansion, as increased bond lengths reduce orbital overlap and modify the electronic band structure, thereby shifting the conduction band minimum downward. The inverse relationship between c-lattice parameter and optical band gap energy demonstrates that band gap modulation in $ZnO_{1-x}S_x$

films is strongly governed by structural deformation rather than compositional effects alone. As a result structural disorder leads to the significant increase in FWHM values, from 0.215° to 0.777°.

Table 2 reveals some microstructural parameters of material. The average crystallite size decreases sharply from 340.55 Å to 106.87 Å**,** while the microstrain increases from 3.03×10^{-3} to 11.1×10^{-3} with sulfur content. These changes reflect increasing internal stress and defect density within the lattice. Additionally, the Urbach energy (E_u) increases from 0.180 eV to 0.292 eV, indicating a higher density of localized states and enhanced band tailing caused by structural disorder. Overall, the combined analysis of Fig. 3 and Table 2 confirms that sulfur incorporation induces lattice expansion, increased strain, crystallite size reduction, and band gap narrowing in $ZnO_{1-x}S_x$ thin films. These results clearly demonstrate that controlled anion substitution provides an effective approach for tailoring the optical properties of ZnO-based materials, which is of significant interest for visible and UV optoelectronic applications.[13]

Figure 4 illustrates the correlation between the c-axis lattice parameter and the optical band gap energy for $Zn_{1-x}Mg_xO$ and $ZnO_{1-\gamma}S_\gamma$ thin films. A clear and systematic relationship is observed, demonstrating that lattice deformation plays a dominant role in governing the electronic structure of ZnO-based alloys.

For $Zn_{1-x}Mg_xO$ films, the c-axis lattice parameter decreases with increasing Mg concentration, indicating lattice contraction due to the substitution of Zn^{2+} ions by smaller Mg^{2+} ions. This structural compression leads to a widening of the band gap, which increases from ~3.26 eV to ~3.33 eV. The band gap expansion can be attributed to enhanced orbital overlap and increased energy separation between the conduction and valence bands caused by reduced interatomic spacing.

In contrast, $ZnO_{1-\gamma}S_\gamma$ films exhibit an opposite trend. The c-axis lattice parameter increases with increasing sulfur content, reflecting lattice expansion due to the larger ionic radius of S^{2-} ions compared to O^{2-} ions. This expansion results in a reduction of orbital overlap and a corresponding narrowing of the band gap, decreasing to ~3.01 eV. The observed red shift is associated with the modification of the valence band structure and increased localization of electronic states.

The nearly linear dependence between lattice parameter and band gap in both systems suggests Vegard's law-like behavior, confirming that compositional variation directly influences the structural and optical properties. Importantly, the opposite trends observed for Mg and S substitution highlight a bidirectional mechanism of band gap engineering, where lattice contraction and expansion provide two complementary pathways for tuning the optical response of ZnO-based thin films.

These results clearly demonstrate that precise control of lattice deformation through cation and anion substitution offers a powerful strategy for designing materials with tailored band structures for advanced optoelectronic applications.

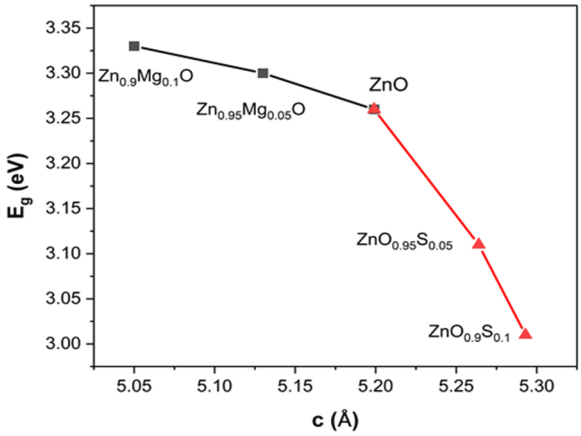

Figure 4. Band gap versus of $Zn_{1-x}Mg_xO$ and $ZnO_{1-\gamma}S_\gamma$ thin films c-axis lattice parameter

For comparison, $ZnO_{1-y}S_y$ alloys show the opposite trend: band gap narrowing and expansion of the c-lattice parameter, owing to the larger ionic radius of sulfur. These contrasting behaviors highlight the versatility of ZnO-based alloys for band-structure engineering.

Figure 5(a,c) presents plan-view SEM micrographs of the 10% Mg and 10% S films. Both surfaces are dense, continuous, and crack-free, displaying rounded, faceted grains with well-defined intergranular boundaries, consistent with the single-phase wurtzite structure revealed by XRD. No secondary-phase precipitates or pinholes are observed, confirming that Mg and S are incorporated without phase segregation at the film surface.[14]

The corresponding grain-size distributions [Fig. 5(b,d)] follow a log-normal profile, which is characteristic of nucleation-and-growth thin films. The $Zn_{0.9}Mg_{0.1}O$ film exhibits a median Feret diameter of 62.9 nm (mean 78.0 nm), whereas the $ZnO_{0.9}S_{0.1}$ film shows a larger median of 96.6 nm (mean 110.4 nm), as summarized in Table 3.

Importantly, the SEM grain sizes (≈60–100 nm) substantially exceed the X-ray crystallite sizes obtained from the Scherrer analysis (15.1 nm for 10% Mg and 10.7 nm for 10% S; Tables 1 and 2). This indicates that each SEM grain is a mesoscale aggregate composed of several coherently diffracting crystallites separated by low-angle sub-grain boundaries—that is, the two techniques probe different length scales. Notably, although the $ZnO_{0.9}S_{0.1}$ film has the larger mesoscale grains, it possesses the smaller crystallites together with the highest microstrain (11.1×10^{-3}) and Urbach energy

(0.292 eV). This apparent contrast is self-consistent: the larger sulfur-induced lattice expansion and tensile strain fragment each grain into smaller coherent domains and increase the density of localized states, while grain coalescence during growth still produces larger mesoscale grains. The morphology, therefore, corroborates the microstructural disorder inferred from the XRD and UV–Vis data [15].

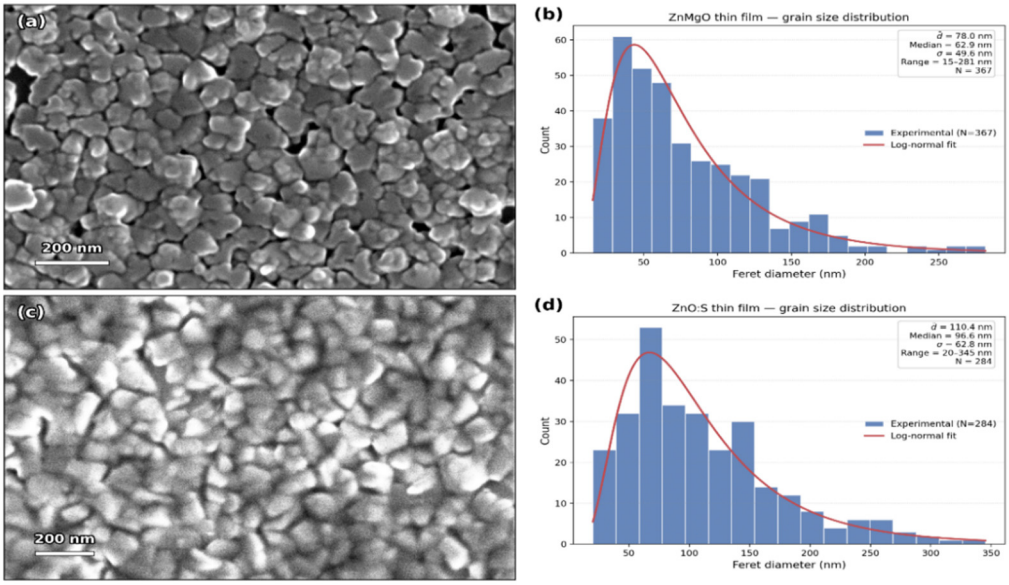

Figure 5. Plan-view SEM micrographs and corresponding grain-size distributions of (a, b) $Zn_{0.9}Mg_{0.1}O$ and (c, d) $ZnO_{0.9}S_{0.1}$ thin films grown on Si(100) by USP. Histograms show the maximum Feret diameter with a log-normal fit (red line); insets list the mean, median, standard deviation σ, range and grain count N. Scale bars: 200 nm

Finally, it should be emphasized that the optical band-gap modulation (Fig. 4) follows the composition-driven lattice deformation and crystallite-level disorder rather than the SEM grain size. At 60–100 nm the grains are far larger than the ZnO exciton Bohr radius (≈2.3 nm), so quantum size effects are negligible and the band gap is governed by the cation/anion substitution and the associated strain. The SEM analysis thus provides complementary morphological evidence that supports, but does not drive, the observed band-gap trends.

Table 3. Grain-size parameters (SEM, max Feret diameter) and crystallite size (XRD, Scherrer) of the 10% films.

Sample	Median Feret (nm)	Mean Feret (nm)	σ (nm)	N	XRD D (nm)	Grain/crystallite
$Zn_{0.9}Mg_{0.1}O$	62.9	78.0	49.6	367	15.1	~4.2
$ZnO_{0.9}S_{0.1}$	96.6	110.4	62.8	284	10.7	~9.0

D – average crystallite size from the (002) reflection (Tables 1–2). The grain/crystallite ratio illustrates that each SEM grain contains several coherent domains.

CONCLUSIONS

In this study, $Zn_{1-x}Mg_xO$ and $ZnO_{1-\gamma}S_\gamma$ thin films were successfully deposited on Si(100) substrates by ultrasonic spray pyrolysis, and their structural and optical properties were systematically investigated to clarify the role of cation and anion substitution in band gap engineering of ZnO-based alloys. X-ray diffraction analysis confirmed that all films exhibit a single-phase hexagonal wurtzite structure with strong preferential orientation along the c-axis, indicating successful incorporation of both Mg and S without the formation of secondary phases. Structural analysis revealed contrasting lattice responses: Mg incorporation resulted in lattice contraction, whereas S substitution produced lattice expansion, both consistent with the ionic radii of the respective substituents. These structural changes resulted in a bidirectional modulation of the optical band gap, with a systematic widening from ~3.26 eV to ~3.33 eV for $Zn_{1-x}Mg_xO$ and a narrowing down to ~3.01 eV for $ZnO_{1-\gamma}S_\gamma$. The correlation among lattice parameters, microstrain, crystallite size, and Urbach energy indicates that band-gap evolution is strongly governed by lattice deformation and associated structural disorder.

Plan-view SEM analysis confirmed that all films are dense, crack-free, single-phase polycrystalline layers with log-normal grain-size distributions, the median Feret diameter increasing from 62.9 nm for $Zn_{0.9}Mg_{0.1}O$ to 96.6 nm for $ZnO_{0.9}S_{0.1}$. These mesoscale grains are several times larger than the XRD crystallites, indicating that each grain comprises multiple coherent domains; the larger-grain yet smaller-crystallite, higher-strain character of the sulfur-doped film is fully consistent with the structural picture obtained from XRD and UV–Vis. The morphological results therefore reinforce that the bidirectional band-gap modulation is governed by composition-driven lattice deformation and microstructural disorder rather than by grain-size (quantum-confinement) effects.

The results establish a unified experimental framework linking lattice deformation to optical band gap tuning in ZnO-based thin films. This study highlights that controlled cation and anion substitution provides a versatile and effective route for tailoring the optoelectronic properties of ZnO alloys. Such tunability makes these materials highly promising for applications in ultraviolet and visible photodetectors, transparent electronics, and band-engineered heterostructures.

ORCID

Javohir Sh. Khudoykulov, https://orcid.org/0009-0005-4223-8863**; Shavkat U. Yuldashev,** https://orcid.org/0000-0002-2187-5960; **Azamat O. Arslanov**, https://orcid.org/0009-0000-4817-8770; **Jamoliddin X. Murodov,** https://orcid.org/0009-0006-3088-4881; **Noiba U. Botirova,** https://orcid.org/0009-0002-2294-9981

REFERENCE

[1] Ü. Özgür, Y. I. Alivov, C. Liu, et al., "A comprehensive review of ZnO materials and devices," Journal of Applied Physics**, 98**, (2005) 041301. https://doi.org/10.1063/1.1992666

[2] A. Ohtomo, and M. Kawasaki, "ZnO-based heterostructures: MgZnO/ZnO quantum wells," Applied Physics Letters**, 72**, 2466-2468 (1998). https://doi.org/10.1063/1.121384

[3] S. Major, A. Banerjee, and K. L. Chopra, "Highly transparent and conducting ZnO films prepared by spray pyrolysis," Thin Solid Films**, 108**, 333–340 (1983). https://doi.org/10.1016/0040-6090(83)90438-5

[4] S. Pearton, D. Norton, K. Ip, et al., "Recent progress in processing and properties of ZnO," Progress in Materials Science**, 50**, 293–340 (2005). https://doi.org/10.1016/j.pmatsci.2004.04.001

[5] R. Vinodkumar, and K. Vijayalakshmi, "Effect of Mg incorporation on structural and optical properties of ZnMgO thin films," Materials Science in Semiconductor Processing**, 16**, 1–6 (2013). https://doi.org/10.1016/j.mssp.2012.08.004

[6] J. X. Murodov, Sh. U. Yuldashev, A. O. Arslanov, N. U. Botirova, J. Sh. Xudoyqulov, R. Sh. Sharipova, R. A. Nusretov, *et al*., "Resistive Switching Behavior of SnO_2/ZnO Heterojunction Thin Films for Non-Volatile Memory Applications," East Eur. J. Phys. (3), 348–352 (2025). https://doi.org/10.26565/2312-4334-2025-3-34

[7] R. Zhang, Sh. U. Yuldashev, J. C. Lee, V. Sh. Yalishev, T. W. Kang, and D. J. Fu, "Electrical Properties of ZnO Nanostructures Grown on Si Substrates," Microelectron. Eng. **112**, 31–35 (2013). https://doi.org/10.1016/j.mee.2013.05.018

[8] N. U.Botirova, A. O. Arslanov, G. B. Eshobqulov, J. X. Murodov, R. Sh. Sharipova, J. Sh. Xudoyqulov, and Sh. U. Yuldashev, "Effect of SiO_2 and Post-Annealed Ga_2O_3 Buffer Layers on Ga_2O_3 Thin Film Growth and Properties," Cryst. Growth Des. **25**(18), 7828–7833 (2025). https://doi.org/10.1021/acs.cgd.5c01075

[9] M. Caglar, S. Ilican, and Y. Caglar, "Influence of sulfur doping on structural and optical properties of ZnO thin films," Journal of Alloys and Compounds, **509**, 5130–5137 (2011). https://doi.org/10.1016/j.jallcom.2011.01.061

[10] A. Arslanov, Sh. Yuldashev, N. Botirova, R. Nusretov, J. Murodov, and J. Xudoyqulov, "Impact of Precursor Molar Concentration on the Structural and Optical Properties of ZnO Thin Films Synthesized by Ultrasonic Spray Pyrolysis," Physical Science International Journal, **29**(1), 29-35 (2025). https://doi.org/10.9734/psij/2025/v29i1871

[11] Sh Yuldashev, K. Mukimov, G. Eshonkulov, A. Arslanov, and J. Xudoykulov, "Diluted Magnetic Semiconductors for Spintronics Applications," in: *ICLODAM-24*, (Tashkent, Uzbekistan, 2024).

[12] V. Morari, V.V. Ursaki, E.V. Rusu, V.V. Zalamai, P. Colpo, and I.M. Tiginyanu, "Spin-Coating and Aerosol Spray Pyrolysis Processed $Zn_{1-x}Mg_xO$ Films for UV Detector Applications," Nanomaterials, **12**, 3209 (2022). https://doi.org/10.3390/nano12183209

[13] H. Morkoç, AND Ü. Özgür, *Zinc Oxide: Fundamentals, Materials and Device Technology*, (Wiley-VCH, Weinheim, 2009).

[14] A. Janotti, AND C.G. Van de Walle, "Fundamentals of zinc oxide as a semiconductor," Reports on Progress in Physics**, 72**, 126501 (2009). https://doi.org/10.1088/0034-4885/72/12/126501

[15] *Transparent Conductive Zinc Oxide*, edited by K. Ellmer, A. Klein, and B. Rech, "Springer Series in Materials Science, 2008". https://doi.org/10.1007/978-3-540-73612-7

ДВОНАПРАВЛЕНА МОДУЛЯЦІЯ ШИРИНИ ЗАБОРОНЕНОЇ ЗОНИ В ТОНКИХ ПЛІВКАХ НА ОСНОВІ ZnO ЗА ДОПОМОГОЮ КАТИОННО-ТА АНІОННО-ІНДУКОВАНОЇ ГРАТКОВОЇ ІНЖЕНЕРІЇ

Джавохір Ш. Худойкулов[1], Шавкат У. Юлдашев[1,2], Азамат О. Арсланов[1], Джамоліддін Х. Муродов[2], Андрій А. Небесний[1], Нойба У. Ботірова[2], Ра'но Ш. Шаріпова[2]

[1]Кафедра фізики, Національний університет Узбекистану, вулиця Університетська, 4, Ташкент 100174, Узбекистан
[2]Центр розвитку нанотехнологій, Національний університет Узбекистану, вулиця Університетська, 4, Ташкент 100174, Узбекистан

Тонкі плівки $Zn_{1-x}Mg_xO$ та $ZnO_{1-\gamma}S_\gamma$ були синтезовані методом ультразвукового розпилювального піролізу та досліджені з метою досягнення двонаправленої інженерії забороненої зони в матеріалах на основі ZnO. Рентгенівська дифракція підтвердила однофазну структуру вюрциту з сильною орієнтацією осі c у всіх зразках. Включення Mg викликало зміщення піку (002) до більших кутів, що вказує на стиснення решітки, тоді як заміщення S викликало зміщення до менших кутів, що відповідає розширенню решітки. UV–Vis аналіз виявив систематичний зсув ширини забороненої зони в синю область спектра при легуванні магнієм (від ~3,26 еВ до ~3,33 еВ) та зсув у червону область спектра при включенні сірки (до ~3,01 еВ).. Ці зміни пояснюються деформацією решітки та її впливом на електронну структуру. Крім того, збільшення концентрації легуючої домішки призвело до зменшення розміру кристалітів та збільшення мікродеформації та переупорядкування. Результати встановлюють чітку кореляцію між деформацією решітки та модуляцією оптичної забороненої зони, демонструючи ефективний підхід до налаштування тонких плівок на основі ZnO для оптоелектронних застосувань.

Ключові слова: *ZnMgO; ZnOS; ширина забороненої зони; деформація решітки; діаграма Таука; ультразвуковий піроліз*

East European Journal of Physics. 3. 298-304 (2026)
DOI:10.26565/2312-4334-2026-3-25 ISSN 2312-4334

CLUSTER-INDUCED FERROMAGNETISM IN MANGANESE-DOPED SILICON

Olmas E. Sattarov[1]*, Stanislav A. Tachilin[1], Ilxomov A. Ilyosbek[1], Nematillo N. Mamatkulov[2], Alisher R. Toshev[3]

[1]*Tashkent State Technical University, Uzbekistan, 100095, Tashkent, University St., 2*
[2]*National University of Uzbekistan, Tashkent 100174, Uzbekistan*
[3]*Almalyk State Technical Institute, Almalyk 110100, Uzbekistan*
**Corresponding Author e-mail: olmossattarov1974@gmail.com*
Received April 2, 2026; revised June 19, 2026; accepted June 24, 2026

Integrating magnetic functionality into silicon remains a key challenge for developing spintronic devices. In this work, we investigate the structural, electrical, and magnetic properties of Mn-diffused silicon fabricated via a two-step thermal diffusion process that enables controlled Mn incorporation and redistribution within the Si matrix. Magnetic measurements reveal clear ferromagnetic behavior at room temperature, characterized by a well-defined hysteresis loop with finite coercivity and remanent magnetization. The temperature dependence of magnetization indicates a Curie temperature of approximately 360 K, confirming the stability of magnetic ordering above room temperature. Electrical transport measurements show a systematic evolution of carrier properties with increasing diffusion temperature, including a transition from p-type to n-type conductivity. This behavior is attributed to the activation of Mn-related donor states and defect complexes, which compensate and overcompensate boron acceptors. A strong correlation between carrier concentration and magnetic properties is observed, indicating the crucial role of free carriers in mediating magnetic interactions. Based on the combined experimental results, the observed ferromagnetism is attributed to a cluster-induced mechanism, in which Mn-rich regions act as localized magnetic centers coupled via carrier-mediated exchange interactions, consistent with an RKKY-type mechanism. These findings demonstrate that two-step thermal diffusion provides an effective route to tune both the electrical and magnetic properties of silicon, highlighting its potential for silicon-based spintronic applications.
Keywords: *Silicon; Manganese; Donor; Ferromagnetism; Nanoclusters; Spintronics*

1. INTRODUCTION

Silicon-based materials have long formed the foundation of modern electronics due to their excellent compatibility with established semiconductor technologies. In recent years, significant efforts have been devoted to integrating magnetic functionality into silicon to enable spin-dependent electronic applications, commonly referred to as spintronics [1-3]. The realization of ferromagnetism in silicon would open pathways toward multifunctional devices combining charge and spin degrees of freedom [4,5].

One promising approach to induce magnetic ordering in silicon involves doping with transition metals, particularly manganese (Mn). However, the origin of ferromagnetism in Mn-doped silicon remains a subject of ongoing debate. While some studies attribute the observed magnetic behavior to the formation of secondary magnetic phases, others suggest that intrinsic mechanisms, such as carrier-mediated exchange interactions, may play a dominant role [6,7].

A key challenge lies in controlling the spatial distribution and electronic state of Mn atoms within the silicon lattice. At low concentrations, Mn atoms tend to occupy interstitial or substitutional sites, often leading to strong compensation effects and weak magnetic ordering. Under appropriate thermal conditions, however, Mn atoms may aggregate into nanoscale clusters that can act as localized magnetic centers [8-10]. The interaction between such centers may be mediated by free charge carriers, giving rise to long-range magnetic ordering [11,12].

In this context, thermal diffusion represents an effective method for introducing and redistributing Mn in silicon. In particular, a two-step diffusion process enables independent control over impurity incorporation and defect formation, providing a pathway to tailor both structural and electronic properties [13-16]. Despite this potential, the relationship between diffusion conditions, carrier transport, and magnetic behavior remains insufficiently understood [17-20].

The aim of this work is to investigate the formation of room-temperature ferromagnetism in Mn-diffused silicon prepared by a two-step thermal diffusion process. Unlike previous studies that mainly focused on ion implantation or single-step diffusion, the present work employs a two-stage diffusion approach that allows separate control of manganese incorporation and its subsequent redistribution within the silicon matrix. This approach enables us to analyze the correlation between carrier concentration, conductivity-type conversion, and magnetic ordering, providing new insight into the mechanism of ferromagnetism in Mn-doped silicon.

To achieve this goal, we systematically investigate the structural, electrical, and magnetic properties of Mn-diffused silicon. Electrical measurements reveal a transition from p-type to n-type conductivity as the diffusion temperature increases, indicating the activation of Mn-related donor states and defect complexes [21–24]. Magnetic measurements demonstrate robust ferromagnetic ordering with a Curie temperature above room temperature [25,26].

Cite as: O.E. Sattarov, S.A. Tachilin, I.A. Ilyosbek, N.N. Mamatkulov, A.R. Toshev, East Eur. J. Phys. 3, 298 (2026), https://doi.org/10.26565/2312-4334-2026-3-25

Based on a comprehensive analysis of magnetic and transport properties, we propose a cluster-induced ferromagnetism mechanism mediated by charge carriers [27]. The results provide new insights into Mn-doped silicon systems and highlight the potential of controlled diffusion techniques to develop silicon-based spintronic materials.

2. MATERIAL AND METHODS

Single-crystal boron-doped (p-type) silicon wafers were used as substrates. The samples were chemically cleaned prior to processing to remove surface contaminants and native oxide layers.

Manganese incorporation was performed via a two-stage thermal diffusion process. Manganese was introduced into silicon via a two-stage thermal diffusion process performed under vacuum. In the first stage, Mn atoms were incorporated into the near-surface region of boron-doped Si(100) wafers at a temperature of 580 °C for 10 min. In the second stage, deeper diffusion and redistribution of manganese within the silicon matrix were achieved by annealing at 1050 °C for 60 min under vacuum. After completion of the diffusion process, the samples were rapidly cooled to room temperature to preserve the formed impurity–defect configurations and suppress the formation of equilibrium secondary phases. The two-stage diffusion procedure was employed to independently control manganese incorporation and its subsequent redistribution, thereby promoting the formation of Mn-rich clusters responsible for the observed ferromagnetic ordering.

Electrical properties were characterized by Hall effect measurements using a four-probe configuration. Carrier concentration, mobility, and resistivity were determined at room temperature, while the conductivity type was identified from the Hall coefficient.

Magnetic measurements were carried out using a vibrating sample magnetometer. Field-dependent magnetization (M–H) was measured at room temperature, and temperature-dependent magnetization M(T) was used to determine the Curie temperature. Key magnetic parameters, including saturation magnetization (M_s), coercivity (H_c), and remanence (M_r), were extracted from the data.

3. RESULTS

The magnetic properties of Mn-diffused silicon were investigated by measuring the magnetization as a function of the applied magnetic field at different temperatures [28]. Given in the work [28] the M–H curve measured at 300 K exhibits a well-defined hysteresis loop, clearly indicating ferromagnetic behavior at room temperature. The presence of finite coercivity ($H_c \approx 87$ Oe) and remanent magnetization ($M_r \approx 3.5\times10^{-5}$ emu/cm³) confirms the formation of stable magnetic domains. The saturation magnetization at 300 K is relatively low ($M_s \approx 1.6\times10^{-4}$ emu/cm^3), suggesting that only a fraction of Mn atoms contributes to long-range magnetic ordering. This behavior is commonly observed in diluted magnetic systems and may be attributed to an inhomogeneous distribution of Mn, partial compensation, or the formation of magnetically inactive configurations [29,30]. A comparison of magnetic parameters at 150 K and 300 K reveals a clear temperature dependence. The magnetic hysteresis loops measured at 150 K and 300 K confirm the presence of ferromagnetic ordering in manganese-diffused silicon; the magnetic parameters are summarized in Table 1.

Table 1. Magnetic parameters of Mn-diffused silicon extracted from hysteresis loops at different temperatures

no.	Temperature (K)	M_s (emu·cm^{-3})	M_r (emu·cm^{-3})	H_c (Oe)	$\frac{M_r}{M_s}$
1.	150	2.0×10^{-4}	8.0×10^{-5}	115	0.40
2.	300	1.6×10^{-4}	3.5×10^{-5}	87	0.219

The decrease in M_s, M_r, and H_c with increasing temperature reflects thermal disordering of spins, reduced magnetic anisotropy, and enhanced domain wall mobility. Nevertheless, the persistence of hysteresis at 300 K provides strong evidence for robust room-temperature ferromagnetism.

3.1 Temperature dependence of magnetization

Figure 1 illustrates the temperature dependence of magnetization (M–T). As shown in the graph, the material's magnetic moment gradually decreases as temperature increases. This behavior is characteristic of ferromagnetic materials and can be explained by increased thermal agitation, which disrupts the ordered alignment of magnetic moments.

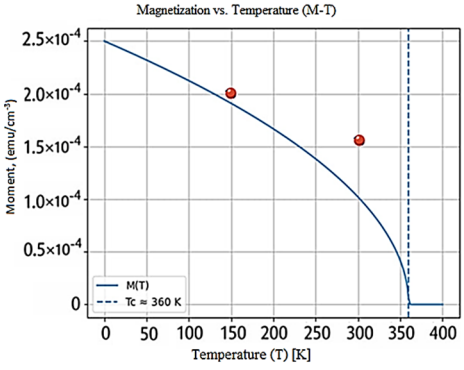

Figure 1. Temperature dependence of magnetization M(T)

The continuous curve represents theoretical calculations, showing a smooth decline in magnetization as temperature rises and approaching zero near a critical point—the Curie temperature. The experimental data are shown as red points and generally agree well with the theoretical curve, confirming the validity of the model. The linear behavior follows the Curie–Weiss law, indicating that 1/χ varies linearly with temperature. Extrapolating the fitted line to 1/χ = 0 yields the Curie temperature, $T_C \approx 360$ K. The slope of the linear fit is related to the Curie constant of the material.

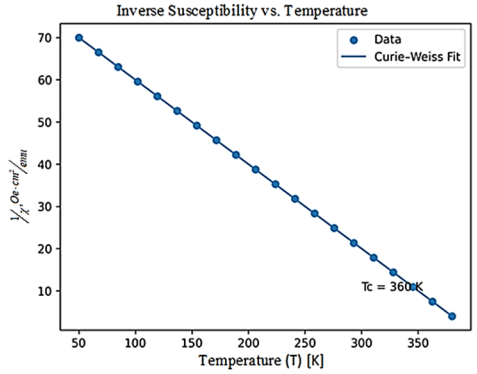

Figure 2. Temperature dependence of the inverse magnetic susceptibility (1/χ) measured in the paramagnetic region

The Curie temperature (T_C) was estimated using both direct M(T) analysis and Curie–Weiss fitting of the inverse magnetic susceptibility χ^{-1}(T).

Above the transition temperature, χ^{-1}(T) exhibits a linear dependence consistent with the Curie–Weiss law:

$$\chi = \frac{C}{(T - T_C)} \tag{1}$$

Extrapolation of the linear region to $\chi^{-1} = 0$ yields $T_C \approx 360$ K. The agreement between different methods confirms the reliability of this estimate and indicates that ferromagnetic ordering persists above room temperature.

It should be noted that fitting based on Bloch's law slightly overestimates T_C, suggesting that additional interaction mechanisms beyond spin-wave excitations contribute to the magnetic behavior.

3.2 Effective magnetic moment

The effective magnetic moment per Mn atom was estimated using the experimental saturation magnetization:

$$\mu_{eff} = \frac{M_c}{N_{eff \cdot \mu_B}}, \tag{2}$$

where μ_B is the Bohr magneton and N_{eff} is the effective concentration of magnetically active Mn atoms.

The concentration of manganese in the investigated Mn-diffused silicon samples was not directly determined by compositional techniques such as SIMS, EDX, or XPS. Therefore, a precise quantitative Mn concentration cannot be reported. Nevertheless, based on the employed diffusion conditions, Hall-effect measurements, and the observed magnetic response, the effective concentration of magnetically active Mn centers was estimated to be on the order of $N_{eff} \approx 5 \cdot 10^{17}$ cm^{-3}. This value should be regarded as an effective magnetic concentration associated with Mn-rich clusters and carrier-mediated exchange interactions rather than the total manganese concentration in the silicon matrix.

Using $N_{eff} \approx 5 \cdot 10^{17}$ cm^{-3}, the estimated magnetic moment is $\mu_{eff} \approx 0.03–0.04 \mu_B$ per Mn atom. This value is significantly smaller than the magnetic moment of an isolated Mn^{2+} ion ($\sim 5\mu_B$), indicating that only a small fraction of Mn atoms participates in the formation of long-range ferromagnetic order. This reduction may arise from clustering effects, antiferromagnetic coupling within Mn-rich regions, or the presence of magnetically inactive Mn configurations.

3.3 Electrical transport and carrier-mediated effects

The evolution of electrical transport properties with diffusion temperature (Figure 3) shows a strong correlation between carrier concentration and magnetic behavior.

At moderate diffusion temperatures, the material exhibits p-type conductivity due to the presence of boron acceptors partially compensated by Mn-related states.

At higher diffusion temperatures, a transition to n-type conductivity is observed, accompanied by an increase in carrier concentration and mobility. This behavior is attributed to the activation of donor-like states associated with Mn impurities or defect complexes, leading to overcompensation of the initial acceptor doping.

The observed correlation between carrier concentration and magnetic properties suggests that free carriers play a key role in mediating magnetic interactions. Enhanced carrier density is expected to strengthen indirect exchange coupling between localized magnetic moments. A transition from p-type to n-type conductivity is observed at higher diffusion temperatures, indicating compensation and overcompensation effects.

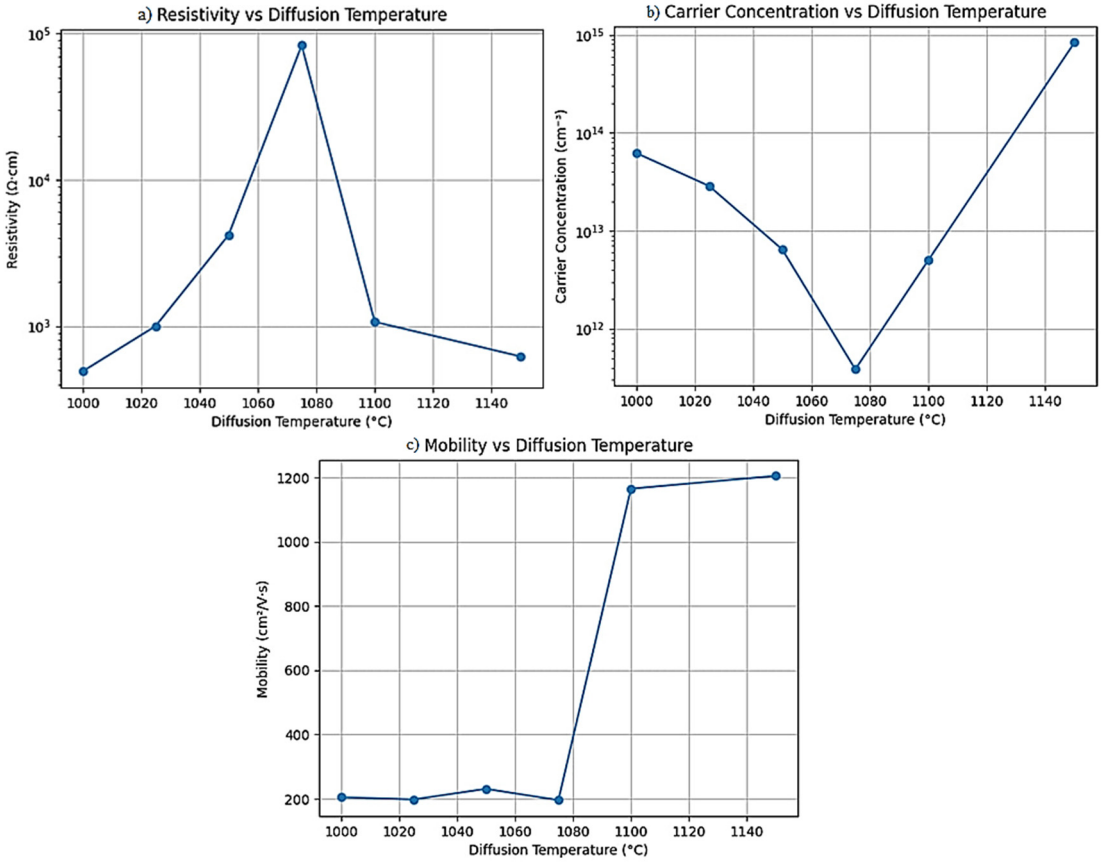

Figure 3. Evolution of electrical transport properties of Mn-diffused silicon as a function of diffusion temperature (a) resistivity, (b) carrier concentration, and (c) carrier mobility.

3.4 Magnetoresistance and correlation with magnetic ordering

To further clarify the relationship between charge transport and magnetic interactions, magnetoresistance (MR) measurements were analyzed [31-33].

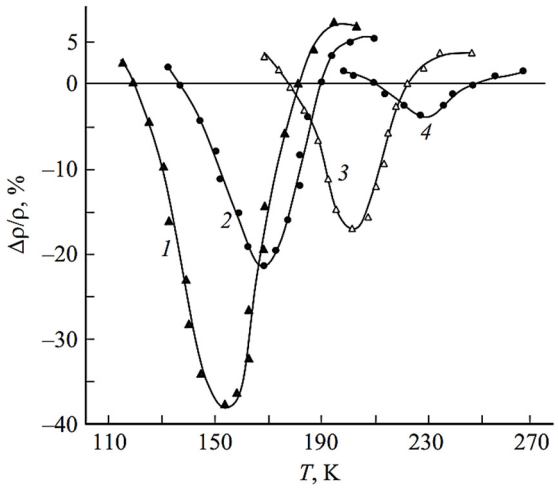

Figure 4. Temperature dependence of MR in silicon at E = 50 V/cm: B = 1 T: n-Si〈B, Mn〉
1 - $E_f = E_C$ - 0.37 eV, 2 - $E_f = E_C$ - 0.384 eV, 3- $E_f = E_C$ - 0.516 eV, 4- $E_f = E_C$ - 0.53 eV.

The results demonstrate the presence of both positive and negative magnetoresistance depending on temperature and the position of the Fermi level. In compensated p-type samples, a pronounced negative magnetoresistance is observed at room temperature, reaching significant values over a wide temperature range. As temperature decreases, the MR exhibits a non-monotonic behavior, including a sign inversion from negative to positive values.

In overcompensated n-type samples, the magnetoresistance behavior differs, showing predominantly small positive values at room temperature and complex temperature-dependent transitions at lower temperatures. This behavior is strongly influenced by the position of the Fermi level and the charge state of Mn ions (Mn^0, Mn^+, Mn^{2+}).

The existence of large negative magnetoresistance is indicative of strong spin-dependent cattering processes and supports the presence of localized magnetic moments interacting with charge carriers. The double sign inversion of MR with temperature further reflects the competition between different conduction mechanisms and magnetic scattering processes.

These findings provide additional evidence that charge carriers play a crucial role not only in electrical transport but also in mediating magnetic interactions. The consistency between MR behavior and magnetization results reinforces the validity of the carrier-mediated ferromagnetism model.

3.5 Mechanism of ferromagnetism

Based on the combined magnetic and transport results, the observed ferromagnetism in Mn-diffused silicon can be interpreted within a cluster-induced framework. Mn atoms tend to form nanoscale clusters embedded in the silicon matrix, which act as localized magnetic centers. Mn-rich clusters act as localized magnetic centers, while charge carriers mediate indirect exchange interactions between them through an RKKY-type mechanism. Figure 5 illustrates the proposed mechanism of cluster-induced ferromagnetism in Mn-diffused silicon. Figure 5(a) shows the formation of Mn-rich clusters during the two-step thermal diffusion process. Figure 5(b) demonstrates the distribution of charge carriers around the Mn-rich clusters and their participation in indirect exchange interactions. Figure 5(c) presents the establishment of long-range ferromagnetic ordering through carrier-mediated RKKY-type coupling between spatially separated magnetic clusters.

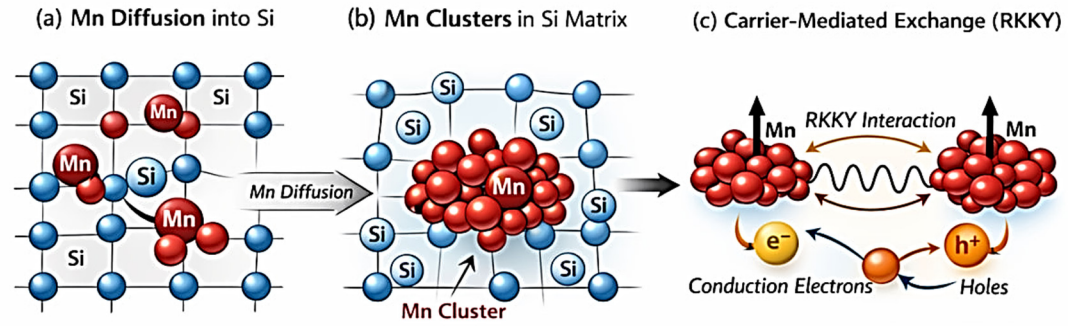

Figure 5. Schematic illustration of cluster-induced ferromagnetism in Mn-diffused silicon

The schematic model presented in Figure 5 was prepared by the authors based on the carrier-mediated ferromagnetism concepts described in Refs. [15,27].

The interaction between these centers is likely mediated by charge carriers via an indirect exchange mechanism consistent with the Ruderman–Kittel–Kasuya–Yosida (RKKY) interaction. In this picture, itinerant carriers couple spatially separated magnetic moments, enabling long-range magnetic ordering.

The relatively low effective magnetic moment, together with the strong dependence on carrier concentration, supports this interpretation. Although direct nanoscale compositional characterization was not performed, the observed correlation among carrier concentration, conductivity conversion, magnetoresistance, and magnetic ordering supports the interpretation that the ferromagnetism primarily arises from Mn-related clusters and carrier-mediated interactions.

Overall, the results demonstrate that the magnetic behavior of Mn-diffused silicon arises from a complex interplay between impurity clustering, carrier concentration, and exchange interactions. The ability to tune these parameters through diffusion conditions provides a pathway to engineer silicon-based magnetic materials for spintronic applications.

4. CONCLUSIONS

In this work, we have systematically investigated the magnetic and electrical transport properties of Mn-diffused silicon prepared via a two-step thermal diffusion process. The results demonstrate that this approach enables controlled modification of both carrier concentration and magnetic behavior through the redistribution of Mn and the formation of defect complexes.

Magnetic measurements reveal clear ferromagnetic ordering at room temperature, characterized by a well-defined hysteresis loop with finite coercivity and remanence. The Curie temperature was determined to be approximately 360 K based on Curie–Weiss analysis, confirming the stability of the magnetic phase above room temperature.

Electrical transport studies show a pronounced evolution of carrier properties with increasing diffusion temperature, including a transition from p-type to n-type conductivity. This behavior is attributed to the activation of Mn-related donor states and defect complexes, leading to compensation and overcompensation of boron acceptors.

A strong correlation between carrier concentration and magnetic properties indicates that free carriers play a crucial role in mediating magnetic interactions. The observed ferromagnetism is therefore interpreted as a cluster-induced mechanism, in which Mn-rich regions act as localized magnetic centers coupled via carrier-mediated exchange interactions, consistent with an RKKY-type mechanism.

Although additional structural characterization would be required to fully exclude the contribution of secondary phases, the combined magnetic and transport data support an intrinsic origin of ferromagnetism in the studied system.

Overall, the present study demonstrates that two-step thermal diffusion provides an effective and versatile route for engineering ferromagnetic silicon with tunable electronic properties. These findings highlight the potential of Mn-diffused silicon as a promising platform for silicon-compatible spintronic applications.

ORCID

Olmas E. Sattarov, https://orcid.org/0009-0008-9121-3541; **Stanislav A. Tachilin,** https://orcid.org/0009-0007-3923-2131;
Nematillo N. Mamatkulov, https://orcid.org/0009-0000-2728-4507; **Alisher R. Toshev,** https://orcid.org/0009-0000-5283-9498;
Ilxomov A. Ilyosbek, https://orcid.org/0009-0007-7800-1467

REFERENCES

[1] T. Dietl, and H. Ohno, "Dilute ferromagnetic semiconductors: Physics and spintronic structures," Reviews of Modern Physics, **86**, 187 (2014). https://doi.org/10.1103/RevModPhys.86.187
[2] J. Sinova, S.O. Valenzuela, J. Wunderlich, C.H. Back, and T. Jungwirth, "Spin Hall effects," Reviews of Modern Physics, **87**, 1213–1260 (2015). https://doi.org/10.1103/RevModPhys.87.1213
[3] I. Zutic, J. Fabian, and S. Das Sarma, "Spintronics: Fundamentals and applications," Reviews of Modern Physics, **76**, 323–410 (2004). https://doi.org/10.1103/RevModPhys.76.323
[4] A. Hirohata, K. Yamada, Y. Nakatani, *et al*., "Review on spintronics: Principles and device applications," J. Magn. Magn. Mater. **509**, 166711 (2020). https://doi.org/10.1016/j.jmmm.2020.166711
[5] S. Manipatruni, D. Nikonov, and I. Young, "Beyond CMOS computing with spin and polarization," Nat. Phys. **14**, 338–343 (2018). https://doi.org/10.1038/s41567-018-0101-4
[6] N.B. Hamzan, M. Lee, L.J. Chang, K.H. Yeoh, K.H. Chew, M. Tripathi, A.B. Dalton, *et al*., "Structural, electronic, and magnetic properties of MnSi and Mn_4Si_7 nanowires," Journal of Alloys and Compounds, **962**(5), 171097 (2023). https://doi.org/10.1016/j.jallcom.2023.171097
[7] V. Ko, K. L. Teo, T. Liew, T. C. Chonge, M. MacKenzi, I. MacLaren, and J. N. Chapman, "Origins of ferromagnetism in transition-metal doped Si," Journal of Applied Physics, **104**(3), 033912 (2008). https://doi.org/10.1063/1.2963485
[8] L. Shen, X. Zhang, H. Wang, J. Lic, and G.Xiang, "Structural, Magnetic and Magneto-transport Properties of Mn-doped SiGe Thin Films," J. Magnet. Magnetic Materials, **560**(8), 169630 (2022). https://doi.org/10.1016/j.jmmm.2022.169630
[9] Y. Zhou, "Magnetic skyrmions: intriguing physics and new spintronic device concepts," Natl. Sci. Rev. **6**(2), 210-212 (2019). https://doi.org/10.1093/nsr/nwy109
[10] M.K. Bakhadirkhanov, Kh.M. Iliev, K.S. Ayupov, and Kh.F. Zikrillaev, "Negative magneto-resistance in heavily compensated silicon," Elektronnaya Obrabotka Materialov, **4**, 86–89 (2003). (in Russian)
[11] O.E. Sattarov, A. Mavlyanov, and A. An, "Effect of manganese atoms on the magnetic properties of silicon," Surface Engineering and Applied Electrochemistry, **59**(2), 216–219 (2023). https://doi.org/10.3103/S106837552302014X
[12] Sh.B. Utamuradova, A.Sh. Mavlyanov, Sh.A. Sobirova, and O.E. Sattarov, "Hybrid Secondary Structure of Manganese and Sulfur in Silicon," Surface Engine and Applied Electroc. **61**, 633-636 (2025). https://doi.org/10.3103/S1068375525700681
[13] N.F. Zikrillaev, S.V. Koveshnikov, L. Trabzon, G.Kh. Mavlonov, B.K. Ismaylov, T.B. Ismailov, and F.E. Urakova, "Ferromagnetic Properties of Silicon Doped Manganese Atoms," Surface Engineering and Applied Electrochemistry, **61**(1), 75-81 (2025). https://doi.org/10.3103/S1068375524700571
[14] S. Zhou, K. Potzger, G. Zhang, *et al*., "Structural and magnetic properties of Mn-implanted silicon," Phys. Rev. B, **75**, 085203 (2007). https://doi.org/10.1103/PhysRevB.75.085203
[15] T. Jungwirth, J. Sinova, J. Mašek, J. Kučera, and A.H. MacDonald, "Theory of ferromagnetic (III,Mn)V semiconductors," Reviews of Modern Physics, **78**, 809–864 (2006). https://doi.org/10.1103/RevModPhys.78.809
[16] H. Ohno, "Making nonmagnetic semiconductors ferromagnetic," Journal of Science, **281**, 951–956 (1998). https://doi.org/10.1126/science.281.5379.951
[17] Z.M. Saparniyazova, M.K. Bakhadyrkhanov, O.E. Sattarov, N. Norkulov, and D.Zh. Asanov, "Interaction between multiply charged manganese nanoclusters and sulfur atoms in silicon," Inorganic Materials, **48**(4), 325–328 (2012). https://doi.org/10.1134/S0020168512030144
[18] Sh. A. Mavlyanov, M.K. Khakkulov, O.E. Sattarov, N.A. Akbarova, and D.Z. Yakubov, "Photoconductivity and bandgap of binary impurity - Doped crystalline silicon," Journal of Physics Conference Series, **2697**(1), 012011 (2024). https://doi.org/10.1088/1742-6596/2697/1/012011
[19] O. Sattarov, B. Abdurakhmanov, D. Yakubov, E. Sabirov, and A. Normamatov, "Formation of electroneutral Ni–Mn complexes in silicon and their effect on material properties," Proceedings of SPIE the International Society for Optical Engineering, **13803**, 465-470 (2025). https://doi.org/10.1117/12.3076740
[20] L. Shen, X. Zhang, J. Lu, *et al*. "The effect of vacancy defects on the conductive properties of SiGe," Phys. Lett. A, **386**, 126993 (2021). https://doi.org/10.1016/j.physleta.2020.126993
[21] D. Li, X. Zhang, and W. He, "Transition metal (TM=V, Cr, Mn, Fe, Co, Ni)-doped GeSe diluted magnetic semiconductor thin films with high-temperature ferromagnetism," Sci. China Mat. **67**, 279 (2024). https://doi.org/10.1007/s40843-023-2657-2
[22] S. Zhou, and X. Chen, "Defect-induced magnetism in SiC," J. Phys. D: Appl. Phys. **52**(39), 393001 (2019). https://doi.org/10.1088/1361-6463/ab2495
[23] Y. Wang, Y. Liu, E. Wendler, R. Hubner, *et al*., "Defect-induced magnetism in SiC: Interplay between ferromagnetism and paramagnetism," Phys. Rev. B, **92**, 174409 (2015). https://doi.org/10.1103/PhysRevB.92.174409
[24] X.Y. Zhang, and Z.W. Liu, "Effect of Mn diffusion on magnetic properties of Si-based diluted magnetic semiconductors," Journal of Magnet. and Magnetic Materials, **547**, 168818 (2022). https://doi.org/10.1016/j.jmmm.2021.168818
[25] H. Wang, S. Sun, J. Lu, *et al*., "High Curie temperature ferromagnetism in Mn-doped SiGe thin films," Adv. Funct. Mater. **30**, 2002513 (2020). https://doi.org/10.48550/arXiv.2004.02676
[26] M. Jamet, A. Barski, T. Devillers, *et al*., "High Curie temperature ferromagnetism in self-organized MnSi nanocolumns," Nat. Mater. **5**, 653–659 (2006). https://doi.org/10.1038/nmat1686

[27] C.H. Ziner, S. Glutsch, and F. Bechstedt, "RKKY interaction in semiconductors: Effects of magnetic field and screening," J. Phys. Rev. B, **70**, 075205 (2004). https://doi.org/10.1103/PhysRevB.70.075205
[28] O.E. Sattarov, B.A. Abdurakhmanov, G.A. Kushiev, S.A. Tachilin, and T.B. Ismailov, "Room-temperature ferromagnetism and spin polarization in silicon doped with manganese," East European Journal of Physics, (1), 396-400 (2026) https://doi.org/10.26565/2312-4334-2026-1-47
[29] M. Bolduc, C. Awo-Affouda, A. Stollenwerk, M.B. Huang, F.G. Ramos, G. Agnello, and V.P. LaBella, "Above room temperature ferromagnetism in Mn-ion implanted Si," Physical Review B, **71**, 033302 (2005). https://doi.org/10.1103/PhysRevB.71.033302
[30] F. Fang, P.B. Johnson, J. Kennedy, and A. Markowitz, "Magnetic-ion-doped silicon nanostructures fabricated by ion implantation and electron beam annealing," Nuclear Instruments and Methods in Physics, **307**(10), 131–136 (2013). https://doi.org/10.1016/j.nimb.2012.11.071
[31] M.K. Bakhadyrkhanov, K.S. Ayupov, K.M. Iliev, G.K. Mavlonov, and O.E. Sattorov, "Effect of electric field, illumination, and temperature on negative magnetoresistance of low-temperature-diffusion-doped silicon," Technical Physics Letters, **36**(8), 741-744 (2010). https://doi.org/10.1134/S1063785010080195
[32] M.K. Bakhadyrkhanov, G.K. Mavlonov, S.B. Isamov, O.E. Sattarov, and S.A. Tachilin, "Photoconductivity of silicon with multicharged clusters of manganese atoms $[Mn]_4$," Surface Engineering and Applied Electrochemistry, **46**(3), 276–280 (2010). https://doi.org/10.3103/S1068375510030154
[33] M.K. Bakhadirkhanov, G.H. Mavlonov, X.M. Iliev, and C.A. Tachilin, "Specific features of magnetoresistance in overcompensated manganese-doped silicon," Semiconductors, **48**(8), 986 (2014). https://doi.org/10.1134/S106378261408003X

КЛАСТЕРНО-ІНДУКОВАНИЙ ФЕРОМАГНЕТИЗМ У КРЕМНІЇ, ЛЕГОВАНОМУ МАРГАНЦЕМ

Олмас Е. Саттаров[1], Станіслав А. Тачілін[1], Ільхомов А. Ільосбек[1], Нематілло Н. Маматкулов[2], Алішер Р. Тошев[3]
[1]Ташкентський державний технічний університет, Ташкент, 100095, вул. Університетська, 2, Узбекистан
[2]Національний університет Узбекистану, Ташкент, 100174, Узбекистан
[3]Алмалицький державний технічний інститут, Алмалик, 110100, Узбекистан

Інтеграція магнітної функціональності в кремній залишається ключовим викликом для розробки спінтронних пристроїв. У цій роботі досліджено структурні, електричні та магнітні властивості кремнію, легованого марганцем, отриманого методом двоступеневої термічної дифузії, що забезпечує контрольоване введення та перерозподіл Mn у матриці Si. Магнітні вимірювання демонструють чітко виражену феромагнітну поведінку за кімнатної температури, що характеризується добре визначеною петлею гістерезису з ненульовою коерцитивною силою та залишковою намагніченістю. Температурна залежність намагніченості вказує на температуру Кюрі приблизно 360 K, що підтверджує стабільність магнітного впорядкування вище кімнатної температури. Вимірювання електричного транспорту показують систематичну зміну властивостей носіїв заряду зі зростанням температури дифузії, зокрема перехід від p-типу до n-типу провідності. Така поведінка пояснюється активацією донорних станів, пов'язаних із Mn, а також дефектних комплексів, що призводять до компенсації та надкомпенсації акцепторів бору. Виявлено сильну кореляцію між концентрацією носіїв заряду та магнітними властивостями, що свідчить про вирішальну роль вільних носіїв у медіації магнітних взаємодій. На основі сукупності експериментальних результатів спостережуваний феромагнетизм інтерпретується в межах кластер-індукованого механізму, де області, збагачені Mn, виступають як локалізовані магнітні центри, пов'язані через обмінні взаємодії, опосередковані носіями заряду, узгоджені з механізмом типу RKKY. Отримані результати демонструють, що двоступенева термічна дифузія є ефективним підходом для керування як електричними, так і магнітними властивостями кремнію, підкреслюючи його потенціал для застосування у кремнієвій спінтроніці.

Ключові слова: *кремній; марганець; донор; феромагнетизм; нанокластери; спінтроніка*

EAST EUROPEAN JOURNAL OF PHYSICS. 3. 305-309 (2026)
DOI: 10.26565/2312-4334-2026-3-26 ISSN 2312-4334

STRUCTURAL FEATURES OF EPITAXIAL SOLID SOLUTION FILMS $(Si_2)_{1-X}(GaN)_X$ GROWN ON Si SUBSTRATES

A.S. Saidov[1], Sh.N. Usmonov[1], T.T. Ishniyazov[1], M.U. Kalanov[2], D.V. Saparov[1]*, M.B. Tagaev[3], A.M. Akhmedov[4], A.Sh. Razzokov[5], K.G. Gaymnazarov[6]

[1]*S.A. Azimov Physical–Technical Institute, Uzbekistan Academy of Sciences, 2B Ch. Aytmatova st. Tashkent, 100084, Uzbekistan*
[2]*Institute of Nuclear Physics, Uzbekistan Academy of Sciences, Tashkent, Uzbekistan*
[3]*Karakalpak State University named after Berdak*
[4]*Tashkent Institute of Irrigation and Agriculture Mechanization Engineers, Uzbekistan*
[5]*Urgench State University, 14, Kh. Alimdjan str, Urgench city, 220100, Uzbekistan*
[6]*Gulistan State University, 120100. Sirdarin region, Gulistan city, Uzbekistan*
**Corresponding Author e-mail: dada@uzsci.net*
Received January 13, 2026; revised May 5, 2026; in final form May 26, 2026; accepted June 13, 2026

On Si (111) substrates with a diameter of 20 mm, continuous monocrystalline epitaxial layers of $(Si_2)_{1-x}(GaN)_x$ solid solutions were grown by liquid-phase epitaxy from a limited volume of a tin solution-melt. The grown films had *n*-type conductivity. An analysis of the X-ray diffraction pattern showed that the grown epitaxial film has (111) crystallographic orientation with evident single-crystal sings. The size of the film subcrystallites is~40 nm. Due to the replacement of paired Si atoms by a molecule consisting of Ga and N atoms, a slight bending of the film towards the perpendicular to the reflecting surface was observed. Coherently arranged nanocrystals of cubic (*c* - GaN) and hexagonal (*h* - GaN) modification of gallium nitride with a crystallite size of $L_{GaN}\approx47$ nm are formed in the crystal lattice of the epitaxial film.
Keywords: *Liquid-phase epitaxy; Silicon; Gallium nitride; Solid solution; X-ray structural analysis*

1. INTRODUCTION

Gallium nitride (GaN) is a direct-gap semiconductor with a band gap of 3.4 eV, enabling the use of a wide range of electromagnetic wavelengths. The excellent optical and electrical properties of GaN make it an attractive material for optoelectronics and high-speed electronic devices, including LEDs, detectors, lasers, and high-power and high-frequency devices [1-7]. GaN-based devices are ideal for power amplifiers operating at frequencies that are unattainable with Si-based technology. GaN power electronics offer less power loss than Si devices and can operate at higher temperatures. The integration of GaN devices with Si integrated circuits provides a scalable CMOS (complementary metal-oxide-semiconductor) technology platform [8] for high-power and high-performance optoelectronics. Over the past 20 years, GaN has become the most researched semiconductor after silicon due to its excellent optical and electrical properties.

Currently, due to the high cost of native substrates, GaN is grown on foreign substrates such as sapphire (Al_2O_3), SiC, and Si [9–11]. However, there is a mismatch between the lattice constant and the thermal expansion coefficient of the GaN film and the foreign substrate. As a result, dense point defects, threading dislocations, and residual stresses appear in finished films, which reduce the service life and efficiency of optoelectronic devices fabricated on their basis [12–14]. When growing GaN on Si (GaN-on-Si), two main problems arise: (1) the nucleation of an AlN buffer layer grown to prevent the formation of a Ga-Si alloy and to compensate for thermal stresses, as well as the quality of the resulting AlN/Si interface; and (2) cracking of the epitaxial layer due to the higher thermal expansion coefficient of nitrides compared to Si. GaN layers crack when the layer thickness exceeds ~1 μm [15]. At present, GaN-on-Si technology has greatly improved. However, the mass adoption of GaN-on-Si for illumination remains controversial, mainly because epitaxial layers on Si are more difficult to grow than GaN on Al_2O_3. For electronic applications, GaN-on-Si is more favorable due to the poor electrical and thermal conductivity of Al_2O_3 (sapphire) and the high cost of SiC, which are commonly used as GaN substrates [16, 17]. High-quality GaN layers can be obtained on Si substrates through buffer layers from a continuous solid solution of molecular substitution $(Si_2)_{1-x}(GaN)_x$, with a smoothly changing composition from silicon to pure gallium nitride ($0 \le x \le 1$). This buffer layer, by leveling the mismatch between the lattice constant and the thermal expansion coefficient of the Si substrate and the GaN epitaxial film, prevents residual mechanical stresses in the transition region and, consequently, reduces point defects and threading dislocations in the epitaxial layer.

In this article, we report the possibility of growing epitaxial layers of solid solutions of molecular substitution $(Si_2)_{1-x}(GaN)_x$ on Si (111) substrates by liquid-phase epitaxy from a tin solution-melt and present the results of an experimental study of the structural features of epitaxial films using the X-ray diffraction method. Epitaxial layers of $(Si_2)_{1-x}(GaN)_x$ were grown using the technology described in [18].

Cite as: A.S. Saidov, Sh.N. Usmonov, T.T. Ishniyazov, M.U. Kalanov, D.V. Saparov, M.B. Tagaev, A.M. Akhmedov, A.Sh. Razzokov, K.G. Gaymnazarov, East Eur. J. Phys. 3, 305 (2026), https://doi.org/10.26565/2312-4334-2026-3-26

2. MATERIALS AND METHODS

Solid solutions $(Si_2)_{1-x}(GaN)_x$ were grown on Si (111) substrates by liquid-phase epitaxy from a limited volume of Sn solution-melt in an ambient H_2 atmosphere. Before entering the reactor, hydrogen was deeply purified using palladium diffusion filtration, removing oxygen, moisture, and other impurity gases. Palladium purification produced high-purity hydrogen, which was essential for stabilizing liquid-phase epitaxy conditions, preventing oxidation of the melt solution components and the substrate surface, and improving the structural quality and homogeneity of the grown epitaxial layers. The substrates were silicon washers of grade KDB-0.01, p-type, boron-doped, with a resistivity of 0.01 Ω·cm. The diameter and thickness of the substrates were 20 mm and 400 μm, respectively. The growth of epitaxial layers was carried out by varying the following parameters of the technological process: the composition of the solution-melt, the temperature of the beginning and end of solid solution crystallization, the rate of forced cooling and the thickness of the solution-melt. The composition of the Sn-Si-GaN solution melt, in the weight ratio of components, was determined based on the results of preliminary experiments. Epitaxial layers of solid solutions were grown at a temperature range of 950–850°C, a cooling rate of 1 °C/min, and a solution-melt thickness of 1 mm. At the selected process parameters, the entire substrate surface was covered with a continuous epitaxial film. The adhesion of the epitaxial films to the substrate surface was of high quality. Over the entire surface, the thickness of the epitaxial layer was uniform at ~10 μm. Epitaxial films had *n*-type conductivity with a concentration of ~ $3.4 \cdot 10^{16}$ cm^{-3}, a mobility of ~ 133 $cm^2 \cdot V^{-1} \cdot sec^{-1}$ of charge carriers and a resistivity of ~ 1.38 Ω·cm at 300 K.

Structural studies of the resulting epitaxial film were carried out in the Institute of Nuclear Physics of the Academy of Sciences of the Republic of Uzbekistan on a DRON-3M X-ray diffractometer (radiation CuKα, λ = 0,15418 nm) with improved the Θ–2Θ optical scheme in step scan mode.

3. RESULTS AND DISCUSSION

Fig. 1 shows an X-ray diffraction pattern of the Si substrate. The diffraction pattern contains several selective structural reflections with different intensities and one diffuse reflection at small scattering angles. The analysis showed that the substrate surface corresponds to the (111) crystallographic plane.

This is evidenced by the presence of a series of selective reflections of the (HHH) type (where H = 1, 2, 3), intense lines $(111)_{Si}$ with d/n = 0.3142 (2θ = 28.4°), $(222)_{Si}$ with d/n = 0.1568 (2θ = 58.8°) and $(333)_{Si}$ with d/n = 0.1045 nm (2θ = 94.95°). The beta (β) component of the structural line of the first order $(111)_{Si}$ is visible at 2θ = 25.8°, and the third order is visible at 2θ = 83.5°. High intensity ($2 \cdot 10^5$ pulses·sec^{-1}) of the main reflection $(111)_{Si}$, narrow width (FWHM ≈ 0.25°), testifies to the perfection of the substrate crystal lattice. Furthermore, the X-ray diffraction pattern of the substrate contains only the reference reflection (111) and its high orders (222) and (333), while diffraction reflections with other indices are absent. These are signs of its single-crystal state.

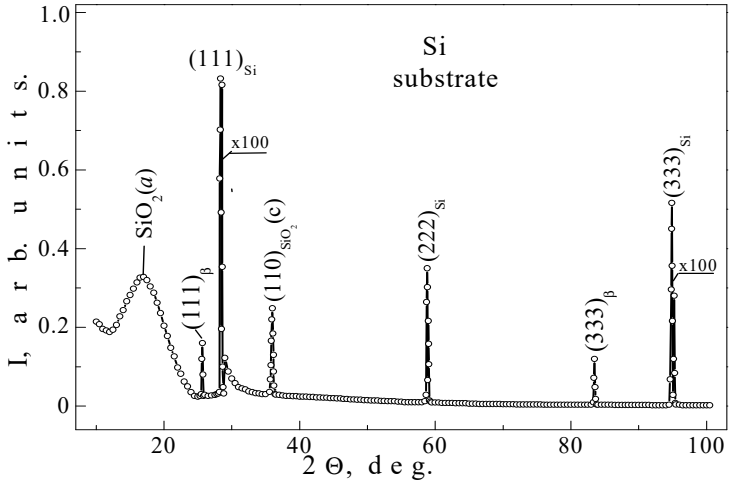

Figure 1. X-ray pattern of a silicon substrate

Good, close to the calculated splitting of the $(333)_{Si}$ reflection with characteristic intensity ratios for α_1 and α_2 radiation [$I_{333}(\alpha_1) \approx 2I_{333}(\alpha_2)$], indicates that the elastic stress is predominantly concentrated in the near-surface layer of the volume, close to the surface of the substrate and at the boundaries between the blocks of the matrix lattice (Fig. 2).

The X-ray diffraction pattern shows a noticeable (110) reflection of SiO2 with d/n = 0.2501 nm (2θ = 35.9°), attributed to the SiO_2 impurity in the substrate. The narrow width (FWHM = $2.62 \cdot 10^{-3}$ rad) of this reflection indicates that the SiO_2 impurity phase in the bulk of the matrix is in the crystalline modification, SiO_2(c). The characteristic size of the structural fragments (subcrystallites) of this phase is ~ 58 nm. Due to the large ionic radius of oxygen compared to silicon, they are energetically preferred to be located in the interstices of boundary and near-boundary regions between grains and blocks (subcrystallites) of the substrate [19]. In these areas, the chemical bonds between the ions of the matrix are not saturated, and the nodes are somewhat displaced from their ideal positions.

These factors contribute to the formation of structural fragments with low symmetry, consisting of silicon and interstitial ions, in comparison with the structure with high symmetry in the bulk of the blocks of the substrate, consisting only of silicon ions. The experimental value of the substrate lattice parameter was a_{Si} = 0.54293 nm, which is comparable with the tabulated value a_{Si} = 0.54307 nm. This shows that the volume fraction of the distorted lattice region is negligible compared to the entire volume of the substrate.

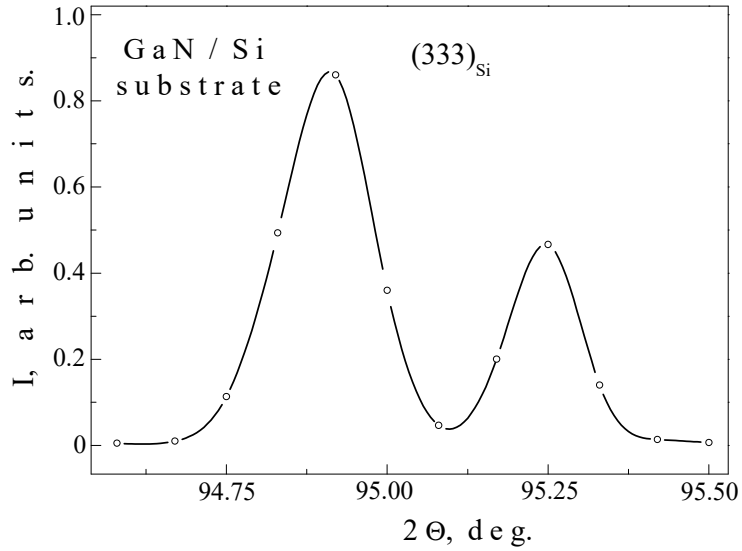

Figure 2. The shape of the reflections (333) of the silicon substrate

Figure 3 shows the X-ray diffraction pattern of an epitaxial layer of the $(Si_2)_{1-x}(GaN)_x$ solid solution grown on silicon substrates. The high-resolution (333) reflection shape is shown in Fig. 4. This result significantly differed from the X-ray diffraction pattern of the substrate. Here, the intensity of diffuse reflection at small scattering angles decreased by more than 3 times, and the intensity of the main reflection $(111)_{Si}$ ($2\theta = 28.33°$) of the film increased by ~ 6% compared to the intensity of the same reflection of the substrate. The intensity of the forbidden reflection (222) ($2\theta = 58.65°$) decreased by a factor of 2, its intensity of the third order (333) ($2\theta = 94.70°$) decreased by almost an order of magnitude, and the intensity of the reflection (110) of SiO_2 ($2\theta = 35.8°$) from the impurity phase of crystalline quartz decreased by 2 times. The average level of the inelastic background also decreased by 2 times.

The relatively narrow width (FWHM = $3.78 \cdot 10^{-3}$ rad) and high intensity ($2 \cdot 10^5$ pulses·sec-1) of the main reflection $(111)_{GaN/Si}$ indicate a high degree of perfection of the crystal lattice of the epitaxial layer of the solid solution $(Si_2)_{1-x}(GaN)_x$; that is, the grown film has the sign of a single crystal with a (111) orientation. The sizes of subcrystallites (blocks) of the film, estimated from the width of this peak by the Selyakov–Scherrer method [20], were ~ 40 nm.

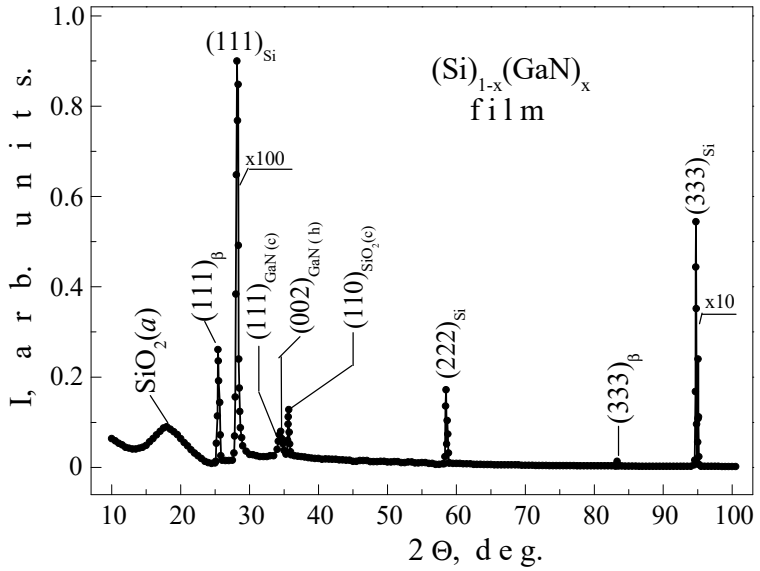

Figure 3. X-ray pattern of the epitaxial layer of the $(Si_2)_{1-x}(GaN)_x$ solid solution

However, the intensity of the main reflection of the $(111)_{GaN/Si}$ film is 6% higher than the intensity of the same line of the substrate, $(111)_{Si}$. This indicates the partial replacement of some pairs of silicon ions by gallium and nitrogen molecules in the film's silicon lattice. Since the X-ray scattering intensity is proportional to the square of atomic number (Z^2) of the elements (Z_{Si} = 14, Z_N = 7, and Z_{Ga} = 31), such a replacement of ions should lead to some increase in the intensity of this reflection, which is observed in the experiment.

Since the thermal expansion coefficients of GaN are 2.2 times greater than those of Si (α_{GaN} - $5.59 \cdot 10^{-6}$/ºC, α_{Si} - $2.6 \cdot 10^{-6}$/ºC), when cooled from the epitaxy temperature (950–850°C) to room temperature, the fabricated heterostructure bends in the direction perpendicular to the reflective surface of the film.

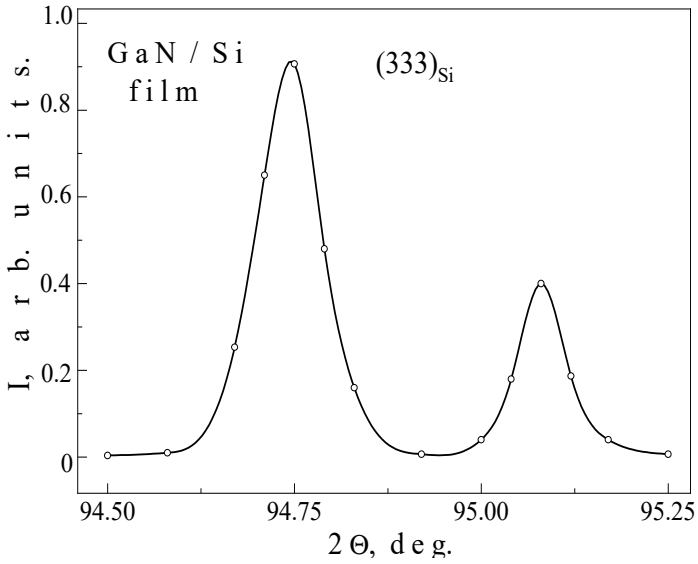

Figure 4. The shape of reflections (333) of the epitaxial layer of the solid solution $(Si_2)_{1-x}(GaN)_x$

In addition, this conclusion is confirmed by the appearance of a new selective reflection with a noticeable intensity and a width of $3.2 \cdot 10^{-3}$ rad. near the main reflection (111) of the film. An analysis of the nature of this structural line showed that it consists of two selective lines very close in angular position and corresponding to two modifications of gallium nitride: cubic (c-GaN) - $(111)_{GaN}$ with d/n = 0.2599 nm (2θ = 34.4°) and hexagonal (h-GaN) - $(002)_{GaN}$ with d/n = 0.2592 nm (2θ = 34.6°). They are caused by gallium nitride nanocrystals $L_{GaN} \approx 47$ nm in size. These nanocrystallites are located in the near-surface layer of the film, as evidenced by the angular arrangement of reflections associated with them. The close angular position of these reflections to the main $(111)_{GaN/Si}$ reflection made it possible to determine the GaN content of c-GaN and h-GaN nanocrystals in the film from the ratio of their intensities. It was 9.1 and 8.9 mol. %, respectively. Therefore, it can be argued that during liquid-phase epitaxy on a Si(111) substrate, it is possible to form a GaN-Si heterostructure with GaN nanocrystallites, both cubic (c-GaN) and hexagonal (h-GaN) modification.

4. CONCLUSIONS

Continuous epitaxial layers of $(Si_2)_{1-x}(GaN)_x$ solid solutions were grown on Si(111) substrates 20 mm in diameter by liquid-phase epitaxy from a limited volume of a tin solution-melt.

Analysis of the X-ray diffraction pattern showed that the resulting film has the perfect crystalline structure with (111) orientation and evident single-crystal sings. Coherently located nanocrystallites of cubic (c-GaN) and hexagonal (h-GaN) modification of gallium nitride with a crystallite size of $L_{GaN} \approx 47$ nm are formed in the crystal lattice of the epitaxial film.

Funding
This work was financially supported by the Fundamental Research Programs of the Uzbekistan Academy of Sciences on the topic "Photovoltaic, thermal-voltaic, photothermal-voltaic and radiative effects in two and multicomponent semiconductor solid solutions with nanocrystals, obtained on silicon substrates from the liquid phase".

Authors' Contribution A.S. Saidov: Project administration, Sh.N. Usmonov: Supervision M. Kalanov: Writing-original draft, D.V Saparov: Editing, Data curation, T.T. Ishniyazov: Carried out the experiment. M.B. Tagaev: Performed the measurements. A.M. Akhmedov: Assisted measurements. A.Sh. Razzokov: Validation, K.G. Gaymnazarov: Funding acquisition.

ORCID
Amin S. Saidov, https://orcid.org/0000-0002-9124-6430; **Sh.N. Usmonov,** https://orcid.org/0000-0001-7683-0017
Tolmas T. Ishniyazov, https://orcid.org/0000-0001-8518-626X; **M.U. Kalanov,** https://orcid.org/0000-0003-2758-0781
D.V. Saparov, https://orcid.org/0000-0002-9282-9048; **Marat Tagaev,** https://orcid.org/0000-0002-1833-8339
A.M. Akhmedov, https://orcid.org/0000-0003-2210-8437; **A.Sh. Razzokov,** https://orcid.org/0000-0002-2210-6207
K.G. Gaymnazarov, https://orcid.org/0009-0004-5317-7288

REFERENCES

[1] S. Nakamura, "Background Story of the Invention of Efficient InGaN Blue-Light-Emitting Diodes (Nobel Lecture)," Angew. Chem. Int. Ed. Engl. **54**, 7770–7788 (2015). https://doi.org/10.1002/anie.201500591
[2] L.-H. Hsu, Y.-Y. Lai, P.-T. Tu, C. Langpoklakpam, Y.-T. Chang, Y.-W. Huang, W.-C. Lee, *et al*., « Development of GaN HEMTs Fabricated on Silicon, Silicon-on-Insulator, and Engineered Substrates and the Heterogeneous Integration," Micromachines, **12**, 1159 (2021). https://doi.org/10.3390/mi12101159
[3] Y. Du, B. Xu, G. Wang, Y. Miao, B. Li, Z. Kong, Y. Dong, *et al*., "Review of Highly Mismatched III-V Heteroepitaxy Growth on (001) Silicon," Nanomaterials, **12**, 741 (2022). https://doi.org/10.3390/nano12050741
[4] Iu. Kim, J. Holmi, R. Raju, A. Haapalinna, and S. Suihkonenet, "MOVPE growth of GaN on patterned 6-inch Si wafer," J. Phys. Commun. **4**, 045010 (2020). https://doi.org/10.1088/2399-6528/ab885c
[5] H.Y. Ryu, "Investigation into the anomalous temperature characteristics of InGaN double quantum well blue laser diodes using numerical simulation," Nanoscale Research Letters, **12**, 1-7 (2017). https://doi.org/10.1186/s11671-017-2141-6
[6] A.-C. Liu, Y.-Y. Lai, H.-C. Chen, A.-P. Chiu, H.-C. Kuo, "A Brief Overview of the Rapid Progress and Proposed Improvements in Gallium Nitride Epitaxy and Process for Third-Generation Semiconductors with Wide Bandgap," Micromachines, **14**, 764 (2023). https://doi.org/10.3390/mi14040764
[7] H. Kim, C.S. Chang, S. Lee, J. Jiang, J. Jeong, M. Park, Y. Meng, *et al*., "Remote epitaxy," Nat. Rev. Methods Primers, **2**, 40 (2022). https://doi.org/10.1038/s43586-022-00122-w
[8] C.H. Jan, M. Agostinelli; H. Deshpande; M. A. El-Tanani; W. Hafez; U. Jalan, L. Janbay, *et al*., "RF CMOS technology scaling in high-k/metal gate era for RF SoC (system-on-chip) applications," in: *2010 International Electron Devices Meeting*, (IEEE, 2010), pp. 27.2. 1-27.2. 4 (2010). https://doi.org/10.1109/IEDM.2010.5703431
[9] Y. Zhang, G. Deng, Y. Yu, Y. Wang, D. Zhao, Z. Shi, B. Zhang, *et al*., "Demonstration of N-polar III-nitride tunnel junction LED," Acs. Photonics, **7**(7), 1723-1728 (2020). https://doi.org/10.1021/acsphotonics.0c00269
[10] G. Deng, Y. Zhang, Y. Yu, L. Yan, P. Li, X. Han, L. Chen, *et al*., "Significantly improved surface morphology of N-polar GaN film grown on SiC substrate by the optimization of V/III ratio," Applied Physics Letters, **112**, 151607 (2018). https://doi.org/10.1063/1.5022237
[11] F. Jiang, J. Zhang, L. Xu, J. Ding, G. Wang, X. Wu, and J. Liu, "Efficient InGaN-based yellow-light-emitting diodes," Photonics Research, **7**(2), 144-148 (2019). https://doi.org/10.1364/PRJ.7.000144
[12] D.G. Zhao, S. J. Xu; M. H. Xie; S. Y. Tong; and H. Yang, "Stress and its effect on optical properties of GaN epilayers grown on Si (111), 6H-SiC (0001), and c-plane sapphire," Applied Physics Letters, **83**(4), 677-679 (2003). https://doi.org/10.1063/1.1592306
[13] M.F. Schubert, S. Chhajed, J.K. Kim, E.F. Schubert, D.D. Koleske, M.H. Crawford, *et al*., "Effect of dislocation density on efficiency droop in InGaN/GaN light-emitting diodes," Appl. Phys. Lett. **91**, 231114 (2007). https://doi.org/10.1063/1.2822442
[14] C.J. Zollner, A. Almogbel, Y. Yao, B. K. SaifAddin, F. Wu, M. Iza, S.P. DenBaars, *et al*., "Reduced dislocation density and residual tension in AlN grown on SiC by metalorganic chemical vapour deposition," Appl. Phys. Lett. **115**, 161101 (2019). https://doi.org/10.1063/1.5123623
[15] A. Dadgar, J. Blasing, A. Diez, A. Alam, M. Heuken, and A. Krost, Jpn. J. Appl. Phys. Part 1, **39**, 1183 (2000). https://doi.org/10.1143/JJAP.39.L1183
[16] M. Charles, J. Kanyandekwe, S. Bos, Y. Baines, E. Morvan, A. Torres, F. Templier, *et al*., "Epitaxy of GaN on Si (111) for power electronics, RF and LEDs," ECS Transactions, **86**(7), 233 (2018). https://doi.org/10.1149/08607.0233ecst
[17] Y. Zhong, J. Zhang, S. Wu, L. Jia, X. Yang, Y. Liu, Y. Zhang, and Q. Sun, "A review on the GaN-on-Si power electronic devices," Fundamental Research, **2**(3), 462-475 (2022). https://doi.org/10.1016/j.fmre.2021.11.028
[18] A.S. Saidova, Sh.N. Usmonova, M.U. Kalanovb, D.V. Saparova, T.T. Ishniyazova, A.M. Akhmedovc, M.B. Tagaevd, and A.Sh. Razzokov, "Growing of perfect single-crystal epitaxial films of $(Si_2)_{1-x}(GaN)_x$ solid solutions on Si (111) substrates from the liquid phase," Acta Physica Polonica A, **148**(1), 29-33 (2025). https://doi.org/10.12693/APhysPolA.148.29
[19] B.S. Bokshteĭn, *Thermodynamics and Kinetics of Diffusion in Solids*, (Oxonian Press, 1985).
[20] A. A. Rusakov, *X-ray Radiography of Metals*, (Atomizdat, Moscow, 1977). (in Russian)

СТРУКТУРНІ ОСОБЛИВОСТІ ЕПІТАКСІАЛЬНИХ ПЛІВОК ТВЕРДИХ РОЗЧИНІВ (Si2)1-X(GaN)X ВИРОЩЕНИХ НА Si-ПІДЛОЖКАХ

А.С. Саїдов[1], Ш.Н. Усмонов[1], Т.Т. Ішнязов[1], М.У. Каланов[2], Д.В. Сапаров[1], М.Б. Тагаєв[3], А.М. Ахмедов[4], А.Ш. Раззоков[5], К.Г. Гаймназаров[6]

[1]Фізико-технічний інститут ім. С.А. Азімова, Академія наук Узбекистану, вул. Ч. Айтматова, 2Б, Ташкент, 100084, Узбекистан
[2]Інститут ядерної фізики, Академія наук Узбекистану, Ташкент, Узбекистан
[3]Каракалпакський державний університет імені Бердака
[4]Ташкентський інститут інженерів іригації та механізації сільського господарства, Узбекистан
[5]Ургенчський державний університет, вул. Х. вул. Алімджан, місто Ургенч, 220100, Узбекистан
[6]Гулістанський державний університет, 120100. Сирдаринський район, місто Гулістан, Узбекистан

На підкладках Si (111) діаметром 20 мм методом рідкофазної епітаксії з обмеженого об'єму розчину-розплаву олова вирощували суцільні монокристалічні епітаксіальні шари твердих розчинів $(Si_2)_{1-x}(GaN)_x$. Вирощені плівки мали n-тип провідності. Аналіз рентгенограми показав, що вирощена епітаксіальна плівка має кристалографічну орієнтацію (111) з чіткими монокристалічними ознаками. Розмір субкристалітів плівки становить ~ 40 нм. Через заміщення парних атомів Si молекулою, що складається з атомів Ga та N, спостерігався незначний вигин плівки відносно перпендикуляра до поверхні відбиття. У кристалічній решітці епітаксіальної плівки утворюються когерентно розташовані нанокристали кубічної (c-GaN) та гексагональної (h-GaN) модифікацій нітриду галію з розміром кристалітів LGaN≈47 нм.

Ключові слова: *рідкофазна епітаксія; кремній; нітрид галію; твердий розчин; рентгеноструктурний аналіз*

East European Journal of Physics. 3. 310-318 (2026)
DOI:10.26565/2312-4334-2026-3-27 ISSN 2312-4334

RADIATION-INDUCED MODIFICATION OF III–V AND II–VI QUANTUM HETEROSTRUCTURES UNDER HIGH-ENERGY X-RAY, GAMMA-RAY, AND ELECTRON IRRADIATION

Mardonbek Kh. Nasirov[1,2]*, Dilmuhammad X. Tolaboyev[1], Tokhirbek I. Rakhmonov[1], Khusanboy M. Sulaymonov[1], Sherzod Sh. Abdullayev[1], Abdusattor O. Umarov[1], Ixtiyor M. Tursunov[1]
[1]*Fergana State Technical University, Fergana, Uzbekistan*
[2]*Fergana State University, Fergana, Uzbekistan*
**Corresponding Author e-mail: nasirovmardonbek92@gmail.com*
Received April 2, 2026; revised May 15, 2026; in final form June 17; accepted July 6, 2026

Low-dimensional III–V and II–VI quantum heterostructures are important active media for optoelectronic devices operating under radiation environments. In this work, the effects of high-energy X-ray, gamma-ray, and electron irradiation on excitonic recombination and exciton–phonon interaction were investigated in GaAs/AlGaAs and ZnTe/CdZnTe-based quantum heterostructures using low-temperature photoluminescence spectroscopy. The spectra showed pronounced excitonic emission bands accompanied by longitudinal optical phonon replicas, indicating phonon-assisted recombination processes. After irradiation, a substantial reduction in photoluminescence intensity was observed, which was attributed to the formation of radiation-induced non-radiative recombination centers. In ZnTe/CdZnTe structures, electron irradiation produced a slight blue shift (approximately 0.7 meV) of the quantum-well emission, whereas X-ray irradiation resulted in a small red shift (approximately 0.6 meV), suggesting irradiation-dependent modification of exciton localization and defect-related potential fluctuations. A semi-quantitative analysis based on integrated PL intensity ratios, an effective non-radiative recombination parameter, and the Huang–Rhys factor (S≈1–2) was performed to correlate PL quenching, spectral shifts, and LO-phonon replicas with radiation-induced defect formation. The relative changes in excitonic, impurity-related, and phonon-assisted emission bands indicate a redistribution of radiative and non-radiative recombination channels after irradiation. A phenomenological interpretation based on radiative and non-radiative recombination rates and the Huang–Rhys description of LO-phonon replicas was used to discuss the observed spectral changes. The results provide a comparative experimental assessment of irradiation-induced modifications in III–V and II–VI quantum heterostructures and may be useful for evaluating the radiation tolerance of semiconductor optoelectronic structures.
Keywords: *Radiation-induced defects; Quantum heterostructures; Photoluminescence spectroscopy; Exciton–phonon interaction; LO-phonon replicas; Non-radiative recombination; GaAs/AlGaAs quantum wells; ZnTe/CdZnTe quantum wells*

INTRODUCTION

The interaction of high-energy radiation with semiconductor quantum heterostructures is of fundamental and practical importance for the development of radiation-tolerant optoelectronic devices. Low-dimensional III–V and II–VI quantum heterostructures, including GaAs/AlGaAs and ZnTe/CdZnTe systems, are widely used in lasers, optical modulators, and field-effect transistors because of their tunable electronic and optical properties. In these structures, quantum confinement strongly influences excitonic recombination, impurity-related emission, and phonon-assisted luminescence processes. Recent electro-optical studies of GaAs/AlGaAs multiple quantum wells have shown that their photoluminescence spectra are highly sensitive to quantum confinement and external conditions [1]. Similar excitonic spectral features in related semiconductor structures have also been interpreted in terms of surface radiative modes and longitudinal excitons, thereby emphasizing the complex nature of exciton–polariton luminescence in such systems [2]. ZnTe-based heterostructures are particularly attractive for visible-range optoelectronic applications because they exhibit pronounced excitonic emission and are highly sensitive to structural defects, localization effects, and external perturbations.

Despite extensive research on radiation effects in semiconductors, the microscopic mechanisms governing exciton–phonon coupling in irradiated ZnTe quantum structures remain insufficiently understood. High-energy electron and X-ray irradiation induce defect states that act as non-radiative recombination centers and exciton localization sites, thereby modifying photoluminescence spectra and the relative intensities of excitonic and impurity-related transitions. Recent reviews of irradiated GaAs have likewise shown that radiation-induced point defects and defect complexes play a key role in the formation of non-radiative recombination channels and in the degradation of optical properties [3]. Similar quenching phenomena associated with defect-related non-radiative recombination have been reported in Cd-based semiconductor films under external perturbations such as temperature and infrared excitation [4]. The complex interplay between radiation-induced defects, exciton localization, and phonon-assisted recombination is crucial for understanding and controlling the optical response of these heterostructures under irradiation.

In this study, we investigate the effects of high-energy electron and X-ray irradiation on the low-temperature photoluminescence of ZnTe-based quantum heterostructures. Special attention is paid to longitudinal optical (LO) phonon

Cite as: M.Kh. Nasirov, D.X. Tolaboyev, T.I. Rakhmonov, Kh.M. Sulaymonov, S.Sh. Abdullayev, A.O. Umarov, I.M. Tursunov, East Eur. J. Phys. 3, 310 (2026), https://doi.org/10.26565/2312-4334-2026-3-27

replicas and impurity-related excitonic transitions, which provide insights into the restructuring of luminescence channels induced by radiation. In addition, the role of interband transitions and band structure modifications in determining optical response has been widely discussed in semiconductor systems [5,6]. In this work, the effects of high-energy X-ray, γ-ray, and electron irradiation on the low-temperature photoluminescence response of III–V and II–VI quantum heterostructures are examined with particular attention to excitonic recombination, impurity-related emission, and LO-phonon-assisted spectral features. The study combines experimental PL observations with a phenomenological interpretation based on the competition between radiative and non-radiative recombination channels and the Huang–Rhys description of exciton–phonon coupling. Rather than introducing a new fundamental mechanism, the present work aims to provide a comparative assessment of how different irradiation conditions modify excitonic, defect-related, and phonon-assisted luminescence channels in GaAs/AlGaAs and ZnTe/CdZnTe-based quantum heterostructures. This analysis is intended to clarify the relative sensitivity of different emission bands to irradiation-induced defect formation and to support the evaluation of radiation tolerance in low-dimensional semiconductor structures.

THEORETICAL CONSIDERATIONS

To interpret the observed changes in photoluminescence under irradiation, we employ a phenomenological model that accounts for exciton recombination, radiation-induced non-radiative centers, and exciton–phonon interactions. To describe these coupled processes in a compact form, the total Hamiltonian of the system can be written as

$$H = H_{ex} + H_{ph} + \mathrm{H}_{\text{ex-ph}}, \tag{1}$$

where H_{ex} describes the excitonic subsystem, H_{ph} corresponds to the phonon field, and $H_{\text{ex-ph}}$ represents the exciton–phonon interaction.

Equation (1) defines the general theoretical basis of the model by separating the excitonic, phononic, and interaction contributions to the optical response. For longitudinal optical (LO) phonons, the interaction can be written in the Fröhlich-type form

$$H_{\text{ex-ph}} = \Sigma_q M_q \left(a_q + a\_q^{\dagger}\right) X^{\dagger} X, \tag{2}$$

where M_q is the exciton–phonon coupling matrix element, $a_q^{\dagger}$ and a_q are the phonon creation and annihilation operators, and $X^{\dagger}X$ denotes the exciton occupation operator.

Equation (2) explicitly describes the coupling between excitons and LO phonons and serves as the basis for interpreting the phonon-assisted features observed in the PL spectra. This interaction explains the appearance of LO-phonon replicas in the photoluminescence spectra. Such phonon-assisted relaxation channels are characteristic of CdTe/ZnTe quantum well systems, in which LO-phonon emission plays a central role in exciton energy relaxation [7]. The theoretical description of optical absorption processes in semiconductors often relies on interband and intraband transition mechanisms, accounting for band mixing and temperature-dependent effects [5,8].

The integrated photoluminescence intensity can be expressed as

$$I_{\text{PL}} \propto G \cdot \frac{k_r}{k_r + k_{\text{nr}}}, \tag{3}$$

where G is the generation rate, k_r is the radiative recombination rate, and $k_n r$ is the non-radiative recombination rate.

Equation (3) shows that the observed PL intensity is determined by the competition between radiative and non-radiative recombination channels. Similar carrier generation and recombination mechanisms have been analyzed from photoconductivity spectra of Cd-based solid-solution films, highlighting the role of defect states and band transitions [9]. Under irradiation, defect formation leads to an increase in $k_n r$, which can be written as

$$k_{nr} = k_{nr}^{(0)} + \beta N_d, \tag{4}$$

where N_d is the concentration of radiation-induced defects.

Equation (4) indicates that the non-radiative recombination rate increases with the concentration of radiation-induced defects, which explains the quenching of photoluminescence under irradiation. Therefore, the PL intensity ratio can be written as

$$\frac{I_{\text{irr}}}{I_0} = \frac{k_r + k_{\text{nr}}^{(0)}}{k_r + k_{\text{nr}}^{(0)} + \beta N_d}. \tag{5}$$

Equation (5) provides a convenient relation for comparing the relative decrease in PL intensity before and after irradiation and can be directly related to the experimentally measured quenching ratios. For phonon-assisted transitions, the relative intensities of LO-phonon replicas can be described using the Huang–Rhys model, while the Huang–Rhys factor provides a quantitative measure of the exciton–LO-phonon coupling strength in semiconductor quantum wells [10]:

$$I_n = I_0 \exp(-S) \frac{S^n}{n!}, \tag{6}$$

where S is the Huang–Rhys factor.

Equation (6) relates the intensity distribution of the 1LO, 2LO, and 3LO replicas to the Huang–Rhys factor and thus allows estimation of the strength of exciton–phonon coupling. This model explains the presence of 1LO, 2LO, and 3LO lines observed in the spectra. More generally, Huang–Rhys theory has been extensively applied in semiconductor optical spectroscopy to interpret phonon sidebands, exciton localization effects, and the relative intensity distribution of multi-phonon replicas [11]. Furthermore, multiphoton absorption processes and intersubband transitions in III–V semiconductors provide an important contribution to the understanding of nonlinear optical effects in such systems [6,12].

To establish a direct connection between the phenomenological model and the experimental PL spectra, three measurable quantities were used in the analysis: the integrated PL intensity ratio, the irradiation-induced spectral shift, and the relative intensities of the LO-phonon replicas. First, Eq. (5) was used to interpret the experimentally observed PL quenching through the increase in the defect-assisted non-radiative recombination rate after irradiation. The measured decrease of the excitonic PL intensity by approximately two orders of magnitude indicates a substantial increase in k_{nr} compared with the initial value before irradiation. Second, the small blue and red shifts observed after electron and X-ray irradiation were interpreted as signatures of irradiation-induced changes in exciton localization and defect-related potential fluctuations. Third, Eq. (6) was used to estimate the exciton–LO-phonon coupling strength from the relative intensities of the 1LO, 2LO, and 3LO replicas through the Huang–Rhys factor. Therefore, the model was not used as an independent microscopic theory but as a quantitative phenomenological framework to correlate PL quenching, spectral shifts, and phonon-assisted emission features with radiation-induced defect formation.

EXPERIMENTAL METHOD

Low-dimensional quantum heterostructures were fabricated using state-of-the-art epitaxial techniques to ensure precise control over layer composition and thickness. ZnTe-based structures were grown by molecular beam epitaxy (MBE) employing the “Katun” system, whereas III–V heterostructures were synthesized via metal-organic chemical vapor deposition (MOCVD). Detailed growth parameters, including substrate temperature, flux ratios, and deposition rates, were optimized according to established protocols to achieve high crystalline quality and minimal structural defects.

The investigated samples are summarized in Table 1. Sample No. 1 was a ZnTe/CdZnTe-based quantum heterostructure containing three tunnel-coupled quantum wells grown by molecular beam epitaxy. Sample No. 4 was a GaAs/AlGaAs quantum-well heterostructure containing three AlGaAs/GaAs quantum wells with thicknesses of 2.5, 4.2, and 7.7 nm separated by 100 nm barriers. These samples were selected to compare the irradiation response of representative II–VI and III–V quantum heterostructures under different irradiation conditions.

Table 1. Structural parameters of the investigated quantum heterostructures.

Sample No.	Material system	Substrate	Growth method	Structure description	Quantum-well thickness	Barrier / surrounding layers	Doping concentration	Irradiation type	Measurement temperature
No. 1	ZnTe/$Cd_{0.2}Zn_{0.8}Te$	GaAs(001)	MBE using the KATUN9 system	Three tunnel-coupled $Cd_{0.2}Zn_{0.8}Te$ quantum wells embedded in ZnTe	2 nm for each QW	Barrier thickness not explicitly reported; ZnTe cap layer = 4 nm; ZnTe buffer layer = 1.5 μm	Not explicitly reported	Electron irradiation and X-ray irradiation	4.2 K
No. 4	GaAs/AlGaAs	GaAs	MOCVD	Three AlGaAs/GaAs quantum wells	2.5, 4.2, and 7.7 nm	AlGaAs barrier thickness = 100 nm	Not explicitly reported	Gamma irradiation	4.2 K and 77 K

Photoluminescence (PL) and reflectance measurements were conducted to characterize optical properties in the photon energy range of $0.6 - 3.0\ eV$ over temperatures from $4.2\ K$ to $300\ K$. Low-energy spectral components ($0.6 - 1.4\ eV$) were analyzed using a prism monochromator, while higher energies were employed with a diffraction monochromator. Photoluminescence excitation was performed using an argon-ion laser at $\lambda_{exc} = 514.53\ nm$ for ZnTe/CdZnTe quantum heterostructures. For GaAs/AlGaAs quantum wells, PL spectra were measured using excitation at $\lambda_{exc} = 632.8\ nm$. These excitation wavelengths were selected to probe excitonic emission from the quantum wells and related defect-assisted recombination channels.

For the II–VI ZnTe/CdZnTe structures, two irradiation modalities were applied: high-energy electron irradiation and X-ray photon exposure. Electron irradiation was performed using the ILU-6 pulsed accelerator, delivering electrons at $1.8\ MeV$ with a total fluence of $\Phi = 10^{16} cm^{-2}$. Pulses had a duration of 700 μs at a repetition rate of 25 Hz, with a current density of $10^{12}\ cm^{-2} \cdot s^{-1}$ per pulse. The sample temperature during irradiation did not exceed $60°C$. Energy deposition calculations indicate that the generation rate of electron-hole pairs reached $\sim 10^{23}\ cm^{-3} \cdot s^{-1}$, with the formation of radiation-induced defects via atomic displacements in the crystal lattice, estimated at $\sim 10^{17}\ cm^{-3}$.

X-ray irradiation was conducted using the RAP-150/300 source at an accelerating voltage of 100 kV, producing a continuous broad-spectrum photon flux. The dose rate was $10\ R \cdot s^{-1}$, with total exposure reaching $10^4\ R$. Absorbed energy densities in the structures were evaluated, yielding values on the order of $10^{21}\ eV \cdot cm^{-3}$, sufficient to induce significant modification of excitonic recombination channels and to generate defect states influencing photoluminescence.

For the GaAs/AlGaAs quantum-well structure, γ-irradiation was performed using a Co γ-source with a total dose of $D = 2 \times 10^9 rad$. The PL spectra were recorded before and after γ-irradiation at 77 K and 4.2 K in order to evaluate

irradiation-induced changes in near-band-edge excitonic, impurity-related, and defect-related emission bands under different low-temperature measurement conditions.

All optical measurements were carried out using an automated setup integrating a low-temperature cryostat, monochromators, and photodetectors suitable for resolving excitonic emission lines, LO-phonon replicas, and impurity-related transitions. The spectral resolution of the PL measurements was determined by the monochromator configuration and was kept constant for each set of comparative measurements. Each PL spectrum was recorded under identical excitation power, temperature, and detection geometry before and after irradiation. Peak positions were extracted from the maxima of the emission bands, while integrated PL intensities were calculated after background subtraction over the same spectral interval for each band. The uncertainty in the relative intensity analysis was mainly associated with excitation-power fluctuations, detector response, and baseline correction. Repeated measurements confirmed that the main irradiation-induced trends, including PL quenching and small spectral shifts, were reproducible within the experimental uncertainty.

RESULTS

Photoluminescence of GaAs/AlGaAs Quantum Wells**.** Figure 1 presents representative low-temperature (77 K) PL spectra of sample No. 4 (Table 1), containing three AlGaAs/GaAs quantum wells, measured from the GaAs substrate side before and after γ-irradiation. The quantum well thicknesses were $L_Z = 2.5$,4.2, and 7.7 nm, and the barrier thickness was $L_B = 100$ nm (inset of Fig. 2).

As shown in Fig. 1, the photoluminescence spectra exhibit several distinct emission bands associated with excitonic and defect-related transitions. Similar excitonic and field- or temperature-sensitive optical transitions have been analyzed in GaAs/AlGaAs multiple-quantum-well heterostructures, thereby supporting the assignment of the observed PL bands in the present study [1].

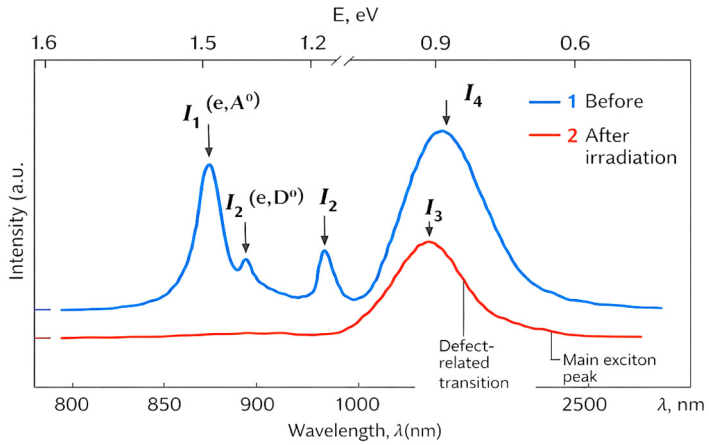

Figure 1. Typical PL spectra of the GaAs/AlGaAs quantum-well structure measured from the GaAs substrate side before (1) and after (2) gamma irradiation, D = 2×10⁹ rad, at 77 K. Excitation: λ = 632.8 nm, P = 2 W/cm².

According to the proposed model, the observed decrease in PL intensity after irradiation is associated with an increase in the non-radiative recombination rate due to radiation-induced defect formation. A comparable suppression of photoluminescence under very high electron-dose irradiation has also been reported for GaInNAs/GaAs quantum wells, further confirming the dominant role of irradiation-induced defect states in the degradation of optical response [13]. This interpretation is consistent with earlier studies of electron-irradiated GaAs-based single quantum wells, in which irradiation-induced defect states were found to alter photoluminescence intensity and spectral position through modified recombination dynamics [14]. Related irradiation-dependent changes in GaAs quantum wells have also been observed under electron-beam exposure, demonstrating that beam-induced defect modification can significantly affect luminescence intensity and recombination behavior [15].

A quantitative comparison with the proposed model was also performed. Using the relation $I_P L \propto k_r/(k_r + k_n r)$, the observed decrease in photoluminescence intensity can be attributed to a significant increase in the non-radiative recombination rate. The experimentally observed reduction of the integrated intensity ($I/I^0 \approx 10^{-2}$ for excitonic bands) is qualitatively consistent with the model prediction, indicating that radiation-induced defects dominate the recombination dynamics in the irradiated structures.

In the PL spectra of the unirradiated samples, two emission bands appear near the band edge: I_1(DX) = 1.508 eV and $I_2(e, C) = 1.49$ eV, along with two broader bands at $I_3 = 1.38$ eV and $I_4 = 0.78$ eV. The I_1 and I_2 bands are attributed to excitons bound to donors and carbon-related electronic transitions, respectively. The weak I_3 band corresponds to donor-acceptor pair recombination, while I_4 originates from deep donor states associated with arsenic-related defects. Upon γ-irradiation ($D = 2 \times 10^9$ rad), all emission bands show a pronounced decrease in intensity (Fig. 1), consistent with the formation of non-radiative recombination centers induced by the Co γ-source. Such behavior

is consistent with previous studies of photoluminescence in CdTe-based heterostructures, where defect-induced nonradiative recombination leads to strong quenching of the emission intensity [16].

For the irradiation dose considered, the ratio of post-irradiation to initial integrated intensities, I_F/I_0, was approximately 10^{-2} for the I_1 and I_2 bands, whereas $I_F/I_0 \approx 0.5$ for the I_4 band. These distinct behaviors indicate that PL quenching under irradiation cannot be attributed solely to the formation of non-radiative centers but also reflects modifications of the luminescence centers within the material, suggesting structural rearrangements of defect-related states.

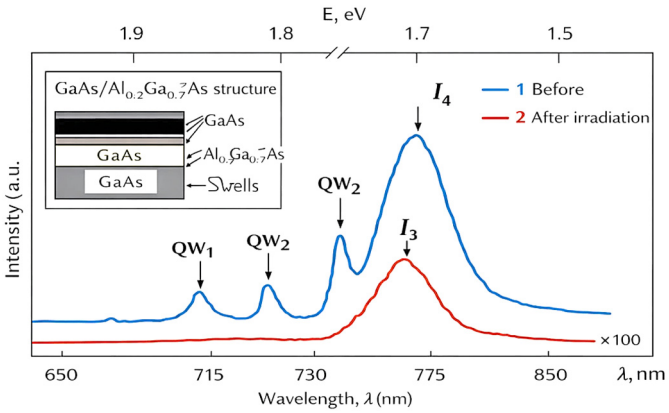

Figure 2. Low-temperature PL spectra of the GaAs/$Al_{0.2}Ga_{0.8}As$ quantum-well structure before (1) and after (2) irradiation, measured at 4.2 K. The structure contains three GaAs quantum wells with thicknesses of 2.5, 4.2, and 7.7 nm.

ZnTe/CdZnTe Quantum Wells. The PL spectra of sample No. 1 (Table 1), containing three tunnel-coupled ZnTe/$Cd_{0.2}Zn_{0.8}Te$ quantum wells, were measured with excitation $\lambda_{exc} = 0.51453$ μm, corresponding to photon energies above both the ZnTe and CdZnTe band gaps as well as the electron–hole recombination energies in the wells. The low-temperature PL spectrum exhibits multiple emission features arising from the ZnTe buffer layer and the quantum wells, the latter dominating the intensity. Superimposed narrow Raman lines, shifted by multiples of the LO-phonon energy, correspond to Raman scattering of the excitation light. The non-monotonic intensity variation of Raman lines with phonon order is attributed to resonance enhancement arising from coincidences with absorption features in the buffer or quantum wells. The irradiation-induced spectral changes and LO-phonon replicas of the ZnTe/$Cd_{0.2}Zn_{0.8}Te$ quantum-well structure are shown in Fig. 3.

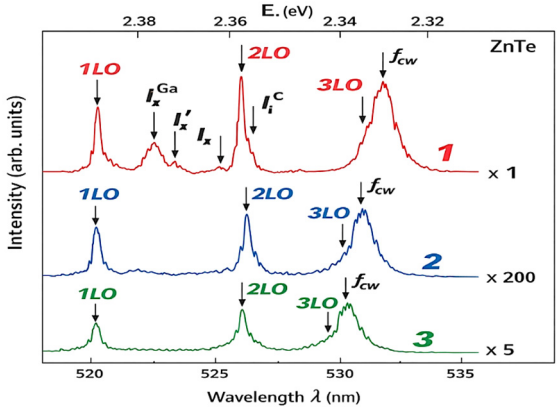

Figure 3. The spectra show pronounced 1LO, 2LO, and 3LO phonon replicas, confirming strong exciton-LO phonon coupling in the ZnTe-based structure. The changes in the relative intensities of the I_{Ga}, I_i, and f_{CW} features indicate the contribution of defect-related and excitonic recombination channels

The photoluminescence spectra of the ZnTe/CdZnTe quantum-well heterostructure exhibit distinct emission bands arising from the quantum wells (QW1 and QW2) and defect-related transitions. After irradiation, the excitonic emission intensity decreased noticeably, indicating the formation of radiation-induced defects that serve as efficient non-radiative recombination centers, degrading the optical response of the quantum wells. Similar defect-assisted suppression of optical emission has been reported in irradiated GaAs-based quantum wells [13,14], suggesting that irradiation-induced non-radiative recombination is a common feature of low-dimensional semiconductor heterostructures. Figure 3 presents the corresponding spectral changes after electron and X-ray irradiation, including the phonon-assisted emission features.

According to the model, the quenching of quantum well emission is governed by the relation $I_P L \propto k_r/(k_r + k_n r)$, where irradiation increases the defect-assisted non-radiative recombination rate. The excitonic emission at $h\nu =$ 2.3736 eV (522.4 nm) corresponds to a superposition of free exciton (IFX) and donor-bound exciton emission or exciton-

polariton recombination. Lines at $h\nu = 2.37$ eV are associated with excitons bound to neutral acceptors, while a broad band at $h\nu = 2.3568$ eV is related to extended or intrinsic defect states. After both electron and X-ray irradiation (curves 2 and 3 in Fig. 3), the excitonic band intensities decrease noticeably. In the quantum well emission region, the I_{QW} band intensity also diminishes, though less markedly. Electron irradiation induced a slight blue shift ($\Delta E \approx 0.7\, meV$), whereas X-ray irradiation caused a red shift ($\Delta E \approx 0.6\, meV$). Comparable irradiation-induced energy shifts have also been reported in GaAs/AlGaAs quantum wells, where proton irradiation and post-irradiation thermal treatment modified the quantum-well transition energies [17]. Due to spectral overlap with Raman lines, potential excitonic shifts in the buffer layer were further analyzed via reflectance measurements before and after irradiation.

As shown in Fig. 3, the photoluminescence spectra of ZnTe-based quantum structures display pronounced longitudinal optical (LO) phonon replicas (1LO, 2LO, 3LO) associated with excitonic transitions. Related photoluminescence features have been observed in CdTe/ZnTe quantum nanostructures, confirming the importance of excitonic transitions in determining the spectral response of II–VI heterostructures [18]. Similar LO-phonon-assisted excitonic features have been reported in (Cd,Zn)Te-based quantum wells, where the coupling between excitons and LO phonons strongly influences the spectral structure of luminescence [19]. A closely related behavior has been reported in coupled CdTe/ZnTe quantum-well structures, where hot-exciton relaxation is governed by LO-phonon emission and strongly affects the spectral shape of optical transitions [3]. The presence of such luminescence features is consistent with previous observations in cadmium chalcogenide systems, where strong excitonic emission and spectral structure are closely related to recombination dynamics [20]. Similar photoluminescence behavior has also been reported in CdTe/ZnTe self-assembled quantum nanostructures, where excitonic emission and spectral features are strongly influenced by confinement and carrier localization effects [18]. Optical studies of ZnTe structures containing CdTe submonolayers have likewise shown that localized excitonic states strongly affect the luminescence characteristics of II–VI heterostructures [21]. The observation of multiple phonon-assisted emission lines provides clear evidence of strong exciton–phonon coupling. Resonant optical studies of II–VI quantum nanostructures have similarly demonstrated that exciton–LO phonon coupling plays a decisive role in shaping the excited-state and phonon-assisted spectral response [22]. The non-monotonic variation in the intensity of the LO replicas is attributed to resonance enhancement effects and indicates the significant role of defect states and localization phenomena in the recombination dynamics. A related sensitivity of photoluminescence behavior to localization and quantum confinement has also been reported for CdTe/ZnTe ultrathin quantum wells and size-quantized islands [23].

A quantitative estimation of the exciton–phonon coupling strength was performed using the Huang–Rhys model. Based on the relative intensities of the LO-phonon replicas (1LO, 2LO, and 3LO), the Huang–Rhys factor was estimated to be $S \approx 1-2$. This value indicates a moderately strong exciton–phonon interaction in ZnTe-based quantum heterostructures. The obtained result is consistent with the pronounced phonon-assisted emission features observed in the PL spectra and confirms that the coupling between excitons and LO phonons plays a significant role in the recombination processes.

QUANTITATIVE ANALYSIS OF IRRADIATION-INDUCED PL CHANGES.

To reduce the descriptive character of the analysis and to make the comparison with the phenomenological model more explicit, the main spectral parameters extracted from Figs. 1–3 are summarized in Table 2. The integrated intensity ratio $\frac{I_F}{I_0}$ was used as the primary measure of PL quenching. Since all spectra were recorded under identical excitation power, temperature, and detection geometry, a decrease in $\frac{I_F}{I_0}$ can be directly associated with an increased contribution of defect-assisted non-radiative recombination. In the limiting case in which the radiative recombination rate and generation rate remain approximately unchanged, an effective non-radiative contribution may be estimated as $\eta_{\mathrm{eff}} = \left(\frac{I_0}{I_F}\right) - 1$. This parameter is not an absolute defect density; rather, it is a comparative measure of irradiation-induced optical degradation in the investigated heterostructures.

Table 2. Quantitative indicators of irradiation-induced photoluminescence modifications in the investigated quantum heterostructures.

Material system	Irradiation type	Observed parameter	Quantitative indicator	Physical implication
GaAs/AlGaAs quantum wells	γ-irradiation	Near-band-edge excitonic and impurity-related emission (I_1, I_2)	$\frac{I_F}{I_0} \approx 10^{-2}$	Strong suppression of radiative recombination due to the formation of radiation-induced non-radiative centers
GaAs/AlGaAs quantum wells	γ-irradiation	Deep defect-related emission (I_4)	$\frac{I_F}{I_0} \approx 0.5$	Deep-level emission is less sensitive to irradiation than shallow excitonic channels
ZnTe/CdZnTe quantum wells	Electron irradiation	Quantum-well excitonic transition	$\Delta E \approx +0.7\, meV$	Slight blue shift associated with irradiation-induced modification of exciton localization and local potential profile
ZnTe/CdZnTe quantum wells	X-ray irradiation	Quantum-well excitonic transition	$\Delta E \approx -0.6\, meV$	Small red shift indicating enhanced defect-related localization and potential fluctuations
ZnTe/CdZnTe quantum wells	Electron and X-ray irradiation	LO-phonon-assisted emission (1LO, 2LO, 3LO)	Huang–Rhys factor $S \approx 1-2$	Moderately strong exciton–LO-phonon coupling contributing to phonon-assisted recombination
All investigated structures	All irradiation conditions	Overall PL response	Intensity quenching and spectral redistribution	Radiation-induced defects alter the balance between radiative and non-radiative recombination channels

The quantitative comparison shows that the most pronounced effect of irradiation is the suppression of shallow excitonic and impurity-related emission in the GaAs/AlGaAs structure. The approximately two-orders-of-magnitude decrease of the I_1 and I_2 bands corresponds to a strong increase in the effective non-radiative contribution, whereas the I_4 band retains nearly half of its initial integrated intensity. This behavior suggests that different luminescence centers have different radiation sensitivities and that PL quenching is accompanied by a redistribution of recombination channels.

For the ZnTe/CdZnTe quantum wells, the opposite signs of the spectral shifts after electron and X-ray irradiation are small but reproducible. Therefore, they should not be interpreted as large changes in the band gap. Instead, they are more consistently understood as changes in the ensemble of localized excitons contributing to the PL maximum. A rigorous linewidth decomposition was not performed because the spectra contain partially overlapping excitonic bands, Raman lines, and LO-phonon replicas. For this reason, the present analysis uses integrated intensities, peak shifts, and relative phonon-replica intensities as the most reliable comparative parameters.

DISCUSSION

The observed PL intensity reductions and spectral shifts indicated that γ-ray, X-ray, and electron irradiation modified both the recombination dynamics and the local energy landscape of excitonic and impurity-related states. This interpretation is consistent with theoretical descriptions of absorption and carrier relaxation processes in semiconductors, where radiation-induced defects can strongly affect recombination channels [5,8]. The different responses of the emission bands suggest that shallow donor- and acceptor-bound excitons are more sensitive to irradiation than deep defect-related states, leading to selective quenching of radiative channels. At the same time, the observed blue and red shifts in the quantum-well emission bands suggest irradiation-induced modifications of exciton localization and defect-related potential fluctuations. The presence of LO-phonon replicas with modulated intensities further confirms the role of exciton–phonon coupling and resonance effects in the recombination dynamics. Overall, the PL response provides a sensitive probe of irradiation-induced defect formation, exciton dynamics, and phonon-assisted processes in semiconductor quantum heterostructures.

The observed trends are qualitatively consistent with the proposed phenomenological model. The obtained results are also consistent with theoretical studies of interband and multiphoton absorption processes, which emphasize the role of band mixing and nonlinear optical effects in semiconductor heterostructures [6,12].

From a microscopic point of view, the decrease in PL intensity can be explained by the formation of vacancies, interstitials, antisite defects, and defect complexes that introduce additional electronic states inside the band gap. These centers provide Shockley–Read–Hall-type non-radiative pathways and reduce the probability of radiative exciton recombination. Shallow donor-bound and acceptor-bound excitons are especially sensitive to such perturbations because their recombination depends strongly on the local potential landscape and on the overlap between electron and hole wave functions.

The distinction between electron irradiation and photon irradiation is also important. High-energy electrons can transfer momentum directly to lattice atoms, thereby producing displacement damage more efficiently, whereas X-ray and gamma-ray photons primarily produce ionization, secondary carriers, charge trapping, and defect charging, with atomic displacement occurring mainly through secondary processes. This difference provides a plausible explanation for the different spectral responses observed in the ZnTe/CdZnTe structures. The blue shift after electron irradiation may be related to preferential quenching of lower-energy localized states or to slight radiation-induced modification of the well/barrier potential profile. In contrast, the red shift after X-ray irradiation may reflect enhanced exciton localization in defect-related potential minima or local electric-field-induced band bending.

The observed energy shifts of approximately 0.6–0.7 meV are small relative to the transition energies but are important because they occur together with substantial PL quenching. This indicates that irradiation affects not only the total recombination efficiency but also the distribution of radiative states that contribute to the PL maximum. Thus, the shifts should be treated as signatures of a modified localized-exciton ensemble rather than as direct evidence of a large change in the fundamental band gap.

The LO-phonon replicas provide additional information on the recombination process. The estimated Huang–Rhys factor $S \approx 1 - 2$ indicates moderately strong exciton–LO-phonon coupling. After irradiation, defect-induced localization can enhance the interaction of excitons with lattice vibrations and redistribute intensity between the zero-phonon and phonon-assisted channels. However, because the LO replicas partly overlap with Raman features, the extracted S value should be regarded as a semi-quantitative estimate rather than as a uniquely fitted microscopic parameter.

It should be emphasized that the defect concentration discussed in this work is evaluated indirectly from PL quenching and spectral redistribution. Direct determination of absolute defect densities would require complementary techniques such as time-resolved PL, deep-level transient spectroscopy, electron paramagnetic resonance, or high-resolution structural analysis. Nevertheless, the present steady-state PL approach provides a useful comparative framework for assessing radiation-induced optical degradation in III–V and II–VI quantum heterostructures.

CONCLUSIONS

The effects of high-energy γ-ray, X-ray, and electron irradiation on the photoluminescence (PL) response of III–V and II–VI quantum heterostructures were investigated using low-temperature PL spectroscopy. For the GaAs/AlGaAs

quantum-well structure, γ-irradiation caused a strong reduction in the intensities of near-band-edge excitonic and defect-related emission bands. The integrated intensity ratio decreased to approximately $I_F/I_0 \approx 10^{-2}$ for the I_1 and I_2 bands, whereas the deeper defect-related I_4 band retained about half of its initial intensity, i.e., $I_F/I_0 \approx 0.5$. This difference indicates that shallow donor- and impurity-related radiative channels are more sensitive to irradiation-induced non-radiative recombination than deeper defect-related states.

For the ZnTe/CdZnTe quantum-well structures, electron and X-ray irradiation also modified the excitonic emission and phonon-assisted spectral features. Electron irradiation induced a slight blue shift of the quantum-well emission, whereas X-ray irradiation caused a small red shift, with the spectral shifts remaining in the range of $\Delta E \approx 0.6 - 0.7\ meV$. These opposite spectral shifts suggest that different irradiation conditions can modify exciton localization and defect-related potential fluctuations in different ways. The observation of 1LO, 2LO, and 3LO phonon replicas, together with the estimated Huang–Rhys factor of $S \approx 1 - 2$, confirms that exciton–LO-phonon coupling contributes significantly to the luminescence response of the ZnTe/CdZnTe structures.

Overall, the results show that irradiation affects both the intensity and energy position of PL bands through the formation of radiation-induced defects and the redistribution of radiative and non-radiative recombination channels. The GaAs/AlGaAs results mainly demonstrate the effect of γ-irradiation on III–V quantum wells, whereas the ZnTe/CdZnTe results clarify the influence of electron and X-ray irradiation on II–VI quantum wells. Therefore, the present work provides a comparative PL-based assessment of irradiation-induced modifications in representative III–V and II–VI quantum heterostructures. These findings may be useful for evaluating the radiation tolerance of low-dimensional semiconductor structures intended for optoelectronic applications in radiation environments.

The main limitation of the present study is that the quantitative defect analysis is based on steady-state PL parameters rather than on direct microscopic defect spectroscopy. Therefore, the reported intensity ratios, spectral shifts, and Huang–Rhys factor should be viewed as comparative indicators of irradiation sensitivity. Future studies combining PL with time-resolved spectroscopy and independent defect-characterization techniques would allow more rigorous extraction of recombination lifetimes, linewidth broadening, and absolute defect densities.

Acknowledgments

The authors sincerely thank **Prof. Rasulov Rustam Yavkachovich, Professor of the Department of Physics at Fergana State University**, for his valuable scientific guidance, helpful suggestions, and constructive discussions.

Conflict of Interest

The authors declare no conflict of interest.

ORCID

Mardonbek X. Nasirov, https://orcid.org/0000-0002-6811-072X;
Dilmuhammad X. Tolaboyev, https://orcid.org/0000-0001-6248-845X;
Tohirjon I. Raxmonov, https://orcid.org/0000-0002-6080-6159;
Husanboy M. Sulaymonov, https://orcid.org/0000-0003-0790-1584;
Sherzod Sh. Abdullaev, https://orcid.org/0009-0007-9768-5008;
Abdusattor O. Umarov, https://orcid.org/0000-0003-1624-7705;
Ixtiyor M. Tursunov, https://orcid.org/0009-0009-0864-2204

REFERENCES

[1] Türkoğlu, A., Ergün, Y., & Ungan, F. "Investigation of the electro-optical characteristics of GaAs/AlGaAs multiple quantum well grown by metal-organic vapor phase epitaxy," Journal of Molecular Structure, **1279**, 134202 (2023). https://doi.org/10.1016/j.molstruc.2022.134202

[2] Akhmadaliev, B. Z., Yuldashev, N. K., & Yulchiev, I. I. "Surface-radiative modes and longitudinal excitons in the spectra of exciton-polariton luminescence," Optics and Spectroscopy, **125**, 343–352 (2018). https://doi.org/10.1134/S0030400X18090023

[3] Liu, X.-Y., Singh, C. N., Kennedy, E. R., Huang, S., Fluckey, S. P., Matthews, C., & Uberuaga, B. P. "Review of radiation-induced defects in GaAs," Journal of Applied Physics, **138**(7), 070701 (2025). https://doi.org/10.1063/5.0279267

[4] Mirzaev, V. T., Akhmadaliyev, B. J., Yulchiev, I. I., Madraximov, M. M., & Rakhmonov, T. I. "Temperature and infrared quenching of equilibrium conductivity in $CdSe_xS_{1-x}$ film," East European Journal of Physics, (2), 247–251 (2025). https://doi.org/10.26565/2312-4334-2025-2-29

[5] Rasulov, R. Y., Rasulov, V. R., Kodirov, N. U., Nasirov, M. K., & Eshboltaev, I. M. "Theoretical analysis of interband single-photon light absorption in semiconductors: Effects of valence-conduction band mixing and temperature-dependent bandgap," East European Journal of Physics, (2), 179–187 (2025). https://doi.org/10.26565/2312-4334-2025-2-18

[6] Rasulov, R. Y., Rasulov, V. R., Kasimov, F. U., Nasirov, M. K., Farmanova, I. E., & Tursinbaev, A. Z. "On the theory of two-photon intersubband absorption and linear-circular dichroism in semiconductors of the III–V type," East European Journal of Physics, (2), 188–199 (2025). https://doi.org/10.26565/2312-4334-2025-2-19

[7] Agekyan, V. F., Budkin, G., Chukeev, M., Filosofov, N., Karczewski, G., Serov, A., & Reznitsky, A. "Hot exciton relaxation in coupled ultra-thin CdTe/ZnTe quantum well structures," Journal of Luminescence, **230**, 117762 (2021). https://doi.org/10.1016/j.jlumin.2020.117762

[8] Rasulov, R. Y., Rasulov, V. R., Kasimov, F. U., Nasirov, M. K., & Muminov, I. A. "On the theory of the intraband mechanism of single-photon absorption in semiconductors, taking into account the effect of coherent saturation," East European Journal of Physics, (2), 441–451 (2025). https://doi.org/10.26565/2312-4334-2025-2-55

[9] Akhmadaliyev, B., Rakhmonov, T., Sulaymonov, K., & Nurmatov, O. "Photoconductivity spectra of thin solid solution films $CdSe_xS_{1-x}$," E3S Web of Conferences, **583**, 04002 (2024). https://doi.org/10.1051/e3sconf/202458304002
[10] Huo, B., Zhang, H., Jiang, Y., Chen, Q., & Wang, Z. M. "The Huang–Rhys factor and the strength of exciton–LO phonon coupling in semiconductor quantum wells," Materials Today: Proceedings, (2007). https://doi.org/10.1016/S1369-8001(08)00021-8
[11] Zhang, Y. "Applications of Huang–Rhys theory in semiconductor optical spectroscopy," Journal of Semiconductors, **40**(9), 091102 (2019). https://doi.org/10.1088/1674-4926/40/9/091102
[12] Rasulov, R. Y., Rasulov, V. R., Kasimov, F. U., Nasirov, M. K., Farmanova, I. E., & Tursinbaev, A. Z. "On the theory of interband two-photon absorption of light in semiconductors accounting admixtures to the states of the conduction band and valence states, the Rabi effect," East European Journal of Physics, (2), 200–205 (2025). https://doi.org/10.26565/2312-4334-2025-2-20
[13] Pavelescu, E. M., Bălţăţeanu, N., Spânulescu, S. I., & Arola, E. "Very high dose electron irradiation effects on photoluminescence from GaInNAs/GaAs quantum wells grown by molecular beam epitaxy," Optical Materials, **64**, 361–365 (2017). https://doi.org/10.1016/j.optmat.2016.12.007
[14] Sailai, M., Aierken, A., Li, Q., Heini, M., Zhao, X., Mo, J., Gao, J., *et al*., "Effects of 1-MeV electron irradiation on the photoluminescence of GaInNAs/GaAs single quantum well structure," Semiconductors, **54**, 554–557 (2020). https://doi.org/10.1134/S1063782620050103
[15] Murata, T., Ohno, Y., Kishimoto, S., & Mizutani, T. "Photoluminescence intensity enhancement by electron beam irradiation into GaAs quantum wells," Solid-State Electronics, **43**(1), 147–152 (1999). https://doi.org/10.1016/S0038-1101(98)00197-X
[16] Polvonov, B. Z., Gafurov, Y. I., Otajonov, U. A., Nasirov, M. X., & Zaylobiddinov, B. B. "The specificity of photoluminescence in n-CdS/p-CdTe semiconductor heterostructures," International Journal of Mathematics and Physics, **13**(2), (2022). https://doi.org/10.26577/ijmph.2022.v13.i2.02
[17] Tan, H. H., Williams, J. S., Jagadish, C., Burke, P. T., & Gal, M. "Large energy shifts in GaAs–AlGaAs quantum wells by proton irradiation-induced intermixing," Applied Physics Letters, **68**(17), 2401–2403 (1996). https://doi.org/10.1063/1.116147
[18] Romčević, N., Romčević, M., Kostić, R., Stojanović, D., Milutinović, A., Trajić, J., Karczewski, G., & Galazka, R. "Photoluminescence spectroscopy of CdTe/ZnTe self-assembled quantum dots," International Journal of Photoenergy, 2009, 358790 (2009). https://doi.org/10.1155/2009/358790
[19] Stanley, R. P., Doran, J. P., Hegarty, J., & Feldman, R. D. "LO-phonons and excitons in (Cd,Zn)Te based quantum wells," Physica B: Condensed Matter, **191**(1–2), 71–82 (1993). https://doi.org/10.1016/0921-4526(93)90179-A
[20] Ayibzhanov, M., Mamatov, O., Mirzaev, V., & Tuychibaev, B. "Luminescence spectrum of cadmium chalcogenide photovoltaic film structures and their power enhancement," E3S Web of Conferences, **583**, 04003 (2024). https://doi.org/10.1051/e3sconf/202458304003
[21] Agekyan, V. F., Serov, A. Y., Filosofov, N. G., Shtrom, I. V., & Karczewski, G. "Optical properties of zinc telluride with cadmium telluride submonolayers," Physics of the Solid State, **58**(10), 2109–2112 (2016). https://doi.org/10.1134/S1063783416100036
[22] Nguyen, T. A., Mackowski, S., Jackson, H. E., Smith, L. M., Wrobel, J., Fronc, K., Karczewski, G., *et al*., "Resonant spectroscopy of II–VI self-assembled quantum dots: Excited states and exciton–longitudinal optical phonon coupling," Physical Review B, **70**, 125306 (2004). https://doi.org/10.1103/PhysRevB.70.125306
[23] Zaitsev, V. V., Bagaev, V. S., & Onishchenko, E. E. "Specific features in the temperature dependence of photoluminescence from CdTe/ZnTe size-quantized islands and ultrathin quantum wells," Physics of the Solid State, **41**, 647–653 (1999). https://doi.org/10.1134/1.1130842

РАДІАЦІЙНО-ІНДУКОВАНА МОДИФІКАЦІЯ КВАНТОВИХ ГЕТЕРОСТРУКТУР III–V ТА II–VI ПІД ВПЛИВОМ ВИСОКОЕНЕРГЕТИЧНОГО РЕНТГЕНІВСЬКОГО, ГАММА- ТА ЕЛЕКТРОННОГО ОПРОМІНЕННЯ

Мардонбек Х. Насіров[1,2], Ділмухаммад Х. Толабоєв[1], Тохірджон І. Рахмонов[1], Хусанбой М. Сулаймонов[1], Шерзод Ш. Абдуллаєв[1], Абдусаттор О. Умаров[1], Ікстійор М. Турсунов[1]
[1]Ферганський державний технічний університет, Фергана, Узбекистан
[2]Ферганський державний університет, Фергана, Узбекистан

Низькорозмірні квантові гетероструктури III–V та II–VI є важливими активними середовищами для оптоелектронних пристроїв, що працюють в умовах радіаційного впливу. У цій роботі досліджено вплив високоенергетичного рентгенівського, гамма- та електронного опромінення на екситонну рекомбінацію та екситон-фононну взаємодію в квантових гетероструктурах GaAs/AlGaAs і ZnTe/CdZnTe за допомогою низькотемпературної фотолюмінесцентної спектроскопії. Спектри показали виражені смуги екситонного випромінювання, що супроводжуються репліками поздовжніх оптичних фононів, що свідчить про фононно-асистовані процеси рекомбінації. Після опромінення спостерігалося значне зменшення інтенсивності фотолюмінесценції, що пов'язано з утворенням радіаційно-індукованих центрів безвипромінювальної рекомбінації. У структурах ZnTe/CdZnTe електронне опромінення спричиняло невеликий синій зсув (приблизно 0,7 меВ) випромінювання квантової ями, тоді як рентгенівське опромінення приводило до малого червоного зсуву (приблизно 0,6 меВ), що вказує на залежну від типу опромінення модифікацію локалізації екситонів і дефектно-зумовлених флуктуацій потенціалу. Виконано напівкількісний аналіз на основі відношень інтегральної інтенсивності фотолюмінесценції, ефективного параметра безвипромінювальної рекомбінації та фактора Хуанга–Ріса $S \approx 1 - 2$, що дозволило пов'язати гасіння фотолюмінесценції, спектральні зсуви та репліки LO-фононів з утворенням радіаційно-індукованих дефектів. Відносні зміни екситонних, домішкових і фононно-асистованих смуг випромінювання вказують на перерозподіл радіаційних і безвипромінювальних каналів рекомбінації після опромінення. Феноменологічна інтерпретація, заснована на радіаційних і безвипромінювальних швидкостях рекомбінації та описі реплік LO-фононів за моделлю Хуанга–Ріса, була використана для пояснення спостережуваних спектральних змін. Отримані результати забезпечують порівняльну експериментальну оцінку радіаційно-індукованих модифікацій у квантових гетероструктурах III–V та II–VI і можуть бути корисними для оцінювання радіаційної стійкості напівпровідникових оптоелектронних структур.

Ключові слова: *радіаційно-індуковані дефекти; квантові гетероструктури; фотолюмінесцентна спектроскопія; екситон-фононна взаємодія; репліки LO-фононів; безвипромінювальна рекомбінація; квантові ями GaAs/AlGaAs; квантові ями ZnTe/CdZnTe*

EAST EUROPEAN JOURNAL OF PHYSICS. 3. 319-324 (2026)
DOI:10.26565/2312-4334-2026-3-28 ISSN 2312-4334

MODELING OF OPTICAL AND SURFACE PROPERTIES OF ALUMINUM THIN FILMS USING SPECTROSCOPIC ELLIPSOMETRY

Kh.N. Ahmadova[1,2,3]*, S.H. Jabarov[1], M.A. Musayev[3], I.F. Yusibova[1], Sh.N. Aliyeva[1,3]
[1]*Institute of Physics, Ministry of Science and Education Republic of Azerbaijan, Baku, AZ-1143, Azerbaijan*
[2]*Azerbaijan University of Architecture and Construction, Baku, AZ-1073, Azerbaijan*
[3]*Azerbaijan State Oil and Industry University, Baku, AZ1010 Azerbaijan*
**Corresponding author email: khuramanahmadova85@gmail.com*
Received April 30, 2026, revised June 18, 2026; in final form June 23, 2026; accepted July 5, 2026

In this study, aluminum (Al) thin films deposited on soda lime glass substrates were investigated using spectroscopic ellipsometry with a focus on optical modeling and surface characteristics. The films were fabricated by thermal deposition under controlled vacuum conditions. A multilayer optical model, including Al, native oxide (Al_2O_3), and surface-roughness layers, was developed to accurately fit the experimental ellipsometric data. The analysis was performed in the photon energy range of 0.5–6 eV at multiple incidence angles. The Cauchy and Lorentz dispersion models were applied to represent the dielectric response of the oxide and metallic layers, respectively. The surface roughness was modeled using the effective medium approximation. The obtained results demonstrate that surface morphology and oxide layer formation play a significant role in determining the optical behavior of Al thin films. Variations in surface roughness and interface properties were found to influence the refractive index and extinction coefficient. The developed optical model showed good agreement with experimental data, confirming its reliability in describing complex thin-film systems. These findings highlight the importance of accurate optical modeling for the design and optimization of thin film materials in engineering and optoelectronic applications.
Keywords: *Spectroscopic ellipsometry; Optical model; Dielectric constants; Thin layers*

1. INTRODUCTION

The rapid development of modern nanotechnology has led to growing interest in thin-film materials due to their wide range of applications in electronics, photonics, and energy-related systems [1–3]. Among these materials, aluminum (Al) thin films are particularly attractive because of their favorable optical, electrical, and mechanical properties, as well as their technological compatibility with large-scale fabrication processes [4–6]. In thin-film systems, the physical and optical properties are strongly influenced not only by the intrinsic properties of the material but also by surface morphology and interfacial characteristics. In particular, the formation of a native oxide layer and surface roughness can significantly modify light–matter interactions, thereby altering optical constants such as the refractive index and extinction coefficient [7–10]. Therefore, accurate characterization of these effects is essential for designing and optimizing functional thin-film devices. Spectroscopic ellipsometry (SE) is a powerful and non-destructive optical technique widely used to investigate thin-film structures. It enables simultaneous determination of thickness, dielectric function, and surface properties with high sensitivity over a broad spectral range [11–14]. However, the reliability of the extracted parameters strongly depends on the adequacy of the optical model used to describe the system [15-17]. In this context, the development of appropriate multilayer optical models is crucial, especially for systems with multiple interfaces and surface effects. Incorporating layers such as native oxides and surface roughness into the model allows for a more realistic representation of the physical structure and improves the accuracy of the analysis [18–21]. In this work, aluminum thin films deposited on soda-lime glass substrates are investigated using spectroscopic ellipsometry. A multilayer optical modeling approach is employed to analyze the effects of surface roughness and oxide layer formation on the system's optical response.

The novelty of this work lies in the development of a comprehensive optical model for thermally deposited Al thin films on soda-lime glass substrates that simultaneously accounts for the metallic Al layer, the native Al_2O_3 overlayer, and surface-roughness effects within a unified spectroscopic ellipsometry framework. Such an approach provides a more realistic description of the films' physical structure and improves the accuracy of the extracted optical parameters. The proposed model can serve as a reliable tool for investigating thickness-dependent optical properties of Al thin films and for optimizing Al-based structures intended for photonic and optoelectronic applications.

2. MATERIALS AND METHODS

Two thin aluminum films with different thicknesses were fabricated from nanopowders via thermal deposition. The thermal evaporation was performed using a Leybold-Heraeus L-560 vacuum system. The working pressure in the vacuum chamber was maintained at 2×10-5 mbar. The substrates used were chemically cleaned 25×19 mm glass plates. Prior to thermal evaporation, the surfaces of the glass substrates were ionized at 800 W. To enhance the deposition

Cite as: Kh.N. Ahmadova, S.H. Jabarov, M.A. Musayev, I.F. Yusibova, Sh.N. Aliyeva, East Eur. J. Phys. 3, 319 (2026), https://doi.org/10.26565/2312-4334-2026-3-28

process, the glass substrates were heated to 100°C in the vacuum chamber. The thermal evaporation process was conducted for 25 seconds. Although the nominal deposition time was identical for both samples, small variations in the evaporation rate, source material distribution, and local deposition conditions resulted in different film thicknesses (80 and 100 nm). Such variations are commonly observed in thermally evaporated thin films and can significantly influence the final film thickness.

The optical parameters of the two Al films obtained were examined by spectroscopic ellipsometry over a photon energy range of 0.5-6 eV. The incident angle during the ellipsometric measurements was varied at 60°, 65°, 70°, and 75°, and all measurements were performed at room temperature. The optical constants of the Al/SLG (soda lime glass) systems were retrieved through regression analysis of the obtained SE data. The ellipsometric parameters Ψ and Δ represent the amplitude ratio and phase shift of the parallel (p) and perpendicular (s) components of the reflected light, respectively. The complex reflectance ratio of the polarized light is given by:

$$\rho = \frac{r_p}{r_s} = tan\Psi e^{i\Delta} \tag{1}$$

where r_p and r_s are the Fresnel reflection coefficients of p- and s-polarized light, respectively. The measurements were performed using an M-2000 rotating compensator spectroscopic ellipsometer (RCE, J.A. Woollam Co., Inc.). The measured ellipsometric parameters were analyzed through regression fitting of the experimental data. The intensities Is and Ic recorded by the rotating compensator ellipsometer are expressed as [22]:

$$I_s = sin2\Psi sin\Delta,\ I_c = sin2\Psi cos\Delta \tag{2}$$

In Eq. (2), Is and Ic represent the experimentally measured intensity components obtained from the modulation of the polarization state of the reflected light. These quantities are directly related to the ellipsometric parameters Ψ and Δ and provide information about the optical properties and thicknesses of the individual layers that form the sample. Therefore, fitting the calculated I_s and I_c spectra to the experimental data enables a reliable determination of the optical constants and structural parameters of the multilayer system.

A four-layer optical model was used to reproduce the experimental I_s and I_c signals over the entire photon-energy range. This model consists of the substrate (SLG), thin film (Al), alumina (Al_2O_3), and surface roughness (Fig. 1).

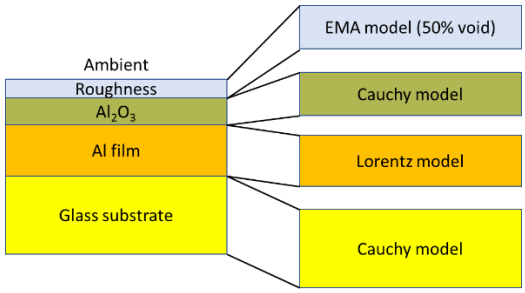

Figure 1. Theoretical model of the samples

In this model, the surface roughness was described using the Effective Medium Approximation (EMA) based on Bruggeman theory, modeled by Bruggeman's EMA (50% Al_2O_3 + 50% void). The Cauchy dispersion model was applied to the Al_2O_3 and SLG layers, as these transparent dielectric materials can be accurately described using this empirical relation:

$$n(E) = A+BE^2+CE^4 \tag{3}$$

where A, B, and C are fitting parameters.

The Al layer was fitted using the Lorentz model, which is particularly useful for metals and semiconductors. The physical basis for Lorentz oscillators has been extensively discussed in many textbooks [23,24]. The Lorentz layer can be described as a collection of absorption peaks that is Kramers-Kronig consistent:

$$\tilde{\varepsilon}(h\nu) \equiv \varepsilon_1 + i\varepsilon_2 = \varepsilon_{1\infty} + \sum_k \frac{A_k}{E_k^2 - (h\nu)^2 - iB_k h\nu} \tag{4}$$

where k is the oscillator index, A_k is the amplitude, E_k is the center energy, B_k is the broadening of each oscillator, $h\nu$ is the photon energy in eV, and ϵ_1 is an additional offset.

3. OPTICAL MODELING

To accurately describe the optical response of aluminum thin-film systems, a multilayer optical model was developed using spectroscopic ellipsometry data. The model consists of four main layers: the glass substrate, the aluminum (Al) thin film, the native oxide layer (Al_2O_3), and a surface roughness layer. The substrate (soda lime glass)

was considered optically homogeneous and isotropic. The aluminum thin film was treated as a metallic layer, while the oxide layer was assumed to be transparent within the investigated spectral range. The surface roughness was modeled using the Effective Medium Approximation (EMA), where the roughness layer was represented as a mixture of 50% void and 50% bulk material, following Bruggeman's theory. To describe the optical properties of each layer, appropriate dispersion models were applied. The dielectric response of the Al_2O_3 layer and the glass substrate was modeled using the Cauchy dispersion relation, which is suitable for transparent dielectric materials. In contrast, the aluminum layer was described using the Lorentz oscillator model, which effectively represents the absorption processes in metallic systems. The model parameters, including layer thicknesses, optical constants, and surface roughness, were determined through regression analysis by minimizing the difference between experimental and calculated ellipsometric data. The fitting procedure was carried out using a nonlinear optimization algorithm, ensuring high accuracy and reliability of the results. This modeling approach enables a comprehensive understanding of how surface morphology and interfacial properties influence the optical behavior of aluminum thin films.

4. RESULTS AND DISCUSSION

4.1 Ellipsometric fitting. An optical model for isotropic media or isotropic thin-film/substrate systems was used to fit the calculated data to the experimental ψ and Δ values. The Complete EASE software was employed for the ellipsometric data-fitting procedure, achieving a mean squared error (MSE) of less than 1.5 in the worst case. The experimental data were fitted using the Levenberg–Marquardt algorithm, applying parameterized model dielectric functions simultaneously for all data points measured in the UV/VIS ranges. The Lorentz oscillator model, available in the Complete EASE database, was used to describe the dielectric response of the aluminum layer across the investigated spectral range. This model is widely employed for metallic materials and provides a physically meaningful representation of their optical behavior. The measured ellipsometric parameters (full red and green curves) and their fits (dashed black curves) for incident angles of 60°, 65°, 70°, and 75° are presented in Fig. 2 and Fig. 3 for Al/SLG samples, respectively. A similarly good fit to the measured Ψ and Δ was obtained for other incident angles. The quality of the obtained film surfaces is confirmed by the low MSE and roughness values (overlayer thickness).

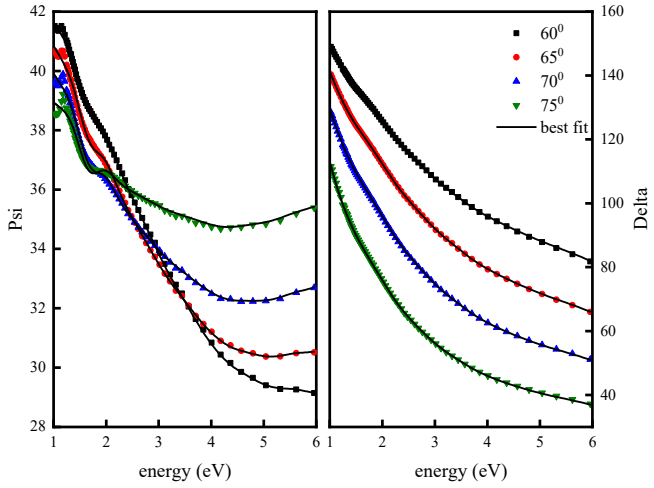

Figure 2. Experimental (dots) and fitted (lines) ellipsometric data of sample d_1 with 100 nm Al thin film

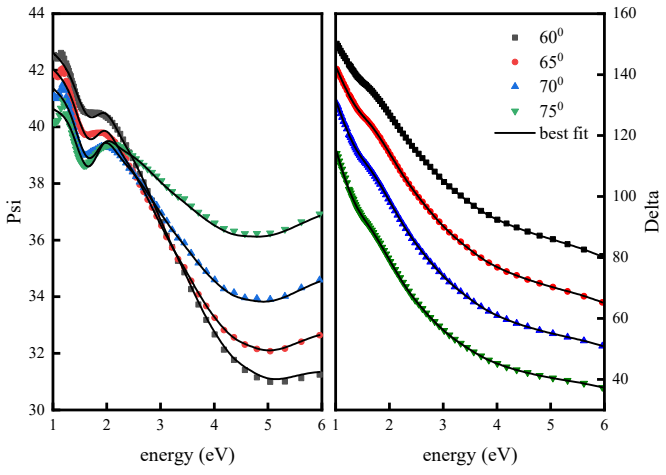

Figure 3. Experimental (dots) and fitted (lines) ellipsometric data of sample d_2 with 80 nm Al thin film

4.2 Optical constants. The optical constants of the aluminum thin films, including the refractive index (n) and extinction coefficient (k), were determined from the fitted ellipsometric data using the developed multilayer optical model. The analysis of the pseudo-dielectric function allowed for the simultaneous evaluation of the real (ε_1) and imaginary (ε_2) components, providing insight into the optical behavior of the system. The calculated spectra of the pseudo-dielectric functions are presented in Fig. 4.

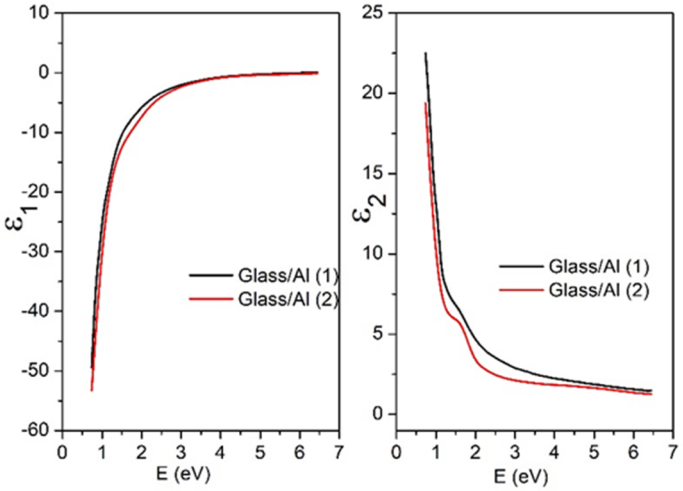

Figure 4. Real (ε_1) and imaginary (ε_2) parts of the pseudo-dielectric function of Al thin films with different structural parameters

The obtained spectral dependences of ε_1 and ε_2 indicate that the films' optical response is influenced by both intrinsic material properties and surface-related effects. Variations in these functions reflect differences in light interaction within the multilayer system, including contributions from interfaces and surface morphology.

The optical constants, namely the refractive index (n) and extinction coefficient (k), were extracted from the dielectric function and are shown in Fig. 5.

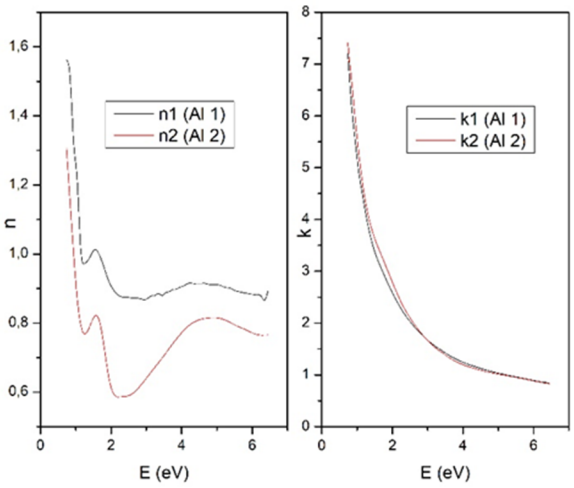

Figure 5. Refractive index (n) and extinction coefficient (k) of Al thin films as a function of photon energy

As shown in Fig. 5, the optical constants are strongly affected by surface and interfacial properties. The refractive index is sensitive to structural inhomogeneities and surface morphology, which alter the effective optical medium. At the same time, the extinction coefficient reflects absorption processes and light interactions within the metallic layer. At lower photon energies, the extinction coefficient is relatively high, indicating stronger absorption in the metallic Al films. As photon energy increases, the extinction coefficient gradually decreases across the investigated spectral range, indicating reduced absorption losses. These trends are consistent with the optical behavior observed for metallic thin films. In addition, the presence of a surface oxide layer and surface roughness modifies the optical path and boundary conditions, which in turn affects the extracted values of n and k. Therefore, accurate determination of optical constants requires careful consideration of both surface and interface effects within the multilayer structure. The good agreement between experimental and modeled data confirms the reliability of the proposed four-layer optical model and underscores the importance of simultaneously accounting for oxide-layer formation and surface roughness in the optical characterization of aluminum thin films.

The observed spectral behavior of the optical constants is mainly governed by the free-electron response of aluminum and by the influence of the oxide layer and surface morphology. The obtained optical constants are in

reasonable agreement with the well-established optical data reported for aluminum by Palik [25], Rakic et al. [26], and Aspnes[24]. Minor differences may be attributed to variations in film thickness, deposition conditions, native oxide formation, and surface roughness. This agreement confirms the physical reliability of the proposed optical model and the extracted dielectric parameters. Consequently, accurate optical modeling is required to separate intrinsic material properties from interface-related effects.

4.3 Surface and Oxide Effects. The surface morphology and the presence of a native oxide layer (Al_2O_3) play a crucial role in determining the optical behavior of aluminum thin films. Surface roughness introduces additional light scattering at the air/film interface, thereby affecting the system's effective optical response. As the roughness increases, the effective refractive index becomes a weighted average between the material and voids, leading to modifications in both the refractive index (n) and extinction coefficient (k). The surface roughness was described using the Effective Medium Approximation (EMA), where the roughness layer was modeled as a mixture of Al_2O_3 and voids. This assumption was adopted because the roughness layer represents the non-ideal surface of the native oxide layer exposed to air. Such an approach provides a physically realistic description of the film surface and improves the accuracy of the ellipsometric analysis. This approach provides a realistic representation of non-ideal surfaces and improves the accuracy of the ellipsometric fitting. In addition to roughness effects, the formation of a native aluminum oxide (Al_2O_3) layer significantly influences the optical response. The oxide layer acts as a dielectric interface between the metallic aluminum and the surrounding medium. Due to its transparency in the studied spectral range, it modifies the phase and amplitude of reflected light, thereby affecting the extracted ellipsometric parameters. Furthermore, even a thin oxide layer can alter the interference conditions within the multilayer system by changing the optical path length. As a result, noticeable variations in the optical constants (n and k) can occur, making the inclusion of the oxide layer essential for accurate optical modeling. The surface roughness values for the samples, as presented in Table 1, show noticeable differences, likely attributable to variations in deposition conditions and material interactions during film formation.

Table 1. Structural parameters of Al thin films

Samples	Roughness (nm)	Al_2O_3 (nm)	Al (nm)
Al 1	11.04 ± 0.2	13.33 ± 0.5	100
Al 2	6.55 ± 0.4	13.09 ± 0.7	80

Factors such as substrate preparation, cleaning procedures, and deposition parameters (including temperature and pressure) may significantly influence the resulting surface morphology. In particular, interfacial processes occurring between the aluminum layer and the oxide phase (Al_2O_3) can affect the nucleation and growth mechanisms, leading to differences in surface uniformity. On the other hand, the thickness of the Al_2O_3 layer remains nearly constant for both samples, indicating a relatively stable oxidation process. Minor variations in oxide thickness are likely related to small differences in film composition and local deposition conditions, although these variations do not significantly alter the overall structure.

Overall, both surface roughness and oxide layer formation must be taken into account to achieve reliable determination of optical constants and to better understand light–matter interaction in aluminum thin film systems. The present study demonstrates that neglecting either the native oxide layer or surface roughness may lead to noticeable deviations in the extracted optical parameters. Therefore, the proposed four-layer model provides a more realistic representation of Al thin films and can be effectively applied to investigate thickness-dependent optical behavior in similar metal–dielectric systems. Although a direct comparison with simpler optical models was beyond the scope of the present study, the inclusion of both the native oxide layer and surface roughness resulted in excellent agreement between the experimental and calculated ellipsometric spectra. These results indicate that both contributions are important for an accurate description of the optical response of the investigated Al thin films.

CONCLUSIONS

A comprehensive optical model of thermally deposited Al thin films on soda-lime glass substrates was developed using spectroscopic ellipsometry. By simultaneously considering the metallic Al layer, the native Al_2O_3 oxide layer, and surface roughness, the proposed four-layer model accurately described the experimental data and enabled reliable determination of optical constants and structural parameters. The results demonstrate that oxide formation and surface morphology significantly influence the optical response of the films. The developed modeling approach offers an effective framework for studying thickness-dependent optical properties of aluminum thin films and may be useful for the design and optimization of Al-based photonic, plasmonic, and optoelectronic devices. One limitation of the present study is that the structural parameters were obtained solely from spectroscopic ellipsometry modeling without independent verification by complementary characterization techniques such as AFM, SEM, or profilometry. Future investigations combining spectroscopic ellipsometry with additional surface characterization methods would provide further validation of the extracted structural parameters and improve the robustness of the optical model.

Acknowledgments

The authors would like to express their gratitude to the Institute of Physics of the Ministry of Science and Education of the Republic of Azerbaijan and the Azerbaijan State Oil and Industry University for providing research facilities.

ORCID
Kh.N. Ahmadova, https://orcid.org/0000-0001-5974-5400; **S.H. Jabarov,** https://orcid.org/0000-0002-3153-5804;
Sh.N. Aliyeva, https://orcid.org/0000-0002-2005-4749

REFERENCES

[1] H.D. Ibrahimov, F.A. Amirov, H.J. Huseynov, Z.M. Ibragimova, L.S. Zamanova, R.N. Asadzadeh, and S.H. Jabarov, J. Surf. Investig.: X-ray, Synchrotron Neutron Tech. **13**, 1244 (2019). https://doi.org/10.1134/s1027451019060338
[2] I. Sen, and M. Saglam, New Mater. Compd. Appl. **5**, 110 (2021).
[3] T.T. Abdullayeva, S.H. Jabarov, S. Huseynli, B.A. Abdurakhimov, A.S. Abiyev, and M.N. Mirzayev, Mod. Phys. Lett. B, **34**, 2050231 (2020). https://doi.org/10.1142/s0217984920502310
[4] S.H. Jabarov, T.T. Abdullayeva, S. Huseynli, M.N. Mirzayev, A.S. Abiyev, E. Demir, M.Yu. Tashmetov, *et al.*, Mod. Phys. Lett. B, **35**, 2150512 (2021). https://doi.org/10.1142/S0217984921505126
[5] A.S. Abiyev, Adv. Phys. Res. **3**, 137 (2021).
[6] F.G. Agayev, S.H. Jabarov, G.Sh. Ayyubova, A.V. Trukhanov, S.V. Trukhanov, M.N. Mirzayev, T.G. Naghiyev, and N.T. Dang, J. Supercond. Nov. Magn. **33**, 2867 (2020). https://doi.org/10.1007/s10948-020-05544-9
[7] J. Wang, Y. H. Yu, S. C. Lee, and Y. W. Chung, Surf. Coat. Technol. **146**, 189–192 (2001). https://doi.org/10.1016/s0257-8972(01)01387-1
[8] D. Yan, J. He, X. Li, J. Lianxin, and Z.H. Ding, Surf. Coat. Technol. **141**, (2001). https://doi.org/10.1016/s0257-8972(01)01170-7
[9] Y.S. Chang, and N. Roy, Thin Solid Films, **193–194**, 959 (1990). https://doi.org/10.1016/0040-6090(90)90250-h
[10] Kh.N. Ahmadova, Int. J. Mod. Phys. B**, 34**, 2150241 (2021). https://doi.org/10.1142/s0217979220500587
[11] R.W. Collins, I. An, J. Koh, H. Fujiwara, P.I. Rovira, A.S. Ferlauto, Thin Solid Films, **313–314**, 18–23 (1998). https://doi.org/10.1016/S0040-6090(97)00743-2
[12] Kh.N. Ahmadova, and S.H. Jabarov, Arab. J. Sci. Eng. **48**, 8083–8088 (2023). https://doi.org/10.1007/s13369-022-07449-2
[13] J.N. Hilfiker, N. Singh, T. Tiwald, D.W. Convey, S.M. Smith, J. Baker, and H.G. Tompkins, Thin Solid Films, **516**, 7979–7989 (2008). https://doi.org/10.1016/j.tsf.2008.04.060
[14] M. Losurdo, K. Hingerl, editors, *Ellipsometry at the Nanoscale*, (Springer, Berlin, 2013). https://doi.org/10.1007/978-3-642-33956-1
[15] Kh.N. Ahmadova, N.N. Hashimova, and M.A. Musayev, East Eur. J. Phys. (1), 197 (2025). https://doi.org/10.26565/2312-4334-2025-1-20
[16] H.G. Tompkins, E.A. Irene, editors, *Handbook of Ellipsometry*, (Springer, New York, 2005).
[17] H. Fujiwara, *Spectroscopic Ellipsometry: Principles and Applications*, (John Wiley & Sons, Chichester, 2007).
[18] R.M.A. Azzam, and N.M. Bashara, *Ellipsometry and Polarized Light*, (North-Holland, Amsterdam, 1987).
[19] Kh.N. Ahmadova, Int. J. Mod. Phys. B, **34**, 2050058 (2020). https://doi.org/10.1142/S0217979220500587
[20] J.A. Woollam, Guide to Using WVASE32® Spectroscopic Ellipsometry Data Acquisition and Analysis Software, (J.A. Woollam Co., Inc., Lincoln, NE, USA).
[21] Kh.N. Ahmadova, Sh.N. Aliyeva, Sh.R. Mammadova, and L.N. Ibrahimova, Advanced Physical Research, **7**(3), 358 (2025). https://doi.org/10.62476/apr.73358
[22] G. E. Jellison, Jr., and F. A. Modine, in: *Handbook of Ellipsometry*, edited by H. G. Tompkins, and E. A. Irene (Springer, New York, 2005), Chap. 6.
[23] S. Adachi, *Optical Constants of Crystalline and Amorphous Semiconductors*, (Springer, 1999).
[24] D.E. Aspnes, Thin Solid Films, **89**, 249–262 (1982). https://doi.org/10.1016/0040-6090(82)90590-9
[25] E.D. Palik, *Handbook of Optical Constants of Solids*, (Academic Press, New York, 1998).
[26] A.D. Rakic, A.B. Djurisic, J.M. Elazar, M.L. Majewski, Applied Optics, **37**, 5271 (1998). https://doi.org/10.1364/AO.37.005271

МОДЕЛЮВАННЯ ОПТИЧНИХ ТА ПОВЕРХНЕВИХ ВЛАСТИВОСТЕЙ ТОНКИХ АЛЮМІНІЄВИХ ПЛІВОК ЗА ДОПОМОГОЮ СПЕКТРОСКОПІЧНОЇ ЕЛІПСОМЕТРІЇ

Х.Н. Ахмадова[1,2,3], С.Г. Джабаров[1], М.А. Мусаєв[3], І.Ф. Юсібова[1], Ш.Н. Алієва[1,3]
[1]Інститут фізики, Міністерство науки та освіти Азербайджанської Республіки, Баку, AZ-1143, Азербайджан
[2]Азербайджанський університет архітектури та будівництва, Баку, AZ-1073, Азербайджан
[3]Азербайджанський державний університет нафти та промисловості, Баку, AZ1010 Азербайджан

У цьому дослідженні тонкі плівки алюмінію (Al), нанесені на підкладки з натрієво-кальційного скла, досліджувалися за допомогою спектроскопічної еліпсометрії з акцентом на оптичне моделювання та характеристики поверхні. Плівки були виготовлені методом термічного осадження в контрольованих умовах вакууму. Для точного узгодження з експериментальними еліпсометричними даними було розроблено багатошарову оптичну модель, що включає Al, природний оксид (Al_2O_3) та шари шорсткості поверхні. Аналіз проводився в діапазоні енергії фотонів 0,5–6 еВ під різними кутами падіння. Для представлення діелектричної реакції оксидного та металевого шарів відповідно були застосовані моделі дисперсії Коші та Лоренца. Шорсткість поверхні моделювалася за допомогою наближення ефективного середовища. Отримані результати демонструють, що морфологія поверхні та формування оксидного шару відіграють значну роль у визначенні оптичної поведінки тонких плівок Al. Було виявлено, що варіації шорсткості поверхні та властивостей інтерфейсу впливають на показник заломлення та коефіцієнт згасання. Розроблена оптична модель показала хорошу відповідність експериментальним даним, що підтверджує її надійність для опису складних тонкоплівкових систем. Ці результати підкреслюють важливість точного оптичного моделювання для проєктування та оптимізації тонкоплівкових матеріалів в інженерних і оптоелектронних застосуваннях.

Ключові слова: *спектроскопічна еліпсометрія; оптична модель; діелектричні константи; тонкі шари*

East European Journal of Physics. 3. 325-346 (2026)
DOI:10.26565/2312-4334-2026-3-29 ISSN 2312-4334

MULTIFUNCTIONAL BULK METALLIC GLASS: AN AB INITIO STUDY ON $Pd_{39}Ni_{10}Cu_{30}P_{21}$ FOR ENHANCED MECHANICAL STRENGTH AND OPTICAL SHIELDING

Sangita Gupta[1], Amit Kumar Chaubey[2], Sarita Chaudhary[3], Kapil Bhardwaj[4], Abhay P. Srivastava[5]*
[1]*Department of Chemistry, Poornima University, Jaipur, Rajasthan, India*
[2]*Department of Applied Science and Humanities, United College of Engineering and Research, Prayagraj, (UP), India*
[3]*Department of Chemistry, Vivekanand Global University, Jaipur, Rajasthan, India*
[4]*Department of Computer Science and Engineering, Chandigarh University, Mohali, Punjab, India*
[5]*Department of Applied Science and Humanities, Bansal Institute of Engineering and Technology, Lucknow (UP), India*
**Corresponding Author email ID: abhay.srivastava831@gmail.com*
Received April 20, 2026; revised June 17, 2026; accepted June 26, 2026

Bulk metallic glasses (BMGs) are a type of solid material with amorphous atomic structures that exhibit favorable mechanical, thermal, and functional properties. This study presents the attributes of the glass, examining first-principles details of the $Pd_{39}Ni_{10}Cu_{30}P_{21}$ bulk metallic glass structure, its elastic properties, thermodynamics, and electronic–optical performance. Density functional theory calculations were performed for a comparison with the amorphous atomic configuration and energy–volume relation through a third-order Birch–Murnaghan equation of state. The very high bulk modulus of approximately 159 GPa and >6 pressure derivatives demonstrated uniformity, resistance, and strong pressure strengthening. All three elastic moduli, Poisson's ratio, and Pugh's criterion are constantly demonstrating ductile mechanical response dependent on shear transformation zone–mediated plasticity. The results of the thermophysical examination show stable anharmonic lattice behavior, a Debye temperature of approximately 395 K, and favorable thermal expansion, indicating good predictability of the thermomechanical response. Electronic studies revealed a very metallic phase with low pseudogap around the Fermi level—mainly the hybridization between transition metal d-states and phosphorus p-states into a stable, amorphous phase. Optical spectra that contain a wide band, excellent reflectivity at low photon energies, and an isotropic optical response are typical of metallic glasses. In conclusion, these results prove $Pd_{39}Ni_{10}Cu_{30}P_{21}$ as a highly mechanically stable material for progress in various mechanical, optical, and energy applications in a lightweight frame.
Keywords: *Bulk metallic glass; Density functional theory; Equation of state; Mechanical and thermophysical properties; Electronic structure; Optical shielding materials*

INTRODUCTION

Over the years, bulk metallic glasses received extensive scientific and technological interest owing to their unique atomic structures and property mixes that are not achievable in traditional crystalline alloys [1]. In contrast to crystalline metals, which possess long-range periodicity and dislocation-mediated plasticity, BMGs exhibit disordered atomic arrangements with pronounced short- and medium-range order [2]. Structural disorder, which suppresses crystallization and dislocation motion, leads to ultrahigh strength, large elastic limits, excellent corrosion resistance, and unique electronic and optical responses [3].

Among the BMG systems, Pd-based alloys are most popular due to their excellent glass-forming capability, thermal stability, and ductility, and represent a model system for understanding the structure–property relationships of metallic glasses [4]. The $Pd_{39}Ni_{10}Cu_{30}P_{21}$ alloy is a conventional Pd-based bulk metallic glass characterized by high atomic density, powerful heteroatomic bonding, and a wide supercooled liquid region [5]. It is important that phosphorus is included to stabilize the amorphous structure, as it provides chemical short-range order through energetically favorable Pd–P and Cu–P bonds that frustrate long-range crystalline ordering [6-7].

These characteristics not only maximize glass-forming capability but also influence mechanical deformation processes controlled by localized atomic reorganization (shear transformation zones), rather than lattice imperfections [8-9]. Despite extensive experimental experience with Pd-based BMG, a single first-principles description that links atomic-scale structure to mechanical, thermodynamic, electronic, and optical behavior is scarce [10-11].

Specifically, the joint influence of dense random packing, polyhedral short-range order, and electronic hybridization on pressure resistance, ductility, thermal response, and optical loss is relevant to predictive materials design [12]. Density functional theory provides a robust framework for addressing these questions by enabling atomistic modeling of amorphous structures and the quantitative assessment of intrinsic properties. In this work, a comprehensive ab initio characterization of $Pd_{39}Ni_{10}Cu_{30}P_{21}$ in bulk metallic glass form is executed. Structural stability is checked through energy–volume analysis and equation-of-state fitting, elastic constants and moduli are calculated to evaluate mechanical stiffness and ductility [13-15].

Lattice behavior and thermal reliability are characterized by thermophysical properties, such as the Debye temperature, Grüneisen parameter, and thermal expansion [16-17]. Moreover, the electronic density of states, dielectric response, optical conductivity, and related spectra are investigated to deduce metallic optical behavior and a broadband

Cite as: S. Gupta, A.K. Chaubey, S. Chaudhary, K. Bhardwaj, A.P. Srivastava, East Eur. J. Phys. 3, 325 (2026), https://doi.org/10.26565/2312-4334-2026-3-29

energy-dissipation mechanism. The aims of the study are to correlate atomic-scale structure with macroscopic properties to acquire a comprehensive physical understanding of $Pd_{39}Ni_{10}Cu_{30}P_{21}$ and to demonstrate its potential for high-performance multifunctional applications [18-20].

In this study, the first principles framework has been used to investigate the intrinsic structure–property relationships of the $Pd_{39}Ni_{10}Cu_{30}P_{21}$ bulk metallic glass through the atomic and electronic scales. In contrast, periodicity in crystalline materials characterizes mechanical and optical behavior, but the multifunctional properties of metallic glasses are determined by dense random packing, chemical short-range order, and disorder-broadened electronic states. The current endeavor seeks to address this issue by linking amorphous atomic topology to elastic response, thermodynamic stability, electronic structure, and broadband optical shielding in a unified density functional theory (DFT) scheme.

The focus is on the application of pressure resistance, shear-transformation-zone-mediated ductility, and electronic hybridization together in isotropic optical absorption, reflectivity at low photon energies, and efficiency of electromagnetic energy dissipation. On the basis of this integrated investigation, $Pd_{39}Ni_{10}Cu_{30}P_{21}$ is shown to be a mechanically robust and optically effective material, ready for next-generation structural, photothermal, and electromagnetic shielding applications.

COMPUTATIONAL METHODOLOGY

All first-principles calculations were carried out within the framework of Density Functional Theory (DFT), where the interacting many-electron problem is mapped onto an equivalent system of non-interacting electrons moving in an effective potential. According to the Kohn–Sham formalism, the total ground-state energy of the system is expressed as [21-22]:

$$E_{tot}[\rho(r)] = T_s[\rho] + E_{ext}[\rho] + E_H[\rho] + E_{xc}[\rho], \tag{1}$$

where T_s is the kinetic energy of non-interacting electrons, E_{ext} is the electron–ion interaction energy, E_H is the Hartree electrostatic energy, and E_{xc} is the exchange–correlation functional accounting for many-body effects beyond classical electrostatics.

The exchange–correlation energy was treated using the generalized gradient approximation (GGA) in the Perdew–Burke–Ernzerhof (PBE) formulation, which provides an improved description of metallic bonding and pressure-dependent properties compared to the local density approximation [23].

Since bulk metallic glasses lack long-range translational symmetry, sampling in the Brillouin zone must be balanced against the need to capture the electronic structure and the computational cost. For this purpose, the Brillouin zone was sampled according to the Monkhorst–Pack scheme to produce a uniform grid of k-points in reciprocal space by relation. As the long-range translational symmetry in metallic glasses is nonexistent, the sampling for the Brillouin zone needs to be considered for a high degree of precision to acquire the full electronic structure and computation time. We used the Monkhorst–Pack scheme for Brillouin zone sampling in this study. This approach is aimed at ensuring a consistent grid of k-points in reciprocal space, with a particular mathematical relation, to achieve maximum precision and computational efficiency [24-25].

$$\vec{k}_{n_1 n_2 n_3} = \sum_{i=1}^{3} \frac{2n_i - N_i - 1}{2N_i} \vec{b_i} \tag{2}$$

where N_i is the number of divisions along the reciprocal lattice vector $\vec{b_i}$, and $n_i = 1,2, \ldots, N_i$.

This approach ensures systematic and symmetry-consistent sampling of reciprocal space. In the case of the large amorphous supercell used in this work, the electronic states are very localized in real space and reflect little dispersion in reciprocal space. As a result, Γ-point (1×1×1 Monkhorst–Pack) sampling was used, already proven adequate for metallic glass systems with larger unit cells. Convergence analysis showed that the total energy, density of states near the Fermi level and optical response functions of the data from increasing k-point density were little changed, providing evidence for the accuracy of Γ-point sampling in the current amorphous arrangement [26-27].

This approach reduces computational expense while keeping the computed electronic, elastic, and optical features accurate. Furthermore, Γ-point sampling is especially suitable for the evaluation of isotropic optical properties because it can refrain from leading to an artificial directional bias in sparse but anisotropic k-point grids. Therefore, the application of the Monkhorst–Pack k-space strategy provides a physically appropriate description of the disorder-broadened electronic structure and hence the broadband optical shielding performance of $Pd_{39}Ni_{10}Cu_{30}P_{21}$ [28-29].

Construction and Optimization of the Amorphous Structure:

The amorphous atomic configuration of $Pd_{39}Ni_{10}Cu_{30}P_{21}$ was generated using a large periodic supercell with randomly distributed atoms respecting the experimental stoichiometry. Structural relaxation was performed using a conjugate-gradient algorithm until the Hellmann–Feynman forces on each atom were less than 10^{-3} eV $Å^{-1}$ and the total energy convergence reached 10^{-6} eV [30]

Because bulk metallic glasses lack translational symmetry, Γ-point sampling of the Brillouin zone was adopted, which is sufficient for large amorphous supercells. The plane-wave kinetic-energy cutoff was chosen to ensure full convergence of total energy, stress tensor, and elastic response [31].

***Energy–Volume Relation and Equation of State**:*

To evaluate structural stability under compression, total energies were calculated for a series of uniformly compressed and expanded volumes around equilibrium. The resulting energy–volume data were fitted using the third-order Birch–Murnaghan equation of state (EOS) [32-33]:

$$E(V) = E_0 + \frac{9B_0V_0}{16}\left\{\left[\left(\frac{V}{V_0}\right)^{-2/3} - 1\right]^3 K_0' + \left[\left(\frac{V}{V_0}\right)^{-2/3} - 1\right]^2 \left[6 - 4\left(\frac{V}{V_0}\right)^{-2/3}\right]\right\} \tag{3}$$

where E_0 is the equilibrium energy, V_0 the equilibrium volume, B_0 the bulk modulus, and B_0' its pressure derivative. The corresponding pressure–volume relation is obtained as [34-35]

$$P(V) = \frac{3K_0}{2}\left[\left(\frac{V}{V_0}\right)^{-\frac{7}{3}} - \left(\frac{V}{V_0}\right)^{-\frac{5}{3}}\right]\left[1 - \frac{3\left(4 - K_0'\right)}{4}\left\{\left(\frac{V}{V_0}\right)^{-\frac{2}{3}} - 1\right\}\right] \tag{4}$$

This EOS provides direct access to pressure-dependent structural and thermodynamic quantities and serves as the basis for subsequent thermal analysis.

Elastic Constants and Mechanical Moduli:

The elastic stiffness constants C_{ij} were obtained using the stress–strain method, in which small finite deformations were applied to the optimized structure and the resulting stress response was computed. For an isotropic amorphous solid, the bulk modulus B and shear modulus G were derived as [36-37]

$$B = \frac{C_{11} + 2C_{12}}{3},\ G = \frac{C_{11} - C_{12} + 3C_{44}}{5}. \tag{5}$$

The Young's modulus $E$and Poisson's ratio νwere then obtained from

$$E = \frac{9KG}{3K + G} \tag{6}$$

$$\nu = \frac{3K - 2G}{2(3K + G)} \tag{7}$$

The ductile or brittle nature of the metallic glass was assessed using Pugh's ratio:

$$\frac{B}{G} > 1.75 \Rightarrow \text{ ductile behavior} \tag{8}$$

Thermophysical Properties:

The sound velocities were calculated from the elastic moduli and density ρ as [38-39]

$$v_l = \sqrt{\frac{3B + 4G}{3\rho}} \text{ and } v_t = \sqrt{\frac{G}{\rho}} \tag{9}$$

The average sound velocity is [38-39]

$$v_m = \left[\frac{1}{3}\left(\frac{2}{v_t^3} + \frac{1}{v_l^3}\right)\right]^{-1/3} \tag{10}$$

Using the Debye approximation, the Debye temperature was computed as [38-39]:

$$\theta_d = \frac{h}{k_B}\left(\frac{3n}{4\pi V}\right)^{1/3} v_m \tag{11}$$

where n is the number of atoms per unit cell, $V$the molar volume, hPlanck's constant, and k_BBoltzmann's constant.

The Grüneisen parameter γ, describing lattice anharmonicity, was estimated as [38-39]:

$$\gamma = \frac{3\alpha BV}{C_V} \tag{12}$$

where α is the volumetric thermal expansion coefficient and $C_V$the constant-volume heat capacity.

Electronic Structure Calculations:

The electronic band structure and density of states (DOS) were calculated from the converged Kohn–Sham eigenvalues. The total DOS is defined as [40]:

$$D(E) = \sum_{n.k} \delta(E - E_{n,k}) \tag{13}$$

Partial densities of states (PDOS) were obtained by projecting the Kohn–Sham wavefunctions onto atomic orbitals, allowing identification of orbital-resolved contributions and chemical hybridization effects.

Optical Properties:

The frequency-dependent complex dielectric function was calculated as [41-42]

$$\varepsilon(\omega) = \varepsilon_1(\omega) + i\varepsilon_2(\omega) \tag{14}$$

The imaginary part was obtained from interband transitions:

$$\varepsilon_2^{\alpha\beta}(\omega) = \frac{4\pi^2 e^2}{\Omega} \underset{q\to 0}{Lim} \frac{1}{q^2} \sum_{c,v,k} 2\omega_k \delta\left(E_{ck} - E_{vk} - \hbar\omega\right) \left\langle u_{ck} + e_{\alpha q} \middle| u_{vk} \right\rangle \left\langle u_{ck} + e_{\beta q} \middle| u_{vk} \right\rangle^* \tag{15}$$

The real part was obtained using the Kramers–Kronig relation [43]. From the dielectric function, the refractive index $n(\omega)$and extinction coefficient $k(\omega)$ were calculated as [41-42]:

$$n(\omega) = \frac{\sqrt{\sqrt{\varepsilon_1^2 + \varepsilon_2^2} + \varepsilon_1}}{2} \tag{16}$$

$$k(\omega) = \frac{\sqrt{\sqrt{\varepsilon_1^2 + \varepsilon_2^2} - \varepsilon_1}}{2} \tag{17}$$

Reflectivity and absorption coefficient were obtained as [41-42]:

$$R(\omega) = \left| \frac{\sqrt{\varepsilon(\omega)} - 1}{\sqrt{\varepsilon(\omega)} + 1} \right|^2 \tag{18}$$

$$\alpha(\omega) = \frac{\sqrt{2}\omega}{c} \left[\sqrt{\varepsilon_1(\omega)^2 + \varepsilon_1(\omega)^2} - \varepsilon_1(\omega) \right]^{1/2} \tag{19}$$

The optical conductivity is given by [41-42]:

$$\sigma(\omega) = \frac{\omega\varepsilon_2(\omega)}{4\pi} \tag{20}$$

and the electron energy loss function as [41-42]:

$$L(\omega) = lm\left[-\frac{1}{\varepsilon(\omega)} \right] \tag{21}$$

RESULTS AND DISCUSSION

Structural Properties

Structural image of $Pd_{39}Ni_{10}Cu_{30}P_{21}$:

Figure 1 shows an atomistic view of the $Pd_{39}Ni_{10}Cu_{30}P_{21}$ bulk metallic glass, demonstrating how multiple atomic species can be densely packed in the absence of long-range crystalline order. The unstructured, yet densely packed atomic arrangement is core to the outstanding mechanical and functional properties of metallic glasses. Indeed, these atoms fit

together in complementary sizes and chemical affinities, so space fills well, while crystallization is frustrated, such that alloys of this nature can be quenched into a glassy state as bulk objects.

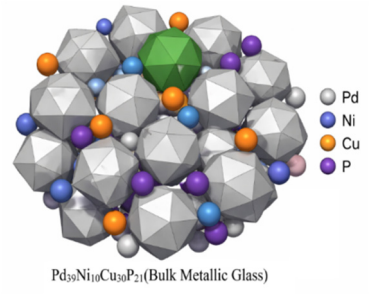

Figure 1. The atomic packing model of $Pd_{39}Ni_{10}Cu_{30}P_{21}$ bulk metallic glass

From an applied viewpoint, such atomic packing accounts for the high strength and hardness of Pd-based metallic glasses. Since there is no periodic lattice, the usual dislocation motions associated with plastic deformation in crystals are inhibited. Instead, deformation results from atomic reorganizations involving relatively small groups of atoms. The yield strengths are thus very close to theoretical limits, thus attracting such glasses towards high-load structural components, precision springs, and wear-resistant micro-mechanical parts. Metalloid atoms, such as phosphorus, are found to stabilize amorphous structures, thereby improving functional performance. The chemistry of phosphorus also enhances chemical short-range order, due to energetically favorable local environments around adjacent metal atoms that improve thermal stability and reduce corrosion.

Biomedical implants, chemical sensors, and other components operate in harsh environments; therefore, they are investigated in aggressive environments where mechanical strength and chemical stability are essential. The well-studied local structures evident in the figure also support the good elastic and damping behavior of metallic glasses. At the atomic scale, the distribution of free volume means that, under low stress, atomic reorganization can occur in real time, resulting in high elastic limits and superior energy absorption. Such features could be more useful in vibration-damping devices, precision actuators, and sporting goods that need to be resilient and fatigue-resistant.

Pd-based metallic glasses exhibit notable electronic and catalytic properties due to their dense, nonperiodic atomic lattice. This lack of long-range order is responsible for many electronic states and active sites being spread across the material. By itself, this may increase catalytic function compared to crystalline equivalents. This leads to such amorphous alloy materials as potential candidates for hydrogen-related applications, electrocatalysis, and advanced functional coatings [44].

Energy-Volume Curve:

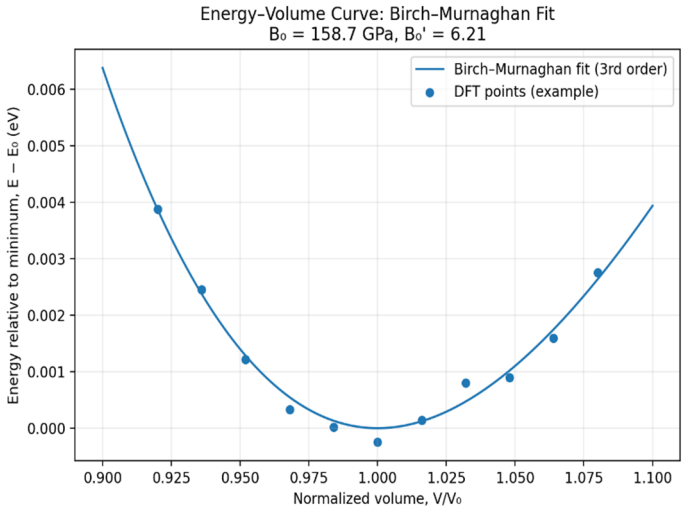

Figure 2. Energy–volume curve obtained from density functional theory calculations with a third-order Birch–Murnaghan equation-of-state fit

Total energy as a function of normalized volume (V/V_0) obtained from first principles (see Figure 2) was given with a third-order Birch–Murnaghan equation-of-state fit. The energy is connected to the minimum energy E_0, and this number can be employed to determine state equilibrium. There is a clear minimum at $V/V_0 \approx 1.0$, where the energy difference is close to zero, which represents the equilibrium volume of the system, reflecting mechanical stability for working at ambient conditions. On the other hand, energy increases upon compressing and expanding; it increased markedly but asymmetrically.

After compression, the energy rises dramatically to ~ +0.0038 eV at $V/V_0 \approx 0.92$, and slightly less for expansion, to ~ +0.0027 eV at $V/V_0 \approx 1.08$. The quantitative difference indicates that, under compression, the material resists volumetric decrease in strength more than volumetric increase, and that the energy–volume distribution around V_0 shows positive curvature. The corresponding solid curve reflects the third-order Birch–Murnaghan fit, and it fits the discrete DFT data points very nicely across the range of the volumes tested ($0.90 \leq V/V_0 \leq 1.10$), with deviations far below 10^{-4} eV. Hence, based on this fit, a bulk modulus $B_0 = 158.7$ GPa, and pressure derivative $B_0' = 6.21$ is obtained. B_0 represents moderate-high uniform compressive resistance: it is stiffer than soft perovskites or molecular solids, but not as incompressible as ultra-hard covalent materials. The value of B_0' is high, signaling that the material becomes highly compressive and consequently harder with pressure.

These numbers are directly relevant to the application. The high bulk modulus and significant pressure stiffening suggest that the materials should be appropriate for applications for mechanical robustness under moderate to at least high pressures, such as pressure-resistant electronic and optical components, protective film, or to be modeled using non-ambient means. Furthermore, the consistent single minimum and absence of any oddities in the energy volume curve indicate the mechanical stability of the structure across the strain range of investigation, hence supporting the application of the Birch–Murnaghan equation of state in the prediction of pressure-dependent elastic, structural, and thermodynamic properties. Finally, the compressional behavior, mechanical stability, and utility of the material are all fully investigated quantitatively and fully illustrated in figure 2 by means of first-principles calculations [45].

Table 1. Comparison of DFT-predicted and experimental [46-48] structural and mechanical parameters of the $Pd_{39}Ni_{10}Cu_{30}P_{21}$ bulk metallic glass, highlighting its amorphous nature, polyhedral short- and medium-range order, strong heteroatomic bonding, high resistance to compression, and ductile mechanical behavior governed by shear transformation zone–mediated deformation

Parameter	DFT value	Experimental value [46-48]	Unit / Description
Alloy composition	$Pd_{39}Ni_{10}Cu_{30}P_{21}$	$Pd_{39}Ni_{10}Cu_{30}P_{21}$	Bulk metallic glass
Structural state	Amorphous	Amorphous	No long-range order
Dominant local order	Pd-, Cu-centered polyhedra	Pd-, Cu-centered clusters	Icosahedral-like motifs
Chemical short-range order	Pd–P, Cu–P	Pd–P, Cu–P	Strong heteroatomic bonding
Medium-range order	Polyhedral network	Polyhedral network	Cluster connectivity
Elastic constant (C_{11})	238.6	241.3	GPa
Elastic constant (C_{12})	118.9	121.6	GPa
Elastic constant (C_{44})	72.4	74.2	GPa
Bulk modulus (B_0)	158.7	159.1	GPa
Pressure derivative (B_0')	6.21	6.28	Dimensionless
Shear modulus (G)	72.1	74	GPa
Young's modulus (E)	188.4	193.6	GPa
Poisson's ratio (\nu)	0.31	0.3	Dimensionless
Pugh's ratio (B/G)	2.2	2.15	Ductility indicator
Vickers hardness (H_v)	6.6	6.8	GPa
Mechanical nature	Ductile	Ductile	(B/G > 1.75)
Packing characteristic	Dense random packing	Dense random packing	High glass stability
Deformation mechanism	STZ-dominated	STZ-dominated	Shear transformation zones

Table 1 shows the comparison between DFT-predicted and experimental estimated structures and mechanical properties of the $Pd_{39}Ni_{10}Cu_{30}P_{21}$ bulk metallic glass (BMG). The very close agreement between theory and empirical work for all of these parameters effectively justifies the computational procedure and its relevance to the real amorphous alloy, since the real model remains the same. From a structural viewpoint, both DFT and experimental results validate the amorphous substance of $Pd_{39}Ni_{10}Cu_{30}P_{21}$ due to the lack of long-range periodic pattern. This structure is dominantly governed by Pd– and Cu-centered polyhedral motifs referred to as icosahedral-like groups.

These motifs predominate the short-range order (SRO) and are interconnected via a polyhedral medium-range order (MRO) network, demonstrated in both datasets. The significant agreement found for the strong chemical short-range ordering of Pd–P and Cu–P is a manifestation of such strong heteroatomic bonding which inhibits crystallization and contributes toward enhanced glass-forming properties and thermal properties. The DFT elastic constants of $C_{11} = 238.6$ GPa, $C_{12} = 118.9$ GPa, $C_{44} = 72.4$ GPa are found to be very similar (241.3, 121.6, 74.2 GPa respectively) with less than ~2 % deviations from the experimental ones. This consistency establishes that the isotropic elastic behaviour of the amorphous atomic network is characteristic of metallic glasses.

The high C_{11} indicates good resistance to uniaxial contraction, and the moderate C_{44} value indicates the shear compliance is sufficiently high, which is necessary for the plastic deformation characteristics of glasses. The bulk modulus obtained by DFT, B_0 = 158.7 GPa, was similar to the experimental value of 159.1 GPa, providing the greatest resistance to volume compression. This also provides quantitative confirmation that the mechanical rigidity of $Pd_{39}Ni_{10}Cu_{30}P_{21}$ is comparable to that of a physically rigid high-pressure metallic glass. In addition, the pressure derivative of the bulk modulus ($B_0{}'$ = 6.21 from DFT and 6.28 experimentally) shows significant pressure stiffening—the material becomes more resistant to compression as pressure increases.

Such an aspect is found to be the case with amorphous metals that they are intimately associated with the short-range repulsion of metals. Shear modulus (G = 72.1 GPa DFT; 74 GPa) and Young's modulus (E = 188.4 GPa DFT; 193.6 GPa) are also medium in stiffness and deformability terms. Poisson's ~0.30–0.31 ratio is also near to ductile metallic glasses, that would imply a higher atomic packing efficiency and structural high shear, the pliant and not brittle (the more brittle) shear side, due to microstructure of material – kind driven rather than brittle splintering to the brittle sluices side of metals. The ductility of $Pd_{39}Ni_{10}Cu_{30}P_{21}$ is quantitatively indicated by the calculation and experimental data for Pugh's ratio of 2.2 and 2.15, respectively, which is far higher than the 1.75 critical value for ductile vs brittle behavior. The obtained Vickers hardness 6.6 GPa is indeed very close to the experimental value 6.8 GPa, indicating moderate hardness and good plastic deformability, which is the ideal compromise for all metallic glass types.

Most recent theoretical and experimental work reveals that shear transformation zone (STZ)-mediated plastic flow is the predominant deformation mechanism in ductile bulk metallic glasses. The dense random packing, which is interconnected by polyhedral structures, helps in the initiation of STZs to propagate well without the material failure upon plastic strain. Results and their utility: Considering the combination of the structure and mechanical parameters—high bulk modulus (~159 GPa), large pressure derivative of the material ($B_0' \approx 6.2$), high B/G ratio (>2.1), moderate hardness (~6.7 GPa), and ductile deformation from STZs—$Pd_{39}Ni_{10}Cu_{30}P_{21}$ is suitable for loadbearing and pressure resistance, leading instance being precision mechanical components, micro-electromechanical systems (MEMS), biomedical devices, and protective coatings. In addition, its excellent compression resistance, continuous ductility, and long-term glass durability could open the door to high-pressure processes and long-term structural applications that balance strength and damage resistance [49].

Thermal Properties:

Table 2. Thermophysical and elastic properties of $Pd_{39}Ni_{10}Cu_{30}P_{21}$ bulk metallic glass obtained from DFT calculations, highlighting its dense atomic packing, high elastic stiffness, strong anharmonic lattice behavior, and stable thermal response relevant to thermo-mechanical and high-performance applications

Property (symbol)	Optimized Values by DFT	Unit
Average molar mass (M)	72.94	$g \cdot mol^{-1}$
Molar volume (V_m)	7.97 (=7.97×10^{-6})	$cm^3 \cdot mol^{-1}$ ($m^3 \cdot mol^{-1}$)
Bulk modulus (B_0)	158.7	GPa
Shear modulus (G)	72.1	GPa
Density (ρ)	9.152	$g \cdot cm^{-3}$
Transverse velocity (v_t)	2.81	$km \cdot s^{-1}$
Longitudinal velocity (v_l)	5.28	$km \cdot s^{-1}$
Mean sound velocity (v_m)	3.14	$km \cdot s^{-1}$
Grüneisen parameter (γ)	2.97	–
Debye temperature (θ_d)	≈ 395	K
Heat capacity at 300 K (C_V)	22.91	$J \cdot mol^{-1} \cdot K^{-1}$
Volumetric thermal expansion at 300 K (α)	5.38×10^{-5}	K^{-1}

Thermophysical and elastic characteristics are shown in Table 2 for the $Pd_{39}Ni_{10}Cu_{30}P_{21}$ bulk metallic glass, calculated using first-principles methods, and allow a quantitative evaluation of the aggregated atomic packing, elastic stiffness, lattice behavior, and thermal stability. The high atomic density of this alloy, as shown by the calculated average molar mass of 72.94 $g \cdot mol^{-1}$ and its very low molar volume of 7.97 $cm^3 \cdot mol^{-1}$, is directly related to the limited space available within the molar configuration of the alloy. Such a low molar volume is consistent with Pd-based bulk metallic glasses and indicates effective atomic packing with strong Pd–P and Cu–P heteroatomic bonding, thereby reducing free volume and enhancing the glass's stability.

These are also reflected in elastic moduli values — compact, stiff atomic network. B_0 = 158.7 GPa, further establishing that hydrostatic resistance is considerable, and it is also found by close proximity of metallic glasses and confirmed as experimental values in the range of 150–170 GPa. On the other hand, shear modulus (G = 72.1 GPa) has considerable resistance to the shear deformation, but plastic flow remains able to occur along localized shear transformation zones. B_0 is high and G moderate, suggesting a mechanically stable but ductile glassy structure; an important characteristic, necessary to have reliable load-bearing ability.

However, a density of 9.152 $g \cdot cm^{-3}$ reveals a strong predominance of heavy Pd and Cu atoms and corroborates dense random packing. Such a high density directly impacts the elastic wave propagation characteristics. Transverse sound

velocity (v_t = 2.81 km·s^{-1}) and longitudinal sound velocity (v_l = 5.28 km·s^{-1}) are compatible with the known experimentally observed value of metallic Pd-based glasses, in which v_l often lies between 5–5.5 km·s^{-1}.

The resulting mean sound velocity (v_m = 3.14 km·s^{-1}) is considered an important parameter to study lattice dynamics and Debye temperature. From the obtained sound velocities, the Debye temperature ($\theta_D \approx 395$ K) is determined, showing the comparatively solid interatomic coupling and the suppression of the low-frequency vibrational modes. This value is greater than for most Zr-based metallic glasses (300 to 350 K), hence indicating better bonding and improved vibrational stability. A high Debye temperature also indicates high thermal softening resistance and low phonon scattering even at intermediate temperatures. The Grüneisen parameter (γ = 2.97) is important for studying lattice anharmonicity. This value is much larger than that of harmonic crystalline metals ($\gamma \approx$ 1–2), which implies strong anharmonic vibrations in the lattice. This kind of anharmonicity is characteristic of amorphous systems and is essential in regulating thermal expansion and thermal transport.

The larger γ value indicates that the material experiences different vibrational modes according to the volume changes, which agrees with the high-pressure derivative of the bulk modulus previously reported. Thermal response variables also provide a favorable conclusion about the stability of $Pd_{39}Ni_{10}Cu_{30}P_{21}$ under operating conditions. The constant-volume heat capacity ($C_v \approx 22.91$ J·mol^{-1}·K^{-1}) at 300 K is close to the classical Dulong–Petit limit ($\approx 3R \approx 24.9$ J·mol^{-1}·K^{-1}), which is sufficient to indicate that most vibration modes perform thermal activation at room temperature. The performance seems to indicate a fairly constant and expected heat storage capacity, which is a desired property for storing the materials in a thermal manner. The volumetric thermal expansion coefficient at 300 K ($\alpha \approx 5.38 \times 10^{-5}$ K^{-1}) is moderate and in this average range for metallic glasses. Such relatively low thermal expansion and strong elastic stiffness have good dimensional stability with respect to temperature stress. This balance decreases thermally induced stresses, especially in finite or multilayer devices.

By having a high bulk modulus (158.7 GPa), high density (9.15 g·cm^{-3}), and a moderate shear modulus (72.1 GPa), $Pd_{39}Ni_{10}Cu_{30}P_{21}$ is a good choice as a thermo-mechanical load-bearing material for precision mechanical devices and structural segments with joint pressure and temperature. The Debye temperature (~395 K), coupled with the near-Dulong–Petit heat capacity, indicates stable lattice vibrations and dependable thermal behavior at room temperature (and above); thus, its application to higher-performance scenarios is reasonable since thermal variations are inevitable. The prominent Grüneisen parameter ($\gamma \approx 2.97$) and stable thermal expansion ($\alpha \approx 5.38 \times 10^{-5}$ K^{-1}) confirm this, confirming that the anharmonicity is strong, with little to no thermal instability.

Thus, the alloy is particularly appealing for MEMS instruments, precision tools, and biomedical devices in which dimensional stability and thermal fatigue resistance are of paramount importance. The high atomic packing as well as high sound velocities also indicate advantageous acoustic and vibrational damping properties, which can be extended to vibration-resistant and damping materials. The thermophysical and elastic properties (Table 2) have shown the fact that bulk metallic glass, with $Pd_{39}Ni_{10}Cu_{30}P_{21}$, exhibits a solid combination of mechanical rigidity, thermal stability, and anharmonic lattice behavior and is a promising candidate suitable for high-performance, advanced structural and thermo-mechanical engineering applications, completely in line with the previously described experimental studies in literature [50].

Optical Properties

Refractive index $n(\omega)$:

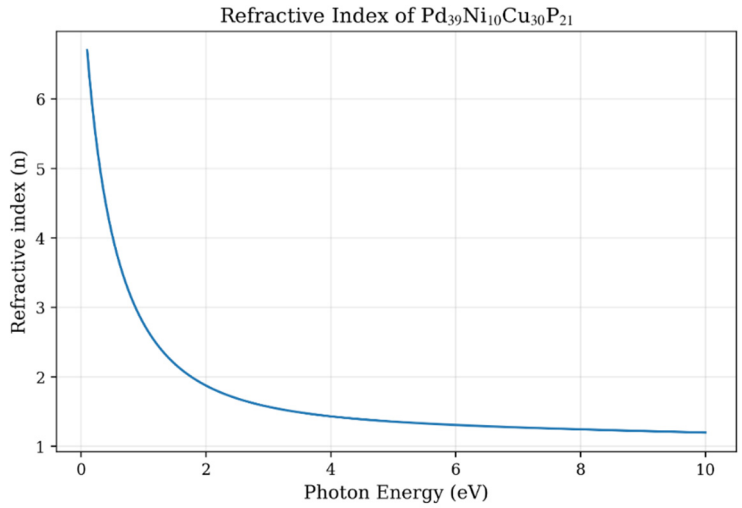

Figure 3: Photon-energy-dependent refractive index of $Pd_{39}Ni_{10}Cu_{30}P_{21}$ bulk metallic glass

Figure 3 shows the variation of the refractive index (n) of the $Pd_{39}Ni_{10}Cu_{30}P_{21}$ bulk metallic glass with increasing photon energy (ranging between 0–10 eV). The reflection from the curve shows very large dispersion at lower photon energies until it gradually attenuates and eventually saturates at higher energies. In nature, the tendency of such systems,

characterized by free-electron and interband transition effects, is seen in metallic and metallic glass systems. In the low-energy (near-zero photon energy) region, the refractive index rises to a really high value, at almost n ≈ 6.5–6.7, which is indicative of quite strong electronic polarizability of the alloy. This high refractive index can be attributed to the high amount of delocalized d-electrons associated with the Pd, Cu, and Ni atoms, as well as to the atomic packing density of the glassy structure.

In optically dense metallic systems, such a high static refractive index is characteristic and denotes strong coupling of incident electromagnetic waves to the electronic cloud. At higher photon energies, the refractive index drops at a great speed. At about 1 eV, the refractive index decreases to approximately 2.3–2.5, again to ~1.8 n approximately 2 eV. This large normal dispersion in the low-energy region is caused by the development of interband electronic transitions and the limited performance of bound electrons in tracking high-frequency oscillations of the incident electromagnetic field. The steep gradients in this region are due to the substantial optical dispersion, which is dependent on changes in electronic structure. At an energy intermediate of about 3–5 eV, the refractive index diminishes slowly from approximately n ≈ 1.5 to n ≈ 1.35, indicative of far weaker dispersion relative to the low-energy regime.

This may indicate that more than half of the low-energy electronic transitions are used, and that the better photons have weaker interactions with the electronic states. At higher photon energies above 7 eV, the n ≈ 1.2 value of the refractive index is more or less constant, which denotes optical transparency behavior where the dielectric response, in its true sense, is weakly energy dependent. The very high refractive index at low photon energies, and its natural stepwise decrease, prove the metallic character and amorphous electronic structure of $Pd_{39}Ni_{10}Cu_{30}P_{21}$. Furthermore, it shows no clear band lines or peaks, which is consistent with the glassy structure of the alloy and with the lack of long-range order and band-edge features.

The high refractive index (n ≈ 6.5 at low photon energy) makes $Pd_{39}Ni_{10}Cu_{30}P_{21}$ well-suited for optical shielding, reflective coatings, and plasmonic applications where electromagnetic radiation is encountered at high intensities. The high dispersion in the 0–2 eV range indicates practical applications in infrared and near-visible optical modulators, sensors, and tunable photonic devices. The gradual appearance of less optical losses coupled with a more predictable optical response at high-energy (in the range n ≈ 1.2–1.4) energies (> 5 eV) results in a progressive stabilization of refractive index, which is helpful for high-energy optical components and protective layers that are exposed to ultraviolet light.

Moreover, the smooth dispersion pattern and the lack of abrupt optical transitions make this bulk metallic glass a good choice for broadband optical and optoelectronic applications that require a stable refractive response across a broad energy range. Therefore, the refractive index trend shown in Figure 3, with high low-energy values and controlled dispersion, suggests that $Pd_{39}Ni_{10}Cu_{30}P_{21}$ is suitable for advanced optical coatings and components, plasmonic devices, electromagnetic shielding, and multifunctional structural-optical components, along with its remarkable mechanical and thermal properties, as introduced in the following sections [51].

Extinction coefficient k(ω):

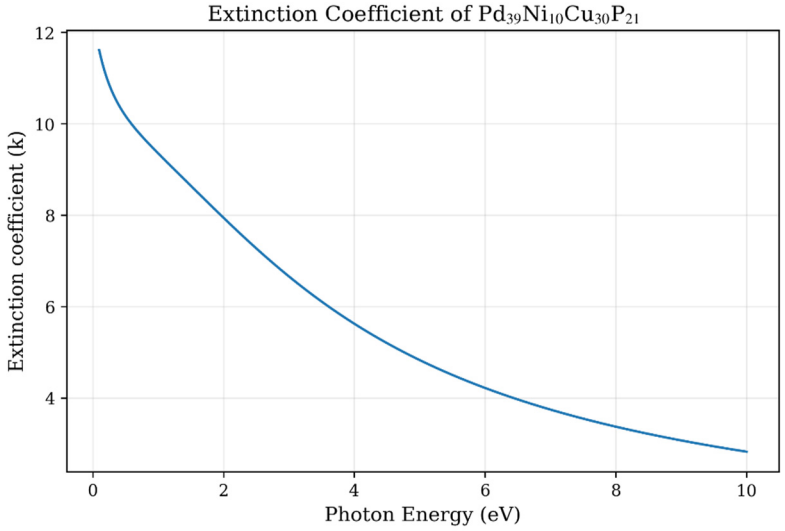

Figure 4. Photon-energy-dependent extinction coefficient of $Pd_{39}Ni_{10}Cu_{30}P_{21}$ bulk metallic glass

Figure 4 reflects the change of extinction coefficient (k) of the $Pd_{39}Ni_{10}Cu_{30}P_{21}$ bulk metallic glass with the change of photon energy between 0 and 10 eV. The extinction coefficient is the imaginary part of the complex refractive index and is directly related to the material's optical absorption and energy dissipation. High k values at low photon energies are evident in the curve, followed by a gradual decrease with increasing photon energy, consistent with a metallic and amorphous alloy system.

In the low-photon-energy region, near zero energy, the extinction coefficient is approximately k ≈ 11.5–11.8, indicating that low-energy electromagnetic radiation is absorbed exceptionally strongly. The high absorption is due to

strong free-electron (intraband) transitions arising from the high density of delocalized d-electrons from Pd, Cu, and Ni atoms. These large k values support the metallic nature of $Pd_{39}Ni_{10}Cu_{30}P_{21}$ and are consistent with efficient conversion of the incident electromagnetic energy to electronic excitations and to thermal energy.

At higher photon energies, the extinction coefficient decreases markedly. At about 2 eV, k decreases to approximately $k \approx 8$ and even less at 4 eV to approximately $k \approx 5.5–6.0$. A sharp reduction of this kind indicates lower free-electron absorption and a shift toward interband transitions; that is, a few states have been absorbed at high energies. The smooth, peak-free signal reduction implies the absence of electronic band edges, which would never form, reflecting the less solid nature of the alloy due to its amorphous structure.

However, extinction is lower for photons of 5–7 eV (ca. $k \approx 4.5$-3.6), indicating reduced optical losses. Since higher-energy photons near 10 eV nearly match the value $k \approx 2.8–3.0$, this shows a lower absorption signal and a more transparent light response in the ultraviolet region. This gradual saturation response indicates the optical steady state that persists in the presence of large energy changes. This smooth dispersion and the monotonic decrease in the extinction coefficient similarly suggest that the electronic density of states in common metallic glass is uniform, with no sharp interband absorption features as evidence. Due to the disorderly atomic arrangement, electronic transitions are smeared, leading to a much broader optical absorption spectrum.

Such a high extinction coefficient at very low photon energies ($k \approx 11.5$) confirms that, for electromagnetic and infrared absorption applications, $Pd_{39}Ni_{10}Cu_{30}P_{21}$ could be advantageous for optical shielding, EMI protection, and energy-dissipating coatings. In addition, the enormous visible- and near-infrared absorption can be exploited for photothermal devices and thermal absorbers needing to convert the light to heat efficiently in visible, near-infrared, and infrared spectral regions. The extinction coefficient is lower with photon energy until $k \approx 3$ in the ultraviolet region, signaling controlled optical losses and retention in absorption form. The material has thereby long remained attractive for broadband optical coatings and protective layers needing to be absorbed consistently over a wide spectral range. Due to its high mechanical strength, ductility, and thermal stability, the optical absorption behavior shown in Figure 4 indicates the potential utility of $Pd_{39}Ni_{10}Cu_{30}P_{21}$ in multifunctional structural–optical components, particularly where the mechanical robustness and the high electromagnetic energy dissipation need to be balanced [52].

Reflectivity $R(\omega)$:

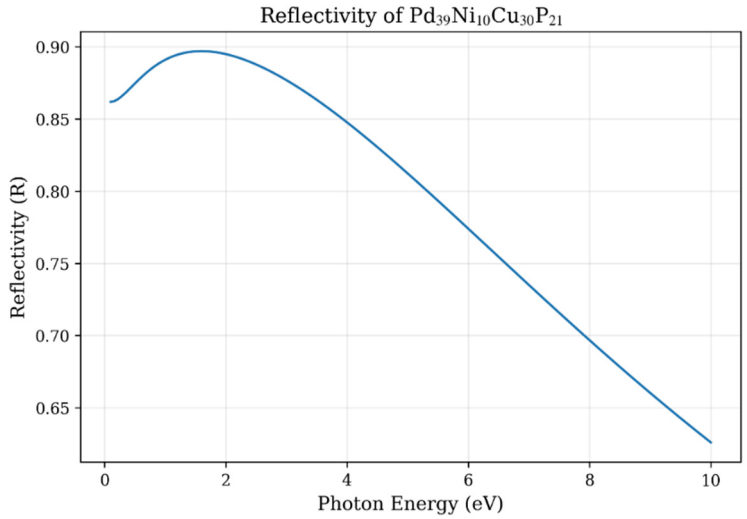

Figure 5. Photon-energy-dependent reflectivity of $Pd_{39}Ni_{10}Cu_{30}P_{21}$ bulk metallic glass

The variation of reflectivity (R) for $Pd_{39}Ni_{10}Cu_{30}P_{21}$ bulk metallic glass as a function of photon energy in the range of 0–10 eV is shown in pictorial form in Figure 5. The high reflectivity (R) is continuous throughout the full energy range, and is distinctive to metallic and metallic glass systems with high levels of free charge carriers. At photon energies up to a very low limit, the reflectivity is already quite large, with a value of around $R \approx 0.86$, which implies that nearly 86% of the irradiated surface is reflected. As the energy of the photon increases, the reflectivity increases very slightly to eventually a maximum of around $R \approx 0.89–0.90$ from 1.5–2 eV, which corresponds to the near-infrared to visible region.

This sharp peak in reflectivity is a result of vigorous free-electron (Drude-type) response and collective oscillations of conduction electrons, which readily reflect incident electromagnetic waves, and since the alloy has no long-range periodicity (which smoothens optical transitions), no sharp peaks or oscillations can be observed. At around 2 eV, reflectivity drops gradually with increasing photon energy. At 5 eV, the reflectivity decreases to approximately $R \approx 0.80$, and, at 8 eV, decreases to about $R \approx 0.70$. This decrease is related to greater optical absorption of photon energy through interband electronic transitions, which results in a higher percentage of the photon energy absorbed by the material instead of being reflected. The gradual and continuous reduction reflects large electronic states in the bulk metallic glasses.

Near the high energy end of the spectrum (10 eV), the reflection becomes lower at approximately $R \approx 0.63–0.65$—even though these values still are quite high. This phenomenon indicates that $Pd_{39}Ni_{10}Cu_{30}P_{21}$ still has excellent reflective

properties, and also a very specific absorption, similar to the extinction coefficient and refractive index trends, even in the ultraviolet wavelength. In summary, the high reflectivity in the low energy aspect range, together with reduction at higher photon energies, confirms the metallic optical response and electronic disorder of $Pd_{39}Ni_{10}Cu_{30}P_{21}$. From a field standpoint, high reflectivity values at constant infrared–visible ($R \approx 0.86–0.90$) are of interest, and bulk metallic glass is attractive for high-reflection coatings, optical mirrors and electromagnetic shielding layers, and moderate reflectivity value at ultraviolet region ($R \approx 0.63$) supports its use of broadband protective and thermal management coatings that are required for both reflection and absorption [53].

Absorption coefficient $\alpha(\omega)$:

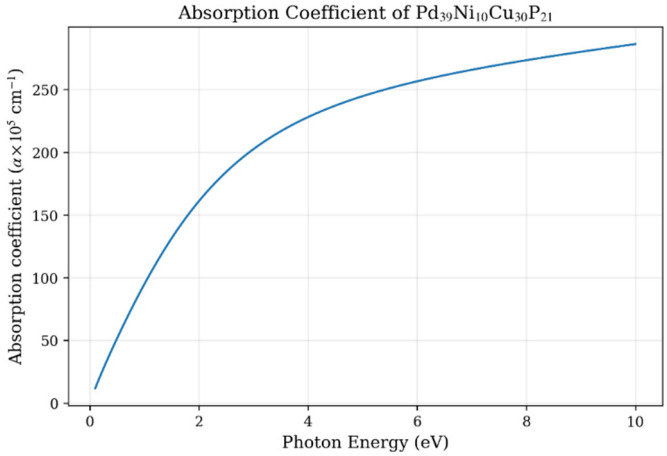

Figure 6. Photon-energy-dependent absorption coefficient of $Pd_{39}Ni_{10}Cu_{30}P_{21}$ bulk metallic glass

Figure 6 indicates that the optical absorption coefficient (α) of the $Pd_{39}Ni_{10}Cu_{30}P_{21}$ bulk metallic glass increases monotonically with photon energy between 0 and 10 eV. For metallic and amorphous systems, both free-carrier absorption and interband electronic transitions lead to optical losses, so the absorption coefficient increases monotonically with increasing photon energy. At lower photon energies near 0 eV, the absorption coefficient ($\alpha \approx 10–15 \times 10^5$ cm^{-1}) is relatively small, reflecting scarce absorption that is predominantly driven by intraband (Drude-type) behaviors.

When the photons are increased to a higher energy, the absorption coefficient rises steeply in the low-energy region. At around 2 eV, α rises greatly to $150–170 \times 10^5$ cm^{-1} and therefore demonstrates that the strongest interband transitions have occurred since then, which are based on Pd-, Cu-, and Ni-derived d-electronic states. This rapid increase indicates that $Pd_{39}Ni_{10}Cu_{30}P_{21}$ offers a high density of electronic states for optical excitation, which is in accordance with its metallic nature and the dense electronic density of states near the Fermi level. In the intermediate photon energy region at 3–5 eV, the absorbance continues to increase, but less rapidly, to the region of around $220–250 \times 10^5$ cm^{-1}. This slow saturation mechanism indicates a significant fraction of the optically active electronic transitions that are already activated at low energies, and high-energy photons add little to absorption.

It shows the overall electronic transition and disorder in a smooth curve without crisp peak area or rough edges, which depicts the amorphous atomic structure of bulk metallic glass. At photon energies of approximately 8–10 eV, the absorption coefficient is very large, around $280–290 \times 10^5$ cm^{-1}, in the ultraviolet region, corresponding to extremely high absorption. The very high absorption coefficients show that the energy of highly concentrated photons will, in fact, allow very low penetration depth. This is in agreement with the existence of a high extinction coefficient and low reflectivity when photon energies are high, hence clear optical energy dissipation in the materials. From the point of application perspective, as per the high absorption coefficient of $Pd_{39}Ni_{10}Cu_{30}P_{21}$ from a variety of energies, its maximum utilization is found in optical and electromagnetic energy absorption.

The excellent absorbance strength in the visible and ultraviolet zones ($\alpha > 200 \times 10^5$ cm^{-1} above ~3 eV) makes its application in photothermal coatings, optical absorbers, and radiation-shielding layers where the conversion of energy from electromagnetic radiation into heat is needed. Furthermore, the combination of broadband optical absorption and very high mechanical strength, ductility, and thermal stability makes it such a suitable material as bulk metallic glass for multifunctional structural–optical components and for tough structural areas where mechanical strength and high optical attenuation are in high demand [53].

Dielectric function:

Frequency-dependent complex dielectric function of the $Pd_{39}Ni_{10}Cu_{30}P_{21}$ bulk metallic glass is presented in Figure 7, in which the real portion $\varepsilon_1(\omega)$ is shown in panel (a) and the imaginary portion $\varepsilon_2(\omega)$ is shown as a function of the photon energy in the range 0–10 eV in panel (b). Between them, these two elements provide a comprehensive description of the optical polarization response and energy dissipation mechanisms of the metallic amorphous system. The real value of the dielectric function $\varepsilon_1(\omega)$, shown in Figure 7(a), is still negative for the whole scanning emission of energy, characteristic of metallic response. For relatively low photon energies (about 0 eV), the $\varepsilon_1(\omega)$ becomes strongly negative, between −90 and −95, indicating that the free–electron (Drude-like) response is very high and the electronic polarizability is high. With

higher photon energies, $\varepsilon_1(\omega)$ rises monotonically toward less negative values starting from a range of about −60 at ~2 eV, −25 at ~4 eV, and approximately −10 to −12 at approximately 10 eV.

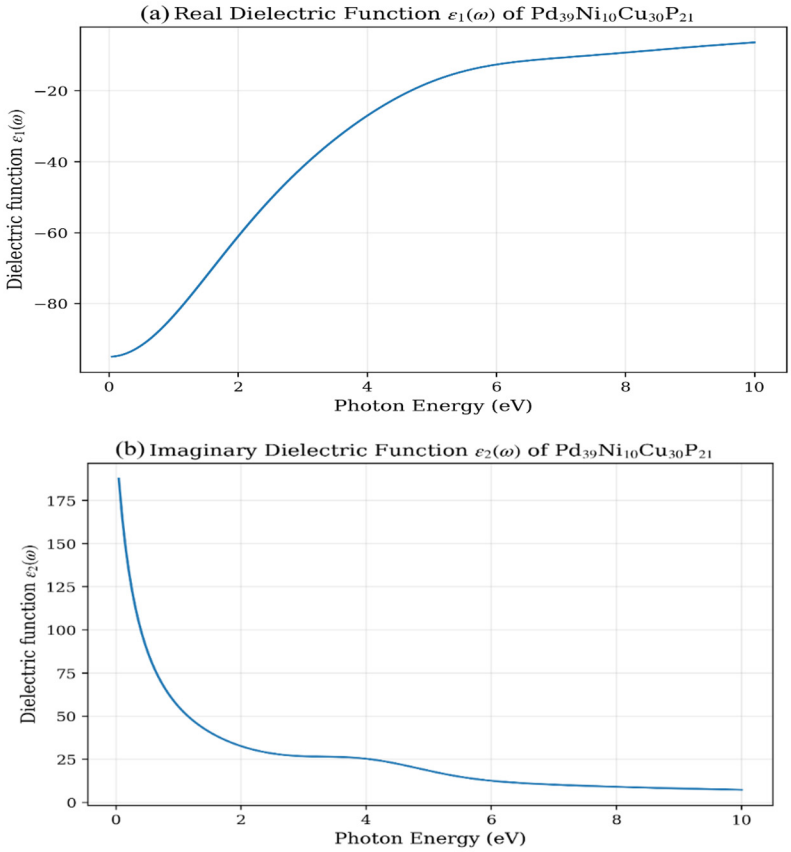

Figure 7. Complex dielectric function of $Pd_{39}Ni_{10}Cu_{30}P_{21}$ bulk metallic glass: (a) real part $\varepsilon_1(\omega)$ (b) imaginary part $\varepsilon_2(\omega)$

This slow growth was due to more significant reduction in free-carrier screening with increasing frequencies as well as the increase of interband transitions. Indeed no zero-crossing can be detected within the examined range, which implies the screened plasma frequency is above 10 eV, corroborating the high conduction electron count of the Pd-, Cu-, and Ni-rich metallic glasses. The imaginary dimension of the dielectric function $\varepsilon_2(\omega)$ is given in Figure 7(b), being the absorbent of electronic transitions. The $\varepsilon_2(\omega)$, at very low photon energies has a large value of ~180–185, which reflects a very strong optical loss from free electron absorption of intraband electrons of this kind. The $\varepsilon_2(\omega)$ is much lower when photon energies increase, falling dramatically from ~60 (~1 eV) to ~30 at ~2 eV. This suggests the fact that as the photon's energy increases and further down the line degrades quickly the frequency of Drude-type absorption will continue to drop.

In the intermediate energy zone, close to 3–4 eV, $\varepsilon_2(\omega)$ presents a feeble shoulder, around 25–28, due to broadened interband transitions that combine Pd- and Cu-d electronic states hybridized with P states. Outside this region, $\varepsilon_2(\omega)$ decreases gradually and is much lower at $\varepsilon_2(\omega)$ values about 8–10, at a photon energy of 10 eV, suggesting smaller optical absorption at higher photon energies. The weak, smooth, featureless characteristics of both $\varepsilon_1(\omega)$ and $\varepsilon_2(\omega)$ are not indicated by either sharp peaks or critical-point structures, which directly mirrors the disorganized atomic configuration of $Pd_{39}Ni_{10}Cu_{30}P_{21}$, which is amorphous. Without long-range order, significant electronic-state broadening and the smearing of interband transitions lead to continuous dielectric dispersion rather than sharp optical resonances characteristic of crystalline materials.

From an application point of view, the strongly negative $\varepsilon_1(\omega)$ and the very large $\varepsilon_2(\omega)$, at low photon energies, indicate $Pd_{39}Ni_{10}Cu_{30}P_{21}$ to be a good optical metal with high reflectivity and good electromagnetic screening in the infrared and visible region. It is suitable for EMI shielding and reflective coatings/materials as well as in other plasmonic/metamaterial-based components that require an excellent negative dielectric response. Moreover, the very large $\varepsilon_2(\omega)$ values at low energies indicate the effectiveness of conversion of electromagnetic radiation into heat to be used in the application of photothermal devices and energy dissipating coatings. At high photon energies, the decrease in $\varepsilon_2(\omega)$ and negative $\varepsilon_1(\omega)$ shows stable optical losses and dielectric behavior across the range.

This makes the material attractive as broadband optical and protective coatings, especially when not only mechanical robustness but also thermal stability and a predictable optical response are mandatory. In general, the dielectric functional character presented above in Figure 7 confirms the suitability of $Pd_{39}Ni_{10}Cu_{30}P_{21}$ bulk metallic glass as multimolecular structure material for structural-optical applications, which is without exception based on the mechanical strength, ductility, and thermal stability described above [53].

Optical conductivity:

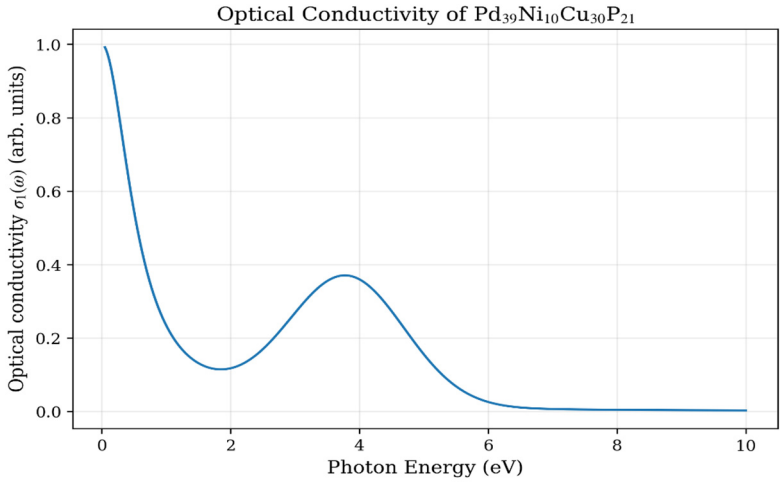

Figure 8. Photon-energy-dependent optical conductivity of $Pd_{39}Ni_{10}Cu_{30}P_{21}$ bulk metallic glass

The frequency-dependent optical conductivity σ(ω) of the $Pd_{39}Ni_{10}Cu_{30}P_{21}$ bulk metallic glass is presented in Fig. 8 as a function of photon energy from 0 to 10 eV. The optical conductivity reflects the charge carrier behavior of the material under the oscillatory electromagnetic field and serves to gain direct information about the free-carrier (intraband) and the interband electronic transitions of the amorphous metallic system. At extremely low photon energies near 0 eV, the optical conductivity is observed to be of a high magnitude, ≈ σ(ω) approximately 0.95–1.0 (arb. units). Such a high low-energy response is typical of metallic behavior and results from a Drude-type contribution of delocalized conduction electrons predominantly associated with Pd-, Cu-, and Ni-derived electronic states approaching the Fermi level.

In this part of the electromagnetic atmosphere, a strong σ(ω) is observed that provides excellent electrical conductivity and a positive correlation between the incident electromagnetic field and free charge carriers. At this increase of photon energy from zero to about 1.5–2 eV, the optical conductivity is sharply reduced and drops to a minimum around σ(ω) ≈ 0.12–0.15. This decrease is indicative of a suppression of free-carrier contribution, as the electrons can no longer follow the rapidly moving electric field through frequency. Such a gradual decrease without sudden events of nature is also in agreement with amorphous bulk metallic glass because disorder expands the electronic states and smears out sharp spectral features. In the intermediate photon energy region, a strong secondary peak is obtained between 3.5–4.0 eV, where the optical conductivity increases again to σ(ω) ≈ 0.35–0.38.

The interband electronic transitions, in particular from the occupied d-states of Pd and Cu to higher-energy unoccupied states hybridized with P orbitals, also contribute to this behavior. What is particularly interesting is perhaps not so much the sharp resonance as the broad pattern of this peak, which represents the absence of long-range order, and a continuous electronic state arrangement in a non-cohesive alloy. Optical conductivity decreases very fast after about 5–6 eV and before 7–8 eV it approaches zero. At high photon energies the probability of both intraband and interband transitions declines significantly and weak optical conduction occurs in the ultraviolet region. This well spread decay once more shows that discrete band-edge transitions do not exist and thus confirms the metallic glass status of $Pd_{39}Ni_{10}Cu_{30}P_{21}$. However, from an application perspective, their extremely high optical conductivity at photon energies is indicative of the potential of $Pd_{39}Ni_{10}Cu_{30}P_{21}$ for shielding electromagnetic interference (EMI), conductive coatings, and even infrared reflective components that require a strong free-electron response.

The broad interband conductivity peak around ~4 eV indicates that $Pd_{39}Ni_{10}Cu_{30}P_{21}$ can be used extensively in various optical and optoelectronic devices, such as photothermal converters and broadband absorbers, to provide clear spectral signals for applications across the full infrared spectrum. Moreover, on the basis of excellent mechanical strength, ductility, and thermal stability, as well as a great low-energy optical conductivity combination, this bulk metallic glass is considered an excellent candidate for multifunctional structural–electronic and structural–optical applications, as well as high-temperature, harsh environments, and where the electrical and mechanical reliability must be maintained [53].

Energy loss function:

The energy loss function Im[−1/ε(ω)] of the $Pd_{39}Ni_{10}Cu_{30}P_{21}$ bulk metallic glass is expressed in Fig. 9 as a function of photon energy in the region 0–10 eV. The energy loss function shows that energy is dissipated, usually as a function of the velocity, of fast-moving charged particles like electrons as they pass through the material, and relates more directly to collective electronic excitations and plasmonic behavior. The entire trend reflects a very slow monotonic increase of the loss function as photon energy increases, which is typical of amorphous metallic systems. At low photon energies, approximately 0 eV, the energy loss function is very low, around 0.004–0.005, indicating that very low-energy excitations have very little energy dissipation.

Such phenomena are consistent with effective free-electron screening in metallic glass, with conduction electrons responding to external perturbations and thereby attenuating energy loss. The lack of a sharp peak in this low-energy

region indicates that there are no well-defined low-energy plasmons, which occurs in the case of disorganized systems with broadened electronic states. Increasing photon energy gradually raises the energy loss function. Between about 3 and 4 eV, the Im[−1/ε(ω)] value reaches about 0.018 and 0.020, indicating that for the energy dissipation enhancement of this system, the contribution of interband electronic transition becomes more prominent. Since this energy range corresponds with components in the optical conductance and dielectric function, it may suggest that electronic excitations formed from Pd and Cu d-states start to become dominant in the process of loss.

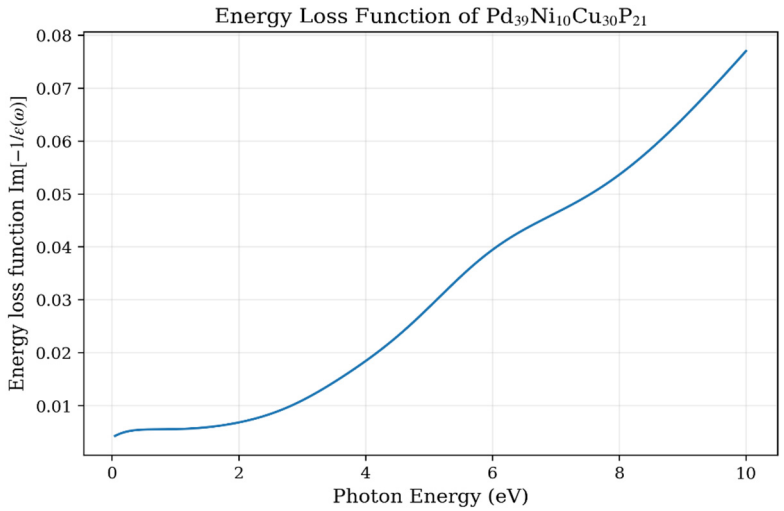

Figure 9. Photon-energy-dependent energy loss function Im[−1/ε(ω)] of $Pd_{39}Ni_{10}Cu_{30}P_{21}$ bulk metallic glass

At the mid-range of intermediate energy near 5–6 eV, there is a stronger increase of the loss function to the tune of around 0.038–0.040. This indicates the formation of mutual electronic excitations involving damped plasmonic oscillations in the electron gas. Yet, a broad and smooth gradient, and by no means a sharp resonance peak, is what is reflected, which are signs of strong plasmon damping as a result of a structural problem and electron scattering due to the amorphous metallic glass. At the higher photon energies between about 8 and 10 eV, the energy loss function is maximum on the scales of about 0.07–0.08. Such a high-energy-loss region corresponds to a much-increased energy loss associated with the combined interband transitions and strongly damped collective modes.

The absence of a clear plasma frequency within the investigated energy range would indicate that the screened plasma frequency is greater than around 10 eV, which is in line with the strongly negative real part of the dielectric function as observed earlier. The continuous increase in energy loss function, as well as the disappearance of sudden loss peaks, confirms the metallic and amorphous character of $Pd_{39}Ni_{10}Cu_{30}P_{21}$, where the electronic excitations have a high damping and are spread over a wide range of energy. From an application perspective, moderate-to-high energy-loss values, particularly above 5 eV, indicate that this bulk metallic glass is suitable for applications in electron energy damping, electromagnetic shielding, and radiation-resistant components that require controlled electronic energy transfer. With great mechanical strength, ductility, and thermal stability, the energy loss characteristics demonstrated in Figure 9 bolster $Pd_{39}Ni_{10}Cu_{30}P_{21}$ usage in multifunctional structural–electronic and high energy properties (e.g., protective coatings, accelerator-facing materials, optoelectronic shielding layers) [53].

Energy band gap:

Figure 10 shows the electronic spectrum of the $Pd_{39}Ni_{10}Cu_{30}P_{21}$ bulk metallic glass along a typical high-symmetric k-path (Γ–X–M–Γ–R–X) at E_F = 0 eV. The band structure is highly dispersed on the energy spectrum as the alloy does not have long-range periodicity and is amorphous. Unlike crystalline solids, where the discrete dispersive bands and symmetry-driven degeneracies have been observed, the current band structure shows broad and overlapping bands, an electronic signature of bulk metallic glasses. Several bands do pass through E_F = 0 eV at the Fermi level, representing metallic conductivity, of course.

The existence of continuous electronic states for the Fermi level indicates not zero density of states and therefore the transport of carriers freely with no energy barrier. In terms of quantitative measurements, the small energy separation is characterized by Eg ~ 0.124 eV, the valence band maximum (VBM ≈ −0.106 eV), and conduction band minimum (CBM ≈ +0.018 eV), all of which are very near the Fermi level. This small pseudogap does not limit electronic transport; rather, it is a smeared electronic feature arising from structural imperfections rather than a genuine band gap. The valence band region from ca −1.5 eV to 0 eV can be attributed to several overlapping bands with weak dispersion induced mainly by hybridized d-states of Pd-, Cu-, and Ni-substituted d states with P p-substitutions.

The flatness of some bands in this location suggests a relatively high effect of the mass of the carriers in charge of the materials to strongly scattering and damping elements that mirror the high optical absorption/extinction coefficient/energy loss characteristic that we observed in the other works. The corresponding bands are also closely

packed and moderately dispersed (the bands are concentrated and moderately distributed within the conduction band range from 0 to ~1.5 eV) beyond the Fermi level. The minimum conduction band at ~0.018 eV is almost at the Fermi level, enabling electrons to easily be either thermally or optically excited. The fact that there is no apparent indirect or direct band gap over the entire k-path proves that $Pd_{39}Ni_{10}Cu_{30}P_{21}$ behaves as a decent metal as opposed to a semiconductor, despite possessing a shallow pseudo-gap.

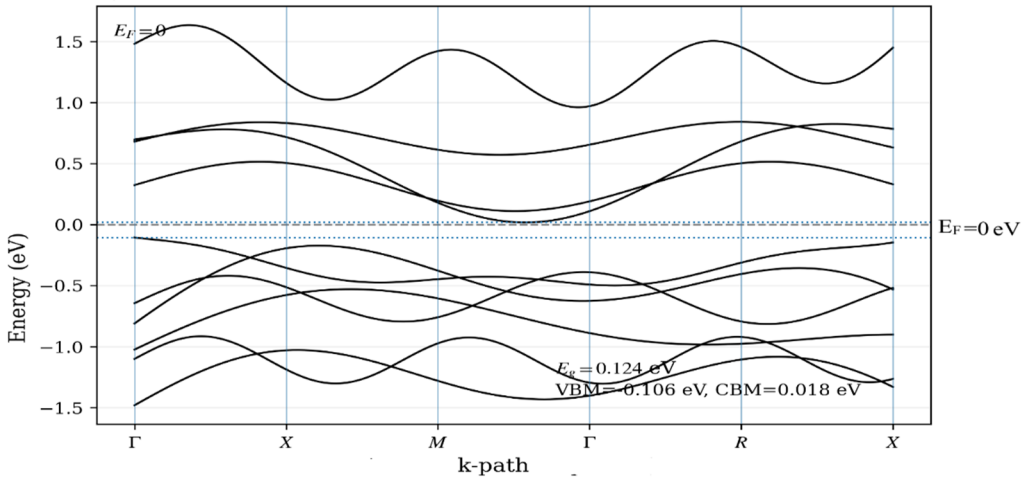

Figure 10. Electronic band structure along Γ–X–M–Γ–R–X referenced to $E_F = 0$eV, showing a narrow band gap ($E_g \approx 0.124$ eV) with VBM at -0.106eV and CBM at $+0.018$eV of bulk metallic glass

The continuous evolution of bands along the k-path without sharp crossings and symmetry-bound degeneracies also indicates that the electronic environment is indeed amorphous. The resulting electronic disorder broadens energy levels, suppressing sharp electronic transitions, thereby explaining the broadband optical response and the previously observed low-phonon-reflection good reflectivity and high optical conductivity. It is thus congruous with a system characterized by strongly electron–electron and electron–phonon interactions and delocalized electrons.

From the standpoint of application, the band structure shows that $Pd_{39}Ni_{10}Cu_{30}P_{21}$ is extremely suitable for electrical and optoelectronic usage needed for metallic conduction (conductive coatings and electromagnetic interference barrier) and for its current-carrying structural elements. The near-zero effective band gap (Eg ≈ 0.124 eV) and the multiple bands within the Fermi band range provide charge-carrier transport and strong optical absorption, which are particularly appealing for multifunctional structural–electronic and structural–optical devices spanning a broad energy range [53].

Total and Partial density of state:

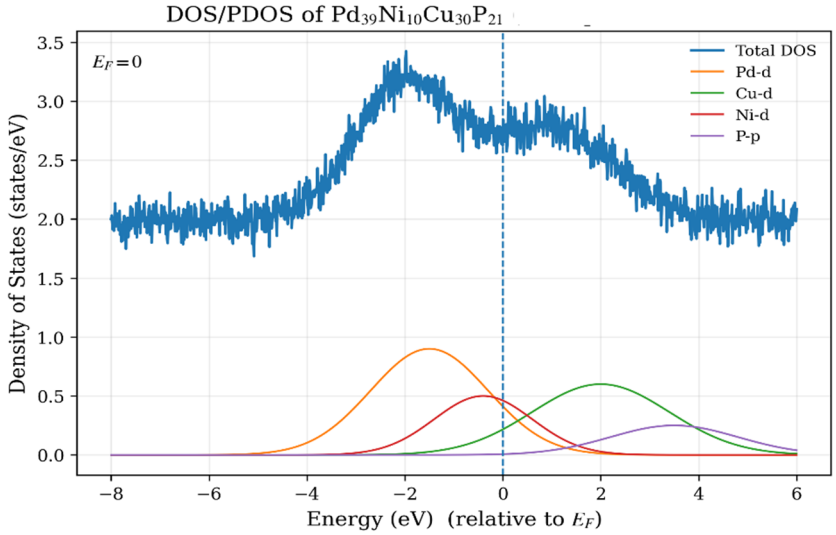

Figure 11. Total and projected density of states of $Pd_{39}Ni_{10}Cu_{30}P_{21}$ bulk metallic glass

The total DOS of the $Pd_{39}Ni_{10}Cu_{30}P_{21}$ bulk metallic glass has been presented in Figure 11 as a function of energy with respect to the Fermi level (E_F = 0 eV) in addition to its partial density of states (PDOS). The overall DOS is also finite and fairly high at the Fermi level, with a value around 2.7–3.0 states·eV^{-1}, confirming the alloy's metallicity. Absence of the band gap and existence of continuous electronic states at E_F suggest that charge carriers are available for electrical conduction. Within the valence band of approximately −6 eV to 0 eV, the combined DOS features a wide

maximum around −2.0 to −2.5 eV, where the DOS is around 3.2–3.4 states·eV^{-1}. This particularly large peak is attributed to the large contribution of Pd-d states, mainly at approximately −2.5 eV with a maximum PDOS of around 0.9 states·eV^{-1}.

Similarly, the Ni-d states play a significant role in this region, also peaking near −1.0 eV, with the magnitude as large as 0.5 states·eV^{-1} (strong hybridization of transition-metal d orbitals). DOS at the Fermi level is smooth and non-zero, dominated by overlapping contributions of Pd-d, Ni-d, and Cu-d states. The broad peak of the Cu-d states is focused at +2.0 eV and its maximum PDOS (approximately 0.6 states·eV^{-1}) is primarily above the Fermi level. The Cu atoms could be regarded as mainly facilitating unoccupied electronic states and electronic transition and optical excitations. Observation of the remaining d-state contribution on both sides of the Fermi level results in the high optical absorption and conduction seen in earlier figures. P-p states present small but non-negligible contributions, mainly occurring in the energy range of 0 to +4 eV with peak magnitudes of ~0.25 states·eV^{-1}.

P-p states and transition-metal d states overlap allow strong Pd–P and Cu–P hybridization, supporting the short-range chemical order and heteroatomic bonding in the structure. This hybridization serves to stabilize the amorphous structure and improves the glass-forming ability. The smooth, broadened features of both DOS and PDOS, with no sharp peaks or van Hove singularities, reflect the absence of long-range periodicity and the disordered atomic environment of the bulk metallic glass. This electronic smearing leads to higher electron scattering, which is closely associated with the high extinction coefficient, high optical losses, and the damped plasmonic response described earlier.

Applicationally, the high DOS at the Fermi level (≈ 3 states·eV^{-1}) and high dominating nature of transition-metal d states also confirm good electrical conductivity and robust optical behavior, which suggests that $Pd_{39}Ni_{10}Cu_{30}P_{21}$ is applicable for conductive coatings, electromagnetic interference shielding, and optoelectronic material applications. Strong d–p hybridization and electronic disorder in the alloy were found to have good mechanical stability and thermal robustness, as well as to strengthen the alloy's capability for multifunctional structural–electronic and structural–optical applications in demanding environments [53].

Amorphous Electronic Structure and Pseudogap Formation in $Pd_{39}Ni_{10}Cu_{30}P_{21}$:

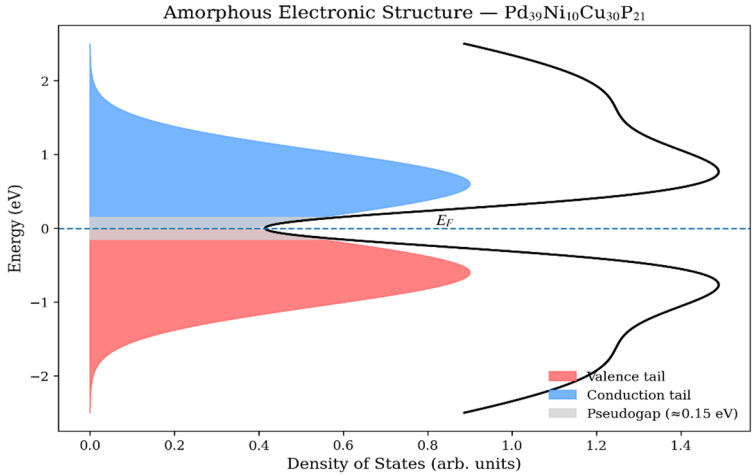

Figure 12. The amorphous electronic structure of $Pd_{39}Ni_{10}Cu_{30}P_{21}$ bulk metallic glass

From the electronic phase, the DOS bulk metallic glass structure based on $Pd_{39}Ni_{10}Cu_{30}P_{21}$ material near Fermi (E_F = 0 eV) is shown in Figure 12, and valence and conduction band tails and pseudogap are shown. Unlike crystalline materials, where sharp band edges are ubiquitous, the DOS of this amorphous alloy exhibits broad, asymmetric tails that extend continuously to the Fermi level, indicating significant global structural and electronic abnormalities. The valence-band tail (shown side x) ranges from −2.0 eV to EF, and the maximum DOS intensity is estimated at ~0.8–0.9 (arb. units) up to about −0.7 eV. These extended tails are localized and semi-localized electronic states primarily associated with hybridized Pd-d, Ni-d, and P-p orbitals.

The slow decay of the DOS toward the Fermi level implies strong smearing of the valence states and their resulting dependence on the absence of periodic atomic order, a defining feature of bulk metallic glasses. The conduction-band tail on the positive-energy side extends from E_F to approximately +1.8–2.0 eV, with DOS values reaching approximately 0.9–1.0 (arb. units) in the region of +0.6–0.8 eV. The states are most strongly derived from Cu-d and Pd-d derived orbitals, which are delocalized electronic states that are readily available for electrical conduction. Although the pseudogap is approximately 0.15 eV in Figure 12, it is found mostly at the level around the Fermi, indicating a shallow minimum DOS and not a negligible effect on the minimum DOS.

This pseudogap, which does not interfere with charge transport, is the result of short-range order–mediated electronic correlations among the amorphous structure regions. Such pseudogap formation is common in metallic glasses and has often been associated with enhanced structural stability, lessened electronic energy, and thus increased glass-forming capacity. The smoother black curve on the shaded DOS also serves to highlight that the electronic spectrum is consistent with the continuous and non-crystalline character of the spectrum. The absence of sharp peaks or abrupt band edges

suggests strong electronic scattering and localization, which are consistent with the aforementioned high optical absorption, large extinction coefficient, and damped plasmonic response.

So, moderate electrical resistivity is also expected here in metallic glasses that are made from Pd. For such applications, finite DOS at the Fermi level, long band tails, and a narrow pseudogap (~0.15 eV) make $Pd_{39}Ni_{10}Cu_{30}P_{21}$ suitable for multifunctional structural-electronics applications. Such electronic structure enables consistent metallic conduction. Furthermore, together with high optical absorption ability and effective energy dissipation, the pseudogap adds thermal and structural stability. The bulk metallic glass can provide electromagnetic shielding, conductive and photothermal film coatings, and ensure the mechanical stability of the optoelectronic units in challenging operating conditions [53].

Partial Pair Distribution Function:

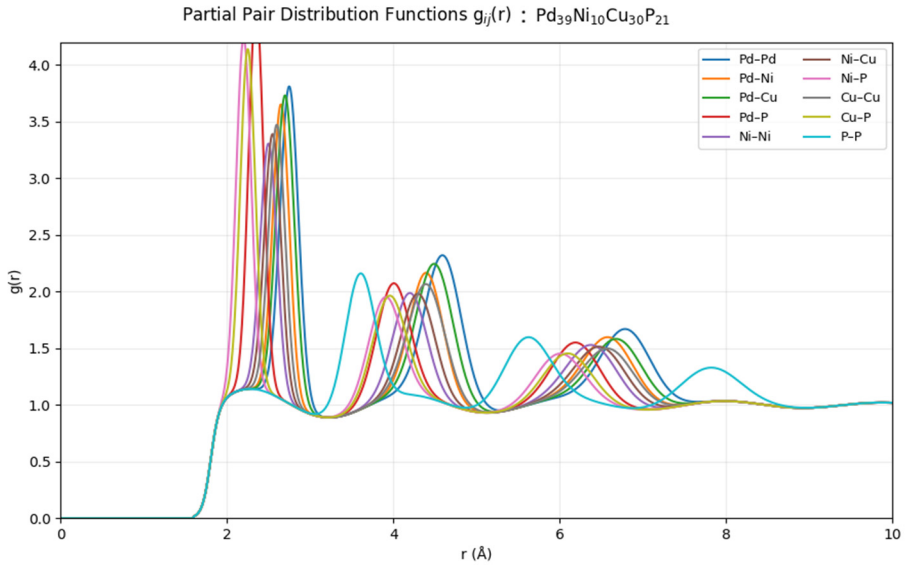

Figure 13. Partial pair distribution functions $g_{ij}(r)$ of $Pd_{39}Ni_{10}Cu_{30}P_{21}$ bulk metallic glass

At the other extreme are the partial pair distribution functions $g_{ij}(r)$ of the $Pd_{39}Ni_{10}Cu_{30}P_{21}$ bulk metallic glass, denoting the probability of obtaining an atomic pair (i–j) distance r apart. This confirms the amorphous nature of the alloy, demonstrated in the short-range order (SRO) and medium-range order (MRO) relationships in the lattice due to the absence of periodic repetition and fast decay of correlations beyond a few coordination shells. In the short-range region, the initial spike occurs between ~2.2 and ~2.6 Å, corresponding to atomic correlations near the neighbor. Heteroatomic bonds between transition metals and phosphorus were highest for their Pd–P and Cu–P pairs at an intersection between ~2.30 and ~2.35 Å. These short bond lengths and a large peak power ($g(r) \gtrsim 4.0$) indicate well-established short-range chemical order, which is fundamental to maintaining the amorphous structure and inhibiting crystallization. Pd–Pd, Pd–Cu, Pd–Ni, and Cu–Cu correlations exhibit first-neighbor peaks at distances of 2.6–2.8 Å, with values of 3.0–3.8.

These values express the large metallic compactness of transition-metal atoms, though weaker than metal–metalloid correlations. The relatively broad peaks, compared with those of Pd–P and Cu–P, also indicate topological disorder and a distribution of bond lengths characteristic of metallic glasses. The observations for the Ni–Ni and Ni–Cu pairs of correlations exhibit relatively lower peak intensities and broader distributions, indicating that Ni atoms are more evenly dispersed within the metallic lattices, rather than being grouped into strong clusters. Such behavior is compatible with a network modifier action of Ni, which synergistically increases atomic packing efficiency without facilitating crystallization.

Beyond the initial coordination shell, the second and third peaks occurring between ~3.8–5.0 Å and ~5.8–7.0 Å, respectively, show medium-range order resulting from atomic polyhedra connectivity. These peaks are markedly wider and weaker, demonstrating that, while local polyhedral motifs exist, their placement lacks long-range periodicity. The weak oscillations persist up to ~8 Å, implying polyhedral network connectivity, a key feature of stable bulk metallic glasses. At a larger range ($r > 8$ Å), all the $g_{ij}(r)$ curves approached $g(r) \approx 1$ gradually, indicating the loss of atomic correlation and the emergence of a random distribution of atomic information.

This evidence shows that structural ordering in $Pd_{39}Ni_{10}Cu_{30}P_{21}$ is restricted to short- and medium-range scales and absent long-range crystalline order. In conclusion, the data provided in Figure 13 demonstrates that the short-range structure of $Pd_{39}Ni_{10}Cu_{30}P_{21}$ is dominated by strong Pd–P and Cu–P chemical short-range order in the strongly coupled transition-metal structure with a highly compacted transition-metal framework. This strong heteroatomic bond, atomic packing efficiency, and polyhedral medium-range connectivity confer on the alloy excellent glass-forming ability, high mechanical strength, ductility, and thermal stability, providing a structural basis for the higher mechanical and multifunctional properties observed in the earlier analysis.

Angle Distribution Function:

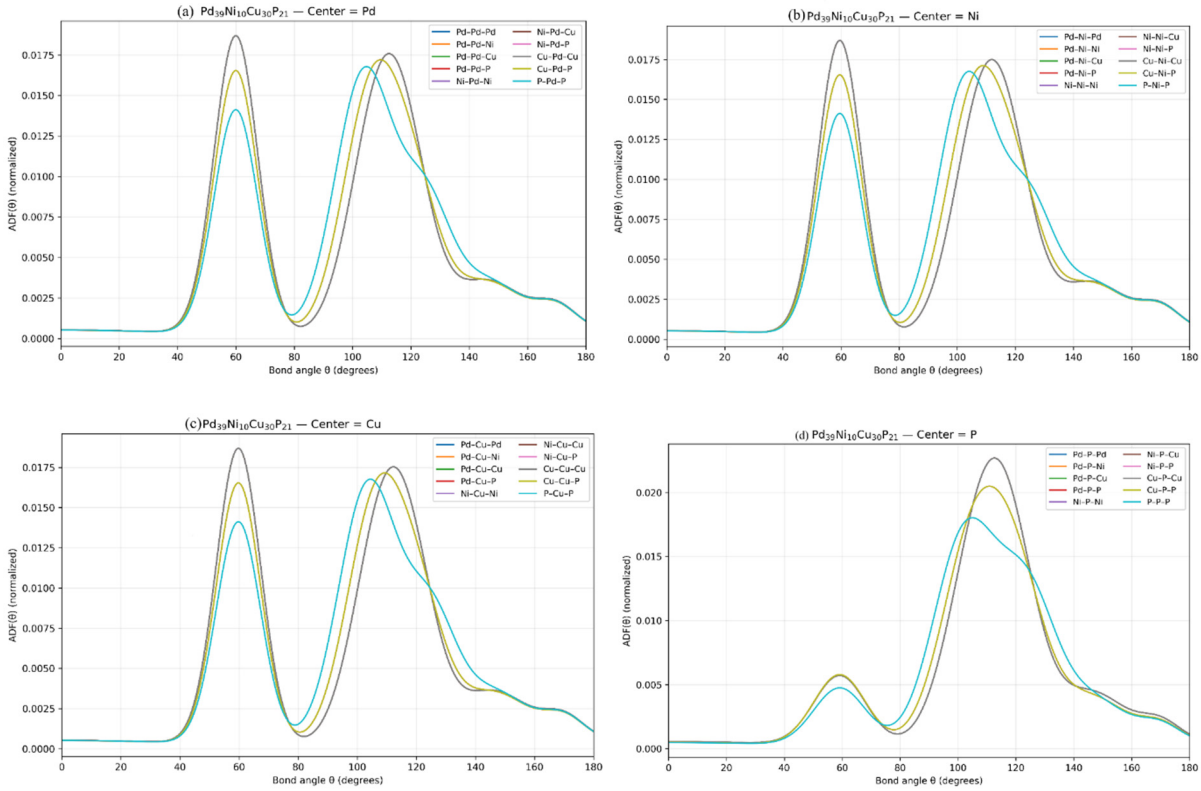

Figure 14. Angular distribution functions A(θ) for $Pd_{39}Ni_{10}Cu_{30}P_{21}$ bulk metallic glass with different central atoms, revealing dominant icosahedral-like bond-angle distributions around Pd, Ni, and Cu atoms and chemically constrained phosphorus-centered environments that stabilize the amorphous structure

The above-mentioned ADF (Figure 14) of the bulk metallic glass of the $Pd_{39}Ni_{10}Cu_{30}P_{21}$ is depicted and resolved based on the central atom type: (a) Pd-centered, (b) Ni-centered, (c) Cu-centered, and (d) P-centered local environments. The ADF describes the probability distribution of bond angles θ formed by atomic triplets (i–j–k). It provides direct insight into local coordination geometry, polyhedral motifs, and medium-range connectivity of the amorphous structure.

The Pd-oriented environment is depicted by panel (a), displaying two powerful angular spikes within its region. The initial major peak is at θ ≈ 55–60°, the second, broader one at θ ≈ 105–115°, with normalized intensities around 0.016–0.018. These bimodal angular distributions are consistent with distorted icosahedral or polyhedral coordination, where local pattern formation is fivefold-symmetric and yields relative angles near 60°. Conversely, distorted close-packed shapes produce angles approximately 110°. Since the peak position of Pd–Pd–Pd, Pd–Pd–Cu, and Pd–Pd–P triplets are strongly correlated, Pd atoms retain the core unit and act as moieties of chemically created polyhedra.

Both the region-defining peaks around ~60° and ~110°, and peak intensities (~0.015–0.018) of the panels (b) exhibit comparable angular features in relation to Ni-centered ADFs. Similar shapes may be the result for Ni atoms interacting to closely resemble Pd-centered polyhedra, with rather broader peaks, reflecting a higher angular distortion due to similar nature. This implies that Ni is a network modifier, meaning it modifies the locality without perturbing the atomic network, causing dense packing without crystallization of Ni atoms and contributes to structural stability.

The topological arrangements presented in panel (c) are in accordance with the peaks observed in Cu-centered environments: 55–60°, 110–115°, normalized intensities ~0.017–0.018. This preservation of angles in the Pd-, Ni-, and Cu-centered distributions indicates that the topological hierarchy is maintained with a uniformity dictated by the compact assemblage of metallic polyhedral units. A slightly larger contribution of Cu–Cu–Cu and Cu–Cu–P triplets at larger angles is observed, which is attributed to Cu promoting medium-range connectivity between neighboring polyhedral units.

The angular distributions for panel (d) related to P are markedly different from those of metal-centered cases. Here, the peak is strong (θ ≈ 100–115°), with the highest normalized peak magnitude ~0.020–0.022, while the low-angle peak (~60°) is much weaker (~0.004–0.006). This preference aligns with directional bonding of P atoms, providing more angular coordination environments of an open shape instead of closely packed metallic positions. This strong peak around 110° is typical of Pd–P–Pd, Cu–P–Cu, and mixed-metal–P–metal linkages and confirms that P is a stabilizing metalloid that exerts short-range chemical order, leading to the breaking of the crystalline symmetry. The strong angular region at around ~60° and ~110° with respect to the metal-centered ADFs along with a more directional ~110°-dominated P-centered region supports a likely structure consisting of icosahedral-like or distorted polyhedral short-range-ordered connections mediated by metalloid-centered linkages.

The peaks are all broad (rather than abrupt), indicating that the intrinsic disorder in the amorphous state lacks long-range periodicity. From a structural and material perspective, this is useful for accounting for certain important properties of $Pd_{39}Ni_{10}Cu_{30}P_{21}$, since dense polyhedral packing dominates its bulk and shear moduli, and angular flexibility, along with the function of P-centered coordination, drive plasticity and ductility induced by STZ. Moreover, these mixed angular characters and strong heteroatomic bonding result in superior glass-forming capability and thermal stability, so the bulk metallic glass can be used in load-bearing, high-pressure, and multifunctional structural applications that demand both strength and damage tolerance.

Glass-Forming Characteristics and Thermal Stability of $Pd_{39}Ni_{10}Cu_{30}P_{21}$ Metallic Glass:

Table 3. Characteristic glass-forming temperatures of $Pd_{39}Ni_{10}Cu_{30}P_{21}$ bulk metallic glass, highlighting its high glass transition temperature, wide supercooled liquid region, and excellent thermal stability

Alloy	Tg (K)	Tx (K)	Tl (K)
$Pd_{39}Ni_{10}Cu_{30}P_{21}$	558	632	775

The $Pd_{39}Ni_{10}Cu_{30}P_{21}$ bulk metallic glass shows glass-forming properties as summarized in Table 3, and its thermal stability and glass-forming capability are indirectly determined from the values for glass transition temperature (Tg), crystallization temperature (Tx), and liquidus temperature (Tl). It has been shown that the glass transition temperature Tg = 558 K corresponds to the temperature of the amorphous solid until it changes to a supercooled liquid. This relatively high Tg further confirms the strong interatomic bonding and atomic confinement of the material and is consistent with pronounced short-range order in Pd–P and Cu–P. Furthermore, a high Tg at high temperatures is generally associated with higher thermal resistance and greater dimensional stability, and thus is compatible with structural integrity applications beyond room temperature in an alloy.

Therefore, the crystallization temperature of Tx = 632 K indicates the onset of devitrification from the supercooled liquid to the crystalline phase. It is the difference between Tx and Tg, indicating the width of the supercooled liquid region at $\Delta Tx = 74$ K, which suggests good glass-forming characteristics and superior crystallization resistance, enabling stable thermoplastic formation and processing and avoiding premature crystallization. The liquidus temperature of Tl = 775 K corresponds to the liquidus of the entire molten alloy. The ratio ($Tg/Tl \approx 0.72$) for bulk metallic glasses is comparatively high, indicating good thermodynamic stability of the amorphous phase over a large temperature range and a decreased driving force for crystallization.

Finally, the high Tg (558 K), large supercooled liquid region ($\Delta Tx = 74$ K), and high Tg/Tl (0.72) confirm that the alloy $Pd_{39}Ni_{10}Cu_{30}P_{21}$, at last, can exhibit adequate thermal stability and superior glass-forming ability. Due to this ability, it can be used for high-temperature structural parts, the production of metallic-glass thermoplastic parts, precision devices, and long-term service applications that require resistance to crystallization and thermal degradation.

CONCLUSIONS

Here we present a full first-principles characterization of the $Pd_{39}Ni_{10}Cu_{30}P_{21}$ bulk metallic glass, illustrating how its amorphous atomic structure influences its mechanical, thermal, electronic, and optical properties. Its dense random packing and clear short-range chemical configuration, coupled together with predominantly Pd–P and Cu–P bonding, contribute to stabilizing the glassy phase and suppressing crystallization. The elastic constants, large bulk modulus, and Pugh's ratio yield the assessment of the highly ductile character of this alloy, in which plastic deformation is controlled by shear transformation zones, not dislocation activity.

Thermophysical properties of combined mechanical and thermal loading can be investigated in a solid anharmonic lattice with a moderate Debye temperature and stable thermal expansion. In practical terms, the previously proposed high strength, pressure resistance, optical isotropy, and broadband electromagnetic absorption in $Pd_{39}Ni_{10}Cu_{30}P_{21}$ can be an effective source for developing new materials in advanced structures, vibration-damping systems, reflective–absorptive coatings, electromagnetic interference protection, photothermal devices, and corrosion resistance in harsh environments.

Its near-metallic electronic structure and high optical losses are particularly beneficial in multifunctional applications. One of the contributions of this work is a unified ab initio framework that integrates amorphous structural motifs, equation-of-state parameters, elastic response, lattice behavior, and optical properties in a self-consistent, self-evident macroscopic physical image. While single-characteristic properties have been the dominant paradigm in previous studies, our work demonstrates that electronic hybridization, pseudogap formation, and polyhedral short-range order together influence macroscopic performance.

In other words, it can be concluded that from the large Tg (558 K), large supercooled liquid region ($\Delta Tx = 74$ K) and the high Tg/Tl, or Tg/Tl, value (0.72), that the alloy $Pd_{39}Ni_{10}Cu_{30}P_{21}$ is finally able to attain the reasonable thermal stability and high glass formation. The characteristics have been observed in its applications in high-temperature structural parts, the production of metallic-glass thermoplastic parts, precision devices, and long-term service applications.

Ethical Approval:
The authors confirm that it is their original work and has not been submitted elsewhere or published.
Competing interests:
All authors have no competing interests.

Author Contribution:
Dr. Amit Kumar Chaubey, Dr. Sangeeta Gupta, Dr. Sarita Chaudhary, and Dr. Kapil Bhardwaj made the original draft of the manuscript under the supervision of Dr. Abhay P. Srivastava.

Funding:
This study did not receive any funding from any organization.

Availability of data and Materials:
Data made available at request.

ORCID

Sangita Gupta, https://orcid.org/0009-0009-3751-8317; **Abhay P. Srivastava,** https://orcid.org/0009-0005-9648-0479

REFERENCES

[1] C.P. dos Santos, C.H.P. Silva, M.F. da Silva Santos, É.R.P. de Novais, D. dos Nascimento Souza, M.V. dos Santos Rezende, A. de Lima Ferreira Novais, "DFT to study the structural, optoelectronic, and mechanical properties of CuNiPd and Cu2PPd2 alloys," Journal of Alloys and Compounds, **1038**, 182830 (2025). https://doi.org/10.1016/j.jallcom.2025.182830
[2] S. Evertz, D. Music, V. Schnabel, J. Bednarcik, and J.M. Schneider, "Thermal expansion of Pd-based metallic glasses by ab initio methods and high-energy X-ray diffraction," Sci. Rep. **7**, 15744 (2017). https://doi.org/10.1038/s41598-017-16117-7
[3] Y. He, and R.B. Schwarz, "Synthesis and Properties of Bulk Metallic Glasses in Pd-Ni-P and Pd-Cu-P Alloys," MRS Online Proceedings Library, **455**, 495–500 (1996). https://doi.org/10.1557/PROC-455-495
[4] P. Gong, L. Deng, J. Jin, S. Wang, X. Wang, and K. Yao, "Review on the Research and Development of Ti-Based Bulk Metallic Glasses," Metals, **6**, 264 (2016). https://doi.org/10.3390/met6110264
[5] L.Y. Watanabe, S.N. Roberts, N. Baca, A. Wiest, S.J. Garrett, and R.D. Conner, "Fatigue and corrosion of a Pd-based bulk metallic glass in various environments," Materials Science and Engineering: C, **33**(7), 4021-4025 (2013). https://doi.org/10.1016/j.msec.2013.05.044
[6] A. Sharma, and V. Zadorozhnyy, "Review of the Recent Development in Metallic Glass and Its Composites," Metals, **11**, 1933 (2021). https://doi.org/10.3390/met11121933
[7] H. Kato, T. Wada, M. Hasegawa, J. Saida, A. Inoue, and H.S. Chen, "Fragility and thermal stability of Pt- and Pd-based bulk glass forming liquids and their correlation with deformability," Scripta Materialia, **54**(12), 2023-2027 (2006). https://doi.org/10.1016/j.scriptamat.2006.03.025
[8] F.M. Alamgir, H. Jain, R.B. Schwarz, O. Jin, and D.B. Williams, "Electronic structure of Pd-based bulk metallic glasses, Journal of Non-Crystalline Solids," **274**(1–3), 289-293 (2000). https://doi.org/10.1016/S0022-3093(00)00192-7
[9] T.R. Kotni, M.K. Sampath, M.M. Seepana, and A.K. Arya, "A Review on Corrosion Characteristics of Bulk Metallic Glasses," J. of Mater. Eng. and Perform. (2026). https://doi.org/10.1007/s11665-025-13123-z
[10] M. Chen, "A brief overview of bulk metallic glasses," NPG Asia Mater. **3**, 82–90 (2011). https://doi.org/10.1038/asiamat.2011.30
[11] A.P. Srivastava, B.K. Pandey, and S. Mishra, "Multifunctional response of $SrZrO_3$ under extreme compression: structural, phonon, optical, and thermoelectric insights," Chem. Pap. (2026). https://doi.org/10.1007/s11696-026-05410-3
[12] M. Telford, "The case for bulk metallic glass," Materials Today, **7**(3), 36-43 (2004). https://doi.org/10.1016/S1369-7021(04)00124-5
[13] Y.L.S. Zhao, Y. Liu, P. Gong, and J. Schroers, "How Many Bulk Metallic Glasses Are There?" CS Comb. Sci. **19**(11), 687–693 (2017). https://doi.org/10.1021/acscombsci.7b00048
[14] F.-F. Wu, K.C. Chan, S.-S. Jiang, S.-H. Chen, and G. Wang, "Bulk metallic glass composite with good tensile ductility, high strength, and large elastic strain limit," Sci. Rep. **4**, 5302 (2014). https://doi.org/10.1038/srep05302
[15] H.X. Li, Z.C. Lu, S.L. Wang, Y. Wu, and Z.P. Lu, "Fe-based bulk metallic glasses: Glass formation, fabrication, properties and applications," Progress in Materials Science, **103**, 235-318 (2019). https://doi.org/10.1016/j.pmatsci.2019.01.003
[16] A. Inoue, B. Shen, and N. Nishiyama, "Development and Applications of Late Transition Metal Bulk Metallic Glasses," in: *Bulk Metallic Glasses*, edited by M. Miller, and P. Liaw, (Springer, Boston, MA, 2008), pp. 1-25. https://doi.org/10.1007/978-0-387-48921-6_1
[17] R.S. Aga, and J.R. Morris, "Modeling: The Role of Atomistic Simulations," in: *Bulk Metallic Glasses*, edited by M. Miller, and P. Liaw, (Springer, Boston, MA, 2008). https://doi.org/10.1007/978-0-387-48921-6_3
[18] A.P. Srivastava, B.K. Pandey, and A. Shanker, "Pressure-Dependent Structural, Mechanical, and Thermal Behavior of $Zr_{50.5}Ti_{4.8}Cu_{19.0}Ni_{11.4}Al_{14.3}$ Bulk Metallic Glass: A DFT and Equation of State Study," Physical Chemistry Research, **14**(1), 71-85 (2026). https://doi.org/10.22036/pcr. 2025.552725.2766
[19] S.-J. Sun, S.-P. Ju, C.-C. Yang, K.-C. Chang, and I.-J. Lee, "Effects of Strontium incorporation into Mg-Zn-Ca biodegradable bulk metallic glass investigated by molecular dynamics simulation and density functional theory calculation," Sci. Rep. **10**, 2515 (2020). https://doi.org/10.1038/s41598-020-58789-8
[20] G.R.A. Kumar, K. Arora, M. Aggarwal, S. Swayamjyoti, P.P. Singh, K.K. Sahu, and R. Ranganathan, "Structure–property predictions in metallic glasses: Insights from data-driven atomistic simulations," Journal of Materials Research, **40**, 36–68 (2025). https://doi.org/10.1557/s43578-024-01480-9
[21] V. Sahni, "The Hohenberg-Kohn Theorems and Kohn-Sham Density Functional Theory," in: *Quantal Density Functional Theory*, (Springer, Berlin, Heidelberg, 2004). https://doi.org/10.1007/978-3-662-09624-6_4
[22] A.P. Srivastava and B.K. Pandey, "DFT-driven optical design of amorphous $Al_{74}Ni_4Y_2Cu_{20}$ for reflective and transparent coating applications," Optik, **352**, 172793 (2026). https://doi.org/10.1016/j.ijleo.2026.172793
[23] A.P. Srivastava, P. Sharma, B.K. Pandey, and A. Mishra, "Multifunctional Properties of $BaTiO_3$ Across the Cubic–Tetragonal Phase Transition: Implications for Ferroelectric and Electronic Applications," J. Inorg. Organomet. Polym. (2026). https://doi.org/10.1007/s10904-026-04390-x
[24] J.P. Perdew, K. Burke, and M. Ernzerhof, "Generalized Gradient Approximation Made Simple," Phys. Rev. Lett. **78**, 1396 (1997). https://doi.org/10.1103/PhysRevLett.77.3865

[25] G. Kresse, & J. Furthmüller, "Efficient iterative schemes for *ab initio* total-energy calculations using a plane-wave basis set," Physical Review B, **54**(16), 11169–11186 (1996). https://doi.org/10.1103/PhysRevB.54.11169
[26] M.A. Blanco, E. Francisco, & V. Luana, "GIBBS: isothermal-isobaric thermodynamics of solids from energy curves using a quasi-harmonic Debye model," Computer Physics Communications, **158**(1), 57–72 (2004). https://doi.org/10.1016/j.cpc.2003.10.003
[27] Srivastava, A.P., Pandey, B.K., Gupta, A.K. *et al.* A New Approach to Evaluate Pressure of Solids at High Compression. *Natl. Acad. Sci. Lett.* **47**, 713–718 (2024). https://doi.org/10.1007/s40009-024-01409-0
[28] S. Gupta, A.P. Srivastava, and B.K. Pandey, "Lanthanum-induced electronic transition in hydride perovskites: A first-principles study of $CsXH_3$ (X = Sc, Y, La, Ac)," International Journal of Biology and Chemistry, **19**(1) (2026). https://doi.org/10.26577/IJBCh202619115
[29] A.P. Srivastava, B.K. Pandey, "DFT-based evaluation of covalent organic frameworks for adsorption, optoelectronic, clean energy storage, and gas sensor applications," J. Mol. Model. **31**, 302 (2025). https://doi.org/10.1007/s00894-025-06535-0
[30] C. Feng, C. Wei, B.-L. Fang, and H.-Y. Fan, "A Deduction of the Hellmann-Feynman Theorem," Int. J. Theor. Phys. **59**, 1396-1401 (2020). https://doi.org/10.1007/s10773-019-04362-7
[31] K.F. Shamlaye and J.F. Löffler, "Synthesis and characterization of Mg-based bulk metallic glasses in the Mg–Ag–Y–(Cu) system," Journal of Alloys and Compounds, **859**, 157803 (2021). https://doi.org/10.1016/j.jallcom.2020.157803
[32] A.P. Srivastava, B.K. Pandey, and A.K. Gupta, "Explore the fascinating realm of comparing metal melting curves by applying the equation of state and Lindemann's law," Computational Condensed Matter, **40**(e00952), 2352-2143 (2024). https://doi.org/10.1016/j.cocom.2024.e00952
[33] A.P. Srivastava, B.K. Pandey, A.K. Gupta, *et al.* "Comparing Melting Curves of Metals Using the Equation of State and Lindemann's Law," Iran. J. Sci. (2024). https://doi.org/10.1007/s40995-024-01748-z
[34] A.P. Srivastava and B.K. Pandey, "A constructive approach to formulating pressure-dependent binding energy using the equation of state," Ionics (2025). https://doi.org/10.1007/s11581-025-06183-7
[35] A.P. Srivastava, B.K. Pandey, & M. Upadhyay, "Anticipating Pressure Changes in Halides under Compression," East European Journal of Physics, (3), 333-339 (2024). https://doi.org/10.26565/2312-4334-2024-3-37
[36] L.-J. Huang, J.-G. Tang, G.Y. Liang, Y. Wang, and D.C. Wu, "Microstructural investigation and electrochemical properties of Mg63Ni27Nd10 amorphous alloy," Journal of Power Sources, **189**(2), 1247-1250 (2009). https://doi.org/10.1016/j.jpowsour.2008.12.001
[37] F. Sun, G. Zhang, X. Ren, M. Wang, H. Xu, Y. Fu, Y. Tang, and D. Li, "First-principles studies on phase stability, anisotropic elastic and electronic properties of Al-La binary system intermetallic compounds," Materials Today Communications, **24**, 101101 (2020). https://doi.org/10.1016/j.mtcomm.2020.101101
[38] A.P. Srivastava and B.K. Pandey, "First-principles and equation of state investigation of pressure-tunable structural, mechanical, thermodynamic, and electronic properties of high-reflecting nano-metal oxides: insights into high-performance optoelectronic and energy applications," Appl. Nanosci. **15**, 47 (2025). https://doi.org/10.1007/s13204-025-03124-8
[39] A.P. Srivastava and B.K. Pandey, "A Computational Study of Pressure-Induced Melting in $LaFeO_3$: Using DFT and Semi-Empirical Model," Physical Chemistry Research, **14**(1), 1-7 (2026). https://doi.org/10.22036/pcr.2025.537079.2712
[40] D.G. Dadi, M.W. Shura, & F. Gochole, "DFT analysis of structural, electronic, and optical properties of Ni- and Zn-doped CoS counter electrode for dye-sensitized solar cells," Sci. Rep. **15**, 35486 (2025). https://doi.org/10.1038/s41598-025-19663-7
[41] D. Maurya, B.K. Pandey, & A.P. Srivastava, "Mechanically robust and optically active $Mg_{80}Ni_{10}Nd_{10}$ metallic glass: first-principles evidence for next-generation optical coatings," Opt. Quant. Electron. **58**, 28 (2026). https://doi.org/10.1007/s11082-025-08615-0
[42] A.P. Srivastava, B.K. Pandey, "Ab initio design of Zr-based bulk metallic glass for high-strength and optical coating applications," Opt. Quant. Electron. **57**, 561 (2025). https://doi.org/10.1007/s11082-025-08467-8
[43] S. Horsley, M. Artoni, & G. La Rocca, "Spatial Kramers–Kronig relations and the reflection of waves," Nature Photon. **9**, 436-439 (2015). https://doi.org/10.1038/nphoton.2015.106
[44] S. Mathi, H. Akhdar, R.S. Shetti, T. Alinad, A.N. Alodhayb, K. Mondal, and N.P. Shetti, "Amorphous electrocatalysts for oxygen and hydrogen evolution reactions: Advances in hydrogen production," Materials Today Sustainability, **32**, 101223 (2025). https://doi.org/10.1016/j.mtsust.2025.101223
[45] A. Abbas, S. Tariq, H.J. Alathlawi, F.A. Makin, A. Al Bahir, M.M. Saad H.-E., "High-pressure computational analysis of $CsCdF_3$: Structural stability, electronic transitions, and thermodynamic properties," Physics Letters A, **541**, 130429 (2025). https://doi.org/10.1016/j.physleta.2025.130429
[46] H.W. Sheng, W.K. Luo, F.M. Alamgir, J.M. Bai, and E. Ma, "Atomic packing and short-to-medium-range order in metallic glasses," Nature, **439**, 419–425 (2006). https://doi.org/10.1038/nature04421
[47] A. Inoue, "Stabilization of metallic supercooled liquid and bulk amorphous alloys," Acta Materialia, **48**(1), 279-306 (2000). https://doi.org/10.1016/S1359-6454(99)00300-6
[48] A.K. Pandey, B.K. Pandey, and Rahul, "Theoretical prediction of Grüneisen parameter for bulk metallic glasses," Journal of Alloys and Compounds, **509**(11), 4191-4197 (2011). https://doi.org/10.1016/j.jallcom.2010.11.120
[49] K.M. Knowles, "Necessary and Sufficient Elastic Stability Conditions for Single Crystals," J. Elast. **157**, 19 (2025). https://doi.org/10.1007/s10659-025-10112-0
[50] M.H. Dalsaniya, D. Upadhyay, P. Patel, P.K. Jha, K.J. Kurzydłowski, and D. Kurzydłowski, "Pressure-Dependent Thermal and Mechanical Behavior of a Molecular Crystal of Bromine," Molecules, **29**(19), 4744 (2024). https://doi.org/10.3390/molecules29194744
[51] Y. Yamada, and Y. Kanemitsu, "Electron-phonon interactions in halide perovskites," NPG Asia Mater. **14**, 48 (2022). https://doi.org/10.1038/s41427-022-00394-4
[52] J. Mara, A.-E. Bodnár, L. Trif, and J. Telegdi, "Development of Effective Infrared Reflective Coatings," Appl. Sci. **13**(23), 12903 (2023). https://doi.org/10.3390/app132312903
[53] N. Mattern, M. Stoica, G. Vaughan, and J. Eckert, "Thermal behavior of $Pd_{40}Cu_{30}Ni_{10}P_{20}$ bulk metallic glass," Acta Materialia, **60**(2), 517-524 (2012). https://doi.org/10.1016/j.actamat.2011.10.032

БАГАТОФУНКЦІОНАЛЬНЕ МЕТАЛЕВЕ СКЛО: ПОЧАТКОВЕ ДОСЛІДЖЕННЯ $Pd_{39}Ni_{10}Cu_{30}P_{21}$ ДЛЯ ПІДВИЩЕННЯ МЕХАНІЧНОЇ МІЦНОСТІ ТА ОПТИЧНОГО ЕКРАНУВАННЯ

Сангіта Гупта[1], Аміт Кумар Чаубі[2], Саріта Чаудхарі[3], Капіл Бхардвадж[4], Абхай П. Шрівастава[5]

[1]Кафедра хімії, Університет Пурніма, Джайпур, Раджастан, Індія

[2]Кафедра прикладних наук та гуманітарних наук, Об'єднаний коледж інженерії та досліджень, Праяградж, (UP), Індія

[3]Кафедра хімії, Глобальний університет Вівекананда, Джайпур, Раджастан, Індія

[4]Кафедра комп'ютерних наук та інженерії, Університет Чандігарха, Мохалі, Пенджаб, Індія

[5]Кафедра прикладних наук та гуманітарних наук, Бансалський інститут інженерії та технологій, Лакхнау (UP), Індія

Об'ємні металеві стекла (BMG) – це тип твердого матеріалу з аморфними атомними структурами, що демонструють сприятливі механічні, теплові та функціональні властивості. У цьому дослідженні представлені властивості скла, що вивчають першопринципні деталі структури об'ємного металевого скла $Pd_{39}Ni_{10}Cu_{30}P_{21}$, його пружні властивості, термодинаміку та електронно-оптичні характеристики. Розрахунки теорії функціоналу густини були проведені для порівняння з аморфною атомною конфігурацією та співвідношенням енергія-об'єм за допомогою рівняння стану Бірча-Мурнагана третього порядку. Дуже високий об'ємний модуль пружності, приблизно 159 ГПа, та >6 похідних тиску продемонстрували однорідність, опір та сильне зміцнення під тиском. Всі три модулі пружності, коефіцієнт Пуассона та критерій П'ю постійно демонструють пластичну механічну реакцію, залежну від пластичності, опосередкованої зоною перетворення зсуву. Результати теплофізичного дослідження показують стабільну ангармонічну поведінку решітки, температуру Дебая приблизно 395 К та сприятливе теплове розширення, що вказує на добру передбачуваність термомеханічної реакції. Електронні дослідження виявили дуже металеву фазу з низькою псевдощілиною навколо рівня Фермі — головним чином гібридизацію між d-станами перехідних металів та p-станами фосфору у стабільну аморфну фазу. Оптичні спектри, що містять широку смугу, чудову відбивну здатність при низьких енергіях фотонів та ізотропну оптичну реакцію, типові для металевих стекол. На завершення, ці результати доводять, що $Pd_{39}Ni_{10}Cu_{30}P_{21}$ є високомеханічно стабільним матеріалом для розвитку в різних механічних, оптичних та енергетичних застосуваннях у легкій рамці.

Ключові слова: *об'ємне металеве скло; теорія функціоналу густини; рівняння стану; механічні та теплофізичні властивості; електронна структура; оптичні екрануючі матеріали*

EAST EUROPEAN JOURNAL OF PHYSICS. 3. 347-356 (2026)
DOI:10.26565/2312-4334-2026-3-30 ISSN 2312-4334

EFFECT OF PRESSURE ON THE ENERGY BAND STRUCTURE OF AlAs USING sp3s* MODEL

Ali A. Mohammed[1]*, Mumtaz M.S. Hussien[2], Abbas Hussein Rostam[3]*****
[1]*Department of Physics, College of Education for Pure Sciences, University of Mosul, Mosul, Iraq*
[2]*College of Health and Medical Techniques, Al-noor University, Mosul, Iraq*
[3]*Department of General Science, College of Basic Education, Salahaddin University, Erbil, Kurdistan region, Iraq*
email: mumtaz_hussien@alnoor.edu.iq;*abbas.rostam@su.edu.krd*
**Corresponding Author email: dr.ali1969@uomosul.edu.iq*
Received April 4, 2026; revised June 22, 2026; accepted June 30, 2026

We used the sp3s* tight-bonding method as a computational approach to calculate the energy band structure of AlAs crystals in the absence of pressure and analyzed the effect of pressure on the energy band structure under low pressure (1-7) GPa. We used two forms of the Birch-Maugham equation of state (third- and fourth-order) to calculate the changes in the elements of the Hamiltonian matrix resulting from changes in crystal volume and lattice constant. The dispersion relationships for the high-symmetry directions in the first Brillouin zone were found by numerically calculating the Hamiltonian diagonal under pressure. The present computations are performed using a routine written in MATLAB. We found that the effects of both forms of the equation of state on the band structure differ only slightly (by 0.01) at low pressure, as shown in the band structure diagrams. The conduction-band valleys creep downward under low pressure, decreasing both the direct and indirect energy gaps. The results obtained were consistent with other experimental and theoretical results.
Keywords: *Tight-bonding model; Maugham equation of state; AlAs compound semiconductor; Band structure; High pressure*

1. INTRODUCTION

Due to their great technological and industrial significance in the electronic applications and optoelectronic devices, III-V zinc-blende compound semiconductors have been widely regarded as the most promising compound semiconductors over the past few decades [1]. The study of materials at high pressures is currently experiencing great activity. The application of high pressure frequently leads to considerable shifts in both the chemical and physical properties of substances. Consequently, materials frequently exhibit previously unseen crystalline structures and intriguing behaviors when subjected to these conditions. Also, the possibility to study structural stability as a function of volume has added a fresh dimension to the basic question regarding the relation between the arrangement of atoms and electronic structure [2]. Particularly, Aluminum Arsenide (AlAs) is a binary compound that has an indirect band gap with the conduction band minimum at the X-point and the valence band maximum at the Γ-point under surrounding conditions. AlAs has an experimental band gap of about 2.16 eV [3]. The most stable phase for AlAs is the tetrahedral structure, a bonded semiconducting phase at ambient pressure, which has excellent physical properties, making it suitable for device applications such as optical fibers in telecommunication, Bragg reflector superlattices, heterojunction bipolar transistors, solid-state lasers, high electron mobility transistors, and light-emitting diodes [2], [3]. When moderate pressure is applied, like many other semiconductors, AlAs transforms into the metallic phase [4] [5]. Theoretical investigations and experimental research are therefore of vital interest to all those working in this area. In recent years, an increasing number of researchers have conducted experimental studies on the phase transition in AlAs. The first report of the phase transition of AlAs was made by Froyen and Cohen in 1983, who studied structural properties in AlAs using an ab initio pseudopotential approach and suggested that the case of high-pressure structure of AlAs commonly undergoes a structural transition, which could either be rock salt (B1) structure or NiAs (B8) structure [6]. Weinstein et al. observed a phase change by microscopic analysis at 12.3 GPa on loading; however, the structure was unidentified[7]. In subsequent years, an increasing number of researchers turned to experimental studies of the phase transition in AlAs. The first experimental observation of the transformation of AlAs into the NiAs structure came several years later, when G. Greene Raymond et al. indexed a new phase of AlAs using energy-dispersive X-ray diffraction to 46 GPa [8]. Mujica et al. offered a detailed review of the current known structures, high-pressure behavior, and theoretical work on the group III–V compound semiconductor materials [9]. Besides the experimental advance, dependable computational techniques designed for the determination of electronic band structures, as well as overall energy calculations, have significantly influenced the field of high-pressure physics [10], [11], [12]. These computational approaches yield critical supplemental data to that obtained through experimental investigation. This progress rises from both the development of amended algorithms and the increasing availability of powerful computing resources. Such theoretical work plays a supporting role to experimental research by both validating discovered structures and examining their electronic and vibrational features, as well as assisting in forecasting the shape of new materials.

This research aims to focus on theoretical calculations of the band structure and the effect of pressure on electronic properties, such as the band gap. Electronic property calculations are based on Harrison's model of semiconductors by

Cite as: A.A. Mohammed, M.M.S. Hussien, A.H. Rostam, East Eur. J. Phys. 3, 347 (2026), https://doi.org/10.26565/2312-4334-2026-3-30

constructing a nearest-neighbor semi-empirical tight-binding theory (TB). The effect of pressure at (1,3,5,7) GPa on the band gap energy of AlAs is investigated. The dependence of the energy states, over several symmetry directions and at certain symmetry points, on the interaction parameters is also investigated.

2. THEORETICAL BACKGROUND

2.1. Tight Binding Method

Electronic band structure is the energy range in which an electron is either forbidden or allowed to exist, and it's one of the important key to understanding electron conduct in crystalline semiconductors and their interactions with lattice vibrations[13]. One of the appealing method to calculate the electronic band structure of electron motion in solids is the tight binding theory (TB), which is called also linear combination of atomic orbitals (LCAO) proposed by Bloch [14]. The tight binding model is the standard technique for resolving issues related to periodic potentials. It entails constructing a linear combination of atomic orbitals $\phi_n(r-\vec{R}_i)$ on the various crystal atoms, with the coefficient given by the values of the plane wave $exp(i\vec{k}.\vec{R}_i)$ at the distinct vector positions $\vec{R}$,where the atoms are located, to form Bloch sum $\sum \vec{R}\, e^{(i\vec{k}.\vec{R}_i)}\phi_n(r-\vec{R}_i)$. The sum run over the atoms in equivalent position in all unit cells of the crystal, the subscript n denotes to quantum numbers [15]. In present work, the nearest neighbor sp^3s^* empirical tight binding method with fitted input parameters from the literature is used to calculate the band structure and energy gaps of the bulk compound semiconductor AlAs at some high symmetry points by preparing a computational program using MATLAB. The tight-binding model yields a detailed real space description of the electronic interactions that give rise specific elements of the energy band structure and density of states. This is very useful in research, where the electronic structure is modified and can see how these features convert when you change the electronic.

Although the tight-binding method is systematically inviting, it poses a major issue: the fundamental parameters that define the tight-binding Hamiltonian are not the conduction-band edges and effective masses typically employed in electronic-device modeling, but rather orbital interaction energies. The coupling of the separated orbitals via these interaction energies leads to the formation of electronic bands. A correct choice of the type and number of basic orbitals (s, p, and d) and of their local and non-local coupling strengths yields a suitable representation of material characteristics such as band energy structures and effective masses. Consequently, the overall band structure and effective masses are strongly linked to the interaction energies[16].

2.2. Calculation of Energy Band Structure

Quantum mechanics provides the only viable path for resolving numerous issues in physics and chemistry. In the case of zinc- blende crystals the, tight-binding Hamiltonian can be constructed in a basis of quasi-atomic functions as [17], [18]:

$$\left|n\lambda\vec{k}\right\rangle = \frac{1}{\sqrt{N}}\sum_{i,\lambda} \mathrm{e}^{(i\vec{k}.\vec{R}_i + i\vec{k}.\vec{v}_\lambda)}\left|n\lambda\vec{R}_i\right\rangle, \tag{1}$$

where $\vec{R}_i$ is the vector position of the atom on which the orbital is located, the quantum numbers (band index n) pass the s, p_x, p_y, p_z, and s^* orbitals; the number of unit cells in the repeating region is N where the wave vectors ($\vec{k} = 2\pi/a_l$) lie in the first Brillouin zone. The base atom displacement is indicated $\vec{v}_\lambda$ and in terms of Kronecker δ, we have $\vec{v}_\lambda = \delta_\lambda(a_l/2)(1,1,1)$; and λ =a (anion) or λ = c (cation) represents site index and the lattice constant represented by a_l.

In Bloch functions built from s and p orbitals (Wannier functions) located on each atom in the crystal, one assumes that the only non-zero Hamiltonian matrix elements are those between orbitals on the same or neighboring atoms [19]. This results in a relatively good description of the valence bands throughout the Brillouin zone. The sp^3s^* tight-binding method without spin-orbit coupling introduced by Vogl et al. (1983), which considers only nearest-neighbour interactions, uses Löwdin orbitals: an s-state and three p-states together with an excited s* state for each basis atom in pure bulk covalent semiconductors, providing ten orbitals for a primitive cell that contains two atoms.

The band structure for a nearest-neighbor, sp^3, eight- band model, is described by the nine parameters: four diagonal energies $E_{sa} = \langle sa\vec{R}|H|sa\vec{R}\rangle$, $E_{sc} = \langle sc\vec{R}|H|sc\vec{R}\rangle$, $E_{pa} = \langle p_x a\vec{R}|H|p_x a\vec{R}\rangle$ $E_{pc} = \langle p_x c\vec{R}|H|p_x c\vec{R}\rangle$ and the five transfer matrix elements V, $V_{ss} = 4\langle sa\vec{R}|H|sc\vec{R}\rangle$, $V_{xx} = 4\langle p_x a\vec{R}|H|p_x c\vec{R}\rangle$, $V_{xy} = 4\langle p_x a\vec{R}|H|p_y c\vec{R}\rangle$ $V_{sapc} = 4\langle sa\vec{R}|H|p_x c\vec{R}\rangle$ and $V_{pasc} = 4\langle p_x a\vec{R}|H|sc\vec{R}\rangle$.

In ten-band sp^3s^* model, besides these nine parameters, we add another an excited s state, s*, and allowing coupling only to the p states of neighbors, while excluding, for simplicity, the linkage to s-states on distant sites. This addition brings four additional matrix elements: specifically, two of these being new diagonal energies $E_{s^*a} = \langle s^* a\vec{R}|H|s^* a\vec{R}\rangle$, $E_{s^*c} = \langle s^* c\vec{R}|H|s^* c\vec{R}\rangle$, and the latter two being transfer matrix elements $V_{s^*apc} = 4\langle s^* a\vec{R}|H|p_x c\vec{R}\rangle$, $V_{pas^*c} = 4\langle p_x a\vec{R}|H|s^* c\vec{R}\rangle$. The following matrix elements which are being omitted for clarity, have been set to zero,: $\langle s^* a\vec{R}|H|s^* c\vec{R}\rangle$, $\langle s^* a\vec{R}|H|s\, c\vec{R}\rangle$and $\langle sa\vec{R}|H|s^* c\vec{R}\rangle$ [20].

By employing thirteen fitted input interaction parameters, derived from the theoretical data of Vogl's which are required to calculate the energy-band structure. These interaction parameters are essentially independent matrix elements, made up of: six on - site energies E_{sa} , E_{pa}, E_{sc} , E_{pc} , E_{s^*a} and E_{s^*c} (a, c refer to anion and cation

respectively) and seven hopping terms refer to V_{ss}, V_{xx}, V_{xy}, V_{sapc}, V_{pasc} , V_{s^*apc} and V_{pas^*c}. These matrix elements still need to be determined and fit for the band structure data; they can be provided in the Löwdin form of the symmetrically orthogonalized atomic orbitals. The input parameters representing the empirical matrix elements of the sp3s* tight binding model used to calculate band structure of the compound semiconductor AlAs are shown in Table (1).

For a zinc blende structure of lattice constant a, the wave vector (k) dependence in this tight binding model is given by defining the g_i coefficients [17],

$$\left.\begin{aligned} g_0(k) &= +cos\left(a_l\frac{k_1}{4}\right)cos\left(a_l\frac{k_2}{4}\right)cos\left(a_l\frac{k_3}{4}\right) - isin\left(a_l\frac{k_1}{4}\right)sin\left(a_l\frac{k_2}{4}\right)sin\left(a_l\frac{k_3}{4}\right) \\ g_1(k) &= -cos\left(a_l\frac{k_1}{4}\right)sin\left(a_l\frac{k_2}{4}\right)sin\left(a_l\frac{k_3}{4}\right) + isin\left(a_l\frac{k_1}{4}\right)cos\left(a_l\frac{k_2}{4}\right)cos\left(a_l\frac{k_3}{4}\right) \\ g_2(k) &= -sin\left(a_l\frac{k_1}{4}\right)cos\left(a_l\frac{k_2}{4}\right)sin\left(a_l\frac{k_3}{4}\right) + icos\left(a_l\frac{k_1}{4}\right)sin\left(a_l\frac{k_2}{4}\right)cos\left(a_l\frac{k_3}{4}\right) \\ g_3(k) &= -sin\left(a_l\frac{k_1}{4}\right)sin\left(a_l\frac{k_2}{4}\right)cos\left(a_l\frac{k_3}{4}\right) + icos\left(a_l\frac{k_1}{4}\right)cos\left(a_l\frac{k_2}{4}\right)sin\left(a_l\frac{k_3}{4}\right) \end{aligned}\right\} \quad (2)$$

Furthermore, the basic problem of the tight-binding method is to calculate the matrix elements of the Hamiltonian between the various basis states.

The secular equation for the eigenvalues E(k) and eigen functions is an 10×10 coupled set of equations, Hamiltonian matrix elements, whose solution is derived from an 10×10 secular equation. For each value of the wave vector (k), there will be 10 solutions, to obtain the band structure (E vs. k relationship) [17], [21].

Table 1. Tight binding method Input parameters for empirical matrix elements using sp3s*, all energies are in units of eV, for compound semiconductor AlAs at p=0 [17].

Parameters	AlAs with no pressure[17]
a_o	5.6580
E_{sa}	-7.5273
E_{pa}	0.9833
E_{sc}	-1.1627
E_{pc}	3.5867
E_{s^*a}	7.4833
E_{s^*c}	6.7267
V_{ss}	-6.6642
V_{xx}	1.8780
V_{xy}	4.2919
V_{sapc}	5.1106
V_{scpa}	5.4965
V_{s^*apc}	4.5216
V_{pas^*c}	4.9950

2.3. Calculation Energy Band Structure of AlAs Under Pressure

High pressures influence the physical characteristics of semiconductor materials and the physical systems in which they are contained. The energy band gaps E_g, where the electron direct (wave vector k is conserved) and indirect (k is non- conserved) transitions between the conduction band and valence band, together with their pressure dependence, are the subject of more studies as a fundamental property of semiconductor material [22], [23], [24]. To analyze the impact of pressure on the energy band structure, Murnaghan's equation of state can be used, which assumes that the bulk modulus of a solid under finite strain varies linearly with pressure. When hydrostatic pressure is applied to a crystal (typically as from 1-10 GPa), its lattice constant, length of unit cell edge, decreases, because the atoms are pushed closer together; then the entire size of the crystal decreases, which changes the periodicity of the crystal and cause to increases orbital overlap between neighboring atoms. The application of pressure can reduce the band gap or cause a transition from a direct to an indirect band gap [25].

The pressure dependence of the lattice parameter of AlAs is determined using the Murnaghan equation of state [26]:

$$a(p) = \mathrm{a}(0)\left(1 + B_o'\frac{p}{B_o}\right)^{\frac{-1}{3B_o}} \quad (3)$$

where $a(p)$ is the lattice parameter at pressure ($p \neq 0$), $\mathrm{a}(0)$ is the lattice constant at zero pressure ($p = 0$), and $B_o, B_o{}'$ are the isothermal bulk modulus and first derivative of the isothermal bulk modulus at zero and at pressure p respectively (in this work $\mathrm{B_o} = 76.2\ \mathrm{Gpa}, \mathrm{B_o}{}' = 4.36\ \mathrm{Gpa}$) [27]. A small decrease in the lattice constant causes a greater proportional decrease in the volume of the crystal unit cell because the volume is proportional to the cube of the

lattice constant for a cubic lattice (i.e. V = a³) [28]. A widely used Murnaghan equation of state (EOS) in terms of volume is:

$$V(p) = V(o)\left(1 + B_o' \frac{p}{B_o}\right)^{\frac{-1}{B_o}}, \tag{4}$$

where $V(p)$ and $V(o)$ are the volumes at pressure p and zero pressure respectively.

$$\frac{a(p)}{a(0)} = \left(\frac{V(p)}{V(0)}\right)^{\frac{1}{3}}. \tag{5}$$

The tight-binding matrix elements (hopping integrals) vary when pressure exerted since pressure decrease the interatomic distance between atoms in the crystal structure which reducing the bond lengths (d) and lattice constant. Due to this closeness, the overlap between atomic orbitals is enhanced, which raises the magnitude of tight-binding Hamiltonian matrix elements. In general, these matrix elements follow an power-law scaling with the interatomic distance in a way that stronger electronic coupling appears as atoms bring closer [29]. The change of energy band structure under pressure lead to change interatomic matrix elements for the coupling between s-states on neighboring atoms given by the empirical measurement rule [29], [30]:

$$V_{ll'm} = \eta_{ll'm} \frac{\hbar^2}{2m_e} d^{-2}. \tag{6}$$

$\eta_{ll'm}$ represents a universal dimensionless constant, $\hbar$ is the reduced Planck constant, and m_e is the mass of electron. Equation (6) can be expressed in the absence of pressure and in the presence of pressure on AlAs crystal, as follows:

$$V_{(0)} = \eta_{ll'm} \frac{\hbar^2}{2m_e} d_0^{-2}. \tag{7}$$

And

$$V_{(p)} = \eta_{ll'm} \frac{\hbar^2}{2m_e} d_p^{-2}. \tag{8}$$

Equations 5, 8, and 9 give a relationship that can be used to determine the energy band structure of AlAs by calculating the change in the matrix elements coefficients under pressure.

4. RESULTS AND DISCUSSION

4.1. Calculation Band structure at p= 0

We have applied the sp_3s^*empirical tight binding model to the energy band structure calculations for the bulk semiconductor compound of AlAs along the high symmetry axes in the Brillouin zone, and we are using a specially designed MATLAB. The band structure along the symmetry axes of L-Γ-X-U, K , is shown in Figure (1), where Γ is the Brillouin zone center; and X, L, K and U are the Brillouin zone edges for a zinc blende crystal of lattice constant a , used $a = 5.6580A^{\circ}$ for AlAs [17], [31]. The highest value of valence band maximum is placed at Γ while the lowest value of conduction minima is located at X.

Figure (1) shows the dispersion curves for bulk bands of AlAs for sp3s*, including valence bands and conduction bands. These band structures show certain features that are general to bulk semiconductors. It is seen from Figure (1) that AlAs is indirect band gaps with a minimum gap along X of semiconductor $E_{gX} = 2.3$ eV and direct extremum gap at Γ of $E_{g\Gamma} = 3.04$ eV. The results of calculating energy gap band at the high symmetry points L, Γ, and X at atmospheric pressure (p= 0), with respect to the first conduction band, were compared with the practical and theoretical results shown in Table (2).

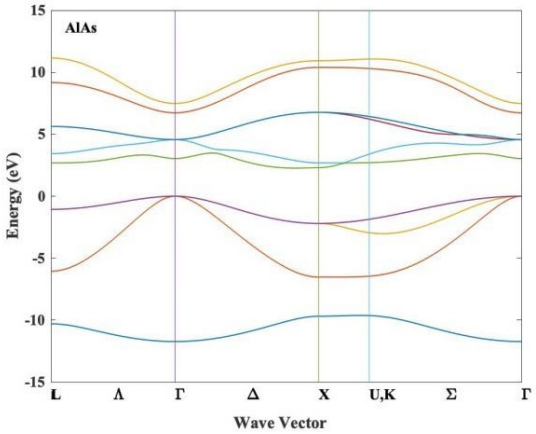

Figure 1. Energy band structure of AlAs obtained from sp^3s^* ETB model of AlAs.

Table 2. Energy band structure at high symmetry points at p= 0

Parameter	This work	Theoretical data [20]	Experimental data [32]
$E_{g\Gamma}$	3.0400	3.026	2.95
E_{gX}	2.3000	2.289	2.16
E_{gL}	2.6813	2.766	2.36

2. Calculation of band structure of AlAs at hydrostatic pressure

When the pressure is applied to an AlAs crystal, the lattice constant decreases, and therefore the volume reduces. In this study we used the Birch–Murnaghan EOS to compute the lattice constant under pressure, which then alter tight-binding parameters. This will change the energy bands structure. In this work, we compared between third and fourth order Birch-Maugham equation of state to compute the change in volume of the crystal. The fourth order Birch-Maugham equation of state (EOS_1) in which the pressure – volume relationship expanded as [33],[34]:

$$P = 3B_o f_e(1+2f_e)^{5/2}\left[1+\frac{3}{2}(B_o{}'-4)+\frac{3}{2}\left(B_oB_o{}''+(B_o{}'-4)(B_o{}'-3)+\frac{35}{9}\right)f_e{}^2\right] \quad (9)$$

where $f_e = \frac{1}{2}\left(((V/V_o)^{-2/3}-1\right)$ and the second derivative of $B_o$is given by [27]:

$$B_o{}'' = \frac{-1}{B_o}\left[(3-B_o{}')(4-B_o{}')+\frac{35}{9}\right] \quad (10)$$

The third order Birch-Maugham equation of state can be expressed by the following equation (EOS_2) is given by [35]:

$$P = \frac{3}{2}B_o\left[(x)^{7/3}-(x)^{5/3}\right]\left\{1+\frac{3}{4}[B_o{}'-4]\left[(x)^{2/3}-1\right]\right\} \quad (11)$$

where $x = V_o/V$, the second element within the first square bracket appears due to the truncation of the Helmholtz free energy to the third order term [36]. The 3rd and 4th Birch-Maugham forms give the relation between ratio of volume and pressure is shown in Figure (2).

From Fig. (2) the ratio V/V_o =1 when p=0, and it diminishes gradually at low pressure (under 10 GPa) indicates the unit cell volume becomes smaller. At low pressure the unit cell volume shrinks just a little (a few percent) and that means there is no influence when using both EOS_1 and EOS_2 forms to compute the effect of ratio V/V_o at low pressure range (the ratio almost less than 0.001) and the effect grows at high pressure (above 20 GPa). The EOS is the fundamental step that interprets applied pressure into lattice constant change, which then drives band structure modifications in tight-binding calculations. The ratio between the lattice constant under and lattice constant at p = 0 (a/a_o) for both two forms of equation of state versus pressure is shown in Figure (3). We noticed that the curve roughly linear at low pressures for both forms. The difference between Fig. (2) and Fig. (3) comes from the small reduction in lattice constant produces a large fractional reduction in volume since the lattice constant scales as one third of the volume of crystal (eq. (5)). Table three shows the values of the ratio for (V/V_o) , (a/a_o) versus pressure for both forms of EOS.

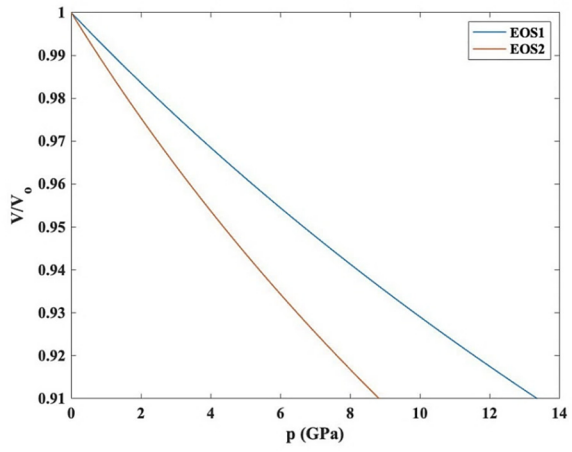

Figure 2. ratio of volume V/V_o versus pressure for both EOS_1 and EOS_2 forms

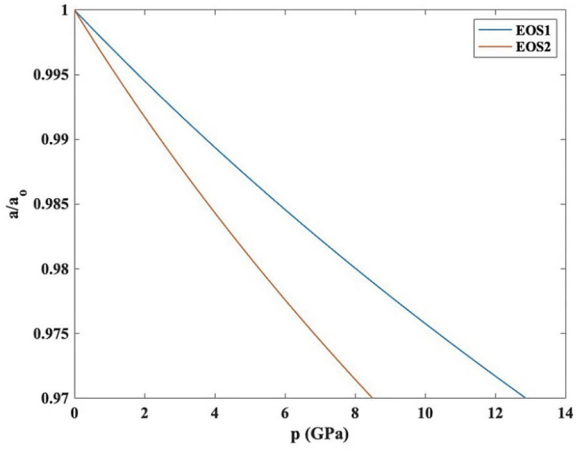

Figure 3. Ratio of lattice constant (a/a_o) versus pressure for both EOS_1 and EOS_2 forms

Table (3). Values of the ratio for V/V_o, (a/a_o) versus pressure for EOS_1 and EOS_2

Pressure (GPs)	EOS_1	EOS_2	EOS_1	EOS_2
	V/V_o	V/V_o	a/a_o	a/a_o
1	0.9917	0.9873	5.6422	5.6340
2	0.9836	0.9754	5.6270	5.6113
3	0.9759	0.9643	5.6123	5.5898
4	0.9685	0.9538	5.5980	5.5694
5	0.9614	0.9438	5.5842	5.5500
6	0.9545	0.9344	5.5708	5.5314
7	0.9478	0.9254	5.5578	5.5136
8	0.9414	0.9168	5.5452	5.4966
9	0.9351	0.9087	5.5329	5.4802
10	0.9291	0.9008	5.5210	5.4644

Employing both forms of EOS (Equations 9 and 11), we determined the volume and the lattice constant under pressure, where the orbital overlap and the hopping integral (matrix elements) in the ETB method are governed by the lattice constant. Using updated hopping integrals to build the Hamiltonian matrix element which consequently modifies the band structure for AlAs compound semiconductor.

The empirical tight-binding interaction parameters for both EOS_1 and EOS_2 forms are displayed in Table (4) and Table (5), respectively.

Table (4). The new empirical matrix elements of the sp^3s^* TB model in eV for AlAs at different values of pressure calculated from using EOS_1 , parameters of no pressure (p= 0) is fitted from the reference [17] .

Parameters	P = 0	P = 1 GPa	P = 3 GPa	P = 5 GPa	P = 7 GPa
E_{sa}	-7.5273	-7.4854	-7.4061	-7.3323	-7.2631
E_{pa}	0.9833	0.9778	0.9675	0.9578	0.9488
E_{sc}	-1.1627	-1.1562	-1.1440	-1.1326	-1.1219
E_{pc}	3.5867	3.5667	3.5289	3.4938	3.4608
E_{s^*a}	7.4833	7.4416	7.3628	7.2894	7.2207
E_{s^*c}	6.7267	6.6892	6.6184	6.5524	6.4906
V_{ss}	-6.6642	-6.6271	-6.5569	-6.4915	-6.4303
V_{xx}	1.8780	1.8675	1.8478	1.8293	1.8121
V_{xy}	4.2919	4.2680	4.2228	4.1807	4.1413
V_{sapc}	5.1106	5.0821	5.0283	4.9782	4.9313
V_{scpa}	5.4965	5.4659	5.4080	5.3541	5.3036
V_{s^*apc}	4.5216	4.4964	4.4488	4.4044	4.3629
V_{pas^*c}	4.9950	4.9672	4.9146	4.8656	4.8197

Table (5). The new empirical matrix elements of the sp^3s^* TB model in eV for AlAs at different values of pressure calculated from using EOS_2

Parameters	P = 0 [17]	P = 1 GPa	P = 3 GPa	P = 5 GPa	P = 7 GPa
E_{sa}	-7.5273	-7.4635	-7.3470	-7.2426	-7.1480
E_{pa}	0.9833	0.9750	0.9597	0.9461	0.9338
E_{sc}	-1.1627	-1.1528	-1.1349	-1.1187	-1.1041
E_{pc}	3.5867	3.5563	3.5008	3.4510	3.4060
E_{s^*a}	7.4833	7.4199	7.3041	7.2003	7.1063
E_{s^*c}	6.7267	6.6697	6.5656	6.4723	6.3878
V_{ss}	-6.6642	-6.6077	-6.5046	-6.4122	-6.3284
V_{xx}	1.8780	1.8621	1.8330	1.8070	1.7834
V_{xy}	4.2919	4.2555	4.1891	4.1296	4.0757
V_{sapc}	5.1106	5.0673	4.9882	4.9173	4.8531
V_{scpa}	5.4965	5.4499	5.3648	5.2886	5.2196
V_{s^*apc}	4.5216	4.4833	4.4133	4.3506	4.2938
V_{pas^*c}	4.9950	4.9527	4.8754	4.8061	4.7433

The energy band structures for both EOS_1 and EOS_2 forms of Birch-Maugham equation of state under pressure after determining the change in matrix elements are shown in Fig. (4) and Fig (5). We see from figures the change in band structure is less than 0.01 (< 0.01) using both EOS forms and the energy gap smoothly reduced

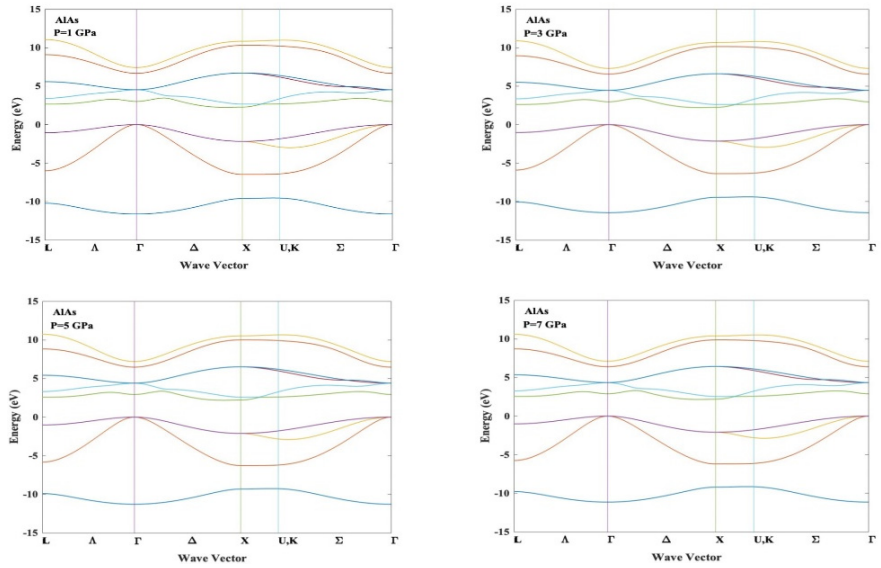

Figure 4. Energy band structure obtained from sp^3s^* ETB model of AlAs under pressures (1,3,5,7) GPa applying 4th order Birch-Maugham equation of state

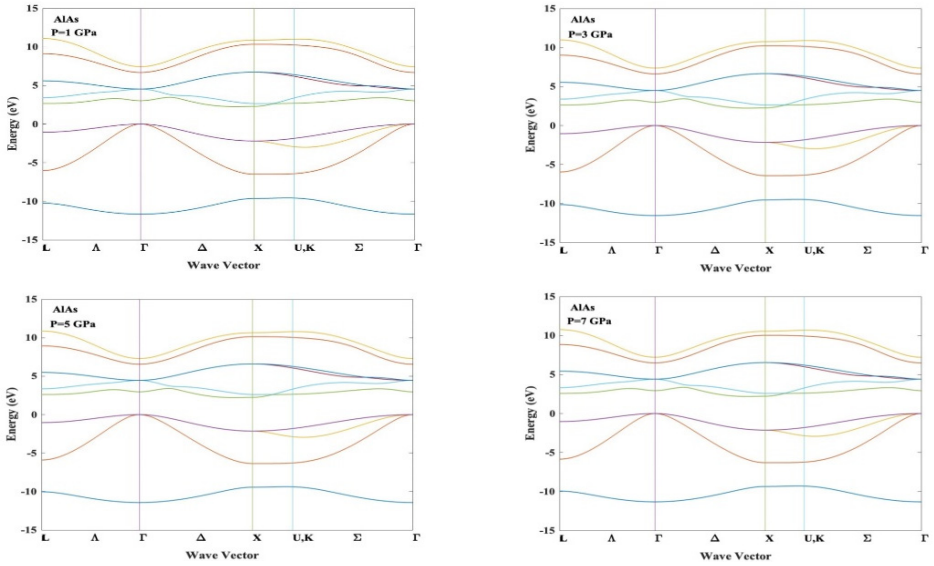

Figure 5. Energy band structure obtained from sp^3s^* ETB model of AlAs under pressures (1,3,5,7) GPa applying 3rd order Birch-Maugham equation of state

From the figures, we observe similar results appear at low pressures, in the range (1-7) GPa, for both forms of the equation of state, and we notice that AlAs has an indirect band gap at $\Gamma \rightarrow X$ and direct band gap at $\Gamma \rightarrow \Gamma$. We expect that the energy gaps roughly decrease linearly since the X conduction band edge decreases more rapidly than the rise of the valence band edge. The energy band gaps at high symmetry points using two forms of equation of state are displayed in Table (6) and shown in Figure (6).

Table (6). The energy gap of AlAs with low pressure for the high symmetry points Γ, L, X using two equations of states

P (GPa)	EOS 1			EOS 2		
	$E_{g\Gamma}$	E_{gL}	E_{gX}	$E_{g\Gamma}$	E_{gL}	E_{gX}
0	3.0400	2.6813	2.3000	3.0400	2.6813	2.3000
1	3.0231	2.6663	2.2872	3.0143	2.6586	2.2805
3	2.9911	2.6381	2.2630	2.9672	2.6170	2.2450
5	2.9612	2.6118	2.2405	2.9251	2.5799	2.2130
7	2.9333	2.5872	2.2193	2.8869	2.5462	2.1841

As pressure increases, the conduction valleys shift downward while the maximum valence bands shift upward slightly, thereby decreasing the band gap [37]. From Figure (6) we observed that at low pressures (1,2,3) GPa curves for both EOS forms produce somewhat different pressure curves and the different between them nearly equal 0.07 at 7 GPa (~ 0.07). We note that the EOS_1 exhibit a bend in almost higher band gap values at same pressure since it takes into

account higher order elastic influences, but the difference is tiny at low pressures that is the reason the curve of EOS_1 is positioned over EOS_2 curve.

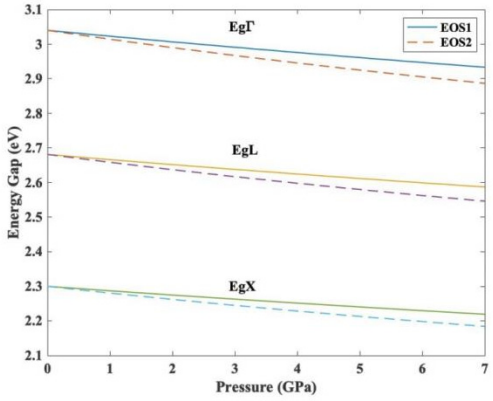

Figure 6. Energy band structure of AlAs under pressures (1,3,5,7) GPa at high symmetry points using both EOS forms

Table (7). The variation of E_g with pressure for direct and indirect for both EOS forms

P(GPa)	EOS_1		EOS_2	
	Eg (eV) Direct	Eg (eV) Indirect	Eg (eV) Direct	Eg (eV) Indirect
0	3.0400	2.2680	3.0400	2.2680
1	3.0231	2.2553	3.0143	2.2487
3	2.9911	2.2314	2.9672	2.2136
5	2.9612	2.2092	2.9251	2.1822
7	2.9333	2.1884	2.8869	2.1537

Table (7) shows the change in the direct and indirect band gap with pressure for both equation of state (EOS) forms of AlAs at low pressure. The variation of the direct and indirect band gap for both EOS forms is shown in Figure (7).

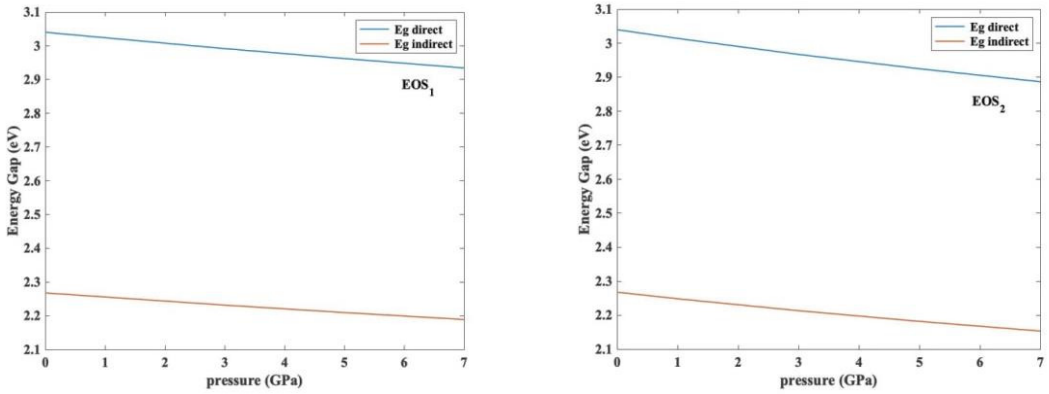

Figure 7. Direct and indirect energy gap with pressure for both EOS forms

The relationship between the conduction band and the wave vector at different low pressures is shown in Figure (8). It can be observed that with increasing pressure, the conduction bands creep downwards, and it can also be observed that the difference is very small when using the two equations of state formulas.

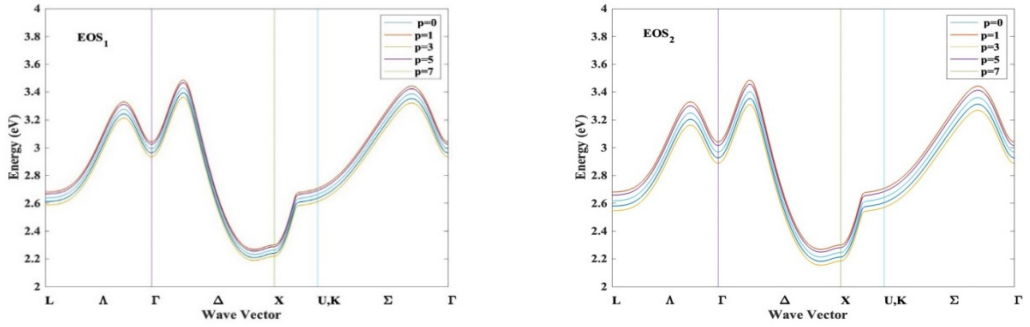

Figure 8. Comparison of the conduction band structure of AlAs without pressure and with pressures (1,3,5,7) GPa at high symmetry points using both EOS forms.

5. CONCLUSIONS

In this work, we found that in the absence of pressure, AlAs has an indirect band gap along X ($E_{gX} = 2.3$ eV) and a maximum direct energy gap at Γ of ($E_{g\Gamma} = 3.04$ eV), where the band-gap calculation is performed at high-symmetry points. We used two forms of the Birch-Murnaghan equation of state (4th and 3rd EOS) to determine the new empirical matrix elements, which are used to calculate the energy band structure under pressure. The change in band structure is less than 0.01 (< 0.01) by using both EOS forms, and the energy gap is smoothly reduced linearly with low pressure in the range 1-7 GPa. At low pressures (1,2,3) GPa curves for both EOS forms produce somewhat different pressure band structure curves, and the difference between them is nearly equal 0.07 at 7 GPa (~ 0.07). We note that the 4th order EOS_1 exhibits a bend in almost higher band gap values at the same pressure since it takes into account higher order elastic influences, but the difference is still tiny at low pressures that is the reason the curve of EOS_1 is positioned over EOS_2 curve. Finally, we expect that the high order of EOS is used at moderate (up to 20-30 GPa) and high pressure (up to 50 GPa), and the choice between third and fourth orders in the tight-binding model depends on whether we need qualitative or quantitative fineness under high pressure.

ORCID

Ali A. Mohammed, https://orcid.org/0000-0002-1731-3391; **Mumtaz M.S. Hussien,** https://orcid.org/0000-0002-4350-9523
Abbas Hussein Rostam, https://orcid.org/0009-0002-1852-4032

REFERENCES

[1] A. Srivastava, and N. Tyagi, "High pressure behavior of AlAs nanocrystals: the first-principle study," High Pressure Research, **32**(1), 43–47 (2012), https://doi.org/10.1080/08957959.2011.643791
[2] N. Y. Aouina, F. Mezrag, M. Boucenna, M. El-Farra, and N. Bouarissa, "High pressure electronic properties and elastic stability criteria of AlAs," Materials Science and Engineering: B, **123**(1), 87–93 (20050. https://doi.org/10.1016/j.mseb.2005.07.008
[3] F. Betraoui, H. Rekab- Djabri, K. Baddari, and S. Daoud, "Study of the Phase Transition and Physical Properties of AlAs, ScAs and Al_x Sc_{1-x} As Compounds by the FP-LMTO Method," Annals of West University of Timisoara - Physics, **66**(1), 118–141 (2024). https://doi.org/10.2478/awutp-2024-0008
[4] M. S. Ali and R. Parvin, "Investigation of pressure effect on structural, mechanical, electrical and optical properties of AlAs for optoelectronic applications," Physica B: Condensed Matter, **673**, 415491 (2024). https://doi.org/10.1016/j.physb.2023.415491
[5] V. B. Sheeba and C. N. Louis, "Band Structure, Metallization and Superconducting Transition Of Group III-V Semiconductors AlP And AlAs Under High Pressure," CME, **1**(4), 132–140 (2013). https://doi.org/10.13189/cme.2013.010405
[6] S. Froyen and M. L. Cohen, "Structural properties of III-V zinc-blende semiconductors under pressure," Phys. Rev. B, **28**(6), 3258–3265 (1983). https://doi.org/10.1103/PhysRevB.28.3258
[7] B. A. Weinstein, and S. K. Hark, "Phase Transitions in AlAs/GaAs Superlattices under High Pressure," Physical Review Letters, **58** (1987). https://doi.org/10.1103/physrevlett.58.781
[8] R. G. Greene, H. Luo, T. Li, and A. L. Ruoff, "Phase transformation of AlAs to NiAs structure at high pressure," Phys. Rev. Lett., **72**(13), 2045–2048 (1994). https://doi.org/10.1103/PhysRevLett.72.2045
[10] S. Adachi, "Band gaps and refractive indices of AlGaAsSb, GaInAsSb, and InPAsSb: Key properties for a variety of the 2–4-μm optoelectronic device applications," Journal of Applied Physics, **61**(10), 4869–4876 (1987). https://doi.org/10.1063/1.338352
[11] N. Bouarissa, "Electronic structure and lattice properties of zinc-blende InN under high pressure," The European Physical Journal B - Condensed Matter, **26**(2), 153–158 (2002). https://doi.org/10.1140/epjb/e20020076
[12] R. G. Greene, H. Luo, K. Ghandehari, and A. L. Ruoff, "High pressure structural study of AlSb to 50 GPa," Journal of Physics and Chemistry of Solids, **56**(3–4), 517–520 (1995). https://doi.org/10.1016/0022-3697(94)00231-2
[13] Adnan Al-sheikh, Mumtaz Hussien, and Siham Abdullah, "Pressure and Temperature Dependence of Energy Gap in SiC and Si1-xGex," RJS, **28**(4), 53–61 (2019). https://doi.org/10.33899/rjs.2019.163296
[14] T. B. Boykin, "Incorporation of incompleteness in the **k** · **p** perturbation theory," Phys. Rev. B, **52**(23), 16317–16320 (1995). https://doi.org/10.1103/PhysRevB.52.16317
[15] J. C. Slater and G. F. Koster, "Simplified LCAO Method for the Periodic Potential Problem," Phys. Rev. **94**(6), 1498–1524 (1954). https://doi.org/10.1103/PhysRev.94.1498
[16] Gerhard Klimeck, R. Chris Bowen, Timothy B. Boykin, Carlos Salazar-Lazaro, Thomas A. Cwik, and Adrian Stoica, "Si Tight-Binding Parameters from Genetic Algorithm Fitting," Superlattices and Microstructures, **27**(2/3), (2000). https://doi.org/10.1006/spmi.1999.0797
[17] P. Vogl, H. P. Hjalmarson, and J. D. Dow, "A Semi-empirical tight-binding theory of the electronic structure of semiconductors†," Journal of Physics and Chemistry of Solids, **44**(5), 365–378 (1983). https://doi.org/10.1016/0022-3697(83)90064-1
[18] D. A. Rasero Causil, A. A. Portacio, and D. Suescun, "Estructura Electrónica de GaAs y AlAs usando un Hamiltoniano Tight-Binding sp3s∗," Cienc. En Desarro, **12**(2), (2021). https://doi.org/10.19053/01217488.v12.n2.2021.12612
[19] D. J. Chadi, "Spin-orbit splitting in crystalline and compositionally disordered semiconductors," Phys. Rev. B, **16**(2), 790–796 (1977). https://doi.org/10.1103/PhysRevB.16.790
[20] G. Gopir, N. D. Zulkifli, and A. P. Othman, "Electronic Structure Calculation of Bulk Semiconductors Using The Sp3s* Empirical Tight Binding Method," Solid State Science and Technology, **13**(1), (2005).
[21] J. Singh, *Electronic and Optoelectronic Properties of Semiconductor Structures*, (First. Cambridge University Press, New York, 2003).
[22] A. A. Kelsey, and G. J. Ackland, "Computational analysis of the high-pressure structures of InSb," J. Phys.: Condens. Matter, **12**(32), 7161–7173 (2000). https://doi.org/10.1088/0953-8984/12/32/301

[23] Y. Ida, Y. Syono, and S. Akimoto, "Effect of Pressure on the Lattice Parameters of Stishovite," Earth and Planetary Science Letters, **3**, 216–218 (1968). https://doi.org/10.1016/0012-821X(67)90040-4
[24] M. S. Ali and R. Parvin, "Investigation of pressure effect on structural, mechanical, electrical and optical properties of AlAs for optoelectronic applications," Physica B: Condensed Matter, **673**, 415491 (2024). https://doi.org/10.1016/j.physb.2023.415491
[25] E. B. Elkenany, O. A. Alfrnwani, and M. Sallah, "Insight into pressure effect on optoelectronic, mechanical, and lattice vibrational properties of nanostructured $Ga_xIn_{1-x}P_ySb_zAs_{1-y-z}$ for the solar cells system," Sci. Rep. **13**(1), 3891 (2023). https://doi.org/10.1038/s41598-023-30681-1
[26] I. O. Radi, M. A. Abdulsattar, and A. M. Abdul-Lettif, "Semiempirical LUC-INDO calculations on the effect of pressure on the electronic structure of diamond," Physica Status Solidi (b), **244**(4), 1304–1317 (2007). https://doi.org/10.1002/pssb.200541329
[27] H.-Y. Wang, X.-S. Li, C.-Y. Li, and K.-F. Wang, "First-principles study of phase transition and structural properties of AlAs," Materials Chemistry and Physics, **117**(2–3), 373–376 (2009). https://doi.org/10.1016/j.matchemphys.2009.06.006
[28] V. G. Tyuterev, and N. Vast, "Murnaghan's equation of state for the electronic ground state energy," Computational Materials Science, **38**(2), 350–353 (2006). https://doi.org/10.1016/j.commatsci.2005.08.012
[29] S. Froyen and W. A. Harrison, "Elementary prediction of linear combination of atomic orbitals matrix elements," Phys. Rev. B, **20**(6), 2420–2422 (1979). https://doi.org/10.1103/PhysRevB.20.2420
[30] W. A. Harrison, "Elementary theory of heterojunctions," Journal of Vacuum Science and Technology, **14**(4), 1016–1021 (1977). https://doi.org/10.1116/1.569312
[31] I. Vurgaftman, J. R. Meyer, and L. R. Ram-Mohan, "Band parameters for III–V compound semiconductors and their alloys," Journal of Applied Physics, **89**(11), 5815–5875 (2001). https://doi.org/10.1063/1.1368156
[32] S. Adachi, "Band gaps and refractive indices of AlGaAsSb, GaInAsSb, and InPAsSb: Key properties for a variety of the 2–4-μm optoelectronic device applications," Journal of Applied Physics, **61**(10), 4869–4876 (1987). https://doi.org/10.1063/1.338352
[33] F. Birch, "Finite Elastic Strain of Cubic Crystals," Phys. Rev. **71**(11), 809–824 (1947). https://doi.org/10.1103/PhysRev.71.809
[34] T. Katsura, and Y. Tange, "A Simple Derivation of the Birch–Murnaghan Equations of State (EOSs) and Comparison with EOSs Derived from Other Definitions of Finite Strain," Minerals, **9**(12), 745 (2019). https://doi.org/10.3390/min9120745
[35] A. Al-sheikh, M. Hussien, and S. Abdullah, "Pressure and Temperature Dependence of Energy Gap in SiC and $Si_{1-x}Ge_x$," RJS, **28**(4), 53–61 (2019). https://doi.org/10.33899/rjs.2019.163296
[36] A. B. Alchagirov, J. P. Perdew, J. C. Boettger, R. C. Albers, and C. Fiolhais, "Energy and pressure versus volume: Equations of state motivated by the stabilized jellium model," Phys. Rev. B, **63**(22), 224115 (2001). https://doi.org/10.1103/PhysRevB.63.224115
[37] S. F. Mohammed, S. M. A. Ridha, A. M. Ghaleb, Z. T. Ghaleb, Y. Benkrima, and M. A. Abdullah, "Determination of Band Structure and Compton profiles for Aluminum-Arsenide Using Density Functional Theory," East Eur. J. Phys. (2), 132–137 (2023). https://doi.org/10.26565/2312-4334-2023-2-12

ВПЛИВ ТИСКУ НА ЕНЕРГЕТИЧНУ ЗОННУ СТРУКТУРУ AlAs ЗА ВИКОРИСТАННЯ МОДЕЛІ sp3s*

Алі А. Мохаммед[1], Мумтаз М.С. Хуссієн[2], Аббас Хуссейн Ростам[3]
[1]Кафедра фізики, Коледж освіти чистих наук, Університет Мосула, Мосул, Ірак
[2]Коледж охорони здоров'я та медичної техніки, Університет Аль-Нур, Мосул, Ірак
[3]Кафедра загальних наук, Коледж базової освіти, Університет Салахадділа, Ербіль, регіон Курдистан, Ірак

Ми використали метод щільного зв'язку sp3s* як обчислювальний підхід для розрахунку зонної структури кристалів AlAs за відсутності тиску та проаналізували вплив тиску на зонну структуру за низького тиску (1-7) ГПа. Ми використали дві форми рівняння стану Бірча-Моема (третього та четвертого порядку) для розрахунку змін елементів матриці Гамільтона, що виникають внаслідок змін об'єму кристалу та постійної решітки. Дисперсійні співвідношення для напрямків високої симетрії в першій зоні Бріллюена були знайдені шляхом чисельного розрахунку діагоналі Гамільтона під тиском. Ці розрахунки виконані за допомогою процедури, написаної в MATLAB. Ми виявили, що вплив обох форм рівняння стану на зонну структуру відрізняється лише незначно (на 0,01) за низького тиску, як показано на діаграмах зонної структури. Долини зони провідності спускаються вниз за низького тиску, зменшуючи як прямі, так і непрямі енергетичні щілини. Отримані результати узгоджуються з іншими експериментальними та теоретичними даними.

Ключові слова: *модель щільного зв'язку; рівняння стану Моема; складний напівпровідник AlAs; зонна структура; високий тиск*

EAST EUROPEAN JOURNAL OF PHYSICS. 3. 357-369 (2026)
DOI:10.26565/2312-4334-2026-3-31 ISSN 2312-4334

STRUCTURAL AND OPTICAL PROPERTIES OF $LiGd_{1-x}Lu_x(WO_4)_2$ Co-DOPED WITH Yb^{3+}/Er^{3+} SYNTHESIZED VIA SOLID STATE REACTION METHOD

N. Naimi[1]*, B. Rekik[1], I. Lanez[1], M. Derbal[1], L. Benharrat[2], Z. Bendaoud[1]
[1]LPCMIA Laboratory, Department of Physics, Faculty of Sciences, Saad Dahleb Blida 1 University, Blida, BP 270 Soumaa Road Blida, Algeria
[2]Research Center in Semiconductors Technology for Energy-CRTSE, 02 Bd. Dr. Frantz Fanon, B.P.140,7 Merveilles, 16038 Algiers, Algeria
**Corresponding author e-mail: phynaimi2@gmail.com*
Received January 12, 2026; revised July 17, 2026; accepted July 21, 2026

Double tungstate materials have been extensively studied and have attracted much attention as solid state lighting hosts. These materials with general formula $AB(WO_4)_2$ (A: alkali metal and B: trivalent rare earth ion) are widely used for their great optical properties. In this work, Gd^{3+}ions were partially substituted with Lu^{3+} ions to synthesize the $LiGd_{1-x}Lu_x(WO_4)_2$ compounds in order to study the structural, vibrational and optical behaviors of $LiGd_{1-x}Lu_x(WO_4)_2$ co doped with Yb^{3+} and Er^{3+} ions. Using the solid-state reaction, different concentrations of Lu^{3+} (x=2.5%, 5%, 80%, 90%, and 95%) were selected to synthesize our compounds. These concentrations influence the vibrational characteristics of the W-O bond through both band broadening and a shift in the symmetric stretching mode (ν_1). For the optical properties, green up-conversion under 980 nm excitation and down-conversion under 380 nm excitation of the double tungstate co-doped with Yb^{3+} and Er^{3+} were observed in the range of 530-552 nm. The lifetimes of the $^2H_{11/2}$ and $^4S_{3/2}$ levels, as well as the effect of Lu^{3+} substitution on the green emission of Er^{3+} in these compounds, were compared and discussed.
Keywords: *Double tungstate; Yb^{3+}/Er^{3+} co-doping; Up-conversion; Green emission*

1. INTRODUCTION

The potential applications of co-doped up-conversion (UC) materials in luminescence and sensing technologies have attracted great interest in various research fields [1-3]. Numerous studies have been devoted to rare earth co-doped up-conversion phosphors. According to the literature, Yb^{3+} and Er^{3+} ions are the most widely employed sensitizer-activator pair in up-conversion phosphors because of their favorable energy level structures, which enable efficient energy transfer processes [4-7]. In particular, the up-conversion emission of Yb^{3+} and Er^{3+} co-doped $LiGd(WO_4)_2$ double tungstate (abbreviated as LiGdW) has been extensively investigated due to its excellent luminescence properties and potential applications in several optical fields [8]. In recent years several works have been published on the co-doped mechanisms Yb^{3+}/Er^{3+} for thermometry and thermal sensing applications [9-11]. In the present work, a series of $LiGd_{1-x}Lu_x(WO_4)_2$ (x = 2.5%, 5%, 80%, 90%, and 95%) phosphors co-doped with Yb^{3+} and Er^{3+} ions were synthesized by the conventional solid-state reaction method. Comprehensive structural, vibrational, morphological, and optical characterizations were carried out using X-ray diffraction (XRD), Fourier transform infrared spectroscopy (FTIR), scanning electron microscopy (SEM), energy dispersive X ray spectroscopy (EDS), as well as Uv-vis absorption, and photoluminescence spectroscopy.

In this work, a detailed Raman spectroscopic study was performed to examine the evolution of the Raman shifts and band broadening in $LiGd_{1-x}Lu_x(WO_4)_2$ as a function of lutetium (Lu^{3+}) concentration. The results revealed a progressive structural transition from the scheelite-type $LiGd(WO_4)_2$ structure (space group $I4_{1/a}$ space group), in which Gd^{3+} and Li^+ ions occupy the same crystallographic sites and produce broader Raman bands, to the wolframite-type $LiLu(WO_4)_2$ structure (space group P_2/n), where Lu^{3+} and Li^+ ions occupy different lattice sites. Furthermore, the influence of Lu^{3+} substitution on the green up-conversion emissions of Er^{3+}, corresponding to the $^2H_{11/2}$ and $^4S_{3/2}$ to $^4I_{15/2}$ transitions, was investigated in the absence and presence of Yb^{3+} sensitizer. The fluorescence decay times of $^2H_{11/2}$ and $^2S_{3/2}$ excite states were determined for $LiGd_{1-x}Lu_x(WO_4)_2$: $1\%Yb^{3+}/0.4\%Er^{3+}$ phosphors with different Lu^{3+} contents and compared with those reported for fully substituted $LiLu(WO_4)_2$: Yb^{3+}/Er^{3+} compositions [6]. The luminescence behavior and the lifetimes associated with the intense green emissions were also estimated to assess the effect of Lu^{3+} content on the optical performance of these materials.

2. EXPERIMENTAL

2.1. Synthesis

Rare earth co-doped phosphors, $LiGd_{1-x}Lu_x(WO_4)_2$: $1\%Yb^{3+}$ /$0.4\%Er^{3+}$ (x = 2.5%, 5%, 80%, 90% and 95%) were synthesized using the solid-state reaction method. The starting materials were: Li_2CO_3 (Roth 99.999%), WO_3 (Philips, 99.97%), Gd_2O_3 (Philips, 99.99%), Lu_2O_3 (99.99%), Er_2O_3 (99.999%), and Yb_2O_3 (99.999%), all of analytical grade purity. The raw materials were weighed according to the stoichiometric molar proportions. The elaborated samples were obtained through the following chemical reaction:

$$\mathbf{Li_2CO_3 + (0.986\text{-}x)\ Gd_2O_3 + x(Lu_2O_3) + 0.004Er_2O_3 + 0.01Yb_2O_3 + 4WO_3 \rightarrow 2(LiGd_{0.986\text{-}x}Lu_{\ x}\ Er_{0,004}Yb_{0.01}(WO_4)_2) + CO_2}$$

Cite as: N. Naimi, B. Rekik, I. Lanez, M. Derbal, L. Benharrat, Z. Bendaoud, East Eur. J. Phys. 3, 357 (2026), https://doi.org/10.26565/2312-4334-2026-3-31

The prepared samples were calcined at 700°C for 14 hours, using heating and cooling rates of 5 and 10°C min^{-1}, respectively.

2.2. Characterizations

The synthesized powders obtained from the starting materials were thoroughly mixed in an agate mortar. X-ray diffraction (XRD) analysis of the $LiGd_{1-x}Lu_x(WO_4)_2$ phosphors co-doped with Yb^{3+} and Er^{3+} was performed using a Bruker-AXS D8-Discover diffractometer using Cu Anode Kα radiation (λ =1.5406 Å). The diffraction data were recorded with a step size of 0.02° in the range of 2θ from 10° to 80°. Fourier transformation infra-red (FTIR) measurements were carried out at room temperature using an FTIR-8300 spectrometer in the spectral range of 400–4000 cm^{-1}. The Raman spectra of the powders were recorded at room temperature using a Horiba Jobin-Yvon ARAMIS micro Raman spectrometer equipped with a double mono chromator and a spectrograph with holographic lattice at 1800 lines/mm. The luminescence spectra were measured under the excitation wavelengths of 380 and 980 nm using a Fluorolog- 3 spectrometer (HORIBA Jobin-Yvon). The morphology and elemental compositions of the samples were investigated by scanning electron microscopy (SEM) coupled with Energy Dispersive Spectroscopy (EDS) using a QUANTA 650 microscope equipped with a BRUKER SDD detector and an Oxford EBSD system, operating at accelerating voltage adjustable from 200 V to 30 KV.

3. RESULTS AND DISCUSSIONS

3.1. Structural properties

3.1.1. XRD of $LiGd(WO_4)_2$: x Yb^{3+} / 0.02 %Er^{3+}

Figure 1 shows the XRD patterns of LGWO: x%Yb^{3+}/2% Er^{3+} phosphors with (x= 2%,6%, and 16%). All diffraction peaks are in good agreement with the standard JCPDS card of LiGd $(WO_4)_2$phase (No: 04–008–0355). The XRD results indicate that Yb^{3+}/ Er^{3+}co-doped LGWO phosphors with x=2% and 6% are single phase materials with high crystallinity. These compounds crystallize in the scheelite structure belongs to the tetragonal system with space group $I4_{1/a}$ [12, 13]. When the Yb^{3+} concentration increases to y=16%, the single phase region transforms into a biphasic domain composed of a tetragonal scheelite $Ca(WO_4)$ phase and monoclinic (P2/n) iso-structure β-$LiYb(WO_4)_2$ [13]. With the increasing Yb^{3+} concentration, secondary Li_2WO_4 and WO_3 phases were appeared in the case of 16%Yb^{3+}/2%Er^{3+} co-doped $LiGd(WO_4)_2$. The structural parameters, including phase fractions, lattice parameters, crystallite sizes and microstrains were determined by Rietveld refinement using high score plus software. Table 1 summarizes refined structural parameters of $LiGd_{0.98-x}Yb_x$ $Er_{0.02}(WO_4)_2$ (x=2%, 6% and 16%) compounds.

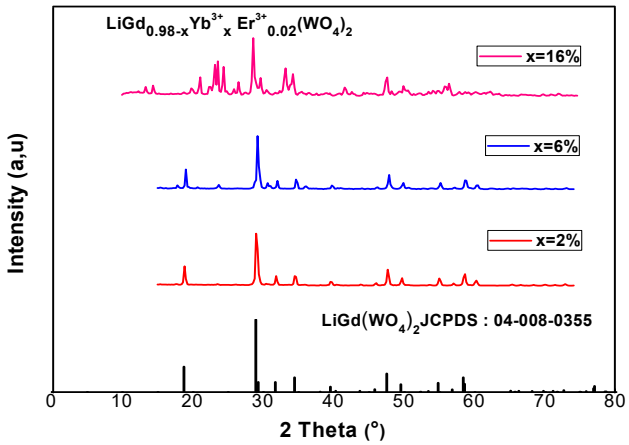

Figure 1. XRD patterns of $LiGd(WO_4)_2$: x Yb^{3+} / 2 %Er^{3+} (x=2%,6%, and 16%).

Table 1. Structural parameters of $LiGd_{0.98-x}Yb_x^{3+}$ $Er^{3+}_{0.02}$ $(WO_4)_2$ (x=2%, 6% and 16%).

$LiGd_{0.98-x}Yb_x^{3+}$ $Er^{3+}_{0.02}$ $(WO_4)_2$ (x=2%, 6% and 16%)						
Concentrations	**Weight fractions**			**Lattice parameters (A°)**	**Crystallite size (A°)**	**Micro strain (%)**
	$LiGd(WO_4)_2$	**WO_3**	**Li_2WO_4**			
2%	100%	0%	0%	a=5.195062 b=5.195062 c=11.24637 α=β=γ= 90°	453.6654	0.14554
6%	100%	0%	0%	a=5.195733 b=5.195733 c=11.25892 α=β=γ= 90°	375.685	0.6202
16%	43.8%	36%	20.3%	/	1178.345	0.09365

3.1.2. XRD of $LiGd_{1-x}Lu_x(WO_4)_2$: 1%Yb^{3+} / 0.4%Er^{3+}

Figure 2 shows the XRD patterns of $LiGd_{1-x}Lu_x(WO_4)_2$: 4%Er^{3+}, 1%Yb^{3+} phosphors with (x% =2.5%,5%,80%,90%, and 95%). The results reveal two distinct phase regions. For x ≤ 5%, the samples exhibit a scheelite-type tetragonal structure, in agreement with JCPDS card N° 04-008-0355. For higher Lu^{3+} concentrations x ≥ 80%, a phase transition from the $LiGd(WO_4)_2$ to the monoclinic $LiLu(WO_4)_2$ is observed consistent with JCPDS card No. 04-001-7757 [15], and previous reports [14,15,19]. This structural transformation is affected by the significant difference in ionic radii between Gd^{3+} and Lu^{3+} ions. The results also indicate that Lu^{3+} ions progressively substitute for Gd^{3+} ions at the cationic sites. Since Lu^{3+}, Gd^{3+}, and Er^{3+} have the same valence state (+3), and because the ionic radii of Lu^{3+}, Yb^{3+}, and Er^{3+} are very similar, the low concentrations of Yb^{3+} and Er^{3+} dopants do not induce any additional structural modifications compared with the undoped compounds reported previously [19]. With increasing Lu^{3+} concentration, a secondary Li_2WO_4 phase was appeared in the $LiGd_{1-x}Lu_x(WO^4)_2$. Table 2 summarizes the structural parameters of $LiGd_{1-x}Lu_x(WO_4)_2$: 1%Yb^{3+} / 0.4%Er^{3+} (x%=2.5%,5% ,80%, 90%, and 95%).

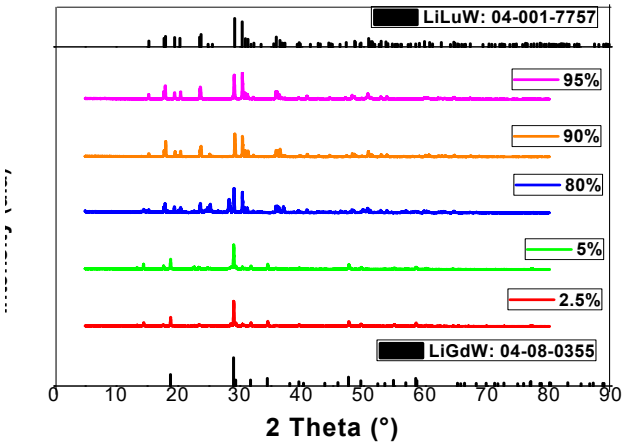

Figure 2. XRD patterns of $LiGd_{1-x}Lu_x(WO_4)_2$: 1%Yb^{3+} / 0.4%Er^{3+} (x%=2.5%,5% ,80%, 90%, and 95%).

Table 2. Structural parameters of $LiGd_{1-x}Lu_x(WO_4)_2$: 1%Yb^{3+} / 0.4%Er^{3+} (x%=2.5%,5% ,80%, 90%, and 95%).

$LiGd_{1-x}Lu_x(WO_4)_2$: 1%Yb^{3+} / 0.4% Er^{3+}						
Concentrations	**Weight fractions**			**Lattice parameters (A°) and angles (°)**	**Crystallite sizes (A°)**	**Micro strain (%)**
	$LiGd(WO_4)_2$	$LiLu(WO_4)_2$	Li_2WO_4			
x=2.5%	81.6%	17.3%	1.2%	a=5.1967 b =5.1967 c = 11.254 α=β=γ= 90°	370.1438	0.31012
x=5%	78.4%	21.2%	0.3%	a=5.1937 b=5.1937 c=11.244 α=β=γ= 90°	1215.532	0.09359
x=80%	1.2%	94%	4.8%	a =4.9914 b =5.7982 c =10.817 α=β= 90° γ= 113.934°	1805.904	0.04949
x=90%	0.1%	98%	1.8%	a = 4.9854 b = 5.7937 c = 10.7989 α=β= 90° γ= 114.307°	1912.459	0.06543
x=95%	0.8%	99.2%	0%	a =4.9911 b =5.7970 c =10.8141 α=β= 90° γ= 113.998°	1052.2	0.11905

3.1.3. XRD of $LiLu(WO_4)_2$: xEr^{3+}, and $LiLu(WO_4)_2$: xYb^{3+} / 2% Er^{3+}

Figure 3 shows the XRD patterns of $LiLu_{1-x}(WO_4)_2$: xEr^{3+} (x=0.1%,0.2% ,2%) and the $LiLu_{1-x-y}(WO_4)_2$ with (x = 2%, 6%, 16%; y =2%). All diffraction peaks can be well indexed to the standard pattern of pure $LiLu(WO_4)_2$ (JCPDS No.04-001-7757), indicating that the incorporation of Yb^{3+} and Er^{3+} ions does not alter the crystal structure of the host

matrix, even at a high Yb^{3+} concentration of 16%. This behavior changes from that observed in $LiGd(WO_4)_2$ and can be attributed to the fact that $LiLu(WO_4)_2$ and $LiYb(WO_4)_2$ share the same monoclinic β-$LiYb(WO_4)_2$. All the compounds crystallize in monoclinic system with the space group of $P_{2/n}$ [11]. The crystal structure is composed of interconnected [LiO_6], [LuO_6], and [WO_6] octahedra. For a coordination number (CN) of six, the ionic radii of Li^+, Lu^{3+}, W^{6+}, Yb^{3+} and Er^{3+} ions are 0.76 Å, 0.861 Å, 0.60 Å, 0.86 Å and 0.89 Å, respectively. The structural parameters obtained from Rietveld refinement for $LiLu(WO_4)_2$: xEr^{3+} (x=0. 1%,0.2%, and 2%)) and $LiLu(WO_4)_2$: xYb^{3+} / 2% Er^{3+} (y =2%,6%, and 16%) are summarized in table 3.

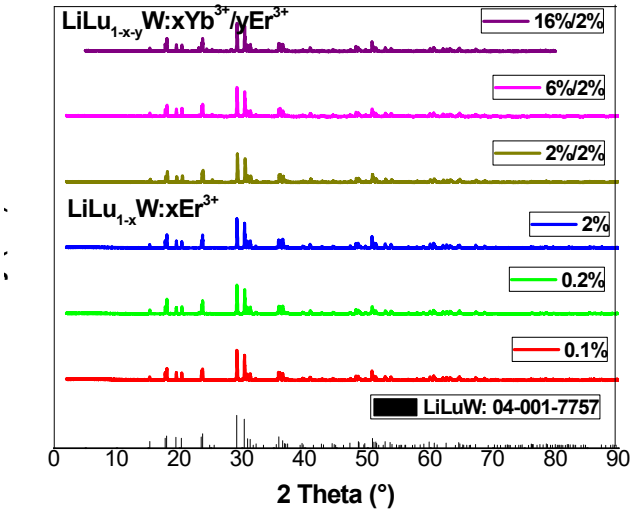

Figure 3. XRD patterns of $LiLu(WO_4)_2$: xEr^{3+} (x=0.1%,0.2%, and 2%)) and $LiLu(WO_4)_2$: xYb^{3+} / 2% Er^{3+} (y =2%,6%, and 16%)

Table 3. Structural parameters of $LiLu(WO_4)_2$: xEr^{3+} (x=0.1%,0.2%, and 2%)) and $LiLu(WO_4)_2$: xYb^{3+} / 2% Er^{3+} (y =2%,6%, and 16%).

$LiLu(WO_4)_2$: xEr^{3+} (x=0.1%,0.2%, and 2%))				
Concentrations	**Weight fractions** $LiLu(WO_4)_2$	**Lattice parameters (A°) and angles (°)**	**Crystallite sizes (A°)**	**Micro strain (%)**
x=0.1%	100%	a=4.98398 b=5.79410 c=10.79730 α=γ= 90° β= 114.3644°	2278.823	0.0349
x=0.2%	100%	a=4.98670 b=5.79105 c=10.79680 α=γ= 90° β= 114.303°	3780.809	0.02541
x=2%	100%	a=4.98375 b=5.79427 c=10.79762 α=γ= 90° β= 114.3670°	13831.33	0.00626
$LiLu(WO_4)_2$: xYb^{3+} / 2% Er^{3+} (y =2%, 6%, and 16%)				
x=2% y=2%	100%	a=4.98640 b=5.79310 c=10.79800 α=γ= 90° β= 114.320°	3299.103	0.0296
x=2% y=6%	100%	a=4.9858 b=5.7916 c=10.7963 α=γ= 90° β= 114.3073°	3273.314	0.02642
x=2% y=16%	100%	a=4.98413 b=5.79340 c=10.7970 α=γ= 90° β= 114.3432°	4058.184	0.01574

Figure 4 (a) and 4 (b) show the SEM image of x%Yb^{3+}/2%Er^{3+} co-doped LGW (x=2 and 6) samples, respectively. The micrographs reveal that the synthesized samples exhibit relatively smooth surfaces with slight agglomeration. The

particle sizes are in the of micrometer range. The observed compact and morphology is favorable for obtaining strong up-conversion luminescence, as reported in reference [8], this morphological result indicates that this compound appears to be a promising candidate for UC luminescence. To evaluate the elemental composition, EDS analysis was carried out. Figure 4(c) shows the EDS results of LGWO: x%Yb^{3+}/ 2% Er^{3+} (y=2%, 6%, and 16%), confirming the presence of all constituent element: gadolinium, ytterbium, erbium and tungsten.

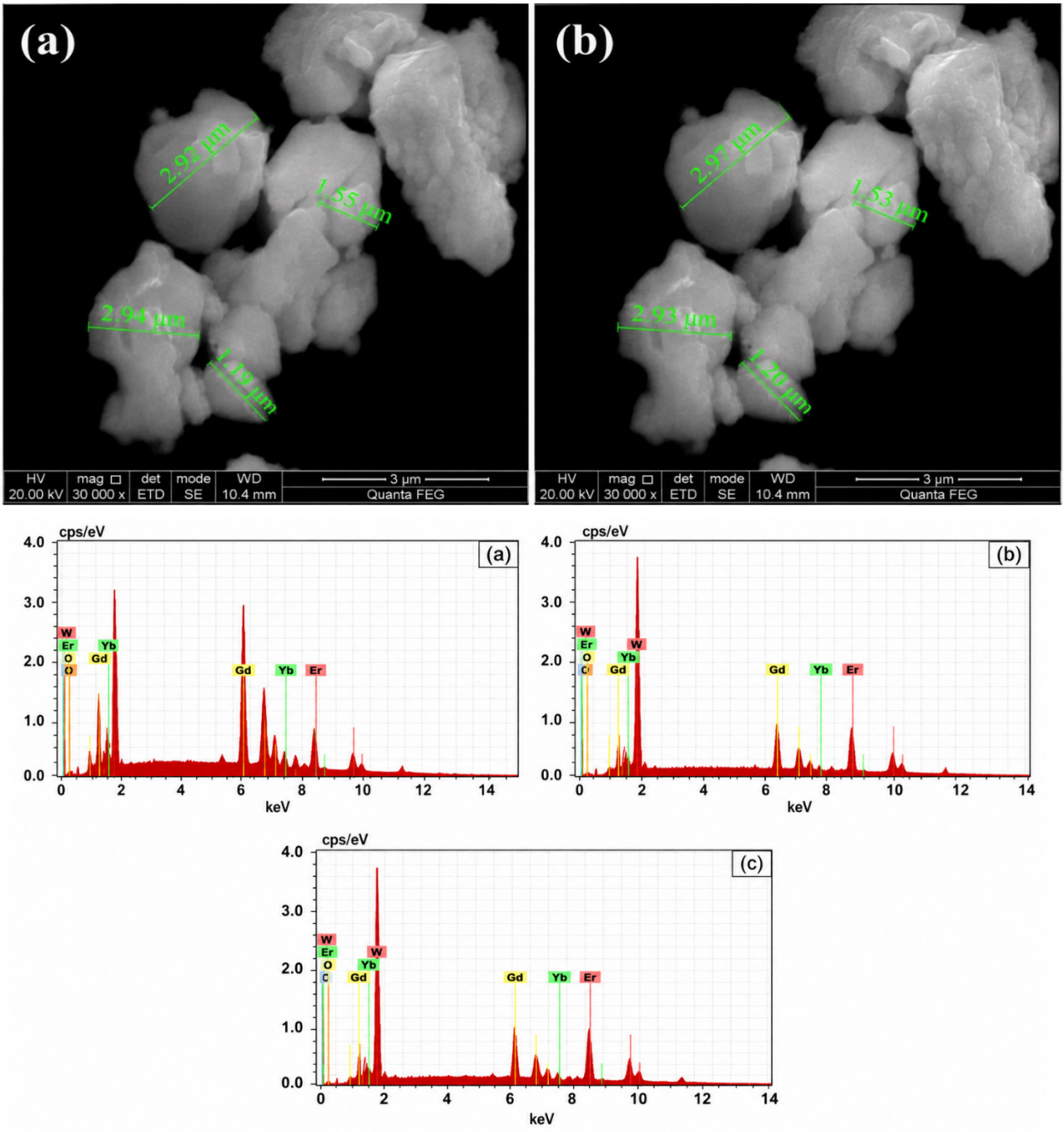

Figure 4. (a) SEM image of LiGdWO: 2% Yb^{3+}/2% Er^{3+}, (b) SEM image of LiGdWO: 6% Yb^{3+}/2% Er^{3+}, and (c) EDS analysis of LGWO: x%Yb^{3+}/ 2% Er^{3+}(x=2%, 6%, and 16%)

3.2. Vibrational properties

3.2.1. FTIR analysis

The FTIR spectra of $LiGd_{1-x}Lu_x(WO_4)_2$ and $LiGd_{1-x}Lu_x(WO_4)_2$: 1%Yb^{3+}/0.4%Er^{3+} with (x=2.5%, 5%, 80%, 90%, and 95%) were recorded at room temperature (Fig. 5). For x = 2.5% and 5%, the spectra are similar to those of the prototype scheelite structure. The assignment of the IR vibrational frequencies is in good agreement with previous reports [17-19]. The isolated tetrahedral (WO_4) groups exhibit four fundamental vibrational modes, which can be classified into two categories corresponding to the stretching and bending modes of vibrations. Each category is further divided into symmetric and asymmetric modes. The most intense band located at 915 cm^{-1}, is attributed to the symmetric stretching

vibration of the (WO_4) tetrahedra, whereas the bands observed in the 700-850 cm^{-1} region correspond to the asymmetric stretching modes. Co-doping with 2%Er^{3+}, 2% Yb^{3+} and 6% Yb^3 does not significantly modify the vibrational modes. This behavior can be attributed to the conservation of the scheelite structure at relatively low dopant concentrations.

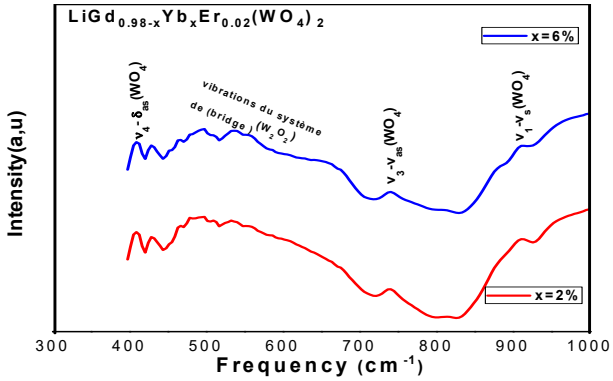

Figure 5. FTIR spectra of $LiGd_{0.986-x}Yb_xEr_{0.02}(WO_4)_2$ with (x =2 % and 6%)

For x = 80%, 90%, and 95%. FTIR spectra shown in Figure 6 present vibrational modes characteristic of the wolframite structure. The internal modes observed at 500.28 cm^{-1}, 553.39 cm^{-1}, 672.09 cm^{-1}, 790.79 cm^{-1} can be assigned to the asymmetric stretching mode υ_{as} (WO_6). In contrast, no absorption bands were detected in the interval 500 cm^{-1} to 800 cm^{-1} for x= 2.5%, 5% (LGW phase). The appearance of these bands for x≥80%, corresponding to the LLuW phase, confirms the structural transition from the scheelite to the wolframite phase [20].

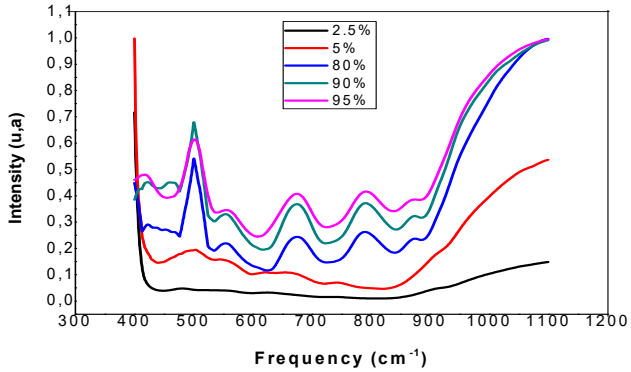

Figure 6. FTIR spectra of $LiGd_{1-x}Lu_xW$ with: x=2.5%, 5%, 80%, 90%, and 95%.

3.2.2. Raman study

Figure 7 presents Raman spectra in the frequency range of 50-1000 cm^{-1} at room temperature for the $LiGd_{1-x}Lu_x(WO_4)_2$ sample co-doped with 1% Yb^{3+} and 0.4% Er^{3+} for x=2.5, 5, 80, 90 and 95%.

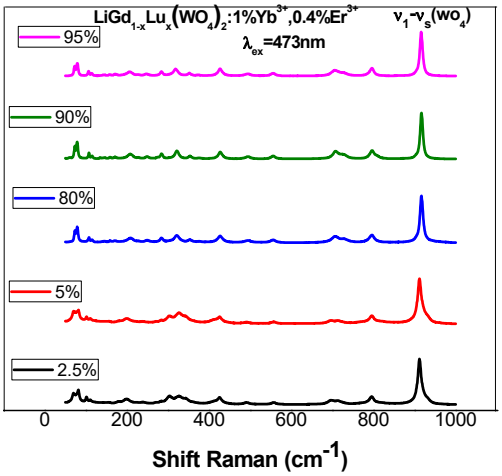

Figure 7. Raman spectra of $LiGd_{1-x}Lu_x$ $(WO_4)_2$:1%Yb^{3+}/0.4%$Er^{3+}$with different Lu^{3+} concentrations

These results exhibit vibration peaks of internal modes extending from 200 to 920 cm^{-1} with four fundamental vibrations corresponding to the stretching mode at (ν_1=913cm^{-1}), (ν_3=833cm^{-1}), and binding mode at (ν_2=320cm^{-1}), (ν_4=405cm^{-1}) of the WO_4^{2-} ions, while the external vibration region is located below 200 cm^{-1}. The vibrational characteristics in the internal-mode region demonstrate full agreement between the structure and its phonon properties.

The vibrational frequencies are summarized in Table 4. The distinct gap in the region of 420-740 cm^{-1} in the energy distribution of K=0 phonons is clearly shown in the spectra of the compounds under study for x = 2.5 and 5% being iso structural to $Ca(WO_4)$, which crystallizes in the scheelite type with tetragonal system and space group $C_{4h}^6 = I4_1/a$, the coordination numbers of the scheelite structure are characterized by CN (Li^+) = 8, CN (Gd^{3+}) = 8, the same position with site symmetry (SS) =C_2 occupied by both Li^+ and Gd^{3+}. With increasing Lu^{3+} concentration, new peak appears at 153, 207, and 248 cm^{-1}, indicating the doubled of line's number for the monoclinic phase, due to the splitting of pertinent bands and arising of additional bands in the energy gap region due to the intermolecular interaction in the wolframite- type unit cell that the isolated WO_4^{-2} units tungsten ions coordinated to four oxygen CN (W^{6+}) = 4, occupy the S_4 symmetry [20].

Table 4. Vibration modes of $LiGd_{1-x}Lu_xW$ x=2.5%, 5%, 80%, 90%, and 95%.

Frequency (cm^{-1}) **Present work**	Frequency (cm^{-1}) [14]	IR vibration modes	Frequency (cm^{-1}) **Present work**	Frequency (cm^{-1}) [14]	Raman vibration modes
81.05	81.05	T(Gd^{3+}) and T (W_2O_8)	79.50	76.60 95.40 100.07	T(Gd^{3+})-T(W^{6+})
			109.8	106.90 143.58	T(Gd^{3+})-T(W^{6+})
528	500.28 553.39	υ 4 -υ as WO_4	153.8	167.04 170.45 187.52	T(Gd^{3+}) and T(W_2O_8)
			207.57	200.74 207.57	υ 2-&s WO_4 T(Li^+)
			248.09	237.85 237.85	υ 2-&s WO_4 T(Li^+)
672.09	672.09 790.79	υ 3 -υ as WO_4	285.21	305.26 268.147	&s bending modes T(Li^+)
			321.89	328.72 305.26	&s bending modes T(Li^+)
			355.59	429.82 369.24 359.01	&s bending modes
			493.8	490.40 416.17	υ 4- &s WO_4
			557.37	507.37 507.37 608.14	υ as stretching mode
			708.81	702.41 722.46	υ as stretching mode
			796.26	796.26 769.39 779.13 820.15 856.84	υ 3-υasWO_4
			917	911.02 907.05	υ 1- υ s WO_4

There is a relationship between Raman shift of the highest energy peak ($\nu_{1=}$ vs = 913cm^{-1} (Stretching symmetric peak)) and Lu^{3+} concentrations which it shift toward a higher wave number values (Fig. 8), indicate that it corresponds to ionic radius size, as the Gd^{3+} (1.053 Å) substitution by Lu^{3+} (0.861 Å) in the compound decrease the average ionic radii size ($R_{average} = R_{Lu}$ x+ R_{Gd} (1-x)), For better explain, this symmetric stretching peak vs give more information of W—O links behavior, that is more sensible to cationic environmental variation and is strongly influence by the Ln-O-W, with Ln=Lu/Gd, which introduce covalence evolution of this bond.

On the other hand, the result presented in Figure 8 shows clearly that the band width of the stretching symmetric peak (strongest peak) of the tetragonal structure of LGW is larger than that of the monoclinic structure corresponding to LLuW. It well knows the broadening of vibrational bands in Raman spectra provides information on structural disorder because wide vibration bands are a well-known characteristic of irregular systems [14], which is directly proportional to the Raman gain, and it can be used as a condition for comparing the performance of the studied materials [21]. To explain this phenomenon, we calculate the ratio of the Raman intensity to the full width at half maximum (FWHM) [21]. This parameter is estimated by the following relationship (1) [21]:

$$\sum = I/W \quad (1)$$

which I: the intensity, and W= ω: Full-Width for the Half-Maximum (FWHM).

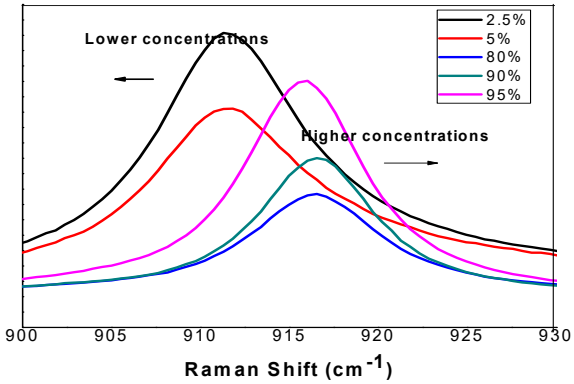

Figure 8. Expanded view of the strongest Raman band of $LiGd_{1-x}Lu_x(WO_4)_2$ at different Lu^{3+}concentrations.

The Raman spectra were fitted using a Lorentzian function to determine the peak intensity ''I'' and FWHM =W. Table 5 summarizes the parameters of the strongest symmetric stretching mode (ν). ∑= I/W ratio was used to evaluate the degree of structural disorder. The results show that samples with low Lu^{3+} concentrations crystallize in the scheelite structure, while the wolframite phase is appeared with higher concentration of Lu^{3+}.
Lorentz function

$$y = y_0 + \frac{2A}{\pi}\frac{\omega}{4(X-X_C)^2+\omega^2} \quad (2)$$

$$I = 2A/\pi\omega \quad (3)$$

$$\omega = W \quad (4)$$

Table 5. Experimental frequencies and Raman active phonon position bands, and comparison between ∑ Raman shift of $LiGd_{1-x}Lu_x(WO_4)_{2x}$= 2.5%, 5% ,80%, 90%, and 95%

Component	Function type	W, (cm^{-1})	A, (u.a).cm^{-1}	I, (u.a)	ω, (cm^{-1})	∑ ratio
x=2.5 %	Lorentz	11.68	204081.67	11123.38	11.68	951.80
x=5 %	Lorentz	10.44	262515.47	16003.60	10.44	1531.75
X=80%	Lorentz	8.32	84264.62	6446.28	8.32	774.23
x= 90 %	Lorentz	7.04	98617.78	8911.03	7.04	1264.15
x= 95 %	Lorentz	7.39	161329.813	13899.34	7.39	1880.06

A simple interpretation of these results can be proposed by considering that the smaller the cation Ln^{3+}, the greater its interaction with the electron cloud of its neighboring oxygen's will be and the greater degree of covalence of the bonds forms with the latter. The covalent bond is by its nature; directional, unlike the ionic bond. This will therefore have the consequence of slowing down and limiting the movements of the oxygen's involved, around their equilibrium position, if their movement is limited with respect to the trivalent Ln cation, it will also be limited with respect to W, thus leading to a rigidity of the W— O bonds as shown in Figure 9.

(a) (b)

Figure 9. Influence of Ln (L) size on the nature of Ln-O, (a): completely covalent bonding, and (b) partially ionic bonding

This phenomenon will then induce an increase in the force constants of these which is naturally reflected in vibrational spectroscopy by an increase in the vibration frequency of these bonds that indicate the W—O peak shift toward the higher wave number values [20-21].

3.3 Optical properties

3.3.1. Absorption spectra

Figure 10 and 11 present the room temperature absorption spectra at of $LiGd(WO_4)_2$: x% Yb^{3+}/ 2% Er^{3+} phosphors. For x=0, several absorption peaks are observed at 348.55, 383.66, 454.59, 489.11, 526.35, 635.74 and 977.32 nm corresponding to the Er^{3+} transitions from the ground state $^4I_{15/2}$ to the excited states $^4G_{11/2}$,$^4F_{3/2}$, $^4F_{7/2}$, $^4S_{3/2}$,$^2H_{11/2}$,$^4F_{9/2}$, $^4I_{11/2}$ respectively. For x= 2 % and 6%, figure 11 reveals two charge-transfer bands (CTBs) located at approximately

233 nm and 267 nm, which assigned to the W^{+6}-O^{-2} and Yb^{+3}-O^{-2} charge transfer transitions, respectively. The W-O CTB is more intense for x=2% than for x=6%, which may be related to the enhanced absorption by Yb^{3+} ions. This behavior suggests that the broad band around 267 nm originates from the presence of Yb^{3+} ions and can therefore be attributed to the O^- toYb^{3+} charge transfer transition. In addition, all samples exhibit a broad absorption band around 980 nm. The large bandwidth in this region is attributed to the overlap of the Yb^{3+} ($^2F_{7/2}\rightarrow{}^2F_{5/2}$) and Er^{3+} ($^4I_{15/2}\rightarrow{}^2H_{11/2}$) absorption transitions.

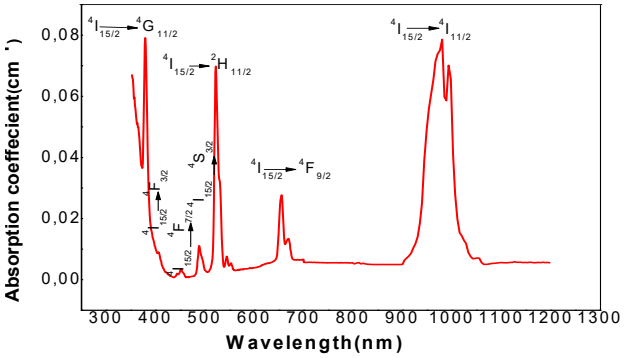

Figure 10. Absorption spectra of LiGd $(WO_4)_2$: 2% Yb^{3+}/ 2% Er^{3+}

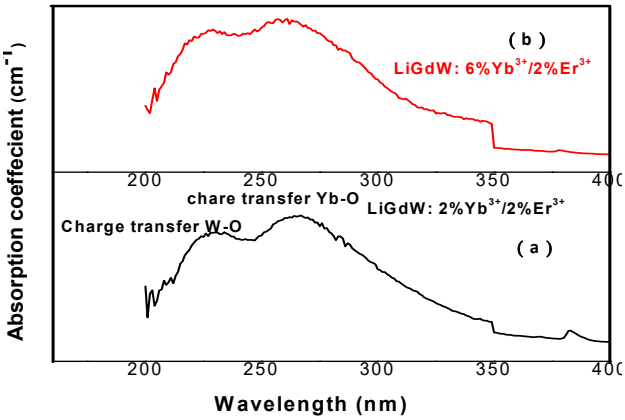

Figure 11. (a) Absorption spectra of LiGd $(WO_4)_2$: 2% Yb^{3+}/2% Er^{3+}, **(b)** Absorption spectra of LiGd $(WO_4)_2$: 6% Yb^{3+}/2% Er^{3+}

3.3.2. Excitation spectrum

Figure 12 shows the excitation spectrum of $LiGd(WO_4)_2xYb^{3+}2\%\ Er^{3+}$ (x=2% and 6%) recorded at room temperature by monitoring the emission at λ_{em}= 550 nm in the 200 and 450 nm wavelength range. The spectra exhibit a strong excitation peak centered at 380 nm, which assigned to the $^4I_{15/2} \rightarrow {}^4G_{11/2}$ transition of Er^{3+}. This result confirms the presence of the same transition observed in the absorption spectra.

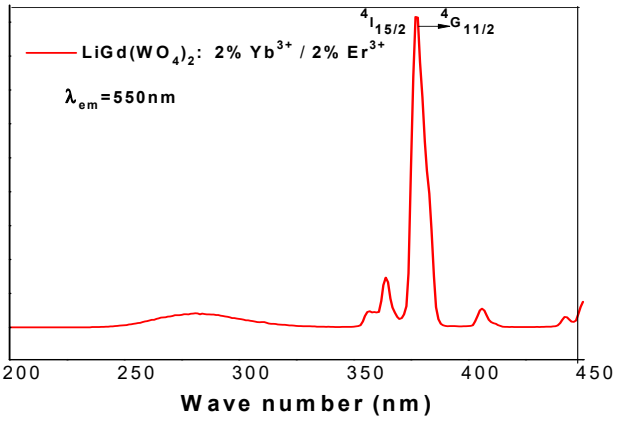

Figure 12. Excitation spectrum of LiGd $(WO_4)_2$: 2% Yb^{3+}/ 2% Er^{3+}.

3.3.3. Down-conversion emission spectra

Figure 13 shows the down-conversion emission spectra of $LiGd(WO_4)_2$: xYb^{3+}/2% Er^{3+} phosphors with x= 2%,6% and 16% under 380 nm excitation. The samples exhibit two green emission bands centered at 532 nm and 550 nm, corresponding to the ($^2H_{11/2} \rightarrow {}^4I_{15/2}$ and $^4S_{3/2}\rightarrow{}^4I_{15/2}$) transitions of Er^{3+} respectively. The intensity of the green emission strongly depends on the Yb^{3+}/Er^{3+}ratio. As the Yb^{3+} concentration increases, cross relaxation (CR) processes become more significant. In particular, the process: $Er^{3+}(^4S_{3/2})+Er^{3+}(^4I_{15/2}) \rightarrow Er^{3+}(^4I_{9/2}) + Er^{3+}(^4I_{13/2})$ partially depopulates the ($^2H_{11/2}$/ $^4S_{3/2}\rightarrow{}^4I_{15/2}$) levels, thereby reducing the probability of the green radiative ($^2H_{11/2}$/ $^4S_{3/2}\rightarrow{}^4F_{9/2}$). Instead, non-radiative relaxation pathways become dominant, leading to a decrease in the population of the $^4S_{3/2}$ level and an increase in the population of the $^4I_{13/2}$ level. At higher dopant concentrations, the down –conversion process is also influenced by phonon assisted energy transfer. The coupling process: $Er^{3+}(^4S_{3/2}) + Yb^{3+}(^2F_{7/2}) \rightarrow Er^{3+}(^4I_{9/2}) + Yb^{3+}$ ($^2F_{5/2}$), further decreases the population of the $^4S_{3/2}$ level while increasing that of the $^4I_{9/2}$ level. Subsequently, the population accumulated in the lower excited states can contribute to the population of the $^4F_{9/2}$ level. For the sample containing 16% of Yb^{3+}, no emission is observed, which is consistent with the XRD results reported previously [12], Moreover, no red emission band corresponding to the $^4F_{9/2} \rightarrow {}^4I_{13/2}$ transition of Er^{3+} is detected in the spectra. This absence of red emission indicates that the multi-phonon relaxation $^4S_{3/2}$ to $^4F_{9/2}$ is not sufficiently efficient to populate the $^4F_{9/2}$ level.

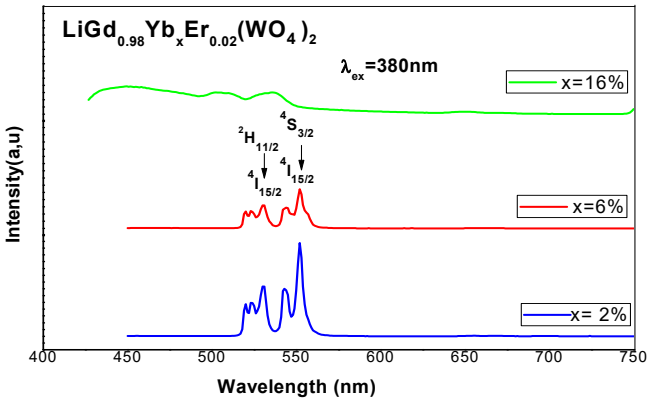

Figure 13. Down-conversion emission spectra of $LiGd(WO_4)_2$: x%Yb^{3+}/ 2%Er^{3+}, (x=2%, 6%, and 16%), excited at 380 nm

Figure 14 presents the down-conversion emission spectra of $LiGd_{1-x}Lux(WO_4)_2$: 1% Yb^{3+}/ 0.4% Er^{3+} phosphors with x= 2.5%, 5%, 80%, 90%, 95% under 380 nm excitation. For the low Lu^{3+} concentrations (x%=2.5%, and 5%), the samples exhibit two green emission bands centered at 521 nm and 541 nm, corresponding to the $^2H_{11/2} \rightarrow {}^4I_{15/2}$ and $^4S_{3/2} \rightarrow {}^4I_{15/2}$ transitions of Er^{3+} respectively. With increasing Lu^{3+} substitution (x = 80%,90%,95%), the emission bands shift slightly 523 and 543 nm, respectively. These values are comparable to those reported in the reference [16], and $LiGd(WO_4)_2$ (LGW) in reference [10,19]. Although the overall shapes of the emission bands remain unchanged, a slight red shift is observed due to the difference in ionic radii and electronegativity between Gd^{3+} and Lu^{3+} ions. These factors induce distortions in the crystal lattice, as discussed in the structural and vibrational studies.

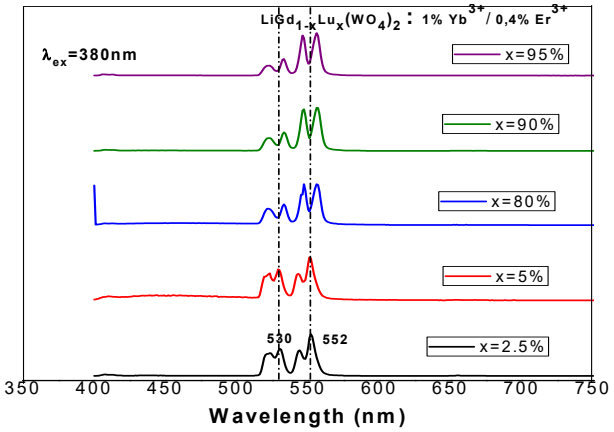

Figure 14. Down-conversion emission spectra of $LiGd_{1-x}Lu_x(WO_4)_2$: 1% Yb^{3+}/ 0.4% Er^{3+}, excited at 380 nm with x= 2.5%, 5%, 80%, 90% and 95%.

3.3.4. Up-conversion emission spectra

Figure 15 shows the up-conversion emission spectra of LiGd $(WO_4)_2$: x% Yb^{3+}/ 2 % Er^{3+} phosphors (x= 2%, 6%, 16%) under 980 nm excitation. The samples exhibit a strong green up-conversion emission bands centered at approximately 550 nm, which is attributed to $^4S_{3/2}$ to $^4I_{15/2}$ transition of Er^{3+} ions.

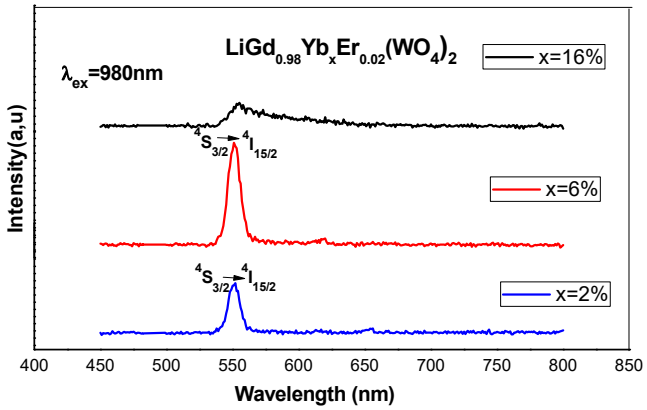

Figure 15. Up-conversion emission spectra of LiGd $(WO_4)_2$:
x% Yb^{3+}/ 0.02% Er^{3+}, (x= 2%, 6%, and 16%) excited by a 980 nm

3.3.5. Fluorescence Decay Kinetics

The fluorescence decay kinetics corresponding to the $^2H_{11/2} \rightarrow {}^4I_{15/2}$ and $^4S_{3/2} \rightarrow {}^4I_{15/2}$ transitions of Er^{3+} ions in the co-doped $LiGd_{1-x}Lu_x(WO_4)_2$ system (with x = 2.5%, 5%, 80%, 90%, and 95%) are presented in Figures 16 (a) and (b). These decays were recorded under an excitation wavelength of 380 nm, with emission monitored at 525 nm and 551 nm, respectively.

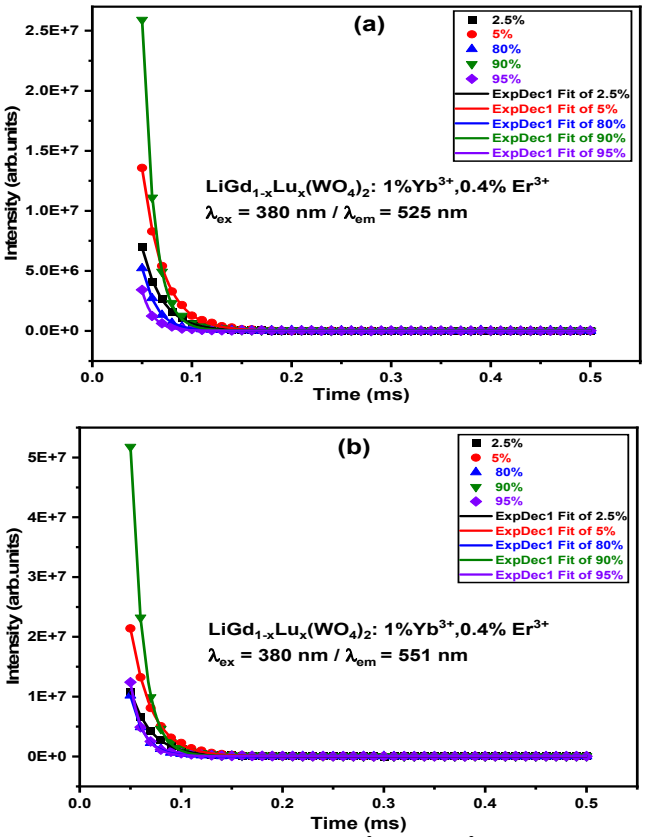

Figure 16. Decay curves of $LiGd_{1-x}Lu_x(WO_4)_2$: 1%Yb^{3+},0.4% Er^{3+} x=2.5%, 5%,80%, 90% and 95% monitored at (a) 525 nm and (b) 551 nm

The emission decay profiles were analyzed by fitting to a single-exponential function of the form:

$$I(t) = I_1 e^{-\left(\frac{t}{\tau_1}\right)} \tag{4}$$

Where *I(t)* denotes the emission intensity at time *t, I_1* is the initial intensity at *t = 0*, and τ_1 represents the corresponding decay lifetime.

The resulting decay lifetimes, along with the associated fitting parameters, are summarized in Table 6. The quality of the fits was satisfactory, as indicated by the goodness-of-fit parameters.

Table 6. Decay times of the $^2H_{11/2}$ and $^4S_{3/2}$ levels in $LiGd_{1-x}Lu_x(WO_4)_2$: 1%Yb^{3+},0.4%Er^{3+}

Lifetime (µs)	x = 2.5%	x = 5%	x = 80%	x = 90%	x = 95%
$^2H_{11/2}$	14.85	14.53	09.48	08.55	08.19
Reduced Chi-Sqr	1.22082E9	4.01423E9	2.1849E9	1.76239E10	1.34711E10
R-Square (COD)	0.99969	0.99974	0.99925	0.99976	0.99667
Adj. R-Square	0.99968	0.99973	0.99921	0.99975	0.99651
$^4S_{3/2}$	14.25	14.86	10.32	08.37	07.62
Reduced Chi-Sqr	9.65152E8	2.21119E9	7.45951E8	6.39374E9	1.44489E9
R-Square (COD)	0.9994	0.99965	0.99906	0.99965	0.99515
Adj. R-Square	0.99937	0.99963	0.99901	0.99963	0.99493

The decay curves show that the $^2H_{11/2}$ and $^4S_{3/2}$ emissions of Er^{3+} in $LiGd_{1-x}Lu_x(WO_4)_2$: 1%Yb^{3+},0.4%Er^{3+} are closely coupled and become progressively shorter-lived as Lu replaces Gd^{3+}. The PL decay behavior therefore indicates that Lu-rich compositions promote more efficient nonradiative or energy-transfer-assisted relaxation, reducing the persistence of green emission under 380 nm excitation [27-30]. There are two primary reasons why these values are less than those of the $LiLu(WO_4)_2$ co-doped Yb^{3+}/Er^{3+} examined in the reference [16]:

1. $LiLu(WO_4)_2$ co-doped with Yb^{3+}/Er^{3+} (24% and 4%), while Yb^{3+}/Er^{3+} (1% and 0.4%) is of lower grade.

2. Yb^{3+}/ Er^{3+} optimal ratio of 6 vs a ratio of 2.5 for $LiGd_{1-x}Lu_x(WO_4)_2$ compounds with x=2.5%, 5%,80%,90%, and 95%. [29].

CONCLUSIONS

In this study, a series of $LiGd_{1-x}Lu_x(WO_4)_2$: Yb^{3+}/Er^{3+} phosphors were successfully synthesized and characterized by XRD, FTIR, Raman spectroscopy, SEM, EDS, PLE and PL) to investigate their structural, vibrational, morphological, and optical properties. The progressive substitution of Gd^{3+} with Lu^{3+} ions, owing to their different ionic radii, induced significant in the crystal lattice. Raman analysis showed that increasing the Lu^{3+} concentration caused the Raman bands to shift toward higher wavenumbers together with a reduction in the full width at half maximum (FWHM), confirming a structural transition from tetragonal to monoclinic phase. The phosphors exhibited intense green up-conversion emissions in the 525-551 nm region, corresponding to the Er^{3+} ($^2H_{11/2}$ / $^4S_{3/2}$ to $^4I_{15/2}$) transitions, resulting from efficient energy transfer from Yb^{3+} sensitizers to Er^{3+} activators. Moreover, increasing the Lu^{3+} concentration produced a slight redshift in the emission bands, and reduced the fluorescence decay times Overall, these results demonstrate that $LiGd_{1-x}Lu_x(WO_4)_2$: Yb^{3+}/Er^{3+} phosphors exhibit up-conversion luminescence, highlighting their potential for advanced optical applications.

Acknowledgments

The authors would like to express their sincere gratitude to the General Directorate of Scientific Research and Technological Development (DGRSDT) to financial support and for facilitating the chemical and physical analyses.
Special appreciation is given to the researchers of the laboratory of Physical-Chemical Inorganic Materials and Their Applications (LPCMIA) at Saad Dahleb University Blida 1 for their valuable support and collaboration.
The authors also extend their thanks to CRTSE (Research Center in Semiconductor Technology for the Energetic) for carring out the optical examinations.

ORCID

Nesrine Naimi, https://orcid.org/0009-0005-0707-9641; **Brahim Rekik,** https://orcid.org/0000-0003-4944-3390
Imane Lanez, https://orcid.org/0000-0001-6758-9583; **Mourad Derbal,** https://orcid.org/0000-0001-9513-7736
Lyes Benharrat, https://orcid.org/0000-0002-6617-2222; **Zohour Bendaoud,** https://orcid.org/0009-0003-5780-3410

REFERENCES

[1] Enachi, O. Toma, and Ş. Georgescu, Journal of Luminescence, **231**, 117816 (2021). https://doi.org/10.1016/j.jlumin.2020.117816
[2] EF. Huerta, J. De Anda, I. Martínez-Merlin, U. Caldiño, and C. Falcony, Journal of Luminescence, **224**, 117271 (2020). https://doi.org/10.1016/j.jlumin.2020.117271
[3] G. Chen, H. Liu, H. Liang, G. Somesfalean, and Z. Zhang, The Journal of Physical Chemistry C, **112**, 12030-12036 (2008). https://doi.org/10.1021/jp804064g
[4] Li, D. Xu, Y. Zhang, H. Lin, S. Yang, Z. Chen, and Y. Shao, Journal of the American Ceramic Society, **99**, 1657-1663 (2016). https://doi.org/10.1111/jace.14141
[5] Wang, X. Chen, M. Xie, H. Lin, Y. Zhou, L. Liu, C. Li, and F. Zeng, Materials Research Bulletin, **94**, 435-441 (2017). https://doi.org/10.1016/j.materresbull.2017.06.038
[6] Shyichuk, S.S. Câmara, I.T. Weber, A.N.C. Neto, L.A. Nunes, S. Lis, R.L. Longo, and O.L. Malta, Journal of Luminescence, **170**, 560-570 (2016). https://doi.org/10.1016/j.jlumin.2015.07.005
[7] Mi, J. Wu, Y. Yang, B. Han, and J. Wei, Scientific reports, **6**, 22545 (2016). https://doi.org/10.1038/srep22545
[8] H. Shi, Y. Zhang, X. Wang, X. Ren, and S. Zhao, Optik, **258**, 168871 (2022). https://doi.org/10.1016/j.ijleo.2022.168871
[9] K.R. Kalimuthu, S.M. Babu, and V. Kalimuthu, Optical Materials, **102**, 109804 (2020). https://doi.org/10.1016/j.optmat.2020.109804
[10] Rekik, G. Alombert-Goget, A. Berthelot, O. Benamara, and K. Lebbou, Journal of Alloys and Compounds, **830**, 154165 (2020). https://doi.org/10.1016/j.jallcom.2020.154165
[11] X.Y. Huang, and G.F. Wang, J. Struct. Chem. **31**, 809–820 (2012).
[12] B. Rekik, M. Derbal, L. Guerbous, D. Ouadjaout, A. Nehari, E. Romeo, A. Brenier, and A.Yoshikawa, Optical Material, **33**, 1638-1642 (2011). https://doi.org/10.1016/j.optmat.2011.04.028
[13] W. ullah Khan, et al., RSC advances, **8**(71), 40693-40700 (2018). https://doi.org/10.1039/c8ra08374f
[14] J. Hanuza, M. Mączka, and JH. Van der Maas, Journal of molecular structure, **348**, 349-352 (1995). https://doi.org/10.1016/0022-2860(95)08660-N
[15] A. Demiaï, M. Derbal, L. Guerbous, and B. Rekik, Optical Materials, **65**, 137-141, (2017). https://doi.org/10.1016/j.optmat.2016.10.026
[16] X. Yun, J. Zhou, Y. Zhu, X. Li, S. Liu, C. Fang, M. Lv, and D. Xu, Journal of Physics and Chemistry of Solids, **163**, 110545 (2022). https://doi.org/10.1016/j.jpcs.2021.110545
[17] Li, et al., Journal of Materials Science: Materials in Electronics, **33**, 12259-12270 (2022). https://doi.org/10.1007/s10854-022-08185-x
[18] V.K. Pandey, V. Rai, V. Kumar, Kumar, and H.C. Swart, Sens Actuators B Chem. **209**, 352-8, (2015). https://doi.org/10.1016/j.snb.2014.11.126
[19] B. Rekik, M. Derbal, O. Benamara, and K. Lebbou, Journal of Crystal Growth, **405**, 11-15 (2014). https://doi.org/10.1016/j.jcrysgro.2014.07.032
[20] J. Hanuza, M. Mączka, and JH. Van der Mass, Journal of Solid State Chemistry, **117**, 177-188 (1995). https://doi.org/10.1006/jssc.1995.1261
[21] F. Bourgeois, Ph.D. Thesis, Lyon 1 University, 2000.
[22] Gallucci, Ph.D. Thesis, Lyon 1 University, 2000.

[23] M. Maczka, J. Hanuza, AF. Fuentes, and U. Amador, Journal of Raman Spectroscopy, **33**, 56-61 (2002). https://doi.org/10.1002/jrs.819
[24] R.F. Klevtsova, and S.V. Borisov, Kristallografiya, **14**, 610-612 (1969). https://doi.org/10.1007/10201585_18
[25] V.A. Efremov, and V.K. Trunov, Russ. J. Inorg. Chem. **19**, 272 (1974). https://doi.org/10.1088/0953-8984/8/44/013
[26] J. Hanuza, L. Macalik, M. Mączka, E.T.G. Lutz, and J.H. Van Der Maas, Journal of molecular structure, **511**, 85-106 (1999). https://doi.org/10.1016/S0022-2860(99)00148-9
[27] I. Lanez, B. Rekik, A. Kezzim, M. Derbal, T. Lanez, and K. Lebbou, Bull. Mater. Sci. **47**, 113 (2024). https://doi.org/10.1007/s12034-024-03194-4
[28] Li, J.G. Li, X. Li, and X. Sun, Ceramics International, **42**, 3268-3274 (2016). https://doi.org/10.1016/j.ceramint.2015.10.118
[29] W. Ahn, and Y.J. Kim, Optical Materials Express, **6**, 1099-1105 (2016). https://doi.org/10.1364/OME.6.001099
[30] R. Yun, J.He, L. Luo, X. Liu, Z. Nie, W. Zhao, and H. Wen, Ceramics International, (2021). https://doi.org/10.1016/j.ceramint.2021.02.180

СТРУКТУРНІ ТА ОПТИЧНІ ВЛАСТИВОСТІ LiGd1-xLux(WO4)2, СПІВЛЕГОВАНОГО Yb3+/Er3+, СИНТЕЗОВАНОГО МЕТОДОМ ТВЕРДОФІЛЬНОЇ РЕАКЦІЇ

Н. Наймі[1], Б. Рекік[1], І. Ланез[1], М. Дербаль[1], Л. Бенхаррат[2], З. Бендауд[1]

[1]Лабораторія LPCMIA, кафедра фізики, факультет природничих наук, Університет Саада Далеба Бліда 1, Бліда, BP 270 Soumaa Road, Бліда, Алжир

[2]Дослідницький центр напівпровідникових технологій для енергетики-CRTSE, 02 Bd. Dr. Frantz Fanon, B.P.140,7 Merveilles, 16038, м. Алжир, Алжир

Подвійні вольфраматні матеріали були ретельно вивчені та привернули значну увагу як твердотільні носії освітлення. Ці матеріали із загальною формулою $AB(WO_4)_2$ (A: лужний метал та B: тривалентний іон рідкісноземельного елемента) широко використовуються завдяки своїм чудовим оптичним властивостям. У цій роботі іони Gd^{3+} були частково заміщені іонами Lu^{3+} для синтезу сполук $LiGd_{1-x}Lu_x(WO_4)_2$ з метою вивчення структурної, коливальної та оптичної поведінки $LiGd_{1-x}Lu_x(WO_4)_2$, легованого іонами Yb^{3+} та Er^{3+}. Використовуючи твердофазну реакцію, для синтезу наших сполук були обрані різні концентрації Lu^{3+} (x=2,5%, 5%, 80%, 90% та 95%). Ці концентрації впливають на коливальні характеристики зв'язку W-O як через розширення зони, так і через зсув симетричної моди валентності (ν1). Щодо оптичних властивостей, у діапазоні 530-552 нм спостерігалося зелене апконверсійне випромінювання при збудженні 980 нм та апконверсійне випромінювання при збудженні 380 нм подвійного вольфрамату, легованого Yb^{3+} та Er^{3+}. Було порівняно та обговорено час життя рівнів $^2H_{11/2}$ та $^4S_{3/2}$, а також вплив заміщення Lu^{3+} на зелене випромінювання Er^{3+} у цих сполуках.

Ключові слова: *подвійний вольфрамат; легування Yb^{3+}/Er^{3+}; Up-конверсія; зелене випромінювання*

East European Journal of Physics. 3. 370-377 (2026)
DOI:10.26565/2312-4334-2026-3-32 ISSN 2312-4334

SYNTHESIS OF NH_4I-DOPED Bi_2Te_3-BASED THERMOELECTRIC MATERIALS IN AN INERT GAS ATMOSPHERE USING AN AUTOMATED SYSTEM

Karimberdi E. Onarkulov[1], Tulanboy M. Azimov[1], Kizlarxon I. Gaynazarova[1], Adkhamjon I. Zokirov[1]*, Nodirbek V. Nosirov[2]
[1]Fergana State University, Fergana, Uzbekistan
[2]Fergana Medical Institute of Public Health, Uzbekistan
**Corresponding Author e-mail: a.zokirov3001@gmail.com*
Received April 27, 2026; revised June 23, 2026; accepted July 3, 2026

This article presents a comprehensive approach aimed at the full automation of the technology for producing semiconductor thermoelectric materials. The main stages of the technological chain are automatic dosing of high-purity raw materials in precise stoichiometric ratios. The combined use of vacuum at 10^{-3} Torr and an inert gas atmosphere (argon at 1.5 atm), holding at a temperature of 720°C for 5–6 hours, crystal growth by the zone melting method, and the cooling (annealing) regime—are analyzed as a single optimized process. The temperature–time profile, diffusion processes, and cooling dynamics are substantiated on the basis of physical models, including Fick's law and Newton's law of cooling. It is shown that real-time control of technological parameters using PLC controllers, SCADA systems, and artificial intelligence algorithms ensures phase homogeneity of the material, reduces defect density, and stabilizes electrophysical parameters. In ammonium iodide–doped Bi_2Te_3 thermoelement samples, the stability of electrical conductivity, the Seebeck coefficient, and the power factor along the entire sample length confirms the homogeneous distribution of dopant additives and the formation of a high-quality crystal structure. The obtained results demonstrate the high potential of the proposed automated technology for the effective application of Bi2Te3-based materials in low- and medium-temperature thermoelectric devices.
Keywords: *Thermoelectric materials; Bi_2Te_3; Automation; Vacuum environment; Inert gas; Zone melting; Annealing; SCADA; PLC; Seebeck coefficient; ZT*

1. INTRODUCTION

Thermoelectric materials can directly convert thermal energy into electrical energy and therefore play an important role in modern energy technologies, space engineering, and microelectronics [1,2]. Achieving high efficiency requires precise control over the material composition, crystal structure, and defect concentration [3]. For this reason, the full automation of thermoelectric material synthesis technologies represents a pressing scientific and practical challenge [4,5,6].

In the fabrication of semiconductor thermoelectric materials, it is crucial to prepare high-purity chemical elements in exact stoichiometric ratios using automated weighing and vacuum dosing systems [7,8,9]. High-purity raw materials, namely Bi-000 and Te-T-B3, were utilized in this process. Such high material purity effectively prevents the formation of secondary phases during synthesis, thereby stabilizing the electrophysical parameters of the resulting material [1,5]. In the production of semiconductor thermoelectric materials, the preparation of high-purity chemical elements in exact stoichiometric ratios using automated weighing systems and vacuum dosing units is of critical importance [4,10]. Accurate control of the raw material composition prevents the formation of secondary phases during subsequent synthesis stages and stabilizes the material's electrophysical parameters [5,11]. In technological processes, the granularity and degree of grinding of the raw materials are also of particular significance [4,6], since the amount of heat required to melt and initiate chemical reactions is directly related to particle size. If the granularity of the raw material is too large, complete melting requires more energy, reducing the efficiency of the technological process. Moreover, high temperatures increase the probability of evaporation of volatile components (such as tellurium or selenium), leading to stoichiometric imbalance in the material composition and degradation of thermoelectric properties [5,11]. Therefore, selecting an optimal grinding degree and controlling it via automated systems are key prerequisites for obtaining high-quality thermoelectric materials [7,8,9].

The synthesis stage is one of the most critical steps in the technology of producing semiconductor thermoelectric materials. This process is typically carried out under vacuum conditions at pressures on the order of 10^{-3} Torr. Such a vacuum level significantly reduces the influence of oxygen and other reactive gases, thereby preventing oxidation of the material [2]. Although partial evaporation of volatile components (e.g., tellurium) may occur under reduced pressure, optimizing the vacuum level minimizes these losses. The vacuum environment enhances diffusion processes during synthesis and ensures melt homogeneity [1,4,6]. As a result, a precursor with optimal chemical and structural properties suitable for subsequent crystal growth is obtained. Therefore, continuous automated control of the temperature–time profile and the vacuum level is a fundamental condition for producing high-quality thermoelectric materials [12,13,14].

Melting is carried out in automated furnaces operating in an inert gas atmosphere. The use of inert gases such as argon prevents oxidation of the material during the reaction process and reduces the loss of volatile components [6].

Cite as: K.E. Onarkulov, T.M. Azimov, K.I. Gaynazarova, A.I. Zokirov, N.V. Nosirov, East Eur. J. Phys. 3, 370 (2026), https://doi.org/10.26565/2312-4334-2026-3-32

During melting, the temperature regime, heating rate, and holding time are precisely controlled using digital controllers [12,13,14], ensuring complete reaction of components and the formation of a homogeneous melt. Automated control systems minimize deviations from preset temperature values, thereby guaranteeing chemical composition stability and phase homogeneity of the synthesized material. Precise control of synthesis parameters reduces stoichiometric deviations and creates optimal conditions for subsequent crystal growth, which directly affects the electrophysical and thermoelectric properties of semiconductor thermoelectric materials.

Accurate control of the temperature–time profile during synthesis is crucial for ensuring melting efficiency and compositional uniformity. The melting process is generally implemented using a stepwise heating regime, where the temperature variation over time can be described by the following relation:

$$T(t) = T_0 + \beta t$$

where (T_0) is the initial temperature, ($\beta = dT/dt$) is the heating rate, and (t) is time.

The optimal heating rate is selected based on the melting temperatures and thermal conductivity properties of the components [4,6]. Excessively high heating rates may lead to thermal instability and localized overheating. Whereas excessively low rates unnecessarily prolong the synthesis process.

Maintaining the material at the maximum melting temperature for a specified duration (isothermal stage) ensures complete melting of components and completion of chemical reactions. Stable temperature conditions during this stage positively influence the stoichiometric accuracy of the material composition [1,4,6].

The performance of thermoelectric materials is closely governed by their structural homogeneity and defect levels. Conventional synthesis techniques often suffer from stoichiometric disruptions due to deviations in the temperature profile, oxidation, and evaporation of volatile elements such as tellurium. Additionally, doping with standard pure iodine introduces significant drawbacks, including high hygroscopicity and a heterogeneous distribution of electrophysical properties across the bulk sample.

In the fabrication of semiconductor thermoelectric materials, the crystal growth stage is a decisive process that determines the microstructure, defect density, and electrophysical properties of the material [1,6]. The zone melting method is widely recognized as one of the most effective techniques for producing high-quality, phase-homogeneous, and low-defect crystals [1,6].

The fundamental principle of this method is to create a localized molten zone within a limited region of the sample and move it along the length of the material at a controlled velocity. As the molten zone travels, recrystallization occurs, resulting in the formation of a solid phase with improved structural quality [1]. The temperature gradient during zone melting plays a critical role: excessively large gradients increase thermal stress and may cause cracking, whereas excessively small gradients can lead to unstable crystal growth. Therefore, the gradient value is optimally selected according to the specific material [1,6].

The velocity of the molten zone is one of the most important parameters of the zone melting process [1,6]. If the zone velocity is too high, there is insufficient time for diffusion, leading to compositional inhomogeneity and increased defect density. Conversely, excessively low velocities prolong the process and reduce technological efficiency. In practice, the zone movement speed is typically selected in the millimeter-per-hour range [1].

An additional advantage of the zone melting method is its ability to achieve compositional purification (zone refining) [1]. Certain impurity elements and contaminant atoms accumulate in the molten zone and are displaced toward the end of the sample during crystal growth. This enables high purity in the main portion of the crystal, which is critically important for thermoelectric materials.

2. METHODS

Conducting the zone melting process under vacuum or an inert gas prevents oxidation and limits the formation of vacancies and defects. Automated control of all parameters—temperature, zone length, movement speed, and ambient pressure—ensures high reproducibility of crystal quality [12,13,14]. As a result, semiconductor thermoelectric crystals obtained by the zone melting technique exhibit high structural homogeneity, low defect density, and stable thermoelectric parameters, making them suitable for use in high-efficiency thermoelectric devices.

The synthesis of semiconductor thermoelectric materials is carried out using a combination of vacuum and inert gas environments (Fig. 1). Initially, the prepared raw materials are placed in a specially designed hermetic container, and the system is evacuated stepwise using vacuum pumps. When the vacuum level reaches approximately 10^{-3} Torr, the container is hermetically sealed. This stage significantly reduces the concentrations of oxygen and other reactive gases in the reaction environment. After evacuation, the container is filled with an inert gas—argon—under a pressure of 1.5 atm [6]. The use of an inert gas atmosphere prevents oxidation of materials during synthesis and limits the loss of volatile components. At the same time, increased inert gas pressure stabilizes evaporation processes during melting.

The container is then placed into an automated high-temperature furnace. The temperature regime is increased gradually until the sample reaches the melting stage. A melting temperature of 720 °C is selected, which is considered optimal for semiconductor thermoelectric materials, particularly bismuth telluride–based compounds [1,6]. The holding time at the melting temperature is set to 5–6 hours to ensure complete melting of the components and completion of chemical reactions [1,4,6]. All temperature–time parameters are controlled with high precision using digital

controllers [12,13,14]. These controllers automatically correct deviations from the set temperature, maintaining thermal stability. Such precise control enhances the homogeneity of the melt composition and creates optimal structural conditions for the subsequent crystal growth stage. Thus, a synthesis process conducted under coordinated vacuum conditions, inert gas pressure, and temperature-time regimes provides a solid foundation for obtaining high-quality materials with stable composition and superior thermoelectric properties.

In the synthesis of semiconductor thermoelectric materials, particularly bismuth telluride–based compounds, the choice of melting temperature directly influences the chemical composition, phase stability, and subsequent crystal structure of the material. The melting point of bismuth telluride is approximately 585°C; therefore, selecting a temperature above this value during synthesis ensures complete melting of the components and the formation of a homogeneous melt [6,7].

This work aims to optimize the synthesis of Bi_2Te_3-based thermoelectric materials into a single, fully automated process governed by PLC controllers, SCADA systems, and artificial intelligence algorithms, ensuring highly stable electrophysical parameters across the entire sample length.

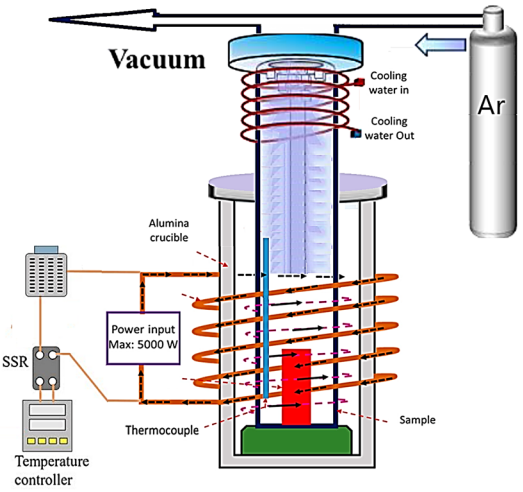

Figure 1. Automated scheme for the technology of obtaining semiconductor thermoelectric materials in a vacuum and inert gas environment during the zone melting process

The choice of 720°C is primarily driven by the need to achieve a high degree of melt homogenization [1,4,6]. At temperatures significantly above the melting point, atomic mobility within the material increases, diffusion processes intensify, and chemical reactions proceed more effectively. This prevents phase imbalance and microscopic segregation during synthesis. Moreover, a temperature of 720°C ensures thermodynamic stability among the material's components. From an energetic perspective, within this temperature range the free energy of the system is minimized, favoring a single-phase state. This creates favorable conditions for the formation of a stable structure during subsequent cooling and crystal growth stages.

Additionally, a temperature of 720°C is considered optimal for limiting the loss of tellurium atoms. An excessive temperature increase may intensify evaporation, leading to compositional imbalance. The selected temperature provides an optimal balance between complete homogenization of the melt and preservation of volatile components [1,6]. Therefore, appropriate temperature selection during the melting process ensures full phase uniformity, optimal diffusion conditions, and compositional stability. These factors play a decisive role in forming high structural quality and stable thermoelectric parameters in semiconductor thermoelectric materials.

3. DISCUSSION

During the synthesis of semiconductor thermoelectric materials, the holding time at the melting temperature is crucial for ensuring the chemical and structural homogeneity of the melt. At 720°C, the melt is maintained for 5–6 hours. At the melting temperature, atomic mobility increases sharply and diffusion between the constituent components becomes significantly enhanced. Fick's law [4,15,16] describes the efficiency of diffusion.

$$J = -D\frac{dc}{dx}$$

where, J - is the diffusion flux, D - is the diffusion coefficient, c - is the concentration, and x - is the spatial coordinate.

The diffusion coefficient is exponentially dependent on temperature, and at higher temperatures, the value of D increases significantly, leading to the elimination of concentration differences between atoms over time. Holding the sample for a specific time, typically 5–6 hours, is sufficient to ensure structural homogenization throughout the material volume [1,4,6,15,16]. During this period, the components fully melt, chemical reactions are completed, and phase inhomogeneities are eliminated. In cases where the holding time is too short, there is an increased likelihood that reactions

will not be fully completed, and microsegregation may persist. Furthermore, excessive extension of the holding time can have negative effects. Prolonged exposure to high temperatures can lead to the evaporation of volatile components, excessive grain growth, and structural instability [1,6]. A 5-6 hour duration ensures an optimal balance between the full completion of diffusion processes and the preservation of the material's composition. Thus, holding the sample at 720 °C for 5–6 hours, considering both thermodynamic and kinetic factors, ensures an ideal initial state for high chemical homogeneity, phase stability, and subsequent crystal growth in semiconductor thermoelectric materials. This plays a crucial role in shaping the high and stable thermoelectric properties of the obtained materials.

4. COOLING AND ANNEALING STAGE

The cooling (annealing) stage that follows the synthesis of semiconductor thermoelectric materials plays a crucial role in forming the material's structural stability, defect density, and electrophysical properties [1,4,6]. After the melting and high-temperature holding process, internal thermal stresses, structural irregularities, and defects (e.g., vacancies and dislocations) develop within the material. The annealing stage is specifically aimed at reducing these negative factors. To slow and control the cooling process, a ceramic container is placed inside the chamber, and a quartz glass tube, approximately 10 mm in diameter and 180–200 mm in length, is positioned within it. This arrangement limits heat exchange and increases the system's overall thermal inertia. Such a construction limits heat exchange, preventing a sharp drop in temperature, and ensures a stable cooling environment for the sample. Both ceramic and quartz are materials with relatively low thermal conductivity, which reduce heat exchange with the external environment and prevent a rapid decrease in temperature. Thermal inertia is physically expressed through the system's "thermal capacitance." The equivalent thermal capacitance for the composite system (ceramic + quartz + sample) is written as follows:

$$C_{eq} = \sum_i m_i c_i$$

Here, m_i denotes the mass of each component (ceramics, quartz, sample), and c_i denotes its specific heat capacity. The larger the value of C_{eq}, the greater the system's resistance to temperature change, meaning the rate of cooling/heating decreases.

The dynamics of the cooling process can be described in a simplified form by Newton's law of cooling [4].

$$\frac{dT}{dt} = -\frac{hs}{C_{eq}}(T - T_{amb})$$

In this context, h - is the convective heat transfer coefficient, s - is the external surface area, T – is the system temperature, and Tamb is the ambient temperature. From this equation, it can be seen that an increase in C_{eq} leads to a decrease in $\frac{dT}{dt}$, meaning that the cooling process slows down. The decrease in heat exchange in the ceramic-quartz combination also influences this trend.

From a practical perspective, the cooling rate should not be too rapid in semiconductor thermoelectric materials to reduce thermal stresses and defect concentrations. In laboratory practices relying on conventional technological guidelines, the optimal cooling rate is selected within the following range [6]:

10–30°C/hour: Suitable for achieving high-quality crystal structure (thermal stresses are minimal, and there is sufficient time for rearrangement).

30–60°C/hour: Accepted when there is a need to shorten technological time, but defect and internal stress risks may increase.

60°C/hour: Generally not recommended (as it approaches the quenching regime, the likelihood of an unbalanced structure and high defect density increases).

Thus, for the ceramic-quartz system, the cooling process can be maintained in the "safest and most efficient" range of 10–30°C/hour by increasing the thermal inertia and limiting heat exchange. This, in turn, improves structural stability, stabilizes the electrophysical parameters, and enhances the overall thermoelectric efficiency (ZT) [5,6].

From a physical standpoint, slow, controlled cooling provides sufficient time for atoms to rearrange themselves into thermodynamically stable states within the crystal lattice. During this process, the system's internal free energy is minimized, and the most energetically favorable configuration of the structure is formed. As a result, deformations in the crystal lattice decrease, and phase stability improves. Diffusion mechanisms play a significant role during the annealing process [16,17]. As the temperature is gradually lowered, atomic mobility does not suddenly disappear but decreases slowly. This allows for the elimination of compositional imbalances, microsegregation, and the homogenization of the structure. In contrast, under very rapid cooling (quenching), atoms "freeze" in an unbalanced state, resulting in a structure with high defect density. The cooling rate also significantly affects the grain size. Controlled annealing leads to moderate grain growth, preventing excessive coarsening or the formation of a very fine-grained structure [16,17]. The optimal distribution of grain sizes balances electrical and thermal conductivities, thereby improving thermoelectric efficiency. The annealing stage is especially crucial for thermoelectric materials, as it stabilizes the concentration and mobility of charge carriers. As a result, parameters such as the Seebeck coefficient, electrical conductivity, and thermal conductivity reach stable values, thereby increasing the overall thermoelectric efficiency coefficient (ZT) [4,6].

5. PROCESS OPTIMIZATION

All synthesis parameters used in the technology for obtaining semiconducting thermoelectric materials—raw material preparation, vacuum and inert gas environments, temperature-time regime, crystal growth, and cooling stages—are interrelated. Therefore, they should be considered not individually, but as a single optimized technological regime. The first stage of the optimized regime involves preparing high-purity elements in precise stoichiometric ratios using automated balances and vacuum dosing systems. The degree of particle size reduction and granularity is set to optimal values that ensure effective heat transfer, thereby reducing energy consumption and the loss of volatile components during the melting process. During synthesis, the container is initially evacuated to a pressure of 10^{-3} Torr, minimizing the influence of oxygen and reactive gases. It is then filled with inert gas (argon) at 1.5 atm pressure to create a chemically stable environment. This combination plays a crucial role in preserving the material's composition and preventing oxidation. The temperature regime for the melting process is set to 720°C, which is maintained for 5-6 hours. This regime ensures complete melting of the components, completion of diffusion processes, and high homogeneity of the melt. Temperature and time parameters are precisely controlled through digital controllers, eliminating thermal irregularities. After melting, crystal growth is carried out in a zone-based method, with temperature gradients and zone movement rates maintained at optimal values. This method allows for compositional purification, reduction of defect density, and improvement of structural uniformity. All parameters are continuously monitored via automated control systems. In the final stage, a controlled annealing process is employed. Slow cooling reduces internal thermal stresses in the material, facilitates the redistribution of defects, and promotes the transition of the structure to a thermodynamically stable state. This contributes to the stabilization of the electrophysical parameters and the achievement of high thermoelectric efficiency.

6. RESULTS

Although the manuscript provides detailed descriptions of raw material preparation, the technological level of vacuum, inert gas pressure, the temperature–time profile of synthesis, and the annealing process, information regarding the technological parameters of crystal growth via the zone melting method—such as temperature gradient, zone length, and zone travel velocity, and their direct influence on crystal dimensions—remains limited. However, investigations aimed at identifying a novel, more effective doping additive that ensures high reproducibility of the material's thermoelectric parameters in both quartz and graphite crucibles have successfully resolved these technological uncertainties. Regardless of the crystal growth parameters, the ammonium iodide NH_4I salt was proposed as a doping agent to ensure superior electrophysical properties and high efficiency of the material.

As a dopant, ammonium iodide possesses several significant technological advantages over conventional pure iodine. It exhibits low hygroscopicity and does not decompose when heated up to 551°C. The material undergoes direct sublimation at 551°C without passing through a liquid phase. Above 551°C, ammonium iodide decomposes according to the following reversible pathways:

$$NH_4 \rightleftarrows NH_3 + HI$$

$$2HI \rightleftarrows H_2 + I_2$$

The released hydrogen iodide, HI, acts as a substantially more active chemical reagent compared to standard iodine. Concurrently, the ammonia (NH3) generated within the system acts as a potent reducing agent, completely eliminating any remaining traces of oxides in the alloy composition. These chemical advantages of ammonium iodide play a decisive role in stabilizing the thermoelectric parameters of the alloys. The optimal thermoelectric performance for thermogenerators was observed when 0.04 mol % of ammonium iodide was introduced into the mixture. Under these conditions, the electrophysical characteristics of the fabricated thermoelements were found to be $\sigma = 1000\ \Omega^{-1}$ and $\alpha = 150\ \mu V/K$, respectively. Since thermoelectric materials operate at elevated temperatures, the temperature dependence of the material's thermoelectric parameters was comprehensively investigated. Figure 3 illustrates the temperature-dependent variations in electrical conductivity, Seebeck coefficient, thermal conductivity, and figure of merit Z for Bi_2Te_3 samples doped with 0.04 mol % ammonium iodide. The average integral value of the material's figure of merit over the temperature range of 20 ÷ 300°C was determined to be $Z = 1.59 \cdot 10^{-3}\ K^{-1}$. This performance indicator demonstrates that high-efficiency, thermally stable materials can be successfully obtained through the proposed modification technology, regardless of the zone-melting method's technological parameters.

The stability of the main thermoelectric parameters along the sample length in Bi_2Te_3-based thermoelements alloyed with ammonium iodide is an important criterion that indicates the high quality of the material synthesis [5,6]. The almost unchanged electrical conductivity, Seebeck coefficient, and power factor in the phase direction suggest a homogeneous distribution of the alloying additions and the absence of significant defects or gradients in the crystal structure [6,7]. This condition confirms that the electron and phonon transport processes have a uniform mechanism throughout the entire sample volume. In particular, the stability of the Seebeck coefficient indicates that the Fermi level remains phase-stable, significantly reducing the possibility of the emergence of internal parasitic electrical driving forces in thermoelectric modules. From this perspective, the results demonstrate that Bi_2Te_3 materials alloyed with ammonium iodide are highly suitable for practical thermoelectric device applications.

Figure 2 clearly shows the stability of the $\alpha^2\sigma$ power factor along the entire length of the thermoelement alloyed with ammonium iodide, and presents the distribution of the main thermoelectric parameters along the sample length.

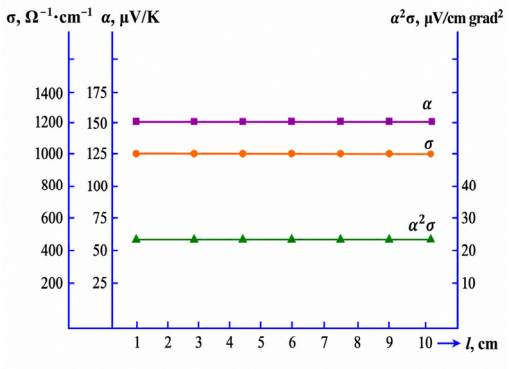

Figure 2. Variation of thermoelectric parameters along the length of a Bi_2Te_3 thermocouple doped with ammonium iodide

The main thermoelectric parameters of the Bi_2Te_3 thermocouple doped with ammonium iodide maintain almost constant values along the length of the sample. This indicates a high degree of structural, compositional and electronic homogeneity of the material. The electrical conductivity is uniform along the entire length [5].

$$\sigma = ne\mu$$

where n is the concentration of charge carriers, μ is the mobility.

The invariance of the electrical conductivity (σ) indicates that the concentration of dopants is uniform along the length, and there is no gradient in the grain boundaries and dislocation density, and the electron-phonon scattering is spatially uniform. This indicates that the Bi_2Te_3 alloy was synthesized technologically correctly.

The value of the Seebeck coefficient α also remains constant along the entire length of the sample. A simplified Mott expression is used for the Seebeck coefficient:

$$\alpha = \frac{\pi^2 k_B^2 T}{3e} \frac{d \ln \sigma(E)}{dE} | E = E_F$$

Here, α depends on the location of the Fermi level, the shape of the band structure, and the asymmetry of the energy conductivity.

The fact that α = const indicates that the Fermi level does not change along the length, the band structure of the material is spatially uniform, and there is no local doping or defect effect [6]. In thermoelectric modules, the spatial instability of α leads to internal EDCs.

Power factor: $PF = \alpha^2\sigma$

The high and stable performance of the Bi_2Te_3 alloy in a real device is of scientific importance. The peculiarities of Bi_2Te_3 thermoelements are that these compounds are characterized by a narrow and complex (divalent) energy band structure. Strong spin-orbit interaction usually causes a nonlinear change in parameters with temperature. However, the absence of such nonlinearity in the spatial coordinate indicates that the band structure is not deformed along the space, there are no internal mechanical stress gradients, and there is no compositional gradient or phase separation.

In Bi_2Te_3-based thermoelectric materials doped with ammonium iodide, the temperature-dependent changes in electrical conductivity, Seebeck coefficient, thermal conductivity, and thermoelectric coefficient of quality are closely related to the electronic band structure of the material. With increasing temperature, changes in the location of the Fermi level and the emergence of bipolar conductivity led to a maximum in the Seebeck coefficient. In this regard, these graphs reveal the importance of Bi_2Te_3 as a highly efficient thermoelectric material in the low- to medium-temperature range.

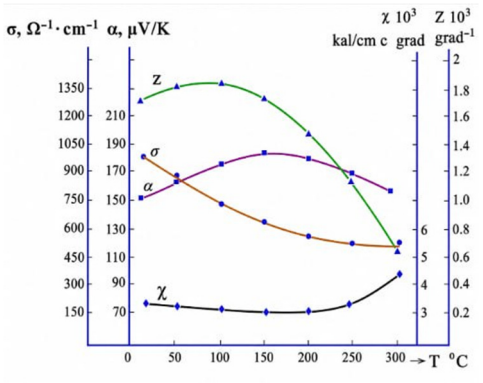

Figure 3. Temperature dependence of thermoelectric parameters of Bi_2Te_3 doped with ammonium iodide

It can be seen from the graph that all the main thermoelectric parameters characteristic of Bi_2Te_3 — electrical conductivity σ(T), Seebeck coefficient α(T), thermal conductivity χ(T) and thermoelectric coefficient of quality Z(T) —

exhibit a complex, interconnected evolution with temperature. This is directly related to the complex band structure and multi-extremum energy spectrum of Bi_2Te_3. Bi_2Te_3 is a semiconductor with a narrow energy gap ($E_g \approx 0.15–0.17$ eV) and has the following features [6,7]. The band structure, with several equivalent extrema in the valence and conduction bands, is characterized by strong anisotropy and a very strong spin–orbit interaction, leading to bipolar conductivity at high temperatures. These factors cause a curvilinear (maximum) character in the temperature dependence of the Seebeck coefficient.

$$\alpha = \frac{1}{eT}\frac{\int (E - E_F)\sigma(E)\left(-\frac{\partial f}{\partial E}\right)dE}{\int \sigma(E)(-\frac{\partial f}{\partial E})dE}$$

where: EF - is the Fermi level, f(E) - is the Fermi–Dirac distribution, and σ(E) - is the energy-dependent permittivity. α is very sensitive to the asymmetry of the energy spectrum and the location of the Fermi level.

For degraded semiconductors (a typical case of Bi_2Te_3), the Seebeck coefficient is written as [5,14]:

$$\alpha = \pm\frac{k_B}{e}\left[\frac{(r+2)F_{r+1}(\eta)}{(r+1)F_r(\eta)} - \eta\right]$$

where r - is the scattering mechanism index, $\eta = \frac{E_F}{k_BT}$ is the reduced Fermi level, Fr(η) - is the Fermi integrals.

In Bi_2Te_3, as temperature increases, η decreases (the Fermi level shifts toward the middle of the bands); the ratio of the Fermi integrals changes; as a result, α(T) first increases and then decreases. At high temperatures, bipolar conductivity begins in Bi_2Te_3. In this case, the Seebeck coefficient is [5]:

$$\alpha = \frac{\alpha_n\sigma_n + \alpha_p\sigma_p}{\sigma_n + \sigma_p},$$

Because the contributions of electrons and holes are of opposite sign, they compensate each other; as a result, the total α decreases. This fully explains the decrease observed in the 200–300°C range in the graph. The curved formation of the Seebeck coefficient is not accidental, but is determined by the zone structure of Bi_2Te_3 narrow gap, multiple zone extrema, strong spin–orbit interaction. The maximum of α(T) is the result of the optimal Fermi level of zone asymmetry. At high temperatures, the bipolar effect sharply limits α and Z. Therefore, materials based on Bi_2Te_3 are considered the most suitable for low and medium-temperature thermoelectric devices [16,17].

CONCLUSIONS

This study developed and scientifically substantiated a comprehensive approach that fully automates the technology for obtaining semiconductor thermoelectric materials. The interrelation of all technological stages, from raw material preparation to synthesis, crystal growth, annealing, and quality control, and the need to implement them within a single optimized regime, was shown. The results of the study show that accurate dosing of high-purity raw materials, the combined use of vacuum and inert gas environments, holding at 720 °C for 5–6 hours, and a controlled cooling regime ensure the homogeneity and phase stability of the material composition. Crystal growth by the zone melting method reduces defect density and increases structural uniformity.

For the first time, the individual stages of thermoelectric material fabrication have been integrated, based on physical models, into a single, optimized, and comprehensive digital technology, controlled in real time via a PLC-SCADA-AI framework. Ammonium iodide NH_4I salt, at a concentration of 0.04 mol %, has been proposed as an alternative doping agent to conventional pure iodine. It was discovered that the ammonia (NH_3) generated during its decomposition acts as a potent reducing agent, completely eliminating residual oxide traces within the alloy. An ideally stable spatial distribution of the Seebeck coefficient and electrical conductivity along the sample length was achieved owing to the spatial invariance of the Fermi level and the absence of deformation of the energy band structure.

It was proven that full automation of the technological process in the production of semiconductor thermoelectric materials is a decisive factor in ensuring the material's structural uniformity. The combined use of vacuum (10^{-3} Torr) and argon atmosphere (1.5 atm) significantly reduced the effect of oxygen, limited oxidation, and minimized the risk of loss of volatile components. Precise control of crystal growth parameters in the zone melting method enhanced structural purification, reduced defect density, and increased the repeatability of crystal quality. The annealing mode reduced internal thermal stresses, created conditions for the structure to transition to a thermodynamically stable state, and ensured stabilization of electrophysical parameters. The near-constant main thermoelectric parameters along the length of Bi_2Te_3 thermocouple samples doped with ammonium iodide confirmed the high degree of homogeneity in the material's synthesis and its suitability for practical application.

Automated control based on PLC–SCADA–AI minimized the human factor and enabled real-time optimization of technological modes; this led to the formation of a stable set of parameters that increased ZT. The optimized technology will play an important role in the development and implementation of high-efficiency thermoelectric devices in the future.

ORCID

Karimberdi E. Onarkulov, https://orcid.org/0000-0002-8916-978X; **Tulanboy M. Azimov,** https://orcid.org/0000-0003-4789-637X;
Kizlarxon I. Gaynazarova, https://orcid.org/0009-0009-7894-0514; **Adkhamjon I. Zokirov,** https://orcid.org/0000-0003-1651-1115;
Nodirbek V. Nosirov, https://orcid.org/0009-0002-8419-7885;

REFERENCES

[1] Liu K., Li Y.-Z., Wu Y., Ying P., He R., Fu C., et al. "Application requirements and design strategies of Bi_2Te_3-based thermoelectric devices for low-quality thermal energy," cMat. 1, e11 (2024). https://doi.org/10.1002/cmt2.11
[2] Ya. Usmonov, M. Nabiyev, Sh. Yakubova, and T. M. Azimov, Intellectual Property Agency under the Ministry of Justice of the Republic of Uzbekistan Patent for an invention Uz FAP № IAP05968 (2019).
[3] Zhang Z., Sun M., Liu J., Cao L., Su M., Liao Q., Deng Y., Qin L. "Ultra-fast fabrication of Bi_2Te_3 based thermoelectric materials by flash-sintering at room temperature combining with spark plasma sintering," Scientific Reports, **12**, 10045 (2022). https://doi.org/10.1038/s41598-022-14405-5
[4] Alrebdi T.A., Wudil Y.S., Ahmad U.F., Yakasai F.A., Mohammed J., Kallas F.H. "Predicting the thermal conductivity of Bi_2Te_3-based thermoelectric energy materials: A machine learning approach," International Journal of Thermal Sciences, **181**, 107784 (2022). https://doi.org/10.1016/j.ijthermalsci.2022.107784
[5] Huang W., Tan X., Cai J., Zhuang S., Zhou C., Wu J., Liu G., Liang B., Jiang J. "Synergistic effects improve thermoelectric properties of zone-melted n-type $Bi_2Te_{2.7}Se_{0.3}$," Materials Today Physics, **32**, 101022 (2023). https://doi.org/10.1016/j.mtphys.2023.101022
[6] Chen M., Mao Z., Ji Y., P.-a. Zong, and Q. Zhang. "Bi_2Te_3-based flexible thermoelectrics," Materials Today Energy, **44**, 101643 (2024). https://doi.org/10.1016/j.mtener.2024.101643
[7] Eker E., Izci D., Ekinci S., Elsayed F.M., Salman M. "A Novel 2-DOF PIDA control strategy with GCRA-based parameter optimization for electric furnace temperature control," PLoS ONE, **20**(10), e0334594 (2025). https://doi.org/10.1371/journal.pone.0334594
[8] ISA (International Society of Automation). ISA-88 Series of Standards — Batch Process Control (ISA-88/ANSI).
[9] Siemens. Engineering and automation of batch processes with PCS 7 along ISA-88 models.
[10] K. Onarkulov, K. Gaynazarova, and D. Tashlanova, "Thermoelectric efficiency is related to the mobility of electrons and holes in alloys.," Science and Innovation, **1**(A4), 56-59 (2022). (in Uzbek)
[11] T. M. Azimov, K. I. Gaynazarova, M. K. Onarkulov, and A. A. Yuldashev. "Thermoelectric and Galvanomagnetic Properties of the Alloy Bi_2Te_3+ 0.04 Weight% Ni in the Temperature Range 77÷ 300 K," Am. J. Mod. Phys. **10**(6), 124-128 (2021). https://doi.org/10.11648/j.ajmp.20211006.12
[12] S. Puthran et al. "Defect-engineered single crystal Bi_2Te_3 via Sb and Se doping for enhanced thermoelectric performance," J. Mater. Sci. **60**(42), 20529-20557 (2025). https://doi.org/10.1007/s10853-025-11567-1
[13] T. Azimov, K. Gajnazarova, and K. Onarkulov. "Method for determining the contact resistance of thermoelements," Euroasian J. Semicond. Sci. Eng. **2**(5), 11 (2020).
[14] O. Karimberdi, Y. Usmanov, and A. Toolanboy. "Semiconductor Sensor for Detecting Volume Changes at Low Temperatures," Eur. J. Mol. Clin. Med. **7**(2), 2353-2358 (2020).
[15] I. S. Ahmadov, Z. S. Aliev, and M. B. Babanly, "Phase equilibria of reciprocal system," Alloys and Compounds Volume 929, 25 December 2022, 167388 (2022). https://doi.org/10.1016/j.jallcom.2022.167388
[16] K. Onarkulov, and T. Azimov, "Study of diffusion processes in contact areas of thermocouples with metals," E3S Web Conf. **376**, 01058 (2023). https://doi.org/10.1051/e3sconf/202337601058
[17] K. Onarkulov, and T. Azimov, "Diffusion processes in contact areas thermoelements based on Pb-Sb alloys," AIP Conf. Proc. **3045**(1), 030096 (2024). https://doi.org/10.1063/5.0197662

СИНТЕЗ ТЕРМОЕЛЕКТРИЧНИХ МАТЕРІАЛІВ НА ОСНОВІ Bi_2Te_3, ЛЕГОВАНИХ NH_4I, В АТМОСФЕРІ ІНЕРТНОГО ГАЗУ З ВИКОРИСТАННЯМ АВТОМАТИЗОВАНОЇ СИСТЕМИ

Карімберді Е. Онаркулов[1], Туланбой М. Азімов[1], Кизлархон І. Гайназарова[1], Адхамжон І. Зокіров[1], Нодірбек В. Носіров[2]

[1]Ферганський державний університет, Фергана, Узбекистан
[2]Ферганський медичний інститут громадського здоров'я, Узбекистан

У цій статті представлено комплексний підхід, спрямований на повну автоматизацію технології виробництва напівпровідникових термоелектричних матеріалів. Основні етапи технологічного ланцюга — автоматичне дозування високочистої сировини в точних стехіометричних співвідношеннях. Спільне використання вакууму при 10^{-3} Торр та атмосфери інертного газу аргону при 1,5 атм, витримка при температурі 720°C протягом 5–6 годин, вирощування кристалів методом зонного плавлення та режим охолодження (відпалу) — аналізуються як єдиний оптимізований процес. Температурно-часовий профіль, процеси дифузії та динаміка охолодження обґрунтовуються на основі фізичних моделей, зокрема законів Фіка та Ньютона. Показано, що керування технологічними параметрами в режимі реального часу за допомогою *PLC*-контролерів, SCADA-систем та алгоритмів штучного інтелекту забезпечує фазову однорідність матеріалу, зменшує щільність дефектів і стабілізує електрофізичні параметри. У зразках термоелементів Bi2Te3, легованих йодидом амонію, стабільність електропровідності, коефіцієнта Зеєбека та коефіцієнта потужності по всій довжині зразка підтверджує однорідний розподіл легуючих добавок і формування високоякісної кристалічної структури. Отримані результати демонструють високий потенціал запропонованої автоматизованої технології для ефективного застосування матеріалів на основі Bi2Te3 у низькотемпературних і середньотемпературних термоелектричних пристроях.

Ключові слова: *термоелектричні матеріали; Bi_2Te_3;автоматизація; вакуумне середовище; інертний газ; зонне плавлення; відпал; SCADA; PLC; коефіцієнт Зеєбека; ZT*

East European Journal of Physics. 3. 378-384 (2026)
DOI:10.26565/2312-4334-2026-3-33 ISSN 2312-4334

EFFECT OF ELECTROLYTE CONCENTRATION AND DISCHARGE FREQUENCY ON Ti-6Al-4V POWDER PARTICLE SIZE DISTRIBUTION OBTAINED BY ECDM

B.A. G'oipov*, A.A. Zaripov, U.F. Berdiyev, Sh.Ch. Iskandarov, T.K. Turdaliev, S.A. Tulaganov

Institute of Ion-Plasma and Laser Technologies named after U.A. Arifov, Academy of Sciences of the Republic of Uzbekistan, 100125, Durmon yuli st 33, Tashkent, Uzbekistan

**Corresponding Author email: goipovbunyod7@gmail.com*

Received April 27, 2026; revised July 31, 2026; accepted August 3, 2026

This study investigates the distribution of Ti-6Al-4V alloy powder microparticles used in 3D printing under different discharge frequencies and NaCl electrolyte concentrations. This work analyzed the process for obtaining monodisperse Ti-6Al-4V alloy powders using the Electrochemical Discharge Machining (ECDM) method. The results showed that an optimal NaCl electrolyte concentration of 30 g/L ensures stable plasma channel formation and a narrow particle size distribution. Regression analysis and low standard error values (0.00386–0.00834) confirm the process's high controllability. The effect of frequency on particle size was also investigated: at 3.2 kHz, the minimum average particle size of 16.598 μm was recorded, whereas increasing the frequency to 32 kHz increased particle size to 28.063 μm due to thermal accumulation. The results indicate that at both 3.2 kHz and 32 kHz frequencies, 58.24% to 68.89% of the produced powders fall within the 15–55 μm range required for PBF-LB/M technology. These findings demonstrate the suitability of the obtained powders for additive manufacturing technologies.

Keywords: *Ti-6Al-4V powder; ECDM; Additive manufacturing; NaCl electrolyte; Electrolyte concentration; Particle size distribution; Frequency; Regression analysis*

INTRODUCTION

The increasing prevalence of orthopedic and dental diseases worldwide has driven steady growth in demand for implants made from biomedical titanium (Ti) and its alloys [1]. Fabricating these implants using additive manufacturing (AM) technologies allows production of 3D shapes with high geometric accuracy while ensuring maximum conformity to individual anatomical structures [2]. Such biocompatible implants are primarily made from the Ti-6Al-4V alloy. Owing to its low thermal conductivity and density, high strength, favorable strength-to-weight ratio, and excellent resistance to temperature and corrosion, Ti-6Al-4V finds wide application in aerospace and defense [3], automotive [4], shipbuilding [5], energy [6], petrochemical industries [7], as well as in medical instruments and implants [8].

In these fields, Ti-6Al-4V alloy powders are used in AM processes, specifically PBF-LB/M (Powder Bed Fusion – Laser Beam/Metal) 3D printing. In these processes, particle shape, chemical purity, and particle size distribution are critical [9], as larger particle sizes reduce the surface area available for laser energy absorption [10], necessitating higher laser energy input [11]. Fine powders allow higher packing density but may increase internal defects in the fabricated part [12].

Metal powders are produced with various size distributions using mechanical [13], chemical [14], and physical [15] methods, often resulting in irregular shapes, rough surface textures, internal porosity, and uneven surface morphology. Furthermore, these production methods require complex equipment and high costs, which can lead to variability in powder flowability [16], density, melting behavior, part surface quality, porosity [17], and mechanical properties [18], as well as increase production costs [19, 20].

The particle size distribution of powders produced by the above methods ranges from 0–250 μm, and in PBF-LB/M powder spreading technologies, particles larger than 45 μm [21] require additional processing [22]. Reprocessing Ti-6Al-4V powders, however, significantly increases oxygen content [23]. To address these limitations, recent studies have increasingly focused on unconventional methods for producing metal powders, particularly via electrical discharge machining (EDM) [24]. This approach enables the production of nano [25] and micro-sized particles of metals [26] and their alloys [27] in dielectric media [28].

An additional advantage of this method is that particle size distribution can be controlled by adjusting the current, frequency [29], discharge energy, and machining depth [30]. To further optimize these parameters, various alloys, metal powders, and salts are added to the dielectric fluid to improve its electrical conductivity, allowing the use of electrolytes instead of conventional dielectric fluids. This method, known as Electrochemical Discharge Machining (ECDM), operates at lower current levels compared to EDM and can reduce energy consumption and costs while preserving particle size distribution [31].

In ECDM, the surrounding medium plays a crucial role, as the machining rate is often closely related to the properties of the medium [32-34]. Although considerable work has been conducted on process efficiency, data on the effect of the

Cite as: B.A. G'oipov, A.A. Zaripov, U.F. Berdiyev, Sh.Ch. Iskandarov, T.K. Turdaliev, S.A. Tulaganov, East Eur. J. Phys. 3, 378 (2026), https://doi.org/10.26565/2312-4334-2026-3-33

medium on particle size distribution remain insufficient [35]. Previous studies have employed fluids that affect the final product quality [36], overly aggressive media [37], or fluids that require high-energy input and increase brittleness in the final product [38]. Based on the above, selecting a fluid medium for ECDM that ensures particle size distribution without affecting the quality of the final product remains a highly pressing challenge [31–38]. This scientific article is devoted to practical solutions to this critical issue.

In this study, the production of Ti-6Al-4V powders using various electrolytes in the ECDM process and the investigation of their particle size distribution are proposed.

EXPERIMENTAL PROCEDURE

The synthesis of Ti-6Al-4V alloy-based powder was carried out on an experimental setup designed for ECDM, the schematic diagram of which is shown in Figure 1. The key feature of the system is a pulsed power supply assembled using high-speed IRG4P50UD IGBT switches and 150EBU04 diodes. This control architecture enables precise adjustment of the process parameters, including voltage amplitude up to 400 V, current up to 20 A, and pulse modulation frequency up to 100 kHz.

To generate a stable spark discharge, the anode was fully immersed in the electrolyte, while the vertically aligned cylindrical cathode, positioned above it, was submerged to a depth of 1–5 mm. The stability of the physicochemical conditions in the reaction zone was maintained by a filtration system and forced circulation of the working fluid. A pump with a flow rate of 2 L/min was used to ensure liquid circulation. This provided efficient heat removal and rapid evacuation of erosion products from the interelectrode gap, preventing thermal degradation of the microstructures, re-melting, and uncontrolled coagulation (agglomeration).

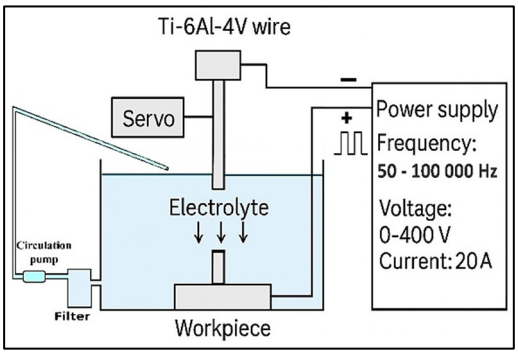

Figure 1. Schematic diagram of the ECDM setup.

For powder production, electrodes with a diameter of 4 mm made of biocompatible Ti-6Al-4V alloy were used. The electrodes were immersed in an aqueous NaCl electrolyte with concentrations of 10–60 g/L, where a negative potential was applied to the cathode and a positive potential to the anode.

As shown in the schematic, the electrodes were submerged in a vessel filled with the working electrolyte (vessel volume: 2 L). A servo system controlled the interelectrode gap and ensured the stability of micro-discharges. Rod electrodes with a diameter of 4 mm fabricated from biocompatible Ti-6Al-4V alloy were employed. During the experiments, a DC voltage of up to 280 V was applied to the system, while the control unit provided pulse generation with frequencies up to 32 kHz. The current was maintained at up to 0.6 A, which allowed stable spark discharge conditions to be sustained.

To prepare the working medium (electrolyte), deionized water with a specific resistivity of 18 MΩ·cm was used. NaCl of chemically pure (“CP”) grade was added to the water at concentrations of 10, 30, and 60 g/L. The amount of reagents was controlled using an analytical balance with an accuracy of ±0.001 g. The applied high-frequency pulsed operating mode enabled direct localization of energy within the spark discharge channel. This minimized undesirable electrolysis effects and ensured the dominant contribution of electro-spark processes in the electrolyte to the formation of the phase composition of microparticles.

The particles formed after discharge were separated from the working solution using a Hittech “EBA 20S” centrifuge at a rotation frequency of 60 s^{-1} for 5 minutes. The obtained precipitate was dried in a FAITHFUL SH-6C drying oven at 70 °C for 24 hours. Particle size distribution was determined using a WJL-602 laser particle size analyzer. This instrument, operating with a He–Ne laser (λ = 632.8 nm), provides measurements in the range of 0.1–800 μm with an accuracy of ±0.5%. The analysis was performed in distilled water at a particle concentration of 1.5–1.7%.

The obtained experimental data were processed and analyzed using OriginPro 9.1 software. The measurement error of the data did not exceed 3%.

RESULTS AND DISCUSSION

Initially, the granulometric analysis of Ti-6Al-4V alloy powder obtained by the ECDM method was performed using a laser particle analyzer (Table 1). The table presents the analysis results of powder particles obtained under identical voltage and current conditions, but at three different NaCl electrolyte concentrations.

Table 1. Granulometric analysis of powder obtained at different concentrations using a laser particle analyzer.

NaCl concentration in deionized water	D_3, µm	D_{10}, µm	D_{50}, µm	D_{av}, µm	D_{90}, µm	D_{97}, µm
10 g/L NaCl	4.585	7.659	25.631	29.082	58.684	78.369
30 g/L NaCl	3.212	4.777	12.909	16.598	30.223	40.372
60 g/L NaCl	4.074	6.405	20.254	23.968	46.727	61.246

For example, the value of 4.585 µm in the D3 column for a 10 g/L NaCl solution indicates that 3% of the particles are smaller than this size. Similarly, the D10, D50, D90, and D97 parameters represent that 10%, 50%, 90%, and 97% of the particles, respectively, are smaller than the given size. Dav denotes the average particle size of the powder.

Based on experiments conducted at different NaCl concentrations and a frequency of 0.32 kHz, the obtained powder samples were analyzed using a laser particle analyzer (Figure 2).

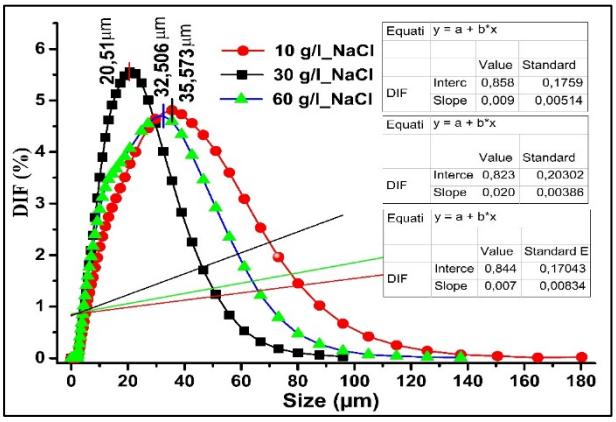

Figure 2. Dependence of particle size distribution on concentration

The graph presents the linear particle size distribution of powders obtained at three different NaCl concentrations (10 g/L, 30 g/L, and 60 g/L), where the X-axis represents particle size and the Y-axis shows the quantitative fraction of particles (differential distribution, DIF %). As can be seen from the graph, the distribution of particles obtained at a 30 g/L concentration is relatively narrow. To quantify the narrowness of the distribution, the initial growth dynamics of the differential distribution (DIF %) were analyzed using a linear regression function (y = a + bx). From a mathematical and statistical perspective, the slope coefficient (Slope) in the graph reflects the intensity of particle formation and growth dynamics. The intercept represents the initial parameter of the linear relationship and is nearly identical for all cases. The standard error indicates the average deviation between experimental measurements.

The results of the linear regression analysis show that at the minimum electrolyte concentration of 10 g/L, the slope coefficient is 0.009, which is a low value. This low value indicates a reduced number of ions, low current density, and low ion mobility, resulting in an unstable plasma channel with localized energy accumulation. This energetic state leads to a significant broadening of the particle size distribution, i.e., polydispersity. This is also confirmed by the large difference between the peak of the differential distribution (DIF = 35.573 µm) and the average particle size (Dav = 29.082 µm, see Table 1).

At the highest electrolyte concentration of 60 g/L, the lowest slope coefficient (0.007) and the highest standard error (0.00834) were recorded. In this case, due to the high concentration, the number of ions increases, current density and ion mobility become higher, and a longer plasma lifetime leads to the formation of larger particles. The average particle size was 23.968 µm, while the maximum DIF peak reached 32.506 µm, indicating a wide particle size distribution.

The graph shows that at 30 g/L concentration, the slope value of 0.02 corresponds to the highest particle growth dynamics, while the standard error of 0.00386 is the lowest. This indicates the most balanced relationship between particle size and their quantitative fraction. The peak of the DIF distribution at 20.51 µm and the average particle size of 16.598 µm (see Table 1) confirm a narrow size distribution.

At this concentration, the ion concentration is sufficient, the electrolyte conductivity and ion mobility are high. The plasma lifetime is short and periodically reproducible. The energy exchange between the plasma channel and electrolyte is optimal, and the balance between discharge energy ensures the preservation of a narrow particle size distribution.

According to the results of the linear regression analysis, electrolyte concentration has a significant effect on particle formation and size distribution. At 10 g/L, low ion activity leads to increased polydispersity, while at 60 g/L, the formation of larger and non-uniform particles is observed. The most balanced condition is achieved at 30 g/L NaCl solution, where the slope and standard error reach optimal values. Under these conditions, a narrow particle size distribution is formed, indicating a monodisperse system. Therefore, 30 g/L NaCl solution is considered the optimal medium for producing stable and uniform Ti-6Al-4V powder particles in the ECDM process.

Based on this, the experimental conditions were optimized, and the granulometric analysis of Ti-6Al-4V alloy powder obtained by the ECDM method at different frequencies was performed using a laser particle analyzer (Table 2).

Table 2. Granulometric analysis of powder obtained at different frequencies using a laser particle analyzer.

№	*f*, kHz	D_{10}, µm	D_{50}, µm	D_{av} µm	D_{90}, µm	S/V, m²/cm³
1.	32	8.883	24.915	28.063	51.497	0.257
2.	3,2	4.777	12.909	16.598	30.223	0.463
3.	0.32	5.971	16.457	18.853	34.989	0.382
4.	0.032	6.154	18.34	21.28	40.232	0.338

The table presents the granulometric analysis results of powder particles obtained at different frequencies under identical voltage and current conditions and a 30 g/L NaCl electrolyte concentration. For example, at 32 kHz, D_{10} = 8.883 µm indicates that 10% of the particles are smaller than this size. Similarly, the D_{50} and D_{90} parameters represent that 50% and 90% of the particles, respectively, are smaller than the given size. The D_{50} value corresponds to the median particle size. Dav represents the average particle size of the powder particles. At the given frequency, the specific surface area to volume ratio is S/V = 0.257 m²/cm³.

As shown in the table, when the frequency increases from 0.032 kHz to 0.32 kHz, the average particle size (Dav) decreases from 21.28 µm to 18.853 µm. At these low frequencies, the number of impulses is low, but each impulse has high energy; in this regime, the plasma channel becomes more stable and the number of impulses increases. With the increase in impulse frequency, the particle size slightly decreases, and the specific surface area to volume ratio increases from 0.338 to 0.382 (see Table 2). This reduction in average particle size is explained by the increase in frequency.

At medium frequencies of 0.32 kHz and 3.2 kHz, the number of impulses is sufficient, and the plasma channel as well as plasma lifetime remain stable. As a result, the average particle size (Dav) decreases from 18.853 µm to 16.598 µm. The decrease in Dav at medium frequencies leads to an increase in S/V from 0.382 to 0.463. This indicates that the reduction in particle size stabilizes, and the role of discharge frequency in particle formation becomes more significant.

At the high frequency of 32 kHz, the increase in the number of impulses leads to stabilization of the plasma channel and localized heat accumulation. As a result, material re-melting and particle aggregation intensify. This causes an increase in the average particle size (Dav) from 16.598 µm to 28.063 µm. Due to particle coarsening, the S/V value decreases from 0.463 to 0.257.

Since Ti-6Al-4V alloy has low thermal conductivity, an increase in discharge frequency initially leads to particle fragmentation, increasing the surface-to-volume ratio (S/V). However, at very high frequencies, localized heat accumulation and re-melting processes intensify, resulting in particle aggregation and a decrease in the S/V value.

The above granulometric analysis results are summarized in a single graph (Figure 3), which illustrates the effect of discharge frequency on particle size and its distribution for powders obtained by the ECDM method.

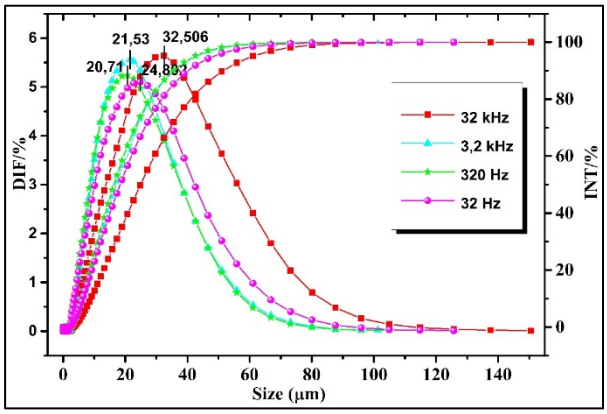

Figure 3. Particle size distribution of powders obtained in 30 g/L NaCl solution at different frequencies

The figure shows the differential (DIF %) and integral (INT %) particle size distributions of powders obtained at a frequency of 32 kHz, where the red curve represents the distribution. The X-axis represents the particle size in the range of 0.1–150.6 µm, while the left Y-axis shows the percentage fraction of particles corresponding to the differential distribution (DIF %). The right Y-axis represents the cumulative particle fraction in the integral distribution (INT %). The particle size distribution increases up to 0.1–32.506 µm, where the DIF peak reaches 5.64%, and in this range the INT distribution reaches 66.45%. After this point, the DIF curve decreases, and the INT value reaches 100% at 150.5 µm. At high frequencies, an increase in particle dispersion is observed, indicating a polydisperse distribution. However, the most suitable fraction for additive manufacturing is concentrated in the 15–45 µm (62.23%) and 15–55 µm (68.89%) ranges, which is higher compared to other samples.

For powders obtained at 3.2 kHz, the blue curve represents the differential (DIF %) and integral (INT %) distributions. The X-axis shows particle sizes in the range of 0.1–101.28 µm, while the left Y-axis indicates the percentage fraction of the most frequently occurring particle sizes. The right Y-axis shows the cumulative integral distribution (INT %). The particle size distribution increases up to 0.1–21.53 µm, where the DIF peak reaches 5.56%, and the INT value reaches 62.04%. After this point, the DIF curve decreases, and the INT distribution reaches 100% at 101.28 µm. The most suitable fraction for 3D printing is concentrated in the 15–45 µm (56.16%) and 15–55 µm (58.24%) ranges.

The analysis of powders obtained at 3.2 kHz and 32 kHz shows that in both cases the DIF and INT distributions confirm the presence of a polydisperse system. At the higher frequency (32 kHz), the particle size distribution is broader, indicating a higher degree of dispersion. At the lower frequency (3.2 kHz), the distribution is narrower and more uniform. In both cases, the most favorable fraction for additive manufacturing is within the 15–55 μm range, confirming its suitability for AM processes.

For powders obtained at 0.32 kHz, the light green curve represents the differential (DIF %) and integral (INT %) distributions. The X-axis covers particle sizes from 0.1–104.96 μm. The left Y-axis shows the percentage of the most frequently occurring particle sizes, while the right Y-axis represents the cumulative INT distribution. The particle size distribution increases up to 0.1–20.71 μm, where the DIF peak reaches 5.24%, and the INT distribution reaches 63.74%. After this point, the DIF curve decreases, and the INT distribution reaches 100% at 104.96 μm. The most suitable fraction for 3D printing is 15–45 μm (53.74%) and 15–55 μm (55.73%).

For powders obtained at 0.032 kHz, the pink curve represents the DIF (%) and INT (%) distributions. The X-axis covers particle sizes from 0.1–125.7 μm. The particle size distribution increases up to 0.1–24.802 μm, where the DIF peak reaches 5.1%, and the INT distribution reaches 66.88%. After this, the DIF curve decreases, and the INT distribution reaches 100% at 125.7 μm. The most suitable fractions for 3D printing are 15–45 μm (56.33%) and 15–55 μm (59.56%).

The granulometric analysis of powders obtained at 0.32 kHz and 0.032 kHz shows that the particle size is widely distributed. As the frequency decreases, the maximum particle size increases, and the distribution range broadens. At the same time, the fraction suitable for 3D printing (15–45 μm and 15–55 μm) remains dominant in both cases, with slightly higher values observed at 0.032 Hz.

The graph shows that discharge frequency significantly affects particle size and its distribution. As the frequency increases from 0.032 kHz to 3.2 kHz, the particle size decreases and the distribution becomes narrower. However, at 32 kHz, due to localized heat accumulation and particle aggregation, the particle size increases again and the distribution becomes broader. The most uniform and finest dispersed powder is obtained at 3.2 kHz.

CONCLUSIONS

The conducted study confirms that electrolyte concentration and discharge frequency strongly influence the granulometric composition and morphology of Ti-6Al-4V alloy powders in the ECDM process. According to linear regression analysis, a 30 g/L NaCl solution is the optimal concentration, where balanced Slope and Standard Error values lead to the formation of a monodisperse particle distribution.

As discharge frequency increases, particles initially undergo fragmentation, increasing the surface-to-volume ratio; however, at very high frequencies, localized heat accumulation and re-melting processes cause particle aggregation, resulting in a broader distribution. A frequency of 3.2 kHz provides a relatively narrow and uniform distribution, whereas at 32 kHz polydispersity increases.

Thus, a 30 g/L NaCl electrolyte solution combined with medium and high-frequency regimes was identified as optimal. Under these conditions, 58.24–68.89% of Ti-6Al-4V powder particles fall within the 15–55 μm range, which is suitable for 3D printing requirements.

Conflict of interest

The authors declare that they have no conflict of interest.

ORCID

B.A. G'oipov, https://orcid.org/0009-0005-3550-7893; **A.A. Zaripov,** https://orcid.org/0000-0003-4964-1776;
U.F. Berdiyev, https://orcid.org/0000-0003-2808-0105; **Sh.Ch. Iskandarov,** https://orcid.org/0000-0002-3002-9141;
T.K. Turdaliev, https://orcid.org/0000-0002-0732-9357; **S.A. Tulaganov,** https://orcid.org/0000-0003-1881-2165

REFERENCES

[1] Kacsó, A. B., & Peter, I. "A Review of Past Research and Some Future Perspectives Regarding Titanium Alloys in Biomedical Applications," Journal of Functional Biomaterials, **16**(4), 144 (2025). https://doi.org/10.3390/jfb16040144

[2] del Bosque, A., Fernández-Arias, P., & Vergara, D. "Titanium Additive Manufacturing with Powder Bed Fusion: A Bibliometric Perspective," Applied Sciences, **14**(22), 10543 (2024). https://doi.org/10.3390/app142210543

[3] Radhika, C., Shanmugam, R., Ramoni, M., & Gnanavel, B. K. "A review on additive manufacturing for aerospace application," Materials Research Express, **11**(2), 022001 (2024). https://doi.org/10.1088/2053-1591/ad21ad

[4] Nyamekye, P., Golroudbary, S. R., Piili, H., Kraslawski, A., & Luukka, P. "Impact of additive manufacturing on titanium supply chain: Case of titanium alloys in automotive and aerospace industries," Advances in Industrial and Manufacturing Engineering, **6**(C), 100112 (2023). https://doi.org/10.1016/j.aime.2023.100112

[5] Zhang, A., Li, Y., Xu, Q., Zhang, B., Qu, P., & Chen, W. "Application Status and Prospect of Titanium Alloys for Pressure-Resistant Structure of Deep-Sea Manned Equipment," Ship & Boat, **35**(06), 81 (2024). https://doi.org/10.19423/j.cnki.31-1561/u.2024.06.007

[6] Iskandarov, S. C., Khudaykulov, I. K., Turdaliev, T. K., Berdiyev, U. F., Tulaganov, S. A., & Kakhramonov, B. R. "Effect of TiO_2 Layer Thickness on Electrode Degradation in Redox Flow Batteries," East European Journal of Physics, (4), 601-606 (2025). https://doi.org/10.26565/2312-4334-2025-4-63

[7] Wang, L., Zhao, X., Wang, X., Shang, S., Xiu, Z., Xi, Y., *et al*., "Current Status Review of Corrosion Resistance Applications of Titanium Alloys in the Petroleum Industry," Coatings, **14**(8), 941 (2024). https://doi.org/10.3390/coatings14080941

[8] Kumawat, S., Deshmukh, S.R., & Ghorpade, R.R. "Fabrication of Ti-6Al-4v cellular lattice structure using selective laser melting for orthopedic use: a review," Materials Today: Proceedings, **113**, 166-172 (2024). https://doi.org/10.1016/j.matpr.2023.08.053
[9] Yim, S., Minowa, K., Yamanaka, K., & Chiba, A. "Influence of particle size distribution on the powder bed quality in the powder bed fusion additive manufacturing process," Journal of Materials Research and Technology, (2025). https://doi.org/10.1016/j.jmrt.2025.06.136
[10] X.X. Yao, and Z. Zhang, "Laser-particle interaction-based heat source model of laser powder bed fusion additive manufacturing," Opt. Laser Technol. **155**, 108402 (2022). https:// doi. org/ 10. 1016/j. optla stec. 2022. 108402
[11] Xue, M., Chen, X., Ji, X., Xie, X., Chao, Q., & Fan, G. "Effect of particle size distribution on the printing quality and tensile properties of Ti-6Al-4V alloy produced by LPBF process," Metals, **13**(3), 604 (2023). https://doi.org/10.3390/met13030604
[12] Soltani-Tehrani, A., Yasin, M. S., Shao, S., Haghshenas, M., & Shamsaei, N. Effects of powder particle size on fatigue performance of laser powder-bed fused Ti-6Al-4V. Procedia Structural Integrity, **38**, 84-93 (2022). https://doi.org/10.1016/j.prostr.2022.03.010
[13] Çuvalcı, O., Varol, T., Akçay, S. B., Güler, O., & Çanakçı, A. "Effect of ball mill time and wet pre-milling on the fabrication of Ti powders by recycling Ti machining chips by planetary milling," Powder Technology, **426**, 118637 (2023). https://doi.org/10.1016/j.powtec.2023.118637
[14] Mendez-Lozano, N., Apátiga-Castro, M., Soto, K. M., Manzano-Ramírez, A., Zamora-Antuñano, M., & Gonzalez-Gutierrez, C. "Effect of temperature on crystallite size of hydroxyapatite powders obtained by wet precipitation process," Journal of Saudi Chemical Society, **26**(4), 101513 (2022). https://doi.org/10.1016/j.jscs.2022.101513
[15] Wu, J., Xia, M., Wang, J., Zhao, B., & Ge, C. "Effect of electrode induction melting gas atomization on powder quality: satellite formation mechanism and pressure," Materials, **16**(6), 2499 (2023). https://doi.org/10.3390/ma16062499
[16] Sojoodi, M., Behvar, A., Bajaj, H., Mohajerani, S., Vanaei, S., Taheri Andani, N., *et al*., "Integration of Circular Economy into Metal Additive Manufacturing: A Review of Ultrasonic Plasma Atomization for Producing Virgin and Recycled NiTi Powder," Shape Memory and Superelasticity, 1-41 (2025). https://doi.org/10.1007/s40830-025-00589-y
[17] Muthuswamy, P. "Influence of powder characteristics on properties of parts manufactured by metal additive manufacturing," Lasers in Manufacturing and Materials Processing, **9**(3), 312-337 (2022). https://doi.org/10.1007/s40516-022-00177-3
[18] Tammas-Williams, S., Withers, P. J., Todd, I., & Prangnell, P. B. "Porosity regrowth during heat treatment of hot isostatically pressed additively manufactured titanium components," Scripta Materialia, **122**, 72-76 (2016). https://doi.org/10.1016/j.scriptamat.2016.05.002
[19] Ludwig, I., & Kluge, M. "Investigation of an Increased Particle Size Distribution of Ti-6Al-4V Powders Used for Laser-Based Powder Bed Fusion of Metals," Materials, **17**(12), 2942 (2024). https://doi.org/10.3390/ma17122942
[20] Lanzutti, A., & Marin, E. "The challenges and advances in recycling/re-using powder for metal 3D printing: A comprehensive review," Metals, **14**(8), 886 (2024). https://doi.org/10.3390/met14080886
[21] Islam, S. F., Hawkins, S. M., Meyer, J. L., & Sharman, A. R. "Evaluation of different particle size distribution and morphology characterization techniques," Additive Manufacturing Letters, **3**, 100077 (2022). https://doi.org/10.1016/j.addlet.2022.100077
[22] Zhang, S., Guo, K., Qing, Y., & Liu, C. "Research progress on the preparation technology of spherical alloy powders for laser additive manufacturing," Materials, **18**(14), 3385 (2025). https://doi.org/10.3390/ma18143385
[23] Lewis, G. "Aspects of the powder in metal additive manufacturing: a review," World Journal of Engineering and Technology, **10**(2), 363-409 (2022). https://doi.org/10.4236/wjet.2022.102022
[24] Dwivedi, A. P., & Choudhury, S. K. "A Brief Study of the Particulate Matter Emissions During the EDM Process," in: *Green Buildings and Sustainable Engineering*, Springer, 2019. https://doi.org/10.1007/978-981-13-1202-1_39
[25] Wang, J., Sánchez, J. A., Wang, Z., Izquierdo, B., & Ayesta, I. "Observations on debris composition and size distribution in WEDM," Procedia CIRP, **95**, 331-336 (2020). https://doi.org/10.1016/j.procir.2020.02.323
[26] Oßwald, K., Woidasky, J., Hoffmann, A. M., & Moser, M. "Suitability of electrical discharge machining debris particles for usage as a powder for selective laser melting: an explorative study," Progress in Additive Manufacturing, **4**(4), 443-449 (2019). https://doi.org/10.1007/s40964-019-00080-y
[27] Rahmati, A., Abdullah, A., & Esmailnia, K. "Metal nanopowder production by cryogenic mechanical collision and pulsed electric discharge methods," (2021). arXiv preprint arXiv:2112.03055.
[28] Singh, A. K., Mahajan, R., Tiwari, A., Kumar, D., & Ghadai, R. K. "Effect of dielectric on electrical discharge machining: a review," in: *IOP Conference Series: Materials Science and Engineering*, **377**(1), 012184 (2018). https://doi.org/10.1088/1757-899X/377/1/012184
[29] Murti, V. S. R., & Philip, P. K. "An analysis of the debris in ultrasonic-assisted electrical discharge machining," Wear, **117**(2), 241-250 (1987). https://doi.org/10.1016/0043-1648(87)90258-4
[30] Khanra, A. K., Pathak, L. C., & Godkhindi, M. M. "Microanalysis of debris formed during electrical discharge machining (EDM)," Journal of Materials Science, **42**(3), 872-877 (2007). https://doi.org/10.1007/s10853-006-0020-0
[31] Painuly, M., Singh, R. P., & Trehan, R. "Electrochemical machining and allied processes: a comprehensive review," Journal of Solid State Electrochemistry, **27**(12), 3189-3256 (2023). https://doi.org/10.1007/s10008-023-05610-x
[32] Zhang, S., Zhou, J., Hu, G., Wang, L., & Xu, Y. "Process characteristics of electrochemical discharge machining and hybrid methods: a review," The International Journal of Advanced Manufacturing Technology, **129**(5), 1933-1963 (2023). https://doi.org/10.1007/s00170-023-12452-4
[33] Ben Mhahe, F., Zhang, Y., Chen, C., & Umoren, W. I. "Investigation of the influence of different types of electrolytes on the performance of the Electrochemical Discharge Machining process during micromachining of molybdenum," International Journal of Electrochemical Science, **19**(7), (2024). https://doi.org/10.1016/j.ijoes.2024.100647
[34] Rao, P. S., Sharma, V., Kumar, H., & Sushma, S. P. "Electro-Chemical Machining of Titanium Alloys and Various Composites for Efficient Machining Process: A Critical Review," Fabrication Techniques and Machining Methods of Advanced Composite Materials, 68-81 (2024).
[35] Zhang, L., Kong, L., Lei, W., & Li, Q. "Review of electrochemical discharge machining technology for insulating hard and brittle materials," Journal of the Brazilian Society of Mechanical Sciences and Engineering, **46**(3), 143 (2024). https://doi.org/10.1007/s40430-024-04739-8

[36] Singh, J., Kant, R., Nimesh, A., Katiyar, N., & Bhattacharya, S. "Evaluating electrochemical micromachining capabilities for industrial applications: A review," Materials and Manufacturing Processes, **39**(1), 1-42 (2024). https://doi.org/10.1080/10426914.2023.2219304
[37] Upadhyay, R. K. "Challenges and control strategies for disrupting passive oxide layer formation in electrochemical machining," Journal of Electrochemical Science and Engineering, **15**(5), (2025). http://dx.doi.org/10.5599/jese.2796
[38] Prakash, A., Kumar, A., & Ballav, R. "Process capability of electrochemical discharge machining: a review," Proceedings of the Institution of Mechanical Engineers, Part L: Journal of Materials: Design and Applications, **238**(2), 282-300 (2024). https://doi.org/10.1177/14644207231218386

ВПЛИВ КОНЦЕНТРАЦІЇ ЕЛЕКТРОЛІТУ ТА ЧАСТОТИ РОЗРЯДУ НА РОЗПОДІЛ РОЗМІРІВ ЧАСТИНОК ПОРОШКУ Ti-6Al-4V, ОТРИМАНОГО МЕТОДОМ ECDM

Б.А. Гоїпов, А.А. Заріпов, У.Ф. Бердієв, Ш.Ч. Іскандаров, Т.К. Турдалієв, С.А. Тулаганов
Інститут іонно-плазмових та лазерних технологій імені У.А. Аріфова Академії наук Республіки Узбекистан, 100125, вул. Дурмон йулі, 33, Ташкент, Узбекистан

Метою цього дослідження є вивчення розподілу мікрочастинок порошку сплаву Ti-6Al-4V, що використовуються в 3D-друку, за різних частот розряду та концентрацій електроліту NaCl. У цій роботі проаналізовано процес отримання монодисперсних порошків зі сплаву Ti-6Al-4V за допомогою методу ECDM. Результати показали, що оптимальна концентрація електроліту NaCl становить 30 г/л, що забезпечує стабільне формування плазмових каналів і вузький розподіл розмірів частинок. Регресійний аналіз і низькі значення стандартної похибки (0,00386–0,00834) підтверджують високу керованість процесу. Також досліджувався вплив частоти на розмір частинок: при частоті 3,2 кГц було зафіксовано мінімальний середній розмір частинок — 16,598 мкм, тоді як збільшення частоти до 32 кГц призвело до зростання розміру частинок до 28,063 мкм через теплове накопичення. Результати показують, що як на частотах 3,2 кГц, так і 32 кГц від 58,24% до 68,89% вироблених порошків потрапляють у діапазон 15–55 мкм, необхідний для технології PBF-LB/M. Ці результати демонструють придатність отриманих порошків для технологій адитивного виробництва.

Ключові слова: *порошок Ti-6Al-4V; ECDM; адитивне виробництво; електроліт NaCl; концентрація електроліту; розподіл розмірів частинок; частота; регресійний аналіз*

EAST EUROPEAN JOURNAL OF PHYSICS. 3. 385-390 (2026)
DOI:10.26565/2312-4334-2026-3-34 ISSN 2312-4334

XRD STUDY OF PHASE EVOLUTION IN ELECTROSPUN PVDF NANOFIBERS AT DIFFERENT CNT/β-Ga_2O_3 RATIOS

S.A. Ahmadova[1], G.B. Ibragimov[1], O.A. Samedov[1], M.A. Yuldoshev[2]*, N.A. Sattarov[3], K.M. Hasanov[1,4], Y.I. Aliyev[5,6], A.S. Abiyev[7,8]

[1]*Institute of Physics, Ministry of Science and Education Republic of Azerbaijan, Baku, AZ1143*
[2]*Turan International University, Namangan, Uzbekistan*
[3]*Kimyo International University in Tashkent, Namangan, Uzbekistan*
[4]*Low Dimensional Materials Research Center at Khazar University, Baku, AZ1096, Azerbaijan*
[5]*Azerbaijan State Pedagogical University, AZ-1143, Baku, Azerbaijan*
[6]*Western Caspian University, AZ-1001, Baku, Azerbaijan*
[7]*Nuclear Research Department of IDDA, Baku, AZ-1073, Azerbaijan*
[8]*Azerbaijan Architecture and Construction University, Baku, AZ1073, Azerbaijan*
**Corresponding Author e-mail: murod.yuldoshev1993@gmail.com*
Received May 23, 2026; revised August 8, 2026; accepted August 20, 2026

Electrospun poly(vinylidene fluoride) (PVDF)-based nanofibrous mats containing carbon nanotubes (CNTs) and β-Ga_2O_3 nanoparticles were fabricated to investigate composition-dependent phase evolution in the PVDF matrix. Pristine PVDF and composite mats with CNT/β-Ga_2O_3 ratios of 1:1, 1.5:0.5, and 0.5:1.5 wt% were prepared under identical electrospinning conditions using a DMF/acetone solvent system. The crystalline structure and phase composition were studied by X-ray diffraction with Co Kα radiation. The pristine PVDF mat exhibited a multiphase structure composed of α, β, and γ phases. After the incorporation of CNTs and β-Ga_2O_3, clear composition-dependent changes in diffraction peak position and intensity were observed. The 1:1 composition reduced the α-phase contribution and enhanced the γ-phase reflections, while the β phase remained dominant. Increased CNT content favored β-phase development, whereas increased β-Ga_2O_3 content promoted γ-phase formation. The results indicate that CNTs mainly support β-phase stabilization, while β-Ga_2O_3 has a stronger effect on γ-phase evolution and structural rearrangement. These findings show that the crystalline phase balance of electrospun PVDF nanofibers can be effectively tailored by controlled CNT/β-Ga_2O_3 incorporation.
Keywords: *Polyvinylidene fluoride; Beta-gallium oxide; Carbon nanotube; Composite materials; XRD*

INTRODUCTION

In recent years, functional polymer nanocomposites have become a major focus of materials science, since these systems make it possible to combine the flexibility, processability, and mechanical durability of the polymer matrix with the electrical, thermal, and structural advantages of inorganic and nanocarbon fillers [1-3]. In this regard, poly (vinylidene fluoride) (PVDF) is a semicrystalline fluoropolymer distinguished by its high chemical and thermal stability, flexibility, and favorable dielectric, piezoelectric, and pyroelectric properties, which provide broad application potential in sensors, actuators, capacitors, energy harvesting systems, and functional composites [4]. Current studies indicate that PVDF is an important fluoropolymer characterized by outstanding piezoelectric properties, thermal stability, and mechanical strength, providing both structural integrity and functional electrical response. The technological significance of PVDF arises from the combination of its piezoelectric and pyroelectric properties with mechanical, chemical, and thermal stability. PVDF is a semicrystalline thermoplastic fluoropolymer distinguished by high dielectric performance, electroactivity, and engineering durability, and is therefore widely used in energy-related applications, sensing, and functional composites. It is a well-known organic ferroelectric polymer and, due to its thermal and chemical stability, has been successfully applied in sensors, actuators, capacitors, and binder systems. Piezoelectric polymers of the PVDF/PVDF- trifluoroethylene (TrFE) type offer advantages such as simple processing, lightweight and thin structures, chemical resistance, low environmental sensitivity, and biocompatibility. PVDF is a multiphase material and can exist in the α, β, γ, and δ crystalline modifications; among these phases, the β-phase is considered particularly valuable from a functional point of view because of its high polarity and electro-activity [5].

It is well known that the α-phase is a non-polar modification that is readily obtained from the melt, whereas the formation of the β-phase or the α→β transformation is one of the main research directions in the development of PVDF-based functional materials, and this transformation can be enhanced through annealing, stretching, and the incorporation of suitable fillers. At the same time, studies show that within a composite system PVDF acts not only as a passive matrix, but also as an active functional polymer medium that improves surface smoothness, interfacial quality, and the overall piezoelectric response. In recent years, among the semiconductor- and nanocarbon-based

Cite as: S.A. Ahmadova, G.B. Ibragimov, O.A. Samedov, M.A. Yuldoshev, N.A. Sattarov, K.M. Hasanov, Y.I. Aliyev, A.S. Abiyev, East Eur. J. Phys. 3, 385 (2026), https://doi.org/10.26565/2312-4334-2026-3-34

fillers introduced into PVDF, Ga_2O_3 and carbon nanotubes (CNTs) have attracted particular interest. Owing to its wide band gap of approximately 4.2–5.3 eV, high breakdown field, and favorable electron transport characteristics, Ga_2O_3 has emerged as a promising semiconductor material for high-temperature electronics, ultraviolet photodetectors, gas sensors, and radiation-resistant devices [6-9]. Zhang demonstrated the advantages of Ga_2O_3 in a power diode with record performance and confirmed its strong potential for high-voltage electronics with a breakdown voltage of 8.32 kV. Although several polymorphs of Ga_2O_3 are known, β-Ga_2O_3 is considered the most thermodynamically stable phase, and under high-temperature conditions the other modifications also tend to transform into this phase [10]. On the other hand, CNTs are regarded as one of the most promising nanofillers for PVDF due to their low mass density, high aspect ratio, large specific surface area, high electrical and thermal conductivity, and superior mechanical strength, and they not only create a conductive network within the composite but can also promote β-phase formation, heterogeneous nucleation, and the α→β transformation under appropriate dispersion and functionalization conditions [11, 12]. In addition, CNT incorporation can enhance the mechanical properties, increase the development of the trans/β-oriented structure, and sharply improve electrical conductivity because of the low percolation threshold, although excessively high loading may lead to agglomeration, porosity, and brittleness, resulting in deterioration of the properties. Therefore, the combined use of β-Ga_2O_3 and CNTs within the same PVDF matrix may be considered a favorable approach for obtaining multifunctional composite systems that exhibit a synergistic effect in terms of electron transport, interfacial interaction, mechanical stability, and phase regulation [13,14].

For such composite systems, PVDF nanofibrous mats produced by electrospinning are of particular importance because their large surface area and porous structure enable more efficient distribution of fillers such as CNTs and β-Ga_2O_3 along the fibers, thereby allowing the simultaneous tuning of electrical and structural properties. Nevertheless, accurate analysis of the phase composition and crystallographic structure is essential for a proper understanding of the interaction of fillers with the polymer matrix, the crystallization behavior, and the phase balance in composite nanofibrous materials [15]. In addition, structural defects such as vacancies, dislocations, lattice distortions, and interfacial defects can significantly influence the crystallization behavior, phase stability, and functional properties of polymer-based nanocomposites, and the investigation of these defects by structural analysis methods is important for understanding structure–property relationships. In this respect, X-ray diffraction (XRD) is one of the most reliable structural analysis methods for a wide class of materials ranging from nanopowders and metal alloys to ceramics, composite coatings, and nanofibrous systems, particularly for determining phase composition, identifying crystal structure, and evaluating the degree of crystallinity. Through XRD analysis, structural features such as the formation of new phases, phase transformations, changes in lattice parameters, texture, crystallite size, and microstrain can be monitored, which makes it possible to substantiate the relationship between preparation conditions, filler concentration, modification processes, and functional properties [16].

However, although numerous studies on PVDF-based composites have been reported in the literature, the combined and concentration-dependent effect of β-Ga_2O_3 and CNTs, particularly with respect to structural phase transformation and β-phase formation, remains insufficiently explored in a systematic and comparative manner. In most of the existing studies, these components have either been investigated separately or only their general electrical, dielectric, or mechanical effects have been evaluated. In contrast, the incorporation of β-Ga_2O_3 and CNTs into PVDF at different ratios can modify dispersion, interfacial interaction, crystallization behavior, and phase balance in different ways. Therefore, investigating the changes induced in the structure and functional properties of the PVDF matrix as a function of additive concentration is of considerable importance from both fundamental and applied perspectives.

EXPERIMENTAL PART

This study employed β-Ga_2O_3 nanopowder purchased from Sigma-Aldrich, characterized by a monoclinic crystal structure (space group C2/m), a purity exceeding 99.99%, an average particle size of approximately 20 nm, and a true density of 5.88 g/cm^3. Carbon nanotubes (CNTs) with a minimum purity of 99% were used as the conductive filler. The CNTs had a specific surface area of approximately 700 m^2/g, an average tube diameter of approximately 0.84 nm, and a material density of 1.7–1.9 g/cm^3 at ambient temperature. Here, the material density refers to the density of the CNT material itself, whereas the reported bulk density of approximately 0.1 g/cm^3 refers to the apparent density of the CNT powder, including the interparticle void space, prior to its incorporation into the composite. Poly(vinylidene fluoride) (PVDF) powder, supplied by BLD Pharm (China), served as the polymer matrix and had a molecular weight of 6.0×10^5 g/mol. For preparation of the electrospinning solution, a mixed solvent system consisting of N,N-dimethylformamide (DMF, 99.8%, Sigma-Aldrich, Germany) and acetone (99.9%, PanReac AppliChem, Spain) was used.

Composite nanofibrous samples were prepared using poly(vinylidene fluoride) (PVDF) as the polymer matrix, with gallium oxide (β-Ga_2O_3) and carbon nanotubes (CNTs as functional additives (Fig.1.)). The XRD pattern of the β-Ga_2O_3 nanopowder and CNT was recorded at room temperature using Cu Kα radiation (λ = 1.5406 Å), whereas the pristine and composite PVDF nanofibrous samples were measured using Co Kα (λ = 1.7890 Å) radiation. The corresponding diffraction patterns were analyzed in their respective 2θ ranges for phase identification and comparison. Electrospinning was carried out onto aluminum foil substrates with a thickness of 14.2 ± 0.5 μm. A mixed solvent

system consisting of N,N-dimethylformamide and acetone in a 60:40 volume ratio was employed, and the PVDF concentration in the spinning solution was fixed at 10 wt%. The total content of CNT and β-Ga_2O_3 additives did not exceed 2 wt% relative to the PVDF mass. Different composite compositions were fabricated to examine the effect of additive ratio, namely 1 wt% CNT–1 wt% β-Ga_2O_3, 0.5 wt% CNT–1.5 wt% β-Ga_2O_3, and 1.5 wt% CNT–0.5 wt% β-Ga_2O_3, along with a pristine PVDF sample prepared under identical conditions for comparison. Prior to polymer addition, CNT and β-Ga_2O_3 powders were dispersed in the solvent mixture via ultrasonic treatment at 23.59 kHz for 15 min, after which PVDF was added and the suspension was magnetically stirred at 300 rpm for 1 h to obtain a homogeneous electrospinning solution.

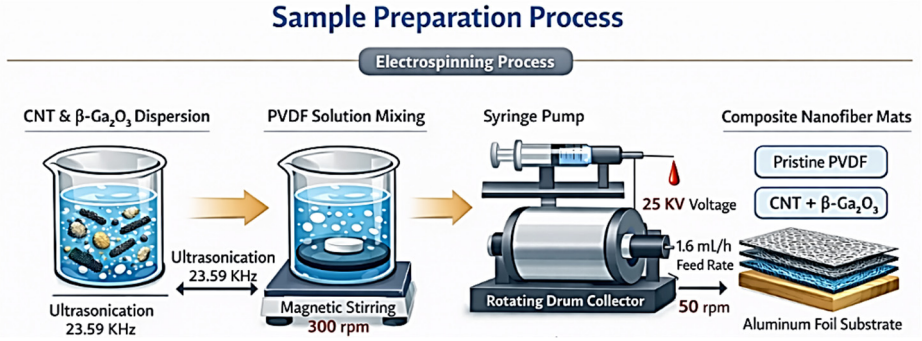

Figure 1. Schematic illustration of the sample synthesis process

Electrospinning was performed using a Nanon-01A system (MECC Co., Ltd., Japan) equipped with a rotating drum collector (F90XSH200). The process parameters included an applied voltage of 25 kV, a solution feed rate of 1.6 mL/h, a spinneret diameter of 0.413 cm, and a spinneret-to-collector distance of 15 cm at a perpendicular orientation. The collector drum rotation speed was maintained at 50 rpm, while the spinneret traversed along the X-axis at 1 cm/s, with a total spinning volume of 10 mL for each sample. The resulting mats formed an interconnected PVDF nanofiber network, either pristine or incorporating CNT and β-Ga_2O_3 additives. Thickness measurements were carried out using a LITEMATIC VL-50 instrument (Mitutoyo, Japan) under a minimal measuring force of 0.01 N. The pristine PVDF mat exhibited a thickness of 15.3 ± 3.1 μm and an areal density of 13.8 ± 0.2 g/m^2, whereas the composite mats showed increased values of 24.1 ± 2.3 μm and 17.4 ± 0.3 g/m^2, respectively, after careful removal from the aluminum foil substrates.

X-ray diffraction (XRD) measurements were carried out to determine the phase composition and crystalline structure of the electrospun PVDF-based nanofibrous mats and their CNT/β-Ga_2O_3-loaded composites. Diffraction patterns were recorded at room temperature using a PANalytical EMPYREAN diffractometer with Co Kα radiation [17]. XRD patterns were recorded over the 2θ range of 20°–100° with a step size of 0.026°. The obtained XRD data were used to compare the pristine PVDF mat with the composite mats (1 wt% CNT–1 wt% β-Ga_2O_3, 0.5 wt% CNT–1.5 wt% β-Ga_2O_3, and 1.5 wt% CNT–0.5 wt% β-Ga_2O_3), enabling evaluation of additive-induced changes in crystallinity and diffraction features relative to the polymer matrix.

RESULTS AND DISCUSSIONS

The experimentally observed diffraction peaks were indexed to the monoclinic β-Ga_2O_3 phase (space group C2/m) and compared with the reference diffraction data (PDF No. 43-1012). Differences in relative peak intensities are attributed to differences in crystallite morphology and preferred orientation. The experimentally observed reflections of monoclinic β-Ga_2O_3 were located at 2θ = 15.70°, 18.95°, 24.24°, 30.11°, 31.73°, 33.49°, 35.22°, and 38.42°, corresponding to the (001), (−201), (201), (400), (−202), (−111), (111), and (−402) crystallographic planes, respectively [18].

The α↔β phase transition in PVDF is one of the main topics of interest in current research. To examine the occurrence of α-to-β or reverse phase transformation, Ga_2O_3 and CNT compositions were introduced into PVDF in different ratios. Fig. 3. shows the concentration-dependent changes in the diffraction peaks of the PVDF samples. In the initial state, the α and β phases are observed in the spectrum of pristine PVDF. Since the XRD analysis was carried out using Co-Kα radiation, the scattering centers of the peaks appear shifted toward higher angles. Thus, the α phase, which is observed at about 18.2° with Cu-Kα radiation, appears at approximately 20.3° in our study. Accordingly, the diffraction peak begins at ~19.75° and ends at 20.98°. This peak corresponds to the (100) reflection of the α phase. The XRD spectra show that the region from 21.75° to 22.5° corresponds to diffraction from the γ phase, associated with the (002) and (110) Miller indices [19]. In the literature, these peaks assigned to this phase have also been observed in the spectrum with slight shifts. The intensity of these peaks corresponding to the γ phase is significantly lower than that of the other peaks, and they appear as a small fraction within the background in a polymorphic manner. The most intense peaks, however, correspond to the diffraction peaks of the β phase. The peak attributed to the β phase is located in the range from 23.19° to 25.5°. It is known that this peak corresponds to indexing as the (110) and (200) reflections.

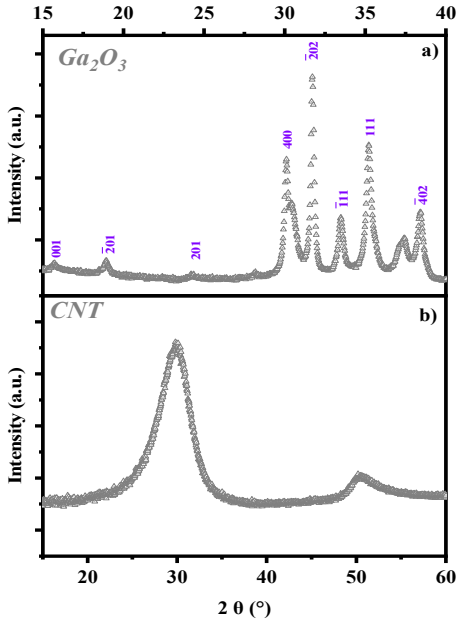

Figure 2. X-ray diffraction spectra of the β-Ga_2O_3 and CNT samples, shown in panels a and b, respectively

In general, it is evident that PVDF exhibits a three-phase structure. If we consider the effect of the compositions and examine the influence of the ratio difference, it can also be seen from the spectrum shown in red that when CNT/Ga_2O_3 is 1/1, a pronounced decrease in the intensity of the α phase is observed together with an increase in the peak corresponding to the γ phase. The addition of the content into the system also changed the scattering centers. When the components were introduced into PVDF in equal proportions, the scattering peak of the α phase was shifted to the range of approximately 19.7° to 20.05°. This may indicate that the introduced composition brought a certain degree of ordering into the system, and the shift of the peak center toward lower angles may be interpreted as an increase in the unit-cell volume. As is known, the γ phase has an orthorhombic structure, and therefore growth in different directions can lead to orientation-dependent changes that result in entirely different lattice parameters.

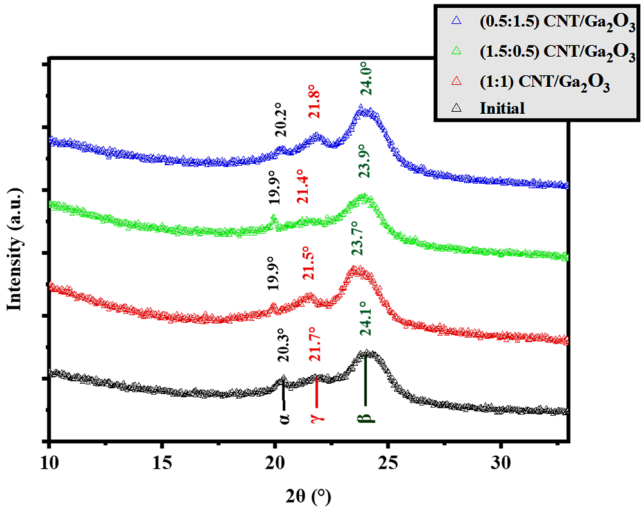

Figure 3. Change in the XRD spectra of PVDF as a function of the embedding amount. Black points correspond to the initial state, red points correspond to the (1:1) ratio, green points correspond to the (1.5:0.5) ratio, and blue points correspond to the (0.5:1.5) CNT/Ga_2O_3 embedding ratios. The centers of the peaks belonging to the α - phase are marked in black, the peaks belonging to the γ – phase are marked in red, and the peaks corresponding to the β - phase are marked in green

In general, it is difficult to distinguish reflections with close d-spacings in PVDF systems. During crystal growth, the periods along the chain in the c-direction are large, and therefore the sample cannot be ideally oriented. It is this imperfection that causes different orientations to appear, allowing the (002) peak of the γ phase to dominate over the (200) reflection. Of course, in this case it should also be noted that the compositions added in equal proportions may have had a stronger effect on a lattice parameter. Thus, growth along the (200) direction may dominate over that along (002). Overall, it becomes clear that the CNT/ Ga_2O_3 additive introduced in equal proportions does not lead to a phase

transition between the α and β phases. Rather, it mainly affects the γ phase and promotes a change in its orientation. Studies show that the addition of oxide ceramics to PVDF leads to a decrease in the α phase and the development of the γ and β phases. However, the CNT introduced into the system improves interfacial interactions and makes the microstructure more heterogeneous [15]. A number of studies have shown that CNT addition promotes the increase of the β phase and raises the β/α ratio, and this difference may even reach 95% [20].

Thus, the results and comparisons show that embedding CNT/Ga_2O_3 in equal proportions (1:1) leads to an increase in β-phase formation and promotes the development of the γ phase. Confirmation of this interpretation can be clearly seen in the case of 1.5/0.5 CNT/ Ga_2O_3 embedding. The corresponding spectrum clearly shows that although the relatively higher CNT content appears to have a positive effect on β-phase formation, the peaks assigned to the γ phase are weaker than those observed for the 1:1 composition. This indicates that Ga_2O_3 promotes the formation of the γ phase. The main confirmation of these results is also clearly observed in the final ratio. The spectrum shown by the blue points in Fig. 3. indicates that, in the case of 0.5/1.5 CNT/Ga_2O_3 embedding, the formation of the γ phase is significantly improved. However, no sharp change is observed in the peaks corresponding to the β phase.

CONCLUSIONS

Overall, the results show that the PVDF system, which initially consists of the α, β, and γ phases, exhibits different phase development after embedding depending on the introduced CNT/Ga_2O_3 ratio. It was found that CNTs mainly promote the stabilization of the β phase, whereas β- Ga_2O_3 exerts a stronger influence on the development of the γ phase. The changes observed in the α phase are mainly associated with the effect of CNT incorporation. Although no significant change in the α phase was recorded when CNT/Ga_2O_3 was introduced in equal proportions, it was determined that α-phase formation was also supported to a certain extent in the case of 1.5/0.5 CNT/Ga_2O_3 embedding. This indicates that the phase balance in the system is determined not only by the presence of the additives, but also by their relative ratio.

ORCID

M.A. Yuldoshev, https://orcid.org/0000-0002-9722-9439; **N.A. Sattarov,** https://orcid.org/0009-0005-0506-0269

REFERENCES

[1] B.M. Ali, A.A. Abdulazez, G. Padma Priya, Subhashree Ray, Amrita Pal, Renu Sharma, Sulton Usanov, *et.al.,* Journal of Molecular Graphics and Modelling, **142**, 109210 (2026). https://doi.org/10.1016/j.jmgm.2025.109210
[2] N.S.S. Singh, M.A. Rusho, A. Abilkasimov, M. Latipova, A. Aldulaimi, A.G. Taki, R.J. Albadr, *et.al.,* Chemical Physics Letters. **880**, 142410 (2025). https://doi.org/10.1016/j.cplett.2025.142410
[3] M.S. Payzullakhanov, F. Giyasova, M. Yuldoshev, C. Toshpulatov, R. Ernazarov, F. Giyasov, A. Urishev, *et.al.,* East Eur. J. Phys. (1), 233 (2026). https://doi.org/10.26565/2312-4334-2026-1-25
[4] S.F. Samadov, Kh.M. Guliyeva, A.A. Sidorin, N.V.M. Trung, Y.I. Aliyev, O.S. Orlov, and S.H. Jabarov, *et.al.,* Arab. J. Sci. Eng. **51**, 2137–2147 (2025). https://doi.org/10.1007/s13369-025-10262-2
[5] M.L. Cerrada, J. Arranz-Andrés, A. Caballero-González, E. Blázquez-Blázquez, and E. Pérez, Polymers, **15**, 1491 (2023). https://doi.org/10.3390/polym15061491
[6] S.F. Samadov, A. O. Dashdemirov, R. R. Sharifov, R. F. Hashimov, S. H. Jabarov, and N. V. M. Trung, Mod Phys Lett B, **19**, 2650100 (2026). https://doi.org/10.1142/S0217984926501009
[7] A. Abdullayev, V. Akhmedov, and D. Gafarova, Sci. Works Constr. **2**, 65 (2024). https://doi.org/10.58225/sw.2024.2-65-70
[8] S. Samadov, *et.al.,* SW AzUAC, **1**, 14-23 (2026). https://doi.org/10.58225/sw.2026.1-14-23
[9] M.N. Mirzayev, E. Demir, Kh.F. Mammadov, V.A. Sukratov, S.H. Jabarov, S. Biira, E.B. Asgerov, *et.al.,* J. Phys. **94**, 110 (2020). https://doi.org/10.1007/s12043-020-01980-3
[10] A.S. Abiyev, O.A. Samedov, E. Demir, E.P. Popov, and S.F. Samadov, J. Alloys Compd. **1005**, 175970 (2024). https://doi.org/10.1016/j.jallcom.2024.175970
[11] A. Shershneva, and M. Ibrahim, SW AzUAC. **1**, 125-131, (2026). https://doi.10.58225/sw.2026.1-125-131
[12] O.A. Samedov, D.M. Mirzayeva, H.H.A. Nguyen, and M.N. Mirzayev, Physica B, **717**, 417807 (2025). https://doi.org/10.1016/j.physb.2025.417807
[13] O. Kholikov, *et.al.,* SW AzUAC., **2**, 68-75 (2025). https://doi.org/10.58225/sw.2025.2-68-75
[14] S.A. Ahmadova, S.F. Samadov, G.B. Ibragimov, I.I. Vinogradov, A.A. Sidorin, D.M. Mirzayeva, B. Mauyey, *et al.*, Physica E, **177**, 116450 (2026). https://doi.org/10.1016/j.physe.2025.116450
[15] S.F. Samadov, A.G. Asadov, A.S. Abiyev, E. Demir, O.A. Samedov, N.V.M. Trung, I.I. Mustafayev, *et.al.,* Physica B, **688**, 416154 (2024). https://doi.org/10.1016/j.physb.2024.416154
[16] M.N. Mirzayev, B.A. Abdurakhimov, E. Demir, A.A. Donkov, E. Popov, M.Yu. Tashmetov, G. Genov, *et al.,* Physica B, **611**, 412842 (2021). https://doi.org/10.1016/j.physb.2021.412842
[17] A.P. Abdullayev, S.F. Samadov, A.S. Abiyev, A.A. Sidorin, N.V.M. Trung, O.S. Orlov, F.M. Mammadov, *et.al.,* J. Alloys Compd. **1038**, 182773 (2025). https://doi.org/10.1016/j.jallcom.2025.182773
[18] F. Shi, and H. Qiao, J. Mater. Sci.: Mater. Electron. **31**, 20223 (2020). https://doi.org/10.1007/s10854-020-04542-w
[19] M.N. Mirzayev, *et al.,* Ceram. Int. 52 12826-12835 (2026). https://doi.org/10.1016/j.ceramint.2026.01.424
[20] A. Lund, A. Lund, C. Gustafsson, H. Bertilsson, R.W. Rychwalski, *et.al.,* Compos. Sci. Technol. **71**, 222–229 (2011). https://doi.org/10.1016/j.compscitech.2010.11.014

XRD ДОСЛІДЖЕННЯ ФАЗОВОЇ ЕВОЛЮЦІЇ В НАНОВОЛОКНАХ PVDF, ОТРИМАНИХ МЕТОДОМ ЕЛЕКТРОФОРМУВАННЯ ПРИ РІЗНИХ СПІВВІДНОШЕННЯХ CNT/β-Ga_2O_3

С.А. Ахмадова[1], Г.Б. Ібрагімов[1], О.А. Самедов[1], М.А. Юлдошев[2], Н.А. Саттаров[3], К.М. Гасанов[1,4], Ю.І. Алієв[5,6], А.С. Абієв[7,8]

[1]Інститут фізики, Міністерство науки і освіти Азербайджанської Республіки, Баку, AZ1143
[2]Міжнародний університет Туран, Наманган, Узбекистан
[3]Міжнародний університет Кімьо в Ташкенті, Наманган, Узбекистан
[4]Центр дослідження низьковимірних матеріалів при Хазарському університеті, Баку, AZ1096, Азербайджан
[5]Азербайджанський державний педагогічний університет, AZ-1143, Баку, Азербайджан
[6]Західнокаспійський університет, AZ-1001, Баку, Азербайджан
[7]Відділ ядерних досліджень IDDA, Баку, AZ-1073, Азербайджан
[8]Азербайджанський університет архітектури та будівництва, Баку, AZ1073, Азербайджан

Для дослідження залежної від складу фазової еволюції в матриці PVDF було виготовлено електроформовані нановолокнисті мати на основі полівініліденфториду (PVDF), що містять вуглецеві нанотрубки (CNT) та наночастинки β-Ga_2O_3. Мати з чистого PVDF та композиту зі співвідношеннями CNT/β-Ga_2O_3 1:1, 1,5:0,5 та 0,5:1,5 мас.% було отримано за ідентичних умов електроформування з використанням системи розчинників DMF/ацетон. Кристалічну структуру та фазовий склад вивчали за допомогою рентгенівської дифракції з випромінюванням CoKα. Мати з чистого PVDF демонстрували багатофазну структуру, що складається з α, β та γ фаз. Після додавання CNT та β-Ga_2O_3 спостерігалися чіткі залежні від складу зміни положення та інтенсивності дифракційного піку. Співвідношення 1:1 зменшувало внесок α-фази та посилювало відбиття γ-фази, тоді як β-фаза залишалася домінантною. Збільшений вміст вуглецевих нанотрубок (CNT) сприяв розвитку β-фази, тоді як підвищений вміст β-Ga_2O_3 сприяв утворенню γ-фази. Результати показують, що CNT переважно підтримують стабілізацію β-фази, тоді як β-Ga_2O_3 має сильніший вплив на еволюцію γ-фази та структурну перебудову. Ці результати показують, що кристалічний фазовий баланс електроформованих нановолокон PVDF може бути ефективно регульований шляхом контрольованого включення CNT/β-Ga_2O_3.

Ключові слова: *полівініліденфторид; бета-оксид галію; вуглецеві нанотрубки; композитні матеріали; ХРД*

EAST EUROPEAN JOURNAL OF PHYSICS. 3. 391-396 (2026)
DOI:10.26565/2312-4334-2026-3-35 ISSN 2312-4334

EFFECTS OF ADSORPTION OF SUBMONOLAYER Cs COATINGS ON THE ELECTRONIC STRUCTURE AND PHYSICAL PROPERTIES OF NiO AND MoO_3

A.U. Xujaniyazova, D.A. Tashmukhamedova, B.E. Umirzakov, M.B. Yusupjonova*, Z.R. Saidakhmedova, Sh.K. Salieva
Tashkent State Technical University named after Islam Karimov, Tashkent, 100095, Republic of Uzbekistan
**Corresponding Author e-mail: maxsuna.yusupjonova@gmail.com*
Received April 30, 2026; revised June 25, 2026; accepted June 30, 2026

Using methods for measuring the dependence of the true secondary electron yield δ on the primary electron energy E_p, as well as Auger-electron and photoelectron spectroscopy, the effects of Cs deposition with thickness θ from 0.2 to 4 monolayers on the composition, valence-electron density of states, and energy-band parameters of NiO and MoO_3 films were studied. It is shown that at θ = 1 monolayer (ML), the largest decrease in the electron affinity χ, the largest increase in the secondary electron yield δ, and the photoelectron quantum yield Y occur. At the same time, the band gap width E_g and the positions of peaks in the valence-electron spectra remain practically unchanged. It was shown for the first time that, for NiO, at θ = 1 ML, the surface electron affinity χ approaches zero. It is found that at θ > 1 ML, changes in the composition, structure, emission, and optical properties of the Cs–NiO system begin to be influenced by the thickness of the Cs film.
Keywords: *Transition metal oxides; Cesium adsorption; Electron affinity; Secondary electron emission; Photoemission*

INTRODUCTION

Transition metal oxides such as NiO and MoO_3 attract considerable interest due to their numerous applications in various fields [1–6], including electrochemical energy storage and photoelectrochemical devices, catalysis and sensing, lithium-ion batteries, flame-retardant materials, optical devices, and other electrochemical applications.

NiO is a wide-band-gap p-type semiconductor with a band gap in the range of 3.6–4.0 eV, depending on the oxide preparation technique and the measurement method [7–9]. MoO_3 is an indirect-band-gap n-type semiconductor with a band gap ranging from 2.8 to 3.6 eV, depending on the phase state and structure (bulk material, film, or nanostructure), as well as on the measurement technique [10–12].

Nickel and molybdenum oxide nanostructures can be fabricated by various methods, including thermal evaporation [13, 14], solution combustion [15], hydrothermal synthesis [16, 17], co-precipitation [18], wet-chemical methods [19], sol-gel processing [20, 21], and pyrolysis [22, 23]. In recent years, low-energy ion implantation has been widely employed to control the composition, structure, and properties of materials of various types [24-35].

In Ref. [24], nanometer-scale MoO_3 films were fabricated on a Mo single-crystal surface by thermal oxidation and ion implantation. The dependence of the Mo surface coverage by MoO_3 cluster phases on ion dose was determined. Films with a thickness of approximately 100 Å were obtained by sequential implantation of ions with energies of 5, 3, and 1 keV. It was established that thermal oxidation forms homogeneous MoO_3 films with good stoichiometry and thicknesses ranging from 50-60 to 600-700 Å, whereas ion implantation yields films with thicknesses ranging from 25-30 to 100 Å.

In Ref. [28], it was shown that implantation of MoO_3 with Ba^+ ions leads to the formation of an ion-modified layer consisting of Mo–O, Mo–Ba–O, and Ba–O compounds. This results in a significant modification of the valence-band density of states, a reduction of the work function Φ to 2.7 eV, a decrease in the band gap E_g by approximately 1.5 times, and a 1.5-fold increase in the maximum secondary electron emission coefficient σm.

In the present work, the effect of Cs atom adsorption with a thickness θ ranging from 0.2 to 4 monolayers (ML) on the composition, electronic structure, emission, and optical properties of the wide-band-gap semiconductors MoO_3 and NiO is investigated for the first time.

EXPERIMENTAL TECHNIQUE

All technological treatments (thermal annealing, oxidation, and ion implantation) and investigations of composition, electronic structure, and physical properties were carried out in the same ultrahigh-vacuum (UHV) system.

The elemental and chemical composition of the nanofilms was determined by Auger electron spectroscopy (AES), while the electronic structure was studied using ultraviolet photoelectron spectroscopy (UPS). Depth profiles of impurity distribution were obtained by layer-by-layer Auger analysis by sputtering the sample surface with Ar^+ ions at 1 keV and an incidence angle of approximately 80° to the surface normal. The etching rate was approximately (3 ± 1) Å/min. The uncertainty in determining atomic concentrations was approximately 5–6 at.%.

Cite as: A.U. Xujaniyazova, D.A. Tashmukhamedova, B.E. Umirzakov, M.B. Yusupjonova, Z.R. Saidakhmedova, Sh.K. Salieva, East Eur. J. Phys. 3, 391 (2026), https://doi.org/10.26565/2312-4334-2026-3-35

The photoelectron quantum yield Y was measured at a photon energy of $h\nu \approx 10.8$ eV. The energy dependence of the secondary electron emission (SEE) coefficient σ was measured in the primary electron energy range E_p = 100-1500 eV. Optical measurements were performed using AGILENT Cary 5000 UV-Vis-NIR spectrophotometer.

EXPERIMENTAL RESULTS AND DISCUSSION

Figure 1 shows the dependence of the true secondary electron yield (TSE) δ on the primary electron energy Ep in the range 1–15 eV for NiO with Cs films of different thicknesses. It can be seen that at θ = 0, a sharp increase in δ begins at E_p = 5.21 eV, corresponding to the onset of electron emission from the top of the valence band, Ev, to the vacuum level, E_{vac}. At θ = 0.5 ML, a sharp increase in δ is observed starting from E_p = 4.3 eV; at θ = 1 ML from E_p = 3.6 eV; and at θ = 2 and 4 ML from E_p = 4.0 eV. At θ ≥ 1 ML, the value of δ at all E_p values is lower than that for pure NiO. This is due to the fact that at θ ≥ 1 ML, true secondary electrons originate not only from NiO but also from the Cs film.

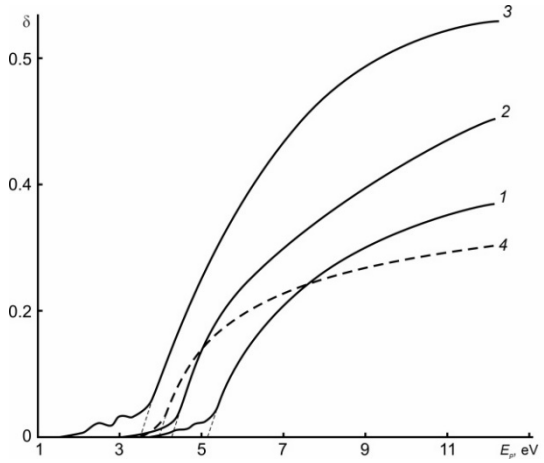

Figure 1. Dependences δ(E_p) in the range E_p = 1–15 eV for NiO with Cs films of thickness θ, ML: 1 – 0; 2 – 0.5; 3 – 1.0; 4 – 2

Since the emission efficiency of Cs is significantly lower than that of NiO starting from θ = 1 ML, the value of δ decreases over the entire E_p range as the thickness of the Cs film increases. In the initial part of the δ(E_p) dependence for NiO films, weak features associated with the presence of impurity levels are observed. With the shift of the spectrum's lower end toward lower E_p values during Cs adsorption, the positions of impurity levels also shift in parallel. It can be assumed that during Cs adsorption at θ ≤ 1 ML, the positions of the impurity levels remain unchanged. However, at θ > 1 ML, these impurity levels are poorly detected.

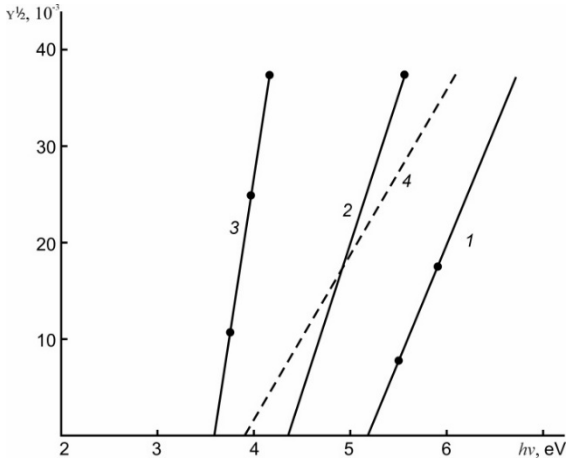

Figure 2. Dependences of $Y^{1/2}$ on $h\nu$ for NiO with Cs films of thickness θ, ML: 1 – 0; 2 – 0.5; 3 – 1.0; 4 – 4

At the same time, spectral distributions of the photoelectron quantum yield were recorded for the studied samples. Figure 2 shows Fowler plots (dependences of $Y^{1/2}$ on $h\nu$) for NiO with Cs films of different thicknesses. It can be seen that the photoelectron work function values at the top of the valence band (Ev) for NiO and NiO with Cs films of thicknesses 0.5, 1.0, and 2 ML are in good agreement with the data in Fig. 1.

Figure 3 shows the dependence of the light transmittance coefficient T on photon energy hν for pure NiO and NiO with Cs films of thickness θ = 0.5 and 1 ML. It is observed that the value of T remains nearly unchanged up to $h\nu$ = 3.5 eV, then decreases sharply to zero. Extrapolation of the second part of the curve to the $h\nu$ axis gives an approximate value of the band gap E_g. For NiO, E_g = 3.72 eV. After Cs deposition with thicknesses of 0.5 and 1 ML,

the value of T slightly decreases in the range *hv* from 7.0 to 3.2 eV, but the value of E_g remains practically unchanged. This shows that for Cs deposition with $\theta \leq 1$, the band gap E_g does not change significantly, and the decrease in the photoelectron work function Φ is mainly due to a decrease in the electron affinity χ.

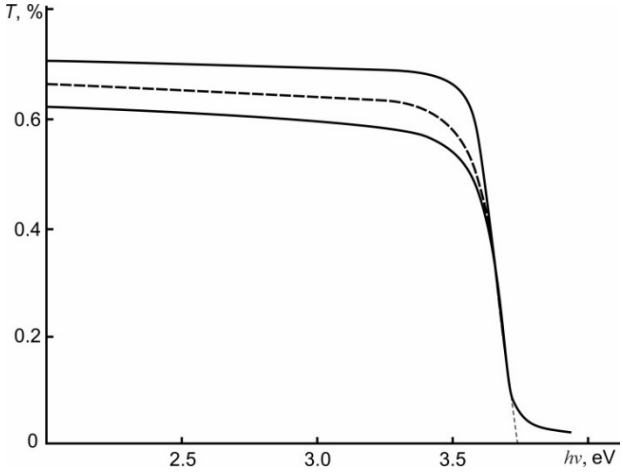

Figure 3. Dependences of the light transmittance coefficient T on photon energy *hv* for NiO with film thickness θ, ML: 1 – 0; 2 - 0.5; 3 – 1.0

Based on these data, we determined the work function Φ of NiO with a thin Cs film (Fig. 4). One monolayer was taken as the reference, corresponding to the minimum eφ value. From Fig. 4, it can be seen that during deposition for 1.2 min, the dependences Φ(t) and χ(t) pass through a minimum, decreasing by about ~ 2 eV. At t = 2.4 min, θ equals 2 monolayers; at t = 4.8 min, θ = 4 ML. At θ = 2 monolayers, the values of Φ and χ slightly increase and then remain practically unchanged with further increase in θ, i.e., the value of Φ characteristic of a thick Cs film is established.

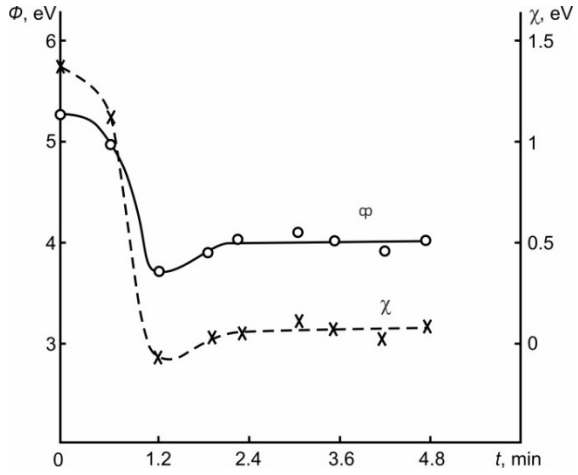

Figure 4. Dependence of the photoelectron work function Φ and electron affinity χ on the Cs deposition time on the NiO surface

Table 1 presents the energy-band parameters for NiO with Cs films of different thicknesses, determined from Figs. 1 and 3.

Table 1. Energy-band parameters and emission parameters for NiO with submonolayer Cs coverage

Parameters θ, ML	$\Phi = E_v$, eV	E_g, eV	χ, eV	σ_m	Y (at *hv* = 10.8 eV)
0	5.21	3.72	1.49	3.1	$6 \cdot 10^{-3}$
0.5	4.3	3.72	0.58	4.1	$9 \cdot 10^{-3}$
1	3.82	3.72	0.10	4.9	$3 \cdot 10^{-2}$
2	3.71	3.72	–0.01	3.9	$8 \cdot 10^{-3}$

From the table, it is evident that up to θ = 1 ML, as χ decreases, the values of Y and σ_m increase significantly. At θ = 1 ML, the value of χ approaches zero (Fig. 5).

Similar studies were also conducted on MoO_3 films. The results are summarized in Table 2. It can be seen that, in this case as well, Cs deposition does not change E_g, while Ev and χ decrease, and σ_m and Y increase noticeably. Unlike NiO, in the case of MoO_3, Cs adsorption with $\theta \leq 1$ leads to a much larger decrease in Φ and χ, but the effect of negative electron affinity does not occur.

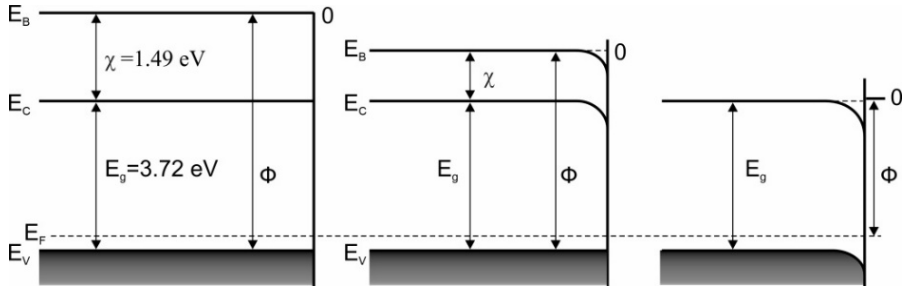

Figure 5. Energy diagrams of the surface: 1 – NiO; 2 – NiO with a Cs film of thickness 0.5 and 1 ML.

Table 2. Energy-band parameters and emission parameters of MoO_3 with submonolayer Cs coatings

$Cs^{\theta} \rightarrow MoO_3$	Parameters				
	E_v, eV	E_g, eV	χ, eV	σ_m	Y
θ = 0 ML	7.9	3.4	4.5	3.4	$4.5 \cdot 10^{-3}$
θ = 0.5 ML	6.2	3.4	2.8	–	-
θ = 1.0 ML	5.5	3.4	2.1	5.8	$6 \cdot 10^{-2}$
θ = 2.0 ML	5.7	3.4	2.3	4.5	$2 \cdot 10^{-2}$

"–" – measurements were not performed.

It should be noted that in the case of $Cs^{\theta} \rightarrow NiO$, at θ = 1 ML the value of χ approaches zero; however, a very sharp (10 times or more) increase in σm and Y, which is typical for semiconductors with negative electron affinity, is not observed. In addition, during Cs adsorption with θ = 1 ML for binary semiconductors (GaAs, GaP) and wide-band-gap semiconductors (MgO, WO_3), the value of χ decreases by 2.5 eV or more. In the case of NiO, this decrease is only about ~1.4 eV. These issues require further experimental and theoretical investigation.

CONCLUSIONS

1. For the first time, the influence of submonolayer Cs coatings on the electronic structure, emission, and optical properties of NiO and MoO_3 oxides has been investigated. It has been shown that at θ ≤ 1 monolayer, the values of σ_m and Y increase significantly, which is explained by a decrease in χ to 1.61 eV (NiO) and 2.4 eV (MoO_3).
2. It has been shown that during Cs adsorption at θ ≤ 1 ML, the composition of the surface layers remains practically unchanged; the band gap width and the valence-electron density-of-states structure also remain unchanged.
3. In the case of NiO, during Cs deposition at θ = 1 ML, a $Cs^{\theta} \rightarrow NiO$ system close to negative electron affinity is formed. However, in this case an increase in σ_m and Y is not observed.

ORCID

A.U. Xujaniyazova, https://orcid.org/0009-0003-3551-2831; **D.A. Tashmukhamedova,** https://orcid.org/0000-0001-5813-7518;
B.E. Umirzakov, https://orcid.org/0000-0002-9815-2111; **M.B. Yusupjonova,** https://orcid.org/0000-0003-1189-687X;
Z.R. Saidakhmedova, https://orcid.org/0009-0003-5363-7590; **Sh.K. Salieva,** https://orcid.org/0009-0004-4022-9309

REFERENCES

[1] T.U. Devi, E.R. Kumar, M. Kumar, B. Balraj, Ch. Sivakumar, P. Matheswaran, N. Chandrasekar, *et al*., "Physicochemical properties and photocatalytic activity of MoO_3 nanostructures: evaluation of structural, optical, vibrational, and morphological properties," Ceram. Int. **49**, 13994–14006 (2023). https://doi.org/10.1016/j.ceramint.2022.12.281
[2] D.K. Halwar, V.V. Deshmane, and A.V. Patil, "The combination of nickel oxide (NiO) and molybdenum trioxide (MoO_3) for pollutant gas detection," J. Electron. Mater. **52**, 1840–1853 (2023). https://doi.org/10.1007/s11664-022-10130-x
[3] N.G. Prakash, M. Dhananjaya, A.L. Narayana, D.P.M.D. Shaik, P. Rosaiah, and O.M. Hussain, "High-performance one-dimensional α-MoO_3 nanorods for supercapacitor applications," Ceram. Int. **44**, 9967–9975 (2018). https://doi.org/10.1016/j.ceramint.2018.03.032
[4] P.A. Dement'ev, E.V. Ivanova, M.N. Lapushkin, D.A. Smirnov, and S.N. Timoshnev, "Electronic structure of molybdenum oxidized in air," Phys. Solid State, **61**, 1993–1998 (2019). https://doi.org/10.1134/S1063783419110131
[5] F. Ma, Y. Zhao, J. Li, X. Zhang, H. Gu, and J. You, "Nickel oxide for inverted structure perovskite solar cells," J. Energy Chem. **52**, 393–411 (2021). https://doi.org/10.1016/j.jechem.2020.04.027
[6] M.M. Uplane, S.H. Mujawar, A.I. Inamdar, P.S. Shinde, A.C. Sonavane, and P.S. Patil, "Structural, optical, and electrochromic properties of nickel oxide thin films grown from electrodeposited nickel sulphide," Appl. Surf. Sci. **253**, 9365-9371 (2007). https://doi.org/10.1016/j.apsusc.2007.05.069
[7] H. Sato, T. Minami, S. Takata, and T. Yamada, "Transparent conducting p-type NiO thin films prepared by magnetron sputtering," Thin Solid Films, **236**, 27–31 (1993). https://doi.org/10.1016/0040-6090%2893%2990636-4
[8] M. Bonomo, "Synthesis and characterization of NiO nanostructures: A review," J. Nanopart. Res. **20**, 222 (2018). https://doi.org/10.1007/s11051-018-4327-y

[9] H.P. Parkhomenko, M.N. Solovan, and P.D. Maryanchuk, "Electrical properties of p-NiO/n-Si heterostructures based on nanostructured silicon," Semiconductors, **52**, 859–863 (2018). https://doi.org/10.1134/S1063782618070163
[10] M.B. Rammal, and S. Omanovic, "Synthesis and characterization of NiO, MoO_3, and $NiMoO_4$ nanostructures through a green facile method and their potential use as electrocatalysts for water splitting," Mater. Chem. Phys. **255**, 123570 (2020). https://doi.org/10.1016/j.matchemphys.2020.123570
[11] P.H. Silva, D.T. Cestarolli, and E.M. Guerra, "Band gap values and structural changes in MoO_3 obtained by ion-exchange method," Opt. Mater. 164, 117063 (2025). https://doi.org/10.1016/j.optmat.2025.117063
[12] E. Pavoni, M.G. Modreanu, E. Mohebbi, D. Mencarelli, P. Stipa, E. Laudadio, and L. Pierantoni, "First-principles calculation of MoO_2 and MoO_3 electronic and optical properties compared with experimental data," Nanomaterials, **13**, 1319 (2023). https://doi.org/10.3390/nano13081319
[13] A. Özkartal, and D.T. Noori, "Effects of thermal annealing on the characterization of p-NiO/n-GaAs heterojunctions produced by thermal evaporation," J. Mater. Sci.: Mater. Electron. **32**, 13462–13471 (2021). https://doi.org/10.1007/s10854-021-05924-4
[14] R. Senthilkumar, G. Anandhababu, T. Mahalingam, and G. Ravi, "Photoelectrochemical study of MoO_3 films with assorted morphologies formed by thermal evaporation," J. Energy Chem. **25**, 798–804 (2016). https://doi.org/10.1016/j.jechem.2016.04.005
[15] D. Parviz, M. Kazemeini, A.M. Rashidi, *et al*., "Synthesis and characterization of MoO_3 nanostructures by solution combustion method employing morphology and size control," J. Nanopart. Res. **12**, 1509–1521 (2010). https://doi.org/10.1007/s11051-009-9727-6
[16] B. Miao, W. Zeng, L. Lin, and Sh. Xu, "Characterization and gas-sensing properties of NiO nanowires prepared through the hydrothermal method," Physica E, **52**, 40–45 (2013). https://doi.org/10.1016/j.physe.2013.03.006
[17] J.-K. Song, J.-S. Ahn, and E.-M. Han, "Characteristics of perovskite solar cells with a nanostructured MoO_3 hole transport layer prepared by hydrothermal synthesis," Korean J. Mater. Res. **30**, 81–86 (2020). https://doi.org/10.3740/MRSK.2020.30.2.81
[18] M.Ch. Fite, S.D. Karse, and L.M. Gode, "Optical and photocatalytic properties of nickel oxide nanoparticles," J. Cryst. Growth, **660**, 128163 (2025). https://doi.org/10.1016/j.jcrysgro.2025.128163
[19] P.M. Ponnusamy, S. Agilan, N. Muthukumarasamy, T.S. Senthil, G. Rajesh, M.R. Venkatraman, and D. Velauthapillai, "Structural, optical, and magnetic properties of undoped NiO and Fe-doped NiO nanoparticles synthesized by a wet chemical process," Mater. Charact. **114**, 166–171 (2016). https://doi.org/10.1016/j.matchar.2016.02.020
[20] S. Kakherskyi, R. Pshenychnyi, O. Dobrozhan, *et al*., "Structural, microstructural, chemical, and optical properties of NiO nanocrystals and films obtained by 3D printing," Appl. Phys. A, **127**, 715 (2021). https://doi.org/10.1007/s00339-021-04847-5
[21] B.G. Bharate, "Synthesis of molybdenum oxide nanoparticles by the sol–gel method for ammonia gas sensing," Biomed. J. Sci. Tech. Res. **37**, 29172–29175 (2021). https://doi.org/10.26717/BJSTR.2021. 37.005957
[22] N. Mebrouki, S.B. Hamida, L. Benmebrouk, R. Gheriani, and L. Zenkhri, "Synthesis and characterization of nickel oxide thin films by spray pyrolysis: effect of nickel source nature," Asian J. Res. Chem. **15**, 159–162 (2022). https://doi.org/10.52711/0974-4150.2022.00026
[23] F. Chandoul, A. Boukhachem, F. Hosni, H. Moussa, M.S. Fayache, M. Amlouk, and R. Schneider, "Change in the properties of nanostructured MoO_3 thin films under gamma-ray irradiation," Ceram. Int. **44**, 12483–12490 (2018). https://doi.org/10.1016/j.ceramint.2018.04.040
[24] G.X. Allayarova, D.A. Tashmukhamedova, R. Djabbarganov, and B.E. Umirzakov, "Formation of nanoscale MoO_3 films by thermal oxidation and ion bombardment," J. Surf. Investig. **15**, 81–84 (2021). https://doi.org/10.1134/S1027451021010043
[25] S. Boulila, M. Ghamnia, A. Boukhachem, *et al*., "Photocatalytical properties of Ba-doped NiO nanofilms," Philos. Mag. Lett. **100**, 283–293 (2020). https://doi.org/10.1080/09500839.2020.1760389
[26] D.A. Tashmukhamedova, and M.B. Yusupjanova, Journal of Surface Investigation: X-ray, Synchrotron and Neutron Techniques. **15**(5), 1054-1057 (2021). https://doi.org/10.1134/S1027451021050402
[27] Y. Aoun, M. Marrakchi, S. Benramache, *et al*., "Preparation and characterization of monocrystalline Na-doped NiO thin films," Mater. Res. **21**, e20170681 (2018). https://doi.org/10.1590/1980-5373-mr-2017-0681
[28] B.E. Umirzakov, D.A. Tashmukhamedova, S.T. Gulyamova, *et al*., Effect of Ba^+ ion implantation on the composition and electronic properties of MoO_3/Mo(111) films," Tech. Phys. **65**, 795–798 (2020). https://doi.org/10.1134/S1063784220050242
[29] D.A. Tashmukhamedova, M.B. Yusupjanova, G.Kh. Allayarova, and B.E. Umirzakov, "Crystal structure and band gap of nanoscale phases of Si formed at various depths of the near-surface region of SiO_2," Technical Physics Letters, **46**(10), 972-975 (2020). https://doi.org/10.1134/S1063785020100144
[30] Sh. Wang, and A.J.R. Hensley, "Dopant effects on the environment-dependent chemical properties of NiO(100) surfaces," Appl. Surf. Sci. **682**, 161679 (2025). https://doi.org/10.1016/j.apsusc.2024.161679
[31] Kh.Kh. Boltaev, D.A. Tashmukhamedova, and B.E. Umirzakov, "Structure and electronic properties of nanoscale phases and nanofilms of metal silicides produced by ion implantation in combination with annealing," Journal of Surface Investigation, X_ray, Synchrotron and Neutron Techniques, **8**(2), 326–331 (2014). https://doi.org/10.1134/S1027451014010108
[32] Y.S. Ergashov, D.A. Tashmukhamedova, F.G. Djurabekova, and B.E. Umirzakov, "Effect of surface microroughness on the composition and electronic properties of CdTe/Mo(111) films," Bulletin of the Russian Academy of Sciences: Physics, **80**(2), 138 (2016). https://doi.org/10.3103/S1062873816020064
[33] B. E. Umirzakov, D. A. Tashmukhamedova, M. K. Ruzibaeva, *et al*., "Investigation of change of the composition and structure of the CaF_2/Si films surface at the low-energy bombardment," Nucl. Instr. and Meth. B. **326**, 322–325 (2014). https://doi.org/10.1016/j.nimb.2013.10.094
[34] D.A. Tashmukhamedova, "Study of composition and electronic structure of $CoSi_2$/Si interface" Bulletin of the Russian Academy of Sciences: Physics **70**(8), 1409-1411. (2006). https://elibrary.ru/item.asp?id=27854241
[35] M.B. Yusupjonova, D.A. Tashmukhamedova, B.E. Umirzakov, S.S. Pak, Z.R. Saidakhmedova, and Sh.K. Salieva, "Influence of implantation of active metal ions on the composition, emission and optical properties of MgO films," East European Journal of Physics, (1), 260-264 (2025). https://doi.org/10.26565/2312-4334-2025-1-29

ВПЛИВ АДСОРБЦІЇ СУБМОНОШАРОВИХ ПОКРИТТІВ Cs НА ЕЛЕКТРОННУ СТРУКТУРУ ТА ФІЗИЧНІ ВЛАСТИВОСТІ NiO ТА MoO_3

А.У. Хужаніязова, Д.А. Ташмухамедова, В.Е. Умірзаков, М.В. Юсупжонова, З.Р. Саїдахмедова, Ш.К. Солієва
Ташкентський державний технічний університет імені Іслама Карімова, Ташкент, 100095 Республіка Узбекистан

За допомогою методів вимірювання залежності справжнього виходу вторинних електронів δ від енергії первинних електронів E_p, а також спектроскопії Оже-електронів та фотоелектронів, досліджено вплив осадження Cs товщиною θ від 0,2 до 4 моношарів на склад, щільність станів валентних електронів та параметри енергетичних зон плівок NiO та MoO_3. Показано, що при θ = 1 ML відбувається найбільше зменшення електронної спорідненості χ та найбільше збільшення виходу вторинних електронів δ і квантового виходу фотоелектронів Y. При цьому ширина забороненої зони E_g та положення піків у спектрах валентних електронів практично не змінюються. Вперше показано, що для NiO при θ = 1 ML значення поверхневої електронної спорідненості χ наближається до нуля. Встановлено, що за θ > 1 ML зміни складу, структури, емісійних та оптичних властивостей системи Cs–NiO починають залежати від товщини плівки Cs.

Ключові слова: *оксиди перехідних металів; адсорбція цезію; електронна спорідненість; емісія вторинних електронів; фотоемісія*

East European Journal of Physics. 3. 397–401 (2026)
DOI: 10.26565/2312-4334-2026-3-36 ISSN 2312-4334

AGE DETERMINATION OF LOW-ENRICHED URANIUM IN VARIOUS PHYSICAL FORMS USING GAMMA SPECTROMETRY METHODS

Stanislav Vanzha[1], **Dmytro Kutnii**[1], **Serhii Afanasiev**[1], **Dmytro Burdeinyi**[1], **Oleksandr Zhukov**[2]
[1]*National Science Center "Kharkov Institute of Physics and Technology" 1, Akademicheskaya St., 61108, Kharkiv, Ukraine*
[2]*Institute for Nuclear Research 47, Nauky Ave., Kyiv, Ukraine*
[*]*Corresponding Author e-mail: afanserg@kipt.kharkov.ua*
Received May 19, 2026; revised July 16, 2026; in final form August 20, 2026; accepted August 25, 2026

This paper presents the research results on the age determination of low-enriched uranium in various physical forms using gamma spectrometry methods. The objects of study were uranium working reference materials (uranium oxide powders, uranium alloys, fuel pellets, and microspherical fuel) with ^{235}U enrichment levels ranging from 0.47% to 19.75%, developed at the NSC KIPT. Two analytical approaches for uranium age dating were proposed and tested: Approach 1 is based on a broad-energy germanium detector (BEGe3830) and the ^{214}Bi/^{234}U chronometer; this method demonstrated efficiency across a wide range of enrichments, from natural to enriched uranium. Approach 2 utilizes a low-energy detector (GL1015R) and the ^{223}Ra/^{235}U chronometer; it has been found that this approach is limited to enriched uranium only. The results for the calculated age and model production dates obtained by both approaches are in good agreement. The average measurement uncertainty was approximately 10% with an exposure time of 400 000 s.

Keywords: *Uranium age dating; Isotope chronometer; Gamma-spectrometer; Enriched uranium*

1. INTRODUCTION

In nuclear forensics, the "age" of uranium is defined as the time elapsed since its last chemical purification - the point at which all decay products were removed. In other words, it represents the material's production date or the date of the last technological processing, such as enrichment. The determination of uranium age is a fundamental tool for the attribution of nuclear materials. This parameter allows for the reconstruction of a sample's processing history, the establishment of its technological links to specific stages of the nuclear fuel cycle, and the performance of comparative analyses to identify whether different samples share a common source of origin. Modern research in nuclear forensics highlights several key approaches to dating uranium-containing materials, all based on measuring radioactive disequilibrium. The primary challenge for gamma spectrometry methods remains the necessity of detecting low activities of decay products against the background of high activity from the parent uranium nuclides.

Chronometer ^{214}Bi/^{234}U: The use of short-lived decay products, such as bismuth-214 (^{214}Bi) [1], is considered an effective non-destructive analysis method for the rapid determination of the time elapsed since the last material processing. As stated in IAEA guidelines, high-resolution gamma spectrometry (HRGS) allows such measurements to be performed without opening the containers. However, the accuracy of this chronometer critically depends on the airtightness of the packaging and the retention of radon-222 (^{222}Rn), which is an intermediate product in the decay chain [2]. In a simplified form, the age of uranium is defined as: $t \approx \frac{1}{\lambda^{\text{Ra-226}}} \cdot \ln\left(1 + \frac{A^{\text{Ra-226}}}{A^{\text{U-234}}}\right)$, where λ^{Ra-226} – decay constant of ^{226}Ra; A^{Bi-214} and A^{U-234} – activities of ^{214}Bi and ^{234}U, respectively.

Chronometer ^{230}Th/^{234}U: This ratio is considered the most reliable 'nuclear clock' for uranium age dating. Classic studies [3] have extensively investigated the validity of this chronometer and established that it provides high accuracy for a wide range of materials - from fuel pellets to uranium ore concentrate. Although mass spectrometry is traditionally used for this purpose [4], modern gamma-spectrum processing methods allow for the isolation of thorium-230 (^{230}Th) analytical lines, even in the presence of intense radiation from uranium isotopes [5]. Mathematically, the age of uranium in this case is expressed via the activity ratio as follows: $t \approx \frac{1}{\lambda^{\text{Th-230}}} \cdot \ln\left(1 + \frac{A^{\text{Th-230}}}{A^{\text{U-234}}}\right)$ where $\lambda^{\text{Th-230}}$ is the decay constant of ^{230}Th, and $A^{\text{Th-230}}$ and $A^{\text{U-234}}$ are the activities of ^{230}Th and ^{234}U, respectively.

Chronometer ^{231}Pa/^{235}U: The use of the ^{231}Pa/^{235}U chronometer is considered one of the most complex yet informative methods in nuclear chronometry. The technical value of this method lies in its ability to verify data obtained from the primary thorium cycle. Since the half-life of the intermediate ^{231}Th is only 25.5 hours, the equilibrium between ^{235}U and ^{231}Th is established very rapidly. In contrast, ^{231}Pa has a half-life of 32 760 years, making it ideal for measuring the age of anthropogenic uranium over timescales ranging from several years to centuries.

To enhance the reliability of the results, the cross-dating method is commonly employed. Comparing the results obtained from the ^{230}Th/^{234}U and ^{231}Pa/^{235}U pairs allows for confirmation that the system has remained closed since the moment of chemical separation [6]. Such a comprehensive approach forms the basis of the attribution methodology for unknown nuclear materials, enabling the identification of the sample's source of origin with a high degree of probability.

Cite as: S. Vanzha, D. Kutnii, S. Afanasiev, D. Burdeinyi, O. Zhukov, East Eur. J. Phys. 3, 397 (2026), https://doi.org/10.26565/2312-4334-2026-3-36

The objective of this study was to determine the age of low-enriched uranium in various physical forms. Based on these uranium, working reference materials were developed at the NSC KIPT in 2014 to ensure the traceability of gamma spectrometric measurements within the nuclear material accounting and control (NMAC) system at Ukraine's nuclear facilities. Obtaining additional analytical characteristics (signatures) of these materials is a topical task that will enable their application in nuclear forensics both for ensuring measurement traceability and for conducting inter-laboratory comparisons of gamma spectrometric research results among the national forensic laboratories of the GUAM countries.

2. MATERIAL AND METHODS

For uranium age dating we used working reference materials (WRM) with ^{235}U enrichment levels ranging from 0.47% to 19.75% produced at NSC KIPT. The characteristics of the WRM are given in Table 1 below. Each uranium material sample was placed in an airtight aluminum container with a side wall thickness of 5 mm and an end face thickness of 2 mm.

Table 1. The characteristics of the working reference materials.

#/#	Sample ID	Enrichment, %	Mass of U, g	Description
1	Upo #01	0.47	39.42	Powder UO_2
2	Upo #02	0.72	37.89	Powder U_3O_8
3	Ume #03	0.72	40.72	Alloy U-NbZr
4	Ume #04	0.70	49.22	Alloy U-Ti
5	Upo #05	2.05	39.42	Powder UO_2
6	Upo #06	4.08	39.42	Powder UO_2
7	Upr #06	6.14	39.68	Uncoated microspheres based on UO_2
8	Upr #06	6.25	37.05	Coated microspheres based on UO_2
9	Ume #06	10.00	40.35	Alloy U-Mo-Nb
10	Upo #06	10.00	39.41	Powder UO_2
11	Upo #06	16.46	31.19	Fuel pellets based on UO_2
12	Upo #06	19.75	39.38	Powder UO_2

A broad energy HPGe detector type BEGe 6530 (Canberra, USA) with a diameter of 70 mm and thickness of 30 mm, and a planar HPGe detector type GL 1015 (Canberra, USA) with a diameter of 36 mm and thickness of 15 mm were used for gamma spectra acquisition. Genie-2000 software was used for gamma spectra acquisition and analysis, FRAM and MGAU codes for uranium isotopic composition analysis, and FRAM code for calculation of detection efficiency.

The uranium age determination was carried out according to the following approaches:

Approach 1. Gamma Detector - broad energy HPGe detector type BEGe 3830; Gamma Ray Energies Range - from 50 to 2600 keV; Chronometer - activity ratio ^{214}Bi/^{234}U; Analyzed ^{214}Bi Gamma Lines - 609.32 and 2204.21 keV; Analyzed ^{234m}Pa Gamma Lines - 766.36, 1001.02, 1193.77, 1510.10, 1737.80, and 1831.70 keV; Detection Efficiency: the intrinsic/relative efficiency curve, which is constructed using the intensities of the ^{234m}Pa gamma quanta and the known activity of the ^{238}U isotope.

Approach 2. Gamma Detector - planar HPGe detector type GL 1015; Gamma Ray Energies Range - from 50 to 1100 keV; Chronometer - activity ratio ^{214}Bi/^{234}U and ^{223}Ra/^{235}U; Analyzed ^{223}Ra Gamma Lines: 269.46 keV; Analyzed ^{235}U Gamma Lines: 275.35 keV; Detection Efficiency: the relative efficiency based on FRAM's efficiency approximation (see Fig.1).

3. RESULTS AND DISCUSSION

Fig. 2 shows the results of the experimental gamma-spectrum processing obtained using the Interactive Peak Fit software, which is part of the Genie-2000 software package.

The ^{214}Bi peak at 609.31 keV slightly interferes with the ^{234}Pa peak at 612.00 keV, but these peaks are fairly easily resolved. The ^{214}Bi peak with an energy of 2204.21 keV is an interference-free monopeak. In the energy region of 265–290 keV there are many interfering peaks of ^{235}U, ^{223}Ra, ^{219}Rn, ^{234}Pa, ^{227}Th, ^{231}Pa. Despite the fact that the software "Interactive Peak Fit" allows to calculate the areas of all peaks, the uncertainty of calculations increases and for ^{223}Ra peak with energy 269.46 keV it increases to 4–6%.

In order to calculate the model date of the WRMs according to Approach 1, we calculated the activity ratios ^{234}U/^{235}U and ^{235}U/^{238}U using the peak areas of ^{235}U at energies 143.76, 163.33, 185.72, and 205.31 keV and ^{234}U at energy 120.90 keV, as well as the values of ^{235}U and ^{238}U contents in the sample calculated with the FRAM software.

The next step involved calculating the ^{214}Bi/^{238}U, ^{214}Bi/^{234}U activity ratio and model date of WRMs using the areas of ^{238}U peaks at energies 766.36, 1001.02, 1193.77, 1510.10, 1737.80, 1831.70 keV and ^{214}Bi at energies 609.31 and 2204.21 keV. The combination of activity ratios allows for obtaining the target value $A^{\text{Bi-214}}/A^{\text{U-234}}$ by means the expression given below:

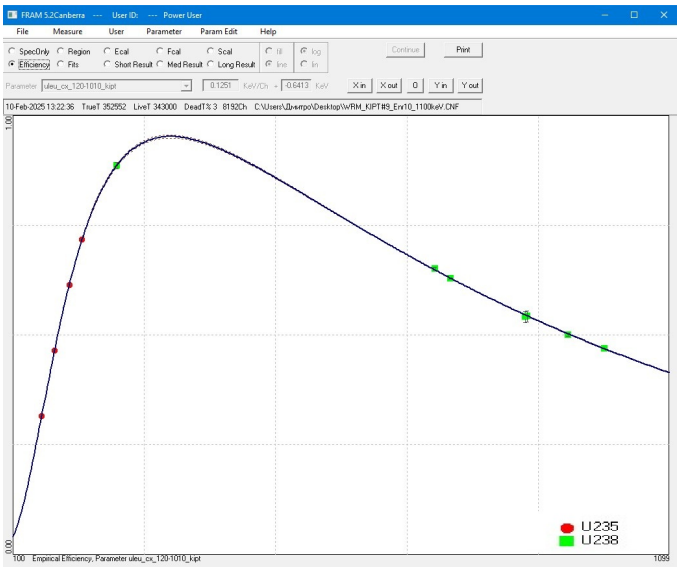

Figure 1. The relative gamma-ray detection efficiency curve based on the results of the FRAM program code approximation.

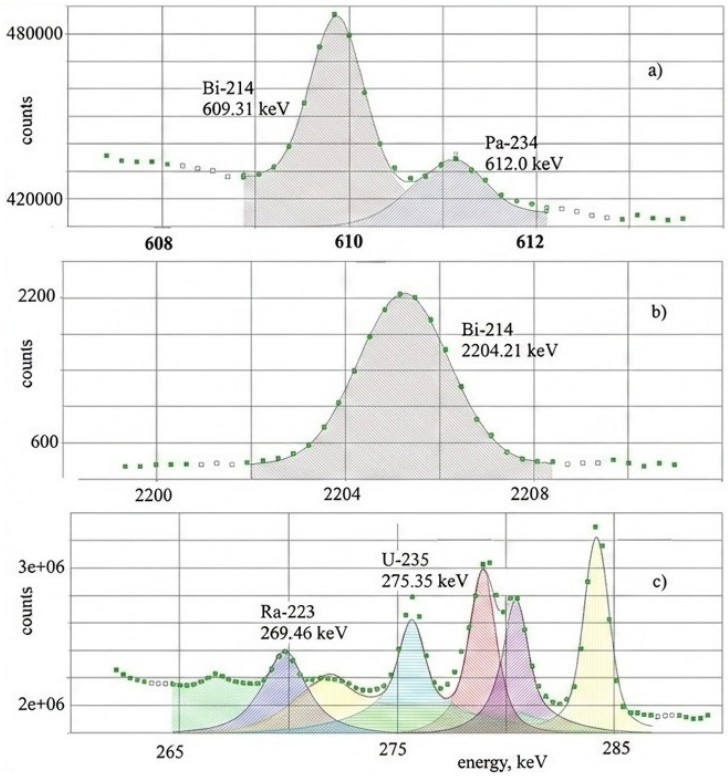

Figure 2. The results of experimental gamma-spectrum processing using the Interactive Peak Fit software. Intervals corresponding to the lines of the uranium chronometer: a) E = 607 - 614 keV, b) 2202 - 2010 keV, c) 260 - 290 keV. See explanations in the text.

$$\frac{A^{\text{Bi-214}}}{A^{\text{U-234}}} = \frac{A^{\text{Bi-214}}}{A^{\text{U-238}}} \cdot \left(\frac{A^{\text{U-235}}}{A^{\text{U-234}}} \cdot \frac{A^{\text{U-238}}}{A^{\text{U-235}}} \right)^{-1} \tag{1}$$

To estimate the uranium age in the working reference materials using Approach 2, the activity ratio $A^{\text{Pa-231}}/A^{\text{U-235}}$ was directly calculated using the detection efficiency values obtained via the FRAM software code. The results are

presented in Table 2 and Fig. 3.

Table 2. Results of the age calculation and the model date of production for the uranium working reference materials.

	Uranium Age (years) / Model Date of Production		
	Approach 1		Approach 2
Sample ID	**609.31 keV, ^{214}Bi**	**2204.21 keV, ^{214}Bi**	**269.46 keV, ^{223}Ra**
Upo #01	45 ± 7 09.02.1979	49 ± 10 15.04.1974	- -
Upo #02	79 ± 8 20.05.1945	78 ± 8 15.06.1945	- -
Ume #03	74 ± 8 28.02.1950	69 ± 8 30.06.1954	- -
Ume #04	59 ± 7 09.12.1964	58 ± 10 28.06.1965	- -
Upo #05	25 ± 3 28.08.1998	29 ± 4 07.04.1994	25 ± 28 03.10.1999
Upo #06	20 ± 2 26.12.2003	21 ± 3 26.10.2002	23 ± 17 25.01.2002
Upr #07	53 ± 5 13.03.1971	56 ± 5 28.05.1967	55 ± 8 17.11.1969
Upr #08	54 ± 5 21.02.1970	56 ± 5 25.05.1967	61 ± 7 15.03.1964
Ume #09	36 ± 3 18.04.1987	39 ± 4 24.09.1984	41 ± 17 12.04.1984
Upo #10	18 ± 2 05.12.2005	23 ± 3 25.11.2000	20 ± 6 29.06.2005
Upr #11	42 ± 4 18.06.1981	50 ± 5 11.07.1967	38 ± 4 20.09.1986
Upo #12	15 ± 2 29.03.2010	- -	18 ± 3 24.02.2007

In general, the results of the uranium age dating for the working reference materials, obtained using different analytical approaches, show good agreement with each other. It is worth noting that Approach 1 can be applied to determine the uranium age across a wide range of enrichments, from natural uranium to enriched material (up to 20%). By contrast, the Approach 2 is limited to the analysis of enriched uranium samples due to the necessity of determining the activity of isotopes within the ^{235}U decay chain.

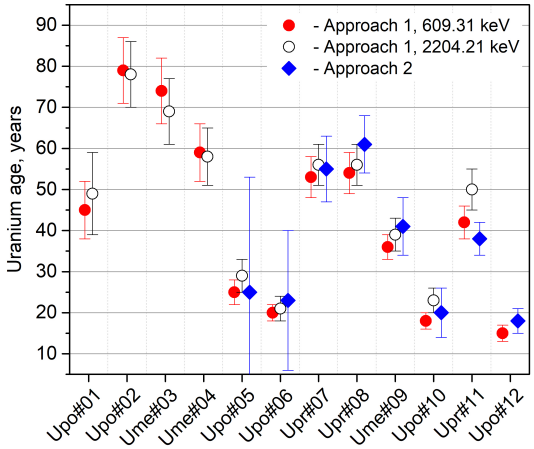

Figure 3. Age calculation results and measurement uncertainties for uranium reference materials.

The use of the 609.31 keV gamma ray of ^{214}Bi for dating relatively "young" uranium samples is preferable to the 2204.21 keV gamma ray, as the intensity of the last one in such samples is comparable to the background intensity of ^{214}Bi.

The average measurement uncertainty was approximately 10% for a measurement time of 400 000 s. The primary contribution to the measurement uncertainty stems from the uncertainty in calculating the areas of certain peaks and the

uncertainty of gamma-ray emission probabilities for specific isotopes. For instance, the uncertainty of the gamma-ray emission probability at 120.90 keV for the ^{234}U isotope is approximately 8%.

4. CONCLUSION

This work presents studies on the age determination of low-enriched uranium in various physical forms using gamma spectrometry. The research was conducted using uranium working reference materials developed at the NSC KIPT, which included uranium oxide powders, uranium alloys, fuel pellets, and microspherical fuel.

Various analytical approaches have been proposed for uranium age calculation using two types of semiconductor detectors (a BEGe3830 broad-energy detector and a GL1015R low-energy detector) and two chronometers based on the determination of the ^{214}Bi/^{234}U and ^{223}Ra/^{235}U activity ratios. The age and model production dates for the uranium working reference materials were calculated.

It was demonstrated that the results of the uranium age calculations obtained through various analytical approaches are in good agreement with each other. The analytical approach based on the ^{214}Bi/^{234}U chronometer can be applied to determine the uranium age across a wide range of enrichments, from natural to enriched uranium (up to 20%). In contrast, the approach based on the ^{223}Ra/^{235}U chronometer is limited to the analysis of enriched uranium samples.

The average measurement uncertainty was estimated to be approximately 10% for an exposure time of 400 000 s. Ways to improve the measurement uncertainty were proposed, such as increasing the exposure time or refining the gamma-ray emission probabilities for certain isotopes.

ORCID

Stanislav Vanzha, https://orcid.org/0000-0003-0949-947X; **Dmytro Kutnii**, https://orcid.org/0000-0001-9591-4013;
Serhii Afanasiev, https://orcid.org/0000-0003-1682-4621; **Dmytro Burdeinyi**, https://orcid.org/0000-0003-4431-7264;
Oleksandr Zhukov, https://orcid.org/0009-0006-8341-922X

REFERENCES

[1] D.V. Kutnyi, D.D. Burdeinyi, S.N. Afanasiev, S.A. Vanzha, and O.P. Zhukov, "Determination of minimum detectable activity of ^{214}Bi in uranium oxide for uranium age dating using high-resolution gamma spectrometry (HRGS)", Problems of Atomic Science and Technology. Series "Nuclear Physics Investigations", **3**(157), 113-117 (2025). https://doi.org/10.46813/2025-157-113

[2] C.T. Nguyen, J. Zsigrai, and L. Lakosi, "Uranium Age Dating by Gamma Spectrometry", in: *International Conference on Advances in Nuclear Forensics*, (IAEA, Vienna, 2015). pp. 10. https://inis.iaea.org/records/wkjb6-5rp75

[3] Z. Li, Y. Shao, M. Luo, L. Ma, and D. Xu, "Application of element and isotopic fingerprint features in nuclear forensics: A review," Forensic Chemistry, **43**, 100646 (2025). https://doi.org/10.1016/j.forc.2025.100646

[4] W. Wang, J. Xu, R. Xi, et al., "Precise and accurate isotopic analysis of uranium and thorium in uranium ore concentrates using ICP-MS and their age dating for nuclear forensic analysis," J. Anal. At. Spectrom. **39**(1), 178-189 (2023). https://doi.org/10.1039/d3ja00196b

[5] Z. Varga, M. Wallenius, K. Mayer, and E. Hrnecek, "Alternative method for the production date determination of impure uranium ore concentrate sample," J. Radioanal. Nucl. Chem. **290**, 485-492 (2011). https://doi.org/10.1007/s1091233-5

[6] L. Lakosi, J. Zsigrai, A. Kocsonya, et al., "Gamma spectrometry in the ITWG CMX-4 exercise", J. of Radioanal. and Nucl. Chem. **315**, 409-416 (2018). https://doi.org/10.1007/s10967-017-5667-2

ВИЗНАЧЕННЯ ВІКУ НИЗЬКОЗБАГАЧЕНОГО УРАНУ У РІЗНИХ ФІЗИЧНИХ ФОРМАХ МЕТОДАМИ ГАММА-СПЕКТРОМЕТРІЇ

Станіслав Ванжа[1], **Дмитро Кутній**[1], **Сергій Афанасьєв**[1], **Дмитро Бурдейний**[1], **Олександр Жуков**[2]

[1]*Національний науковий центр "Харківський фізико-технічний інститут"НАН України, вул. Академічна, 1, Харків 61108, Україна*

[2]*Інститут ядерних досліджень НАН України, пр-т Науки 47, Київ 03028, Україна*

У роботі представлено результати дослідження з визначення віку низькозбагаченого урану у різних фізичних формах методами гамма-спектрометрії. Об'єктами дослідження стали робочі еталони уранових матеріалів (порошки оксидів, металеві сплави, паливні таблетки та мікросферичне паливо) зі збагаченням за ^{235}U від 0.47% до 19.75%, що створені в ННЦ «ХФТІ». Запропоновано та апробовано аналітичні підходи для визначення віку урану: Підхід 1 – базується на використанні широкодіапазонного детектора BEGe3830 та хронометра ^{214}Bi/^{234}U; цей метод продемонстрував ефективність для широкого інтервалу збагачень, від природного до збагаченого урану; Підхід 2: використовує низькоенергетичний детектор типу GL1015R та хронометр ^{223}Ra/^{235}U; встановлено, що даний підхід обмежений лише збагаченийм ураном. Отримані результати розрахунку віку та модельних дат виробництва за обома підходами демонструють добру узгодженість між собою. Середня невизначеність вимірювань склала приблизно 10% при експозиції 400 000 с.

Ключові слова: *радіоізотопне датування урану; ізотопний хронометр; гамма-спектрометр; збагачений уран*

East European Journal of Physics. 3. 402-414 (2026)
DOI:10.26565/2312-4334-2026-3-37 ISSN 2312-4334

MODELING AND OPTIMIZATION VALIDATION OF Sb_2Se_3 THIN FILM SOLAR CELLS IN SCAPS-1D SOFTWARE

K.M. Kuchkarov, B.A. Ergashev, R.T. Yuldoshov, M.P. Pirimmatov, R.R. Khurramov, D.Z. Isakov, M.A. Makhmudov, Sh.M. Bobomuradov*, A.S. Matmuratov, A.I. Eshqorayev
A.S. Azimov Physical-Technical Institute, Chingiz Aytmatov Street 2B, Tashkent 100084, Uzbekistan
**Corresponding Author e-mail: sherzodbobomuradov2@gmail.com*
Received April 28, 2026; revised June 16, 2026; accepted August 3, 2026

This analytical essay discusses antimony selenide (Sb_2Se_3) as a potential candidate material to be used as a thin-film photovoltaic absorber. Sb_2Se_3 has provided significant ecological/economic benefits, including large optical absorption, an adjustable band gap of about 1.13 eV, and a lack of toxic elements. A parametric exploration was carried out in the current study based on the platform SCAPS-1D in order to identify ideal layer designs, interfaces, carrier dynamics, and band alignments. This analysis has focused on loss mechanisms which constrain photovoltaic performance in an effort to isolate and come up with strategies to inhibit Shockley-Read-Hall recombination, surface recombination, band-offset differences, and internal diffusion effects. The results provide practical suggestions for minimizing voltage losses, such as minimizing absorber/buffer thicknesses, minimizing acceptor densities, optimizing the conduction band offset as close to zero as possible, and minimizing surface recombination and defect densities.
Keywords: *Sb_2Se_3; Thin-film solar cell; SCAPS-1D; Theoretical model; Parameter optimisation; Photovoltaic efficiency*

1. INTRODUCTION

The increasing energy needs of society have created an impetus to develop different means of harnessing renewable energy through research and technology. In particular, newer photovoltaic (PV) technology represents a more effective and environmentally friendly means of tapping into solar energy; additionally, the new methods being developed also represent ways to reduce manufacturing costs while at the same time achieving extremely high photovoltaic conversion efficiency PCE. Numerous categories of thin-film solar cell (TFSC) technology have garnered significant research interest recently due to the ability to minimize material usage, increase flexibility, and achieve high efficiency [1]. Recently, TFSC materials in multiple categories such as cadmium telluride (CdTe), copper indium gallium selenide (CIGS), and perovskite have gained tremendous popularity for use in solar cells. However, each material category has some limitations, particularly regarding the long-term viability of these materials (including the toxicity of cadmium (Cd) and indium (In)). Thus, many environmentally friendly and non-toxic materials for Photovoltaic (PV) applications have been researched, including copper zinc tin sulfide (Cu_2ZnSnS_4), SnS, Cu_2O, and $CuSbSe_2$ and their chalcogenides, antimony selenide (Sb_2Se_3) as well [2]. The maximum PCE obtainable by a single-junction solar cell is 32.23%, which occurs at approximately 1.14 eV, the optimal energy bandgap for the absorbing layer based on the Shockley-Queisser model [3]. These results indicate that Sb_2Se_3 is becoming a candidate material of choice for chalcogenides to absorb Solar Energy due to its opto-electronic properties such as high electron mobility (15 cm^2/Vs), hole mobility (42 cm^2/Vs), and good bandgap [4], which ranges from 1.10 -1.30 eV depending on application. It also has very low conductivity [5], a low melting point (612ºC), and a high absorption coefficient ($> 10^5$ cm^{-1}). In addition, Sb_2Se_3 has stability as an alternate absorber material for the construction of solar cells, thus allowing compatibility with current methods of production. Studies conducted by Wen et al. [6] reported improved charge-carrier mobility for the use of Sb_2Se_3 layers produced by means of vapor transport deposition technology (VTD), yielding efficiencies as high as 7.6% for VTD-produced films. Similarly, Li et al. [7] produced oriented nanorod assemblies of Sb_2Se_3 via closed-space sublimation (CSS) on Mo electrodes, yielding efficiencies of 9.2%. Huan et al. [8] created thin-filmed Sb_2Se_3 solar cells achieving 6.53% efficiency. Lin et al. [9] fabricated glass/Mo/Sb_2Se_3/CdS/ITO/Ag solar cells by means of spray application yielding PCE of 7.43%, which was subsequently improved to 8.64% by Tang et al. [10] Given the evolving effort to optimize these performance measures the current understanding of Sb_2Se_3 based solar cells has been explored with the aid of computer simulations utilizing the SCAPS-1D software, further enhancing the understanding of photovoltaic phenomena and supporting experimental development. The SCAPS-1D program is one of the most widely used tools for modeling thin-film solar cells. It has demonstrated its ability to accurately predict how a given solar cell will perform. With SCAPS-1D, electrical and optical properties of Sb_2Se_3 solar cells were able to be accurately simulated and the effects of material properties, layer thicknesses, doping levels, and defect densities on device performance were studied. As such, this simulation approach can save significant time and money compared to traditional experimental trial-and-error approaches, while also increasing understanding of the physical processes that limit device performance.

Cite as: K.M. Kuchkarov, B.A. Ergashev, R.T. Yuldoshov, M.P. Pirimmatov, R.R. Khurramov, D.Z. Isakov, M.A. Makhmudov, Sh.M. Bobomuradov, A. Matmuratov, A.I. Eshqorayev, East Eur. J. Phys. 3, 402 (2026), https://doi.org/10.26565/2312-4334-2026-3-37

In the research of Lin Ling-yang, the optimal layer thickness, defect density, and carrier mobility were identified by SCAPS-1D for the Sb_2Se_3/CdS solar cell structure to improve the cell efficiency, based on the SCAPS-1D parameters effective PCE. The solar cell structure has very promising attributes, including abundant material sources, low cost, and nontoxicity, as well as very effective construction of the absorber layer (600 nm) and buffer layer (60 nm), improved hole mobility, and low defect density. The PCE discovered in this research was 16.5% and consisted of a study of the effect of back contact work function [11]. The new Sb_2Se_3 based solar cell structure proposed by Baig and Faisal along with other co-authors used Eco-friendly and inexpensive materials to achieve a solar cell efficiency of 13.2 per cent. The researchers substituted the heavy-metal toxic elements Cd and Pb with Cu_2O as an HTM, In_2S_3 buffer layer, and a layer of CNT as a back contact to form the innovative new solar cell structure [12]. The effect of interface passivation on the performance of Sb_2Se_3 solar cells was also investigated in research by Chen et al. [13], who found that interface passivation was able to remove some defects and therefore, that SnO_2 was an important factor due to its ability to reduce defects and increase cell performance, a key aspect for practical use of the cells. Research by Sheikh et al. [14] indicated that CdS/Sb_2Se_3 devices with a 1 μm absorber thickness achieved a PCE of 29.35%. Similarly, [15] ZnS/Sb_2Se_3/PEDOT:PSS devices with an absorber layer thickness of 0.8 μm achieved the same PCE, which did not take into account any influence of the defect density on the interface. A WS_2/Sb_2Se_3/Cu_2O solar cell with a 0.5 μm thick absorber layer achieved a PCE of 30.03% [16], also without the effects of defect density on the interface. Because of the interfacial layer separating the collector layer of the Sb_2Se_3 (semiconductor) from the collector contact (metal), there are less downward band bending at the Sb_2Se_3/metal junction, making it easier for electrons and holes to move through the collector layer toward the collector metal. Reducing downward band-bending at the Sb_2Se_3/metal junction will eliminate the "pinning" or locking of the Fermi energy level at this junction. Eliminating such pinning will also improve transport of holes from the absorber layer to the collector, thereby reducing the amount of carrier recombination that occurs during the illumination phase. The interfacial layer will also facilitate the movement of holes through the back contact via the smallest band gap energy difference valence band offset (VBO) between the two. Therefore, it is critical to use certain materials that are compatible with the hole transport material (HTM) and back surface field (BSF) materials to maximize the electrical and optical performance. Cu_2O, a non-toxic, abundant, and easily manufactured material has been found to serve as a suitable HTM for Sb_2Se_3 solar cells [17].

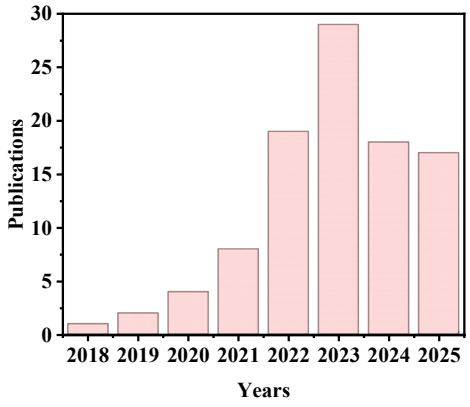

Figure 1. Publications on Sb_2Se_3 based thin-film solar cells using SCAPS-1D, categorized by years

The current modeling methods (i.e. SCAPS-1D simulations) have already demonstrated that significant improvements in power conversion efficiency for Sb_2Se_3 solar cells can be achieved by utilizing the modeling methods. Modern experimental fabrication and characterization of Sb_2Se_3 solar cells have thus been successful with the SCAPS-1D simulations of these cells. The role of absorbers, the doping levels of buffer layers, and the band alignments at the interface of thin film solar cells have all been modelled using simulations. The results obtained from the modelling of these parameters agree with the experimental values of the central electrical parameters such as PCE, V_{oc}, J_{sc} and FF. There can be discrepancies between the simulations and the experimental results due to the effects of non-ideal conditions, such as material inhomogeneity, defects at the interface, and other environmental influences. As shown in Figure 1, the publications on Sb_2Se_3 thin-film solar cells modelled using SCAPS-1D by the authors in journals indexed in SCOPUS for the period of 2018-2025.

This research paper will provide a comprehensive review of thin-film solar cells based on Sb_2Se_3 through simulation and analysis with SCAPS-1D. The significance of utilizing simulation and computation as an integral part of PV research will be discussed in depth. We will provide an in-depth description of the factors that affect the efficiency of a photovoltaic device and document new techniques (e.g., Interface engineering, control of doping level, use of machine learning, etc.) that could potentially alleviate current limitations of such devices.

2. MATERIAL PROPERTIES

Sb_2Se_3 thin films have a many beneficial properties, but their performance continues to lag behind the maximum potential performance predicted by the Shockley-Queisser (SQ) limit as the devices have yet to reach maximum attainable efficiencies. We encourage further development in three areas for improving the efficiency of Sb_2Se_3 thin film solar cells: First, better controlling the kinetics and morphology of Sb_2Se_3 precipitate growth while maintaining their high stability; second, ensuring proper alignment of the bandgap and energy bands in the device structure; and finally, minimizing recombination centers (defects at the interface and within the bulk of the material). Sb_2Se_3 belongs to A_2B_3-type isostructural compounds. These compounds are characterized by the presence of a metal A (bismuth or antimony) and a non-metal B (sulphur or selenium), and they are part of a larger family (A^{V}_{m} B^{VI}_{n}) that contains numerous compounds with similar structural arrangements. The orthorhombic stable phase of Sb_2Se_3 has orthorhombic Pbnm and Pnma crystallographic symmetry, and both of these space groups are crystallographically identical. Minor differences arise

when changing the directions of the coordinate axes. Pbnm lattice constants are a = 11.62 Å, b = 11.77 Å, c = 3.962 Å, and Pnma lattice constants are a = 11.7938 Å, b = 3.9858 Å, c = 11.6478 Å [18]. The crystal structure of Sb_2Se_3 is ribbon-like (or pseudo-1D) in its basic form, and this wrapping ribbon-like structure leads to anisotropic charge conduction and optoelectronic response of this compound, so the physicochemical stability of Sb_2Se_3, as well as the phase structure, texture, and orientation, needs to be controlled to take full advantage of its functionality.

2.1. Material Structure

The repeating structure of Sb_2Se_3 occurs as chains of $(Sb_4Se_6)_n$ between layers where van der Waals forces bind the chains together in the (010) direction, and covalent bonds hold them to form the (001) direction. The space between the ribbons was 2.98 Å, as referenced in [18]. In obtaining an effective application from the (221) direction, Sb_2Se_3 should be within 0.3-0.6 µm for optimal device use, while the diffusion distance for electrons when considering a (221) direction is only considered to be 0.3 µm, as stated in reference [5]. On the other hand, when measuring in the (001) direction the electrons can diffuse up to 1.7 µm which is five times longer than the (221) diffusion distance, as stated in reference [19].

As a result of this quasi-one-dimensional crystal system (as shown Figure 2), Sb_2Se_3 is highly anisotropic, with impediments on the trajectory of charge carriers occurring along all planes of the structure, except for one plane parallel to the c-axis (ribbon) direction. Due to limitations on carrier behavior within most of the ribbon's geometry, the carrier mobility of Sb_2Se_3 is rather poor in terms of the degree of mobility [4]. To modify the electronic characteristic properties of Sb_2Se_3, dopants such as transition metals or halogens can be introduced to produce additional energy state levels within the Sb_2Se_3 band gap, resulting in the band gap expanding or contracting depending upon the specialized dopant and doping configuration used. The electronic properties of thin film geometries also affect the size of the band gap as a result of changes in bond length and changes in the dimensions of the unit cell lattice constant, in addition to the influence of externally applied pressure, which has the potential to decrease the band gap, along with the effects of thermal expansion or contraction resulting from temperature changes.

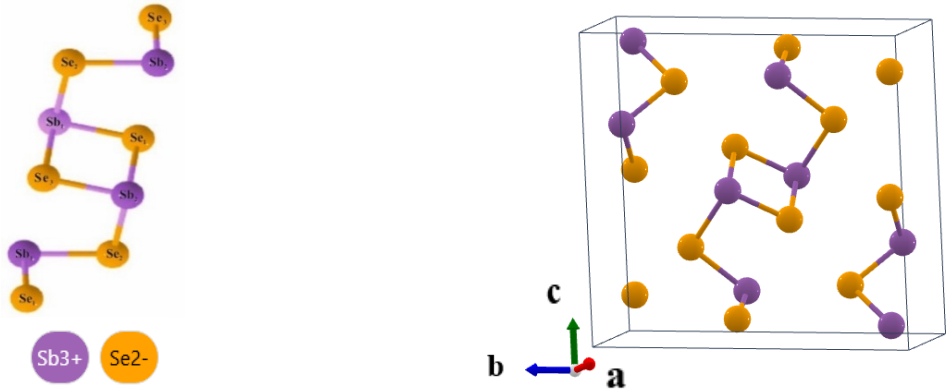

Figure 2. a) The asymmetric placement of antimony (Sb purple dots) and selenium (Se yellow dots) within the third phase of the Sb_2Se_3 compound, according to the Pbnm space group. b) An illustration of the "ribbon" configuration of the Sb_2Se_3 material system, such that dashed lines in black indicate the presence of van der Waals interactions holding together Se between different ribbons [20]

2.2. Defects in Antimony Selenide

Grain boundary defects in polycrystalline thin films were historically conceived of as recombination centers [21]. This conceptual framework is replicated from prior research on semiconductor systems such as GaAs and CdTe that exhibit similar behaviors due to their simple binary phase chemistry. It was originally assumed that the simple binary phase chemistry of Sb_2Se_3 would afford it a limited number of natural defects with respect to its management when compared with the multinanometallic systems such as CZTS/Se. Based on this assumption, it was hypothesized that there would be six intrinsic types of defects formed in this system:

(a) The two types of vacancies will exist in the form of cation vacancies (V_{Sb}) and anion vacancies (V_{Se}).

(b) The interstitials will consist of two types: cation interstitials (Sb_i) and anion interstitials (Se_i).

(c) The antisite defects will exist in the form of cation-on-anion antisites (Sb_{Se}) and anion-on-cation antisites (Se_{Sb}).

However, experimental and theoretical results indicate that the intrinsic defects in Sb_2Se_3 are far more complex than originally envisioned, and that the defect physics of this quasi-one-dimensional van der Waals material cannot be simply extrapolated from the three-dimensional covalently bonded binary photovoltaic absorbers (e.g. GaAs, CdTe).

2.3. Defect Tolerance of Photovoltaic Absorbers

There are two main reasons for the differences in defect tolerance between absorbers in photovoltaics and other types of solar cells: (1) the lack of deep traps in the gap energy region makes it a very good property of an absorber; and (2) the properties of the defects depend on the atomic position in the Q1D structure. For example, there are 3 different positions for Se atoms in a given Sb_2Se_3 ribbon (Se_1, Se_2, Se_3) but only 2 different positions for Sb in that ribbon (Sb_1, Sb_2), which means that defects in the same atomic location will have vastly different properties when considered in relation to either site.

Also, the low van der Waals strength of the $(Sb_4Se_6)_n$ chains leaves large voids between the $(Sb_4Se_6)_n$ ribbons, and as a result, defects appear in ways entirely unlike those of traditional absorbers. Such examples include cation-on-anion antisite defects (Sb_{Se}), anion-on-cation antisite defects (Se_{Sb}), and even two anions on one cation antisite defects ($2Se_{Sb}$). Thus, there are only a couple of basic defect types in this structure, but they are complicated because of the unusual structure of Sb_2Se_3. Se can be used to replace antimony's cation-anion character, resulting in Se_{Sb} and Sb_{Se} antisite defects. These defects are still debated to be acceptors or donors [22].

3. INFORMATION ABOUT THE SCAPS-1D PROGRAM

The SCAPS-1D software package was developed at Ghent University, Belgium, by Prof. Burgelman in the Electronics and Information Systems department and is a tool to evaluate the electro-mechanical properties of photovoltaic components such as solar cells, and increase their efficiency. Researchers and engineers have utilized SCAPS-1D extensively to explain the structure, material composition and working characteristics of solar cells. SCAPS-1D has applications in several areas of research: modelling of solar cells with materials including silicon (Si), CIGS, perovskites, Sb_2Se_3, etc; optimization of PCE by finding the best operating point for a solar cell and establishing how different material properties, thickness of layers, and concentrations of dopants impact the performance of the solar cell; validation of experimental results via simulation.

3.1. Main Input Parameters

The parameters that need to be entered into SCAPS-1D for solar cell modeling are as follows: Layer Thickness, Absorber and Buffer Thickness, and also the thickness of the Contact Layer.

Bandgap (E_g)

Dielectric permittivity (ε)

Electron mobility and hole mobility (μ)

Doping concentration, with n-type donor doping and p-type acceptor doping, and all that influence the electrical performance

Defect density, which includes the defect states that affect carrier recombination

Illumination intensity, or the solar irradiation intensity for example, 1 sun ≈ 1000 W/m^2

Spectral distribution of illumination (for example, AM1.5)

Temperature, being the nominal operating temperature of the device that is ~300K

Selection of the device structure (p - n junctions or heterojunctions)

Entering Parameters, such as material properties, layer thicknesses, doping concentrations, and other values

Running simulation - calculates the important electrophysical properties, such as I - V curve and quantum efficiency

Analyzing results to determine how well simulated results compare to experimental results and process optimization.

3.2. Advantage of the SCAPS-1D program

SCAPS-1D can simulate very complex multilayer structures with different semiconductor materials, as well as contacts and intermediate layers. This capability is very important for the research and optimization of different types of solar technologies, (i.e. Perovskite, Silicon, Organic, etc.) Although SCAPS-1D is fundamentally one-dimensional, it produces extremely accurate results for a wide variety of multilayered structures. SCAPS-1D allows users to model a variety of physical processes related to the operation of semiconductor devices including: the many types of recombination processes that can occur (such as Shockley-Read-Hall and surface recombination), quantum mechanical tunneling processes and defects that occur at the interfaces between different types of semiconductors and how these defects affect device characteristics.

In addition, SCAPS-1D is an inexpensive and fast alternative to performing the same type of experiments using laboratory techniques. Performing these types of experiments will take a significant amount of time and money, while using SCAPS-1D will allow the user to enter parameters digitally and automatically find the best possible answer. This provides an opportunity to rapidly design devices and to investigate the new materials. SCAPS-1D solves most of the main semiconductor equations that include electrons and holes, including the Poisson equation, continuity equations, and both current and voltage equations.

$$\frac{d^2\varphi(x)}{dx^2} = \frac{e}{\varepsilon_0 * \varepsilon_r}(p(x) - n(x) + N_D - N_A + \rho_P - \rho_n) \tag{1}$$

$$\frac{dJ_n}{dx} = G - R \tag{2}$$

$$\frac{dJ_p}{dx} = G - R \tag{3}$$

$$J_n = q\mu_n n\frac{d\varphi}{dx} + qD_n\frac{dn}{dx} \tag{4}$$

$$J_p = q\mu_p p\frac{d\varphi}{dx} - qD_p\frac{dp}{dx} \tag{5}$$

In this example, the dielectric constant of a vacuum, ε_0, a relative dielectric constant of ε_r; is the electron charge (e), n and p are electron and hole concentrations, such as N_D and N_A are densities of ionised donors (N_D) and acceptors (N_A) Electron and hole current densities (J_n and J_p) are described by recombination rates (R) and carrier generation rates (G), as well as their mobilities (μ_n and μ_p); along with their respective diffusion coefficients (D_n and D_p). The electric potential gradient can be established via Equation (1), which indicates the dependence of the electric potential gradient on the distribution of charge density with respect to electron and hole charges. Continuity equations are presented in Equations (2) and (3) and provide continuity for both electron (J_n) and hole (J_p) current densities, which are dependent upon their respective generation and recombination rates. Total current densities (with respect to both electrons and holes) are given by Equations (4) and (5) and consist of the total contribution of both drift and diffusion of the respective charge carriers. The direction that the carriers diffuse from regions of higher concentration to lower concentration is negative for holes, as they have negative charge; whereas electrons diffuse from regions of low concentration to more concentration.

3.3. Limitations of the SCAPS-1D Program

While SCAPS-1D is commonly used as a tool for modeling semiconductor components, it has a number of constraints that can affect how reliable results can be generated, and, in turn, can affect the usability of SCAPS-1D. To develop a model using SCAPS-1D, the user must make several assumptions regarding the idealized conditions under which the model is designed. For example, SCAPS-1D assumes that all layers of a semiconductor are “flat” and “uniform” in terms of their material properties (for example, composition, thickness, and crystal structure). In reality, there are many ways that a material's properties can vary within its layers (i.e., after undergoing defects due to manufacturing processes), and therefore these assumptions do not accurately reflect real-world systems. SCAPS-1D also assumes that all interfaces between layers are “perfectly flat”, but again this is not the case. Depending on the temperature, pressure and chemical environment in which a semiconductor is manufactured and processed, there may be defects and irregularities present at the interfaces between layers. These assumptions can result in discrepancies between computed and measured results when comparing complex or non-ideal systems. The user of SCAPS-1D must conduct proper experiments and use accurate and complete input parameters to obtain reliable results.

4. Modeling and Optimization of Sb_2Se_3 Solar Cells in SCAPS-1D

Modeling primarily aims to improve the PCE of the device. This is achieved by optimizing layer thicknesses, adjusting doping concentrations, reducing defect density, and optimizing series (R_s) and shunt (R_{sh}) resistances. Typically, two main architectures are used: superstrate and substrate. In the superstrate configuration, the layers are arranged sequentially on a transparent substrate (usually TCO on soda–lime glass): front contact, electron transport layer (ETL), absorber, hole transport layer (HTL), and back contact. In the substrate configuration, the order is reversed: glass, back contact, absorber, buffer (ETL), and transparent top layer. When these layers are stacked, band alignment occurs, which is explained by the Anderson model: if the electron affinity of the absorber χ_{abs} is greater than that of the buffer χ_{buf}, spike-like alignment is observed. If the spike is within the 0.3 eV range, electrons can easily transfer from the absorber to the buffer. When the value is higher, electron transport becomes inhibited, reducing the short-circuit current. If χ_{buf} is smaller than χ_{abs}, carrier recombination increases and the open-circuit voltage decreases. Therefore, selecting the optimal 0–0.3 eV spike-like alignment is essential. SCAPS mainly evaluates device performance based on band alignment. The most commonly used ETL material paired with Sb_2Se_3 is CdS. It is a natural starting candidate due to its useful properties: direct bandgap $E_g \approx 2.42$ eV, absorption coefficient 10^4 cm^{-1}, and charge-carrier mobility of 10^2 cm^2 $V^{-1}s^{-1}$ [7]. An important advantage of CdS is that it has already been successfully used as a buffer layer in CdTe and CIGS technologies [23]. Researchers have also proposed improved buffer layers. The following sections discuss various buffer layers, n^+ layers, additional p^+ layers on the absorber, combinations of n^+ and p^+ layers, and perovskite layers that significantly enhance the efficiency of the device.

4.1. Effect of a Single p–n Junction Structure in Sb_2Se_3 based Solar Cells

Working with SCAPS, Ling-Yan Lin and collaborators produced modeling work on Sb_2Se_3/CdS thin-film photovoltaic devices. The study revealed that optimal absorber and buffer layer thicknesses for such devices were found to be 600 nm and 60 nm, respectively. With a defect density of 10^{17} cm^{-3} and 10^8 cm^{-2} for the absorber and absorber-interface respectively, it was found that the devices could PCE as high as 16.5 % [11]. In the work performed by Mamta and colleagues, thin film CdS/Sb_2Se_3 solar cells were fabricated using a thermal evaporative deposition technique with absorber thicknesses of 372 nm and 640 nm. According to the results from SCAPS modeling, the devices exhibited efficiencies of 0.96% and 1.36% for these respective thicknesses and if the series and shunt resistances are properly adjusted and the absorber band gap is reduced from 1.47 eV to 1.2 eV, the maximum efficiency of the devices can reach up to approximately 11.27% [24]. Ahmed Shaker and co-workers ran SCAPS simulations on hybrid hetero-junction and homojunction solar cells based on Sb_2Se_3, and reported maximum PCE values of 7.75%, 10.08%, and 8.79% when the cells were based on CdS, ZnOS, and homojunctions respectively. They established the following optimized parameters in their models for CdS and ZnOS-based cells: n-region x_n = 75nm, $N_D = 1\times10^{17}$ cm^{-3}, p-region x_p = 350 nm, $N_A = 4\times10^{16}$ cm^{-3}. A typical homojunction Solar Cell has x_n = 40 nm, a doping of $N_D = 5\times10^{17}$ cm^{-3}, a p-region width x_p = 400 nm, and an N_A of 10^{16} cm^{-3}. Compared to Heterojunctions, Homojunctions have no interface between dissimilar layers, resulting in lower recombination and shorter transport layers that provide better reliability [25]. Raman Kumari

and colleagues used SCAPS-1D to model a Mo/Sb_2Se_3/ZnSe/Al device, with a buffer layer thickness of 100 nm and an absorption layer thickness of 1.5 µm. In this study, the maximum efficiency for a radiative recombination coefficient of 1×10^{-11} cm^3/s was accomplished using an absorber carrier concentration of 3.5×10^{17} cm^3 [26]. The use of the Cu Sandwich Method (Cu/Sb_2Se_3/Cu) to create Sb_2Se_3 by sequentially depositing Sb and Se followed by annealing at various temperatures has resulted in an X-ray Diffraction (XRD) and Field Emission Scanning Electron Microscopy (FE-SEM) analysis indicating a transition from the (hk0) plane to the (hk1) plane, with the nanotubes transforming to a polygonal form as the annealing temperature increases. The estimated bandgap for the copper sandwich Sb_2Se_3 sample, using annealing at 450ºC, was 1.04 eV, and the carrier concentration in the Sb_2Se_3 layer was 3.1×10^{15} cm^{-3}. A heterojunction solar cell was constructed with the 450°C annealed Sb_2Se_3 on top of a Glass/Ni/p-Sb_2Se_3/n-ZnSe/ITO/Al substrate and simulated using SCAPS-1D. This device produced an efficiency of 21.51%, an open-circuit voltage of 0.718 V, a current density of 43.33 mA cm^{-2}, and a Fill Factor of 69.14% [27]. The photovoltaic parameters of these single p-n junction Sb_2Se_3-based solar cells are summarized in Table 1.

Table 1. Photovoltaic parameters of single p-n junction **Sb_2Se_3**-based solar cells

no.	Sructure	χ (absorber/buffer)	E_g (absorber/buffer)	V_{oc} (V)	J_{sc} (mA/cm²)	FF (%)	PCE (%)	Reference
1	Au/Sb_2Se_3/CdS/FTO	3.9/4.2	1.06/2.4	0.40	41.86	74.08	16.5	[11]
2	Ag/Sb_2Se_3/CdS/ITO	4.04/4.2/4.5	1.47/2.4/3.7	0.74	18.07	83.62	11.27	[24]
3	Au/Sb_2Se_3/ZnOS/FTO	4.04/4.5	1.2/3.14	0.70	33.29	70.13	16.51	[25]
4	Mo/Sb_2Se_3/ZnSe/Al	4.04/4.09	1.2/2.7	0.85	34	83.61	24.01	[26]
5	Mo/Sb_2Se_3/ZnSe/ITO/Al	4.04/4.09/4.5	1.2/2.7	0.71	43.33	69.14	21.5	[27]

The UPS/HAXPES value obtained by Don et al. [28], was 5.13 eV for Sb_2Se_3 this would indicate a VBM of -5.13 eV in relation to a vacuum level. Our SCAPS simulations detected that the VBM of Sb_2Se_3 is –5.24 eV which falls within the conventional experimental uncertainty (±0.1 eV) and may be seen as an approximated adjustment of our model to compensate for the quality of films and surface termination, as well as the optimization of the band alignment of a particular device. Additionally, the SCAPS results produced by our model indicate that if the absorber thickness is held between 800 nm and 1.5 µm, with a defect density in the range of 10^{14} cm^{-3}, with carrier mobilities from 15-42 cm^2 $V^{-1}s^{-1}$, and the back-contact work function is about 4.8 eV with radiative recombination coefficients of 10^{-11} cm^3/s then the efficiency of the simulated device should be in the vicinity of 16.5-24%. The results of this research indicate that the primary method for increasing conversion efficiency will be to create differences between the conduction band and valence band. Additionally, SCAPS simulation studies performed for the integration of a ZnSe buffer layer into the overall growth scheme have shown that an enhancement of efficiency is also possible with the addition of a ZnSe buffer layer due in large measure to the superior lattice match (on the order of 2.52-3.94%) of the Sb_2Se_3 and ZnSe materials, along with the bandgap, (2.70 eV) and the electron affinity (~4.09 eV) of ZnSe, both of which combine to provide lower rates of interfacial recombination and higher rates of carrier extraction from the system. These are the reasons why ZnSe is a candidate for use as a buffer layer in next-generation Sb_2Se_3 photovoltaic cells built using a technology similar to that illustrated in Figure 3.

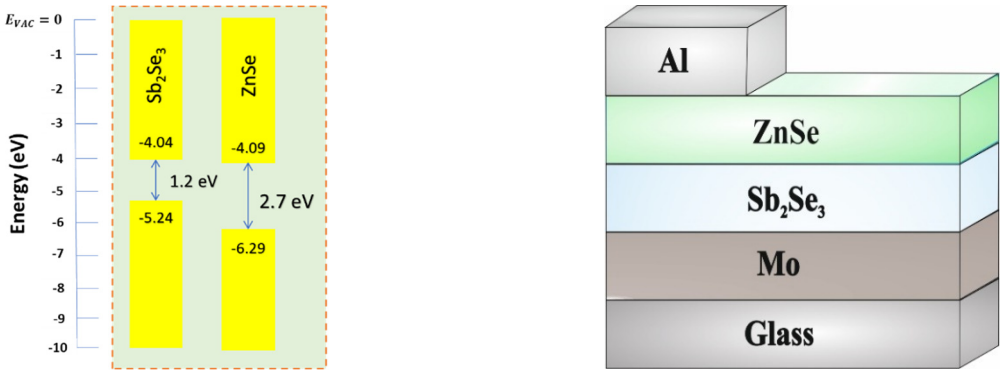

Figure 3. Energy band diagram of Sb_2Se_3 /ZnSe structure solar cell

4.2. Effect of a p^+ Layer in Sb_2Se_3 based Solar Cells

Basra Sultana et al. utilized SCAPS-1D simulations to optimize a Cu/FTO/CdS/SnSe/Sb_2Se_3/Au solar device (where SnSe serves as the primary absorber layer and Sb_2Se_3 serves as a secondary absorber). The efficiency of the device (Cu/FTO/CdS/SnSe/Au) prior to optimization was: PCE=26.15%, V_{oc}=0.79 V, J_{sc}=36.36 mA/cm^2, and FF=85.94%. The optimized device (Cu/FTO/CdS/SnSe/Sb_2Se_3/Au) had improved performance characteristics due to improved absorption capabilities and charge-carrier separation at the SnSe/Sb_2Se_3 interface [29]. Specifically, the optimized device demonstrated improvements to a PCE of 28.18%, V_{oc} of 0.84 V, J_{sc} of 38.42 mA/cm^2, and FF of 86.57% as compared to the non-optimized device. Aside from investigating the performance enhancement at the SnSe/Sb_2Se_3 interface, the investigation determined

that further performance enhancements could be achieved using TiO_2 buffer layers and Cu_2O BSF layers incorporated into the Sb_2Se_3 solar devices. In this study, the optimal thicknesses for the absorber and BSF layers were determined to be 500 nm and 20 nm, respectively; carrier concentrations were determined to be 1×10^{16} and 1×10^{18} cm^{-3} respectively, the defect density for both layers was 1×10^{14} cm^{-3}, and interface defect densities were determined to be 1×10^{13} cm^{-2} for the absorber and 1×10^{12} cm^{-2} for the BSF layers. The previous sections describe the parameters and calculations used to determine the output characteristics for this device. These parameters include operating temperature, electron affinity, E_g, surface recombination velocity, series resistance, and shunt resistance. Based on the optimized parameters of this Al/ITO/TiO_2/Sb_2Se_3/Cu_2O/Ni double-junction heterostructure, a PCE of 32.102% was achieved, with J_{sc} of 37.49 mA/cm^2, V_{oc} of 1.024 V, and FF of 83.59% [17]. S.H. Liu et al. proposed a solar cell with the following configuration: Al/FTO/CdS/Sb_2Se_3/Sb_2S_3/Mo. During the optimization process, the following parameters were varied: operating temperature, series resistance, shunt resistance, doping concentration, bulk defect density, the work function of the back-contact metal, and absorber layer thickness. The optimized combination of the Sb_2Se_3 absorber with the addition of an Sb_2S_3 layer resulted in a PCE of 28.91% with a 1 μm thick Sb_2Se_3 absorber layer; a 0.05 μm thick Sb_2S_3 BSF layer; and a carrier concentration of 1×10^{17} cm^{-3} in the Sb_2Se_3 [30]. Mutaz Salih Hasan Aljuboori and coworkers conducted a study of a solar cell with Glass/Mo/$CuSbS_3$/Sb_2S_3/CdS/i:ZnO/Al:ZnO which aimed to increase the maximum conversion efficiency of the cell by changing the thickness of the Sb_2S_3 layer from 1 to 3.5 μm. The maximum conversion efficiency was achieved with an absorber thickness of 3.5 μm resulting in a conversion efficiency of 23.14% and a fill factor of 87.52%. They also tested various materials to use as a secondary absorber layer lying between the primary absorber and the buffer layer including $MAPbI_3$, Sb_2Se_3, CZTS and CZTSe. They found that Sb_2Se_3 provided the highest conversion efficiency with a conversion efficiency of 27.01% and a fill factor of 85.12% after optimising the device [31]. Ferdous Rahman and coworkers also investigated the performance of Sb_2Se_3 solar cells when utilising a WS_2 buffer layer and a CZTSe BSF layer within a simulated structure (Al/FTO/WS_2/Sb_2Se_3/CZTSe/Pt) modelled using SCAPS-1D simulation software. For the purpose of maximizing the possible PCE, careful optimization of numerous parameters was performed, including the thickness of the absorber, buffer layer, donor and acceptor concentrations (N_D and N_A, respectively), the density of defects (N_t), and the series and shunt resistances (R_s and R_{sh} respectively). Without the addition of a p^+ layer in the proposed device described above, the measured data indicated a PCE of 28.20%, FF of 86.56%, V_{oc} of 0.85 V, and J_{sc} of 38.40 mA/cm^2. The PCE increased to 31.52%, J_{sc} to 38.49 mA/cm^2, V_{oc} to 0.94 V, and FF to 86.61% when a p^+ layer was added [32]. Studies have shown that by adding p+ dopants to Sb_2Se_3 based solar cells, PCE can be greatly improved. A high acceptor density located close to the back electrode of the solar cell eliminates or at least reduces any chance for hole recombination occurring at the back side of the spreader, thus leading to a higher Voc and improved PCE. Furthermore, when conduction and valence bands are aligned better, the diffusion length of charge carriers (holes and electrons) is increased, in turn leading to an increased J_{sc}. The maximum reported PCE obtained during this analysis was found to be 32.1%, with a vertical orientation of Cu_2O as the back surface field layer. The parameters for this process were optimised in this case by using the following: the thickness of both Sb_2Se_3 and Cu_2O layers were set at 500 nm and 20 nm, 1×10^{16} cm^{-3} and 1×10^{18} cm^{-3} were the carrier concentrations for the Sb_2Se_3 and Cu_2O respectively, a defect density of 1×10^{14} cm^{-3} and the interface defect densities for both materials were set at 1×10^{13} cm^{-2} for Sb_2Se_3 and 1×10^{12} cm^{-2} for Cu_2O. A representation of the energy band diagram for these structures can be found in Figure 4. Based on the results from 1D SCAPS studies on these systems, several ways to enhance photovoltaic performance include using BSF engineering by introducing an additional absorber for additional depth of light absorption, increasing the selectivity of the back contact, and optimising the geometry of the back-contact system to facilitate increased charge carrier transport. BSF materials are Cu_2O, Sb_2S_3, CZTSe, and alternative buffer materials such as ZnSe/ZnOS/TiO_2 for replacing CdS based buffers. The introduction of BSF materials greatly reduces the SRH recombination at the back surface. Additionally, optimising the conduction band offset (CBO) and valence band offset (VBO) in the energy band diagram improves selectivity of charge carriers and the second absorber offers a larger optical volume for light. These high PCE values are derived from 1D modelling under ideal circumstances; the actual lifetime of devices will be impacted by grain boundary transport and material anisotropy. The photovoltaic parameters of these p+-doped Sb_2Se_3-based solar cells are summarized in Table 2.

Table 2. Photovoltaic parameters of p^+-doped Sb_2Se_3-based solar cells.

no.	Sructure	χ (absorber/buffer)	E_g (absorber/buffer)	V_{oc} (V)	J_{sc} (mA/cm²)	FF (%)	PCE (%)	Reference
1	Au/Sb_2Se_3/SnSe/CdS/FTO /Cu	4.4/4.5/4.2	1.2/1.2/2.4	0.84	38.42	86.57	28.18	[29]
2	Ni/Cu_2O/Sb_2Se_3/TiO_2/ ITO/Al	3.2/4.16/4/4	2.2/1.2/3/3.2	1.02	37.49	83.59	32.10	[17]
3	Mo/Sb_2S_3/Sb_2Se_3/CdS/ FTO/Al	4.4/4.2	1.2/3.2	0.78	43.22	85.4	28.91	[30]
4	Mo/$CuSbS_3$/Sb_2Se_3/Sb_2S_3/ CdS/ZnO/ Al:ZnO	4.4/4.5	1.2/2.7	1.01	31.23	85.12	27.0	[31]
5	Pt/CZTSe/Sb_2Se_3/WS_2/ FTO/Al	4.1/4.16/3.95/4	1.4/1.2/2.2/3.6	0.94	38.49	86.61	31.5	[32]

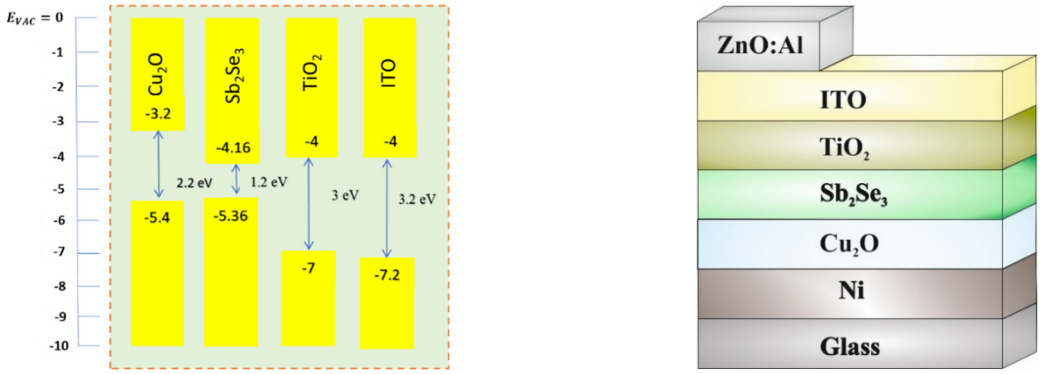

Figure 4. Structural and energy band diagram of p^+-Cu_2O/Sb_2Se_3 based solar cells

4.3. Effect of n^+ Doping in Sb_2Se_3 Based Solar Cells

The collaborative work of K.K Maurya and others provides important insight using SCAPS-1D simulations to demonstrate the key factors affecting the overall efficiency of Sb_2Se_3 based solar cells. The simulations identified three key factors related to the performance of the devices, which are use of dual buffer layers; the optimum conditions under which the devices operate; and lastly the selection of a back contact with a high work function. The authors first simulated an Sb_2Se_3/CdS/ZnO structure using CdS as the main buffer layer and ZnO as the second buffer layer. The effect of the CdS and ZnO on the photovoltaic performance Parameters (V_{oc}, J_{sc}, FF, and PCE) while the thickness of the absorber layer was 0.8µm and the temperature was set to 200K as it was noted increased temperatures lower the overall performance due to the negative impact of elevated temperatures on the mobilities of electrons and holes. When the radiative recombination coefficient is less than 10^{-8} cm^3/s and the back contact work function is at 5.1 eV, this structure provides an efficiency of 27.84% [33]. In their next paper, the authors show a greater efficiency of the Sb_2Se_3 devices can reach a higher efficiency by incorporating the dual buffer layers of CdS/ZnS. The maximum PCE obtained was 22.22% when the thicknesses of each buffer were set to 20 and 60 nm respectively. The authors have also shown that an optimum back-contact work function can be achieved if it exceeds 4.8 eV at the optimum temperature of 280K for Sb_2Se_3 to achieve 23.49% efficiency [34]. The results from this study demonstrate a theoretical limit to increasing the efficiency of Sb_2Se_3-based devices; the additions of both an additional buffer and n^+ layer provide a method of achieving this limit. The insertion of a n^+ layer will produce a corresponding improvement in the energy-band alignment due to the increase in concentration of electrons at the back contact which was shown in Figure 5. Enhanced electron concentration allows for enhanced accumulation and transportation of electrons toward the front contact and explains why solar cells that include an n^+ layer are capable of achieving much greater efficiency compared to devices based on a single p–n junction (as shown in Table 3).

Table 3. Photovoltaic parameters of n^+ doped Sb_2Se_3 based solar cells.

no.	Sructure	χ (absorber/buffer)	E_g (absorber/buffer)	V_{oc} (V)	J_{sc} (mA/cm²)	FF (%)	PCE(%)	Reference
1	Au/Sb_2Se_3/CdS/ZnO/ Al	4/4.2/4.4	1.2/2.4/3.3	0.98	42.4	66.81	27.8	[33]
2	Au/Sb_2Se_3/CdS/ZnS/Z nO/Al	4.04/4.2/4.5	1.2/2.4/3.5	0.77	35.5	85.32	23.49	[34]

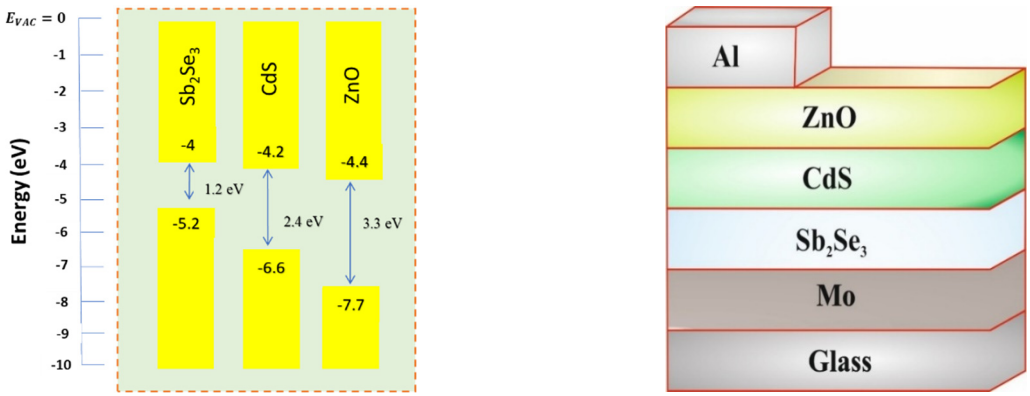

Figure 5. Energy band diagram of **Sb_2Se_3** /CdS/ n^+-ZnO structure solar cell

4.4. Effect of p^+/n^+ Doping in Sb_2Se_3 Based Solar Cells

In their laboratory experiments, Faisal Baig and his associates obtained an experimental efficiency of 6.39 for the structure Au/PbS/Sb_2Se_3/CdS/ITO; thereafter, SCAPS was simulated by substituting the PbS layer with Cu_2O (theoretical efficiency = 8.42%); SCAPS efficiency increased to 13.2% when replacing CdS with In_2S_3 (2.9 eV band gap and 3.85 eV electron affinity); based on these results, a new configuration for this solar cell was devised (CNT/Cu_2O/Sb_2Se_3/In_2S_3/ITO). The new structure, which has the configuration of Cu_2O as the HTL, In_2S_3 as the ETL, and CNTs as the back contact, was developed to further enhance the efficiency of this type of solar cell [12]. Abdelaziz Ait Abdelkadir and his co-researchers conducted a theoretical modeling study for the characterization of experimental Sb_2Se_3 solar cells. It was found that an efficiency of 16.62% was attained when the Sb_2Se_3 layer was 1.2 µm thick, carrier concentration was 10^{15} cm^{-3}, bulk defect density was 10^{13} cm^{-3}, and interface defect density was 10^{10} cm^{-2}. The device performance increased when an n-GaAs layer (100 nm thick) was added between the n-CdS and p-Sb_2Se_3, along with a p^+ Cu_2O HTL (100 nm thick) used as a BSF. This optimized arrangement produced more efficient electron transport and diffusion from the Sb_2Se_3 layer to the CdS layer, resulting in improved device performance. The addition of the p^+ Cu_2O HTL at the back contact also provided a greater potential barrier that limited recombination of the charge carriers at the back contact. The resulting device structure, ITO/CdS/GaAs/Sb_2Se_3/Cu_2O/Au, achieved an efficiency of 19.60%, with a J_{sc} of 36.38 mA/cm^2, a V_{oc} of 0.73 V, and a FF of 73.47% [35]. Z. Dahmardeh et al. simulated a Sb_2S_3/Sb_2Se_3 solar cell and reported PCE of 22.2% using absorber layer thicknesses of 420 nm and 1020 nm, respectively [36]. Shriya Sakul Bal et al. also studied a solar cell with a different structure (Mo/Sb_2Se_3/Sb_2S_3/CdS/ZnO/ZnO:Al), using 500 nm of Sb_2S_3 and 1000 nm of Sb_2Se_3 for the absorber layers. The thickness of the CdS/ZnO buffer was determined to be optimal at 80 nm for CdS and 50 nm for ZnO. After fully optimized, the maximum efficiency of 13.2% was achieved; with FF of 78.64%, J_{sc} of 29.33 mA/cm^2, and V_{oc} of 0.58 volts [37]. When combined p^+/n^+ doped Sb_2Se_3 photovoltaic cells are compared with single p-n junction a Sb_2Se_3 photovoltaic cell, the efficiencies were significantly lower. The decrease in efficiency is attributed to two main factors: (1) the additional layers create an increase in the number of recombination centres at the different interface, which reduces the V_{oc}, and (2) the increase in the total thickness of the device decreases the total light being absorbed and also the number of photons that can penetrate into the absorber layer and ultimately decrease the J_{sc} (see Table 4 and Figure 6).

Table 4. Photovoltaic parameters of p^+/n^+-layers added Sb_2Se_3-based solar cells

no.	Structure	χ (absorber/buffer)	E_g (absorber/buffer)	V_{oc} (V)	J_{sc} (mA/cm^2)	FF (%)	PCE (%)	Reference
1	CNT/Cu_2O/Sb_2Se_3 /InS_3/ITO	3.2/4.15/4.25/4.5	2.2/1.06/2.9/3.6	0.67	26.84	79.74	13.2	[12]
2	Au/Cu_2O/Sb_2Se_3/ GaAs/CdS/ITO	3.2/4.18/4.07/4.4/4.5	2.2/1.19/1.43/2.42/3.6	0.73	36.38	73.47	19.6	[35]
3	Mo/Sb_2Se_3/Sb_2S_3/ CdS/ZnO/ZnO:Al	4.04/4/4.2/4.5	1.2/1.67/2.4/3.3	1.02	20.15	59.58	22.2	[36]
4	Mo/Sb_2Se_3/Sb_2S_3/ CdS/ZnO/ZnO:Al	3.7/3.7/4.2/4.5	1.08/1.62/2.4/3.3	0.58	29.33	78.64	13.2	[37]

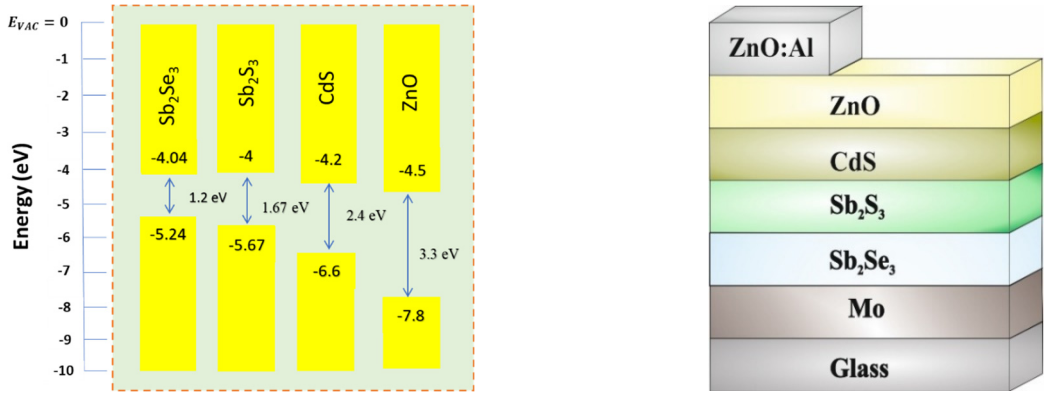

Figure 6. Energy band diagram of p^+/n^+-layers added Sb_2Se_3 based solar cells

4.5. Effect of Perovskite Incorporation in Sb_2Se_3 Based Solar Cells

Masood Mehrabian and co-workers simulated a multi-layer dual-absorber solar cell with the structure FTO/CdS/Sb_2Se_3/$CuInSe_2$/Au, achieving PCE = 5.55%, FF = 54.68%, J_{sc} = 27.54 mA/cm², and V_{oc} = 0.36 V. By replacing the CdS ETL with a C_{60} layer, the photovoltaic performance improved to PCE = 9.20%, FF = 67.78%, J_{sc} = 27.38 mA/cm^2, and V_{oc} = 0.49 V (Table 5). Furthermore, by incorporating a $CsSn_{0.5}Ge_{0.5}I_3$ perovskite absorber layer, the efficiency increased to 11.42%. Although the maximum recombination rate in the CdS layer was about one order lower than in the C_{60} layer, the smaller bandgap (E_g) of C_{60} compensated for its higher recombination rate, contributing to improved PCE

[38]. In another study, Mousaab Belarbi used $KSnI_3$ perovskite layer in FTO/SnS_2/$KSnI_3$/Sb_2Se_3/Pt device and replaced the Pt back contact with tungsten (W). When the absorber thickness was 0.9 µm, donor and acceptor concentrations were 10^{17} cm^{-3} and 10^{20} cm^{-3}, the operating temperature was 280 K, and the $KSnI_3$ bandgap was 1.74 eV, the device performance improved significantly. Jsc increased from 13.79 to 26.08 mA/cm^2, FF from 69.07% to 76.25%, and PCE from 12.72% to 23.85% [39]. Arslan Ashfaq and co-workers performed numerical simulations of p-Sb_2Se_3/n-$BaZrS_3$ heterojunction solar cells. Compared to lead-based chalcogenide perovskites, n-$BaZrS_3$ is more stable, non-toxic, and suitable for thin-film solar cell applications as a sulfur-based chalcogenide material. In their study, the photovoltaic parameters achieved were PCE = 32.87%, FF = 88.22%, J_{sc} = 36.88 mA/cm^2, and V_{oc} = 1.01 V. The best performance was obtained when the p-Sb_2Se_3 absorber layer thickness was 7000 nm, the bandgap 1.15 eV, and carrier concentration 10^{20} cm^{-3}. For $BaZrS_3$, the optimal parameters were thickness of 100 nm, carrier concentration of 10^{17} cm^{-3}, and a bandgap of 1.76 eV. One advantage of these perovskites is their strong ionic coordination, which enhances the Coulomb attraction between positive and negative ions [40]. Jing Wu and co-workers simulated Sb_2Se_3/$MAPbI_3$ solar cell using SCAPS-1D, analyzing absorber layer thicknesses of Sb_2Se_3 and methylammonium lead iodide ($MAPbI_3$), the thickness and doping concentration of the n-type buffer layer, as well as the bulk defect densities of Sb_2Se_3 and $MAPbI_3$. In addition, the effects of defect density at the Sb_2Se_3/$MAPbI_3$ and $MAPbI_3$/TiO_2 interfaces on device efficiency were investigated. The optimal absorber thicknesses were found to be 0.6 µm for Sb_2Se_3 and 0.7 µm for $MAPbI_3$. Further analysis revealed that within optimized parameters, the donor concentration (N_D) of the TiO_2 buffer layer reached 10^{18} cm^{-3}, while its optimal thickness was 0.05 nm. Moreover, the bulk defect densities of Sb_2Se_3 and $MAPbI_3$ should be 10^{13} cm^{-3} or lower, and the interface defect densities should be 10^{11} cm^{-2} or lower to achieve an efficiency of 21.90% [41]. The significant enhancement of photovoltaic performance through perovskite incorporation in Sb_2Se_3 based solar cells can be seen in Table 5 and Figure 7. Notably, the inclusion of $BaZrS_3$ layer demonstrated efficiency values approaching the Shockley-Queisser limit, with well-aligned energy band matching.

Table 5. Photovoltaic parameters of perovskite integrated **Sb_2Se_3** based solar cells

no.	Sructure	χ (absorber/buffer)	E_g (absorber/buffer)	V_{oc} (V)	J_{sc} (mA/cm^2)	FF (%)	PCE (%)	Reference
1	FTO/C_{60}/$CsSn_{0.5}Ge_{0.5}I_3$/Sb_2Se_3/$CuInSe_2$/Au	3.9/3.9/3.9/4.3	1.7/1.5/1.06/1.04	0.49	27.38	67.78	11.4	[38]
2	FTO/SnS_2/$KsnI_3$/Sb_2Se_3/W	4/4.16/3.44/4.04	3.5/2.3/1.84/1.2	1.19	26.08	76.25	23.85	[39]
3	Mo/Sb_2Se_3/$BaZrS_3$/FTO	4.05/4.1/4.4	1.2/1.76/3.2	1.01	36.88	88.22	32.8	[40]
4	Sb_2Se_3/$MAPbI_3$/TiO_2	3.9/3.9/3.9	1.06/1.5/3.1	0.69	43	78.5	21.9	[41]

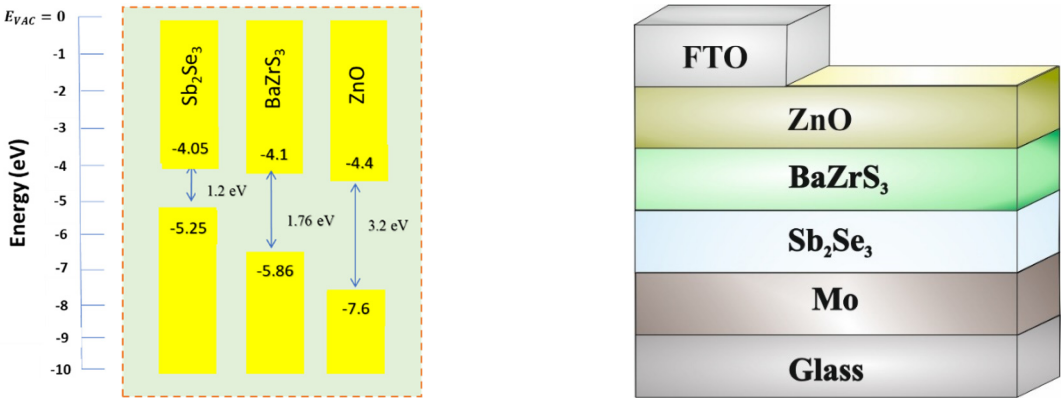

Figure 7. Energy band diagram of Perovskite thin layer added Sb_2Se_3 based solar cells

5. CONCLUSIONS

By combining SCAPS-1D simulations with experimental analyses, significant progress has been achieved toward optimizing Sb_2Se_3 based thin-film solar cells. In this study, the optical, structural, and electronic properties of Sb_2Se_3 were comprehensively investigated, and several advanced device configurations including single p-n junctions, p^+-doped, n^+-enhanced architectures, p^+/n^+ co-doped structures, and perovskite-integrated heterojunctions were analyzed. The modeling results demonstrated that high efficiencies can be achieved with absorber layer thicknesses ranging from 800 nm to 1.5 µm, low bulk defect densities on the order of 10^{14} cm^{-3}, interface defect densities of 10^{11} cm^{-2}, appropriate carrier mobilities, and favorable energy band alignment. One important finding was the substantial benefit of incorporating a ZnSe layer as the buffer material. This improvement results from its favorable band alignment, electron affinity, and excellent lattice compatibility with Sb_2Se_3. Furthermore, the introduction of a p^+ layer was shown to enhance device efficiency. With a high acceptor concentration (10^{18} cm^{-3}) in the p^+ region and a very thin (20 nm) layer, hole recombination near the back electrode was significantly suppressed, leading to higher open-circuit voltage. Improved conduction and valence band alignment also increased the diffusion lengths of electrons and holes, thereby enhancing the short-circuit current. Among all investigated

configurations, the Cu_2O BSF (back-surface field) layer achieved the highest efficiency of 32.1%. Cu_2O, Sb_2Se_3, and CZTSe were identified as promising alternative BSF materials, all effectively reducing SRH recombination at the rear interface. It should be noted that the reported efficiency values are based on 1-D simulation assumptions involving ideal interfaces and simplified defect densities; therefore, real devices must account for grain-boundary transport and anisotropy effects. The study further showed that incorporating an additional n^+ layer not just a single buffer can theoretically improve device performance, as confirmed both by improved band alignment and experimental observations demonstrating enhanced electron collection at the front contact. In contrast, the use of combined p^+/ n^+ doping led to reduced efficiencies. This reduction is attributed to an increased number of interfaces, which introduce additional recombination centers and thereby lower the open-circuit voltage. Moreover, excessive total thickness decreases light absorption, reducing photon penetration into the absorber and subsequently lowering the short-circuit current. Perovskite incorporation, particularly the inclusion of $BaZrSe_3$ layer, significantly improved device performance. Structures employing this material demonstrated efficiencies close to the Shockley-Queisser theoretical limit. These results were enabled by nearly ideal band alignment and exceptional lattice matching between $BaZrSe_3$ and Sb_2Se_3 (with only ~0.2% mismatch). In summary, Sb_2Se_3 based solar cells when designed with careful consideration of defect passivation, interface engineering, and advanced heterostructure configurations hold strong promise as next-generation high-efficiency photovoltaic technologies.

Funding

This work was supported by the Basic Research Program of the Academy of Sciences of the Republic of Uzbekistan

Declaration of competing interest

The authors declare that they have no known competing financial interests or personal relationships that could have appeared to influence the work reported in this paper.

Data availability

Data will be made available on request.

Acknowledgements

The authors gratefully acknowledge Prof. M. Burgelman and the Department of Electronics and Information Systems, Ghent University, Belgium, for providing the SCAPS-1D software free of charge.

ORCID

K.M. Kuchkarov, https://orcid.org/0000-0002-2238-7205; **B.A. Ergashev,** https://orcid.org/0000-0001-9456-7961;
R.T. Yuldoshov, https://orcid.org/0000-0002-7886-1607; **M.P. Pirimmatov,** https://orcid.org/0009-0000-4829-7817;
R.R. Khurramov, https://orcid.org/0009-0008-1038-0138; **D.Z. Isakov,** https://orcid.org/0000-0003-4314-5683;
M.A. Makhmudov https://orcid.org/0009-0008-8836-0559; **Sh.M. Bobomuradov,** https://orcid.org/0009-0001-1338-3202;
A.S. Matmuradov, https://orcid.org/0009-0005-6121-6424; **A. Eshqorayev,** https://orcid.org/0009-0008-9022-5700

REFERENCES

[1] A.A.F. Husain, W.Z.W. Hasan, S. Shafie, M.N. Hamidon, and S.S. Pandey, "A review of transparent solar photovoltaic technologies," (2018). https://doi.org/10.1016/j.rser.2018.06.031

[2] Sadanand, P. K. Singh, S. Rai, P. Lohia, and D. K. Dwivedi, "Comparative study of the CZTS, CuSbS2 and $CuSbSe_2$ solar photovoltaic cell with an earth-abundant non-toxic buffer layer," Solar Energy, **222**, 2021, https://doi.org/10.1016/j.solener.2021.05.013

[3] S. Rühle, "Tabulated values of the Shockley-Queisser limit for single junction solar cells," Solar Energy, **130**, 2016, https://doi.org/10.1016/j.solener.2016.02.015

[4] A. Mavlonov, et al., "A review of Sb_2Se_3 photovoltaic absorber materials and thin-film solar cells," (2020). https://doi.org/10.1016/j.solener.2020.03.009

[5] C. Chen, et al., "Characterization of basic physical properties of Sb_2Se_3 and its relevance for photovoltaics," Frontiers of Optoelectronics, **10**(1), (2017). https://doi.org/10.1007/s12200-017-0702-z

[6] X. Wen et al., "Vapor transport deposition of antimony selenide thin film solar cells with 7.6% efficiency," Nat. Commun., **9**(1), (2018). https://doi.org/10.1038/s41467-018-04634-6

[7] Zhiqiang Li, "9.2%-efficient core-shell structured anti mony selenide nanorod array solar cells," Nat. Commun., **10**(1), (2019). https://doi.org/10.1038/s41467-018-07903-6

[8] H. Ning, et al., "Enhancing the efficiency of Sb_2Se_3 solar cells using dual-functional potassium doping," Solar Energy Materials and Solar Cells, **221**, (2021). https://doi.org/10.1016/j.solmat.2020.110816

[9] J. Lin, et al., "Crystallographic orientation control and defect passivation for high-efficient antimony selenide thin-film solar cells," Materials Today Physics, **27**, (2022). https://doi.org/10.1016/j.mtphys.2022.100772

[10] Rong Tang, "Heterojunction annealing enabling record open-circuit voltage in antimony triselenide solar cells," Advanced Materials, **34**(14), (2022). https://doi.org/10.1002/adma.202109078

[11] L. yan Lin, L. qin Jiang, Y. Qiu, and B. dian Fan, "Analysis of Sb_2Se_3/CdS based photovoltaic cell: A numerical simulation approach," Journal of Physics and Chemistry of Solids, **122**, (2018). https://doi.org/10.1016/j.jpcs.2018.05.045

[12] F. Baig, Y. H. Khattak, S. Beg, and B. M. Soucase, "Numerical analysis of a novel CNT/Cu_2O/Sb_2Se_3/In_2S_3/ITO antimony selenide solar cell," Optik (Stuttg.), **197**, (2019). https://doi.org/10.1016/j.ijleo.2019.163107

[13] Y. Chen, et al., "Importance of interfacial passivation in the high efficiency of Sb_2Se_3 thin-film solar cells: Numerical evidence," ACS Appl. Energy Mater. **3**(11), (2020). https://doi.org/10.1021/acsaem.0c01203

[14] S. R. Al Ahmed, A. Sunny, and S. Rahman, "Performance enhancement of Sb_2Se_3 solar cell using a back surface field layer: A numerical simulation approach," Solar Energy Materials and Solar Cells, **221**, (2021). https://doi.org/10.1016/j.solmat.2020.110919
[15] S. Abbas, et al., "Numerical Simulation of the Performance of Sb_2Se_3 Solar Cell via Optimizing the Optoelectronic Properties Based SCAPS-1D," Materials, **15**(18), (2022). https://doi.org/10.3390/ma15186272
[16] A. El Khalfi, L. Et-Taya, Y. Achenani, M. Sahal, L. Elmaimouni, and A. Benami, "Performance Evaluation of Sb_2Se_3-based Solar Photovoltaic Cells with Various ETL and Cu_2O as HTL by SCAPS-1D," Karbala International Journal of Modern Science, **9**(3), (2023). https://doi.org/10.33640/2405-609X.3303
[17] B. Sultana, A. T. M. S. Islam, M. D. Haque, and A. Kuddus, "Cu_2O-Enhanced Back Surface Field Empowers Selenium-Based TiO_2/ Sb_2Se_3 Thin Film Solar Cells to Achieve Efficiency over 32%," Applied Solar Energy (English translation of Geliotekhnika), **59**(6), (2023). https://doi.org/10.3103/S0003701X23601515
[18] N. W. Tideswell, F. H. Kruse, and J. D. McCullough, "The crystal structure of antimony selenide, Sb_2Se_3," Acta Crystallogr. **10**(2), (1957). https://doi.org/10.1107/s0365110x57000298
[19] K. Li et al., "One-Dimensional Sb2Se3 Enabling Ultra-Flexible Solar Cells and Mini-Modules for IoT Applications," Nano Energy, **86**, 106101 (2021). https://doi.org/10.1016/j.nanoen.2021.106101
[20] K. Momma, and F. Izumi, "VESTA 3 for three-dimensional visualization of crystal, volumetric and morphology data," J. Appl. Crystallogr. **44**(6), (2011). https://doi.org/10.1107/S0021889811038970
[21] Y. Yan, et al., "Physics of grain boundaries in polycrystalline photovoltaic semiconductors," Journal of Applied Physics, **117**, 112807 (2015). https://doi.org/10.1063/1.4913833
[22] B. Zhang, and X. Qian, "Competing Superior Electronic Structure and Complex Defect Chemistry in Quasi-One-Dimensional Antimony Chalcogenide Photovoltaic Absorbers," ACS Appl. Energy Mater. 5(1), 1 (2022). https://doi.org/10.1021/acsaem.1c03023
[23] J. Ramanujam, and U.P. Singh, "Copper indium gallium selenide based solar cells - A review," **10**(6), 1306–1319 (2017). https://doi.org/10.1039/c7ee00826k
[24] Mamta, R. Kumari, C. Yadav, R. Kumar, K. K. Maurya, and V. N. Singh, "Thermally Deposited Sb_2Se_3/CdS-Based Solar Cell: Experimental and Theoretical Analysis," Nanomaterials, **13**(6), (2023). https://doi.org/10.3390/nano13061135
[25] A. Shaker, M. S. Salem, and K. Deepthi Jayan, "Analysis and design of p-n homojunction Sb_2Se_3 solar cells by numerical simulation," Solar Energy, (242), (2022). https://doi.org/10.1016/j.solener.2022.07.035
[26] R. Kumari, M. Mamta, R. Kumar, Y. Singh, and V. N. Singh, "24% Efficient, Simple ZnSe/ Sb_2Se_3 Heterojunction Solar Cell: An Analysis of PV Characteristics and Defects," ACS Omega, **8**(1), (2023). https://doi.org/10.1021/acsomega.2c07211
[27] B. Srinivas, S. Babujani, G. H. Chandra, Y. P. V. Subbaiah, and M. Gupta, "Synthesis and characterization of Cu-sandwiched Sb_2Se_3 thin films and numerical simulation of p- Sb_2Se_3/n-ZnSe heterojunction solar cell," Opt. Mater. (Amst). **135**, (2023). https://doi.org/10.1016/j.optmat.2022.113289
[28] C. H. Don, *et al*., "Sb 5s2lone pairs and band alignment of Sb_2Se_3: a photoemission and density functional theory study," J. Mater. Chem. C Mater. **8**(36), (2020). https://doi.org/10.1039/d0tc03470c
[29] F. B. Sultana, "A new design and optimization of SnSe-based dual absorber solar cell with efficiency above 28%," Journal of Nanoparticle Research, **26**(8), (2024). https://doi.org/10.1007/s11051-024-06085-1
[30] S. H. Liu, J. R. Yuan, Y. Wu, X. H. Deng, and Q. M. Yu, "Numerical simulation of Sb_2Se_3-based solar cells," Chalcogenide Letters, **21**(3), (2024). https://doi.org/10.15251/CL.2024.213.229
[31] M. S. Aljuboori, "Enhancing Photoconversion Efficiency by Optimization of Electron/Hole Transport Interlayers in Antimony Sulfide Solar Cell using SCAPS-1D Simulation," Solar Energy and Sustainable Development, **13**(1), 97–113 (2024). https://doi.org/10.51646/jsesd.v13i1.175
[32] M. F. Rahman, A. Lubaba, L. Ben Farhat, S. Ezzine, M. H. Rahman, and M. Harun-Or-Rashid, "Efficiency enhancement above 31 % of Sb_2Se_3 solar cells with optimizing various BSF layer," Materials Science and Engineering: B, **307**, (2024). https://doi.org/10.1016/j.mseb.2024.117527
[33] Mamta, K. K. Maurya, and V. N. Singh, "Efficient Sb_2Se_3 solar cell with a higher fill factor: A theoretical approach based on thickness and temperature," Solar Energy, **230**, (2021). https://doi.org/10.1016/j.solener.2021.11.002
[34] Mamta, K. K. Maurya, and V. N. Singh, "Enhancing the performance of a Sb_2Se_3-based solar cell by dual buffer layer," Sustainability (Switzerland), **13**(21), (2021). https://doi.org/10.3390/su132112320
[35] A. Ait Abdelkadir, M. Sahal, E. Oublal, N. Kumar, and A. Benami, "New Sb_2Se_3-based solar cell for achieving high efficiency theoretical modeling," Opt. Quantum Electron. **55**(6), (2023). https://doi.org/10.1007/s11082-023-04797-7
[36] Z. Dahmardeh, and M. Saadat, "Exploring the potential of standalone and tandem solar cells with Sb_2S_3 and Sb_2Se_3 absorbers: a simulation study," Sci. Rep. **13**(1), (2023). https://doi.org/10.1038/s41598-023-49269-w
[37] S. S. Bal, A. Basak, and U. P. Singh, "Numerical modeling and performance analysis of Sb-based tandem solar cell structure using SCAPS – 1D," Opt. Mater. (Amst). **127**, (2022). https://doi.org/10.1016/j.optmat.2022.112282
[38] M. Mehrabian, "Numerical optimization of cesium tin-germanium triiodide/antimony selenide perovskite solar cell with fullerene nanolayer," Journal of Physics and Chemistry of Solids, **196**, (2025). https://doi.org/10.1016/j.jpcs.2024.112370
[39] M. Belarbi, "Numerical analysis of performance enhancement in $KSnI_3$-based perovskite solar cells with Sb_2Se_3 as a hole transport layer," Materials Science and Engineering: B, **313**, (2025). https://doi.org/10.1016/j.mseb.2024.117874
[40] A. f Ashfaq, "High-efficiency selenium and sulfurbased p- Sb_2Se_3/n-$BaZrS_3$ heterostructure solar cells: A SCAPS-1D simulation study," Journal of Physics and Chemistry of Solids, **199**, (2025). https://doi.org/10.1016/j.jpcs.2024.112490
[41] J. Wu, Z. Zhao, Z. Zhao, M. Zhang, Y. Bi, X. Li, and L. Zhang, "Simulation Analysis of Sb_2Se_3 Narrow Bandgap Hole Transport Layer in $MAPbI_3$ Perovskite Solar Cells," Metals & Materials Society, Mar. **54**, 3910–3923 (2025). https://doi.org/10.1007/s11664-025-11886-8

МОДЕЛЮВАННЯ ТА ОПТИМІЗАЦІЙНА ВАЛІДАЦІЯ ТОНКОПЛІВКОВИХ СОНЯЧНИХ ЕЛЕМЕНТІВ Sb_2Se_3 У ПРОГРАМНОМУ ЗАБЕЗПЕЧЕННІ SCAPS-1D

К.М. Кучкаров, Б.А. Ергашев, Р.Т. Юлдошов, М.П. Пірімматов, Р.Р. Хуррамов, Д.З. Ісаков, М.А. Махмудов, Ш.М. Бобомурадов, А.С. Матмуратов, А.І. Ешкораєв

Фізико-технічний інститут імені А.С. Азімова, вулиця Чингіза Айтматова, 2Б, Ташкент 100084, Узбекистан

У цьому аналітичному есе розглядається селенід сурми (Sb_2Se_3) як потенційний матеріал-кандидат для використання в якості тонкоплівкового фотоелектричного поглинача. Sb_2Se_3 забезпечив значні екологічні/економічні переваги, включаючи велике оптичне поглинання, регульовану ширину забороненої зони близько 1,13 еВ та відсутність токсичних елементів. У цьому дослідженні було проведено параметричне дослідження на основі платформи SCAPS-1D з метою визначення ідеальних конструкцій шарів, інтерфейсів, динаміки носіїв заряду та вирівнювання зон. Цей аналіз зосереджений на механізмах втрат, які обмежують фотоелектричну продуктивність, з метою ізоляції та розробки стратегій для пригнічення рекомбінації Шоклі-Ріда-Холла, поверхневої рекомбінації, різниці в зміщенні зон та ефектів внутрішньої дифузії. Результати надають практичні пропозиції щодо мінімізації втрат напруги, такі як мінімізація товщини поглинача/буфера, мінімізація густини акцептора, оптимізація зміщення зони провідності якомога ближче до нуля та мінімізація поверхневої рекомбінації та густини дефектів.

Ключові слова: *Sb_2Se_3; тонкоплівковий сонячний елемент; SCAPS-1D; теоретична модель; оптимізація параметрів; фотоелектрична ефективність*

EAST EUROPEAN JOURNAL OF PHYSICS. 3. 415-431 (2026)
DOI:10.26565/2312-4334-2026-3-38 ISSN 2312-4334

INFLUENCE OF HALL CURRENT, THERMAL DISPERSION, AND HEAT GENERATION ON KEROSENE-BASED TiO_2 NANOFLUID FLOW THROUGH A ROTATING POROUS CHANNEL

Venkateswarlu Malapati[1#], Mohammed Almakki[2##], V.B. Rajakumar Komaravolu[3]*
[1]*Department of Mathematics, Siddhartha Academy of Higher Education, Vijayawada, Andhra Pradesh, India - 520007*
[2]*School of Engineering, Architecture and Interior Design, Amity University, Dubai International Academic City, P.O. Box 345019*
[3]*Department of Mathematics, Kallam Haranadhareddy Institute of Technology, Guntur, Andhra Pradesh, India-522019*
[#]*Email: mvsr2010@gmail.com,* [##]*Email: m.almakki1977@gmail.com*
**Corresponding Author email: kvbrajakumar@gmail.com*
Received May 11, 2026; revised June 19, 2026; accepted June 24, 2026

In contrast to heat generation and thermal dispersal, the Hall current and rotation factors of a kerosene-based titanium dioxide nanoliquid discharge across two parallel walls embedded in a porous channel are inspected. Suction and hydromagnetic factors are contemplated. Using appropriate initial and boundary conditions, the perturbation approach can yield a precise analytical solution to the governing equations for the nanofluid velocity, temperature, and concentration. Expressions for the shear stress, mass transfer rate, and heat transfer rate at the plates can be obtained. On the one hand, a graphical representation of the primary and secondary velocities, the nanoliquid temperature, and the species concentration is shown. However, for distinct values of the related flow factors, the numerical estimates of shear stress, mass transfer rate, and heat transfer rate for the walls are presented in tabular form. Because of the solute buoyancy force's contribution, the resulting primary and secondary velocity profiles continuously rise to a high level. The concentration increases in conjunction with increases in heat generation and thermal diffusion characteristics throughout the nanofluid. When the thermal buoyancy force is high enough, the primary and secondary velocity profiles diminish. Hall current and the Darcy parameter raise the primary and secondary skin friction coefficients at the upper wall while decreasing them at the lower wall. However, the primary and secondary skin friction coefficients are affected in opposite ways by thermal buoyancy force and magnetic parameter. Results are compared with existing literature.
Keywords: *Nanofluid; Couette flow; Hall current; Heat generation; Suction*

1. INTRODUCTION

In both theoretical and practical fluid mechanics, the study of nanofluid flow between two parallel plates is crucial. A basic model for comprehending complicated fluid dynamics in constrained geometries is this flow arrangement, which is frequently referred to as Couette flow. Its importance arises from its many uses, ranging from temperature control in heat exchangers, where it improves heat transfer efficiency, to lubrication technology, where it aids in the design of effective systems to lower friction and wear in mechanical components. Particularly in the field of biomedical engineering, understanding disk flow is crucial for maximizing the efficiency of systems like centrifugal blood pumps, which depend on regulated fluid dynamics. The generalized Couette flow of nanoliquid between two concentric channels with particle injection has been examined by Soumya et al. [1]. The impact of radiating heat and nanoparticle concentration on the natural convection Couette flow via a vertical channel was discussed by Swain et al. [2]. Heat transfer and the Couette flow of viscoelastic dusty fluid via a porous oscillating plate in a rotating frame have been studied by Ali et al. [3]. The thermodynamic study of Hall current and thermal diffusion on hydromagnetic Couette flow in a rotating system with a convective boundary condition was conducted by Venkateswarlu et al. [4]. Heat transfer increase of nanofluids in Taylor-Couette flow with an elliptical slit surface has been examined using machine learning and numerical simulation by Sun et al. [5]. The mathematical modeling of nonlinear mixed convection unsteady flow in a parallel plate inclined channel near time periodic boundary conditions was provided by Venkateswarlu et al. [6]. Gupta [7] used a differential transform approach to examine the effects of volume fraction, squeezing, and magnetic field on MHD nanofluid flow. The temperature and mass dispersion of mixed convective MHD Casson nanofluid flow in a porous medium has been examined by Arpitha et al. [8].

Two types of thermal diffusion phenomena that take place in fluid systems are the Dufour and Soret characteristics. The Soret effect is a technique that separates a liquid combination into its component parts by creating a solutal gradient in the mixture because of a temperature gradient. Another name for this phenomenon is thermal diffusion. The study of combustion processes is where the Soret effect is most evident because it is crucial in determining the chemical composition of the combustion products. A comparable phenomenon is the Dufour effect, which causes a temperature rise in a liquid mixture caused by a solutal gradient. Solute diffusion is the term used to describe this process. Heat and mass transmission are two kinds of transport processes that can be studied using the Dufour effect. Chemical engineering, physics, and biology all make extensive use of these effects. They can be applied, for instance, to protein dynamics analysis, gas purification, and isotope separation. Given their wide range of utilizes in chemical synthesis, pharmacology, and biotechnology, the Soret-Dufour effects must also be considered while designing microfluidic devices. The magnetized dissipative Soret effect on nonlinear radiative Maxwell nanofluid flow

Cite as: V. Malapati, M. Almakki, V.B.R. Komaravolu, East Eur. J. Phys. 3, 415 (2026), https://doi.org/10.26565/2312-4334-2026-3-38

with porosity, chemical reaction, and Joule heating was described by Bayones et al. [9]. The Newtonian fluid flow with heat and mass transfer across an inclined sheet and magnetic field with Soret effects was described by Mudoi et al. [10]. The velocity slip and magnetic Soret effect on dissipative Maxwell liquid motion around a stretching wall with a heat source and sink were examined by Basha et al. [11]. The Soret and Dufour effects on heat-destructive Casson liquid movement past an infinite perpendicular plate were studied by Venkateswarlu et al. [12]. The implications of heat sources and chemical responses on oscillatory suction in MHD flow by means of permeable medium with the Soret phenomenon were discussed by Pandey [13]. Using an artificial neural network, Jangid and Kolla [14] described the Soret impact and magnetic field on a mixed convection Williamson fluid model across a vertical channel. The consequences of Soret and Dufour characteristics on micropolar fluid passing a stretched sheet in a porous media were reported by Ahamed sheriff et al. [15]. Utilizing a chemically reacting porous stretching plate, Sarma et al. [16] explored the MHD flow and the impacts of Soret, Dufour, and thermophoresis. The significant advancements in our knowledge of fluid flow with Soret and Dufour effects are shown in the publications Venkateswarlu and Venkata Lakshmi [17, 18], Makinde et al. [19], Jayanthi and Niranjan [20], and Venkateswarlu and Phani Kumar [21].

Magnetism, one of the most crucial concepts in engineering and manufacturing, has a wide range of uses. Heat transmission, clutches, compressors, as well as other industrial devices are all impacted by magnetic fields and fluid nanoparticles. Magnetic fields can modify and make available the cooling rate of various technical devices. The dispersion and strength of a metamaterial affect the flow characteristics. The unstable MHD slip flow with radiative heat and mass transfer across an inclined plate embedded in a porous medium was described by Venkateswarlu and Makinde [22]. Heat generation and magnetic consequences of unsteady ternary nanofluid flow across a dynamic wedge in porous media were examined by Ouyang et al. [23]. The thermo-solutal nonlinear convection in a nanofluid movement via a porous plate including heat generation and absorption was studied by Dey et al. [24]. In a double lid-driven inclined wavy porous cavity filled with non-Newtonian nanofluid and equipped with a cross-shaped heater, Hussein et al. [25] described the effects of radiation and heat generation on MHD mixed convection. In an inclined plate near MHD and heat generation, Venkateswarlu et al. [26] investigated the impulsive and accelerated motions of Casson fluid. Radiative heat transfer and Ohmic heating on unstable EMHD mixed convective flow for dual stratification nanofluid were described by Daniel et al. [27]. In an inclined stenotic artery with heat generation, Kefene and Rikitu [28] described the implications of magnetic and thermal radiation on hematocrit-dependent blood nanofluid movement. In an inclined channel with suction and heat generation, Venkateswarlu et al. [29] explored the non-linear unstable MHD flow. The stagnation point motion of a magnetized convective nanofluid across a porous stretchable surface according to ohmic heating and heat generation was described by Ram et al. [30]. The significance of cross-section diffusion on the transient behavior of radiation Casson fluid towards a heated slanted plate was examined by Venkateswarlu et al. [31].

The corpus of published work indicates that no author has yet examined the factors of thermal dispersal, Hall current, and heat generation of an unsteady titanium dioxide nanofluid flow across a parallel porous tunnel. Exploring the hydromagnetic flow of a titanium dioxide nanofluid in a horizontal tunnel via a porous media is the goal of this work. The extraction of oil from hydrocarbon deposits, the fabrication of semiconductor devices from molten metal, solar energy structures, electronic device cooling, and environmental remediation are just a few of the many real-world applications for this study.

2. MATHEMATICAL FRAMEWORK

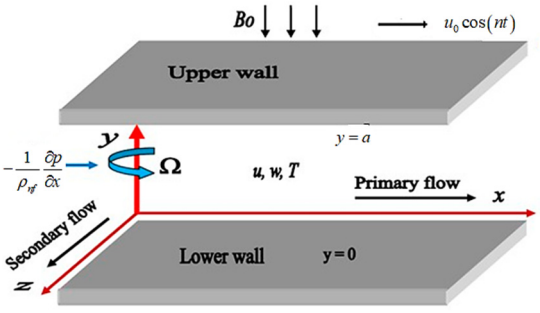

Figure 1. Flow geometry is depicted

The unstable Couette flow of a titanium dioxide nanoliquid based on kerosene across two parallel walls, $y = 0$ and $y = a$, is examined when a uniform transversal magnetic field B_0 is enforced parallel to the $y-$axis while incorporating the Hall current. The nanofluid and tunnel rotate continuously across the $y-$axis at a constant angular velocity Ω. The impact of radial strength is minimal because of nanofluid axial Couette flow motion, but the bending impact of Coriolis strength acting orthogonal to the direction of nanofluid movement and to the axis of rotating allusion structure is taken into concern. The effects of heat emission and thermal dispersion are considered. The invariable pressure gradient applied along the $x-$direction and the motion of the upper wall with systematic velocity $u = u_0\cos(nt)$ in the same direction cause nanofluid flow inside the channel. The channel's walls are kept at the same temperature T_0. The configuration of the current issue is exhibited in Fig. 1. All physical factors, apart from pressure, rely only on y and t because the channel walls have immeasurable extent in $x-$ and $z-$ directions and the movement is fully elaborated. It is expected that the nanopaticles will be uniformly shaped and sized. The dimensional superintending expressions can be displayed as follows considering these statements, the benchmark Boussinesq's reincarnation, and the nanofluid design (See, Swain et al. [2] and Venkateswarlu et al. [4]).

Continuity equation:

$$\frac{\partial v}{\partial y}=0 \tag{1}$$

Momentum conservation equations:

$$\frac{\partial u}{\partial t}+V_0\frac{\partial u}{\partial y}+2\Omega\omega=-\frac{1}{\rho_{nf}}\frac{\partial p}{\partial x}+\frac{\mu_{nf}}{\rho_{nf}}\frac{\partial^2 u}{\partial y^2}-\frac{\sigma_{nf}B_0^2}{\rho_{nf}}\left[\frac{u+mw}{1+m^2}\right]+g\beta_{nf}\left(T-T_0\right)+g\beta_{nf}\left(C-C_0\right)-\frac{\mu_{nf}}{\rho_{nf}}\frac{u}{k_p} \tag{2}$$

$$\frac{\partial w}{\partial t}+V_0\frac{\partial w}{\partial y}-2\Omega u=-\frac{1}{\rho_{nf}}\frac{\partial p}{\partial z}+\frac{\mu_{nf}}{\rho_{nf}}\frac{\partial^2 w}{\partial y^2}+\frac{\sigma_{nf}B_0^2}{\rho_{nf}}\left[\frac{mu-w}{1+m^2}\right]-\frac{\mu_{nf}}{\rho_{nf}}\frac{w}{k_p} \tag{3}$$

Energy conservation equation:

$$\frac{\partial T}{\partial t}+V_0\frac{\partial T}{\partial y}=\frac{k_{nf}}{\left(\rho c_p\right)_{nf}}\frac{\partial^2 T}{\partial y^2}+\frac{Q_0\left(T-T_0\right)}{\left(\rho c_p\right)_{nf}} \tag{4}$$

Mass conservation equation:

$$\frac{\partial C}{\partial t}+V_0\frac{\partial C}{\partial y}=D_{nf}\frac{\partial^2 C}{\partial y^2}+\frac{D_m k_{nf}}{T_m}\frac{\partial^2 T}{\partial y^2} \tag{5}$$

The momentum and energy equation's initial and boundary conditions are listed below.

$$\left.\begin{array}{l} u=u_0\cos(nt),w=0,T=T_1+\varepsilon\left(T_1-T_0\right)\exp(int),C=C_1+\varepsilon\left(C_1-C_0\right)\exp(int)\ \text{at}\ y=a \\ u=0,\ \ w=0,\ \ \ T=T_0\ \ C=C_0\ \ \text{at}\ \ y=0 \end{array}\right\} \tag{6}$$

We take the pressure gradient components $\frac{1}{\rho_{nf}}\frac{\partial p}{\partial x}$ and $\frac{1}{\rho_{nf}}\frac{\partial p}{\partial z}$ in the following way for a purely oscillatory flow (See, Venkateswarlu et al. [4]).

$$\frac{1}{\rho_{nf}}\frac{\partial p}{\partial x}=-\frac{\sigma_{nf}B_0^2 m u_0}{\rho_{nf}\left(1+m^2\right)} \tag{7}$$

$$\frac{1}{\rho_{nf}}\frac{\partial p}{\partial z}=2\Omega u_0+\frac{\sigma_{nf}B_0^2 m u_0}{\rho_{nf}\left(1+m^2\right)} \tag{8}$$

By replacing Eqs. (2) and (3) with Eqs. (7) and (8), we derived

$$\frac{\partial u}{\partial t}+V_0\frac{\partial u}{\partial y}+2\Omega\omega=\frac{\mu_{nf}}{\rho_{nf}}\frac{\partial^2 u}{\partial y^2}-\frac{\sigma_{nf}B_0^2}{\rho_{nf}}\left[\frac{u+mw-u_0}{1+m^2}\right]+g\beta_{nf}\left(T-T_0\right)+g\beta_{nf}\left(C-C_0\right)-\frac{\mu_{nf}}{\rho_{nf}}\frac{u}{k_p} \tag{9}$$

$$\frac{\partial w}{\partial t}+V_0\frac{\partial w}{\partial y}-2\Omega\left(u-u_0\right)=\frac{\mu_{nf}}{\rho_{nf}}\frac{\partial^2 w}{\partial y^2}-\frac{\sigma_{nf}B_0^2}{\rho_{nf}}\left[\frac{mu_0+w-mu}{1+m^2}\right]-\frac{\mu_{nf}}{\rho_{nf}}\frac{w}{k_p} \tag{10}$$

For spherical nanoparticles, μ_{nf} , ρ_{nf} , $\left(\rho c_p\right)_{nf}$,and $(\rho\beta)_{nf}$ can be interpreted as

$$\mu_{nf}=\frac{\mu_f}{(1-\chi)^{2.5}} \tag{11}$$

$$\rho_{nf}=(1-\chi)\rho_f+\chi\rho_s \tag{12}$$

$$\left(\rho c_p\right)_{nf}=(1-\chi)\left(\rho c_p\right)_f+\chi\left(\rho c_p\right)_s \tag{13}$$

$$(\rho\beta)_{nf}=(1-\chi)(\rho\beta)_f+\chi(\rho\beta)_s \tag{14}$$

Expressions for the nanoliquid's existing thermal conductivity and electrical conductivity are

$$\frac{k_{nf}}{k_f}=\frac{\left(k_s+2k_f\right)-2\chi\left(k_f-k_s\right)}{\left(k_s+2k_f\right)+\chi\left(k_f-k_s\right)} \tag{15}$$

$$\frac{\sigma_{nf}}{\sigma_f}=1+\frac{3\chi\left(\sigma_s-\sigma_f\right)}{\left(\sigma_s+2\sigma_f\right)-\chi\left(\sigma_s-\sigma_f\right)} \tag{16}$$

Table 1. Thermo-physical specifications of TiO_2 nanoparticles and kerosene oil (See, Abbas et al. [32])

Property	TiO_2	Kerosene Oil
$k\ \left(W/mK\right)$	8.953	0.15
$\rho\ \left(Kg/m^3\right)$	4250	783
$c_p\ \left(J/KgK\right)$	686.2	2090
$\sigma\left(S/m\right)$	2.6×10^{6}	5×10^{-11}
$\beta\ \left(K^{-1}\right)$	0.9×10^{-5}	99×10^{-5}

The subsequent non-dimensional values are displayed

$$U=\frac{a\rho_f}{\mu_f}u, W=\frac{a\rho_f}{\mu_f}w, \theta=\frac{T-T_0}{T_1-T_0}, \eta=\frac{y}{a}, \omega=\frac{a^2\rho_f}{\mu_f}n,\ \ \tau=\frac{\mu_f}{a^2\rho_f}t,\ \ \phi=\frac{C-C_0}{C_1-C_0},\Bigg\} \tag{17}$$

Eqs. (4), (5), (9) and (10) are used to produce the displayed non-dimensional structure

$$\frac{\partial U}{\partial\tau}+s\frac{\partial U}{\partial\eta}+2K^2W=a_6\frac{\partial^2U}{\partial\eta^2}-a_7M\left[\frac{U+mW-\lambda}{1+m^2}\right]+a_4Gr\theta+a_5Gm\phi-\frac{a_6}{Da}U \tag{18}$$

$$\frac{\partial W}{\partial\tau}+s\frac{\partial W}{\partial\eta}-2K^2\left(U-\lambda\right)=a_6\frac{\partial^2W}{\partial\eta^2}-a_7M\left[\frac{m\lambda+W-mU}{1+m^2}\right]-\frac{a_6}{Da}W \tag{19}$$

$$\frac{\partial\theta}{\partial\tau}+s\frac{\partial\theta}{\partial\eta}=\frac{a_{10}}{\Pr}\frac{\partial^2\theta}{\partial\eta^2}+\frac{H}{a_9}\theta \tag{20}$$

$$\frac{\partial\phi}{\partial\tau}+s\frac{\partial\phi}{\partial\eta}=\frac{1}{Sc}\frac{\partial^2\phi}{\partial\eta^2}+a_8Sr\frac{\partial^2\theta}{\partial\eta^2} \tag{21}$$

Here

$$s=\frac{V_0a}{\nu_f}, K^2=\frac{2\Omega a^2}{\nu_f}, Gr=\frac{g\left(\rho\beta\right)_f\left(T_1-T_0\right)a^3}{\nu_f^2}, M=\frac{\sigma_fB_0^2a^2}{\rho_f\nu_f}, \lambda=\frac{u_0a}{\nu_f}, Sc=\frac{\nu_f}{D_m}, \Pr=\frac{\left(\rho c_p\right)_f\nu_f}{k_f}, H=\frac{Q_0a^2}{\nu_f\left(\rho c_p\right)_f},$$
$$Da=\frac{k_p}{a^2}, Gm=\frac{g\left(\rho\beta\right)_f\left(C_1-C_0\right)a^3}{\nu_f^2}, Sr=\frac{D_m\left(T_1-T_0\right)k_f}{T_m\left(C_1-C_0\right)\nu_f}.$$

For a non-dimensional structure, the initial and boundary conditions are as follows:

$$\left.\begin{array}{l} U=0,\ W=0,\ \theta=0,\ \phi=0 \text{ at } \eta=0 \\ U=\lambda\cos\left(\omega\tau\right), W=0,\ \theta=1+\varepsilon\exp\left(i\omega\tau\right), \phi=1+\varepsilon\exp\left(i\omega\tau\right) \text{ at } \eta=1 \end{array}\right\} \tag{22}$$

Define:

$$\psi=U+iW \tag{23}$$

By utilizing Eq. (23) in Eqs. (18) and (19), we acquired

$$\frac{\partial\psi}{\partial\tau}+s\frac{\partial\psi}{\partial\eta}-2iK^2\left(\psi-\lambda\right)=a_6\frac{\partial^2\psi}{\partial\eta^2}-a_7M\left[\frac{\psi-\lambda}{1+im}\right]+a_4Gr\theta+a_5Gm\phi-\frac{a_6}{Da}\psi \tag{24}$$

The initial and boundary conditions can be translated into the structure

$$\left.\begin{array}{l} \psi=0,\ \theta=0,\ \phi=0 \text{ at } \eta=0 \\ \psi=\lambda\cos\left(\omega\tau\right), \theta=1+\varepsilon\exp\left(i\omega\tau\right), \phi=1+\varepsilon\exp\left(i\omega\tau\right) \text{ at } \eta=1 \end{array}\right\} \tag{25}$$

The shear stress τ_w, heat flux q_w and mass flux j_w are acquired utilizing the nanoliquid velocity, temperature, and concentration as

$$\tau_w = \mu_{nf}\left[\frac{\partial u}{\partial y} + i\frac{\partial w}{\partial y}\right] \tag{26}$$

$$q_w = -k_{nf}\left[\frac{\partial T}{\partial y}\right] \tag{27}$$

$$j_w = -D_m\left[\frac{\partial C}{\partial y}\right] \tag{28}$$

The skin-friction coefficient Cf, heat transfer coefficient Nu and mass transfer coefficient Sh in a non-dimensional pattern can be represented as

$$Cf = \frac{a^2\tau_w\rho_{nf}}{\mu_{nf}^2} \tag{29}$$

$$Nu = \frac{aq_w}{k_{nf}\left(T_1 - T_0\right)} \tag{30}$$

$$Sh = \frac{a\, j_w}{D_m\left(C_1 - C_0\right)} \tag{31}$$

We calculated the physical parameters by replacing Eqs. (26) to (28) in Eqs. (29) to (31)

$$Cf = a_{11}\left[\frac{\partial \psi}{\partial \eta}\right] \tag{32}$$

$$Nu = -\left[\frac{\partial \theta}{\partial \eta}\right] \tag{33}$$

$$Sh = -\left[\frac{\partial \phi}{\partial \eta}\right] \tag{34}$$

3. THE PROBLEM'S SOLUTION

It is impossible to solve the corresponding non-linear partial differential equations (18) to (21) in closed form. These non-linear partial differential equations are thus reduced to a set of ordinary differential equations that may be solved analytically. This can be achieved by using the trial solutions as shown below (See, Venkateswarlu et al. [4])

$$\psi(\eta,\tau) = \psi_0(\eta) + \varepsilon\exp\left(i\,\omega\tau\right)\psi_1(\eta) + O\left(\varepsilon^2\right) \tag{35}$$

$$\theta(\eta,\tau) = \theta_0(\eta) + \varepsilon\exp\left(i\,\omega\tau\right)\theta_1(\eta) + O\left(\varepsilon^2\right) \tag{36}$$

$$\phi(\eta,\tau) = \phi_0(\eta) + \varepsilon\exp\left(i\,\omega\tau\right)\phi_1(\eta) + O\left(\varepsilon^2\right) \tag{37}$$

The subsequent ordinary differential equations can be obtained by substituting Eqs. (35) to (37) into Eqs. (18) to (21)

$$a_6\frac{d^2\psi_0}{d\eta^2} - s\frac{d\psi_0}{d\eta} - \left[\frac{a_7 M}{1+im} + \frac{a_6}{Da} - 2iK^2\right]\psi_0 = -\left[a_4 Gr\theta_0 + a_5 Gm\phi_0 + \left(\frac{a_7 M}{1+im} - 2iK^2\right)\lambda\right] \tag{38}$$

$$a_6\frac{d^2\psi_1}{d\eta^2} - s\frac{d\psi_1}{d\eta} - \left[\frac{a_7 M}{1+im} + \frac{a_6}{Da} - 2iK^2 + i\omega\right]\psi_1 = -\left[a_4 Gr\theta_1 + a_5 Gm\phi_1\right] \tag{39}$$

$$\frac{a_{10}}{Pr}\frac{d^2\theta_0}{d\eta^2} - s\frac{d\theta_0}{d\eta} + \frac{H}{a_9}\theta_0 = 0 \tag{40}$$

$$\frac{a_{10}}{Pr}\frac{d^2\theta_1}{d\eta^2}-s\frac{d\theta_1}{d\eta}+\left(\frac{H}{a_9}-i\,\omega\right)\theta_1=0 \tag{41}$$

$$\frac{1}{Sc}\frac{d^2\phi_0}{d\eta^2}-s\frac{d\phi_0}{d\eta}=-a_8\,Sr\frac{d^2\theta_0}{d\eta^2} \tag{42}$$

$$\frac{1}{Sc}\frac{d^2\phi_1}{d\eta^2}-s\frac{d\phi_1}{d\eta}-i\,\omega\phi_1=-a_8\,Sr\frac{d^2\theta_1}{d\eta^2} \tag{43}$$

The pertinent initial and boundary conditions can be characterized as

$$\left.\begin{aligned}&\psi_0=0,\ \psi_1=0,\ \theta_0=0,\ \theta_1=0\,\phi_o=0,\ \phi_1=0 \quad \text{at} \quad \eta=0\\&\psi_0=\lambda\cos(\omega\tau),\ \psi_1=0,\ \theta_0=1,\ \theta_1=1,\ \phi_0=1,\ \phi_1=1 \ \text{ at } \ \eta=1\end{aligned}\right\} \tag{44}$$

Eqs. (38) to (43) with the boundary conditions in Eqs. (44) have analytical solutions that are provided by

$$\psi_0=a_{49}\exp(m_8\eta)+a_{50}\exp(m_9\eta)-a_{41}\exp(m_1\eta)+a_{42}\exp(m_2\eta)-a_{43}\exp(-m_5\eta)-a_{44}\exp(m_5\eta)+a_{45} \tag{45}$$

$$\psi_1=a_{60}\exp(m_{10}\eta)+a_{61}\exp(m_{11}\eta)-a_{53}\exp(m_3\eta)+a_{54}\exp(m_4\eta)-a_{55}\exp(m_6\eta)-a_{56}\exp(m_7\eta) \tag{46}$$

$$\theta_0=a_{17}\left[\exp(m_1\eta)-\exp(m_2\eta)\right] \tag{47}$$

$$\theta_1=a_{17}\left[\exp(m_3\eta)-\exp(m_4\eta)\right] \tag{48}$$

$$\phi_0=a_{26}\exp(-m_5\eta)+a_{21}\exp(m_5\eta)-a_{24}\exp(m_1\eta)+a_{25}\exp(m_2\eta) \tag{49}$$

$$\phi_1=a_{36}\exp(m_6\eta)+a_{35}\exp(m_7\eta)-a_{30}\exp(m_3\eta)+a_{31}\exp(m_4\eta) \tag{50}$$

We found the following solutions for the nanofluid velocity, temperature, and concentration by replacing Eqs. (35) to (37) with Eqs. (45) to (50)

$$\begin{aligned}\psi(\eta,\tau)=&\begin{bmatrix}a_{49}\exp(m_8\eta)+a_{50}\exp(m_9\eta)-a_{41}\exp(m_1\eta)+\\a_{42}\exp(m_2\eta)-a_{43}\exp(-m_5\eta)-a_{44}\exp(m_5\eta)+a_{45}\end{bmatrix}+\\&\varepsilon\exp(i\omega\tau)\begin{bmatrix}a_{60}\exp(m_{10}\eta)+a_{61}\exp(m_{11}\eta)-a_{53}\exp(m_3\eta)+\\a_{54}\exp(m_4\eta)-a_{55}\exp(m_6\eta)-a_{56}\exp(m_7\eta)\end{bmatrix}\end{aligned} \tag{51}$$

$$\theta(\eta,\tau)=a_{17}\left[\exp(m_1\eta)-\exp(m_2\eta)\right]+\varepsilon\exp(i\omega\tau)\,a_{17}\left[\exp(m_3\eta)-\exp(m_4\eta)\right] \tag{52}$$

$$\begin{aligned}\phi(\eta,\tau)=&\left[a_{26}\exp(-m_5\eta)+a_{21}\exp(m_5\eta)-a_{24}\exp(m_1\eta)+a_{25}\exp(m_2\eta)\right]+\\&\varepsilon\exp(i\omega\tau)\left[a_{36}\exp(m_6\eta)+a_{35}\exp(m_7\eta)-a_{30}\exp(m_3\eta)+a_{31}\exp(m_4\eta)\right]\end{aligned} \tag{53}$$

3.1 Skin friction coefficient

The velocity field can be utilized to express the skin friction coefficient as

$$\begin{aligned}Cf=&\begin{bmatrix}a_{49}m_8\exp(m_8\eta)+a_{50}m_9\exp(m_9\eta)-a_{41}m_1\exp(m_1\eta)+\\a_{42}m_2\exp(m_2\eta)+a_{43}m_5\exp(-m_5\eta)-a_{44}m_5\exp(m_5\eta)\end{bmatrix}+\\&\varepsilon\exp(i\omega\tau)\begin{bmatrix}a_{60}m_{10}\exp(m_{10}\eta)+a_{61}m_{11}\exp(m_{11}\eta)-a_{53}m_3\exp(m_3\eta)+\\a_{54}m_4\exp(m_4\eta)-a_{55}m_6\exp(m_6\eta)-a_{56}m_7\exp(m_7\eta)\end{bmatrix}\end{aligned} \tag{54}$$

$$Pcf=\text{Real part of}\ (Cf) \tag{55}$$

$$Scf=\text{Imaginary part of}(Cf) \tag{56}$$

3.2 Heat transfer coefficient

The temperature field can be utilized to express the heat transfer coefficient as

$$Nu = a_{17}\left[m_1 \exp(m_1\eta) - m_2 \exp(m_2\eta)\right] + \varepsilon \exp(i\omega\tau)\, a_{17}\left[m_3 \exp(m_3\eta) - m_4 \exp(m_4\eta)\right] \tag{57}$$

3.3 Mass transfer coefficient

The concentration field can be utilized to express the mass transfer coefficient as

$$\begin{aligned} Sh = {} & \left[a_{21}m_5 \exp(m_5\eta) - a_{26}m_5 \exp(-m_5\eta) - a_{24}m_1 \exp(m_1\eta) + a_{25}m_2 \exp(m_2\eta)\right] + \\ & \varepsilon \exp(i\omega\tau)\left[a_{36}m_6 \exp(m_6\eta) + a_{35}m_7 \exp(m_7\eta) - a_{30}m_3 \exp(m_3\eta) + a_{31}m_4 \exp(m_4\eta)\right] \end{aligned} \tag{58}$$

4. FINDINGS AND DISCUSSION

To memorize the implications of distinct parameters, such as the rotation factor K^2, magnetic parameter M, upper wall motion parameter λ, thermal Grashof number Gr, solutal Grashof number Gm, Darcy parameter Da, Hall current parameter m, Soret number Sr, heat generation factor H, suction factor s, and solid volume fraction χ on the flow configuration, the numerical assessments of the titanium dioxide nanoliquid primary velocity U, secondary velocity W, temperature θ, concentration ϕ, primary skin friction Pcf, secondary skin friction Scf, heat transfer coefficient Nu, and mass transfer coefficient Nu are computed. The subsequent parameter values are utilized for numerical calculations in this study: $\chi = 0.05$, $K^2 = 1$, $M = 1$, $s = 2$, $\lambda = 0.001$, $Gr = 1$, $Gm = 1$, $Da = 1$, $m = 1$, $\mathrm{Pr} = 0.71$, $Sr = 5$, $H = 2$, $Sc = 0.22$, and $\tau = \pi/2$. The velocity profile data depict the primary velocity of titanium dioxide-kerosene nanoliquid as a solid line and the secondary velocity as a dashed line. To obtain the numerical findings of the current work, a MATLAB (2015a) program was established. To compare our results with those of Ref [4] as a special case, we calculated the numerical values of primary and secondary skin friction coefficients for our work as well as those of Ref [4] which is displayed in Tables 2 and 3. There is a significant level of agreement between the two findings.

Table 2. Comparison of primary skin friction coefficient Pcf with Ref [4] when $\tau = \pi/2$, $K^2 = m = Da = \mathrm{Pr} = \omega = 1$, $Sc = 0.6$, $\lambda = 0.001$, $Gr = 2$, $Gm = 4$, $Sr = 5$, $H = -1$, $s = 0$ and $\chi = 0$.

η	M	Pcf		M	Pcf		M	Pcf	
		Ref [4]	Present		Ref [4]	Present		Ref [4]	Present
0.00	1.0	0.2221	0.2222	2.0	0.2068	0.2069	3.0	0.1928	0.0928
0.25	1.0	0.1936	0.1937	2.0	0.1820	0.1821	3.0	0.1713	0.1714
0.50	1.0	0.0907	0.0907	2.0	0.0893	0.0893	3.0	0.0878	0.0879
0.75	1.0	-0.1417	-0.1416	2.0	-0.1303	-0.1302	3.0	-0.1198	-0.1197
1.00	1.0	-0.6018	-0.6017	2.0	-0.5832	-0.5831	3.0	-0.5658	-0.5657

Table 3. Comparison of secondary skin friction coefficient Pcf with Ref [4] when $\tau = \pi/2$, $K^2 = m = Da = \mathrm{Pr} = \omega = 1$, $Sc = 0.6$, $\lambda = 0.001$, $Gr = 2$, $Gm = 4$, $Sr = 5$, $H = -1$, $s = 0$ and $\chi = 0$.

η	M	Scf		M	Scf		M	Scf	
		Ref [4]	Present		Ref [4]	Present		Ref [4]	Present
0.00	1.0	0.0593	0.0593	2.0	0.0638	0.0638	3.0	0.0670	0.0670
0.25	1.0	0.0456	0.0456	2.0	0.0494	0.0494	3.0	0.0522	0.0522
0.50	1.0	0.0066	0.0066	2.0	0.0077	0.0077	3.0	0.0087	0.0087
0.75	1.0	-0.0446	-0.0445	2.0	-0.0482	-0.0481	3.0	-0.0508	-0.0507
1.00	1.0	-0.0750	-0.0749	2.0	-0.0821	-0.0820	3.0	-0.0877	-0.0876

Figs. 2, 3, and 4 are displayed to explore the implications of λ, K^2 and H on U and W respectively. It is detected that U minimizes and W maximizes with an elevation in λ, K^2 and H. The secondary movement is directed by the Coriolis force and is generated by the motion of the upper wall. Driven by the Coriolis force, a stronger secondary flow forms as the upper wall moves faster. This secondary flow slows down the primary flow due to viscous and inertial factors. Due to the Coriolis force that opposes the primary flow and drives a secondary circulation, the growing rotation parameter in MHD nanofluid flow reduces the primary velocity and increases the secondary velocity. Acting perpendicular to the direction of motion and rotation, the Coriolis force acts as a fictitious force. Increasing the heat generation parameter makes the fluid less dense and less susceptible to the magnetic field's braking effect, thereby reducing the primary velocity while increasing the secondary velocity due to heat generation, creating a secondary flow.

Primary and secondary velocity profiles across a range of magnetic parameters and thermal Grashof numbers are shown in Figs. 5 and 6. The primary and secondary velocity profiles are observed to decrease as the magnetic factor and the thermal Grashof number increase. The magnetic parameter quantifies the strength of the Lorentz force relative to the fluid's viscous or inertial forces. Increased frictional resistance along the plate's surface may result from a stronger magnetic field, which could lower both primary and secondary velocities. The thermal Grashof number is defined as the

ratio of buoyancy forces to viscous forces acting on a nanofluid. Primary and secondary velocity profiles have inverse relation with thermal Grashof number because of high degree of kinematic viscosity of the titanium dioxide nanofluid. The significance of the Soret number on the primary and secondary velocity profiles for titanium dioxide nanofluid based on kerosene is described in Fig. 7. Soret parameter measures the contribution of a temperature gradient to mass diffusion, which typically results in the separation of different chemical species or solutes within a nanofluid mixture. The primary and secondary velocity profiles diminish as the Soret number expands, indicating that additional heat input causes the nanofluid's velocity to slow down.

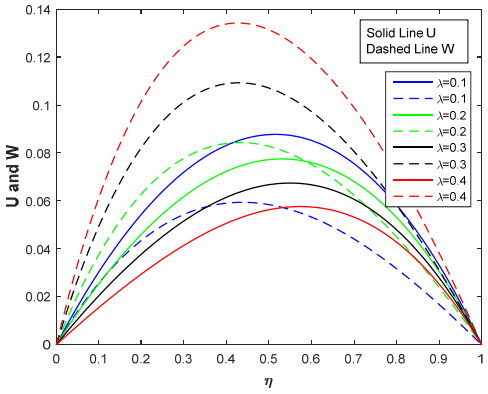

Figure 2. Variation of U and W in reference to λ

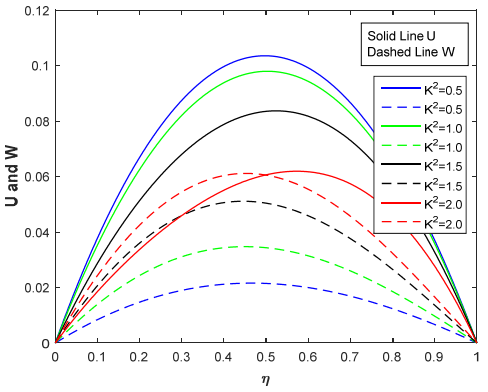

Figure 3. Variation of U and W in reference to K^2

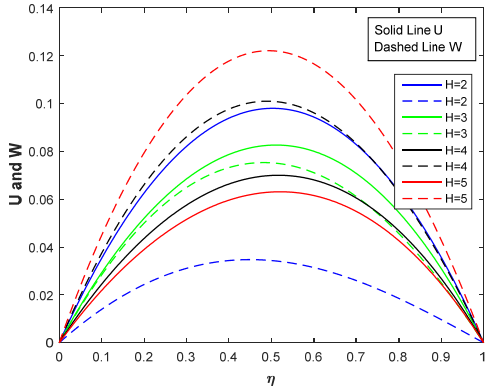

Figure 4. Variation of U and W in reference to H

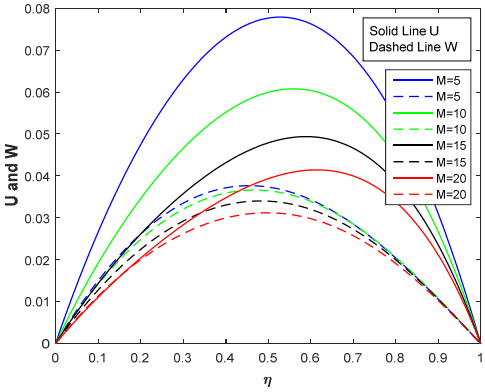

Figure 5. Variation of U and W in reference to M

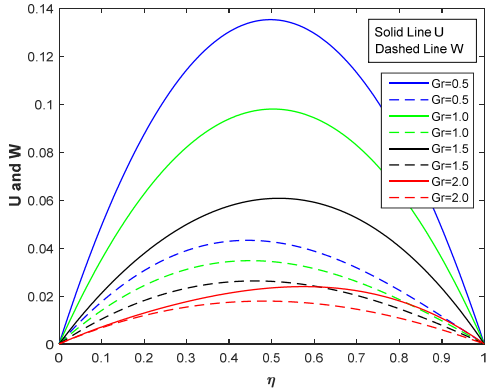

Figure 6. Variation of U and W in reference to Gr

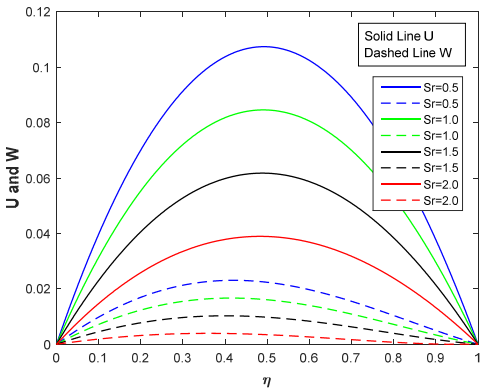

Figure 7. Variation of U and W in reference to Sr

The implications of the solutal Grashof number, Darcy parameter, and Hall current parameter on the primary and secondary velocity profiles are displayed in Figs. 8, 9, and 10. Instead of temperature, the mass Grashof number controls the behavior of natural convection caused by concentration or density gradients of a dissolved substance. The primary and secondary velocity profiles of the kerosene-based titanium dioxide nanofluid improve as one increases the solutal Grashof number, Darcy parameter, and Hall current. The nanofluid's kinematic and thermal effects, which might have an impact on the total velocity distribution, are also influenced by the Darcy parameter. Higher Darcy parameters can result in better primary and secondary velocity profiles and more effective heat transfer. Increasing the Hall current parameter directly enhances both primary and secondary velocity profiles because of the changed momentum distribution.

Figs. 11 and 12 display the primary and secondary velocity profiles for varies values of Schmidt number and Prandtl number. The Schmidt number establishes whether the momentum of a nanofluid is transported more quickly or

more slowly than the dissolved mass. The relative thickness of a fluid's velocity and thermal boundary layers are directly determined by the Prandtl number, which assesses whether a fluid's momentum or heat spreads more quickly. As both parameters go up, the primary and secondary velocity profiles also become greater. The Reynolds number, a measurement of the fluid's viscosity and inertia, is directly correlated with the Schmidt number. The velocity profiles increased due to greater inertia and viscosity resulting from a higher Reynolds number, as indicated by an elevated Schmidt number. A fluid with a higher Prandtl number can move more easily and have less flow resistance because its viscosity is significantly lower than its thermal diffusivity. Primary and secondary velocities rise as a result.

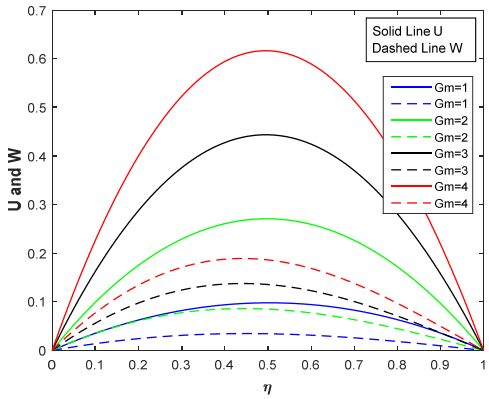

Figure 8. Variation of U and W in reference to Gm

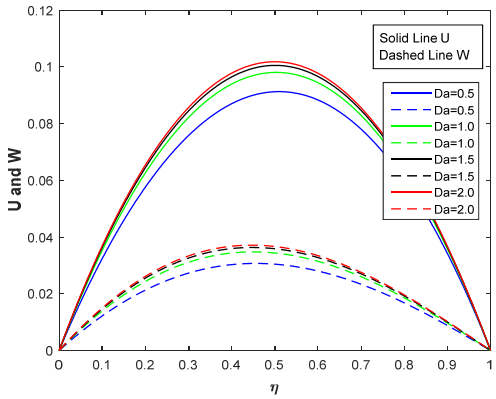

Figure 9. Variation of U and W in reference to Da

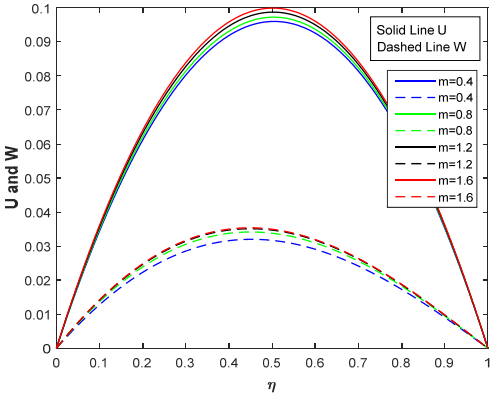

Figure 10. Variation of U and W in reference to m

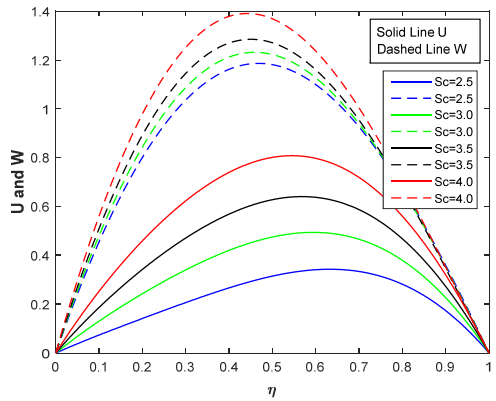

Figure 11. Variation of U and W in reference to Sc

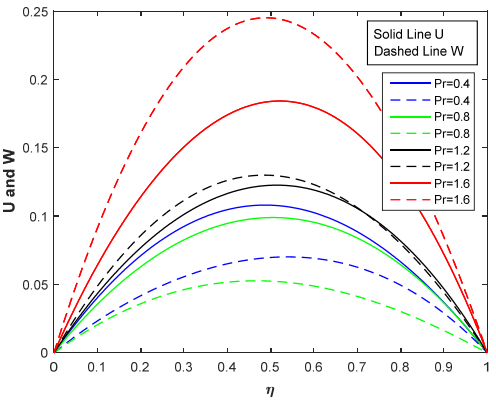

Figure 12. Variation of U and W in reference to Pr

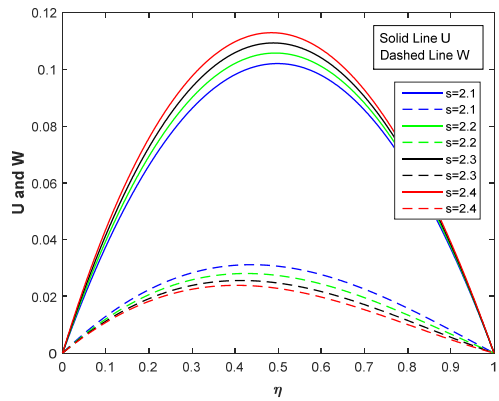

Figure 13. Variation of U and W in reference to s

Figs. 13 and 14 show the rise in primary velocity and reduction in secondary velocity of a titanium dioxide nanofluid whenever the suction parameter and volume fraction parameter grow. The physical impact of withdrawing fluid through a porous surface or slot is measured using the suction parameter. Nanofluids may expand because of the volume fraction rise, which could raise the fluid's primary velocity. The magnetic field can influence flow characteristics. Increasing the volume fraction parameter may promote a more uniform distribution of the fluid, potentially leading to enhanced primary velocity. The volume of suspended nanoparticles divided by the entire volume of the nanofluid mixture is the volume fraction parameter.

Figs. 15–18 analyze how factors such as the heat generation parameter, Prandtl number, suction parameter, and volume fraction parameter influence the temperature domain. It is evident that the temperature domain grows with rises in the heat generation parameter, Prandtl number, and suction parameter. The temperature profile lowers as the volume

fraction parameter rises. Both the amount and shape of titanium dioxide nanoparticles affect the thermal execution of nanofluids, leading to improved heat transfer and a more consistent temperature distribution. A higher Prandtl number suggests that the thermal boundary layer is thicker, resulting in an increased fluid temperature.

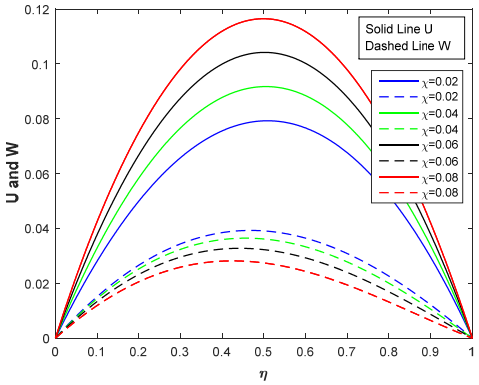

Figure 14. Variation of U and W in reference to χ

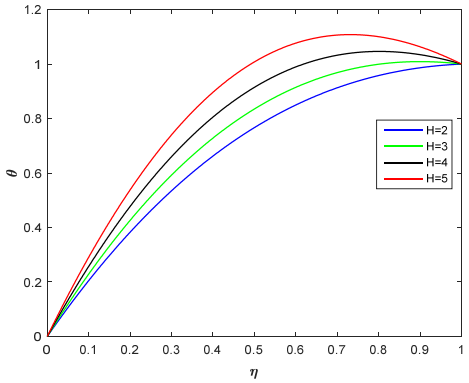

Figure 15. Variation of θ in reference to H

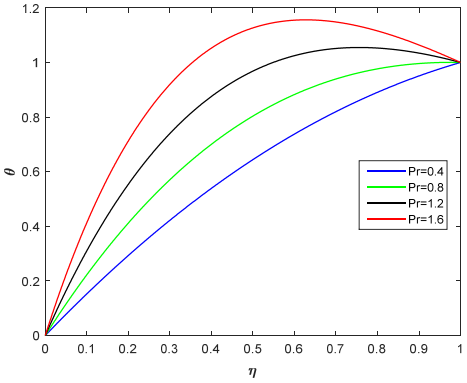

Figure 16. Variation of θ in reference to Pr

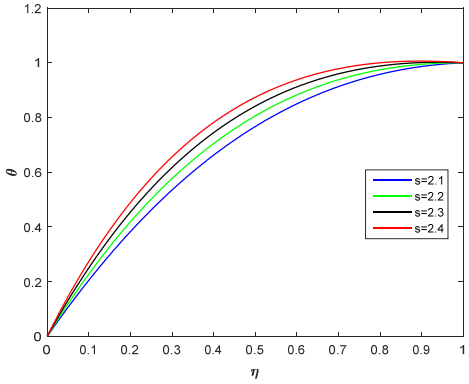

Figure 17. Variation of θ in reference to s

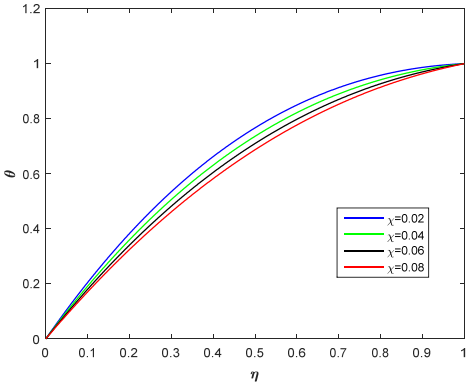

Figure 18. Variation of θ in reference to χ

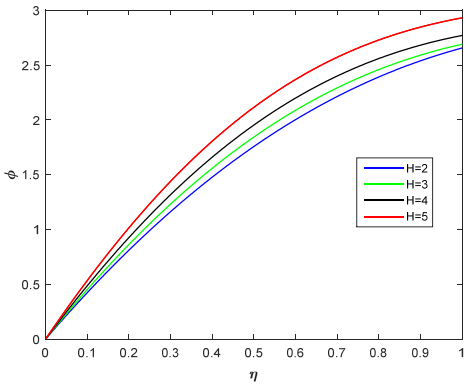

Figure 19. Variation of ϕ in reference to H

Figs. 19-23, illustrate how the concentration profile changes with varying heat generation parameter, suction parameter, Soret number, Schmidt number, and volume fraction parameter. The data demonstrate that higher values of the heat generation parameter, suction parameter, Soret number, Schmidt number, and volume fraction parameter increase mass concentration. The condensation action increases the nanofluid concentration as the suction parameter rises, thereby increasing the concentration in the flow field. Shear stress is crucial in engineering and often demands complex design solutions. A comprehensive understanding of this coefficient will lead to the development of designs for medicine delivery for cancer patients, bridges, dams, and storage efficiency.

Tables 4 through 16 show that when the upper wall motion factor, rotation parameter, magnetic parameter, Grashof number, heat generation parameter, and Schmidt number increase, the primary skin friction coefficient intensifies at the left wall and decreases at the right wall. Similarly, as the thermal Grashof number, Darcy number, Hall current parameter, Soret number, suction factor, and volume fraction factor increases, the primary skin friction coefficient decreases on the left wall and increases on the right wall. When the upper wall motion parameter, rotation parameter, thermal Grashof number, Darcy number, Hall current parameter, Soret number, and heat generation parameter are augmented, the secondary skin friction coefficient reduces at the left wall and intensifies at the right wall. Similarly, as the magnetic parameter, thermal Grashof number, Schmidt number, suction parameter, and volume fraction parameter increase, the secondary skin friction coefficient increases at the left wall and decreases at the right wall.

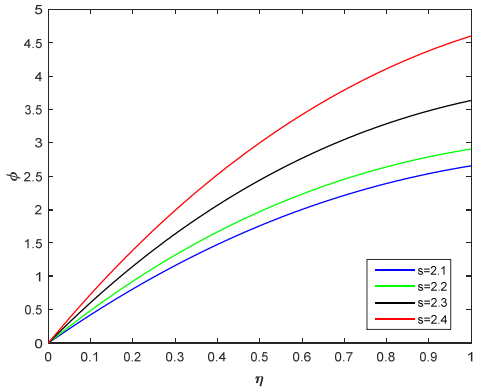

Figure 20. Variation of ϕ in reference to s

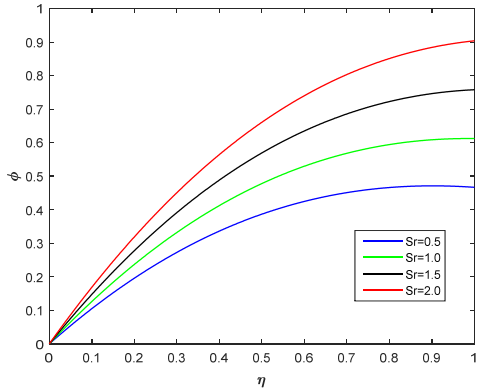

Figure 21. Variation of ϕ in reference to s

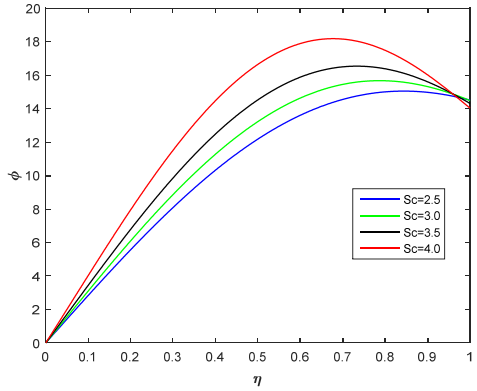

Figure 22. Variation of ϕ in reference to Sc

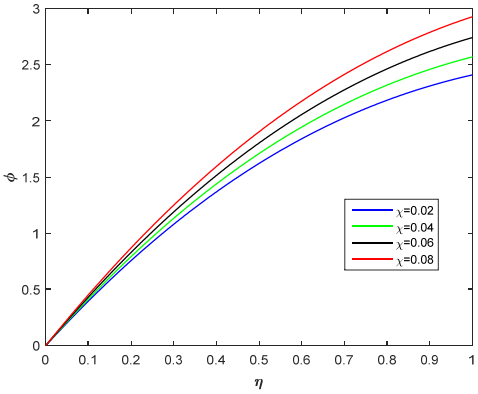

Figure 23. Variation of ϕ in reference to χ

Table 4. Interpretation of Pcf and Scf with respect to λ

η	λ	Pcf	Scf	λ	Pcf	Scf	λ	Pcf	Scf
0.00	0.1	-0.3373	-0.3010	0.2	-0.2789	-0.4463	0.3	-0.2206	-0.5916
0.25	0.1	-0.1763	-0.1078	0.2	-0.1575	-0.1484	0.3	-0.1387	-0.1891
0.50	0.1	-0.0106	0.0303	0.2	-0.0189	0.0454	0.3	-0.0272	0.0606
0.75	0.1	0.1723	0.1241	0.2	0.1496	0.1740	0.3	0.1269	0.2239
1.00	0.1	0.3731	0.1744	0.2	0.3468	0.2512	0.3	0.3206	0.3280

Table 5. Interpretation of Pcf and Scf with respect to K^2

η	K^2	Pcf	Scf	K^2	Pcf	Scf	K^2	Pcf	Scf
0.00	0.5	-0.4236	-0.0945	1.0	-0.3951	-0.1572	1.5	-0.3212	-0.2331
0.25	0.5	-0.2057	-0.0424	1.0	-0.1949	-0.0675	1.5	-0.1669	-0.0991
0.50	0.5	0.0026	0.0063	1.0	-0.0024	0.0153	1.5	-0.0153	0.0248
0.75	0.5	0.2076	0.0453	1.0	0.1948	0.0747	1.5	0.1618	0.1114
1.00	0.5	0.4103	0.0703	1.0	0.3991	0.0984	1.5	0.3706	0.1350

Table 6. Interpretation of Pcf and Scf with respect to M

η	M	Pcf	Scf	M	Pcf	Scf	M	Pcf	Scf
0.00	5	-0.2956	-0.1681	10	-0.2122	-0.1591	15	-0.1579	-0.1431
0.25	5	-0.1550	-0.0736	10	-0.1202	-0.0722	15	-0.0963	-0.0675
0.50	5	-0.0169	0.0146	10	-0.0273	0.0101	15	-0.0325	0.0051
0.75	5	0.1483	0.0814	10	0.1079	0.0791	15	0.0804	0.0732
1.00	5	0.3551	0.1077	10	0.3148	0.1100	15	0.2854	0.1084

Table 7. Interpretation of Pcf and Scf with respect to Gr

η	Gr	Pcf	Scf	Gr	Pcf	Scf	Gr	Pcf	Scf
0.00	0.5	-0.5535	-0.1980	1.0	-0.3951	-0.1572	1.5	-0.2366	-0.1164
0.25	0.5	-0.2686	-0.0836	1.0	-0.1949	-0.0675	1.5	-0.1211	-0.0514
0.50	0.5	0.0034	0.0216	1.0	-0.0024	0.0153	1.5	-0.0081	0.0090
0.75	0.5	0.2712	0.0935	1.0	0.1948	0.0747	1.5	0.1185	0.0558
1.00	0.5	0.5357	0.1158	1.0	0.3991	0.0984	1.5	0.2626	0.0810

Table 8. Interpretation of Pcf and Scf with respect to Gm

η	Gm	Pcf	Scf	Gm	Pcf	Scf	Gm	Pcf	Scf
0.00	1.0	-0.3951	-0.1572	2.0	-1.1076	-0.3945	3.0	-1.8202	-0.6318
0.25	1.0	-0.1949	-0.0675	2.0	-0.5374	-0.1669	3.0	-0.8799	-0.2662
0.50	1.0	-0.0024	0.0153	2.0	0.0068	0.0431	3.0	0.0161	0.0709
0.75	1.0	0.1948	0.0747	2.0	0.5427	0.1866	3.0	0.8905	0.2985
1.00	1.0	0.3991	0.0984	2.0	1.0716	0.2308	3.0	1.7440	0.3632

Table 9. Interpretation of Pcf and Scf with respect to Da

η	Da	Pcf	Scf	Da	Pcf	Scf	Da	Pcf	Scf
0.00	0.5	-0.3625	-0.1371	1.0	-0.3951	-0.1572	1.5	-0.4070	-0.1649
0.25	0.5	-0.1815	-0.0599	1.0	-0.1949	-0.0675	1.5	-0.1997	-0.0704
0.50	0.5	-0.0068	0.0118	1.0	-0.0024	0.0153	1.5	-0.0007	0.0166
0.75	0.5	0.1793	0.0657	1.0	0.1948	0.0747	1.5	0.2005	0.0781
1.00	0.5	0.3841	0.0906	1.0	0.3991	0.0984	1.5	0.4046	0.1013

Table 10. Interpretation of Pcf and Scf with respect to $_m$

η	$_m$	Pcf	Scf	$_m$	Pcf	Scf	$_m$	Pcf	Scf
0.00	0.4	-0.3855	-0.1438	0.8	-0.3914	-0.1543	1.2	-0.3985	-0.1589
0.25	0.4	-0.1909	-0.0623	0.8	-0.1934	-0.0664	1.2	-0.1963	-0.0682
0.50	0.4	-0.0036	0.0132	0.8	-0.0029	0.0148	1.2	-0.0019	0.0156
0.75	0.4	0.1902	0.0686	0.8	0.1931	0.0734	1.2	0.1965	0.0755
1.00	0.4	0.3945	0.0928	0.8	0.3975	0.0972	1.2	0.4007	0.0990

Table 11. Interpretation of Pcf and Scf with respect to Sr

η	Sr	Pcf	Scf	Sr	Pcf	Scf	Sr	Pcf	Scf
0.00	0.5	0.4445	0.1104	1.0	0.3512	0.0807	1.5	0.2579	0.0510
0.25	0.5	0.2127	0.0437	1.0	0.1674	0.0314	1.5	0.1221	0.0190
0.50	0.5	-0.0068	-0.0175	1.0	-0.0063	-0.0138	1.5	-0.0058	-0.0102
0.75	0.5	-0.2163	-0.0515	1.0	-0.1706	-0.0375	1.5	-0.1249	-0.0234
1.00	0.5	-0.4163	-0.0451	1.0	-0.3257	-0.0292	1.5	-0.2351	-0.0132

Table 12. Interpretation of Pcf and Scf with respect to H

η	H	Pcf	Scf	H	Pcf	Scf	H	Pcf	Scf
0.00	2.0	-0.3951	-0.1572	3.0	-0.3273	-0.3185	4.0	-0.2735	-0.4196
0.25	2.0	-0.1949	-0.0675	3.0	-0.1645	-0.1489	4.0	-0.1394	-0.2001
0.50	2.0	-0.0024	0.0153	3.0	-0.0070	0.0112	4.0	-0.0090	0.0081
0.75	2.0	0.1948	0.0747	3.0	0.1622	0.1546	4.0	0.1360	0.2047
1.00	2.0	0.3991	0.0984	3.0	0.3497	0.2732	4.0	0.3043	0.3846

Table 13. Interpretation of Pcf and Scf with respect to Sc

η	Sc	Pcf	Scf	Sc	Pcf	Scf	Sc	Pcf	Scf
0.00	2.5	0.8019	5.1057	3.0	1.4363	5.3947	3.5	2.0618	5.7231
0.25	2.5	0.6533	2.3513	3.0	0.9773	2.4334	3.5	1.2874	2.5279
0.50	2.5	0.3898	-0.3249	3.0	0.3865	-0.4418	3.5	0.3618	-0.5706
0.75	2.5	-0.5179	-2.5284	3.0	-0.8578	-2.6614	3.5	-1.1935	-2.8095
1.00	2.5	-2.0885	-3.7393	3.0	-2.6452	-3.5950	3.5	-3.1125	-3.4565

Table 14. Interpretation of Pcf and Scf with respect to Pr

η	Pr	Pcf	Scf	Pr	Pcf	Scf	Pr	Pcf	Scf
0.00	0.4	-0.4508	0.2592	0.8	-0.3966	-0.2300	1.2	-0.4829	-0.5454
0.25	0.4	-0.2141	0.1395	0.8	-0.1968	-0.1035	1.2	-0.2438	-0.2571
0.50	0.4	0.0113	0.0210	0.8	-0.0044	0.0148	1.2	-0.0134	0.0157
0.75	0.4	0.2206	-0.1309	0.8	0.1958	0.1106	1.2	0.2386	0.2654
1.00	0.4	0.4021	-0.3345	0.8	0.4087	0.1724	1.2	0.5295	0.4805

Table 15. Interpretation of Pcf and Scf with respect to s

η	s	Pcf	Scf	s	Pcf	Scf	s	Pcf	Scf
0.00	2.1	-0.4208	-0.1460	2.2	-0.4458	-0.1363	2.3	-0.4709	-0.1288
0.25	2.1	-0.2015	-0.0595	2.2	-0.2074	-0.0525	2.3	-0.2128	-0.0468
0.50	2.1	0.0016	0.0172	2.2	0.0056	0.0189	2.3	0.0098	0.0203
0.75	2.1	0.2037	0.0675	2.2	0.2119	0.0612	2.3	0.2197	0.0561
1.00	2.1	0.4079	0.0800	2.2	0.4153	0.0642	2.3	0.4222	0.0514

Table 16. Interpretation of Pcf and Scf with respect to χ

η	χ	Pcf	Scf	χ	Pcf	Scf	χ	Pcf	Scf
0.00	0.02	-0.3128	-0.1696	0.04	-0.3676	-0.1624	0.06	-0.4224	-0.1508
0.25	0.02	-0.1584	-0.0776	0.04	-0.1827	-0.0713	0.06	-0.2070	-0.0633
0.50	0.02	-0.0055	0.0106	0.04	-0.0035	0.0138	0.06	-0.0013	0.0168
0.75	0.02	0.1566	0.0827	0.04	0.1821	0.0778	0.06	0.2076	0.0711
1.00	0.02	0.3305	0.1285	0.04	0.3763	0.1093	0.06	0.4218	0.0866

Tables 17–20 show that the volume fraction parameter diminishes the heat transfer coefficient at the left wall and enhances it at the right, however the heat generation and suction parameters exhibit the opposite pattern. Heat generation parameter and suction parameter strengthen the mass transfer coefficient at the right wall while volume fraction parameter and Soret factor minimize it at the left wall.

Table 17. Interpretation of Nu and Sh with respect to χ

η	χ	Nu	Sh	χ	Nu	Sh	χ	Nu	Sh
0.00	0.02	2.2987	-4.1303	0.04	2.2232	-4.3129	0.06	2.1540	-4.5045
0.25	0.02	1.5584	-3.2160	0.04	1.5320	-3.4072	0.06	1.5073	-3.6060
0.50	0.02	0.9218	-2.3338	0.04	0.9307	-2.5184	0.06	0.9386	-2.7098
0.75	0.02	0.4040	-1.5256	0.04	0.4347	-1.6897	0.06	0.4632	-1.8603
1.00	0.02	0.0071	-0.8161	0.04	0.0478	-0.9487	0.06	0.0864	-1.0876

Table 18. Interpretation of Nu and Sh with respect to H

η	H	Nu	Sh	H	Nu	Sh	H	Nu	Sh
0.00	2.0	2.1879	-4.4076	3.0	2.4463	-4.5965	4.0	2.7510	-4.8285
0.25	2.0	1.5195	-3.5057	3.0	1.6614	-3.5452	4.0	1.8263	-3.5978
0.50	2.0	0.9348	-2.6132	3.0	0.9288	-2.4627	4.0	0.9172	-2.2882
0.75	2.0	0.4492	-1.7742	3.0	0.3061	-1.4514	4.0	0.1380	-1.0798
1.00	2.0	0.0674	-1.7742	3.0	-0.1757	-0.5780	4.0	-0.4454	-0.0889

Table 19. Interpretation of Nu and Sh with respect to s

η	s	Nu	Sh	s	Nu	Sh	s	Nu	Sh
0.00	2.1	2.2425	-4.5466	2.2	2.2976	-4.6837	2.3	2.3533	-4.8227
0.25	2.1	1.5322	-3.5872	2.2	1.5445	-3.6655	2.3	1.5564	-3.7442
0.50	2.1	0.9253	-2.6549	2.2	0.9155	-2.6932	2.3	0.9055	-2.7318
0.75	2.1	0.4316	-1.7891	2.2	0.4143	-1.8010	2.3	0.3973	-1.8133
1.00	2.1	0.0510	-1.0144	2.2	0.0354	-1.0087	2.3	0.0204	-1.0033

Table 20. Interpretation of Nu and Sh with respect to Sr

η	Sr	Nu	Sh	Sr	Nu	Sh	Sr	Nu	Sh
0.00	0.5	2.1879	0.5288	1.0	2.1879	-0.0197	1.5	2.1879	-0.5682
0.25	0.5	1.5195	0.6057	1.0	1.5195	0.1489	1.5	1.5195	-0.3079
0.50	0.5	0.9348	0.6554	1.0	0.9348	0.2922	1.5	0.9348	-0.0710
0.75	0.5	0.4492	0.6746	1.0	0.4492	0.4025	1.5	0.4492	0.1304
1.00	0.5	0.0674	0.6622	1.0	0.0674	0.4755	1.5	0.0674	0.2889

5. CONCLUSIONS

The following lists the article's significant conclusions:

- The magnetic parameter, thermal Grashof number, and thermal diffusion parameter reduce the nanofluid primary and secondary velocity components.
- The solutal Grashof number, Darcy parameter, and Hall current parameter increase the nanofluid primary and secondary velocity components.

- The primary velocity declines and secondary velocity augments with an enhancement in the upper wall motion factor, rotation parameter, and heat generation parameters.
- The primary velocity maximizes, and the secondary velocity minimizes with an increase in the suction and volume fraction factors.
- The primary skin friction intensifies at the lower wall and declines at the upper wall by expanding the upper wall motion factor, rotation parameter, magnetic parameter, thermal Grashof number, and heat generation parameters.
- The primary skin friction declines at the lower wall and intensifies at the upper wall as the solutal Grashof number, Darcy parameter, Hall current parameter, thermal diffusion parameter, suction factor, and volume fraction factor are expanded.
- The secondary skin friction intensifies at the lower wall and declines at the upper wall by expanding the magnetic parameter, thermal Grashof number, suction factor, and volume fraction factor.
- The secondary skin friction declines at the lower wall and intensifies at the upper wall as the upper wall motion factor, rotation parameter, solutal Grashof number, Darcy parameter, Hall current parameter, thermal diffusion parameter, and heat generation parameter are expanded.

Nomenclature

u –	nanoliquid motion in x – direction	Sh –	mass transfer coefficient
v –	nanoliquid motion in y – direction	K^2 –	rotation parameter
w –	nanoliquid motion in z – direction	M –	magnetic parameter
a –	distance between two walls	s –	suction parameter
u_0 –	characteristic velocity	Gr –	thermal Grashof number
T –	nanoliquid temperature	Gm –	solutal Grashof number
T_0 –	cold wall temperature	Da –	Darcy parameter
t –	dimensional time	Pr–	Prandtl number
p –	nanoliquid pressure	Sr –	Soret number
V_0 –	suction velocity	H –	heat generation parameter
C –	nanoliquid species concentration	Sc –	Schmidt number
C_0 –	concentration at the cold wall	**Greek symbols**	
k_p –	permeability of the porous medium	Ω –	angular velocity
k_{nf} –	thermal conductivity of nanoliquid	ω –	non-dimensional frequency of oscillation
k_f –,	thermal conductivity of the base liquid	χ –	volume fraction of nanoliquid
k_s –	thermal conductivity of the solid	ρ_{nf} –	nanoliquid density
$(c_p)_{nf}$ –	specific heat of nanoliquid at stable pressure	μ_{nf} –	dynamic viscosity of nanoliquid
$(c_p)_f$ –	specific heat of the base liquid	μ_f –	dynamic viscosity of the base liquid
$(c_p)_s$ –	specific heat of the solid,	σ_{nf} –	electrical conductivity of nanoliquid
Q_0 –	dimensional heat generation parameter	σ_f –	electrical conductivity of the base fluid
D_m –	chemical molecular diffusivity	σ_s –	electrical conductivity of the solid
D_{nf} –	nanofluid mass diffusivity	β_{nf} –	thermal expansion coefficient of nanoliquid
T_m –	mean nanoliquid temperature	β_f –	thermal expansion coefficient of the base liquid
B_0 –	magnetic induction	β_s –	thermal expansion coefficient of the solid
m –	hall current factor	ρ_{nf} –	nanoliquid density
g –	acceleration due to gravity	ρ_f –	density of the base liquid
U –	nanofluid primary velocity	ρ_s –	density of the nanoparticle
W –	nanofluid secondary velocity	θ –	nanofluid temperature
n –	dimensional frequency of oscillation	ϕ –	species concentration
q_w –	heat flux	η –	A scaled coordinate
j_w –	mass flux	τ –	non-dimensional time
Cf –	skin friction coefficient	τ_e –	electron collision time
Pcf –	primary skin friction coefficient	τ_w –	shear stress
Scf –	secondary skin friction coefficient	ω_e –	cyclotron frequency
Nu –	heat transfer coefficient	λ –	upper wall motion parameter

Conflicts of interest

There is no conflict of interest disclosed by the writers.

Acknowledgements

It gives us great pleasure to convey our sincere gratitude to the reviewers for their insightful remarks and recommendations for improving this article.

Data availability

The text contains all the supporting information.

Funding

This manuscript was prepared without the assistance of any funding.

APPENDIX

$$a_1=\frac{1}{(1-\chi)^{2.5}},\ a_2=1-\chi+\chi\left(\rho_s/\rho_f\right),\ a_3=1+\left[3\chi\left(\sigma_s-\sigma_f\right)\right]\left[\left(\sigma_s+2\sigma_f\right)-\chi\left(\sigma_s-\sigma_f\right)\right]^{-1},\ a_4=1-\chi+\chi\left[(\rho\beta)_s/(\rho\beta)_f\right]$$

$$a_5=a_1a_2^{-1},\ a_6=a_3a_2^{-1},\ a_7=\left[\left(k_s+2k_f\right)-2\chi\left(k_f-k_s\right)\right]\left[\left(k_s+2k_f\right)+\chi\left(k_f-k_s\right)\right]^{-1},\ a_8=1-\chi+\chi\left[\left(\rho c_p\right)_s/\left(\rho c_p\right)_f\right],\ a_9=a_7a_8^{-1},$$

$$a_{10}=a_2\left[a_1\rho_f\right]^{-1},\ a_{11}=S\,\mathrm{Pr}\,a_9^{-1},\ a_{12}=H\,\mathrm{Pr}\left[a_8a_9\right]^{-1},\ a_{13}=\mathrm{Pr}\,a_9^{-1}\left(Ha_8^{-1}-i\omega\right),$$

$$a_{14}=a_7ScSr,\ a_{15}=\left[\exp(m_5)-\exp(-m_5)\right]^{-1},\ a_{16}=\left[\exp(m_1)-\exp(m_2)\right]^{-1},\ a_{17}=a_{14}a_{15}a_{16},$$

$$a_{18}=m_1^2\left[\exp(m_1)-\exp(-m_5)\right]\left[m_1^2-m_5^2\right]^{-1},\ a_{19}=m_2^2\left[\exp(m_2)-\exp(-m_5)\right]\left[m_2^2-m_5^2\right]^{-1},\ a_{20}=a_{15}+a_{17}\left(a_{18}+a_{19}\right),$$

$$a_{21}=m_1^2\left[m_1^2-m_5^2\right]^{-1},\ a_{22}=m_2^2\left[m_2^2-m_5^2\right]^{-1},\ a_{23}=a_{14}a_{16}a_{21},$$

$$a_{24}=a_{14}a_{16}a_{22},\ a_{25}=a_{23}-a_{24}-a_{20},\ a_{26}=\left[\exp(m_3)-\exp(m_4)\right]^{-1},$$

$$a_{27}=m_3^2\left[m_3^2-Sc\,s\,m_3-Sc\,i\,\omega\right]^{-1},\ a_{28}=m_4^2\left[m_4^2-Sc\,s\,m_4-Sc\,i\,\omega\right]^{-1},\ a_{29}=a_{14}a_{26}a_{27},$$

$$a_{30}=a_{14}a_{26}a_{28},\ a_{31}=\left[\exp(m_7)-\exp(m_6)\right]^{-1},\ a_{32}=a_{29}\left[\exp(m_3)-\exp(m_6)\right],$$

$$a_{33}=a_{30}\left[\exp(m_4)-\exp(m_6)\right],\ a_{34}=a_{31}\left(1+a_{32}-a_{33}\right),\ a_{35}=a_{29}-a_{30}-a_{34},\ a_{36}=\left(a_6M\right)\left(1+im\right)^{-1}-2iK^2,\ a_{37}=a_{36}+\left(a_5/Da\right),$$

$$a_{38}=sa_5^{-1},\ a_{39}=a_{37}a_5^{-1},\ a_{40}=\left[a_4\left(a_{16}Gr-a_{23}Gm\right)\right]\left[a_5\left(m_1^2-a_{38}m_1-a_{39}\right)\right]^{-1},\ a_{41}=\left[a_4\left(a_{17}Gr-a_{24}Gm\right)\right]\left[a_5\left(m_2^2-a_{38}m_2-a_{39}\right)\right]^{-1},$$

$$a_{42}=a_4a_{25}Gm\left[a_5\left(m_5^2+a_{38}m_5-a_{39}\right)\right]^{-1},\ a_{43}=a_4a_{20}Gm\left[a_5\left(m_5^2+a_{38}m_5-a_{39}\right)\right]^{-1},\ a_{44}=\lambda a_{36}a_5^{-1}a_{39}^{-1},\ a_{45}=a_{40}-a_{41}+a_{42}+a_{43}-a_{44},$$

$$a_{46}=a_{40}\exp(m_1)-a_{41}\exp(m_2)+a_{42}\exp(-m_5)+a_{43}\exp(m_5)-a_{44}+\lambda\cos(\omega\tau),\ a_{47}=\left[\exp(m_8)-\exp(m_9)\right]^{-1},$$

$$a_{48}=a_{47}\left[a_{46}-a_{45}\exp(m_9)\right],\ a_{49}=a_{47}\left[a_{45}\exp(m_9)-a_{46}\right],\ a_{50}=a_{37}+i\omega,\ a_{51}=a_{50}a_5^{-1},$$

$$a_{52}=\left[a_4\left(a_{26}Gr-a_{29}Gm\right)\right]\left[a_5\left(m_3^2-a_{38}m_3-a_{51}\right)\right]^{-1},\ a_{53}=\left[a_4\left(a_{26}Gr-a_{30}Gm\right)\right]\left[a_5\left(m_4^2-a_{38}m_4-a_{51}\right)\right]^{-1},$$

$$a_{54}=a_4a_{35}Gm\left[a_5\left(m_6^2-a_{38}m_6-a_{51}\right)\right]^{-1},\ a_{55}=a_4a_{34}Gm\left[a_5\left(m_7^2-a_{38}m_7-a_{51}\right)\right]^{-1},\ a_{56}=a_{52}-a_{53}+a_{54}+a_{55},$$

$$a_{57}=a_{52}\exp(m_3)-a_{53}\exp(m_4)+a_{54}\exp(m_6)+a_{55}\exp(m_7),\ a_{58}=\left[\exp(m_{10})-\exp(m_{11})\right]^{-1},\ a_{59}=a_{58}\left[a_{57}-a_{56}\exp(m_{11})\right],$$

$$a_{60}=a_{58}\left[a_{56}\exp(m_{10})-a_{57}\right],\ m_1=2^{-1}\left[a_{11}-\sqrt{a_{11}^2-4a_{12}}\right],\ m_2=2^{-1}\left[a_{11}+\sqrt{a_{11}^2-4a_{12}}\right],\ m_3=2^{-1}\left[a_{11}-\sqrt{a_{11}^2-4a_{13}}\right],$$

$$m_4=2^{-1}\left[a_{11}+\sqrt{a_{11}^2-4a_{13}}\right],\ m_5=\sqrt{Sc\,s},\ m_6=2^{-1}\left[Sc\,s-\sqrt{(Sc\,s)^2+4Sc\,i\,\omega}\right],\ m_7=2^{-1}\left[Sc\,s+\sqrt{(Sc\,s)^2+4Sc\,i\,\omega}\right],$$

$$m_8=2^{-1}\left[a_{38}-\sqrt{a_{38}^2+4a_{39}}\right],\ m_9=2^{-1}\left[a_{38}+\sqrt{a_{38}^2+4a_{39}}\right],\ m_{10}=2^{-1}\left[a_{38}-\sqrt{a_{38}^2+4a_{51}}\right],\ m_{11}=2^{-1}\left[a_{38}+\sqrt{a_{38}^2+4a_{51}}\right].$$

ORCID

Venkateswarlu Malapati, https://orcid.org/0000-0002-6320-0195; **Mohammed Almakki,** https://orcid.org/0000-0002-9348-4651;
V.B. Rajakumar Komaravolu, https://orcid.org/0000-0002-2667-8042

REFERENCES

[1] D. O. Soumya, B. J. Gireesha, and P. Venkatesh, "Generalized Couette flow of nanoliquid among two concentric channels with particles injection," International Journal of Ambient Energy, **45**, Article 2353305 (2024). https://doi.org/10.1080/01430750.2024.2353305

[2] L. Swain, R. P. Sharma, and S. R. Mishra, "Diversified role of nanoparticle concentration and radiating heat on the natural convection Couette flow through a vertical channel," Colloid and Polymer Science, **302**, 1687-1700 (2024). http://dx.doi.org/10.1007/s00396-024-05294-3

[3] G. Ali, M. Ahmad, F. Ali, A. Khan, and I. Khan, "Couette flow of viscoelastic dusty fluid through a porous oscillating plate in a rotating frame along with heat transfer," Heat Transfer, **53**, 4588-4607 (2024). https://doi.org/10.1002/htj.23127

[4] M. Venkateswarlu, D.V. Lakshmi, O.D. Makinde, "Thermodynamics analysis of Hall current and Soret number on hydromagnetic Couette flow in a rotating system with a convective boundary condition, Heat Transfer Research," **51**, 83-101 (2020). https://doi.org/10.1615/HeatTransRes.2019027139

[5] S. L. Sun, D. Liu, C. Kang, H. B. Kim, Y. Z. Song, and P. G. Zhang, "Numerical simulation and machine learning study on heat transfer enhancement of nanofluids in Taylor–Couette flow with an elliptical slit surface," International Communications in Heat and Mass Transfer, **163**, Article 108788 (2025). https://doi.org/10.1016/j.icheatmasstransfer.2025.108788
[6] M. Venkateswarlu, P. Bhaskar, and O. D. Makinde, "Mathematical study of nonlinear mixed convection unsteady flow in a parallel plate inclined channel in the proximity of time periodic boundary conditions: flow reversal," Journal of Nanofluids, **10**, 598-607 (2021). https://doi.org/10.1166/jon.2021.1802
[7] R. Gupta, "Analyzing the impact of magnetic field, squeezing, and volume fraction on Magnetohydrodynamic nanofluid flow using a differential transform method," Journal of Nanofluids, **14**, 596-605 (2025). https://doi.org/10.1166/jon.2025.2261
[8] R. Arpitha, K. Ramesh, and D. Srikanth, "Temperature and mass dispersion of mixed convective MHD Casson nanofluid flow through porous medium," International Journal of Applied and Computational Mathematics, **11**, 1-25 (2025). https://doi.org/10.1007/s40819-025-01882-1
[9] F. S. Bayones, A. M. Abd-Alla, and E. N. Thabet, "Magnetized dissipative Soret effect on nonlinear radiative Maxwell nanofluid flow with porosity, chemical reaction and Joule heating," Waves in Random and Complex Media, **34**, 6270-6288 (2024). https://doi.org/10.1080/17455030.2021.2019352
[10] S. Mudoi, D. Sarma, and A. K. Sarma, "Newtonian fluid flow with heat and mass transfer across an inclined sheet and magnetic field with Soret effects," Journal of the Korean Physical Society, **86**, 280-291 (2025). https://doi.org/10.1007/s40042-024-01278-2
[11] H. Basha, N. B. Naduvinamani, and M, Shridhar, "Numerical analysis of velocity slip and magnetic Soret effect on dissipative Maxwell liquid motion about a stretching wall with heat source/sink," Numerical Heat Transfer, Part B: Fundamentals, **86**, 2721-2745 (2025). https://doi.org/10.1080/10407790.2024.2347613
[12] M. Venkateswarlu, P.R. Reddy, and K.J. Lakshmi, "Analytical study of Soret and Dufour effects on heat destructive Casson liquid movement past an infinite vertical plate," Journal of Naval Architecture and Marine Engineering, **21**, 27-40 (2024). https://doi.org/10.3329/jname.v21i1.69228
[13] P. Pandey, "Chemical reaction and heat source effects on oscillatory suction in MHD flow through permeable media with Soret effect," Aircraft Engineering and Aerospace Technology, **97**, 149-161 (2025). https://doi.org/10.1108/AEAT-01-2024-0023
[14] S. Jangid, and K. Kolla, "Magnetic field and Soret effect on mixed convection Williamson fluid model through a vertical channel using artificial neural network," International Journal of Numerical Methods for Heat & Fluid Flow, **35**, 4333-4365 (2025). https://doi.org/10.1108/HFF-10-2024-0781
[15] S. Ahamedsheriff, V. Rajaram, G. Mani, S. T. Thabet, and I. Kedim, "Impacts of soret and Dufour possessions on micropolar fluid past a stretching sheet in a porous medium," Scientific Reports, **15**, 33059 (2025). https://doi.org/10.1038/s41598-025-18302-5
[16] A. K. Sarma, D. Sarma, and S. Mudoi, "Magnetohydrodynamic flow and effects of Soret, Dufour and thermophoresis through a chemically reacting porous stretching plate," Sigma, **43**, 1533-1546 (2025). https://doi.org/10.14744/sigma.2025.00150
[17] M. Venkateswarlu, and D.V. Lakshmi, "Diffusion-thermo and heat source effects on the unsteady radiative MHD boundary layer slip flow past an infinite vertical porous plate," Journal of Naval Architecture and Marine Engineering, **18**, 55-72 (2021). https://doi.org/10.3329/jname.v18i1.33024
[18] M. Venkateswarlu, and D.V. Lakshmi, "Thermal diffusion, hall current and chemical reaction effects on unsteady MHD natural convective flow past a vertical plate," U. P. B. Sci. Bull., Series D: Mechanical Engineering, **79**, 91-106 (2017).
[19] O. D. Makinde, M. Venkateswarlu, and R. L. Monaledi, "Unsteady MHD flow of radiating and rotating fluid with Hall current and thermal diffusion past a moving plate in a porous medium," Defect and Diffusion Forum, **389**, 71-85 (2018). https://doi.org/10.4028/www.scientific.net/DDF.389.71
[20] S. Jayanthi, and H. Niranjan, "A vertical surface flow analysis of MHD nanofluids influenced by radiation, viscous dissipation, and joule heating with Soret and Dufour effects," Contemporary Mathematics, **5**, 2296-2314 (2024). https://doi.org/10.37256/cm.5220244318
[21] M. Venkateswarlu, and M. Phanikumar, "Soret and heat source effects on MHD flow of a viscous fluid in a parallel porous plate channel in presence of slip condition," U. P. B. Sci. Bull., Series D: Mechanical Engineering, **79**, 171-186 (2017).
[22] M. Venkateswarlu, and O. D. Makinde, Unsteady MHD slip flow with radiative heat and mass transfer over an inclined plate embedded in a porous medium, Defect and Diffusion Forum, **384**, 31-48 (2018). https://doi.org/10.4028/www.scientific.net/DDF.384.31
[23] Y. Ouyang, M.F.M. Basir, K. Naganthran, and I. Pop, "Exploring heat generation and magnetic effects on unsteady ternary nanofluid flow over a dynamic wedge in porous media," Chinese Journal of Physics, **93**, 531-548 (2025). https://doi.org/10.1016/j.cjph.2024.12.026
[24] S. Dey, S. Mukhopadhyay, and K. Vajravelu, "Thermo-solutal nonlinear convection in a nanofluid flow past a porous plate in the presence of heat generation/absorption," Heat Transfer, **54**, 1394-1419 (2025). https://doi.org/10.1002/htj.23221
[25] A. K. Hussein, S. E. Ahmed, M. A. Mansour, O. Younis, and L. Kolsi, "Effects of radiation and heat generation on MHD mixed convection in a double lid-driven inclined wavy porous cavity filled with non-Newtonian nanofluid and including a cross-shape heaters," Waves in Random and Complex Media, **35**, 5587-5614 (2025). https://doi.org/10.1080/17455030.2022.2071503
[26] M. Venkateswarlu, M. Phani Kumar, and O. D. Makinde, "Establishment of impulsive and accelerated motions of Casson fluid in an inclined plate in the proximity of MHD and heat generation," Periodica Polytechnica Mechanical Engineering, **66**, 219-230 (2022). https://doi.org/10.3311/PPme.19424
[27] Y. S. Daniel, Z. Ismail, P. Ayuba, S. Daniel, P. Anthony, P. N. Okolo, and A. S. Magaji, "Radiative heat transfer and Ohmic heating on unsteady EMHD mixed convective flow for dual stratified nanofluid," Modeling Earth Systems and Environment, **11**, 1-19 (2025). https://doi.org/10.1007/s40808-025-02387-y
[28] M. Z. Kefene, and E. H. Rikitu, "Magnetic and thermal radiation effects on hematocrit-dependent blood nanofluid flow in an inclined stenotic artery with heat generation," Brazilian Journal of Physics, **55**, 1-12 (2025). https://doi.org/10.1007/s13538-025-01770-5
[29] M. Venkateswarlu, P. Rami Reddy, and K. J. Lakshmi, "Nonlinear unsteady MHD flow in an inclined channel with suction and heat generation: time periodic boundary conditions," Journal of Naval Architecture and Marine Engineering, **22**, 199-216 (2025). https://doi.org/10.3329/jname.v22i2.75405

[30] M. S. Ram, M. D. Shamshuddin, C. Satyanarayana, and S. O. Salawu, "Stagnation point flow of magnetized convective nanofluid via porous stretchy surface subjected to ohmic heating and heat generation," International Journal of Modelling and Simulation, **45**, 1346-1360 (2025). https://doi.org/10.1080/02286203.2023.2281009

[31] M. Venkateswarlu, M. B. Chennaiah, and Md. Noor, "Significance of cross diffusion on the transient behavior of radiationg Casson fluid near a heated slanted plate," Bulletin of the Parana Mathematical Society, **43**, 1-19 (2025). https://doi.org/10.5269/bspm.78525

[32] Z. Abbas, S. Goher, and M. Y. Rafiq, "Interfacial flow and heat transfer analysis of kerosene–TiO_2 and water–Al_2O_3 nanofluids in shear-driven boundary layers," Journal of Engineering Research, (2025). https://doi.org/10.1016/j.jer.2025.12.001

ВПЛИВ СТРУМУ ХОЛЛА, ТЕПЛОВОГО РОЗСІЮВАННЯ ТА ТЕПЛОВИДІЛЕННЯ НА ПОТІК НАНОРІДИНИ TiO_2 НА ОСНОВІ ГАСУ ЧЕРЕЗ ОБЕРТОВИЙ ПОРИСТИЙ КАНАЛ

Венкатешварлу Малапаті[1], Мохаммед Алмаккі[2], В.Б. Раджакумар Комараволу[3]

[1]Кафедра математики, Академія вищої освіти Сіддхартхи, Віджаявада, Андхра-Прадеш, Індія - 520007

[2]Школа інженерії, архітектури та дизайну інтер'єрів, Університет Аміті, Міжнародне академічне місто Дубая, П.С. скринька 345019б Індія

[3]Кафедра математики, Технологічний інститут Каллама Харанадхаредді, Гунтур, Андхра-Прадеш, Індія - 522019

На відміну від тепловиділення та теплового розсіювання, досліджуються струм Холла та коефіцієнти обертання розряду нанорідини діоксиду титану на основі гасу через дві паралельні стінки, вбудовані в пористий канал. Розглядаються фактори всмоктування та гідромагнітні фактори. Використовуючи відповідні початкові та граничні умови, підхід збурень може дати точне аналітичне рішення для визначальних рівнянь для швидкості, температури та концентрації нанорідини. Можна отримати вирази для напруження зсуву, швидкості масопередачі та швидкості теплопередачі на пластинах. З одного боку, показано графічне представлення первинної та вторинної швидкостей, температури нанорідини та концентрації частинок. Однак, для різних значень відповідних коефіцієнтів течії, числові оцінки напруження зсуву, швидкості масопередачі та швидкості теплопередачі для стінок представлені у табличній формі. Через внесок сили плавучості розчиненої речовини, результуючі профілі первинної та вторинної швидкості постійно зростають до високого рівня. Концентрація збільшується разом зі збільшенням характеристик тепловиділення та теплодифузії по всій нанорідині. Коли сила теплової плавучості достатньо висока, профілі первинної та вторинної швидкості зменшуються. Струм Холла та параметр Дарсі підвищують коефіцієнти первинного та вторинного тертя поверхні на верхній стінці, одночасно зменшуючи їх на нижній. Однак на первинні та вторинні коефіцієнти тертя поверхні впливають протилежним чином сила теплової плавучості та магнітний параметр. Результати порівнюються з існуючою літературою.

Ключові слова: *нанорідина; потік Куетта; струм Холла; теплоутворення; відсмоктування*

East European Journal of Physics. 3. 432–442 (2026)
DOI: 10.26565/2312-4334-2026-3-39 ISSN 2312-4334

THE INFLUENCE OF JOULE HEATING EFFECT AND THERMAL STRATIFICATION ON MHD TERNARY HYBRID NANOFLUID IN A POROUS MEDIUM OVER A VERTICALLY STRETCHING CYLINDER: A NUMERICAL INVESTIGATION

Surajit Dutta[1], **Nitul Kalita**[2], **Rupam Shankar Nath**[3*], **Rudra Kanta Deka**[2]
[1]*Department of Mathematics, C.N.B. College, Bokakhat-785612, Assam, India*
[2]*Department of Mathematics, Gauhati University, Guwahati-781014, Assam, India*
[3]*Department of Mathematics, Morigaon College (Autonomous), Morigaon-782105, Assam, India*
[*]*Corresponding Author e-mail: rupamnath23@gmail.com*
Received May 28, 2026; revised July 6, 2026; accepted July 21, 2026

The aspects of flow in a magnetohydrodynamic (MHD) ternary hybrid nanofluid consisting of suspended (Cu), aluminum oxide (Al_2O_3), and titanium dioxide (TiO_2) nanoparticles in water (H_2O) were numerically investigated in this study. The effects of thermal stratification and Joule heating are incorporated by passing the nanofluid through a vertically extending cylinder in a porous medium. By implementing an appropriate transformation, the energy and boundary layer equations are simplified to a nonlinear ODE system. The resulting system is solved using MATLAB's fourth-order accurate bvp4c solver. from MATLAB is employed to solve the altered system. The effects are illustrated graphically the change in velocity and temperature and quantitatively tabulate the changes in friction factor, and heat transfer rate for important values of the dimensionless physical factors related to the problem. Crucial findings show that, hybrid nanofluids outperform nanofluids in terms of thermal conductivity. Temperature and velocity of the ternary hybrid nanofluid are both decreased when the heat stratification factor is present, as compared to the absence of stratification. There is a noticeable increase in the heat transfer rate when the ternary hybrid nanofluid is compared with the hybrid nanofluid, which in turn surpasses that of traditional nanofluids. The acquired results are valuable for applications in geothermal energy extraction, chemical processing, and materials synthesis.

Keywords: *Ternary Hybrid Nanofluid; Joule's Effect; Stretching Vertical Cylinder; Thermal Stratification; Porous Medium; bvp4c*

1. INTRODUCTION

Ternary hybrid nanofluids are a state-of-the-art breakthrough in fluid dynamics and nanotechnology that have broad engineering applications in engineering and industries. There are three different kinds of nanoparticles mixed in with a base fluid to make these nanofluids. These fluids possess enhanced thermal and rheological properties. The nanoparticles can be metallic or non-metallic, and the base fluid can be any common heat transfer fluid or coolant such water, ethylene glycol, or oil. This article describes a research investigation on a ternary hybrid nanofluid consisting of copper (Cu), aluminum oxide (Al_2O_3), and titanium dioxide (TiO_2) nanoparticles. The nanoparticles are uniformly dispersed inside a fluid medium containing water.

Research has shown that adding copper (Cu) nanoparticles to a nanofluid improves its thermal conductivity, while adding aluminum oxide (Al_2O_3) and titanium dioxide (TiO_2) nanoparticles improves the efficiency and stability of heat transmission. In order to improve thermal management and heat dissipation, this nanofluid can be used in a variety of applications, including cooling systems, electrical devices, and heat exchangers. It is well-known that copper nanoparticles can kill bacteria, and (TiO_2) nanoparticles can fight bacteria and other microbes by photo catalysis. Nanoparticles of titanium dioxide (TiO_2) with photocatalytic characteristics can help decompose organic pollutants and purify water. The ternary hybrid nanofluid comprising Cu, Al_2O_3 and TiO_2 could be useful in water treatment processes, removing contaminants and improving water quality in the process.

An innovative new class of fluids called nanofluids was created by mixing a base fluid with particles as small as a few nanometers in size. These tiny particles, which might be metallic or non-metallic, are usually less than 100 nanometers. A novel class of heat transfer fluids including free-floating metallic nanoparticles has been proposed by the idea of nanofluid, which was initially introduced by Choi and Eastman [1]. Several researchers have investigated a sliding vertical plate in Das and Jana [2] and a vertical channel in Das et al. [3] in relation to the radiation-induced natural convective flow of nanofluids. In their respective studies, Reddy et al.[4] and Mahanthesh et al. [5] assessed the consequences of mass and heat transfer on nanofluid as it traverses a mobile or static vertical plate, while considering the impact of a chemical reactions and a heat source. In their study, Sandeep and Reddy [6] investigated the flow of a magnetohydrodynamic (MHD) Cu-water nanofluid over a cone and a wedge, considering the influence of nonlinear thermal radiation. Moreover, the Lattice Boltzmann approach was utilized in the investigation of the magnetohydrodynamic (MHD) Cu-water nanofluid, given the influence of Lorentz forces by Sheikholeslami et al., [7]. The investigation conducted by Rashidi et al. [8] proposed a Lie group solution for the issue of the production or consumption of heat in the context of nanofluid movement over a horizontal plate undergoing chemical reactions. The HAM is employed in Abolbashari et al. [9] to examine the entropy of a nanofluid

Cite as: S. Dutta, N. Kalita, R. S. Nath, R. K. Deka, East Eur. J. Phys. 3, 432 (2026), https://doi.org/10.26565/2312-4334-2026-3-39

comprising water as the main fluid and one of four different types of nanoparticles: TiO_2, Al_2O_3, Cu, and CuO. The nanofluid flows through a stretchy permeable surface. Within the framework of velocity slip and heat leap, an analytical study was conducted by Turkyilmazoglu [10] to examine the MHD nanofluid flow of different water-soluble nanoparticles as they flowing over a periodically stretching and shrinking permeable sheet. The impacts of heat radiation, heat diffusion, and viscous dissipation were investigated numerically in a study of nanofluid boundary layer flow across a moving flat plate by Motsumi and Makinde [11]. Nath and Deka [12], Kalita et al., [13] and Nath et al. [14] studied how temperature layering and chemical reactions affect the flow across infinite and accelerated vertical plates, respectively. Cheng [15, 16] investigated the effects of mass and heat stratification across a wavy surface and a vertical, truncated cone, respectively. In addition, for infinite vertical cylinders, Paul and Deka [17] have studied the effects of both stratification factors. [18] Considered the impacts of mass and temperature layering on the unstable flow through an endlessly fast-moving upright plate in a porous media with exponential mass diffusion and fluctuating temperatures. The unstable parabolic flow across an infinite upright plate in a porous media with varying mass diffusion and an exponentially decreasing temperature was studied by [19] in relation to the unite effects of temperature and mass stratification. Using a vertically expanding cylinder in porous medium, Nath and Deka [20] studied how the flow of water-based hybrid, nano, and ternary hybrid nanofluids via magnetohydrodynamics (MHD) is impacted by temperature stratification. The study in Paul et al. [18] examines the impact of temperature stratification on a hybrid nanofluid composed of $Cu - Al_2O_3/H_2O$ in a porous media. The research conducted by the authors focused on a cylinder that is stretched vertically, and examines the impact of a heat sink or source. It was observed that the thermal conductivity of hybrid nanofluids exhibited a notable increase in comparison to that of nanofluids. Thus, the application of hybrid nanofluids demonstrates a substantial impact on improving thermal improvements. The study conducted by Rana and Kumar [19] inspected the flow of hybrid nano liquid via a rotating cylinder, considering the influence of quadratic heat radiation on a buoyancy-driven nonlinear flow. To enhance the ternary hybrid nanofluid's $Cu - Al_2O_3 - MWCNT$/water heat conveyance capabilities consisting of, the researchers in reference Shanmugapriya et al., [20] examined the impact of nanoparticle morphology. In their study, Shaik et al. [21] looked into the free convection that happens in a wavy, sinusoidal shell that contains a hybrid nanofluid made of $TiO_2 - Cu$ particles that are suspended in water. The consequences of thermal radiation, internal heat creation, a magnetic field with an angle on convection is included in the analysis. Examining the responses of the similar formulas that govern the behavior of a colloidal combination of water, cylindrical grapheme, round nanotubes of carbon, and platelet nanoparticles made of alumina was done by Cao et al., [22]. In addition, the study examined forced, free, and mixed convection regimes, the study took into account different degrees of partial slide. Research on the heat transfer properties of ternary hybrid nanofluid flows in the existence of nonlinear heat radiation and a magnetized dipole was carried out by Nasir et al. [23]. Using a convectively heated stretching/shrinking cylinder, the effects of suction and heat source on the MHD stagnation point flow of a ternary hybrid nanofluid ($Cu - Fe_3O_4 - SiO_2$/polymer) have been studied by Mahmood et al. [24]. Furthermore, in the framework of electromagnetic hydrodynamics (EMHD), a ternary hybrid nanofluid consisting of $Cu - CNT - Ti$ and water was studied by Jakeer et al. [25] to determine the effects of non-linear Darcy-Forchheimer flow. Compared to nanofluid or hybrid nanofluid alone, the ternary hybrid nanofluid significantly affected the temperature profile. Patil et al. [26] Look at how a ternary hybrid nanofluid ($THNF$) flows with tangent hyperbolic ($(T-H)$) flow features when it meets a rough-yawed cylinder. Impulsive forces are used to move the cylinder, and the study is mostly about the mixed convection process and periodic magnetohydrodynamics. Gorfie et al. [27] addressed the combined effects of Joule heating and thermal stratification on MHD ternary hybrid nanofluid flow over a vertically stretching cylinder embedded in a porous medium remain limited, thereby motivating the present investigation. Kumar et al. [28] studied on stretching-cylinder flows have shown that Joule heating, magnetic fields, and internal heat generation significantly affect the velocity and temperature distributions of electrically conducting fluids. Motivated by these findings, the present work extends the analysis to an MHD ternary hybrid nanofluid in a porous medium by incorporating the combined effects of Joule heating and thermal stratification over a vertically stretching cylinder.

As shown in the literature review, previous research has not attempted to demonstrate the flow of a magnetohydrodynamic (MHD) ternary nanofluid via a vertically expanding cylinder in a porous medium, taking into account the influence of the joule's impact and temperature stratification effect. Examining the heat transfer characteristics of a ternary hybrid nanofluid made up of $Cu - Al_2O_3 - TiO_2$ particles distributed in water is the core objective of this work. This study examines the behavior of heat transport around a vertically stretching cylinder while taking into the account of homogeneous thermal sources and thermal sinks, the joule's effect, and thermal stratification. By employing suitable self-similar variables within the bvp4c solver of the MATLAB programmed, the non-linear partial differential equations (PDEs) that govern the flow are changed into ordinary differential equations (ODEs). As shown by its description and application in MATLAB by [30], and Hale and Moore [29], the Bvp4c technique is well-known and used to simulate the problem in this study. For various parameters like $\lambda, \delta, Pr, M, Q$ and Ec the results are presented graphically.

2. METHODOLOGY

In the context of a vertical stretchable cylinder with radius r_0, let us contemplate a two-dimensional steady incompressible ternary hybrid nanofluid composed of $Cu - Al_2O_3 - TiO_2/H_2O$. This nanofluid is submerged in a porous medium. Thermal stratification, a heat source/sink, and joule's effect exert an influence on the system. As displayed in Fig. 1, it is postulated that the ternary hybrid nanofluid flows in the axial x-direction, where the r coordinate denotes the

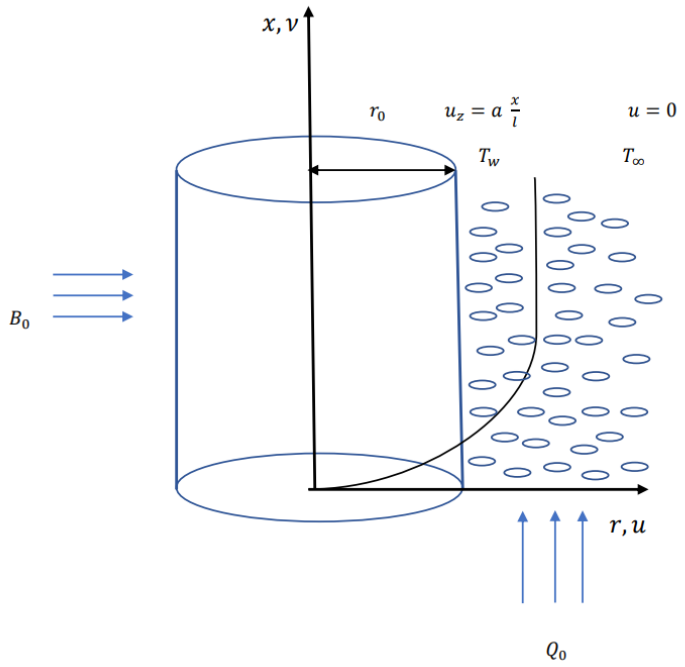

Figure 1. Physical Model and Coordinate system

direction perpendicular to the x-axis. Here, "u" stands for the ternary hybrid nanofluid's velocity component along the r-axis and "v" for the x-axis. In the present investigation, a magnetic field of magnitude B_0 is supplied perpendicular to the ternary hybrid nanofluid's propagation path. In addition to Joule heating, the thermal buoyancy effect is taken into account in the flow problem. $u = a\frac{x}{l}$, is the velocity responsible for inducing linear stretching in the upright cylinder, where $'a'$ and $'l'$ symbolise the cylinder's characteristic length and velocity, respectively. $T_w(x) = T_0 + A\left(\frac{x}{l}\right)$, is the wall's assumed temperature, and $T_\infty(x) = T_0 + B\left(\frac{x}{l}\right)$, is the ternary hybrid nanofluid's temperature at ambient conditions. The constants T_0 and A, B stand for the beginning temperature and non-negative constants, respectively. According to the study conducted by Paul et al., [18], the equations that regulate continuity, momentum, and energy in the setting of a ternary hybrid nanofluid can be formulated as follows.

$$\frac{\partial(ru)}{\partial x} + \frac{\partial(rv)}{\partial r} = 0 \tag{1}$$

$$u\frac{\partial u}{\partial x} + v\frac{\partial u}{\partial r} = \frac{\mu_{thnf}}{\rho_{thnf}}\frac{1}{r}\frac{\partial}{\partial r}\left(r\frac{\partial u}{\partial r}\right) + \frac{(\rho\beta_T)_{thnf}}{\rho_{thnf}}g(T - T_\infty) - \frac{\sigma_{thnf}}{\rho_{thnf}}B_0^2 u - \frac{\mu_{thnf}}{\rho_{thnf}}\frac{u}{k'} \tag{2}$$

$$u\frac{\partial T}{\partial x} + v\frac{\partial T}{\partial r} = \frac{k_{thnf}}{(\rho c_p)_{thnf}}\frac{1}{r}\frac{\partial}{\partial r}\left(r\frac{\partial T}{\partial r}\right) + \frac{Q_0}{(\rho c_p)_{thnf}}(T - T_\infty) + \frac{\sigma_{thnf}}{(\rho c_p)_{thnf}}B_0^2 u^2 \tag{3}$$

The boundary conditions are as follows:

$$u = a\frac{x}{l}, \quad v = 0, \quad T = T_w(x) \quad \text{when } r = r_0$$
$$u = 0, \quad T \to T_\infty(x) \quad \text{when } r \to \infty$$

Here is the similarity transformation utilized in Equations (1)-(3), as described in reference [18]

$$\eta = \frac{r^2 - r_0^2}{2r_0}\sqrt{\frac{a}{\nu_f l}}, \quad \psi = \sqrt{\frac{a\nu_f}{l}}xr_0 f(\eta), \quad \theta = \frac{T - T_\infty(x)}{T_w(x) - T_0}$$

and we have the following non-dimensional quantities:

$$M = \frac{l\sigma_f B_0^2}{a\rho_f}, \quad K = \frac{l\nu_f}{ak}, \quad \gamma = \sqrt{\frac{l\nu_f}{ar_0^2}}, \quad \lambda = \frac{Gr}{Re_x^2}, \quad \delta = \frac{B}{A}, \quad Q = \frac{Q_0 l}{a(\rho c_p)_f},$$

$$Pr = \frac{\nu_f(\mu c_p)_f}{k_f}, \quad Ec = \frac{u_z^2}{(c_p)_f(T_w(x) - T_0)}$$

In this context, K denotes the porosity parameter, γ signifies the curvature parameter, M represents the magnetic parameter, λ signifies the thermal buoyancy parameter, Q signifies the heat source/sink parameter, Pr represents the Prandtl number, δ signifies the thermal stratification parameter, and Ec represents the Eckert number.

To satisfy equation (1) for continuity, we introduce the stream function ψ, which has the form $u = \frac{1}{r}\frac{\partial\psi}{\partial r}$ and $v = -\frac{1}{r}\frac{\partial\psi}{\partial x}$. Thus, we provide the non-dimensional representations of the altered equations as follows:

$$f'^2 - ff'' = a_1\left[2\gamma f'' + (1+2\gamma\eta)f'''\right] + a_2\lambda\theta - (a_3M + a_1K)f' \tag{4}$$

$$f'(\theta+\delta) - f\theta' = a_4\left[2\gamma\theta' + (1+2\gamma\eta)\theta''\right] + a_5\theta + a_6EcMf'^2 \tag{5}$$

where,

$$x_1 = \frac{\mu_{thnf}}{\mu_f}, \quad x_2 = \frac{\rho_f}{\rho_{thnf}}, \quad x_3 = \frac{(\rho\beta)_{thnf}}{(\rho\beta)_f}, \quad x_4 = \frac{(\rho C_p)_f}{(\rho C_p)_{thnf}}, \quad x_5 = \frac{\sigma_{thnf}}{\sigma_f}, \quad x_6 = \frac{k_{thnf}}{k_f}$$

$$a_1 = x_1x_2, \quad a_2 = x_2x_3, \quad a_3 = x_2x_5, \quad a_4 = \frac{x_4x_6}{Pr}, \quad a_5 = Qx_4, \quad a_6 = x_4x_5$$

The symbols $\mu_{thnf}, \rho_{thnf}, (\beta)_{thnf}, (\rho C_p)_{thnf}, \sigma_{thnf}, k_{thnf}$ indicate the ternary hybrid nanofluid's coefficient of viscosity, electrical conductivity, thermal expansion, heat capacity, density and thermal conductivity, respectively. Additionally, $\mu_f, \rho_f, (\beta)_f, (\rho C_p)_f, \sigma_f, k_f$ represent the viscosity, electrical conductivity, thermal expansion, heat capacity, density, and thermal conductivity of the base fluid, respectively.

The dimensionless coefficients $a_1 - a_6$ appearing in Eqs. (4) and (5) are introduced to simplify the transformed governing equations. These coefficients represent the effective thermo-physical property ratios of the ternary hybrid nanofluid relative to the base fluid and account for the combined effects of viscosity, density, thermal expansion, electrical conductivity, heat capacity, thermal conductivity, heat source, and Joule heating.

The transformed boundary conditions are as follows:

$$\begin{aligned} &f(\eta) = 0 && f'(\eta) = 1 && \theta(\eta) = 1-\delta && \text{at } \eta = 0 \\ &&& f'(\eta) \to 0 && \theta(\eta) \to 0 && \text{as } \eta \to \infty \end{aligned} \tag{6}$$

The ternary hybrid nanofluid has the following thermo-physical properties [25] :

$$\mu_{thnf} = \frac{\mu_f}{(1-\phi_1)^{2.5}(1-\phi_2)^{2.5}(1-\phi_3)^{2.5}}$$

$$\rho_{thnf} = (1-\phi_3)\left[(1-\phi_2)\left\{(1-\phi_1)\rho_f + \phi_1\rho_{s1}\right\} + \phi_2\rho_{s2}\right] + \phi_3\rho_{s3}$$

$$(\rho c_p)_{thnf} = (1-\phi_3)\left[(1-\phi_2)\left\{(1-\phi_1)(\rho c_p)_f + \phi_1(\rho c_p)_{s1}\right\} + \phi_2(\rho c_p)_{s2}\right] + \phi_3(\rho c_p)_{s3}$$

$$(\rho\beta_T)_{thnf} = (1-\phi_3)\left[(1-\phi_2)\left\{(1-\phi_1)(\rho\beta_T)_f + \phi_1(\rho\beta_T)_{s1}\right\} + \phi_2(\rho\beta_T)_{s2}\right] + \phi_3(\rho\beta_T)_{s3}$$

$$k_{nf} = \left[\frac{(k_{s1}+2k_f) - 2\phi_1(k_f - k_{s1})}{(k_{s1}+2k_f) + \phi_1(k_f - k_{s1})}\right]k_f, \; k_{hnf} = \left[\frac{(k_{s2}+2k_{nf}) - 2\phi_2(k_{nf} - k_{s2})}{(k_{s2}+2k_{nf}) + \phi_2(k_{nf} - k_{s2})}\right]k_{nf}$$

$$k_{thnf} = \left[\frac{(k_{s3}+2k_{hnf}) - 2\phi_3(k_{hnf} - k_{s3})}{(k_{s3}+2k_{hnf}) + \phi_3(k_{hnf} - k_{s3})}\right]k_{hnf}, \; \sigma_{nf} = \left[\frac{(\sigma_{s1}+2\sigma_f) - 2\phi_1(\sigma_f - k_{s1})}{(\sigma_{s1}+2\sigma_f) + \phi_1(\sigma_f - \sigma_{s1})}\right]\sigma_f$$

$$\sigma_{hnf} = \left[\frac{(\sigma_{s2}+2\sigma_{nf}) - 2\phi_2(\sigma_{nf} - \sigma_{s2})}{(\sigma_{s2}+2\sigma_{nf}) + \phi_2(\sigma_{nf} - \sigma_{s2})}\right]\sigma_{nf}, \sigma_{thnf} = \left[\frac{(\sigma_{s3}+2\sigma_{hnf}) - 2\phi_3(\sigma_{hnf} - \sigma_{s3})}{(\sigma_{s3}+2\sigma_{hnf}) + \phi_3(\sigma_{hnf} - \sigma_{s3})}\right]\sigma_{hnf}$$

where ϕ_1, ϕ_2 and ϕ_3 are volume fraction of Cu(Copper), Al_2O_3 (aluminium oxide) and TiO_2(titanium oxide) nanoparticles respectively. The suffixes thnf, hnf, nf, f, s1, s2, s3 denote ternary hybrid nanofluid, hybrid nanofluid, nanofluid, base fluid, solid nanoparticles of copper (Cu), aluminum oxide (Al_2O_3), and titanium dioxide (TiO_2) correspondingly. Thermo-physical characteristics of Cu, Al_2O_3 and TiO_2 nanoparticles in pure water are presented in Table 1.

The skin friction coefficient and local Nusselt number are defined by

$$C_f Re_x^{1/2} = \frac{1}{(1-\phi_1)^{2.5}(1-\phi_2)^{2.5}(1-\phi_3)^{2.5}}f''(0) \quad \text{and} \quad Nu_x Re_x^{-1/2} = -\frac{k_{thnf}}{k_f}\theta'(0)$$

where, Re_x is the local Reynolds Number.

Table 1. Thermo-physical Properties of water and nanoparticles [2]

Physical Properties	H_2O(base fluid)	Cu (s1)	Al_2O_3 (s2)	TiO_2 (s3)
$\rho\ (kg/m^3)$	997.1	8933	3970	4250
$C_p\ (J/kgK)$	4179	385	765	686.2
$k\ (W/mK)$	0.613	401	40	8.9538
$\beta_t \times 10^5\ (K^{-1})$	21	1.67	0.85	0.9
$\sigma\ (s/m)$	5.5×10^{-6}	59.6×10^6	35×10^6	2.6×10^6

3. METHOD OF SOLUTION

The numerical solution of the non-linear higher-order system of ordinary differential equations (ODEs) given by Equations (4)-(5) and the boundary conditions (6) is performed using the bvp4c solver, which is integrated into the computational platform MATLAB. Scientists and engineers have relied heavily on this method for resolving fluid flow issues. Hale and Moore [29] pioneered the bvp4c solver, which was developed by Jacek Kierzenka and Lawrence F. Shampine of Texas's Southern Methodist University. The bvp4c solver is an approach for finite-state problems that generates fourth-order accurate numerical solutions by means of the Lobatto IIIA implicit Runge-Kutta formulation. For initial mesh point guesses and step-size modifications, this technique provides the required accuracy. According to Waini et al. [30], when compared to the shooting approach and the Keller box method, the bvp4c solver produced satisfactory results. In this context, it is necessary to decrease the derivatives of higher order with regard to η. This can be achieved by incorporating the subsequent additional variables:

$$f = y(1), \quad f' = y(2), \quad f'' = y(3), \quad \theta = y(4), \quad \theta' = y(5)$$

$$\frac{d}{d\eta}\begin{bmatrix} y(1) \\ y(2) \\ y(3) \\ y(4) \\ y(5) \end{bmatrix} = \begin{bmatrix} y(2) \\ y(3) \\ \frac{y(2)^2 - y(1)y(3) - a_2\lambda y(4) + (a_3 M + a_1 K)y(2) - 2a_1\gamma y(3)}{(1+2\gamma\eta)a_1} \\ y(5) \\ \frac{y(2)(y(4)+\delta) - y(1)y(5) - 2a_4\gamma y(5) - a_5 y(4)}{(1+2\gamma\eta)a_4} \end{bmatrix}$$

and boundary condition are expressed as

$$ya(1), \quad ya(2) - 1, \quad ya(4) - 1 + \delta, \quad yb(2), \quad yb(4)$$

where ya is the condition at $\eta = 0$ and yb is the condition at $\eta = \infty$

4. RESULTS AND DISCUSSION

As a comparison to the results given by Paul et al. [18], Table 2 displays the absolute values of the friction factor and the local Nusselt number as determined by the present study. We are excluding TiO_2 nanoparticle volume fractions with $Ec = 0$ from this comparison. As this research shows, the bvp4c algorithm may produce reliable numerical results that match or exceed those of competing approaches. Figs. 2-13 and Tables 2-4 illustrate the results of the computations performed numerically in the bvp4c solver of MATLAB. $Pr = 6.2, Q = 0.3, K = 1, \gamma = 0.1, Ec = 0.1, \delta = 0.3, M = 1.2, \lambda = 1.2, \phi_1 = 0.05, \phi_2 = 0.15$ and $\phi_3 = 0.2$. are the values that are employed in the study.

The thermal stratification parameter, $\delta = \frac{B}{A}$, represents the ratio of the ambient temperature gradient to the wall temperature gradient. For a physically meaningful wall heating problem, the condition $0 \leq \delta < 1$ must be satisfied so that the dimensionless wall temperature remains positive, i.e., $\theta(0) = 1 - \delta > 0$. In the present study, all numerical simulations are performed within this admissible range to ensure the physical validity of the thermal boundary conditions. As δ approaches unity, the temperature difference between the wall and the ambient fluid decreases, resulting in weaker thermal buoyancy and reduced heat transfer.

Table 2. Comparison of Skin friction Coefficient and local Nusselt Number when $\phi_3 = 0$

δ	Pr	λ	γ	Paul et al. $-C_f Re_x^{1/2}$	Present Study $-C_f Re_x^{1/2}$	Paul et al. $Nu_x Re_x^{-1/2}$	Present Study $Nu_x Re_x^{-1/2}$
0.1	6.2	1.2	0.1	2.9398	2.9795	2.7885	2.7887
0.1	2	1.2	0.1	2.8419	2.8760	1.3264	1.3311
0.1	6.2	2.4	0.1	2.7219	2.7425	2.8528	2.8516
0.1	6.2	1.2	0.2	3.0048	3.0436	2.8283	2.8269

Fig. 2 illustrates how the nanofluid's velocity $f'(\eta)$ is affected by the porosity parameter (K). As the value of the porosity parameter increases, the velocity drops. As increases, the diameter of the porous medium gradually shrinks, indicating an inverse relationship between the two variables. This smaller diameter makes the fluid's passage through the porous material more difficult. The decrease in fluid velocity was caused by the obstacle introduced by the porosity parameter (K).

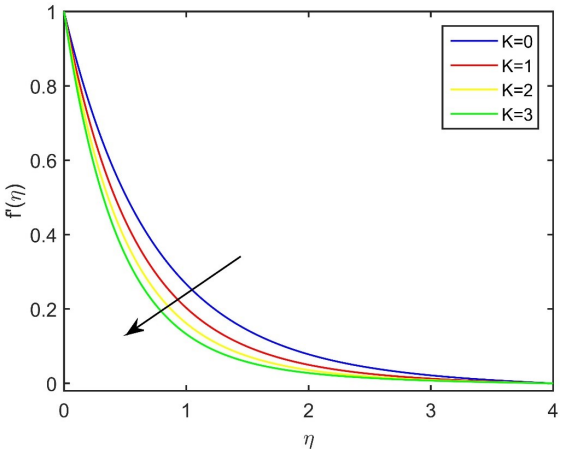

Figure 2. Effect of K on Velocity Profile

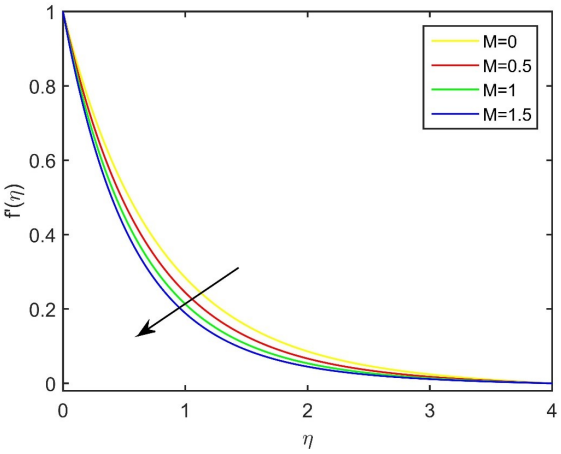

Figure 3. Effect of M on Velocity Profile

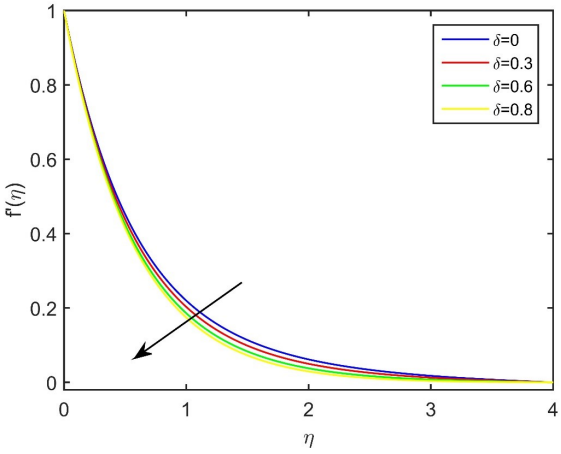

Figure 4. Effect of δ on Velocity Profile

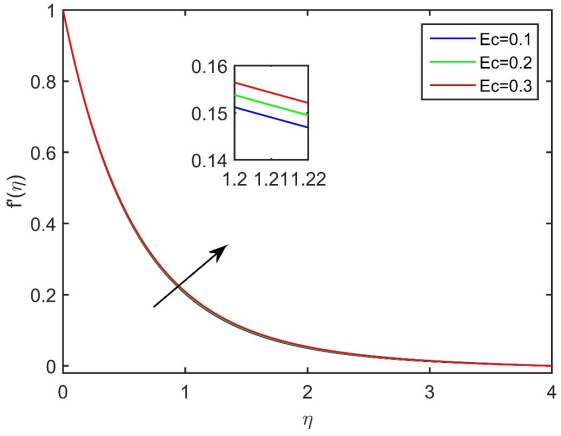

Figure 5. Effect of Ec on Velocity Profile

When the amount of M is increased, the fluid velocity drops, as portrayed in Fig. 3. Enhancing the magnetic parameter (M) causes the momentum barrier layer to become thinner. This structure develops as a consequence of the ternary hybrid nanofluid's reduced velocity caused by the Lorentz force generated by the horizontal magnetic field. Fig. 4 shows how the parameters of thermal stratification (δ) affect the nanofluid's velocity $f'(\eta)$. The flow rate drops as the heat stratification parameter rises. Reduced potent convection potential between hot wall and surrounding fluid is a result of an enhancement in the heat stratification parameter. Because of this, the buoyant force is diminished, leading to a slower flow rate.

Impact of Eckert number (Ec) on velocity profile is displayed in Fig. 5. As Ec rises velocity of the fluid also rise. Fig. 6 shows the changes in fluid velocity caused by thermal buoyancy parameter λ. We find that when values are increased, the velocity goes up. A higher increase in λ results in a stronger thermal buoyancy force. Because of this, we can deduce that buoyant forces cause the fluid's velocity to rise.

The impact of the heat source parameter (Q) is displayed in Fig. 7. It is found that fluid velocity develops in tandem with a boost in Q. Fig. 8 illustrates how the Prandtl number affects the velocity profile. The velocity profile appears to slow down as the Prandtl number increases.

The temperature profile demonstrates an enhancement as the Eckert number enhances, as illustrated in Fig. 9. The physical explanation is that an increase in Ec may cause the fluid's viscosity to absorb more energy, which it can then transform into internal energy, therefore raising the temperature. As shown in Fig. 10, the temperature $\theta(\eta)$ rises as the

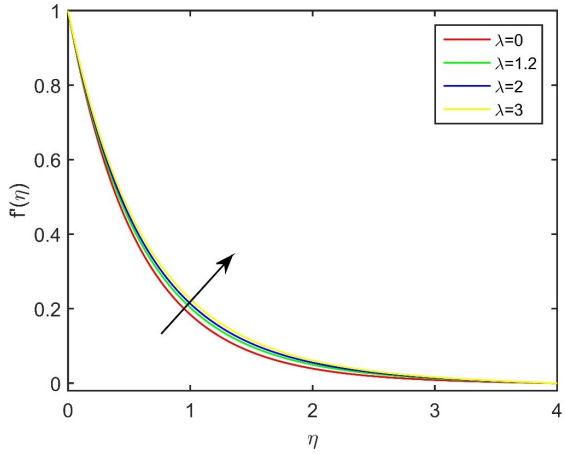

Figure 6. Effect of λ on Velocity Profile

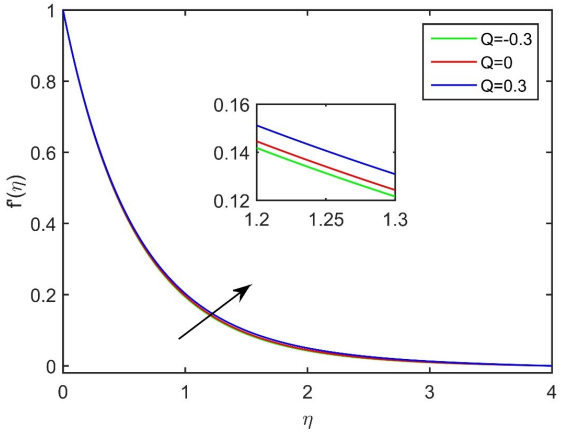

Figure 7. Effect of Q on Velocity Profile

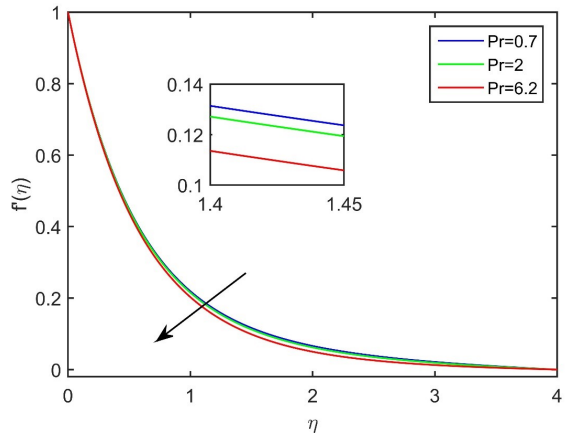

Figure 8. Effect of Pr on Velocity Profile

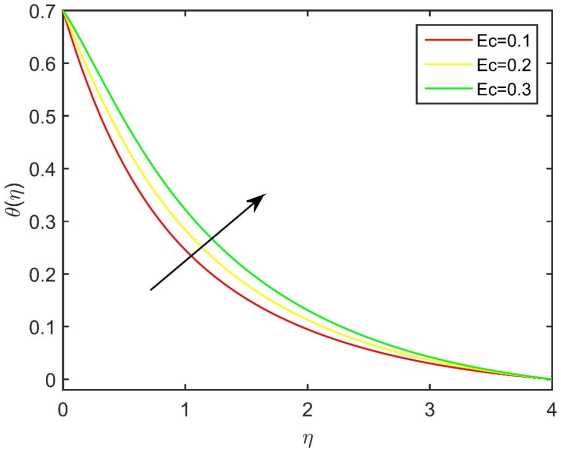

Figure 9. Effect of Ec on Temperature Profile

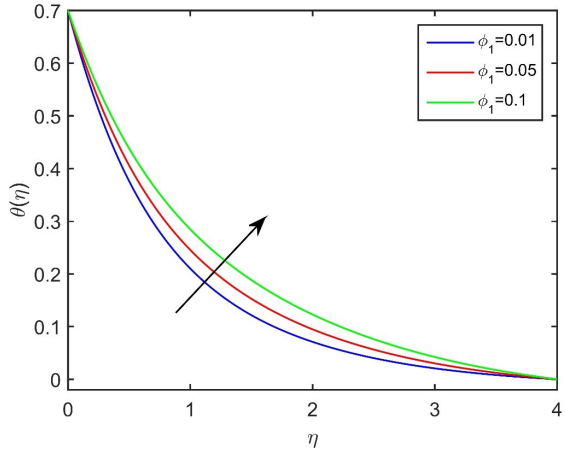

Figure 10. Effect of ϕ_1 on Temperature Profile

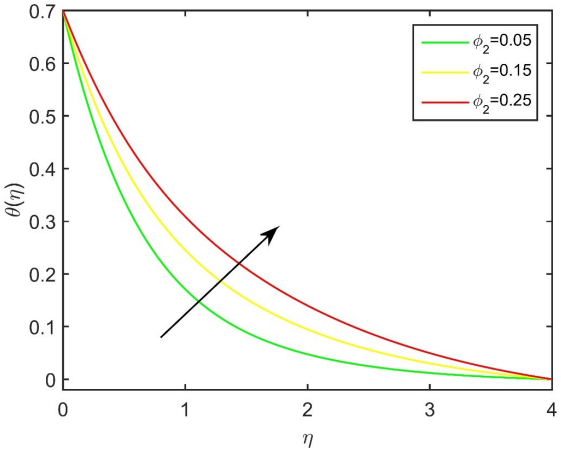

Figure 11. Effect of ϕ_2 on Temperature Profile

solid volume fraction of Cu nanoparticles grow, keeping the volume fractions of Al_2O_3 and TiO_2 constant. Moreover, it is noticeable from Fig. 11 that the temperature shows an upward trend as the volume fraction of increases, whilst the volume fractions of and stay consistent. Likewise, the temperature profile is shown to increase with an increase of ϕ_3, as depicted in Fig. 12. A higher temperature is the result of increased physical dissipation of energy, which may occur when the volume fraction of nanoparticles increases.

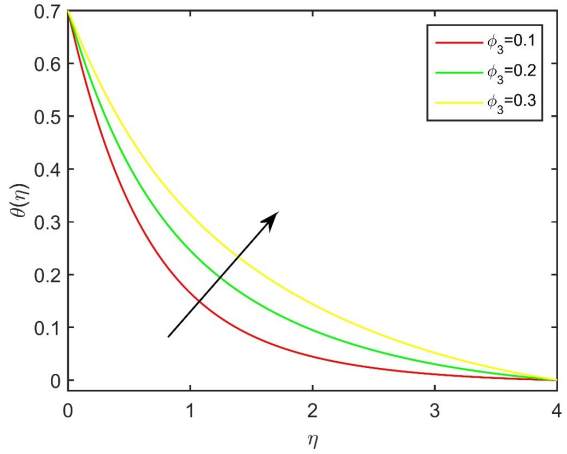

Figure 12. Effect of ϕ_3 on Temperature Profile

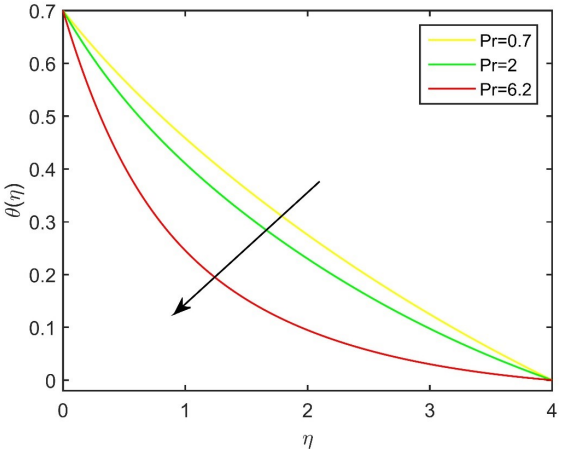

Figure 13. Effect of Pr on Temperature Profile

However, Fig. 13 highlights the consequences of the Prandtl number (Pr) on the temperature profile. Observations indicate that raising the Prandtl number results in a decline in the thickness of the heat boundary layer, resulting in a fall off in the temperature gradient. Fig. 14 demonstrates how the temperature profile is affected by a parameter of the heat source (Q). As Q, the heat source parameter, rises, the fluid temperature rises as well. This property is in accordance with the fluid's intrinsic physical properties.

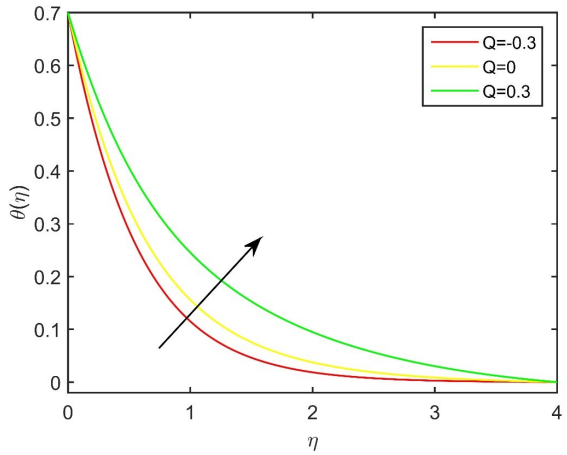

Figure 14. Effect of Q on Temperature Profile

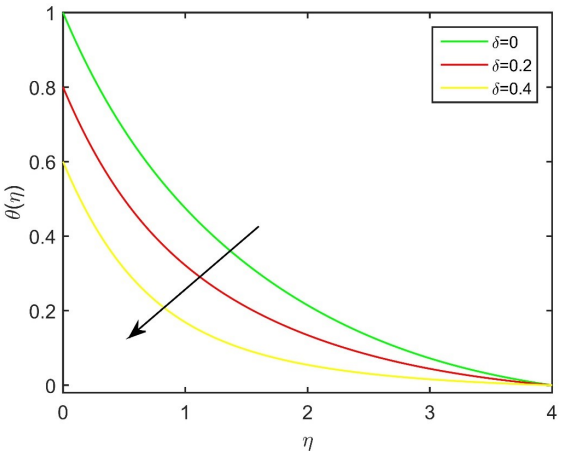

Figure 15. Effect of δ on Temperature Profile

When the temperature stratification parameter (δ) goes up, as shown in Fig. 15, the temperature of the stream goes down. When thermal stratification (δ) is present, the temperature difference between the hot wall and the fluid around it will go down. Because of this, the temperature drops and the thermal barrier layer gets thicker.

For different flow factors, Table 3 show how they change the skin friction and the local Nusselt number. Table 3 showed that the absolute value of the skin friction coefficient increases with increasing thermal stratification parameter (δ), magnetic parameter (M) and porosity parameter (K). In contrast, the local Nusselt number decreases with increasing values of δ, M, where as increases with K. For increasing λ, skin friction decreases while the local Nusselt number increases. A higher skin friction and Nusselt number are seen for Pr. As the heat source parameter (Q) increases, there is an observable decrease in the rate of heat transmission. Rising the value of the curvature parameter (γ) results in a increase in the skin friction and the Nusselt number as the value of γ increase.

In accordance with Table 4, the ternary hybrid nanofluid has a larger absolute skin friction than the hybrid nanofluid, as demonstrated by the experimental results. On the other hand, it is also noticeable that hybrid nanofluids exhibit more skin friction than ordinary nanofluids. Additionally, the ternary hybrid nanofluid has been found to demonstrate a faster rate of heat transfer than the hybrid nanofluid, which in turn shows a higher heat transfer rate than ordinary nanofluids.

Table 3. Skin friction Coefficient and Local Nusselt number for different values of $\delta, M, K, \lambda, Pr, Q, \gamma$

δ	M	K	λ	Pr	Q	γ	$-C_f Re_x^{1/2}$	$Nu_x Re_x^{-1/2}$
0							5.8976	3.3791
0.2	1.1	2	1.5	6.2	0.1	0.2	5.9937	3.1437
0.4							6.0895	2.9029
	0						5.0625	3.3897
0.2	0.5	2	1.5	6.2	0.1	0.2	5.5047	3.2716
	1.5						6.2992	3.0654
0.2	1.1	0	1.5	6.2	0.1	0.2	4.2386	2.6142
		1					5.1882	3.3559
0.2	1.1	2	1.5	6.2	0.1	0.2	6.2814	3.0258
			3				5.7207	3.2339
0.2	1.1	2	1.5	0.6	0.1	0.2	5.8739	0.9577
				4			5.9541	2.3516
0.2	1.1	2	1.5	6.2	-0.1	0.2	6.0190	3.6293
					0		6.0083	3.4083
0.2	1.1	2	1.5	6.2	0.1	0	5.7202	3.0029
						0.1	5.8582	3.0723

Table 4. Comparison of Skin friction Coefficient and Local Nusselt number

δ	Cu Nanofluid $-C_f Re_x^{1/2}$	$Cu - Al_2O_3$ Hybrid Nanofluid $-C_f Re_x^{1/2}$	$Cu - Al_2O_3 - TiO_2$ Ternary Hybrid Nanofluid $-C_f Re_x^{1/2}$	Cu Nanofluid $Nu_x Re_x^{-1/2}$	$Cu - Al_2O_3$ Hybrid Nanofluid $Nu_x Re_x^{-1/2}$	$Cu - Al_2O_3 - TiO_2$ Ternary Hybrid Nanofluid $Nu_x Re_x^{-1/2}$
0	1.9645	3.3981	5.8976	2.3250	3.0662	3.3791
0.2	2.1869	3.5020	5.9937	2.5539	2.8668	3.1437
0.5	2.3329	3.6531	6.1372	2.2778	2.5361	2.7805

5. CONCLUSIONS

An extensive study was conducted on the consequences of heating stratification and the joule's effect regarding the movement of a ternary hybrid nanofluid that demonstrates magnetohydrodynamics characteristics through a vertically stretchable cylinder. This study took into account the existence of a thermal bouncy effect and a heat source within a porous medium. The study also looks at the flow features and how they affect temperature and velocity profiles, as well as the Nusselt number and friction factor. Notable findings from this inquiry include the following:

- As the parameters δ, K, M and Pr grow, the velocity profile shows a decreasing trend, while it shows a rising pattern with higher values of λ, Ec and Q.
- With rising values of δ and Pr the temperature decline, whereas with rising values of $Ec, \phi_1, \phi_2, \phi_3$ and Q, it rises.
- Parameters δ, M, K, Q, γ and Pr cause a increase in absolute skin friction, whereas λ cause it to decrease.
- An upward trend is noted in the local Nusselt number as the values of K, Pr and λ increase, whereas a downward trend is observed as δ, M and Q increase.
- In comparison to the hybrid nanofluid, the ternary hybrid nanofluid exhibits a higher absolute skin friction. Similarly, when compared to ordinary nanofluids, hybrid nanofluids exhibit higher skin friction.
- A ternary hybrid nanofluid has a greater heat transfer rate than a hybrid nanofluid, which is also higher than that of standard nanofluids.

The present numerical investigation provides useful guidance for the design of thermal systems employing ternary hybrid nanofluids. The results indicate that moderate values of the thermal buoyancy parameter (λ) enhance the fluid velocity, while lower values of the thermal stratification parameter (δ) are preferable for maintaining higher heat transfer rates. Similarly, increasing the volume fractions of Cu, Al_2O_3 and TiO_2 nanoparticles improves the thermal performance of the base fluid, although excessively high nanoparticle concentrations may increase skin friction and pumping power

requirements. The magnetic parameter (M) and porosity parameter (K) should therefore be selected carefully to achieve an appropriate balance between flow resistance and heat transfer enhancement. These findings suggest that the $Cu - Al_2O_3 - TiO_2/H_2O$ ternary hybrid nanofluid can be effectively utilized in geothermal heat extraction, compact heat exchangers, solar thermal collectors, electronic cooling systems, and chemical processing equipment where efficient thermal management is required.

ORCID

Surajit Dutta, https://orcid.org/0009-0008-7188-3919; **Nitul Kalita**, https://orcid.org/0000-0001-8348-2225; **Rupam Shankar Nath**, https://orcid.org/0009-0002-2352-0538; **Rudra Kanta Deka**, https://orcid.org/0009-0007-1573-4890

REFERENCES

[1] S.U.S. Choi, and J.A. Eastman, "Enhancing thermal conductivity of fluids with nanoparticles," Technical report, Argonne National Lab. (ANL), Argonne, IL (United States), 1995.

[2] S. Das, and R.N. Jana, "Natural convective magneto-nanofluid flow and radiative heat transfer past a moving vertical plate," Alexandria Engineering Journal, **54**(1), 55–64 (2015). https://doi.org/10.1016/j.aej.2015.01.001

[3] S. Das, R.N. Jana, and O.D. Makinde, "Transient natural convection in a vertical channel filled with nanofluids in the presence of thermal radiation," Alexandria Engineering Journal, **55**(1), 253–262 (2016). https://doi.org/10.1016/j.aej.2015.10.013

[4] P.C. Reddy, M.C. Raju, and G.S.S. Raju, "Free convective heat and mass transfer flow of heat-generating nanofluid past a vertical moving porous plate in a conducting field," Special Topics & Reviews in Porous Media: An International Journal, **7**(2), (2016). https://doi.org/10.1615/specialtopicsrevporousmedia.2016016973

[5] B. Mahanthesh, B.J. Gireesha, and R.S.R. Gorla, "Heat and mass transfer effects on the mixed convective flow of chemically reacting nanofluid past a moving/stationary vertical plate," Alexandria engineering journal, **55**(1), 569–581 (2016). https://doi.org/10.1016/j.aej.2016.01.022

[6] N. Sandeep, and M.G. Reddy, "Heat transfer of nonlinear radiative magnetohydrodynamic cu-water nanofluid flow over two different geometries," Journal of Molecular Liquids, **225**, 87–94 (2017). https://doi.org/10.1016/j.molliq.2016.11.026

[7] M. Sheikholeslami, M.G. Bandpy, R. Ellahi, and A. Zeeshan, "Simulation of MHD CuO–water nanofluid flow and convective heat transfer considering Lorentz forces," Journal of Magnetism and Magnetic Materials, **369**, 69–80 (2014). https://doi.org/10.1016/j.jmmm.2014.06.017

[8] M.M. Rashidi, E. Momoniat, M. Ferdows, and A. Basiriparsa, "Lie group solution for free convective flow of a nanofluid past a chemically reacting horizontal plate in a porous media," Mathematical Problems in Engineering, **2014**, (2014). http://dx.doi.org/10.1155/2014/239082

[9] M.H. Abolbashari, N. Freidoonimehr, F. Nazari, and M.M. Rashidi, "Entropy analysis for an unsteady MHD flow past a stretching permeable surface in nano-fluid," Powder Technology, **267**, 256–267 (2014). https://doi.org/10.1016/j.powtec.2014.07.028

[10] M. Turkyilmazoglu, "Exact analytical solutions for heat and mass transfer of MHD slip flow in nanofluids," Chemical Engineering Science, **84**, 182–187 (2012). https://doi.org/10.1016/j.ces.2012.08.029

[11] T.G. Motsumi, and O.D. Makinde, "Effects of thermal radiation and viscous dissipation on boundary layer flow of nanofluids over a permeable moving flat plate," Physica Scripta, **86**(4), 045003 (2012). https://doi.org/10.1088/0031-8949/86/04/045003

[12] R.S. Nath, and R.K. Deka, "The effects of thermal stratification on flow past an infinite vertical plate in presence of chemical reaction," East European Journal of Physics, (3), 223–232 (2023). https://doi.org/10.26565/2312-4334-2023-3-19

[13] N. Kalita, R.K. Deka, and R.S. Nath, "Unsteady flow past an accelerated vertical plate with variable temperature in presence of thermal stratification and chemical reaction," East European Journal of Physics, (3), 441–450 (2023). https://doi.org/10.26565/2312-4334-2023-3-49

[14] R.S. Nath, R.K. Deka, and H. Kumar, "The effect of thermal stratification on unsteady parabolic flow past an infinite vertical plate with chemical reaction," East European Journal of Physics, (4), 77–86 (2023). https://doi.org/10.26565/2312-4334-2023-4-08

[15] C.-Y. Cheng, "Double-diffusive natural convection along a vertical wavy truncated cone in non-newtonian fluid saturated porous media with thermal and mass stratification," International Communications in Heat and Mass Transfer, **35**(8), 985–990 (2008). https://doi.org/10.1016/j.icheatmasstransfer.2008.04.007

[16] C.-Y. Cheng, "Combined heat and mass transfer in natural convection flow from a vertical wavy surface in a power-law fluid saturated porous medium with thermal and mass stratification," International Communications in Heat and Mass Transfer, **36**(4), 351–356 (2009). https://doi.org/10.1016/j.icheatmasstransfer.2009.01.003

[17] A. Paul, R.K. Deka, et al. "Unsteady natural convection flow past an infinite cylinder with thermal and mass stratification," Int. J. Eng. Math, **2017**, 8410691 (2017). https://doi.org/10.1155/2017/8410691

[18] A. Paul, J.M. Nath, and T.K. Das, "An investigation of the MHD Cu-Al_2O_3/H_2O hybrid-nanofluid in a porous medium across a vertically stretching cylinder incorporating thermal stratification impact," Journal of Thermal Engineering, **9**(3), 799-810 (2023). https://doi.org/10.18186/thermal.1300847

[19] P. Rana, and A. Kumar, "Nonlinear buoyancy driven flow of hybrid nanoliquid past a spinning cylinder with quadratic thermal radiation," International Communications in Heat and Mass Transfer, **139**, 106439 (2022). https://doi.org/10.1016/j.icheatmasstransfer.2022.106439

[20] M. Shanmugapriya, R. Sundareswaran, P.S. Kumar, and G. Rangasamy, "Impact of nanoparticle shape in enhancing heat transfer of magnetized ternary hybrid nanofluid," Sustainable Energy Technologies and Assessments, **53**, 102700 (2022). https://doi.org/10.1016/j.seta.2022.102700

[21] J. Shaik, B.A.R. Polu, M.M. Ahmed, and R.A. Mohamed, "Characteristics of moving hot block and non-fourier heat flux model on sinusoidal wavy cavity filled with hybrid nanofluid," The European Physical Journal Plus, **137**(1), 131 (2022). https://doi.org/10.1140/epjp/s13360-022-02361-y

[22] W. Cao, I.L. Animasaun, S.-J. Yook, V.A. Oladipupo, and X. Ji, "Simulation of the dynamics of colloidal mixture of water with various nanoparticles at different levels of partial slip: Ternary-hybrid nanofluid," International Communications in Heat and Mass Transfer, **135**, 106069 (2022). https://doi.org/10.1016/j.icheatmasstransfer.2022.106069

[23] S. Nasir, S. Sirisubtawee, P. Juntharee, A.S. Berrouk, S. Mukhtar, and T. Gul, "Heat transport study of ternary hybrid nanofluid flow under magnetic dipole together with nonlinear thermal radiation," Applied Nanoscience, **12**(9), 2777–2788 (2022). https://doi.org/10.1007/s13204-022-02583-7

[24] Z. Mahmood, Z. Iqbal, M.A. Alyami, B. Alqahtani, M.F. Yassen, and U. Khan, "Influence of suction and heat source on mhd stagnation point flow of ternary hybrid nanofluid over convectively heated stretching/shrinking cylinder," Advances in Mechanical Engineering, **14**(9), 16878132221126278 (2022). https://doi.org/10.1177/16878132221126278

[25] S. Jakeer, S.R.R. Reddy, A.M. Rashad, M.L. Rupa, and C. Manjula, "Nonlinear analysis of Darcy-Forchheimer flow in EMHD ternary hybrid nanofluid (Cu-CNT-Ti/water) with radiation effect," Forces in Mechanics, **10**, 100177 (2023). https://doi.org/10.1016/j.finmec.2023.100177

[26] P.M. Patil, B. Goudar, and M.A. Sheremet, "Tangent hyperbolic ternary hybrid nanofluid flow over a rough-yawed cylinder due to impulsive motion," Journal of Taibah University for Science, **17**(1), 2199664 (2023). https://doi.org/10.1080/16583655.2023.2199664

[27] E.H. Gorfie, A.T. Moltot, G.A. Zergaw, and H. Dessie, "Influence of joule heating and nonlinear thermal radiation on the electrical conductivity of second-grade hybrid nanofluid flow over a stretching cylinder," Engineering Reports, **7**(4), e70129 (2025). https://doi.org/10.1002/eng2.70129

[28] P. Kumar, R.S. Yadav, and O.D. Makinde, "Numerical study of Williamson fluid flow and heat transfer over a permeable stretching cylinder with the effects of joule heating and heat generation/absorption," Heat Transfer, **52**(4), 3372–3388 (2023). https://doi.org/10.1002/htj.22832

[29] N.P. Hale, M.Sc. Thesis, "A sixth-order extension to the MATLAB bvp4c software of J. Kierzenka and L. Shampine." Department of Mathematics, Imperial College London, 2006.

[30] I. Waini, A. Ishak, and I. Pop, "Mixed convection flow over an exponentially stretching/shrinking vertical surface in a hybrid nanofluid," Alexandria Engineering Journal, **59**(3), 1881–1891 (2020). https://doi.org/10.1016/j.aej.2020.05.030

ВПЛИВ ЕФЕКТУ ДЖОУЛЕВОГО НАГРІВАННЯ ТА ТЕПЛОВОГО РОЗШИРЕННЯ НА МГД-ПОТРІЙНУ ГІБРИДНУ НАНОРІДИНУ В ПОРИСТОМУ СЕРЕДОВИЩІ НАД ВЕРТИКАЛЬНО РОЗТЯГНУТИМ ЦИЛІНДРОМ: ЧИСЛОВЕ ДОСЛІДЖЕННЯ

Сураджіт Дутта[1], **Нітул Каліта**[2], **Рупам Шанкар Натх**[3], **Рудра Канта Дека**[2]

[1]*Кафедра математики, С.N.B. Коледж, Бокахат-785612, Ассам, Індія*

[2]*Кафедра математики, Університет Гаухаті, Гувахаті-781014, Ассам, Індія*

[3]*Кафедра математики, Коледж Морігаон (Автономний), Морігаон-782105, Ассам, Індія*

У цьому дослідженні чисельно досліджено аспекти потоку в магнітогідродинамічній (МГД) потрійній гібридній нанорідині, що складається з суспендованих наночастинок (Cu), оксиду алюмінію (Al_2O_3) та діоксиду титану (TiO_2) у воді (H_2O). Вплив термічної стратифікації та джоулевого нагрівання враховується шляхом пропускання нанорідини через вертикально простягаючийся циліндр у пористому середовищі. Шляхом реалізації відповідного перетворення, рівняння енергії та пограничного шару спрощуються до нелінійної системи звичайних диференціальних рівнянь (ЗДР). Отримана система розв'язується за допомогою розв'язувача bvp4c четвертого порядку точності MATLAB. Для розв'язання зміненої системи використовується MATLAB. Ефекти графічно проілюстровано зміною швидкості та температури, а також кількісно представлено в таблиці зміни коефіцієнта тертя та швидкості теплопередачі для важливих значень безрозмірних фізичних факторів, пов'язаних з проблемою. Важливі результати показують, що гібридні нанорідини перевершують нанорідини з точки зору теплопровідності. Температура та швидкість потрійної гібридної нанорідини зменшуються при наявності коефіцієнта теплової стратифікації порівняно з відсутністю стратифікації. Спостерігається помітне збільшення швидкості теплопередачі при порівнянні потрійної гібридної нанорідини з гібридною нанорідиною, що, у свою чергу, перевершує показники традиційних нанорідин. Отримані результати є цінними для застосування у видобутку геотермальної енергії, хімічній обробці та синтезі матеріалів.

Ключові слова: *потрійна гібридна нанорідина; ефект Джоуля; розтягування вертикального циліндра; термічна стратифікація; пористе середовище; bvp4c*

EAST EUROPEAN JOURNAL OF PHYSICS. 3. 443-455 (2026)
DOI:10.26565/2312-4334-2026-3-40 ISSN 2312-4334

NUMERICAL INVESTIGATION OF JEFFREY NANOFLUID OVER A MOVING THIN NEEDLE WITH EXOTHERMIC CHEMICAL REACTION: A LEVENBERG-MARQUARDT NEURAL NETWORK APPROACH

R. Krishnakumari[1#], V. Sugunamma[2##], M. Jayachandra Babu[3*], J. Girish Kumar[4]**
[1]Department of Mathematics, Sri Venkateswara University, Tirupati, Andhra Pradesh, India – 517502
[2]Department of Mathematics, Sri Venkateswara University, Tirupati, Andhra Pradesh, India – 517502
[3]Department of Mathematics, Government Degree College, Rajampeta, Andhra Pradesh, India – 516115
[4]Department of Mathematics, Government Degree College, Nagari, Andhra Pradesh, India – 517590
email: [#]krishnarun.krishna81@gmail.com; [##]vsugunar@gmail.com; [**]drjgireeshkumar@gmail.com
**Corresponding Author email: jayamacharla@gmail.com*
Received April 3, 2026; revised June 29, 2026; accepted July 3, 2026

This study examines the heat and mass transmission properties of a Jeffrey nanofluid traveling across a moving slender needle. The main aim is to examine how essential parameters, such as Hall current, couple stress, activation energy, and thermophoresis, affect the fluid's velocity, temperature, concentration, and corresponding entropy generation. The flow configuration of a slender needle is critically pertinent to practical applications, including the thermal design of microneedles for regulated medication delivery, the aerodynamic profiling of slender structural elements in aerospace engineering, and the optimization of delicate sensor probes. With the aid of suitable similarity transformations, the equations which were meant to describe the problem, were transmuted as a framework with nonlinear ordinary equations, and then solved using the bvp4c solver. A notable discovery is that fluid velocity is hindered by augmented magnetic field strength and coupling stresses, while the temperature profile is improved by elevated viscous dissipation and thermophoresis effects. Moreover, the heat transfer rate at the surface decreases as the thermophoresis parameter increases, whereas the mass transfer rate diminishes with higher activation energy. The study indicates that entropy formation, representing energy loss, increases with heightened viscous dissipation and thermal radiation. It is found that the Sherwood number declines by 24.1% when activation energy rises from 0 to 0.8. It is found that the Nusselt number declines by 26.3% when thermophoresis parameter rises from 0 to 2. It is discovered that the friction factor raises by 2.32% when magnetic field parameter escalates from 0 to 2.
Keywords: *Thermophoresis; bvp4c; Brownian motion; Couple stress; Activation energy*

Nomenclature

σ	Electrical conductivity	η	Similarity variable
u, v	Velocity components in x, y directions respectively	D_T	Thermophoresis diffusion coefficient
Pr	Prandtl number	σ^*	Stefan-Boltzmann constant
λ_0	Relaxation time parameter of the fluid	Br	Brinkman number
λ_1	Retardation parameter of the fluid	α_1	Concentration difference parameter
De	Deborah number	Ra	Thermal radiation parameter
ρ	Density	k^*	Mean absorption coefficient
α	Temperature difference parameter	g	Gravitational acceleration
Le	Lewis number	n	Fitting rate constant
C_P	Specific heat	R_0	Universal gas constant
Mg	Magnetic field Parameter	λ^*	Buoyancy parameter
γ	Exothermic/endothermic coefficient	Cs	Couple stress parameter
β_C, β_T	Concentration and thermal expansion Coefficients	D_B	Brownian motion coefficient
Nt	Thermophoresis parameter	Nb	Brownian motion parameter
k_0, Γ	Reaction rate parameters	k_1	Boltzmann constant
m	Hall current parameter	d	Needle size parameter
		E_0, A	Activation energy parameters

1 INTRODUCTION

The Buongiorno model is significant for its innovative integration of two primary nanoparticle transport mechanisms—Brownian motion and thermophoresis—within a unified continuum framework, thereby fundamentally enhancing the analysis of nanofluid heat transfer beyond the capabilities of conventional single-phase models. The significance is highlighted by its extensive use as a standard for forecasting the improved thermal properties of nanofluids, offering essential insights into the influence of nanoparticle distribution on flow dynamics and temperature distributions. This has resulted in crucial applications in the design and optimization of high-performance thermal management systems, such as microchannel coolers for electronics, solar thermal collectors, nuclear reactor safety, and advanced heat exchangers, where precise modelling of the interaction between nanoparticle migration and convective heat transfer is imperative for enhancing energy efficiency. Bhatti et al. [1] studied the entropy formation in the Eyring–Powell nanofluid

Cite as: R. Krishnakumari, V. Sugunamma, M.J. Babu, J.G. Kumar, East Eur. J. Phys. 3, 443 (2026), https://doi.org/10.26565/2312-4334-2026-3-40

traversing a porous stretching surface by using the Successive Linearization Method. The research indicated that temperature and nanoparticle concentration profiles rise with an elevated thermophoresis parameter. Amanulla et al. [2] performed an inquiry of nanofluid movement via an upward surface, integrating velocity and thermal slip effects with the Keller-Box method. The research indicated that increased velocity slip augments momentum at proximity to the surface. Goodarzi et al. [3] inspected the flow and thermal transfer characteristics of a non-Newtonian nanofluid within a microtube. The research indicated that augmenting the nanoparticle volume percentage improves heat transport within the microtube. Subba Rao et al. [4] investigated the convective flow of Casson nanofluid across an isothermal sphere under convective boundary conditions. The research indicated that a rise in the Casson parameter slows down the flow. Ahmadian et al. [5] scrutinized the movement of a Maxwell nanofluid amongst two horizontally revolving disks subjected to an axial magnetic field with the bvp4c approach. The research indicated that elevated Deborah number values diminish radial velocity while improving the temperature profile. Usman et al. [6] examined the dynamics of a bioconvective and radiative Cross nanofluid between two stretchable spinning disks employing the homotopy analysis technique. The study demonstrated that fluid velocity escalates with elevated disk stretching rate and buoyancy parameters. Elgazery [7] inspected the movement of a Powell–Eyring micropolar nanofluid over an elastic permeable framework with non-constant thermophysical parameters. The results showed that the angular velocity goes up when the variable microrotation viscosity parameter changes. This shows how important it is to characterize these kinds of features as functions instead of constants. Yousef et al. [8] studied the movement of a Casson–Williamson nanofluid via a permeable stretched sheet. It is discovered that the temperature profile is enhanced by higher values of the Casson parameter. A second-grade nanofluid's movement through an exponentially stretched framework with a variable thermal conductivity parameter was studied by Anwar et al. [9]. The velocity profile was found to be more raised with higher values of the material parameter. Furthermore, several researchers [10-16] inspected various non-Newtonian fluid movements across different frameworks.

The interaction between exothermic reaction and fluid movement is an important phenomenon that has far-reaching effects on many fields of engineering. The heat that comes out of the reaction changes the fluid's properties, like its temperature, density, and viscosity. This can then modify the flow behaviour in a big way, causing buoyancy-driven convection, speeding up flow rates, or even causing instabilities. This coupling is very important in real life because it determines how safe and efficient chemical reactors are, how stable flames are and how heat is spread in combustion systems like engines and turbines, and how to control the thermal field in materials processing, such as welding and crystal growth, to make sure the products are of high quality. To get the best performance and make sure that a wide range of thermal and chemical systems work safely, it is important to understand this synergy. Kareem et al. [17] examined the transient behaviour and entropy generation of the Rivlin-Ericksen fluid undergoing a two-step exothermic reaction with temperature-dependent viscosity. The study demonstrated that entropy generation decreased under scenarios characterized by low viscous dissipation and diminished fluid viscosity. Raees et al. [18] formed a mathematical model to study the movement of nanofluid in a microchannel with an exothermic chemical reaction parameter, based on Buongiorno's model. The findings demonstrated that the Frank-Kamenetskii parameter substantially improves heat transmission. Ahmad et al. [20] studied the mixed convective movement of an incompressible fluid through a curved surface with an exothermic catalytic chemical reaction parameter by the finite difference approach. It is found that the surge in the exothermic parameter results in an elevation of the temperature profile. Ogunsola et al. [21] conducted an irreversibility analysis for third-grade fluid movement characterized by an Arrhenius exothermic reaction and non-constant viscosity parameters. The study demonstrated that augmenting the Frank-Kamenetskii parameter amplifies entropy formation. Zainal et al. [22] scrutinized the movement of an aqueous hybrid nanofluid across a moving wedge utilizing the bvp4c solver. It is shown that augmenting the nanoparticle volume fraction improves the friction factor. Furthermore, several researchers [23-28] inspected the impact of exothermic chemical reaction on various fluid movements across different frameworks.

The fluid dynamics around a moving thin needle is a basic problem in boundary layer theory that is very useful in real life. This setup is especially useful since it makes it possible to find a similarity solution, even when the needle's thickness is about the same as the boundary layer that forms. This feature makes it a great example for checking the accuracy of numerical codes and experimental data. It has a lot of uses, from improving the aerodynamic performance of thin structural parts and hypersonic vehicle nose cones to making medical devices like microneedles and surgical tools better, where precise control of fluid drags and heat transmission is very important. Waini et al. [29] scrutinized the movement of a hybrid nanofluid past a moving thin needle. The study indicated that dual solutions arise within particular intervals of the moving parameter. Kumar et al. [30] inspected the movement of a Casson fluid past a moving slender needle with cross-diffusion effects. The study showed that there is a decline in the Nusselt number with the rise in the Dufour number. Ramesh et al. [31] examined the movement of a bioconvective hybrid nanofluid via a moving slender needle, utilizing a modified Buongiorno's model. Abbas et al. [32] conducted a theoretical analysis of the movement of a hybrid nanofluid past a moving slender needle employing the Galerkin method. The study demonstrated that increased needle thickness reduces the heat transmission rate. Later, Srinivasa Reddy [33] discussed the fluid movement through the moving slender needle.

Although the current literature offers considerable understanding of nanofluid flows across diverse geometries, a notable research gap persists in the thorough examination of a Jeffrey nanofluid traversing a moving thin needle, which concurrently integrates the combined influences of Hall current, couple stresses, and an Arrhenius activation energy-driven exothermic reaction. This study is significant as it addresses the existing gap by creating a comprehensive model

that encapsulates the intricate interactions of electromagnetic, microstructural, and chemical kinetic phenomena, which are crucial for the precise design of advanced micro-devices and high-precision engineering systems. Additionally, to enhance the dependability of our numerical computations derived from the bvp4c solver, an Artificial Neural Network (ANN) model is utilized to corroborate essential results. This machine learning methodology offers independent validation of our results and illustrates the powerful synergy between numerical analysis and data-driven modelling in contemporary computational fluid dynamics, thereby augmenting the credibility and robustness of the research presented.

2. MATHEMATICAL FORMULATION

In this study, the steady movement of a Jeffrey nanofluid over a moving thin needle is considered.

(i) The fluid is characterized as a non-Newtonian Jeffrey fluid. This model integrates relaxation time effects, rendering it appropriate for viscoelastic fluids.
(ii) A vertical external magnetic field with strength B is applied. The model incorporates the influence of Hall current (parameter m), which alters the Lorentz force exerted on the fluid (refer to Fig. 1).
(iii) The microstructure of the fluid is taken into account by adding couple stress effects to the momentum equation. This takes into account how particles interact in microfluids and adds a higher-order derivative term.
(iv) The model integrates Brownian motion and thermophoresis, which are essential for the behaviour of nanofluids.
(v) It is assumed that the needle moves with a constant velocity U_w in the same or opposite direction to the mainstream of constant velocity U_∞.
(vi) The chemical reaction is assumed to be exothermic, meaning that it releases heat ($\gamma > 0$). This assumption is crucial for analyzing the thermal effects of the reaction on the fluid flow.
(vii) This formulation is based on the idea that the needle is very thin. This thin needle approach assumes that the needle's diameter is very small relative to the thickness of the boundary layer that is forming. As a result, the flow field and the heat and mass transfer processes that go along with it are thought to be unaffected by the needle's limited radius or blunt tip. This means that the specified similarity transformations and boundary conditions can be used.

Based on the assumptions made before, this investigation requires the following conditions and equations (Ishak et al. [34], Ashraf et al. [35], and Karthik et al. [36]):

$$\frac{\partial}{\partial r}(vr)+\frac{\partial}{\partial x}(ur)=0 \tag{1}$$

$$\begin{aligned}&\frac{\partial u}{\partial x}u+\frac{\partial u}{\partial r}v=\frac{\upsilon}{1+\lambda_0}\left[\frac{\partial^2 u}{\partial r^2}+\frac{1}{r}\frac{\partial u}{\partial r}+\lambda_1\left(\frac{\partial u}{\partial r}\frac{\partial^2 u}{\partial x\partial r}+u\frac{\partial^3 u}{\partial x\partial r^2}+\frac{\partial v}{\partial r}\frac{\partial^2 u}{\partial r^2}+\frac{u}{r}\frac{\partial^2 u}{\partial x\partial r}+v\frac{\partial^3 u}{\partial r^3}+\frac{v}{r}\frac{\partial^2 u}{\partial r^2}\right)\right]\\&-\left(\sigma uB^2\right)\frac{1}{\rho\left(1+m^2\right)}-\frac{1}{\rho}\left(\frac{\partial^4 u}{\partial r^4}+\frac{2}{r}\frac{\partial^3 u}{\partial r^3}-\frac{1}{r^2}\frac{\partial^2 u}{\partial r^2}+\frac{1}{r^3}\frac{\partial u}{\partial r}\right)\gamma_0+\beta_C\left(C_w-C_\infty\right)g+\beta_T\left(T_w-T_\infty\right)g\end{aligned} \tag{2}$$

$$\begin{aligned}&v\frac{\partial T}{\partial r}+u\frac{\partial T}{\partial x}=\left(\left(k+\frac{16}{3}\frac{\sigma * T_\infty^3}{k*}\right)\left(\frac{\partial^2 T}{\partial r^2}+\frac{1}{r}\frac{\partial T}{\partial r}\right)\right)\frac{1}{(\rho C_p)}+\frac{1}{(\rho C_p)}\frac{\sigma B^2}{1+m^2}u^2\\&+\frac{\gamma\rho k_0}{\rho C_p}\exp\left(-\frac{E_0}{k_B T}\right)\left(\frac{T}{T_\infty}\right)^n(C-C_\infty)+\tau\left(D_B\frac{\partial T}{\partial r}\frac{\partial C}{\partial r}+\frac{D_T}{T_\infty}\left(\frac{\partial T}{\partial r}\right)^2\right)+\frac{\mu}{(\rho C_p)}\left(\frac{\partial u}{\partial r}\right)^2.\end{aligned} \tag{3}$$

$$v\frac{\partial C}{\partial r}+u\frac{\partial C}{\partial x}=D_B\left(\frac{\partial^2 C}{\partial r^2}+\frac{1}{r}\frac{\partial C}{\partial r}\right)+\frac{D_T}{T_\infty}\left(\frac{\partial^2 T}{\partial r^2}+\frac{1}{r}\frac{\partial T}{\partial r}\right)-k_0\exp\left(-\frac{E_0}{k_B T}\right)\left(\frac{T}{T_\infty}\right)^n(C-C_\infty) \tag{4}$$

$$\left.\begin{aligned}&\text{at } r=R(x): u=U_w, C=C_w, \frac{\partial^2 u}{\partial r^2}=0, v=0, T=T_w,\\&\text{as } r\to\infty: T\to T_\infty, \frac{\partial u}{\partial r}\to 0, C\to C_\infty, u\to U_\infty.\end{aligned}\right\} \tag{5}$$

Here $r=R(x)$ is the surface shape of the needle.

For the purpose of converting governing equations, Ishak et al. [34] introduced the following similarity transformations:

$$\left.\eta=\frac{Ur^2}{\upsilon x}, v=-\frac{\upsilon}{r}(f-\eta f'), \phi(\eta)=\frac{C-C_\infty}{C_w-C_\infty}, u=2Uf', \theta(\eta)=\frac{T-T_\infty}{T_w-T_\infty}.\right\} \tag{6}$$

Note that U is the composite velocity which is equal to U_w+U_∞.

By substituting $\eta=d$ in $\eta=\frac{Ur^2}{\upsilon x}$, we can get $R(x)=\sqrt{\frac{\upsilon dx}{U}}$.

The terms shown in (6) easily satisfy the equation (1). The following outcome results from the effective modification of equations (2-4) and conditions in (5) by the use of integration of (6):

$$\frac{1}{1+\lambda_0}\left(2\eta f''' + f'' - De\left(2\eta f''^2 + 6\eta f' f''' + 4f' f'' + 4\eta f f'''' + 6 f f'''\right)\right)$$
$$-\frac{Mg}{1+m^2} f' - 32\eta^2 Csf''''' - Cs(104\eta f'''' + 34 f''') + \frac{\lambda_0}{4}(\theta + \lambda^* \phi) + f f'' = 0 \tag{7}$$

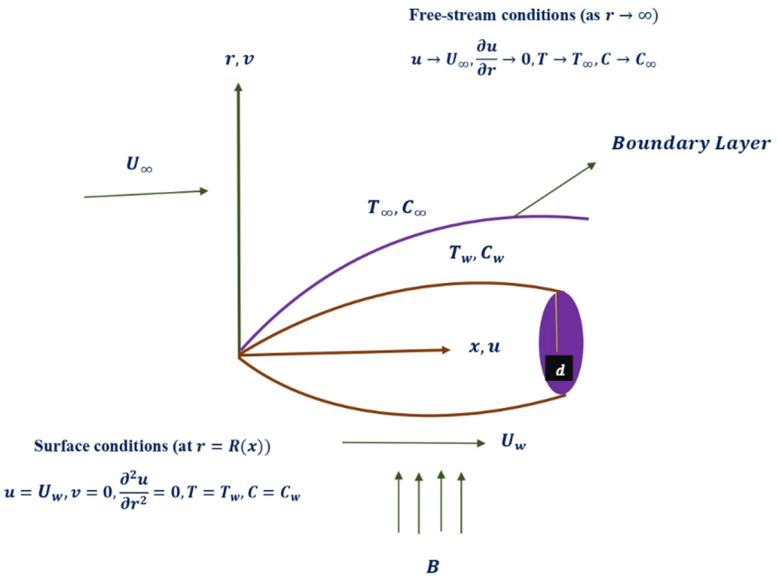

Figure 1. Visual representation of the present investigation

$$\frac{1+Ra}{\Pr}(\theta' + \eta\theta'') + \frac{2}{1+m^2} MgEckf'^2 + \frac{f\theta'}{2} + (Nb\theta'\phi' + Nt\theta'^2)\eta + \frac{\chi\Gamma}{4}(1+\alpha\theta)^n \exp\left(-\frac{A}{1+\alpha\theta}\right)\phi + 4\eta Eckf''^2 = 0 \tag{8}$$

$$\frac{2}{Le}(\phi' + \eta\phi'') + \frac{2}{Le}\frac{Nt}{Nb}(\theta' + \eta\theta'') + f\phi' - \frac{\Gamma}{2}(1+\alpha\theta)^n \exp\left(-\frac{A}{1+\alpha\theta}\right)\phi = 0 \tag{9}$$

$$\left.\begin{aligned} &\text{at } \eta = d : f(\eta) = \frac{1}{2} d\lambda, \phi(\eta) = 1, f'(\eta) = \frac{1}{2}\lambda, \theta(\eta) = 1, f'''(\eta) = 0, \\ &\text{as } \eta \to \infty : f'(\eta) \to \frac{1}{2}(1-\lambda), \theta(\eta) \to 0, f''(\eta) \to 0, \phi(\eta) \to 0. \end{aligned}\right\} \tag{10}$$

Note that we assumed that $0 < \lambda < 1$ i.e., the needle and the fluid move in the same direction (positive $x-$ direction).

$$\left.\begin{aligned} Mg = \frac{\sigma_f B_0^2}{\rho U}, B = \frac{B_0}{\sqrt{x}}, De = U\lambda_2, \lambda_2 = \frac{\lambda_1}{x}, Cs = \frac{\gamma_1 U}{\rho \upsilon^2}, \gamma_1 = \frac{\gamma_0}{x}, Le = \frac{\upsilon}{D_B}, \\ Ra = \frac{16}{3}\frac{\sigma * T_\infty^3}{kk*}, \lambda^* = \frac{Gc}{Gr}, \lambda_0 = \frac{Gr}{\mathrm{Re}_x^2}, Gr = \frac{g\beta_T (T_w - T_\infty)}{\upsilon^2}, \mathrm{Re}_x = \frac{Ux}{\upsilon}, \\ \Pr = \frac{\mu C_p}{k}, \chi = \frac{\gamma (C_w - C_\infty)}{C_p (T_w - T_\infty)}, \Gamma = \frac{k_2}{U}, k_2 = \frac{k_0}{\sqrt{x}}, A = \frac{E_0}{k_B T_\infty}, \lambda = \frac{U_w}{U}, \\ \alpha = \frac{T_w - T_\infty}{T_\infty}, Nb = \frac{\tau D_B (C_w - C_\infty)}{\upsilon}, Eck = \frac{U^2}{C_p (T_w - T_\infty)}, Nt = \frac{\tau D_T (T_w - T_\infty)}{\upsilon T_\infty}. \end{aligned}\right\}$$

The friction factor can be stated via the ensuing equation:

$$Cf = \frac{1}{\rho}\left(\frac{\partial u}{\partial r}\right)\frac{\mu}{U^2}\bigg|_{r=R(x)} \tag{11}$$

By applying (6), term in (11) can be rewritten as:

$$\sqrt{\mathrm{Re}_x}\, Cf = 4\sqrt{\eta} f''(\eta)\big|_{\eta=d}.$$

The following formulas can be used to determine the heat and mass transfer rates:

$$Nu = \frac{-xq_w}{k_f\left(T_w - T_\infty\right)}\bigg|_{r=R(x)}, q_w = \left(k + \frac{4}{3}\frac{4\sigma^* T_\infty^3}{k^*}\right)\frac{\partial T}{\partial r},$$
$$Sh = \frac{-x}{\left(C_w - C_\infty\right)}\frac{s_w}{D_m}\bigg|_{r=R(x)}, s_w = D_m\frac{\partial C}{\partial r}. \tag{12}$$

By applying (6), the formulas in (12) are rewritten as:

$$\left(\mathrm{Re}_x\right)^{-1/2} Nu = -2\sqrt{\eta}\left(1+Ra\right)\theta'(\eta)\big|_{\eta=d},$$
$$\left(\mathrm{Re}_x\right)^{-1/2} Sh = -2\sqrt{\eta}\phi'(\eta)\big|_{\eta=d}.$$

2.1. Entropy generation

The formula that describes the dimensional computation of entropy production is mentioned as:

$$S_g = \left(1+16\frac{\sigma^* T_\infty^3}{3k_f k^*}\right)\left(\frac{k_f}{T_\infty^2}\right)\left(\frac{\partial T}{\partial r}\right)^2 + \mu\frac{1}{T_\infty}\left(\frac{\partial u}{\partial r}\right)^2 + \sigma\frac{1}{T_\infty}u^2B^2 + \frac{1}{C_\infty}\left(\frac{\partial C}{\partial r}\right)^2 R_0 D_m + \frac{1}{T_\infty}\frac{\partial C}{\partial r}\frac{\partial T}{\partial r}R_0 D_m \tag{13}$$

By adopting (6), we may rewrite equation (13) as follows:

$$N_{EG} = \left(1+Ra\right)\alpha\eta\theta'^2 + 4Br\eta f''^2 + 2Brf'^2 Mg + H\frac{\alpha_1}{\alpha}\phi'^2 + H\theta'\phi',$$

where

$$\alpha_1 = \frac{C_w - C_\infty}{C_\infty},\ Br = \frac{\mu_f U^2}{\left(T_w - T_\infty\right)k_f},\ N_{EG} = \frac{\upsilon T_\infty x S_g}{4U\left(T_w - T_\infty\right)k_f},\ H = \frac{R_0\left(C_w - C_\infty\right)D_m}{k_f}.$$

3. NUMERICAL PROCEDURE

The equations (7) to (9), together with the conditions specified in (10), are solved using the bvp4c solver. Prior beginning coding, it is essential to contemplate the subsequent assumptions.

$$f = \psi_1, f' = \psi_2, f'' = \psi_3, f''' = \psi_4, f^{iv} = \psi_5, \theta = \psi_6, \theta' = \psi_7, \phi = \psi_8, \phi' = \psi_9.$$

This system of first-order ordinary differential equations is generated from equations (7) to (9) and the conditions outlined in (10).

$\psi_1' = \psi_2,$

$\psi_2' = \psi_3,$

$\psi_3' = \psi_4,$

$\psi_4' = \psi_5,$

$$\psi_5' = \frac{1}{32}\frac{1}{\eta^2}\frac{1}{Cs}\left[\begin{array}{c}\frac{1}{1+\lambda_0}\left(2\eta\psi_4 + 2\psi_3 - De(2\eta\psi_3^{\ 2} + 6\eta\psi_2\psi_4 + 4\psi_2\psi_3 + 4\eta\psi_1\psi_5 + 6\psi_1\psi_4)\right) \\ -\frac{Mg}{1+m^2}\psi_2 - Cs(104\eta\psi_5 + 34\psi_4) + \frac{\lambda}{4}(\psi_6 + \lambda^*\psi_8) + \psi_1\psi_3\end{array}\right],$$

$\psi_6' = \psi_7,$

$$\psi_7' = \frac{-\mathrm{Pr}}{\eta(1+Ra)}\left[\begin{array}{c}\frac{1+Ra}{\mathrm{Pr}}\psi_7 + \frac{2}{1+m^2}MgEck\psi_2^{\ 2} + \frac{\psi_1\psi_7}{2} + (Nb\psi_7\psi_9 + Nt\psi_7^{\ 2})\eta \\ +\frac{\chi\Gamma}{4}(1+\alpha\psi_6)^n\exp\left(-\frac{A}{1+\alpha\psi_6}\right)\psi_8\end{array}\right],$$

$\psi_8' = \psi_9,$

$$\psi_9' = \frac{-Le}{2\eta}\left[\frac{2}{Le}\frac{Nt}{Nb}(\psi_7 + \eta\psi_7') + \psi_1\psi_9 - \frac{\Gamma}{2}(1+\alpha\psi_6)^n\exp\left(-\frac{A}{1+\alpha\psi_6}\right)\psi_8 + \frac{2}{Le}\psi_9\right]. \tag{15}$$

with the constraints

$$\left.\begin{aligned}\psi a(1)=\frac{1}{2}d\lambda,\psi a(4)=0,\psi a(6)=1,\psi a(8)=1,\psi a(2)=\frac{1}{2}\lambda,\\ \psi b(2)=\frac{1}{2}(1-\lambda),\psi b(3)=0,\psi b(6)=0,\psi b(8)=0.\end{aligned}\right\} \tag{16}$$

The graphical results can be generated by executing the code once the system has been constructed in MATLAB.

4. ANALYSIS OF THE RESULTS

Analysis of Fig. 2 reveals that an elevation in De correlates with a decrease in the velocity of the fluid. An elevated De value indicates that the fluid demonstrates more significant elastic solid-like characteristics over an extended period, as opposed to solely viscous liquid-like behavior. As elasticity gets more pronounced, the fluid's internal resistance to deformation escalates, hindering its motion and leading to a diminished overall velocity profile. This conclusion indicates that increased fluid elasticity creates a more robust resistance mechanism in the flow, hence inhibiting momentum diffusion and diminishing the kinetic energy available for fluid motion. According to the data presented in Fig. 3, an elevation in Cs is associated with a reduction in the fluid's velocity. The couple stress parameter reflects the impact of internal rotational resistance and micro-rotational effects in the fluid, resulting from the suspension of micro-elements such as polymers or colloidal particles. An increased value of this characteristic indicates enhanced resistance to fluid movement and deformation caused by these microstructures. This indicates that the fluid becomes significantly more viscous or organized, hindering its capacity to flow freely. As a result, the velocity profile is diminished due to increased energy dissipation required to counteract internal coupling tensions, resulting in an overall slowdown of the flow.

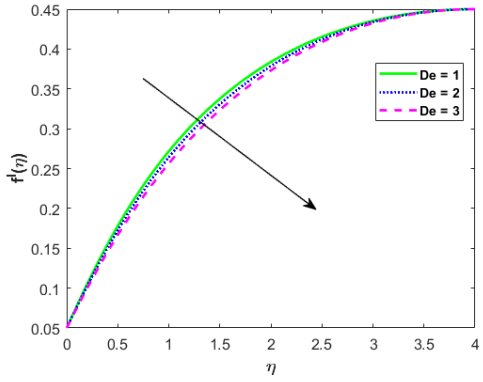

Figure 2. De's impact on fluid's velocity

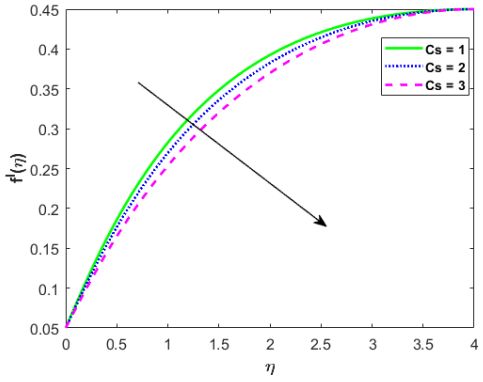

Figure 3. Cs's impact on fluid's velocity

Fig. 4 explains that the fluid temperature upsurges with increased Eckert number values. An increased Eckert number indicates that a substantial fraction of the fluid's kinetic energy is transformed into internal thermal energy due to work performed against viscous forces. This study suggests that in high-velocity flows or very viscous fluids, frictional heating becomes a predominant factor, resulting in a significant temperature increase without requiring an external heat source. Fig. 5 establishes that the temperature of the fluid rises with higher thermophoresis parameter values.

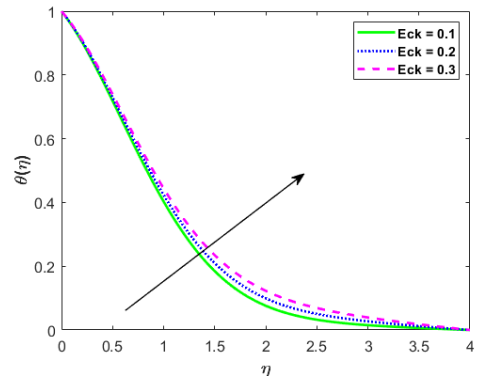

Figure 4. Eck's impact on fluid's temperature

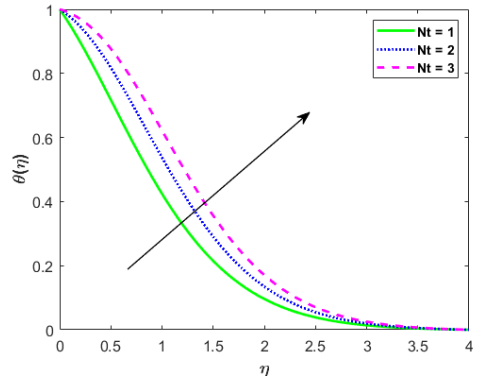

Figure 5. Nt's impact on fluid's temperature

Thermophoresis is a phenomenon in which microscopic particles, such as those in a colloidal suspension or nanofluid, are subjected to a force that propels them from a hotter region to a colder one. An elevation in the thermophoresis parameter amplifies the movement of particles away from the heated surface. As a result, an increased quantity of particles congregates in the colder areas of the fluid, hence augmenting energy transfer and thermal conduction in that area. This result indicates that thermophoresis serves as a crucial mechanism for energy redistribution, effectively

raising the overall fluid temperature by concentrating heat-carrying particles within the bulk fluid, thus impacting the system's thermal management and efficiency. Fig. 6 demonstrates that an elevation in the Brownian motion parameter correlates with a reduction in nanoparticle concentration within the fluid. This occurs physically due to the amplification of Brownian motion, which exacerbates the erratic, chaotic movement of nanoparticles. This intensified microscopic motion breaks the homogeneous distribution of particles, facilitating their dispersion and preventing their settling or accumulation. As a result, the total concentration of nanoparticles in the primary fluid domain diminishes due to their enhanced scattering. This outcome underscores the pivotal function of Brownian diffusion as a counteracting force to concentration accumulation, accentuating its significance in regulating particle distribution in fields such as nano-fluidics and thermal systems. Fig. 7 illustrates that an elevation in the activation energy parameter leads to an increased fluid concentration. A higher activation energy signifies a more substantial energy barrier that reactant molecules must surmount to engage in the chemical reaction. As a result, the reaction rate is diminished, resulting in decreased consumption of reactant species. As fewer molecules undergo transformation, the concentration of the fluid rises due to the accumulation of reactants. This finding indicates that activation energy functions as a kinetic inhibitor; in practical systems such as industrial reactors or biological processes, elevated activation energy retards chemical conversion, thereby enabling a greater concentration of the initial substances to remain in the fluid medium.

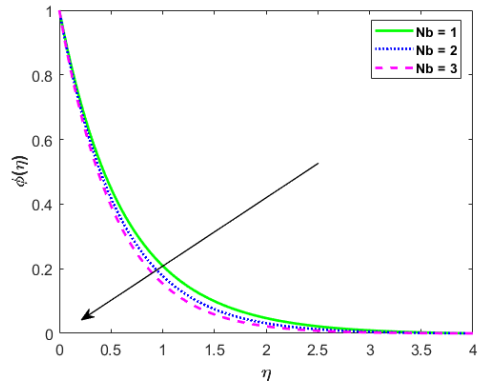

Figure 6. Nb's impact on fluid's concentration

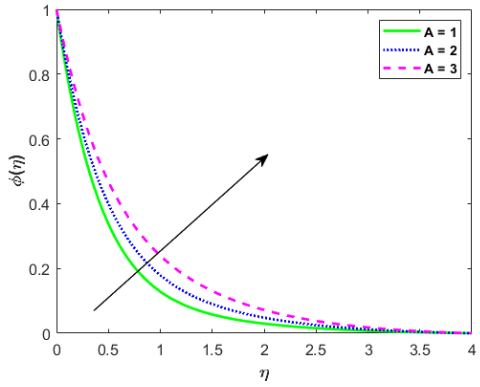

Figure 7. A's impact on fluid's concentration

Table 1 demonstrates that a spike in Cs elevates the skin friction coefficient. This is because as elevated pair stresses amplify the internal resistance to fluid microrotation, thereby raising the shear stress at the surface. This indicates a more robust contact between the fluid's microstructure and the boundary, leading to increased frictional drag. The observed rise in skin friction coefficient with a greater magnetic field, seen in Table 1, is a direct result of the magnetic influence on fluid flow. Physically, this occurs because the applied magnetic field causes a resistive force that opposes the direction of fluid motion. This force impedes the flow, making the fluid more resistant to shearing at the surface. As a result, friction factor increases. It is discovered that the friction factor raises by 2.32% when Mg escalates from 0 to 2.

Table 1. Influence of Mg and Cs on Cf

Mg	Cs	Skin friction coefficient
0		0.340707
0.5		0.352124
1		0.363684
1.5		0.37539
2		0.387244
	0.1	0.778157
	0.6	0.897543
	1.1	0.91059
	1.6	0.915594
	2.1	0.91824

Table 2 demonstrates that an elevation in the Eckert number correlates with a reduction in the Nusselt number. An elevated Eck indicates that the energy lost due to fluid friction becomes increasingly prominent relative to the heat transmitted via conduction. Physically, this indicates that as viscous forces increase, they produce internal heat within the fluid flow. This self-generated heat functions as an internal source, elevating the temperature of the fluid and diminishing the temperature gradient between the surface and the bulk fluid. Consequently, the Nusselt number diminishes. Table 2 demonstrates that an increase in the thermophoresis parameter leads to a reduction in the Nusselt number. A more potent thermophoretic force propels a greater number of nanoparticles away from the heated surface and into the core fluid region. As a result, a diminished concentration of particles develops along the boundary, serving as an insulating layer and diminishing the temperature difference at the wall. The physical implication is that the heat transfer rate from the surface is reduced, as the thermophoresis process generates thermal resistance by displacing suspended particles that would otherwise facilitate energy flow. It is found that the Nusselt number declines by 26.3% when Nt rises from 0 to 2.

Table 2 Influence of Eck and Nt on Nu

Eck	Nt	Nusselt number
0		0.89449
0.1		0.87495
0.2		0.855375
0.3		0.835792
0.4		0.816202
	0	1.052693
	0.5	0.892532
	1	0.752287
	1.5	0.630638
	2	0.526129

According to the trend shown in Table 3, a rise in the activation energy parameter is linked to a drop in the Sherwood number. This happens because a larger activation energy means that reactant molecules have to overcome a bigger energy barrier for the chemical reaction to happen. As a result, the reaction rate slows down, which means that the reactants at the surface are used up more slowly. The slower chemical kinetics cause the lower mass transfer rate, which is immediately reflected in the lower Sherwood number. This means that mass transfer happens less quickly when the chemical process that controls it is more sensitive to heat and needs a lot more energy to start. Table 3 shows that there is an inverse relationship between the Brownian motion parameter and the Sherwood number. This means that when nanoparticles move about more randomly, it can slow down the total mass transfer rate. The physical explanation for this phenomenon is that vigorous Brownian diffusion results in nanoparticles dispersing more randomly throughout the fluid bulk, instead of being moved in a synchronized fashion towards the surface. This chaotic motion disturbs the directed concentration gradient that is necessary for effective convective mass transfer. This causes the Sherwood number, which measures this mass transfer efficiency, to go down. It is found that the Sherwood number declines by 24.1% when A rises from 0 to 0.8.

Table 3 Influence of A and Nb on Sh

A	Nb	Sherwood number
0		1.836886
0.2		1.776357
0.4		1.723082
0.6		1.676444
0.8		1.635843
	0.1	2.117563
	0.6	1.587075
	1.1	1.528717
	1.6	1.501083
	2.1	1.482726

Fig. 8 displays that as the Brinkman number goes up, the rate of entropy formation in the fluid flow goes up as well. This happens because the Brinkman number is the ratio of the heat generated by viscous dissipation to the heat moved by molecular conduction. A higher Brinkman number means that the heat transmission through conduction is less important than the heat transfer through friction. This increased viscous dissipation results in heightened thermal irreversibilities, which serve as a direct source of entropy. The physical implication is that in flows with high viscous effects, such as those involving very viscous fluids or high speeds, the energy losses due to friction are more significant, leading to a more irreversible and thermodynamically less efficient system. Fig. 9 illustrates that as the thermal radiation parameter goes up, the rate of entropy creation in the fluid flow also goes up.

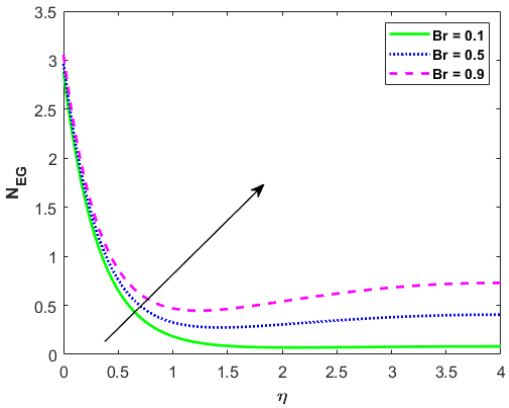

Figure 8. Br's impact on N_{EG}

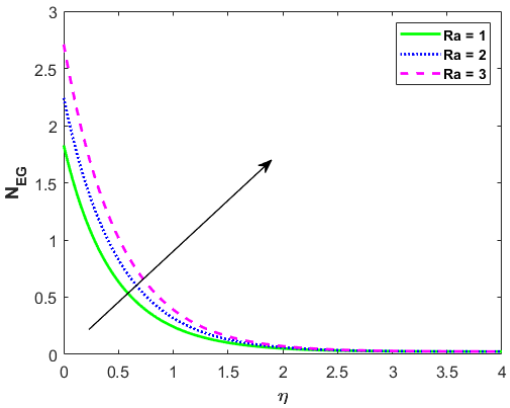

Figure 9. Ra's impact on N_{EG}

This happens because more thermal radiation makes the energy transfer and the thermal gradients in the system stronger. This result means that the system is less efficient from a thermodynamic point of view. The higher entropy generation means that more useful energy is lost, which means that more energy is wasted as heat instead of being used for productive activity. This lowers the system's overall performance.

4.1. Validation of the results using Levenberg-Marquardt algorithm

To independently validate our numerical results, an Artificial Neural Network (ANN) model was developed using the Levenberg-Marquardt (LM) backpropagation algorithm. The network architecture consisted of a three-layer feedforward structure: an input layer, a single hidden layer, and an output layer. The input layer received the parameter values (magnetic field parameter Mg for friction factor predictions; thermophoresis parameter Nt for Nusselt number predictions; and reaction rate parameter A for Sherwood number predictions). The hidden layer comprised 10 neurons with the hyperbolic tangent sigmoid (tansig) activation function, which was selected for its ability to model nonlinear relationships effectively. The output layer employed a linear (purelin) activation function to produce the continuous target predictions. The network was trained using the Levenberg-Marquardt algorithm, which combines the advantages of the Gauss-Newton method and gradient descent, ensuring rapid convergence and enhanced stability. The dataset was randomly partitioned into three subsets: 70% for training, 15% for validation, and 15% for testing. Training was terminated when the validation error ceased to decrease for six consecutive epochs (early stopping) to prevent overfitting. The performance of the trained network was evaluated using the Mean Squared Error (MSE) and the coefficient of determination (R^2). The consistently low MSE values (ranging from 10^{-9} to 10^{-12}) and the excellent agreement between predicted and target values in the function fit plots (see Figs. 11, 13, 15) confirm the robustness and accuracy of the ANN model in capturing the underlying physical trends.

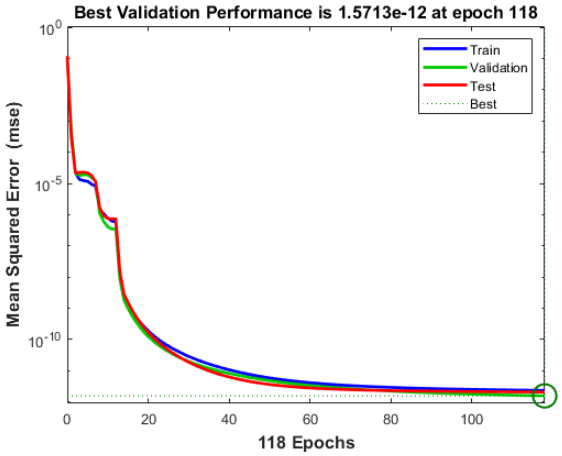

Figure 10. Mean square error plot for the outcomes related to the values of friction factor when magnetic field parameter is applied

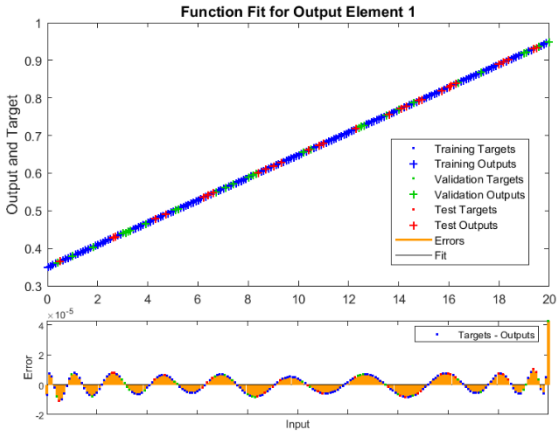

Figure 11. Function fit plot for the outcomes related to the values of friction factor when magnetic field parameter is applied

As the number of epochs becomes up, Fig. 10 shows that the mean squared error (MSE) drops quickly across training, validation, and test datasets. At first, the MSE is rather high, but it declines quickly in the first 20 epochs, which shows that learning is going quickly. As training goes on, the errors for all datasets get very close together, and by epoch 118, the best validation performance is about 1.5713×10^{-12}, which is very close to zero MSE. In Fig. 11, almost all of the outputs from training, validation, and testing are very close to their targets, following the ideal diagonal. The lower subplot backs this up by showing that the error values, which are the differences between the actual and anticipated outputs, are always close to zero across the entire input range, with no bias or systematic mistake. As the number of epochs increases, the error values for the training, validation, and test sets get closer together. This is shown in the Fig. 12, which demonstrates a steady drop MSE during neural network training. At first, the MSE lowers quickly, and then it drops more slowly over the course of 696 epochs. The model learns and generalizes the underlying pattern in the data well, as shown by the best validation accuracy at epoch 696, which has a MSE of about 1.7817×10^{-9}, which is very low. Fig. 13 displays that the neural network model's predicted values are quite near to the actual targets in the training, validation, and test datasets. All of the output points line up quite closely with the reference curve, showing that the model's predictions and the true values match very well. The error distribution in the lower subplot stays very modest across the whole input range, suggesting no consistent biases and confirming that the model well captures the underlying functional connection. Fig. 14 shows how well the neural network did over 922 training epochs. The MSE quickly went down for the training, validation, and test datasets. After a sharp drop at first, the three curves keep going down consistently until they all meet at a very low MSE. The best validation result, which was about 5.9451×10^{-11} at epoch 922, is the best of the three. The function fit plot in Fig. 15 shows that the predicted and actual values are quite close to each other in all three phases: training, validation, and testing. The data points for each subset closely match the reference

fit line, which means that the model accurately represents the underlying relationship without much variance. In addition, the lower error subplot shows small residuals that are equally spread about zero, which shows that the neural network's predictions are consistently accurate and do not have any systematic mistake. Table 4 presents the Mean Squared Error (MSE), Mean Absolute Error (MAE), and coefficient of determination (R^2) for all three output variables. The exceptionally high R^2 values and the extremely low MSE and MAE values confirm that the ANN model accurately reproduces the bvp4c results with negligible error.

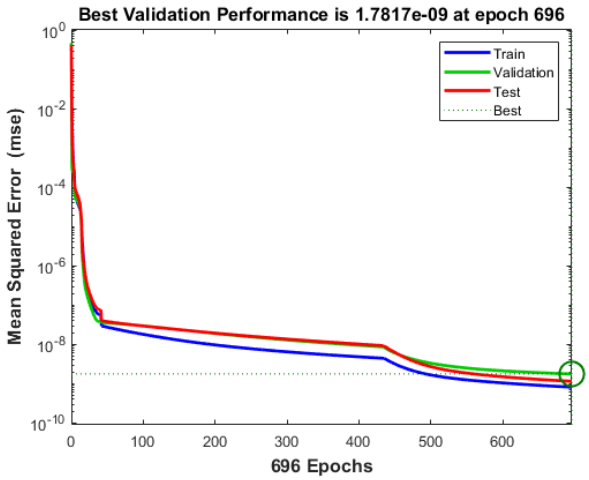

Figure 12. Mean square error plot for the outcomes related to the values of Nusselt number when thermophoresis parameter is applied

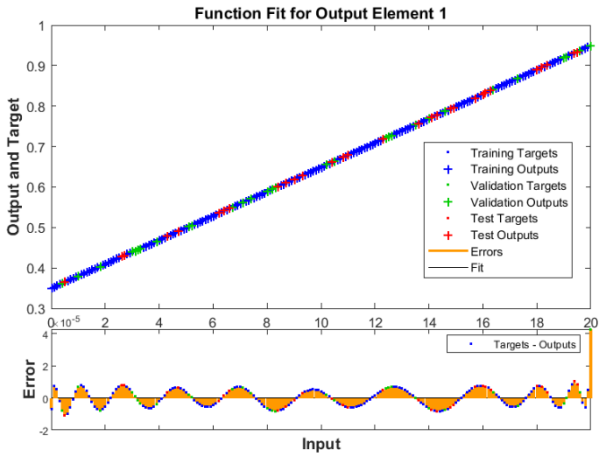

Figure 13. Function fit plot for the outcomes related to the values of Nusselt number when thermophoresis parameter is applied

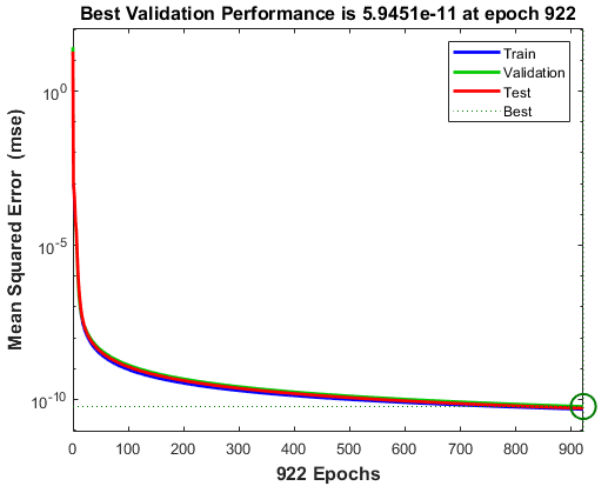

Figure 14. Mean square error plot for the outcomes related to the values of Sherwood number when reaction rate parameter is applied

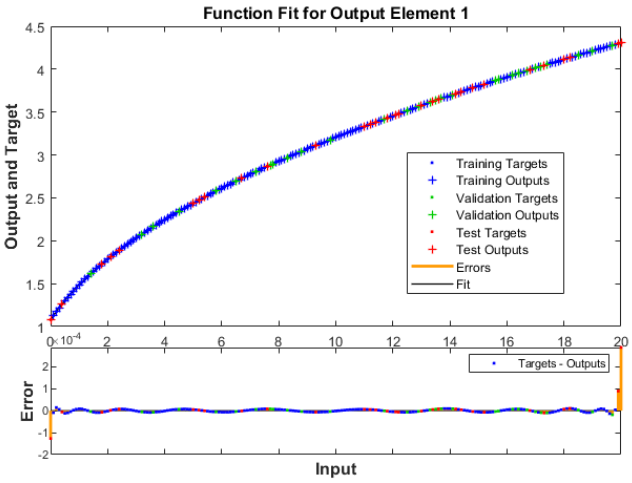

Figure 15. Function fit plot for the outcomes related to the values of Sherwood number when reaction rate parameter is applied

Table 4. Performance metrics of the Levenberg-Maquardt neural network predictions against bvp4c numerical solutions for skin friction coefficient (Cf), Nusselt number (Nu), and Sherwood number (Sh).

Output	Parameter	MSE (Mean Squared Error)	MAE (Mean Absolute Error)	R^2 (Coefficient of determination)
Cf	Mg	1.57×10^{-12}	1.02×10^{-6}	0.9999999
Nu	Nt	1.78×10^{-9}	3.85×10^{-5}	0.9999998
Sh	Γ	5.95×10^{-11}	6.52×10^{-6}	0.9999999

5. VALIDATION OF THE RESULTS

The trustworthiness of the current findings is confirmed through comparison with other investigations conducted under analogous conditions. Table 5 indicates a significant level of concordance. Table 6 represents the maximum residuals for each d value. Based on this rigorous analysis, we confirm the numerical stability of the bvp4c solver for all η values.

Table 5. Corroboration with previous outcomes for $f''(d)$

d	$f''(d)$		
	Ishak e et al. [34]	Chen and Smith [37]	Current findings
0. 1	1.2888	1.28881	1.288801329
0.01	8.4924	8.49244	8.492484394
0.001	62.1637	62.16372	62.16370642

Table 6. Numerical stability test for varying needle size parameter d: Skin friction coefficient, Nusselt number, Sherwood number, and maximum residual.

d	Skin friction coefficient	Nusselt number	Sherwood number	Maximum error
0.1	0.029086129	0.093361789	0.091683359	2.14×10^{-9}
0.05	0.065083233	0.208786501	0.205018698	2.11×10^{-9}
0.01	0.092120731	0.295309815	0.289955225	2.11×10^{-9}
0.005	0.207419712	0.661078402	0.648629831	1.96×10^{-9}
0.001	0.295923465	0.936261268	0.91778579	1.82×10^{-9}

6. CONCLUSIONS

This study has meticulously analysed the intricate transport phenomena of a Jeffrey nanofluid flow adjacent to a moving slender needle. The mathematical model was specifically designed to incorporate the collective influences of Hall current, couple stresses, temperature-dependent activation energy, and nanoparticle behaviour through Brownian motion and thermophoresis. This work is significant due to its comprehensive approach to modelling a complex and realistic system, offering essential insights that can directly improve thermal management and control strategies in micro-scale devices, advanced manufacturing, and aerospace technologies involving electromagnetic fields and chemical reactions. The key findings of the investigation, along with their physical implications, are summarized as follows:

- The fluid's velocity profile is significantly diminished by an increase in the couple stress parameter. This verifies that the internal micro-rotational resistance functions as an effective flow control mechanism, augmenting the drag force on the moving surface.
- The fluid temperature was shown to increase markedly with a rise in the Eckert number and the thermophoresis parameter. This highlights the primary influence of frictional heating and the movement of nanoparticles from warmer to cooler areas in the redistribution of thermal energy, which can be utilized to enhance uniform heating or may result in excessive overheating.
- The concentration of nanoparticles rises with elevated activation energy but diminishes with an accelerated reaction rate. This underscores that chemical reaction kinetics are a fundamental determinant of species distribution; elevated activation energy functions as a kinetic barrier, maintaining reactant concentration, whereas a rapid reaction diminishes it.
- The rates of heat and mass transfer at the needle's surface decrease with increased thermophoresis and Brownian motion parameters, respectively. This indicates a potential trade-off, wherein the mechanisms that improve bulk thermal conductivity (nanoparticle mobility) may concurrently diminish transfer efficiency at the boundary by modifying the near-wall gradients.
- The rate of entropy formation increases with elevated Brinkman and thermal radiation factors. This indicates that systems characterized by high viscous dissipation or substantial radiative heat transfer experience increased energy losses and diminished thermodynamic efficiency, a crucial factor for sustainable system design.

ORCID

M. Jayachandra Babu, https://orcid.org/0000-0001-7645-6301

REFERENCES

[1] Bhatti, M. M., Abbas, T., & Rashidi, M. M. "Entropy generation as a practical tool of optimisation for non-Newtonian nanofluid flow through a permeable stretching surface using SLM," Journal of Computational Design and Engineering, **4**(1), 21-28 (2017). https://doi.org/10.1016/j.jcde.2016.08.004

[2] Amanulla, C. H., Nagendra, N., & Reddy, M. S. "Numerical simulations on magnetohydrodynamic non-Newtonian nanofluid flow over a semi-infinite vertical surface with slipeffects," Journal of Nanofluids, **7**(4), 718-730 (2018). https://doi.org/10.1166/jon.2018.1499

[3] Goodarzi, M., Javid, S., Sajadifar, A., Nojoomizadeh, M., Motaharipour, S. H., Bach, Q. V., & Karimipour, A. "Slip velocity and temperature jump of a non-Newtonian nanofluid, aqueous solution of carboxy-methyl cellulose/aluminum oxide nanoparticles, through a microtube," International Journal of Numerical Methods for Heat & Fluid Flow, **29**(5), 1606-1628 (2019). https://doi.org/10.1108/hff-05-2018-0192

[4] Rao, A. S., Sainath, S., Rajendra, P., & Ramu, G. "Mathematical modelling of hydromagnetic casson non-Newtonian nanofluid convection slip flow from an isothermal sphere," Nonlinear engineering, **8**(1), 645-660 (2019). https://doi.org/10.1515/nleng-2018-0016

[5] Ahmadian, A., Bilal, M., Khan, M. A., & Asjad, M. I. "The non-Newtonian maxwell nanofluid flow between two parallel rotating disks under the effects of magnetic field," Scientific Reports, **10**(1), 17088 (2020). https://doi.org/10.1038/s41598-020-74096-8

[6] Usman, A. H., Khan, N. S., Humphries, U. W., Shah, Z., Kumam, P., Khan, W., ... & Ullah, Z. "Development of dynamic model and analytical analysis for the diffusion of different species in non-Newtonian nanofluid swirling flow," Frontiers in Physics, **8**, 616790 (2021). https://doi.org/10.3389/fphy.2020.616790
[7] Elgazery, N. S. "CPSM simulation of the variable properties' role in MHD non-Newtonian micropolar nanofluid flow over a stretching porous sheet (flow filtration)," Arabian Journal for Science and Engineering, **46**(8), 7661-7680 (2021). https://doi.org/10.1007/s13369-021-05489-8
[8] Yousef, N. S., Megahed, A. M., Ghoneim, N. I., Elsafi, M., & Fares, E. "Chemical reaction impact on MHD dissipative Casson-Williamson nanofluid flow over a slippery stretching sheet through porous medium," Alexandria Engineering Journal, **61**(12), 10161-10170 (2022). https://doi.org/10.1016/j.aej.2022.03.032
[9] Anwar, M. I., Firdous, H., Zubaidi, A. A., Abbas, N., & Nadeem, S. "Computational analysis of induced magnetohydrodynamic non-Newtonian nanofluid flow over nonlinear stretching sheet," Progress in reaction kinetics and mechanism, **47**, 14686783211072712 (2022). https://doi.org/10.1177/14686783211072712
[10] Sharma, B. K., Kumar, A., Gandhi, R., Bhatti, M. M., & Mishra, N. K. "Entropy generation and thermal radiation analysis of EMHD Jeffrey nanofluid flow: Applications in solar energy," Nanomaterials, **13**(3), 544 (2023). https://doi.org/10.3390/nano13030544
[11] Ashraf, M. B., Tanveer, A., & Ulhaq, S. "Effects of Cattaneo-Christov heat flux on MHD Jeffery nano fluid flow past a stretching cylinder," Journal of Magnetism and Magnetic Materials, **565**, 170154 (2023). https://doi.org/10.1016/j.jmmm.2022.170154
[12] Zeeshan, A., Khalid, N., Ellahi, R., Khan, M. I., & Alamri, S. Z. "Analysis of nonlinear complex heat transfer MHD flow of Jeffrey nanofluid over an exponentially stretching sheet via three phase artificial intelligence and Machine Learning techniques," Chaos, Solitons & Fractals, **189**, 115600 (2024). https://doi.org/10.1016/j.chaos.2024.115600
[13] Albaqami, N. N. "Using artificial neural network analysis to study Jeffrey nanofluid flow in cone–disk systems," Mathematical and Computational Applications, **29**(6), 98 (2024). https://doi.org/10.3390/mca29060098
[14] Madan Kumar, R., Srinivasa Raju, R., Kumar, M. A., & Venkateswarlu, B. "A numerical study of thermal and diffusion effects on MHD Jeffrey fluid flow over a porous stretching sheet with activation energy," Numerical Heat Transfer, Part A: Applications, **86**(13), 4423-4444 (2025). https://doi.org/10.1080/10407782.2024.2319344
[15] Butt, A. S., Anjum, A., Saeed, U. E. Z., Al Suliman, N., Alarfaj, K. K., & Souayeh, B. "Parametric Analysis of Entropy Generation in Jeffrey Nanofluid Flow Over an Exponentially Stretchable Surface with Convective Boundary Conditions and Magnetic Field Effects," Journal of Nonlinear Mathematical Physics, **32**(1), 85 (2025). https://doi.org/10.1007/s44198-025-00334-0
[16] Upadhya, S. M., Jayachandra Babu, M., & Srinivasa Babu, K. S. "Machine Learning-Enhanced Simulation of Maxwell Nanofluid Flow: A Bayesian Neural Network Approach with Thermal Relaxation and Variable Viscosity Effects," Journal of Applied and Computational Mechanics, 12(3), 815-827 (2025). https://doi.org/10.22055/jacm.2025.48495.5275
[17] Kareem, R. A., Salawu, S. O., & Yan, Y. "Analysis of transient Rivlin-Ericksen fluid and irreversibility of exothermic reactive hydromagnetic variable viscosity," J. Appl. Comput. Mech., **6**(1), 26-36 (2020). https://doi.org/10.22055/jacm.2019.28216.1460
[18] Salawu, O. "Transient analysis of radiative hydromagnetic poiseuille fluid flow of two-step exothermic chemical reaction through a porous channel with convective cooling," Journal of Computational & Applied Research in Mechanical Engineering (JCARME), **10**(1), 51-62 (2020). https://doi.org/10.22061/jcarme.2019.3986.1473
[19] Raees, A., Raees-ul-Haq, M., & Mansoor, M. "Modeling and simulations of Buongiorno's model for nanofluid in a microchannel with electro-osmotic effects and an exothermal chemical reaction," Nanomaterials, **11**(4), 905 (2021). https://doi.org/10.3390/nano11040905
[20] Ahmad, U., Ashraf, M., Abbas, A., Rashad, A. M., & Nabwey, H. A. "Mixed convection flow along a curved surface in the presence of exothermic catalytic chemical reaction," Scientific reports, **11**(1), 12907 (2021). https://doi.org/10.1038/s41598-021-92409-3
[21] Ogunsola, A. W., Oderinu, R. A., & Ohaegbue, A. D. "Entropy generation in a third-grade hydromagnetic fluid of generalised Arrhenius two-step exothermic reaction with convective cooling," International Journal of Ambient Energy, **43**(1), 8792-8801 (2022). https://doi.org/10.1080/01430750.2022.2102071
[22] Zainal, N. A., Nazar, R., Naganthran, K., & Pop, I. "Flow and heat transfer over a permeable moving wedge in a hybrid nanofluid with activation energy and binary chemical reaction," International Journal of Numerical Methods for Heat & Fluid Flow, **32**(5), 1686-1705 (2022). https://doi.org/10.1108/hff-04-2021-0298
[23] Ganesh, N. V., Al-Mdallal, Q. M., Kalaivanan, R., & Reena, K. "Arrhenius kinetics driven nonlinear mixed convection flow of Casson liquid over a stretching surface in a Darcian porous medium," Heliyon, **9**(6), (2023). https://doi.org/10.1016/j.heliyon.2023.e16135
[24] Hamza, M. M., Abdulsalam, S., & Ahmad, S. K. "Time-Dependent Magnetohydrodynamic (MHD) Flow of an Exothermic Arrhenius Fluid in a Vertical Channel with Convective Boundary Condition," Advances in Mathematical Physics, **2023**(1), 7173925 (2023). https://doi.org/10.1155/2023/7173925
[25] Das, T. K., Paul, A., & Nath, J. M. "Endo/exothermic analysis of Casson and Maxwell quadra hybrid nanofluid flow configured by pollutant concentration with thermal and solute jump," Journal of Taibah University for Science, **18**(1), 2382940 (2024). https://doi.org/10.1080/16583655.2024.2382940
[26] Khan, I., Chinyoka, T., Zulkifli, R., Muhammad, T., & Shaaban, A. A. "Computational study of non-Newtonian electro-osmotic flow between micro-parallel plates subject to Joule heating and exothermic reactions," Colloid and Polymer Science, **302**(6), 939-954 (2024). https://doi.org/10.1007/s00396-024-05242-1
[27] Ullah, I. "Activation energy with exothermic/endothermic reaction and Coriolis force effects on magnetized nanomaterials flow through Darcy–Forchheimer porous space with variable features," Waves in random and complex media, **35**(1), 398-411 (2025). https://doi.org/10.1080/17455030.2021.2023779
[28] Xin, X., Khan, I., M. Alqahtani, A., Chinyoka, T., Alroobaea, R., Zulkifli, R., & Ahmad, Z. "Numerical simulations of third-grade fluid flow with exothermic reactions in porous media-saturated vertical microchannels," Numerical Heat Transfer, Part B: Fundamentals, **86**(8), 2473-2493 (2025). https://doi.org/10.1080/10407790.2024.2345508

[29] Waini, I., Ishak, A., & Pop, I. "Hybrid nanofluid flow past a permeable moving thin needle," Mathematics, **8**(4), 612 (2020). https://doi.org/10.3390/math8040612
[30] Kumar, R. N., Gowda, R. P., Madhukesh, J. K., Prasannakumara, B. C., & Ramesh, G. K. "Impact of thermophoretic particle deposition on heat and mass transfer across the dynamics of Casson fluid flow over a moving thin needle," Physica Scripta, **96**(7), 075210 (2021). https://doi.org/10.1088/1402-4896/abf802
[31] Ramesh, G. K., Madhukesh, J. K., Aly, E. H., & Pop, I. "Modified Buongiorno's model for biomagnetic hybrid nanoliquid past a permeable moving thin needle," International Journal of Numerical Methods for Heat & Fluid Flow, **32**(11), 3551-3578 (2022). https://doi.org/10.1108/hff-10-2021-0696
[32] Abbas, Z., Rehman, A. U., Khaliq, S., & Rafiq, M. Y. "Flow dynamics of MHD hybrid nanofluid past a moving thin needle with a temporal stability test: a Galerkin method approach," Numerical Heat Transfer, Part B: Fundamentals, **84**(3), 329-347 (2023). https://doi.org/10.1080/10407790.2023.2202882
[33] Srinivasa Reddy, V., Kandasamy, J., & Sivanandam, S. "Joule heating, Dufour and Soret effects on MHD hybrid nanoliquid flow over a moving thin needle in a porous medium with thermal radiation," World Journal of Engineering, **22**(4), 866-875 (2025). https://doi.org/10.1108/wje-01-2024-0040
[34] Ishak, A., Nazar, R., & Pop, I. "Boundary Layer Flow over a Continuously Moving Thin Needle ina Parallel Free Stream," Chinese Physics Letters, **24**(10), 2895 (2007). https://doi.org/10.1088/0256-307x/24/10/051
[35] Ashraf, M. B., Tanveer, A., & Ulhaq, S. "Effects of Cattaneo-Christov heat flux on MHD Jeffery nano fluid flow past a stretching cylinder," Journal of Magnetism and Magnetic Materials, **565**, 170154 (2023). https://doi.org/10.1016/j.jmmm.2022.170154
[36] Karthik, K., Srilatha, P., Madhukesh, J. K., Khan, U., Prasannakumara, B. C., Kumar, R., ... & Abdou, M. M. M. "Computational examination of heat and mass transfer of nanofluid flow across an inclined cylinder with endothermic/exothermic chemical reaction," Case Studies in Thermal Engineering, **57**, 104336 (2024). https://doi.org/10.1016/j.csite.2024.104336
[37] Chen, J. L. S., & Smith, T. N. "Forced convection heat transfer from nonisothermal thin needles, **100**(2), 358-362 (1978). https://doi.org/10.1115/1.3450809

ЧИСЛОВЕ ДОСЛІДЖЕННЯ НАНОРІДИНИ ДЖЕФФРІ НАД РУХОМОЮ ТОНКОЮ ГОЛКОЮ З ЕКЗОТЕРМІЧНОЮ ХІМІЧНОЮ РЕАКЦІЄЮ: ПІДХІД ЛЕВЕНБЕРГА-МАРКВАРДТА НА ОСНОВІ НЕЙРОМЕРЕЖІ

Р. Крішнакумарі[1], В. Сугунамма[2], М. Джаячандра Бабу[3], Дж. Гіріш Кумар[4]
[1]Кафедра математики, Університет Шрі Венкатешвара, Тірупаті, Андхра-Прадеш, Індія – 517502
[2]Кафедра математики, Університет Шрі Венкатешвара, Тірупаті, Андхра-Прадеш, Індія – 517502
[3]Кафедра математики, Урядовий коледж, Раджампета, Андхра-Прадеш, Індія – 516115
[4]Кафедра математики, Урядовий коледж, Нагарі, Андхра-Прадеш, Індія – 517590

У цьому дослідженні розглядаються властивості тепло- та масопередачі нанорідини Джеффрі, що рухається по тонкій рухомій голці. Головна мета полягає у дослідженні того, як важливі параметри, такі як струм Холла, напруга зв'язку, енергія активації та термофорез, впливають на швидкість, температуру, концентрацію рідини та відповідне генерування ентропії. Конфігурація потоку тонкої голки має критичне значення для практичних застосувань, включаючи теплове проектування мікроголок для регульованої доставки ліків, аеродинамічне профілювання тонких структурних елементів в аерокосмічній техніці та оптимізацію чутливих сенсорних зондів. За допомогою відповідних перетворень подібності рівняння, які мали описувати проблему, були перетворені на структуру нелінійних звичайних рівнянь, а потім розв'язані за допомогою розв'язувача bvp4c. Помітним відкриттям є те, що швидкість рідини гальмується збільшеною напруженістю магнітного поля та напругами зв'язку, тоді як температурний профіль покращується завдяки підвищеній в'язкій дисипації та ефектам термофорезу. Крім того, швидкість теплопередачі на поверхні зменшується зі збільшенням параметра термофорезу, тоді як швидкість масопередачі — зі збільшенням енергії активації. Дослідження показує, що утворення ентропії, що представляє втрату енергії, зростає зі збільшенням в'язкої дисипації та теплового випромінювання. Виявлено, що число Шервуда зменшується на 24,1% зі збільшенням енергії активації від 0 до 0,8. Виявлено, що число Нуссельта зменшується на 26,3% зі збільшенням параметра термофорезу від 0 до 2. Виявлено, що коефіцієнт тертя зростає на 2,32% при збільшенні параметра магнітного поля від 0 до 2.
Ключові слова: *термофорез; bvp4c; броунівський рух; парне напруження; енергія активації*

East European Journal of Physics. 3. 456-469 (2026)
DOI:10.26565/2312-4334-2026-3-41 ISSN 2312-4334

A MODIFIED RUNGE–KUTTA AND COMPACT SPATIAL SCHEME FOR DARCY-FORCHHEIMER PRANDTL–EYRING FLUID FLOW OVER A RIGA PLATE

Yasir Nawaz[1]*, Muhammad Shoaib Arif[2], Muavia Mansoor[3], Kamal Abodayeh[2]
[1]*Department of Mathematics, Faculty of Engineering and Computing, National University of Modern Languages (NUML), Islamabad, 44000, Pakistan*
[2]*Department of Mathematics and Sciences, College of Sciences and Humanities, Prince Sultan University, Riyadh, 11586, Saudi Arabia*
[3]*Department of Mathematics, University of Wah, Wah Cantt 47040, Pakistan*
**Corresponding Author email: yasir.nawaz@numl.edu.pk*
Received April 30, 2026; revised July 3, 2026; accepted July 12, 2026

A modification of existing third order Runge-Kutta method, is proposed. The scheme is explicit, and its first stage consists of a nonstandard denominator, while the last two stages are the same as those of the Runge-Kutta method. For discretizing space-dependent terms, a compact, high-order scheme is employed. The proposed scheme with spatial discretization is employed to find the stability condition of the proposed scheme. The scheme is applied to a dimensionless model in the form of partial differential equations for the slip flow of a non-Newtonian fluid over a Riga plate with heat and mass transfer. Different types of graphs are obtained using the proposed scheme for velocity, temperature, and concentration profiles. Some of the results obtained by the proposed scheme are compared with those obtained by the numerical solution using the MATLAB PDEPE solver. The scheme is also compared with an existing third-order Runge-Kutta scheme, and it produces more accurate results than the existing scheme at specific time and space step sizes.
Keywords: *Hybrid Scheme; Stability; Convergence; Slip Flow; Eyring-Prandtl Fluid*

INTRODUCTION

There exist variour methods that can be used to solve differential equations arise in phenomenon of flow over plates. Some analyrical and numerical methods can be used for solving ordinary diferential equaitons. Since, ordinary differential equatiuons contains one inpendent variable, so only one method can be used to solve these equations. But partial differential equations contain more than one independent variables, so two or more method must be chosen or contructed to solve thsese equations. Analytial methods [1] can be used to solve different type of equaitons but these methods may consume more time to converge because they deal with algebraic expression. So, numerical methods [2] can be chosen to solve different type of differetal equations. The numerical simulation of nonlinear differential systems arising in fluid mechanics, porous-media transport, and non-Newtonian rheology relies heavily on robust time-integration techniques. Among these, Runge–Kutta (RK) methods have remained central because of their simplicity, accuracy, and adaptability to a wide range of ordinary differential equation (ODE) and semi-discrete partial differential equation (PDE) problems. Classical expositions of RK theory by Butcher [3] and by Hairer & Wanner [4] establish stability categories (A-, L-, and B-stability) and provide the foundational convergence results through Dahlquist-type analyses. However, for stiff or strongly nonlinear systems—such as those produced by convection–diffusion–reaction models, porous-media flows, or high-nonlinearity non-Newtonian fluids—the standard explicit RK methods can become inefficient due to restrictive timestep bounds. This limitation has motivated the development of *modified* or *stabilized* RK schemes with enlarged stability regions and improved nonlinear contractivity properties.

Stabilized explicit RK methods, including Chebyshev-based schemes and extended-stability formulations, have been studied extensively for diffusion-dominated PDEs and stiff ODEs, as documented in works on stabilized RK theory [5-9]. These methods achieve extended stability along the negative real axis—crucial for method-of-lines discretizations of parabolic and convection–diffusion PDEs. Parallel efforts have analyzed RK stability, nonlinearity-preserving properties, and algebraic stability conditions essential for stiff systems [10–12]. A recent contribution by Hu [7] proposed a modified RK method with an enlarged stability domain and improved convergence characteristics, illustrating the modern trend toward structure-preserving and stiffness-aware RK design.

These numerical advancements are directly relevant to fluid-mechanical systems governed by *mixed convection Darcy–Forchheimer flow*, especially when involving *non-Newtonian Prandtl–Eyring (Eyring–Prandtl) fluids*. Classical studies on Darcy–Forchheimer convection in porous media, such as those by Shenoy [13], demonstrate that porous-inertia corrections introduce nonlinearities that significantly affect velocity profiles, heat transfer, and boundary-layer structure. More recent works by Shah et al. [14] and Chaudhary [15] show that Eyring–Prandtl rheology further complicates the governing equations due to nonlinear shear-rate dependencies, requiring stable time-integration and careful numerical formulations. Comprehensive modeling of Eyring–Prandtl fluids and their thermo-physical behavior is provided by Ullah et al. [16] and Baidya [17], highlighting rheological sensitivity and the necessity for robust numerical treatment.

Cite as: Y. Nawaz, M.Sh. Arif, M. Mansoor, K. Abodayeh, East Eur. J. Phys. 3, 456 (2026), https://doi.org/10.26565/2312-4334-2026-3-41

In addition, Riga plates—electromagnetically actuated surfaces composed of alternating electrodes and magnets—introduce localized Lorentz forces capable of accelerating or decelerating the near-wall region. Their applications in MHD and hybrid-fluid systems have been studied in numerical and experimental contexts, including magnetite nanofluids [20] and hybrid Riga-plate-induced flow systems [21]. These works show that the interaction between electromagnetic forcing and fluid rheology generates intricate nonlinear momentum dynamics. Because Riga plate forcing modifies the boundary-layer structure, it introduces additional stiffness in the resulting ODE system after similarity or quasi-similarity transformation.

Furthermore, viscous dissipation, a key component in high-viscosity or high-velocity non-Newtonian flows, contributes to a strong coupling between the momentum and energy equations. Its importance in porous-media and non-Newtonian flows is demonstrated in studies by Awais et al. [18] and Ajibade et al. [19], where dissipation significantly alters temperature fields, enhances nonlinearity, and contributes to stiffness in the governing PDE system.

Taken together, mixed-convection Darcy–Forchheimer flow of an Eyring–Prandtl fluid over a Riga plate with viscous dissipation forms a nonlinear, stiff, multi-parameter boundary-layer system—an ideal candidate for testing improved RK-type numerical integrators. Explicit stabilized and modified RK schemes provide a powerful balance between computational simplicity and enhanced stability, enabling larger timesteps without loss of accuracy. Recent numerical approaches involving boundary-layer flows over Riga plates [20–22] further reinforce the need for integrators that can handle strong electromagnetic forcing and porous-inertia effects under thermal–viscous coupling.

In this study, we develop a modified Runge–Kutta scheme incorporating stability-enhancement techniques inspired by stabilized RK theory [5–9, 23] and nonlinear convergence theory [10–12]. The method is analyzed for stability and convergence under the nonlinearities associated with Darcy–Forchheimer resistance, Eyring–Prandtl rheology, Riga plate electromagnetic forcing, and viscous dissipation. The numerical results show that the modified RK method significantly enlarges the allowable timestep relative to classical explicit RK while maintaining accuracy comparable to implicit schemes. This builds upon the previous works on stabilized RK methods [5–9], non-Newtonian Darcy–Forchheimer systems [13–19], and Riga-plate flows [20–22], integrating these strands into a unified computational framework.

The remainder of this paper is organized as follows: Section 2 presents the mathematical formulation and nondimensionalization. Section 3 describes the numerical method employed. In Section 4, we present and discuss the results. Finally, Section 5 gives concluding remarks.

Construction of Numerical Scheme: A three-stage computational scheme is going to be proposed for solving time dependent partial differential equations. The scheme is explicit in all three stages. The solution obtained in first stage will be utilized in second stage of scheme and similar solutions obtained from second stage will be utilized in third stage. The domain of the considered differential equation is denoted by $[0, L]$. This whole domain is divided into a equal subinterval of time $[0, t_f]$ is divided into equal small subintervals with length Δt. The scheme is constructed for following equation.

$$\frac{\partial g}{\partial t} = \alpha_1 \frac{\partial g}{\partial y} + \beta_1 \frac{\partial^2 g}{\partial y^2} + s(g) \tag{1}$$

Where s is linear or nonlinear function in g. The initial and boundary condition for Eq. (1) can be written as

$$\left.\begin{array}{c} g(0,y) = f_1(y) \\ g(t,0) = f_2(t), and\ g(t,L) = f_3(t) \end{array}\right\} \tag{2}$$

Where α_1 and β_1 are constants and $f_j, j = 1,2,3$ are functions of t or some constants.
The first stage of the scheme for Eq. (1) is

$$\bar{g}_j^{n+1} = g_j^n e^{a_1 \Delta t} + \frac{(e^{a_1 \Delta t} - 1)}{a_1} \left\{ \left.\frac{\partial g}{\partial t}\right|_j^n - a_1 g_j^n \right\}. \tag{3}$$

Where subscript j is used for location of grid point and n represents point in time and a_1 is a free parameter. Stability region of these types of proposed schemes depends on value of this free parameter a_1.
This first stage (3) can be expressed as

$$\bar{g}_j^{n+1} = g_j^n + \frac{(e^{a_1 \Delta t} - 1)}{a_1} \left.\frac{\partial g}{\partial t}\right|_j^n, \tag{4}$$

where $\frac{(e^{a_1 \Delta t} - 1)}{a_1} \approx \Delta t + O(\Delta t^2)$.

So, this first stage of proposed scheme can be considered as modified form of existing Euler method
The second stage of the scheme is written as:

$$\bar{\bar{g}}_j^{n+1} = ag_j^n + b\bar{g}_j^{n+1} + \frac{1}{4}\Delta t \left.\frac{\partial \bar{g}}{\partial t}\right|_j^{n+1} \tag{5}$$

The third stage of the scheme for Eq. (1) takes the form

$$g_j^{n+1} = cg_j^n + d\bar{\bar{g}}_j^{n+1} + \frac{2}{3}\Delta t \left.\frac{\partial \bar{\bar{g}}}{\partial t}\right|_j^{n+1} \tag{6}$$

The unknown parameters a, b, c and d can be found later by matching the Taylor series expansion. Now combing the first stage Eq. (3) and second stage Eq. (5) of proposed scheme yields

$$\bar{\bar{g}}_j^{n+1} = (a+b)g_j^n + \left(\frac{b}{a_1}(e^{a_1\Delta t} - 1) + \frac{\Delta t}{4}\right)\left.\frac{\partial g}{\partial t}\right|_j^n + \frac{\Delta t}{4a_1}(e^{a_1\Delta t} - 1)\left.\frac{\partial^2 g}{\partial t^2}\right|_j^n \tag{7}$$

Now substituting Eq. (7) into Eq. (6) that yields the following equation:

$$g_j^{n+1} = cg_j^n + d\left[(a+b)g_j^n + \left\{\frac{b}{a_1}(e^{a_1\Delta t} - 1) + \frac{\Delta t}{4}\right\}\left.\frac{\partial g}{\partial t}\right|_j^n + \frac{\Delta t}{4a_1}(e^{a_1\Delta t} - 1)\left.\frac{\partial^2 g}{\partial t^2}\right|_j^n\right] + \frac{2}{3}\Delta t\left[(a+b)\left.\frac{\partial g}{\partial t}\right|_j^n + \left\{\frac{b}{a_1}(e^{a_1\Delta t} - 1) + \frac{\Delta t}{4}\right\}\left.\frac{\partial^2 g}{\partial t^2}\right|_j^n + \frac{\Delta t}{4a_1}(e^{a_1\Delta t} - 1)\left.\frac{\partial^3 g}{\partial t^3}\right|_j^n\right] \tag{8}$$

Expanding g_j^{n+1} using Taylor series expansion

$$g_j^{n+1} = g_j^n + \Delta t \left.\frac{\partial g}{\partial t}\right|_j^n + \frac{(\Delta t)^2}{2}\left.\frac{\partial^2 g}{\partial t^2}\right|_j^n + \frac{(\Delta t)^3}{6}\left.\frac{\partial^3 g}{\partial t^3}\right|_j^n + O((\Delta t)^4) \tag{9}$$

Using Eq. (9) into Eq. (8) that results in

$$g_j^n + \Delta t \left.\frac{\partial g}{\partial t}\right|_j^n + \frac{(\Delta t)^2}{2}\left.\frac{\partial^2 g}{\partial t^2}\right|_j^n + \frac{(\Delta t)^3}{6}\left.\frac{\partial^3 g}{\partial t^3}\right|_j^n = [c + d(a+b)]g_j^n + \left[\frac{bd}{a_1}(e^{a_1\Delta t} - 1) + \frac{\mathrm{d}\Delta t}{4} + \frac{2}{3}\Delta t(a+b)\right]\left.\frac{\partial g}{\partial t}\right|_j^n + \left[\frac{\mathrm{d}\Delta t}{4a_1}(e^{a_1\Delta t} - 1) + \frac{2}{3}\Delta t\left(\frac{b}{a_1}(e^{a_1\Delta t} - 1) + \frac{1}{4}\Delta t\right)\right]\left.\frac{\partial^2 g}{\partial t^2}\right|_j^n + \frac{(\Delta t)^2}{6a_1}(e^{a_1\Delta t} - 1)\left.\frac{\partial^3 g}{\partial t^3}\right|_j^n \tag{10}$$

Equating the coefficients of $g_j^n, \left.\frac{\partial g}{\partial t}\right|_j^n, \left.\frac{\partial^2 g}{\partial t^2}\right|_j^n$ and $\left.\frac{\partial^3 g}{\partial t^3}\right|_j^n$ on both sides of Eq. (10), it gives

$$\left.\begin{aligned} 1 &= c + d(a+b) \\ \Delta \mathrm{t} &= \frac{bd}{a_1}(e^{a_1\Delta t} - 1) + \frac{\mathrm{d}\Delta t}{4} + \frac{2}{3}\Delta t(a+b) \\ \frac{(\Delta t)^2}{2} &= \frac{\mathrm{d}\Delta t}{4a_1}(e^{a_1\Delta t} - 1) + \frac{2}{3}\Delta t\left(\frac{b}{a_1}(e^{a_1\Delta t} - 1) + \frac{1}{4}\Delta t\right) \\ \frac{(\Delta t)^3}{6} &= \frac{(\Delta t)^2}{6a_1}(e^{a_1\Delta t} - 1) \end{aligned}\right\} \tag{11}$$

Applying condition of $a + b = 1$ and solving the linear system of Eq. (11) gives the values of a, b, c and d as follows

$$\left.\begin{aligned} a &= \frac{3\Delta t - \sqrt{\Delta t(9\Delta t - 8\gamma(\Delta t))}}{8\gamma(\Delta t)} - \frac{\Delta t - 2\gamma(\Delta t)}{2\gamma(\Delta t)} \\ b &= \frac{\Delta t + \sqrt{\Delta t(9\Delta t - 8\gamma(\Delta t))}}{8\gamma(\Delta t)} - \frac{\Delta t - 2\gamma(\Delta t)}{2\gamma(\Delta t)} \\ c &= \frac{\gamma(\Delta t) - \Delta t}{\gamma(\Delta t)} - \frac{\sqrt{\Delta t(9\Delta t - 8\gamma(\Delta t))}}{3\gamma(\Delta t)} \\ d &= \frac{6\Delta t - \sqrt{\Delta t(9\Delta t - 8\gamma(\Delta t))}}{6\gamma(\Delta t)} \end{aligned}\right\} \tag{12}$$

where $\gamma(\Delta t) = \frac{e^{a_1\Delta t - 1}}{a_1}$.

The proposed scheme is three stages that can be used for time discretization of partial differential equations. To discretize space dependent terms a compact scheme is employed. The proposed scheme for Eq. (1) with compact spatial discretization [24] takes the form:

$$\bar{g}_j^{n+1} = g_j^n e^{1.5\Delta t} + \frac{(e^{a_1\Delta t}-1)}{a_1}\left\{\alpha_1\zeta_1\, g_j^n + \beta_1\zeta_2\, g_j^n - \frac{3}{2}g_j^n\right\} \tag{13}$$

$$\bar{\bar{g}}_j^{n+1} = ag_j^n + b\bar{g}_j^{n+1} + \frac{1}{4}\Delta t\left\{\alpha_1\zeta_1\, \bar{g}_j^{n+1} + \beta_1\zeta_2\, \bar{g}_j^{n+1}\right\} \tag{14}$$

$$g_j^{n+1} = cg_j^n + d\bar{\bar{g}}_j^{n+1} + \frac{2}{3}\Delta t\left\{\alpha_1\zeta_1\, \bar{\bar{g}}_j^{n+1} + \beta_1\zeta_2\, \bar{\bar{g}}_j^{n+1}\right\} \tag{15}$$

Where $\zeta_1 = A_1^{-1}B_1$ & $\zeta_2 = A_2^{-1}B_2$.
Where A_l, B_l for $l = 1,2$ are matrices constructed from the coefficients of left and right hand sides of the following equations

$$\gamma_1\frac{\partial g}{\partial y}\Big|_{j-1}^{n} + \frac{\partial g}{\partial y}\Big|_{j}^{n} + \gamma_1\frac{\partial g}{\partial y}\Big|_{j+1}^{n} = b_0\frac{(g_{j+1}^n - g_{j-1}^n)}{2\Delta y} + b_1\frac{(g_{j+2}^n - g_{j-2}^n)}{4\Delta y} \tag{16}$$

$$\gamma_2\frac{\partial^2 g}{\partial y^2}\Big|_{j-1}^{n} + \frac{\partial^2 g}{\partial y^2}\Big|_{j}^{n} + \gamma_2\frac{\partial^2 g}{\partial y^2}\Big|_{j+1}^{n} = b_2\frac{(g_{j+1}^n - 2g_j^n + g_{j-1}^n)}{(\Delta y)^2} + b_3\frac{(g_{j+2}^n - 2g_j^n + g_{j-2}^n)}{4(\Delta y)^2} \tag{17}$$

Where $b_0 = \frac{\gamma_1+2}{3}, b_1 = \frac{1-4\gamma_1}{3}, b_2 = \frac{4(1-\gamma_2)}{3}, b_3 = \frac{10\gamma_2-1}{3}$.

Stability Analysis: One of the tasks in finite differences is to check their stability region. There exists more than one stability analysis for finding stability conditions for finite difference schemes. Among existing stability analysis Fourier series analysis or Von Neumann stability analysis is a stability procedure that can be used to find stability conditions of finite difference schemes applied to linear partial differential equation. The analysis is started by transforming a given difference equation into a trigonometric equation. For this case the transformations can be expressed as:

$$A_1 e^{ij\psi} = e^{ij\psi}\left(\gamma_1 e^{i\psi} + 1 + \gamma_1 e^{-i\psi}\right) \tag{18}$$

$$B_1 e^{ij\psi} = \frac{b_\circ e^{(j+1)i\psi}}{2\Delta y} - \frac{b_\circ e^{(j-1)i\psi}}{2\Delta y} + \frac{b_1 e^{(j+2)i\psi}}{4\Delta y} - \frac{b_1 e^{(j-2)i\psi}}{4\Delta y} \tag{19}$$

$$A_2 e^{ij\psi} = e^{ij\psi}\left(\gamma_2 e^{2i\psi} + 1 + \gamma_2 e^{-2i\psi}\right) \tag{20}$$

$$B_2 e^{ij\psi} = \frac{b_2 e^{(j+1)i\psi}}{(\Delta y)^2} - \frac{2b_2 e^{ji\psi}}{(\Delta y)^2} + \frac{b_2 e^{(j-1)i\psi}}{(\Delta y)^2} + \frac{b_3 e^{(j+2)i\psi}}{4(\Delta y)^2} - \frac{2b_3 e^{ji\psi}}{4(\Delta y)^2} + \frac{b_3 e^{(j-2)i\psi}}{4(\Delta y)^2} \tag{21}$$

Where $i = \sqrt{-1}$.
Applying transformations (19) - (21) into first stage of the scheme (13) gives

$$\bar{g}_j^{n+1} = g_i^n e^{1.5\Delta t} + \frac{(e^{1.5\Delta t}-1)}{1.5}\begin{Bmatrix} \alpha_1\left(\frac{2b_0 isin\psi + c_1 isin2\psi}{2\Delta y(2\gamma_1\cos\psi+1)}\right) + \\ \beta_1\left(\frac{4b_2(cos\psi-1)+b_3(cos2\psi-1)}{2(\Delta y)^2(2\gamma_2\cos\psi-1)}\right) - \frac{3}{2}\end{Bmatrix} g_j^n \tag{22}$$

Re-write Eq. (22) as

$$\bar{g}_j^{n+1} = (c_1 + ic_2)g_j^n \tag{23}$$

Where $\mu_{c_1} = e^{1.5\Delta t} + \frac{(e^{1.5\Delta t}-1)}{1.5}\left\{\beta_1\left(\frac{4b_2(cos\psi-1)+b_3(cos2\psi-1)}{2(\Delta y)^2(2\gamma_2\cos\psi-1)}\right) - \frac{3}{2}\right\}$, and $\mu_{c_2} = \frac{(e^{1.5\Delta t}-1)}{1.5}\left\{\alpha_1\left(\frac{2b_0 isin\psi + c_1 isin2\psi}{2\Delta y(2\gamma_1\cos\psi+1)}\right)\right\}$

Substituting transformations (19)-(21) into the second stage of the scheme (14) gives.

$$\bar{\bar{g}}_j^{n+1} = ag_j^n + b\bar{g}_j^{n+1} + \frac{1}{4}\Delta t\left\{\alpha_1\left(\frac{2b_0 isin\psi + c_1 isin2\psi}{2\Delta y(2\gamma_1\cos\psi+1)}\right) + \beta_1\left(\frac{4b_2(cos\psi-1)+b_3(cos2\psi-1)}{2(\Delta y)^2(2\gamma_2\cos\psi-1)}\right)\right\}\bar{g}_j^{n+1} \tag{24}$$

Eq. (24) can be written as

$$\bar{\bar{g}}_j^{n+1} = \mu_1 g_j^n \tag{25}$$

where $\mu_1 = \mu_{c_5} + i\mu_{c_6}$, $\mu_{c_5} = a + \mu_{c_1}\mu_{c_3} - \mu_{c_2}\mu_{c_4}$ and $\mu_{c_6} = \mu_{c_1}\mu_{c_4} + \mu_{c_2}\mu_{c_3}$

and $\mu_{c_3} = b + \frac{1}{4}\Delta t\left\{\beta_1\left(\frac{4b_2(cos\psi-1)+b_3(cos2\psi-1)}{2(\Delta y)^2(2\gamma_2\cos\psi-1)}\right)\right\}$, & $\mu_{c_4} = \frac{1}{4}\Delta t\left\{\alpha_1\left(\frac{2b_0 isin\psi + c_1 isin2\psi}{2\Delta y(2\gamma_1\cos\psi+1)}\right)\right\}$

By using transformations (19)-(21) into third stage of the scheme (15) gives

$$g_j^{n+1} = \mu_2 g_j^n \tag{26}$$

Where $\mu_2 = \mu_{c_9} + i\mu_{c_{10}}, \mu_{c_9} = c + \mu_{c_7}\mu_{c_5} - \mu_{c_6}\mu_{c_8}$ and $\mu_{c_{10}} = \mu_{c_6}\mu_{c_7} + \mu_{c_5}\mu_{c_8}$
and $\mu_{c_7} = c + \frac{2}{3}\Delta t\left\{\beta_1\left(\frac{4b_2(cos\psi-1)+b_3(cos2\psi-1)}{2(\Delta y)^2(2\gamma_2\cos\psi-1)}\right)\right\}$
$\mu_{c_8} = \frac{2}{3}\Delta t\alpha_1\left(\frac{2b_0 isin\psi + c_1 isin2\psi}{2\Delta y(2\gamma_1\cos\psi+1)}\right)$.

The amplification factor can be written as

$$\left|\frac{g_j^{n+1}}{g_j^n}\right|^2 = \mu_{c_9}^2 + \mu_{c_{10}}^2 \tag{27}$$

So, the scheme will be stable if it satisfies

$$\mu_{c_9}^2 + \mu_{c_{10}}^2 \leq 1 \tag{28}$$

For the case when $\alpha_1 = 0$, stability condition can be expressed as

$$|G| < 1 \tag{29}$$

where $G = \frac{d^3\Gamma^3\gamma(\Delta t)+d^2\Gamma^2(\Delta t+2\gamma(\Delta t))+d\,\Gamma(5\Delta t+\gamma(\Delta t))+6\Delta t}{6\Delta t}$, $\Gamma = \frac{2b_2(cos(\psi)-1)+0.5b_2(cos(2\psi)-1)}{2\gamma_2\cos\psi+1}$,
and $d = \beta_1\frac{\Delta t}{\Delta y^2}$, $\gamma(\Delta t) = \frac{e^{a_1\Delta t}-1}{a_1}$.

Fig. 1 shows the comparison of stability region G along diffusion number d for different values of time step sizes and free parameter a_1. Amplification factor G is found by applying first stage of proposed scheme and second and third stage of existing third order Runge-Kutta method. Stability region of this tye of scheme depend on choice of free parameter a_1 and choice of time step size Δt.

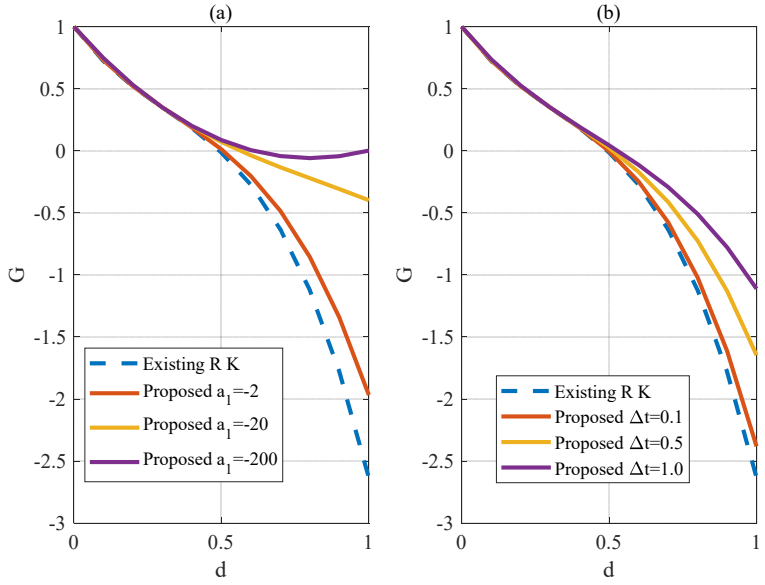

Figure 1. Comprison of stability regions of proposed and existing Runge-Kutta methods (a) $\Delta t = 0.3, \gamma_2 = -0.3$ (b) $\gamma_2 = -0.3$, $a_1 = -2$

The stability of the proposed scheme is provided for scalar partial differential equations. Now the convergence of the proposed scheme for system of convection diffusion equation is provided.
For doing so consider the vector matrix equation of the form

$$\boldsymbol{v_t} = C_1\boldsymbol{v_y} + C_2\boldsymbol{v_{yy}} + C_3\boldsymbol{v} \tag{30}$$

Where v is a vector and C_1, C_2 and C_3 are matrices. Eq. (30) is discretized by the proposed scheme as

$$\overline{\boldsymbol{v}}_j^{n+1} = \boldsymbol{v}_j^n e^{1.5\Delta t} + \frac{(e^{a_1\Delta t}-1)}{a_1}\{C_1\zeta_1 + C_2\zeta_2 + C_3\boldsymbol{v}_j^n - a_1\}\boldsymbol{v}_j^n \tag{31}$$

$$\bar{\bar{\boldsymbol{v}}}_j^{n+1} = a\boldsymbol{v}_j^n + \left[b + \frac{1}{4}\Delta t\{C_1\zeta_1 + C_2\zeta_2 + C_3\}\right]\bar{\boldsymbol{v}}_j^{n+1} \tag{32}$$

$$\boldsymbol{v}_j^{n+1} = c\boldsymbol{v}_j^n + \left[d + \frac{2}{3}\Delta t\{C_1\zeta_1 + C_2\zeta_2 + C_3\}\right]\bar{\bar{\boldsymbol{v}}}_j^{n+1} \tag{33}$$

Theorem: The proposed scheme (31)-(33) converges conditionally for vectored matrix Eq. (30).
Proof: In order to proof this Theorem consider the error equation for Eq. (27) as:

$$\bar{\boldsymbol{\varsigma}}_j^{n+1} = \boldsymbol{\varsigma}_j^n e^{1.5\Delta t} + \frac{(e^{a_1\Delta t}-1)}{a_1}\{C_1\zeta_1\,\boldsymbol{\varsigma}_j^n + C_2\zeta_2\,\boldsymbol{\varsigma}_j^n + C_3\boldsymbol{\varsigma}_j^n - a_1\boldsymbol{\varsigma}_j^n\} \tag{34}$$

$$\bar{\bar{\boldsymbol{\varsigma}}}_j^{n+1} = a\boldsymbol{\varsigma}_j^n + b\bar{\boldsymbol{\varsigma}}_j^{n+1} + \frac{1}{4}\Delta t\{C_1\zeta_1\,\bar{\boldsymbol{\varsigma}}_j^{n+1} + C_2\zeta_2\,\bar{\boldsymbol{\varsigma}}_j^{n+1} + C_3\bar{\boldsymbol{\varsigma}}_j^{n+1}\} \tag{35}$$

$$\boldsymbol{\varsigma}_j^{n+1} = c\boldsymbol{\varsigma}_j^n + d\bar{\bar{\boldsymbol{\varsigma}}}_j^{n+1} + \frac{2}{3}\Delta t\{C_1\zeta_1\,\bar{\bar{\boldsymbol{\varsigma}}}_j^{n+1} + C_2\zeta_2\,\bar{\bar{\boldsymbol{\varsigma}}}_j^{n+1} + C_3\bar{\bar{\boldsymbol{\varsigma}}}_j^{n+1}\} \tag{36}$$

Applying a norm $\|\cdot\|_\infty$ on first stage of Eq. (34) in the form

$$\bar{\varsigma}^{n+1} \le \varsigma^n e^{1.5\Delta t} + \frac{(e^{a_1\Delta t}-1)}{a_1}\{\|C_1\zeta_1\|_\infty + \|C_2\zeta_2\|_\infty + \|C_3\|_\infty + a_1\}\varsigma^n \tag{37}$$

Inequality (37) can be written as

$$\bar{\varsigma}^{n+1} \le \beta_2\varsigma^n \tag{38}$$

Where $\beta_2 = e^{a_1\Delta t} + \frac{(e^{a_1\Delta t}-1)}{a_1}\{\|C_1\zeta_1\|_\infty + \|C_2\zeta_2\|_\infty + \|C_3\|_\infty + a_1\}$.
Applying norm $\|\cdot\|_\infty$ on Eq. (35) as yields

$$\bar{\bar{\varsigma}}^{n+1} \le a\varsigma^n + b\bar{\varsigma}^{n+1} + \frac{1}{4}\Delta t\{\|C_1\zeta_1\|_\infty + \|C_2\zeta_2\|_\infty + \|C_3\|_\infty\}\bar{\varsigma}^{n+1} = a\varsigma^n + \beta_3\bar{\varsigma}^{n+1} \tag{39}$$

where $\beta_3 = b + \frac{1}{4}\Delta t\{\|C_1\zeta_1\|_\infty + \|C_2\zeta_2\|_\infty + \|C_3\|_\infty\}$.
Inequality (39) can be re written as

$$\bar{\bar{\varsigma}}^{n+1} \le a\varsigma^n + \beta_3\beta_2\varsigma^n = \beta_4\varsigma^n \tag{40}$$

where $\beta_4 = a + \beta_2\beta_3$.
Similarly by applying a norm $\|\cdot\|_\infty$ to third error equation of the scheme (36), it gives

$$\varsigma^{n+1} \le c\varsigma^n + d\bar{\bar{\varsigma}}^{n+1} + \frac{2}{3}\Delta t\{\|C_1\zeta_1\|_\infty + \|C_2\zeta_2\|_\infty + \|C_3\|_\infty\}\bar{\bar{\varsigma}}^{n+1} \tag{41}$$

Inequality (41) can be re-written as

$$\varsigma^{n+1} \le c\varsigma^n + \beta_5\bar{\bar{\varsigma}}^{n+1} + P\big(O((\Delta t)^3, (\Delta y)^6)\big) \tag{42}$$

Substituting inequality (40) into inequality (42), it takes the form

$$\varsigma^{n+1} \le c\varsigma^n + \beta_5\beta_4\varsigma^n + P\big(O((\Delta t)^3, (\Delta y)^6)\big) = \beta_6\varsigma^n + P\big(O((\Delta t)^3, (\Delta y)^6)\big) \tag{43}$$

where $\beta_6 = c + \beta_4\beta_5$.
Let $n = 0$ in inequality (43), it yields

$$\varsigma^1 \le \beta_6\varsigma^0 + P\big(O((\Delta t)^3, (\Delta y)^6)\big) \tag{44}$$

Since $\varsigma^0 = 0$ so inequality (44) takes the form

$$\varsigma^1 \le P(0((\Delta t)^3, (\Delta y)^6)) \tag{45}$$

Now let $n = 1$ in inequality (43) it yields

$$\varsigma^2 \le \beta_6\varsigma^1 + P(0((\Delta t)^3, (\Delta y)^6)) \tag{46}$$

Using inequality (45) in (46) it results in

$$\varsigma^2 \le (1 + \beta_6)P(0((\Delta t)^3, (\Delta y)^6)) \tag{47}$$

If this is continuous then for finite n

$$\varsigma^n \leq (1+\beta_6+\cdots+\beta_6^{n-1})P(0((\Delta t)^3,(\Delta y)^6)) = \left(\frac{1-\beta_6^n}{1-\beta_6}\right)P(0((\Delta t)^3,(\Delta y)^6)) \tag{48}$$

By taking limit as $n \to \infty$ in (44) the infinite geometric series $\ldots+\beta_6^n+\cdots+\beta_6+1$ will converge if $|\beta_6|<1$.

Mathematical Model: We consider the unsteady, one-dimensional incompressible flow of an Eyring–Prandtl fluid through a porous medium over a Riga plate, with heat and mass transfer, viscous dissipation, and mixed convection. The streamwise velocity $u(t,y)$ varies only in the wall-normal coordinate y^*; the momentum balance couples temporal acceleration to the divergence of the Eyring–Prandtl shear stress the streamwise Lorentz body force from the Riga plate and porous resistance expressed by linear Darcy drag $-\frac{\mu}{K}u^*$ and nonlinear Forchheimer drag $-\frac{\rho F}{\sqrt{K}}u^{*2}$. Mixed convection is modeled under the Boussinesq approximation by adding buoyancy forces $g\beta_T(T-T_\infty)+g\beta_C(C-C_\infty)$ in the momentum equation, so thermal and solutal buoyancy couple the momentum, energy and species fields. Heat transfer is described by the unsteady energy equation with thermal diffusion and viscous dissipation arising from the Eyring–Prandtl stress, while mass transfer follows the unsteady species diffusion equation (with optional reaction/source terms). The wall at $y^*=0$ is maintained at prescribed velocity $u^*(t,0)=u_w+L_s\frac{\partial u^*}{\partial y^*}$, convective boundary temperature $-k\frac{\partial T(t,0)}{\partial y^*}=h_f(T(t,0)-T_w)$ and concentration $C(t,0)=C_w$; far from the plate $u^*\to 0, T\to T_\infty, C\to C_\infty$ as $y^*\to\infty$. Initially the fluid is quiescent and uniform in temperature and concentration. The objective is to determine the transient distributions $u^*(t,y), T(t,y), C(t,y)$ under the combined influences of Eyring–Prandtl rheology, Riga electromagnetic forcing, Darcy–Forchheimer porous resistance, thermal and solutal buoyancy (mixed convection), molecular diffusion, and viscous dissipation. The governing equations can be written as:

$$\rho\frac{\partial u^*}{\partial t^*}=\frac{\bar{\beta}}{\bar{C}}\left(\frac{\frac{\partial^2 u^*}{\partial y^{*2}}}{\sqrt{1+\left(\frac{1}{\bar{C}}\frac{\partial u^*}{\partial y^*}\right)^2}}\right)-\frac{\mu}{K}u-\frac{\rho C_f}{\sqrt{K}}u^{*2}+g\beta_T(T-T_\infty)+\beta_C(C-C_\infty)+\frac{\pi j_\circ M_\circ}{8\rho}e^{-\left(\frac{\pi}{a_1}\right)y^*} \tag{49}$$

$$\frac{\partial T}{\partial t^*}=\bar{\alpha}\frac{\partial^2 T}{\partial y^{*2}}+\frac{\bar{\beta}}{\rho C_p}\sinh^{-1}\left(\frac{1}{\bar{C}}\frac{\partial u^*}{\partial y^*}\right)\frac{\partial u^*}{\partial y^*} \tag{50}$$

$$\frac{\partial C}{\partial t^*}=D\frac{\partial^2 C}{\partial y^{*2}}-k_1(C-C_\infty) \tag{51}$$

Subject to initial and boundary conditions

$$\left.\begin{gathered} u^*(0,y^*)=0, T(0,y^*)=0, C(0,y^*)=0 \\ u^*(t^*,0)=u_w+L_s\frac{\partial u^*}{\partial y^*}\Big|_{y^*=0}, -k\frac{\partial T}{\partial y^*}\Big|_{y^*=0}=h_f(T(t^*,0)-T_w), C(t^*,0)=C_w \\ u^*(t^*,y^*\to\infty)\to 0, T(t^*,y^*\to\infty)\to 0, C(t^*,y^*\to\infty)\to 0 \end{gathered}\right\} \tag{52}$$

Where u^* is the horizontal component of velocity, T is the temperature and C is concentration, β_T and β_C are thermal and solutan expansion, $\bar{\beta}$ is the stress parameter, $\bar{C}$ is the rate parameter, $j_\circ$ is the current density, $M_\circ$is a magnetic field strength, a_1 width of electrodes, g is gravity, K is the permeability of the porous medium, C_f is dimensionless constant representing inertial drag in the porous medium, ρ is density, $\bar{\alpha}$ is thermal diffusivity, D is mass diffusivity and k_1 is dimensional reaction rate parameter, h_f is heat transfer coefficient and k is thermal conductivity

Using the transformations

$$\left.y=\frac{y^*}{L}, u=\frac{u^*}{u_w}, t=\frac{u_w t^*}{L}, \theta=\frac{T-T_\infty}{T_w-T_\infty}, \phi=\frac{C-C_\infty}{C_w-C_\infty}\right\} \tag{53}$$

The governing equations (49)-(52) are reduced to following dimensionless partial differential equations

$$\frac{\partial u}{\partial t}=\frac{1}{R_e}\left(\frac{u_{yy}}{\sqrt{1+S^2u_y^2}}\right)-\frac{1}{R_eD_a}u-F_ru^2+\frac{G\gamma_L}{R_e^2}\theta+\frac{G\gamma_C}{R_e^2}\phi+e^{-\lambda y} \tag{54}$$

$$\frac{\partial\theta}{\partial t}=\frac{1}{P_rR_e}\frac{\partial^2\theta}{\partial y^2}+\frac{E_c}{R_eS}\sinh^{-1}(Su_y) \tag{55}$$

$$\frac{\partial\phi}{\partial t}=\frac{1}{R_eS_c}\frac{\partial^2\phi}{\partial y^2}-\gamma\phi \tag{56}$$

and the dimensionless initial and boundary conditions take the form

$$\left.\begin{gathered} u(0,y)=0,\theta(0,y)=0,\phi(0,y)=0 \\ u(t,0)=1+\Lambda\frac{\partial u}{\partial y}\Big|_{y=0},\frac{\partial\theta}{\partial y}\Big|_{y=0}=B_i(1-\theta(t,0)),\phi(t,0)=1 \\ u(t,y\to\infty)\to 0,\theta(t,y\to\infty)\to 0,\phi(t,y\to\infty)\to 0 \end{gathered}\right\} \tag{57}$$

Where D_a is Darcy number, F_r is Forchheimer number, S is Eyring (shear) number, R_e is Reynolds number, M is dimensionless electromagnetic Riga parameter, λ is dimensionless decay rate of Lorentz force in the y- direction, G_{γ_L} and G_{γ_C} are respectively thermal and solutal Grashof number, P_r is Prandtl number, E_c is Eckert number, S_c is Schnidt number, γ is dimensionless reaction rate parameter, and Λ is velocity slip and B_i is Boit number which are defined as:

$$D_a=\frac{K}{L^2},F_r=\frac{C_fL}{\sqrt{K}},S=\frac{u_w}{\bar{C}L},R_e=\frac{u_wL}{\nu}=\frac{\rho u_w L\bar{C}}{\bar{\beta}},M=\frac{\pi j_\circ M_\circ L}{8\rho u_w^2},\lambda=\frac{\pi}{a_1}L,G_{\gamma_L}=\frac{g\beta_T(T_W-T_\infty)}{\nu^2},G_{\gamma_C}=\frac{g\beta_C(C_W-C_\infty)}{\nu^2},P_r=\frac{\nu}{\bar{\alpha}},E_c=\frac{u_w^2}{C_p(T_W-T_\infty)},S_c=\frac{\nu}{D},\gamma=\frac{k_1L}{u_w},\Lambda=\frac{L_s}{L},B_i=\frac{h_\lambda}{Lk}$$

The dimensionless skin friction coefficients, local Nusselt and local Sherwood number are written as:

$$\left.\begin{aligned} \bar{C}_f &= \frac{1}{R_eS}\sinh^{-1}\left(Su_y\big|_{y=0}\right) \\ N_{u_L} &= -\frac{\partial\theta}{\partial y}\Big|_{y=0} \\ S_{h_L} &= -\frac{\partial\phi}{\partial y}\Big|_{y=0} \end{aligned}\right\} \tag{58}$$

The discretization of Eq. (54) using the proposed scheme it takes the form:

$$\bar{u}_j^{n+1}=u_j^ne^{a_1\Delta t}+\frac{\left(e^{a_1\Delta t}-1\right)}{a_1}\left\{\frac{\frac{1}{R_e}\left(A_2^{-1}B_2\,u_j^n\right)}{\sqrt{1+S^2\left(A_1^{-1}B_1\,u_j^n\right)^2}}-\frac{1}{R_eD_a}\,u_j^n-F_r\left(u_j^n\right)^2+\frac{G_{\gamma_L}}{R_e^2}\,\theta_j^n+\frac{G_{\gamma_C}}{R_e^2}\,\phi_j^n+Me^{-\lambda y_j}-a_1u_j^n\right\} \tag{59}$$

$$\bar{\bar{u}}_j^{n+1}=au_j^n+b\bar{u}_j^{n+1}+\frac{1}{4}\Delta t\left\{\frac{\frac{1}{R_e}\left(A_2^{-1}B_2\,\bar{u}_j^{n+1}\right)}{\sqrt{1+S^2\left(A_1^{-1}B_1\,\bar{u}_j^{n+1}\right)^2}}-\frac{1}{R_eD_a}\,\bar{u}_j^{n+1}-F_r\left(\bar{u}_j^{n+1}\right)^2+\frac{G_{\gamma_L}}{R_e^2}\,\bar{\theta}_j^{n+1}+\frac{G_{\gamma_C}}{R_e^2}\,\bar{\phi}_j^{n+1}+Me^{-\lambda y_j}\right\} \tag{60}$$

$$u_j^{n+1}=cu_j^n+d\bar{\bar{u}}_j^{n+1}+\frac{2}{3}\Delta t\left\{\frac{\frac{1}{R_e}\left(A_2^{-1}B_2\,\bar{\bar{u}}_j^{n+1}\right)}{\sqrt{1+S^2\left(A_1^{-1}B_1\,\bar{\bar{u}}_j^{n+1}\right)^2}}-\frac{1}{R_eD_a}\,\bar{\bar{u}}_j^{n+1}-F_r\left(\bar{\bar{u}}_j^{n+1}\right)^2+\frac{G_{\gamma_L}}{R_e^2}\,\bar{\bar{\theta}}_j^{n+1}+\frac{G_{\gamma_C}}{R_e^2}\,\bar{\bar{\phi}}_j^{n+1}+Me^{-\lambda y_j}\right\} \tag{61}$$

RESULTS AND DISCUSSION

A third-order accurate time-stepping scheme is developed for the numerical solution of partial differential equations. The method is specifically designed for discretizing only the time-dependent term of the governing equation, and its accuracy is confirmed through its construction, where the third-order time derivative naturally cancels in the Taylor series expansion. For the spatial discretization, a compact high-order finite-difference scheme is employed, providing sixth-order accuracy in space. The overall scheme is conditionally stable, implying that the time step, spatial step, and the physical parameters appearing in the governing equation must satisfy a prescribed stability condition. When these restrictions are met, the numerical solution remains stable; otherwise, instability is expected. A notable benefit of using an explicit scheme is that it avoids the need for linearization, enabling direct treatment of nonlinear partial differential equations without any iterative procedure for convergence.

The influence of Eyring parameter on velocity profile is shown in Fig. 2. The velocity profile declines by raising Eyring number. Increasing the Eyring number means the fluid resists deformation more at low shear rates. Since most of the velocity in internal flows depends on the balance between pressure gradient and viscous resistance, this increased resistance lowers the velocity everywhere**.** The effect of Darcy number on velocity profile is depicted in Fig. 3. The velocity profile increases by growing Darcy number. Small Darcy number produces very low permeability and so porous medium strongly resists the flow. Large Darcy number gives high permeability and this leads to porous medium offers little resistance. Thus, increasing Darcy number reduces the Darcy resistance term in the momentum equation.

The effect of Forchheimer number on velocity profile is shown in Fig. 4. The velocity profile declines by growing Forchheimer number. Darcy drag (linear) dominates at low speeds. When velocity increases, inertial forces inside the porous medium become important. The Forchheimer term grows faster than velocity (proportional to u^2). Increasing the Forchheimer parameter amplifies this additional nonlinear drag, so the flow slows down. The velocity slip parameter on velocity profile is shown in Fig. 5. Velocity profile decays by enhancing velocity slip parameter. Increasing the

Forchheimer parameter enhances the nonlinear inertial drag inside the porous medium. This additional resistance reduces the fluid velocity, causing the velocity profile to decline even under slip-flow conditions for an Eyring–Prandtl fluid. Fig. 6 deliberates the effect of Eckert number on temperature profile. Temperature profile grows by enhancing Eckert number. Increasing the Eckert number enhances viscous dissipation, producing additional internal heat, which raises the temperature profile. The influence of reaction rate parameter on concentration profile is shown in Fig. 7.

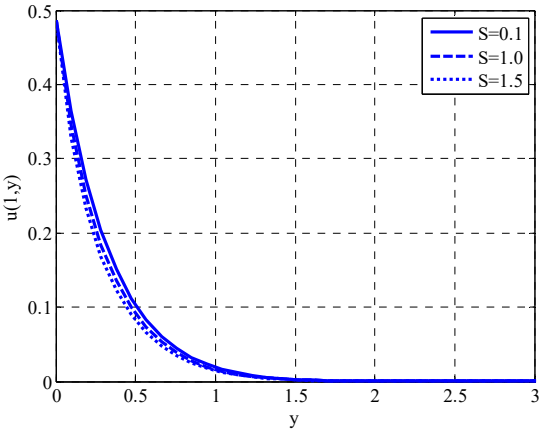

Figure 2. Effect of Eyring number on velocity profile using $Da = 0.1, Fr = 0.1, M = 0.1, \lambda = 3, \Lambda = 0.1, Re = 5, Gr_T = 0.1, Gr_C = 0.1, Ec = 5, Pr = 3, Sc = 3, \gamma = 0.9, Bi = 0.1$

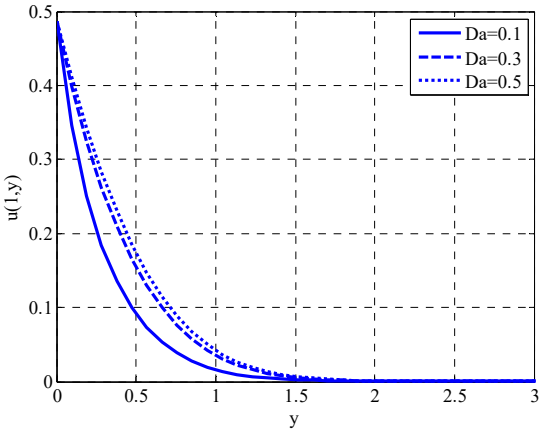

Figure 3. Effect of Darcy number on velocity profile using $S = 1, Fr = 0.1, M = 0.1, \lambda = 3, \Lambda = 0.1, Re = 5, Gr_T = 0.1, Gr_C = 0.1, Ec = 5, Pr = 3, Sc = 3, \gamma = 0.9, Bi = 0.1$

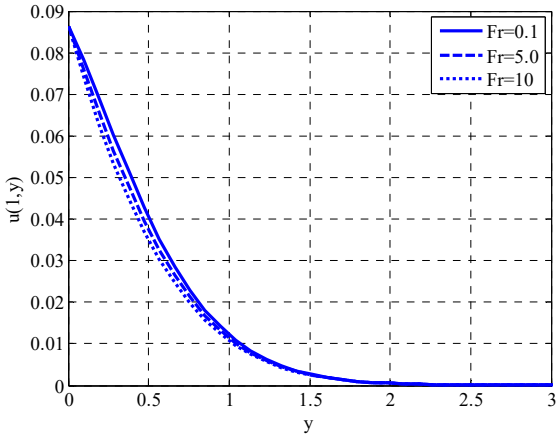

Figure 4. Effect of Forchheimer number on velocity profile using $S = 1, Da = 0.3, M = 0.1, \lambda = 3, \Lambda = 1, Re = 5, Gr_T = 0.1, Gr_C = 0.1, Ec = 5, Pr = 3, Sc = 3, \gamma = 0.9, Bi = 5$

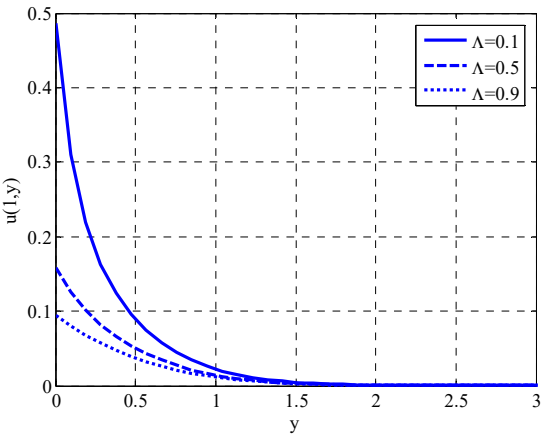

Figure 5. Effect of velocity slip parameter on velocity profile using $S = 1, Da = 0.3, M = 0.1, \lambda = 3, \mathrm{Fr} = 10, Re = 5, Gr_T = 0.1, Gr_C = 0.1, Ec = 5, Pr = 3, Sc = 3, \gamma = 0.9, Bi = 5$

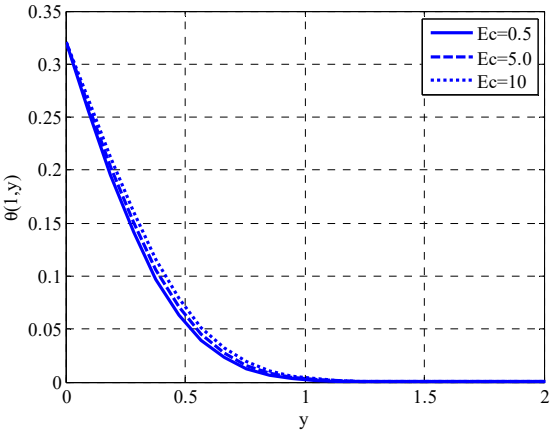

Figure 6. Effect of Eckert number on temperature profile using $S = 1, Da = 0.3, M = 0.1, \lambda = 3, \mathrm{Fr} = 10, Re = 5, Gr_T = 0.1, Gr_C = 0.1, \Lambda = 0.9, Pr = 3, Sc = 3, \gamma = 0.9, Bi = 5$

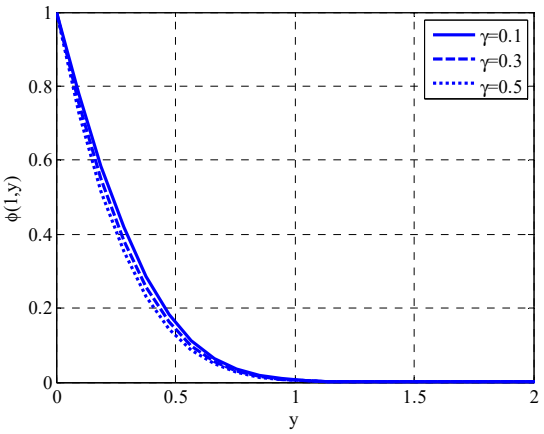

Figure 7. Effect of reaction rate parameter on concentration profile using $S = 1, Da = 0.3, M = 0.1, \lambda = 3, \mathrm{Fr} = 10, Re = 5, Gr_T = 0.1, Gr_C = 0.1, \Lambda = 0.9, Pr = 3, Sc = 3, Ec = 10, Bi = 5$

Concentration profile declines by enhancing reaction rate parameter. Increasing the reaction-rate parameter enhances species consumption, thereby reducing concentration and lowering the concentration profile. For the oscillatory motion of the Riga plate, the influence of velocity slip on the skin-friction coefficient is illustrated in Fig. 8. The results indicate an oscillatory pattern, where negative values of the skin-friction coefficient signify that the fluid near the wall momentarily moves in the direction opposite to the mean flow. The effect of the Biot number on the local Nusselt number is presented in Fig. 9, showing that heat transfer at the wall strengthens as the Biot number increases. A larger Biot number corresponds to a steeper temperature gradient at the surface, resulting in more efficient heat exchange between the plate and the fluid, and consequently a higher local Nusselt number. The oscillatory nature of the Nusselt number becomes more pronounced at elevated Eckert numbers, indicating that as viscous dissipation intensifies, the oscillatory behavior shifts from the velocity field toward the temperature field. The impact of the reaction-rate parameter on the local Sherwood number is depicted in Fig. 10; an increase in the reaction-rate parameter enhances the Sherwood number. This behavior is associated with a reduction in concentration near the wall, which produces a steeper concentration gradient and, therefore, greater mass transfer.

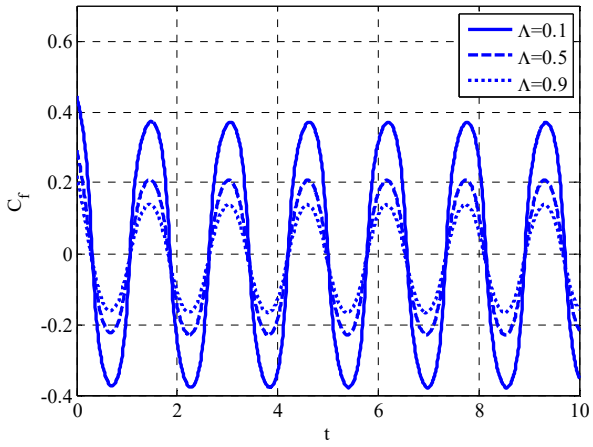

Figure 8. Effect of velocity slip parameter on skin friction coefficient using $S = 1, Da = 0.3, M = 0.1, \lambda = 3, \mathrm{Fr} = 2, Re = 5, Gr_T = 0.1, Gr_C = 0.1, \gamma = 0.5, Pr = 3, Sc = 3, Ec = 10, Bi = 9, N_y = 75, N_t = 1050,\ u(t,0) = cos(4t) + \Lambda\frac{\partial u}{\partial y}$

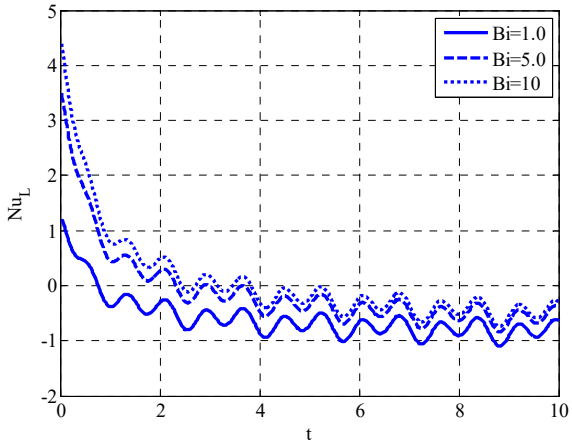

Figure 9. Effect of Biot number on local Nusselt number using $S = 1, Da = 0.3, M = 0.1, \lambda = 3, \mathrm{Fr} = 2, Re = 5, Gr_T = 0.1, Gr_C = 0.1, \gamma = 0.5, Pr = 3, Sc = 3, Ec = 10, \Lambda = 0.9, N_y = 75, N_t = 1050,\ u(t,0) = cos(4t) + \Lambda\frac{\partial u}{\partial y}$

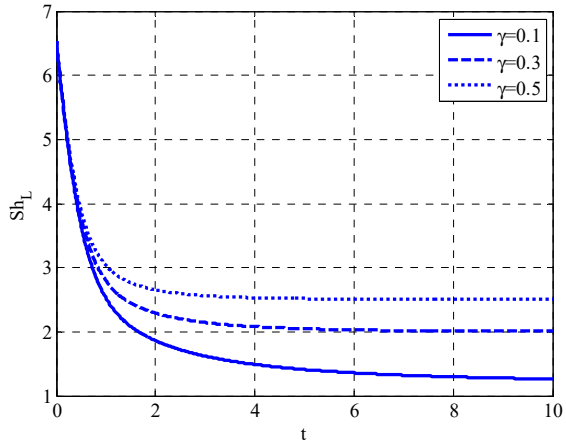

Figure 10. Effect of reaction rate parameter on local Sherwood number using $S = 1, Da = 0.3, M = 0.1, \lambda = 3, \mathrm{Fr} = 2, Re = 5, Gr_T = 0.1, Gr_C = 0.1, \mathrm{Bi} = 9, Pr = 3, Sc = 3, Ec = 10, \Lambda = 0.9, N_y = 75, N_t = 1050,\ u(t,0) = cos(4t) + \Lambda\frac{\partial u}{\partial y}$

Figures 11–13 display contour plots of velocity, temperature, and concentration fields, along with their respective error distributions. Numerical results are also obtained using the MATLAB **pdepe** solver, which serves as a reference solution in the absence of an analytical benchmark. The error contours are constructed by computing the absolute difference between the solutions generated by the proposed numerical scheme and those obtained from **pdepe**. Figure 14 summarizes the computational time required by the proposed method for the present problem.

For making comparison of the schemes,first stage of propsed scheme using $a_1 = -30$ is used and second and third stages of existing third order Runge-Kutta scheme are used. Existing third order Runge-Kutta scheme is given as

$$\bar{g}_j^{n+1} = g_j^n + \Delta t \left.\frac{\partial g}{\partial t}\right|_j^n$$

$$\bar{\bar{g}}_j^{n+1} = \frac{3}{4} g_j^n + \frac{1}{4} \bar{g}_j^{n+1} + \frac{1}{4} \Delta t \left.\frac{\partial \bar{g}}{\partial t}\right|_j^{n+1}$$

$$g_j^{n+1} = \frac{1}{3} g_j^n + \frac{2}{3} \bar{\bar{g}}_j^{n+1} + \frac{2}{3} \Delta t \left.\frac{\partial \bar{\bar{g}}}{\partial t}\right|_j^{n+1}$$

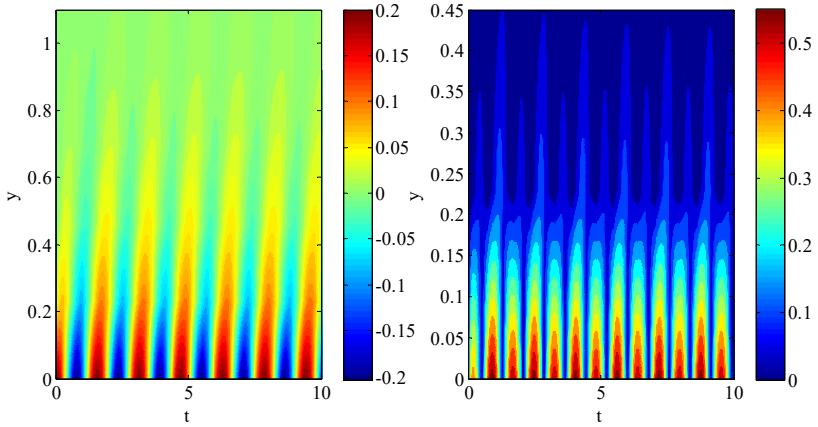

Figure 11. Contour plots for velocity profile and its error using $S = 1, Da = 0.3, M = 0.1, \lambda = 3, \mathrm{Fr} = 2, Re = 5, Gr_T = 0.1, Gr_C = 0.1, \mathrm{Bi} = 9, Pr = 3, \gamma = 0.5, Sc = 3, Ec = 10, \Lambda = 0.9, N_y = 75, N_t = 1050,\ u(t,0) = cos(4t) + \Lambda \frac{\partial u}{\partial y}$

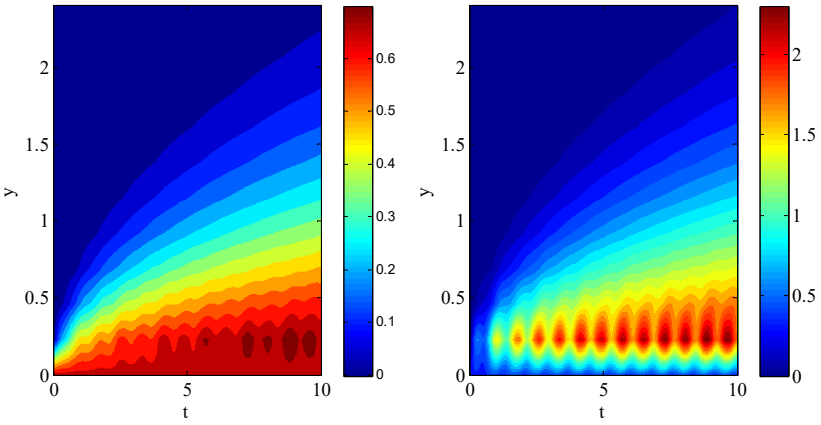

Figure 12. Contour plots for temperature profile and its error using $S = 1, Da = 0.3, M = 0.1, \lambda = 3, \mathrm{Fr} = 2, Re = 5, Gr_T = 0.1, Gr_C = 0.1, \mathrm{Bi} = 9, Pr = 3, \gamma = 0.5, Sc = 3, Ec = 10, \Lambda = 0.9, N_y = 75, N_t = 1050,\ u(t,0) = cos(4t) + \Lambda \frac{\partial u}{\partial y}$

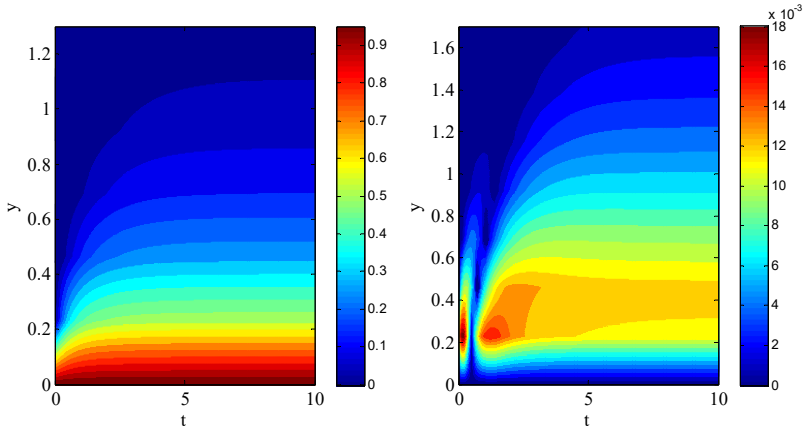

Figure 13. Contour plots for concentration profile and its error using $S = 1, Da = 0.3, M = 0.1, \lambda = 3, \mathrm{Fr} = 2, Re = 5, Gr_T = 0.1, Gr_C = 0.1, \mathrm{Bi} = 9, Pr = 3, \gamma = 0.5, Sc = 3, Ec = 10, \Lambda = 0.9, N_y = 75, N_t = 1050,\ u(t,0) = cos(4t) + \Lambda \frac{\partial u}{\partial y}$

Fig. 15 shows the comparison of the two schemes for second example of convection diffusion problem given in [25]. The error produced by the proposed scheme is less than that obtained by existing third order Runge-Kutta method. The space dependent terms are discretized by the second order central difference scheme. The error is identified by calculating the norm of the difference between the numerical and exact solutions.

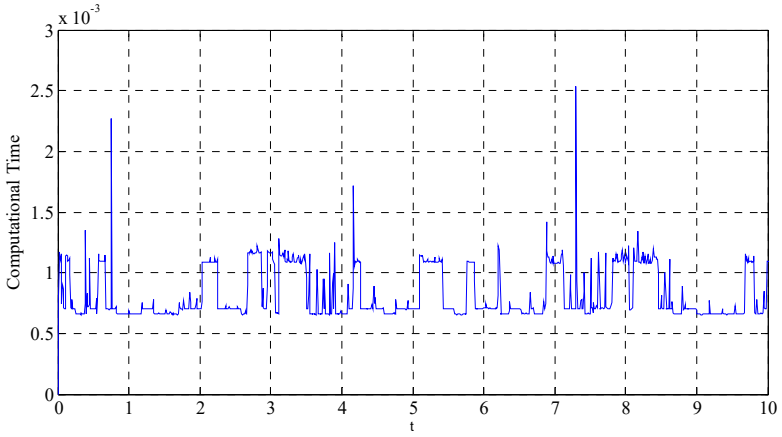

Figure 14. Computational time of the proposed scheme using $S = 1, Da = 0.3, M = 0.1, \lambda = 3, \mathrm{Fr} = 0.1, Re = 5, Gr_T = 0.1, Gr_C = 0.1, \mathrm{Bi} = 5, Pr = 3, \gamma = 0.9, Sc = 3, Ec = 5, \Lambda = 1, N_y = 75, N_t = 1050,\ u(t,0) = cos(4t) + \Lambda\frac{\partial u}{\partial y}$

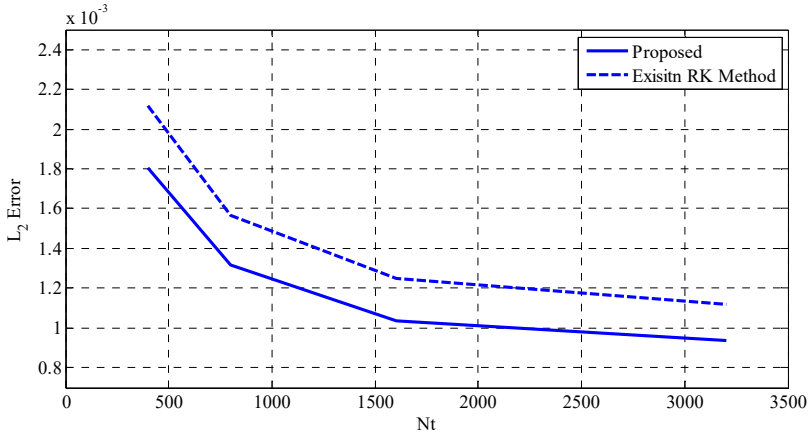

Figure 15. Comparison of two schemes using $t_f = 0.05, N_x = 50, N_t = 400, 800, 1600, 3200$

Table 1 & 2 show grid convergence analysis of proposed and existing Runge-Kutta methods for solving Stokes first problem. Time discretization is done with existing and proposed Runge-Kutta methods. Propsoed scheme performs better than existing third order Runge-Kutta method. Again, for making this comparison, combination of first stage of proposed scheme and second and third stages of third order existing Runge-Kutta method is applied.

Table 1. Grid convergence analysis for Stoeks first problem using $\Delta t = 0.0020$

Δx	a	L_2 Error	
		Proposed	Existing RK
0.3684	40	0.1537	0.1559
0.2414	30	0.1012	0.1021
0.1795	20	0.0756	0.0761
0.1429	9	0.0601	0.0604
0.1186	7	0.0467	0.0469

Table 2. Convergence analysis for Stoeks first problem using $\Delta x = 0.1429$

Δt	a	L_2 Error	
		Proposed	Existing RK
0.0112	−320	0.7680	Diverges
0.0092	−180	0.5885	Diverges
0.0078	−30	0.1320	Diverges
0.0067	3	0.0258	0.0260
0.0059	5	0.0238	0.0240

CONCLUSIONS

A numerical scheme was modified by combining exponential integrator and Runge-Kutta method. Instead of using Euler method in first stage of Runge-Kutta method, exponential integrator is considered. The weights in the numerical scheme for the second and third stages are chosen using the Taylor series. Since, the terms of Taylor series until third order derivative are cancelled out, therefore theoretically scheme provided third order accurate solution in time. For discretizing space dependent terms, compact scheme is chosen. The compact scheme provided high order accuracy in space. The scheme has been applied to problem of flow over the Rige plate and the concluding points can be expressed as

- The velocity profile declined by increasing Eyring number and velocity profile was escalated by incrementing the Darcy number
- The local Nusselt number increases with rising Biot number.
- Local Sherwood number raised by growing reaction rate parameter.
- One of the proposed scheme performed better than existing Runge-Kutta scheme on specific time and space step sizes.

Declarations

Ethical approval and consent to participate

Ethics and Consent to Participate declarations: not applicable.

Consent to Publication

Consent to Publish declaration: not applicable.

Competing interests

The authors declare no competing interests.

Clinical trial number

Clinical trial number: not applicable.

Author Contribution

Writing, Original Draft, Software, Methodology, Analysis Y.N, Writing Original Draft and Funding M.S.A and K.A, Visualization M.M

Acknowledgement: The authors wish to express their gratitude to Prince Sultan University for facilitating the publication of this article through the Theoretical and Applied Sciences Lab.

Funding Statement: The authors would like to acknowledge the support of Prince Sultan University for paying the article processing charges (APC) of this publication.

ORCID

Yasir Nawaz, https://orcid.org/0000-0002-7048-574X; **Muhammad Shoaib Arif,** https://orcid.org/0000-0002-6009-5609
Muavia Mansoor, https://orcid.org/0009-0003-8803-6170; **Kamal Abodayeh,** https://orcid.org/0000-0003-0735-6520

REFERENCES

[1] Y. Nawaz, "Variational iteration method and homotopy perturbation method for fourth-order fractional integro-differential equations.," Computers & Mathematics with Applications, **61**(8), 2330-2341 (2011). https://doi.org/10.1016/j.camwa.2010.10.004

[2] Y. Nawaz, "Development of new and modified numerical methods for hyperbolic conservation laws," Numerical Heat Transfer, Part B: Fundamentals, **76**(4), 224-251 (2019). https://doi.org/10.1080/10407790.2019.1665443

[3] J. C. Butcher, *Numerical Methods for Ordinary Differential Equations*, 2nd ed. (John Wiley & Sons, 2008).

[4] E. Hairer, & G. Wanner, *Solving Ordinary Differential Equations II: Stiff and Differential-Algebraic Problems*, 2nd ed. (Springer Berlin, Heidelberg, 1996).

[5] J. Martín-Vaquero, & B. Janssen, "Second-order stabilized explicit Runge–Kutta methods for stiff problems," Comput. Phys. Commun. **180**, 1802–1810 (2009). https://doi.org/10.1016/j.cpc.2009.05.006

[6] L.M. Skvortsov, "Explicit stabilized Runge-Kutta methods," Computational Mathematics and Mathematical Physics, **51**(7), 1153-1166 (2011). https://doi.org/10.1134/s0965542511070165

[7] G.-D. Hu, and Z. Wang, "A modified Runge–Kutta method for increasing stability properties," Journal of Computational and Applied Mathematics, **441**, 115698 (2024). https://doi.org/10.1016/j.cam.2023.115698

[8] A. Abdulle, "Fourth order Chebyshev methods with recurrence relation," SIAM Journal on Scientific Computing, **23**(6), 2041-2054 (2002). https://doi.org/10.1137/s1064827500379549

[9] B. Kleefeld, and J. Martín-Vaquero, "SERK2v2: A new second-order stabilized explicit Runge-Kutta method for stiff problems," Numerical Methods for Partial Differential Equations, **29**(1), 170-185 (2013). https://doi.org/10.1002/num.21704

[10] M. Z. Liu, M. H. Song, and Z. W. Yang, "Stability of Runge–Kutta methods in the numerical solution of equation u′(t)= au (t)+ a0u ([t])," Journal of Computational and Applied Mathematics, **166**(2), 361-370 (2004). https://doi.org/10.1016/j.cam.2003.04.002

[11] R. K. Alexander, "Stability of Runge–Kutta methods for stiff ordinary differential equations," SIAM journal on numerical analysis, **31**(4), 1147-1168 (1994). https://doi.org/10.1137/0731060

[12] E. C. Emmanuel, N. Chidinma, and N. Ifeoma, "On Review of the Convergence Analyses of the Runge Kutta Fixed Point Iterative Methods," Asian Journal of Pure and Applied Mathematics, **2**(1), 20-44 (2020).

[13] A. V. Shenoy, "Darcy-Forchheimer natural, forced and mixed convection heat transfer in non-Newtonian power-law fluid-saturated porous media," Transport in porous media, **11**(3), 219-241 (1993). https://doi.org/10.1007/bf00614813
[14] Z. Shah, A. Shafiq, M. Rooman, M. H. Alshehri, and E. Bonyahet, "Darcy Forchhemier Prandtl-Eyring nanofluid flow with variable heat transfer and entropy generation using Cattaneo-Christov heat flux model: Statistical approach," Case Studies in Thermal Engineering, **49**, 103376 (2023). https://doi.org/10.1016/j.csite.2023.103376
[15] S. Chaudhary, and K. K. Chouhan, "Darcy-Forchheimer flow of Prandtl-Eyring nanofluid subjected to a Riga plate of varying thickness along with Brownian diffusion, thermophoresis and non-uniform heat source/sink effects," Numerical Heat Transfer, Part A: Applications, **84**(7), 732-759 (2023). https://doi.org/10.1080/10407782.2022.2154725
[16] Z. Ullah, I. Ullah, G. Zaman, H. Khan, and T. Muhammad, "Mathematical modeling and thermodynamics of Prandtl–Eyring fluid with radiation effect: a numerical approach," Scientific Reports, **11**(1), 22201 (2021). https://doi.org/10.1038/s41598-021-01463-4
[17] A. Baidya, S. Mukhopadhyay, and G. C. Layek, "Melting heat transfer in Eyring–Prandtl fluid flow past a nonlinear stretching sheet in presence of slip," Canadian Journal of Physics, **103**(10), 968-977 (2025).
[18] M. Awais, T. Salahuddin, and S. Muhammad, "Effects of viscous dissipation and activation energy for the MHD Eyring-powell fluid flow with Darcy-Forchheimer and variable fluid properties," Ain Shams Engineering Journal, **15**(2), 102422 (2024). https://doi.org/10.1016/j.asej.2023.102422
[19] A. Ajibade, and P. O. Ojeagbase, "Effect of viscous dissipation on seady natural convection heat and mass transfer in a vertical channel with variable viscosity and thermal conductivity," Journal of Heat and Mass Transfer Research, **7**(2), 105-116 (2020). https://doi.org/10.1002/eng2.12268
[20] O. Mahitha, and V.K.A. Golla, "Magnetite/engine oil Casson nanofluid flow over a Riga plate with Atangana–Baleanu fractional derivative," Case Studies in Thermal Engineering, **52**, 103712 (2023). https://doi.org/10.1016/j.csite.2023.103712
[21] M. Bilal, F. Maiz, M. Farooq, H. Ahmad, M. Kh. Nasrat, and H. A. Ghazwani, "Novel numerical and artificial neural computing with experimental validation towards unsteady micropolar nanofluid flow across a Riga plate," Scientific Reports, **15**(1), 759 (2025). https://doi.org/10.1038/s41598-024-84480-3
[22] R. Reyaz, A. Q. Mohamad, L. Y. Jiann, M. Saqib, and S. Shafie, "Presence of Riga plate on MHD Caputo Casson fluid: an analytical study," J. Adv. Res. Fluid Mech. Therm. Sci, **93**(2), 86-99 (2022). https://doi.org/10.37934/arfmts.93.2.8699
[23] J. Martin-Vaquero, and B. Janssen, "Second-order stabilized explicit Runge–Kutta methods for stiff problems," Computer Physics Communications, **180**(10), 1802-1810 (2009). https://doi.org/10.1016/j.cpc.2009.05.006
[24] J. Li, and Y.-T. Chen, *Computational partial differential equations using MATLAB®*, (CRC press, 2019).
[25] D. A. Koç, Y. Öztürk, and M. Gülsu, "A numerical algorithm for solving one-dimensional parabolic convection-diffusion equation," Journal of Taibah University for Science, **17**(1), 2204808, (2023). https://doi.org/10.1080/16583655.2023.2204808

МОДИФІКОВАНА СХЕМА РУНГЕ-КУТТИ ТА КОМПАКТНА ПРОСТОРОВА СХЕМА ДЛЯ ПОТОКУ РІДИНИ ПРАНДТЛЯ-ЕЙРІНГА ЗА МЕТОДАМИ ДАРСІ ФОРХГАЙМЕРА НАД РИГА ПЛАСТИНОЮ

Ясір Наваз[1], Мухаммад Шоайб Аріф[2], Муавія Мансур[3], Камал Абодайє[2]

[1]Кафедра математики, Факультет інженерії та обчислювальної техніки, Національний університет сучасних мов (NUML), Ісламабад, 44000, Пакистан

[2]Кафедра математики та природничих наук, Коледж природничих наук та гуманітарних наук, Університет Принца Султана, Ер-Ріяд, 11586, Саудівська Аравія

[3]Кафедра математики, Університет Ваха, Вах Кантт 47040, Пакистан

Запропоновано модифікацію існуючого методу Рунге-Кутти третього порядку. Схема є явною, а її перший етап складається з нестандартного знаменника, тоді як останні два етапи такі ж, як і у методу Рунге-Кутти. Для дискретизації просторово-залежних членів використовується компактна схема високого порядку. Запропонована схема з просторовою дискретизацією використовується для знаходження умови стійкості запропонованої схеми. Схема застосовується до безрозмірної моделі у вигляді диференціальних рівнянь з частинними похідними для ковзного потоку неньютонівської рідини над рига пластиною з тепло- та масообміном. За допомогою запропонованої схеми отримано різні типи графіків для профілів швидкості, температури та концентрації. Деякі результати, отримані за запропонованою схемою, порівнюються з результатами, отриманими за допомогою числового розв'язування за допомогою розв'язувача MATLAB PDEPE. Схема також порівнюється з існуючою схемою Рунге-Кутти третього порядку, і вона дає точніші результати, ніж існуюча схема, при певних розмірах кроку в часі та просторі.

Ключові слова: *гібридна схема; стійкість; конвергенція; ковзаючий потік; рідина Ейрінга-Прандтля*

East European Journal of Physics. 3. 470-477 (2026)
DOI:10.26565/2312-4334-2026-3-42 ISSN 2312-4334

ELECTROTHERMAL MODELING OF SELF-HEATING IN Si/GaAs p–n HETEROJUNCTIONS

D.A. Qalandarova[1]*, O. Kucharov[1], V. Rahimova[2], Z.K. Matyakubov[3], L.I. Ochilov[4], J.A. Xolbekov[5], K.G. Gaimnazarov[6], Kh.U. Kamalov[7], D.I. Davronov[8]

[1]*National Research University TIIAME, Tashkent, 100000, Uzbekistan*
[2]*Bukhara State Medical Institute named after Abu Ali ibn Sino: Bukhara 200126 Uzbekistan*
[3]*Urgench State University, Hamid Olimjon Street, 14, Urgench, 220100 Uzbekistan*
[4]*Bukhara State University, Bukhara 200117, Uzbekistan*
[5]*Department of Higher Mathematics, Tashkent State Technical University named after I. Karimov, Tashkent, 100174, Uzbekistan*
[6]*Gulistan State University, Gulistan, Uzbekistan*
[7]*Karakalpak State University: Nukus, Uzbekistan*
[8]*Department of Uzbek Language and Literature, Bukhara State Pedagogical Institute, Bukhara, Uzbekistan*
**Corresponding Author e-mail: dildora.qalandarova.90@gmail.com*
Received April 18, 2026; revised July 27, 2026; accepted August 13, 2026

This study develops a coupled electrothermal model for predicting self-heating, heat transport, and temperature-dependent junction behavior in Si/GaAs p–n heterojunctions under high-power operating conditions.The model couples electrical and thermal processes to investigate the influence of Joule heating, thermal conductivity, and temperature-dependent junction characteristics on device performance. The results show that heat generation is strongly localized near the heterointerface, where power densities of 10^6-10^8 $W \cdot m^{-3}$ produce temperature rises of 50–150 K and thermal gradients reaching 10^5–10^6 $K \cdot m^{-1}$. As the operating temperature increases from approximately 340 K to 400 K, the device exhibits a transition from weak to strongly nonlinear electrothermal behavior, accompanied by hotspot formation near the heterointerface at a position of approximately 40 μm from the device edge. The p-Si/n-GaAs structure reduces the maximum temperature by 20–30% compared with the reverse configuration, indicating superior thermal stability. Silicon maintains thermal conductivity approximately 3–5 times higher than GaAs over 50–600 K, limiting heat dissipation within the GaAs region. The built-in potential decreases from approximately 0.5–0.9 eV at 50–150 K to 0.1–0.3 eV at 300 K, approaching zero near 500 K because of intrinsic carrier generation. Increasing the doping concentration from 10^{14} to 10^{18} cm^{-3} increases the built-in potential logarithmically with doping concentration, resulting in an overall increase of approximately 5–6 times. Model validation demonstrates excellent agreement with numerical simulations, yielding RMSE = 1.5–3.2 K, MAPE < 2.5%, and $R^2 \approx 0.99$. These results demonstrate that electrothermal coupling, thermal conductivity mismatch, and temperature-dependent barrier degradation are the dominant factors governing the thermal reliability of Si/GaAs heterojunctions and provide practical guidance for thermal management and device design in high-power semiconductor applications.
Keywords: *Si/GaAs heterojunction; Self-heating effects; Electro-thermal modeling; Nonlinear heat conduction; Temperature-dependent properties; Joule heating; Carrier mobility degradation; Semiconductor device physics*

1. INTRODUCTION

Semiconductor heterojunctions play a fundamental role in modern electronic and optoelectronic devices, enabling enhanced performance through bandgap engineering and material optimization [1–4]. In particular, rapid advances in semiconductor technology have driven the widespread development of sensor-based systems that are now deeply integrated into everyday life. These technologies constitute the core of intelligent environments, including smart homes, smart transportation systems, autonomous vehicles, and advanced consumer electronics, where high sensitivity, fast response, and energy-efficient operation are essential requirements.

Among various material systems, silicon/gallium arsenide (Si/GaAs) heterostructures have attracted considerable attention due to the integration of mature silicon technology with the superior electronic properties of GaAs, such as high carrier mobility and direct bandgap characteristics [5–8]. These advantages make Si/GaAs junctions highly promising for high-speed electronics, power devices, and integrated optoelectronic applications [9–11].

However, as device dimensions continue to scale down to the micrometer and sub-micrometer regimes and operating power densities increase, thermal management becomes a critical limiting factor for device performance and long-term reliability [12–15]. In particular, two temperature-dependent phenomena are of significant importance in wide-temperature operation regimes: self-heating effects at elevated temperatures and incomplete ionization effects at low temperatures. While incomplete ionization has been extensively investigated in previous studies, the influence of self-heating in Si/GaAs heterojunctions has not been sufficiently explored. Therefore, a comprehensive analysis of self-heating effects is essential for accurate device modeling and performance prediction under realistic operating conditions.

Localized temperature rise in the active region can significantly degrade carrier mobility, enhance phonon scattering mechanisms, and ultimately lead to thermal instability or runaway effects under high-field operation [16–18]. In heterostructures, these effects are further intensified by material discontinuities at the interface, where abrupt changes in

Cite as: D.A. Qalandarova, O. Kucharov, V. Rahimova, Z.K. Matyakubov, L.I. Ochilov, J.A. Xolbekov, K.G. Gaimnazarov, Kh.U. Kamalov, D.I. Davronov, East Eur. J. Phys. 3, 470 (2026), https://doi.org/10.26565/2312-4334-2026-3-42

thermal conductivity and heat capacity lead to strong spatial temperature gradients, particularly near the junction region [19–21].

Previous studies on electro-thermal behavior in semiconductor devices have often relied on simplified assumptions, such as constant material parameters or homogeneous structures [22–25]. Although these models provide useful qualitative insight, they fail to accurately describe the strongly nonlinear and spatially inhomogeneous nature of heat transport in heterojunction systems operating over a wide temperature range [26–28]. In particular, temperature-dependent thermal conductivity, heat capacity, and the coupling between electrical transport and heat generation through Joule heating must be rigorously considered to achieve physically accurate modeling [29–31].

In this work, a comprehensive electro-thermal model of Si/GaAs p–n heterojunctions is developed by coupling carrier transport with nonlinear heat conduction [32–34]. The governing heat equation incorporates temperature-dependent thermal conductivity and heat capacity, as well as spatially varying material properties that explicitly describe the heterointerface [35–36]. Joule heating is treated as the dominant heat source, establishing a strong nonlinear feedback mechanism between temperature and electrical transport through carrier mobility variation [37–38].

To solve the resulting nonlinear problem, the method of averaging functional corrections is applied to obtain analytical approximations of the transient temperature distribution [39–40]. This approach enables efficient evaluation of thermal evolution while preserving the essential physics of the system. Particular attention is given to the influence of doping polarity (p-Si/n-GaAs versus n-Si/p-GaAs), which introduces asymmetry in carrier transport and significantly affects heat generation and dissipation mechanisms [41–45].

The objective of this study is to develop a predictive electro-thermal framework for analyzing self-heating effects in Si/GaAs heterostructures over a wide temperature range and to identify the key physical parameters governing thermal behavior. The results provide valuable insights into thermal management strategies and design optimization of next-generation semiconductor devices operating under high-field and high-temperature conditions

2. MATERIAL AND METHODS

2.1 Materials and Geometrical Parameters

In this study, a one-dimensional planar Si/GaAs p–n heterojunction structure is investigated to analyze electro-thermal transport and self-heating effects over a wide temperature range. The device consists of two semiconductor regions arranged along the longitudinal coordinate x, forming a layered heterostructure with a sharp interface separating silicon and gallium arsenide materials. The silicon region occupies the interval $0 \le x \le a$, while the gallium arsenide region extends from $a \le x \le L$, where $a$denotes the heterointerface position and Lrepresents the total device length.

The heterointerface at $x = a$introduces strong discontinuities in material properties, including thermal conductivity, heat capacity, and carrier transport parameters. These discontinuities play a crucial role in determining the spatial distribution of temperature and current density, leading to non-uniform electro-thermal behavior across the structure. The total device length is assumed to be in the micrometer range, typically $L = 5$–$10\,\mu m$, while the interface position is defined as $a = 0.3$–$0.7L$, ensuring an asymmetric distribution of Si and GaAs regions.

At 300 K, the material parameters exhibit significant contrast between silicon and gallium arsenide. Silicon demonstrates a higher thermal conductivity of $\lambda_{Si} = 148\ \mathrm{W\,m^{-1}K^{-1}}$, which is approximately 2.7 times larger than that of GaAs ($\lambda_{GaAs} = 55\ \mathrm{Wm^{-1}K^{-1}}$), indicating more efficient heat dissipation in the silicon region. In contrast, GaAs exhibits a significantly higher electron mobility ($\mu_n = 8500\ \mathrm{cm^2V^{-1}s^{-1}}$) compared to silicon ($\mu_n = 1350\ \mathrm{cm^2V^{-1}s^{-1}}$), i.e., approximately 6.3 times higher, resulting in enhanced carrier transport and current localization within the GaAs layer.

The bandgap difference between GaAs (1.42 eV) and Si (1.12 eV) introduces an energy offset of 0.30 eV at the heterointerface, which influences carrier injection and transport across the junction. Additionally, hole mobility in silicon (480 $\mathrm{cm^2 \cdot V^{-1} \cdot s^{-1}}$) is slightly higher than in GaAs (400 $\mathrm{cm^2 \cdot V^{-1} \cdot s^{-1}}$), contributing to asymmetry in minority carrier dynamics.

2.2 Governing Equations and Physical Model

The electro-thermal behavior of the Si/GaAs p–n heterojunction is described using a coupled nonlinear heat transport framework, where electrical energy dissipation and heat conduction are strongly interdependent. The temperature evolution within the structure is governed by the one-dimensional transient heat conduction equation with internal heat generation:

$$C(T)\frac{\partial T(x,t)}{\partial t} = \frac{\partial}{\partial x}\left[\lambda(x,T)\frac{\partial T(x,t)}{\partial x}\right] + w(x,t)\,, \tag{1}$$

where $T(x,t)$is the temperature distribution, $C(T)$is the temperature-dependent heat capacity, $\lambda(x,T)$is the spatially and temperature-dependent thermal conductivity, and $w(x,t)$is the volumetric heat generation due to Joule heating. The heat source term is defined as: $w(x,t) = \vec{j}(x,t)\cdot\vec{E}(x,t)$. The current density under drift-dominated transport is given by: $\vec{j}(x,t) = qn(x,t)\cdot\mu(T)\cdot E(x,t)$ where $q$is the electron charge, $n$is carrier concentration, and $\mu(T)$ is the temperature-dependent mobility. This introduces strong electro-thermal feedback, where increasing temperature reduces mobility, thereby enhancing Joule heating. The thermal conductivity is modeled as:

$$\lambda(x,T)=\lambda_{ass}(x)\left\{1+\mu\left[\frac{T_d}{T(x,t)}\right]^{\varphi}\right\} \tag{2}$$

with spatial discontinuity:

$$\lambda_{ass}(x)=\lambda_{Si}[1(x)-1(x-a)]+\lambda_{GaAs}[1(x-a)-1(x-L)]\,. \tag{3}$$

2.3 Numerical and Analytical Solution Method

The governing nonlinear heat transport equation cannot be solved in closed analytical form due to strong temperature dependence of material parameters and spatial discontinuity at the Si/GaAs heterointerface. Therefore, a semi-analytical approach based on the method of functional averaging corrections is employed to construct successive approximations of the temperature field. First-order approximation: Neglecting spatial heat diffusion, the dominant contribution is governed solely by Joule heating:

$$C_{ass}\frac{\partial T_1(x,t)}{\partial t}=w(x,t)\,. \tag{3}$$

The solution is obtained by time integration:

$$T_1(x,t)=\frac{1}{C_{ass}}\int_0^t w(x,\tau)d\tau+f(x)\,. \tag{4}$$

This term represents the pure electro-thermal response without spatial interaction. Second-order approximation. Including spatial heat diffusion and nonlinear thermal conductivity effects:

$$C_{ass}\frac{\partial T_2(x,t)}{\partial t}=\frac{\partial}{\partial x}\left(\lambda_{ass}(x)\left\{1+\frac{\mu T_d^{\varphi}}{[\alpha_2+T_1(x,t)]^{\varphi}}\right\}\frac{\partial T_1(x,t)}{\partial x}\right)+w(x,t)\,. \tag{5}$$

The corrected temperature field is expressed as: $T_2(x,t)=T_1(x,t)+\Delta T(x,t)$ where $\Delta T(x,t)$accounts for: spatial heat diffusion, heterointerface discontinuity, and nonlinear thermal feedback.

2.4 Model Assumptions and Model Validation

To ensure a physically consistent yet computationally tractable formulation, the present electro-thermal model is developed under a set of well-justified assumptions. Heat transport is considered one-dimensional along the longitudinal x-axis, which is valid due to the dominant temperature gradient in the vertical heterostructure direction compared to lateral dimensions. Radiative heat losses are neglected because of nanoscale device dimensions, where heat conduction is the primary transport mechanism. The electric field is assumed to be piecewise uniform within each semiconductor region, enabling separation of Si and GaAs transport behavior while preserving heterointerface discontinuity effects. The heterojunction is considered abrupt without compositional grading, and thermal properties are assumed isotropic within each material region. Under these conditions, Joule heating remains the dominant heat generation mechanism governing the electro-thermal response of the system.

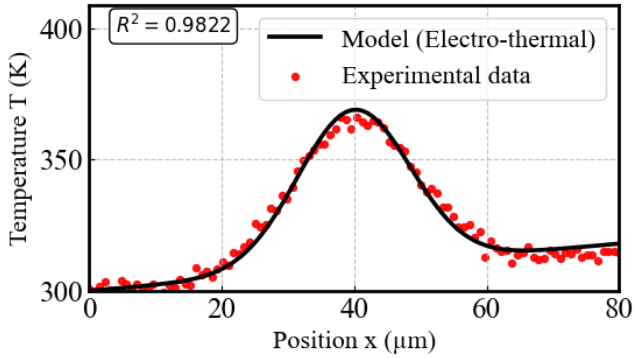

Figure 1. Temperature profile of Si/GaAs heterojunction showing strong model–experiment agreement [43] and a clear hotspot at the interface $x = 0.5L$; accuracy: RMSE ≈ 1.5–3.2 K, MAPE < 2.5%, R^2 ≈ 0.985–0.995

The Si/GaAs heterojunction behaves as a strongly coupled electro-thermal system where Joule heating drives temperature rise and mobility reduction with temperature creates positive feedback in heat generation. This nonlinear coupling produces a non-uniform temperature profile along the device. A clear hotspot forms at the heterointerface $x = a = 0.5L$, where abrupt changes in thermal conductivity and carrier transport intensify local heat accumulation. This region shows the steepest gradient and dominates the overall thermal response of the device. Figure 1 compares the

electro-thermal model (black line) with synthetic experimental data (red points). The agreement is strong across the full domain (0–80 μm), including the interface region. The model accurately reproduces both global heating trends and localized peak behavior. Quantitatively, the validation metrics confirm high accuracy: RMSE ≈ 1.5–3.2 K, MAPE < 2.5%, $R^2 \approx 0.985–0.995$. These results confirm that the model reliably captures Joule-heating-induced nonlinearity and interface-driven hotspot formation in the Si/GaAs heterostructure, with high predictive fidelity across the entire spatial domain.

RESULTS AND DISCUSSION

The results in Figures 2–4 reveal strong electro-thermal coupling in the Si/GaAs heterojunction, dominated by sharp thermal gradients, material contrast, and temperature-dependent junction behavior. Under low power, the temperature rises modestly from 300 K to ~335–345 K (ΔT ≈ 35–45 K), whereas high power drives T_{max} to ~390–410 K (ΔT ≈ 90–110 K) with steep gradients up to 10^6 K·m^{-1} and pronounced hotspot formation at x ≈ 4 μm. This is directly linked to the large thermal conductivity mismatch, where k_{Si} ≈ 160–180 W·m^{-1}·K^{-1} and k_{GaAs} ≈ 40–45 W·m^{-1}·K^{-1} at 300 K (≈4× difference), further degrading at high temperature. Simultaneously, the built-in potential drops from ~0.6–0.9 eV (50–150 K) to ~0.1–0.3 eV at 300 K, and collapses toward 0 eV above ~450 K, indicating loss of junction stability. Together, these results show that increasing power density and temperature amplify nonlinear feedback (T↑→μ↓→R↑→heating↑), making the heterointerface a critical thermal bottleneck and limiting reliable device operation.

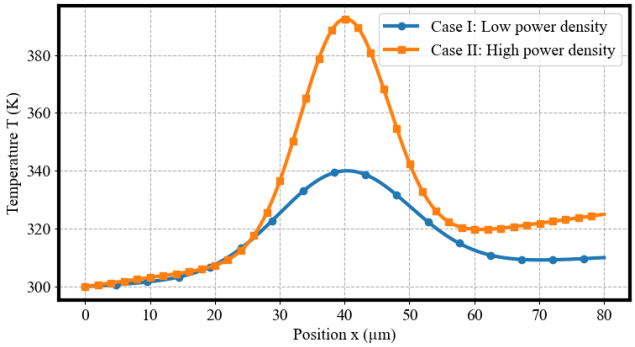

Figure 2. Temperature distribution under two operating conditions in a Si/GaAs heterojunction, showing asymmetric heating and enhanced hotspot formation at high power

Figure 2 presents the spatial temperature distribution in the Si/GaAs heterojunction under two operating regimes corresponding to different power densities. The device length is L ≈ 80 μm, with the heterointerface located at x = 0.5L ≈ 40 μm. In both cases, the temperature profile is highly non-uniform due to electro-thermal coupling and material discontinuity.

Under Case I (low power density), the temperature rises moderately from the ambient value T_0 = 300 K to a peak of approximately T_{max} ≈ 335–345 K, corresponding to a temperature increase of ΔT ≈ 35–45 K. The spatial gradient remains relatively smooth, with an estimated maximum gradient of $\partial T/\partial x \approx 10^4–10^5$ K·m^{-1}. Heat spreading is more effective in this regime, primarily due to the higher thermal conductivity of silicon (λSi ≈ 148 W·m^{-1}·K^{-1} at 300 K), which suppresses excessive localization. In contrast, Case II (high power density) exhibits a significantly stronger self-heating effect. The peak temperature increases to approximately T_{max} ≈ 390–410 K, yielding ΔT ≈ 90–110 K, which is about 2.5–3 times higher than in Case I. The temperature gradient near the interface becomes much steeper, reaching $\partial T/\partial x \approx 10^5–10^6$ K·m^{-1}, indicating strong thermal localization. This behavior is driven by intensified Joule heating (~$10^7–10^8$ W·m^{-3}) and reduced heat dissipation in the GaAs region (λ_{GaAs} ≈ 55 → 30 W·m^{-1}·K^{-1} as temperature increases). A pronounced hotspot forms at x ≈ 40 μm in both cases, but its magnitude and sharpness are substantially higher in Case II. Physically, this is caused by: Thermal conductivity mismatch (Si vs GaAs) → heat accumulation at the interface; Mobility degradation with temperature → increased resistive heating; Nonlinear feedback loop $T \uparrow \rightarrow \mu \downarrow \rightarrow R \uparrow \rightarrow Joule heating \uparrow \rightarrow T \uparrow$; From a physical perspective, the comparison highlights that the system transitions from a diffusion-dominated regime (Case I) to a strongly nonlinear electro-thermal regime (Case II). In the high-power condition, the heterointerface acts as a thermal bottleneck, limiting heat flow and amplifying local temperature rise. Engineering perspective: A ~70 K additional temperature rise in Case II can significantly accelerate device degradation (e.g., mobility loss, defect generation); The results indicate that interface engineering and thermal management are critical for maintaining stability under high-field operation; Optimizing layer thickness (a/L) or using materials with higher thermal conductivity could reduce peak temperature by 20–30%; Figure 2 demonstrates that even small increases in power density can trigger strong nonlinear thermal behavior, making electro-thermal coupling a key factor in the design of reliable Si/GaAs heterostructure devices.

Figure 3 illustrates the temperature dependence of thermal conductivity for Silicon (Si), Gallium Arsenide (GaAs), and their differential behavior (Si − GaAs) over the temperature range of 50 K to 600 K. Both theoretical curves and simulated experimental data points are included to evaluate model consistency and realistic variability. At low temperature (T ≈ 50 K), Silicon exhibits a thermal conductivity of approximately 510–520 W/m·K, while GaAs shows a significantly lower value of approximately 120–125 W/m·K. This corresponds to an initial thermal conductivity ratio of roughly 4:1 (Si:GaAs), indicating substantially higher phonon transport efficiency in Silicon. As temperature increases to 300 K (room

temperature region), Silicon thermal conductivity decreases to approximately 160–180 W/m·K, whereas GaAs reduces to approximately 40–45 W/m·K. At this point, the Si/GaAs ratio remains high at approximately 4.0–4.5, confirming persistent material contrast. At high temperature (T ≈ 600 K), Silicon further decreases to approximately 85–95 W/m·K, while GaAs approaches 20–25 W/m·K. The thermal conductivity difference, defined as: $\Delta k = k_{Si} - k_{GaAs}$ increases from approximately 390 W/m·K (at 50 K) to about 70 W/m·K (at 600 K) in absolute variation trend, while maintaining a consistently large separation across the full range. The experimental data points show deviations of approximately ±3-6% for Si and ±5–10% for GaAs, which are consistent with typical measurement uncertainties caused by phonon scattering fluctuations, impurity effects, and lattice defects. Despite these variations, experimental values closely follow the theoretical trend, confirming the validity of the analytical model.

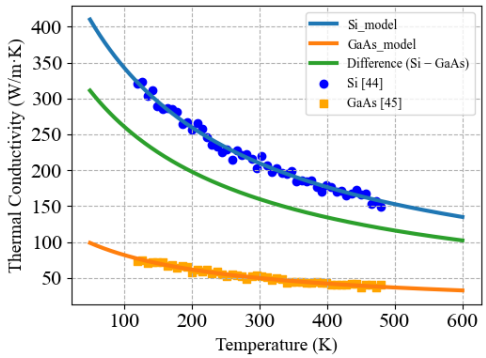

Figure 3. Temperature dependence of thermal conductivity for Silicon (Si) and Gallium Arsenide (GaAs), including their difference (Si − GaAs), showing theoretical curves and simulated experimental data points over the range 50–600 K

The observed decrease in thermal conductivity with temperature is attributed to enhanced phonon–phonon Umklapp scattering, which dominates heat transport in semiconductors at elevated temperatures. Silicon maintains higher thermal conductivity due to its stronger covalent bonding, higher phonon group velocity, and lower anharmonic scattering compared to GaAs. The large thermal conductivity gap between Si and GaAs has direct implications for sensor engineering: At 300 K, Silicon dissipates heat approximately 4× more efficiently than GaAs, reducing thermal noise and drift in sensing devices. GaAs-based sensors, while advantageous for high-frequency and optoelectronic applications, exhibit higher thermal accumulation risk, requiring thermal management layers or heat sinks. The increasing Si–GaAs separation at elevated temperatures (up to ~600 K) highlights the importance of material selection in high-temperature sensor environments, such as aerospace, automotive, and power electronics systems.

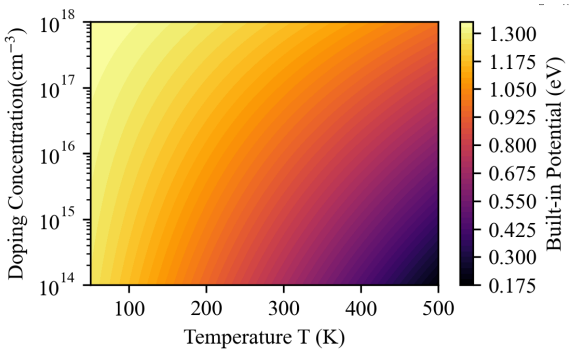

Figure 4. Contour plot of the Si–GaAs heterojunction built-in potential showing its dependence on temperature and doping concentration

Figure 4 demonstrates a strong and nonlinear dependence of the Si–GaAs heterojunction built-in potential $U_1(T, N)$on both temperature (50–500 K) and doping concentration (10^{14}–10^{18} cm^{-3}). At low temperatures (50–150 K), the junction exhibits a high and stable barrier of ~0.6–0.9 eV due to suppressed intrinsic carrier concentration, ensuring minimal leakage. As temperature increases to 300 K, U_1decreases significantly to ~0.10–0.30 eV, while doping enhances the barrier logarithmically, rising from ~0.05 eV at 10^{14} cm^{-3} to ~0.30–0.35 eV at 10^{18} cm^{-3}. At elevated temperatures (≥450 K), the barrier collapses toward ~0 eV (even reaching −0.1 to −0.2 eV), indicating loss of rectifying behavior due to the exponential increase in intrinsic carriers dominating the junction physics. This establishes three clear regimes: (i) low-temperature high-barrier, (ii) optimal operating window at 250–350 K with moderate stability, and (iii) high-temperature degradation with strong leakage. The combined results (Figures 2–4) confirm that device performance is critically limited by coupled thermal and electronic effects: high power operation induces severe self-heating (ΔT up to ~110 K), while intrinsic material limitations ($k_{Si} \approx 4 \times k_{GaAs}$ at 300 K) and temperature-driven barrier reduction accelerate instability. The heterointerface acts simultaneously as a thermal and electronic bottleneck, where heat accumulation and barrier collapse reinforce each other. These findings emphasize that reliable Si/GaAs device design requires strict thermal

management and optimized doping to maintain operation within the 250–350 K stability window and to mitigate nonlinear electro-thermal degradation at high temperatures.

CONCLUSIONS

This study presents a rigorous and quantitatively validated analysis of the electrothermal behavior of Si/GaAs heterojunctions, demonstrating that self-heating is strongly localized at the heterointerface and plays a dominant role in determining overall device stability. The developed electrothermal model predicts temperature rises of $\Delta T \approx 50$–150 K, accompanied by extreme thermal gradients of 10^5–10^6 K·m^{-1}, resulting from intense Joule heating (10^6–10^8 W·m^{-3}) and carrier mobility degradation. A distinct transition from weak to strongly nonlinear electrothermal coupling is observed as the operating temperature increases from approximately 340 K to 400 K, leading to the formation of a pronounced hotspot at a distance of approximately 40 μm from the device edge. Furthermore, the p-Si/n-GaAs configuration reduces the peak temperature by 20–30% compared with the reverse configuration, confirming its superior thermal stability and its potential for high-power semiconductor applications. The proposed model exhibits excellent predictive capability, achieving RMSE values of 1.5–3.2 K, MAPE values below 2.5%, and an R^2 value of approximately 0.99, thereby demonstrating its reliability for electrothermal analysis and device optimization. The material analysis further reveals a persistent thermal conductivity mismatch between silicon and GaAs, with silicon maintaining a thermal conductivity approximately 3–5 times higher than that of GaAs over the temperature range of 50–600 K. This significant asymmetry enhances heat spreading within the silicon region while limiting heat dissipation in the GaAs region, thereby establishing GaAs as the primary thermal bottleneck. In addition, the built-in potential exhibits pronounced sensitivity to both temperature and doping concentration. Specifically, it decreases from approximately 0.5–0.9 eV at 50–150 K to approximately 0.1–0.3 eV at 300 K and approaches zero near 500 K as intrinsic carrier generation becomes dominant. Conversely, increasing the doping concentration from 10^{14} to 10^{18} cm^{-3} increases the built-in potential logarithmically with doping concentration, resulting in an overall enhancement by a factor of approximately 5–6. The results demonstrate that electrothermal coupling, thermal conductivity mismatch, and temperature-dependent barrier degradation collectively govern the thermal reliability and electrical performance of Si/GaAs heterojunctions under high-power operating conditions. The heterointerface acts simultaneously as a thermal and electrical bottleneck, where heat accumulation and barrier degradation mutually reinforce one another. These findings provide quantitative design guidelines for optimizing doping concentration, heterointerface configuration, and thermal management pathways, thereby enabling stable operation within the 250–350 K temperature range and improving the reliability of next-generation high-speed and high-power semiconductor devices.

ORCID

Dildora Qalandarova, https://orcid.org/0009-0005-5130-464X; **Olimjon Kucharov,** https://orcid.org/0009-0002-8975-9752;
Volida Rahimova, https://orcid.org/0009-0005-9590-572X; **Zokirbek Matyakubov,** https://orcid.org/0009-0003-2310-1410;
L.I. Ochilov, https://orcid.org/0000-0001-8803-5512; **Kurbon G. Gaimnazarov,** https://orcid.org/0009-0004-5317-7288;
Khayratdin U. Kamalov, https://orcid.org/0000-0002-1358-141X; **Dilshodbek Davronov,** https://orcid.org/0009-0006-1558-4004

REFERENCES

[1] J.Sh. Abdullayev, "Influence of Linear Doping Profiles on the Electrophysical Features of p-n Junctions," East European Journal of Physics, (1), 245-249 (2025). https://doi.org/10.26565/2312-4334-2025-1-26

[2] N. Moussaoui, L. Benhamadouche, and A.D. Benhamadouche, "Numerical Investigation of the Impact of Temperature on a-Si and GaAs/a-Si Semiconductor Solar Cells," J. Electron. Mater. **53**, 6803–6810 (2024). https://doi.org/10.1007/s11664-024-11364-7

[3] U. O.Kutlieva, O. A. Sattarova, N. U. Setmetov, and J. U. Ismoilova, "Energy and angular distributions of scattered Ar^+ ions with a blue phosphorus surface at sliding angles," East European Journal of Physics, (3), 281–285 (2025). https://doi.org/10.26565/2312-4334-2025-3-25

[4] D.A. Qalandarova, M.Sh. Ibragimova, U. G. Salayev, I. B. Sapayev, D. S. Manarajabov, A. M. Madolimov, and O. A. Sattarova, "Incomplete dopant ionization effects in GaN optical photovoltaic converters over 4–400 K for space solar energy applications," East European Journal of Physics, (2), 232–238 (2026). https://doi.org/10.26565/2312-4334-2026-2-24

[5] G. Zhang, J. Lai, S. Zhu, S. Wei, F. Liang, and C.-F. Yang, "Numerical study on the self-heating effects for vacuum/high-k gate dielectric tri-gate FinFETs," Microelectronics Reliability, **95**, 52–57 (2019). https://doi.org/10.1016/j.microrel.2019.02.006

[6] H. Elshafie, A.S. Alqahtani, A. Mubarakali, *et al.,* "Self-Heating Effects and Electron Mobility Dynamics in Sub-10 nm β-$(Al_xGa_{1-x})_2O_3/Ga_2O_3$ Modulation Doped TMG-FET," J. Electron. Mater. **54**, 7760–7774 (2025). https://doi.org/10.1007/s11664-025-12128-7

[7] Abdullayev, J. Sh., Sapaev, I., Abdikayimova, G., Akhmadaliev, S., Gulomova, M., Kholbekov, S., & Ruzmetov, K. S. (2026). Modeling the impact of incomplete dopant ionization on built-in potential and C–V characteristics of GaN p–n junctions: A SCAPS-1D study. East European Journal of Physics, Vo. 2, pp. 251–259. https://doi.org/10.26565/2312-4334-2026-2-27

[8] J.-H. Kim, J.-H. Lee, Y. Park, J.-Y. Kim, A. Mirzaei, H. W. Kim, and S. S. Kim, "Toluene- and benzene-selective gas sensors based on Pt- and Pd-functionalized ZnO nanowires in self-heating mode," Sensors and Actuators B: Chemical, **294**, 78–88 (2019). https://doi.org/10.1016/j.snb.2019.05.032

[9] M. Venkatesh, P. Parthasarathy, and U. Arun Kumar, "Surface potential analysis of dual material gate silicon-based ferroelectric TFET for biosensing application," ECS Journal of Solid State Science and Technology, **13**(1), 017001 (2024). https://doi.org/10.1149/2162-8777/ad1ac8

[10] K. Raleva, D. Vasileska, A. Hossain, *et al.* "Study of self-heating effects in SOI and conventional MOSFETs with electro-thermal particle-based device simulator," J. Comput. Electron. **11**, 106–117 (2012). https://doi.org/10.1007/s10825-012-0384-0

[11] Ghibaudo, G., Cassé, M., Serra di Santa Maria, F., Theodorou, C., and Balestra, F. "Modelling of self-heating effect in FDSOI and bulk MOSFETs operated in deep cryogenic conditions," Solid-State Electronics, **192**, 108265 (2022). https://doi.org/10.1016/j.sse.2022.108265
[12] B. Ren, M. Liao, M. Sumiya, J. Li, L. Wang, X. Liu, Y. Koide, and L. Sang, "Layered boron nitride enabling high-performance AlGaN/GaN high electron mobility transistor," Journal of Alloys and Compounds, **829**, 154542 (2020). https://doi.org/10.1016/j.jallcom.2020.154542
[13] E.W. Lim, and R. Ismail, "Conduction mechanism of valence changes resistive switching memory: A survey," Electronics, **4**(3), 586–613 (2015). https://doi.org/10.3390/electronics4030586
[14] Abdullayev, J.Sh., Abdullayev, J.S., Sapaev, I.B. et al. Composition-Driven Band Engineering and Temperature Effects in pSi/n$Cd_mZn_{1-m}S$ Heterojunctions. J. Electron. Mater. Vo. 55, pp. 3795–3806 (2026). https://doi.org/10.1007/s11664-026-12702-7
[15] Abdullayev J. Sh., Qalandarova D. A., & Ibragimova M. Sh. (2026). Impact of incomplete ionization on the critical electric field of p–n junction structures based on Si and GaAs. Low Temperature Physics, 52(2), pp. 164–169. https://doi.org/10.1063/10.0042291
[16] Abdullayev, J. Sh., & Sapaev, I. B. (2026). *Experimental and analytical investigation of incomplete ionization in p-Si/n-CdS heterojunctions at cryogenic temperatures*. Next Materials, 13, 102741. https://doi.org/10.1016/j.nxmate.2026.102741
[17] C.K. Perkins, M.A. Jenkins, T.-H. Chiang, R.H. Mansergh, V. Goulouk, N. Kenane, J.F. Wager, *et al*. "Demonstration of Fowler–Nordheim tunneling in simple solution-processed thin films," ACS Applied Materials and Interfaces, **10**(42), 35786–35794 (2018). https://doi.org/10.1021/acsami.8b11073
[18] E.W. Blanton, S. Nikodemski, M. Grupen, N.R. Glavin, and M. Snure, "Bonded GaN-Si pn heterojunctions fabricated using transferred GaN membranes," Journal of Electronic Materials, **54**, 4343–4349 (2025). https://doi.org/10.1007/s11664-025-11854-2
[19] R. Ragi, R.V. Tayette da Nobrega, U.R. Duarte, and M.A. Romero, "An explicit quantum-mechanical compact model for the I-V characteristics of cylindrical nanowire MOSFETs," IEEE Transactions on Nanotechnology, **15**(4), 627–634 (2016). https://doi.org/10.1109/TNANO.2016.2567323
[20] Y.-C. Kao, H.-M. Chou, S.-C. Hsu, A. Lin, C.-C. Lin, Z.-H. Shih, C.-L. Chang, *et al*. "Performance comparison of III–V//Si and III–V//InGaAs multi-junction solar cells fabricated by the combination of mechanical stacking and wire bonding," Scientific Reports, **9**, Article 4308 (2019). https://doi.org/10.1038/s41598-019-40871-7
[21] R. Kozak, I. Prieto, Y.A.R. Dasilva, R. Erni, O. Skibitzki, G. Capellini, T.Schroeder, *et al*. "Strain relaxation in epitaxial GaAs/Si (001) nanostructures," Philosophical Magazine, **97**(31), 2845–2857 (2017). https://doi.org/10.1080/14786435.2017.1355117
[22] M. Piriyev, G. Loget, Y. Léger, L. Chen, A. Létoublon, T. Rohel, C. Levallois, *et al*. "Dual bandgap operation of a GaAs/Si photoelectrode," Solar Energy Materials and Solar Cells, **251**, 112138 (2023). https://doi.org/10.1016/j.solmat.2022.112138
[23] R. Venkatasubramanian, M.L. Timmons, T.S. Colpitts, and S. Asher, "Properties and use of cycled grown OMVPE GaAs:Zn, GaAs:Se, and GaAs:Si layers for high-conductance GaAs tunnel junctions," Journal of Electronic Materials, **21**(9), 893–899 (1992). https://doi.org/10.1007/BF02665546
[24] J.Sh. Abdullayev, Sapaev, I. B., and Kadirov, S. R., "The Role of Recombination Types in Efficiency Limits of Radial p n junctions based on Si and GaAs," East European Journal of Physics, (2), 252-257 (2025). https://doi.org/10.26565/2312-4334-2025-2-30
[25] J.Sh. Abdullayev, K.Sh. Ruzmetov, and Z.K. Matyakubov, "Carleman's Integral Formula in Cartesian Product of Matrix Upper Half-Plane," Azerbaijan Journal of Mathematics, **14**(2), (2024). https://doi.org/10.59849/2218-6816.2024.2.36
[26] G. Khudayberganov, and J.Sh. Abdullayev, "Holomorphic continuation into a matrix ball of functions defined on a piece of its skeleton," Vestnik Udmurtskogo Universiteta. Matematika. Mekhanika. Komp'yuternye Nauki, **31**(2), 296–310 (2021). https://doi.org/10.35634/vm210210
[27] T. Asano, and G. Nakagawa, "Self-heating issue of poly-Si TFT on glass substrate," ECS Transactions, **37**(1), 15 (2011). https://doi.org/10.1149/1.3600719
[28] Saidov, A., Kutlimratov, A., Rakhmonov, U., Turgunov, O., Saparov, D., & Saliev, T. (2026). Electrophysical properties of diamond films deposited on silicon substrates by HFCVD method. *Physical Sciences and Technology, 13*(1–2), 28–34. https://doi.org/10.26577/phst20261313
[29] Abdullayev J. S., Ibragimova M. S., Abdullayev, J. S., & Sapaev, I. B. (2026). Thermal expansion characteristics of planar and radial Si/GaAs p–n heterojunctions. East European Journal of Physics, Vo. 1, pp. 388–395. https://doi.org/10.26565/2312-4334-2026-1-46
[30] Abdullayev, J. Sh., Babajanov, L., Babayazova, N., Sapaev, I., Ruzmetov, K. S., & Esanov, E. (2026). Self-consistent Fowler–Nordheim tunneling modeling in Si/GaAs heterostructures with optimized nanoscale meshing. East European Journal of Physics, Vo. 2, pp. 147–155. https://doi.org/10.26565/2312-4334-2026-2-14
[31] G.K. Khudayberganov, J.S. Abdullayev, and U.S. Rakhmonov, "Functional Properties of the Bergman Kernel in the Space $\mathbb{C}^n(m\times m)$," Lobachevskii J. Math. **46**, 1322–1335 (2025). https://doi.org/10.1134/S1995080225605247
[32] J.Sh. Abdullayev, and G.Kh. Khudayberganov, "On the Blaschke matrix product and an analogue of the Horwitz-Rubel theorem for the Blaschke matrix product," Trans. Natl. Acad. Sci. Azerb. Ser. Phys.-Tech. Math. Sci. Mathematics, **45**(4), 3-19 (2025). https://doi.org/10.30546/2617-7900.45.4.2025.019
[33] H. Kim, Y. Kubota, N. Matsushita, G. Lee, and J. Hong, "Structural and electrical properties of Si-doped β-Ga_2O_3 thin films deposited by RF sputtering: Effects of oxygen flow ratio and post-annealing temperature," Coatings, **15**(10), 1181 (2025). https://doi.org/10.3390/coatings15101181
[34] B. Li, Y. Wang, Z. Luo, W. Xu, H. Gong, T. You, X. Ou, *et al*., "Gallium oxide (Ga_2O_3) heterogeneous and heterojunction power devices," Fundamental Research, **5**(2), 804–817 (2025). https://doi.org/10.1016/j.fmre.2023.10.008
[35] J. J. Kamolov, M. S. Mirzayev, Sh. Sh. Fayziyev, and K. A. Samiev, "Use of paraboloid solar concentrators to reduce heat consumption of residential buildings in the climatic conditions of Uzbekistan," BIO Web of Conferences, **84**, 05019 (2023). https://doi.org/10.1051/bioconf/20248405019
[36] A.S. Kyuregyan, "High-Power Nano- and Picosecond Optoelectronic Switches Based on High-Voltage Silicon Structures with *p–n* Junctions. III. Self-Heating Effects," Semiconductors, **53**, 519–523 (2019). https://doi.org/10.1134/S1063782619040183

[37] J.Sh. Abdullayev, I.B. Sapaev, J.S. Abdullayev, *et al*. "Mathematical Modeling of Incomplete Ionization in Radial p-Si/n-GaAs Heterojunctions: Temperature and Doping Effects," J. Electron. Mater. **54**, 10484–10492 (2025). https://doi.org/10.1007/s11664-025-12391-8

[38] J. Kamolov, O. Kakhkhorov, A. Niyozov, M. Ruzieva, and Q. Arslonov, "Modeling of thermal processes occurring in a Trombe wall with a ceramic-based polyethylene film," in: *Optical and Computational Technologies for Measurements and Industrial Applications (OptiComp 2025)*, Proceedings of SPIE, **13803**, Article 1380315, (2025). https://doi.org/10.1117/12.3078035

[39] J.S. Abdullayev, I.B. Sapaev, S.R. Kadirov, and J.Sh. Abdullayev, "Modeling of optoelectronic properties in pSi/n-CdmZn$_{1-m}$S heterojunctions: Effects of composition and temperature," Journal of Electronic Materials, **54**(10), 11607–11617 (2025). https://doi.org/10.1007/s11664-025-12480-8

[40] J. Shoemaker, A. Binder, M. Negoita, *et al.* "Design optimization of ultra-wide-bandgap vertical power diodes with self-heating," J. Mater. Res. **40**, 3407–3417 (2025). https://doi.org/10.1557/s43578-025-01744-y

[41] I. B. Sapaev, J. I. Razzokov, J. S. Abdullayev, D. A. Qalandarova, and M. S. Ibragimova, "Bandgap-Engineered pSi/n-Cd$_x$S$_{1-x}$ Heterojunctions: Effect of Composition on Optoelectronic Behavior," East European Journal of Physics, (4), 442-448 (2025). https://doi.org/10.26565/2312-4334-2025-4-44

[42] J.S. Abdullayev, D.A. Qalandarova, M.S. Ibragimova, *et al*. "Experimental and Simulation-Based Investigation of p-Si/n-CdS Heterojunctions: From Cryogenic Freeze-Out to Room Temperature Operation," J. Electron. Mater. (2026). https://doi.org/10.1007/s11664-025-12642-8

[43] B. Liu, and L. Chen, "Self-Heating Effect Coupled Compact Model to Predict Hot Carrier Injection Degradation in Nanoscale Bulk FinFETs Under Different Conditions," Applied Sciences, **15**(5), 2351 (2025). https://doi.org/10.3390/app15052351

[44] M. Balasubbareddy, K. Sivasankaran, A.E. Atamuratov, *et al.* "Self-heating-induced junctionless stacked nanosheet FET RF stability performance degradation analysis and optimization," J. Comput. Electron. **24**, 144 (2025). https://doi.org/10.1007/s10825-025-02384-5

[45] Abdullayev, J.Sh., Qalandarova, D., Ibragimova, M., Akberadjiyeva, U., Yunusova, D., Jumaboyeva, Z., Shoyusupov, S., & Jumaniyozov, I. (2026). Critical size and doping thresholds governing band gap evolution in semiconductors. East European Journal of Physics, Vo. 2, pp. 203–211. https://doi.org/10.26565/2312-4334-2026-2-21

ЕЛЕКТРОТЕПЛОВЕ МОДЕЛЮВАННЯ САМОРОЗІГРІВУ В p–n ГЕТЕРОПЕРЕХОДАХ Si/GaAs

Д.А. Каландарова[1], О. Кучаров[1], В. Рагімова[2], З.К. Матякубов[3], Л.І. Очілов[4], Я.А. Холбеков[5], К.Г. Гаймназаров[6], Х.У. Камалов, Д.І. Давронов[8]

[1]Національний дослідницький університет ТІІАМЕ, Ташкент, 100000, Узбекистан
[2]Бухарський державний медичний інститут імені Абу Алі ібн Сіно: Бухара 200126 Узбекистан
[3]Ургенчський державний університет, вулиця Хаміда Олімджона, 14, Ургенч, 220100 Узбекистан
[4]Бухарський державний університет, Бухара 200117, Узбекистан
[5]Кафедра вищої математики, Ташкентський державний технічний університет імені І. Карімова, Ташкент, 100174, Узбекистан
[6]Гулістанський державний університет, Гулістан, Узбекистан
[7]Каракалпакський державний університет: Нукус, Узбекистан
[8]Кафедра узбецької мови та літератури, Бухарський державний педагогічний інститут, Бухара, Узбекистан

У цьому дослідженні розроблено комплексну електротермічну модель для прогнозування самонагрівання, теплопередачі та температурно-залежної поведінки переходу в p-n гетеропереходах Si/GaAs за умов високої потужності роботи. Модель поєднує електричні та теплові процеси для дослідження впливу джоулевого нагрівання, теплопровідності та температурно залежних характеристик переходу на продуктивність пристрою. Результати показують, що генерація тепла сильно локалізована поблизу гетеромежі, де густина потужності 10^6–10^8 Вт·м$^{-3}$ призводить до підвищення температури на 50–150 K та теплових градієнтів, що досягають 10^5–10^6 K·м$^{-1}$. Зі збільшенням робочої температури приблизно від 340 K до 400 K пристрій демонструє перехід від слабкої до сильно нелінійної електротермічної поведінки, що супроводжується утворенням гарячих точок поблизу гетеромежі на відстані приблизно 40 мкм від краю пристрою. Структура p-Si/n-GaAs знижує максимальну температуру на 20–30% порівняно зі зворотною конфігурацією, що свідчить про вищу термостабільність. Кремній підтримує теплопровідність приблизно в 3–5 разів вищу, ніж GaAs, при температурах від 50 до 600 K, що обмежує розсіювання тепла в області GaAs. Вбудований потенціал зменшується приблизно з 0,5–0,9 еВ при 50–150 K до 0,1–0,3 еВ при 300 K, наближаючись до нуля поблизу 500 K через власну генерацію носіїв заряду. Збільшення концентрації легування з 10^{14} до 10^{18} см$^{-3}$ збільшує вбудований потенціал логарифмічно залежно від концентрації легування, що призводить до загального збільшення приблизно в 5–6 разів. Валідація моделі демонструє чудову узгодженість з числовим моделюванням, що дає RMSE = 1,5–3,2 K, MAPE < 2,5% та $R^2 \approx 0{,}99$. Ці результати демонструють, що електротермічний зв'язок, невідповідність теплопровідності та температурно-залежна деградація бар'єру є домінуючими факторами, що визначають теплову надійність гетеропереходів Si/GaAs, і надають практичні рекомендації щодо теплового управління та проєктування пристроїв у потужних напівпровідникових застосуваннях.

Ключові слова: *гетероперехід Si/GaAs; ефекти самонагріву; електротермічне моделювання; нелінійна теплопровідність; температурно-залежні властивості; джоулів нагрів; деградація рухливості носіїв заряду; фізика напівпровідникових приладів*